Processing and Inversion of Arctic Ocean Refraction Data

Gregory Lynn Duckworth

B.S., Rice University (1977)
S.M., Massachusetts Institute of Technology (1980)
E.E., Massachusetts Institute of Technology (1980)

submitted in partial fulfillment
of the requirements for the degree of

Doctor of Science

at the
Massachusetts Institute of Technology
and the
Woods Hole Oceanographic Institution

September 9, 1983

Signature of Author . _____

Certified by _____
Prof. Arthur B. Baggeroer, Thesis Supervisor

Certified by _____
Dr. Ralph A. Stephen, Advisor

Accepted by _____
Arthur B. Baggeroer. Chairman
Joint Committee for Oceanographic Engineering

_____
Arthur C. Smith, Chairman, Electrical Engineering department committee
on graduate students, Massachusetts Institute of Technology

Processing and Inversion of Arctic Ocean Refraction Data

Gregory Lynn Duckworth

Submitted to the
Department of Electrical Engineering and Computer Science
at the Massachusetts Institute of Technology
and the Department of Ocean Engineering
at the Woods Hole Oceanographic Institution
in partial fulfillment of the requirements for the degree of
Doctor of Science

September 9, 1983

ABSTRACT

Several seismic refraction and long-range propagation experiments were carried out during the *Fram 2* experiment in the Pole Abyssal Plain of the Eastern Arctic Ocean (May 1980). This thesis concerns the digital signal processing and inversion methods used to analyse and interpret these data for crustal and oceanic structure, and the results of these analyses. Examined are: i) methods for obtaining the short aperture plane wave decomposition of the data subject to the experimental limitations imposed by the arctic environment and ii) methods for inverting these decompositions for oceanic and crustal structure.

For the plane wave decomposition, conventional time and frequency domain array processing techniques for velocity analysis and slant stacking are contrasted to an optimal adaptive technique. The criteria of phase velocity, group velocity (time of arrival), and amplitude estimator bias and stability are discussed.

To recover the structure, several inversion methods for estimation of the ocean/crust velocity structure from the refraction data are examined. In this work, an emphasis is placed on techniques which fully utilize the data obtained in this experiment. The incorporation of the directly estimated delay time, $\tau(p)$, and offset, $x(p)$, data as a function of horizontal slowness, p, is carried out. In addition, the high processing gain of the data adaptive short aperture slant-stacking technique allows the inclusion of late breaking multiples in the inversions. A primary component of this work deals with the adaptation of a velocity/depth migration technique to the sparsely shot lines available from the arctic.

In addition to the refraction experiments, long-range (341 km) acoustic propagation data are used for the determination of water column and near-bottom sediment velocity structure. The use of both normal mode and WKBJ theory allows development of inversion algorithms for the dispersive water column arrivals and bottom interacting multiples which tightly constrain these velocity structures. The methods allow structural determination from single-shot data as long as the lateral homogeneity of the structure to be examined is sufficient.

Using the techniques developed, refraction and long-range propagation data taken on the *Fram 2* experiment are analysed. These results are some of the most comprehensive determinations of crustal structure in the Fram basin of the Arctic Ocean near the Morris Jessup Rise.

Thesis Supervisor: Dr. Arthur B. Baggeroer,
Professor of Electrical Engineering and Computer Science and
Professor of Ocean Engineering, Massachusetts Institute of Technology

Thesis Advisor: Dr. Ralph A. Stephen,
Associate Scientist, Department of Geology and Geophysics,
Woods Hole Oceanographic Institution

to
Carol Greer Duckworth
and
Clifford Lee Duckworth

"The best thing for being sad," replied Merlyn, beginning to puff and blow, "is to learn something. That is the only thing that never fails. You may grow old and trembling in your anatomies, you may lie awake at night listening to the disorder of your veins, you may miss your only love, you may see the world about you devastated by evil lunatics, or know your honour trampled in the sewers of baser minds. There is only one thing for it then—to learn. Learn why the world wags, and what wags it. That is the only thing which the mind can never exhaust, never alienate, never be tortured by, never fear or distrust, and never dream of regretting."

-T.H. White
from *The Once and Future King*

ACKNOWLEDGEMENTS

There are a great number of people hidden behind the cool, calm, and complete exterior of this work who know the true story. To them I give my thanks for their help, encouragement, and criticism, and request that they keep the facts to themselves. In order that especially damaging evidence be suppressed, the following special thanks are in order.

I wish to extend thanks to all the participants of the Fram 2 experiment for the happy, productive, and safe camp to which everyone contributed, and especially to my WHOI colleagues who made possible the data which drove this thesis. Deserving special mention on this behalf are Keith von der Heydt and Tom O'Brien for making the data acquisition possible, Dave Gever and Ken Prada for the support of the WHOI computer system and much of the software which acquired and manipulated the great volume of data, and Daniel Shaughnessy, Leon Schuyler, and Edward Scheer for their logistical and musical support.

I am indebted to Ruth Jackson of the Bedford Institute of Oceanography for her many and extensive discussions about the geology and tectonics of the arctic, and for teaching me that results which are independent of corroborating evidence should be looked at at least twice.

I must certainly acknowledge the help and influence of my Joint Program friends, and especially that of my fellow students in the Digital Signal Processing Group at MIT. The Education Office at WHOI receives my gratitude for their help, good humor, and sponsorship of the visiting scholar program and multitudinous cookouts. Because the figures constitute such a large part of this work, great credit goes to the perseverance and talent of my illustrator, Donna Carson. I thank my committee members Al Oppenheim and Ira Dyer for their comments, and my defense chairman, George Frisk, for the civil manner in which he conducted my thesis defense.

I must specially thank Ralph Stephen for reading and commenting so carefully on my ever-late drafts, and for the extended discussions resulting from this careful examination which took me from the dreams of signal processing to the realities of geophysics.

I am grateful for the demands and opportunities provided by my six years of close work and friendship with Art Baggeroer, and hope for many more. The rewards have been many. His energy and curiosity have been infectious, and I am afraid that as a result I am in for a lifetime with this affliction.

Finally, I could not have completed the myriad tasks involved in the final stages of the construction of this all-too-thick document without the dedicated and devoted support of my father, Clifford Duckworth, and friend, Beth Parkhurst. To them I also owe my health and sanity.

To leave the spiritual and enter the temporal, I wish to thank the National Science Foundation for their support of my early graduate school career, and the Office of Naval Research and G. Leonard Johnson for the opportunity to carry out this work through his sponsorship of the Fram 2, Fram 4, and MIZEX research programs in the Arctic. These were administered through ONR contracts N 00014-77-C-0256 at MIT, and N 00014-80-C-0161, N 00014-81-C-0161, and N 00014-82-C-0161 at WHOI. In addition to this support, computer work carried out in the Digital Signal Processing Group facility was also sponsored by ARPA contract N 00014-81-K-0742.

TABLE OF CONTENTS

CHAPTER 1: Motivation and Background

INTRODUCTION

This thesis explores the application of array processing and inversion techniques to multichannel seismic refraction and ocean acoustic data from the ice-covered Arctic Ocean. The ultimate goal is estimation of the sound velocity profiles for the crust and water column in the experimental area. In addition to the experimental results presented, it is hoped that the algorithms developed, performance characterizations performed, and philosophies proffered will enhance the analysis of data from other areas of the world and acquired using different experimental procedures.

The data which motivate this work were obtained on Fram 2, a multi-faceted ocean acoustics and seismic experiment in the Eurasian basin of the Arctic Ocean in the spring of 1980. This effort involved the Massachusetts Institute of Technology, Woods Hole Oceanographic Institution, Bedford Institute of Oceanography, Lamont-Doherty Geological Observatory, Naval Undersea System Center, and the University of Washington Polar Science Center. One part of Fram 2 was a series of seismic refraction lines shot to a horizontal 800m by 800m (2-D coverage) 24 channel hydrophone array deployed at the ice station (initially at $86^{o}N$, $24^{o}W$), which drifted with the pack ice 3.8 to 4.0 km above the Pole Abyssal Plain in the eastern Arctic Ocean. From the data acquired on these lines, well constrained crustal compressional and shear velocity profiles are obtained. Another aspect of the experiment to be dealt with in this work is the set of long range propagation experiments in which charges were detonated in the water column near a satellite camp approximately 340 km from the receiving array at the Fram 2 camp. By measuring the dispersion characteristics of the sound received from these shots the water column and near bottom sedimentary structure are obtained.

A broad range of problems are encountered in transforming raw seismic data into models for velocity structure. The data used for this thesis are unique for the Arctic in that they are of exceptionally high quality- an excellent recording system was used, the experiments were highly controlled, signal to noise ratios were good, and the structures probed were reasonably simple. However, logistical considerations dictated the acquisition of a relatively small amount of data when compared with similar refraction experiments in more temperate regions. To a great extent, this thesis deals with methods for fully utilizing data that were taken under these restrictions, although it will be shown that the techniques developed can enhance the results from more conventional datasets. On the other hand, the data acquired from the long range ocean acoustic propagation experiments are among the most complete ever taken because of the use of the large 2-D receiving array. This work will center around the use of array processing techniques for transformation of both of these datasets into decompositions that may be easily related to the model parameters, and the inversion of these decompositions for oceanic and crustal sound and elastic wave propagation velocity structure.

THESIS OUTLINE

As mentioned above, for this work, two main experimental procedures will be employed, the refraction experiment for crustal studies, and the long range propagation experiment for ocean acoustics. This chapter will be devoted to the description, history, and current use of these experiments.

Chapter 2 provides the necessary theoretical background on wave propagation to motivate the array processing and inversion techniques. This includes the relation of slant stacking, the plane wave decomposition, velocity spectral analysis, and spectrogram techniques to the forward problems of the refraction and long range propagation experiments. This work will

center on the use of the WKBJ approximation for identification of crustal models from the refraction data, and on normal mode propagation for the long range data.

Chapter 3 discusses in detail the velocity spectral analysis and slant stacking methods used to process the Arctic data to obtain its plane wave decomposition. This work deals primarily with the use of the Maximum Likelihood Method (MLM) on multichannel short-time Fourier transforms of the transient data. The use of this technique for both velocity spectral analysis, or decomposition of the waves into power as a function of time, frequency, and phase velocity, and as a method for obtaining a high resolution time-domain slant stack from small aperture, non-uniformly sampled array data will be explored. The issues of algorithm bias and estimator performance are discussed.

Chapter 4 discusses the techniques used to invert the reduced data from chapter 3 to obtain oceanic and crustal structure. For the refraction data, the velocity-depth migration techniques of Clayton and McMechan [1981] are considered when the crustal structures are modeled adequately as laterally homogeneous. This method is extended to use the results of velocity spectral processing on short apertures and to utilize amplitude and offset data to further constrain the resulting models. In addition, it is shown how to stabilize the iteration and speed the convergence of this algorithm. Other methods used to analyse the data are the tau-sum method [Diebold and Stoffa, 1981], and a modified version of the linearized least squares inversion technique of Dorman and Jacobson [1981], which uses travel-time and offset data as a function of ray parameter as its input.

One of the primary characteristics of this work is that the free surface multiples that appear as late-breaking arrivals can be picked out in time, frequency, and slowness by the velocity spectral analysis algorithms described in chapter 3. This is a result of using both the

resolution in these three variables, and the signal processing gain over the measurement noise afforded by the use of coherent multichannel processing and temporal filtering. The inversion methods have been modified to fully utilize these data.

Chapter 5 contains the analysis and interpretation of the some of the experimental refraction data obtained on Fram 2 in the eastern Arctic ocean. Three of the total of six refraction lines are analysed using the methods developed in chapters 3 and 4, and crustal structures are given.

Chapter 6 contains the analysis and interpretation of two long range propagation shots obtained during the Fram 2 experiment. This work is separated into two parts. The first is the analysis of the highly dispersive water-borne and very near bottom paths via normal mode techniques and the dispersion characteristics estimated from the spectrogram (also called sonogram) and velocity spectral analyses. From this data we may obtain the water column structure in great detail. Secondly, the deeper bottom interacting paths form a suite of some thirty multiples from a single shot which may be collectively analysed as a multiple offset refraction experiment due to the lateral homogeneity of the propagation path. These data are analysed in the same manner as the refraction data of chapter 5.

EXPERIMENTAL DESIGN OF THE REFRACTION EXPERIMENT

General Structure and Goals

In a *wide angle reflection/refraction* experiment, sources at the surface generate body waves that propagate down into the seismic structure. These waves are reflected by impedance discontinuities or refracted by wave velocity variations within the structure and return to receivers on the surface which are offset along a radial line from the source location (common

source geometry). In the common receiver geometry used in our experiment, the source and receiver locations are exchanged. This experimental geometry is shown schematically in figure 1.1. From these offset surface measurements inferences about the structure through which the waves propagated can be drawn. The primary advantage of this type of experiment is that explosives which produce powerful low frequencies can be used to penetrate deeply into the crust as far as the crust/mantle transition, or Moho. The offset geometry allows the long wavelength disturbances to be refracted back to the surface when the lack of strong discrete reflectors gives very poor normal incidence reflection results. Because of the low frequency of the source and the lack of dependence on reflection mechanisms, such as small changes in the impedance, a larger and deeper region of the crust can be explored with this method, albeit with lower resolution, than with typical normal incidence reflection experiments. Because of these properties, the primary use of the refraction experiment is for large scale tectonic interpretation, not hydrocarbon exploration. The oblique geometry also allows the observation of both compressional and shear wave paths since conversions from P to S type waves can occur at horizontal interfaces with a velocity contrast even when the source is purely compressional [White and Stephen, 1980]. This is fortunate since most powerful man-made sources, and all marine sources, are purely compressional, and invaluable from the viewpoint of structural characterization since the shear and compressional velocities are necessary for a good geological interpretation.

Practical Difficulties in Recovery of the Structure from Refraction Data

In the ideal experiment, the structure underlying the continuous line over which the measurements are made would be laterally homogeneous and monotonically increasing in velocity with depth. In this case, if noiseless arrival time measurements as a continuous function of

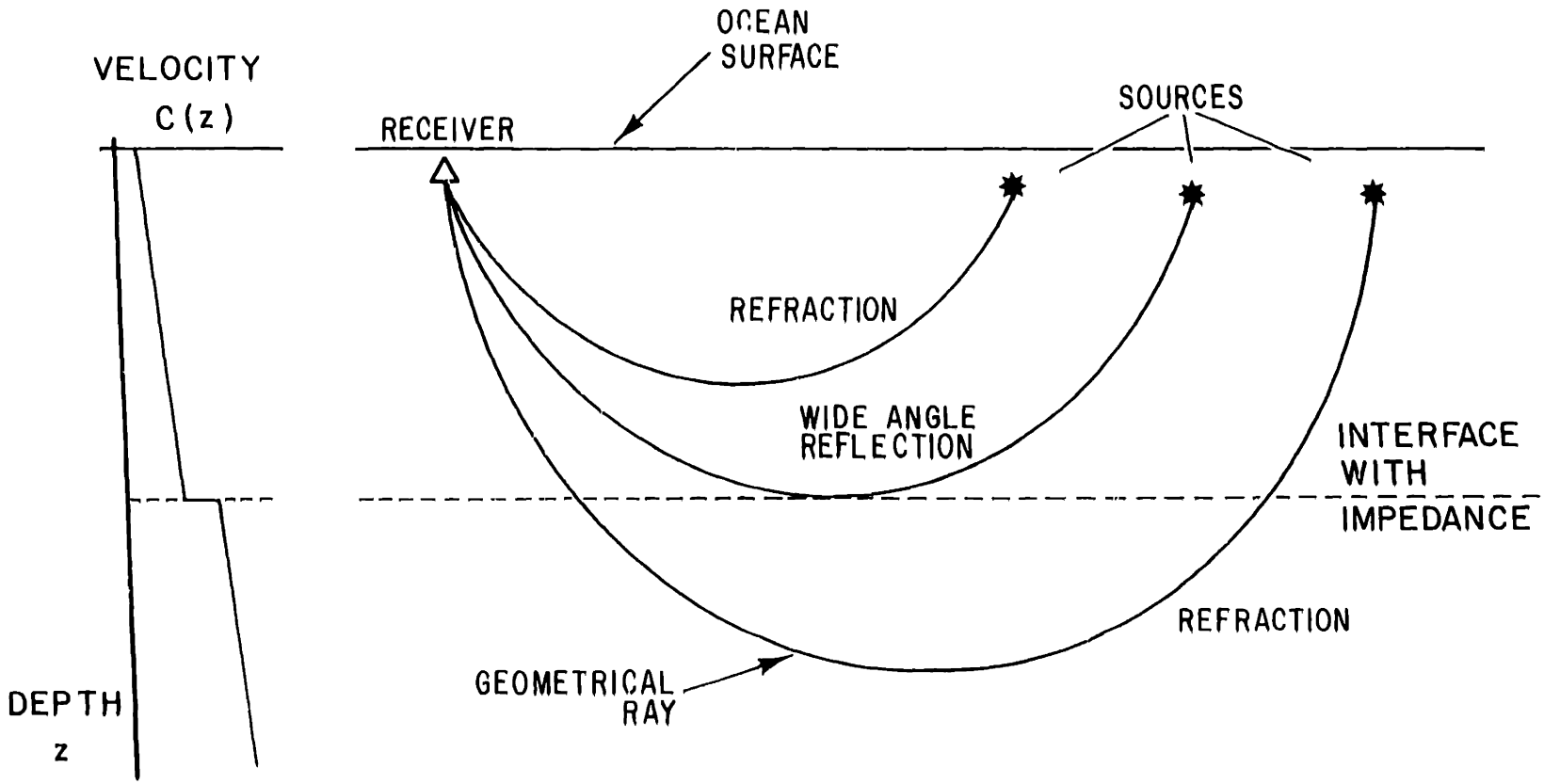

Fig. 1.1) Geometry for refraction/wide angle reflection experiment using the common receiver point geometry.

offset for the geometric ray paths can be made, then the velocity-depth structure can be determined through the Herglotz-Wiechert integral:

$$z(c) = -\frac{1}{\pi}\int_{c^{-1}(0)}^{c^{-1}} \frac{x(p)}{\sqrt{p^2 - c^{-2}}}dp \qquad 1.1$$

In this expression $p = \frac{dt(x)}{dx}$ and $t(x)$ is the arrival time at offset x with ray parameter, p, (variously known as the horizontal slowness or inverse phase velocity). The function $x(p)$ is simply the geometrical offset of the arrival with slowness p.

Unfortunately, obtaining all these measurements is difficult in actual experimental work, and in our analysis the lack of a dense coverage in offset is a primary problem. Even if an infinite bandwidth signal is generated, propagation effects, such as intrinsic attenuation, quickly limit it. In the presense of measurement noise, the finite bandwidth arrivals are subject to errors in estimation of their arrival times, leading to noisy travel time curve, $t(x)$, estimates. In addition, the multiple valued structure of the travel time and offset functions [Kennett, 1976], coupled with the finite bandwidth of the received arrivals causes overlapping, and thus not easily separable arrivals at a given offset [Chapman, 1978]. When these problems are combined with the fact that it is often impractical to either deploy sources, or make measurements at all offsets, it becomes clear that it is difficult to estimate both $t(x)$ and $p(x)$. The branches of the travel time curve must first be resolved (which almost requires knowing the structure), then smoothed and interpolated over offset to obtain reliable p estimates, thus diminishing $x(p)$ resolution. Fortunately, advances in technology have made it possible to record digitally many channels of data simultaneously from an array of hydrophones. With measurements from an array that is adequately sampled in offset, coherent processing of the multichannel data is possible. With this method, the slowness, arrival time, and offset of an

event can all be measured independently and with good resolution. In addition, arrivals overlapping in time, but with different slownesses may be resolved, thus providing information from all branches of the travel time curve regardless of source bandwidth. Direct measurement of all the information needed for subsequent inversion is a main advantage of multichannel acquisition. In this work it is shown that this compensates to a degree for the sparse offset coverage that will be seen to be enforced by Arctic logistics.

Problems Specific to the Arctic

It obviously would be most advantageous if all measurement offsets were covered with sufficient density for coherent processing. However, refraction shooting in the ice covered waters of the Arctic is quite different from that of open ocean where this is possible. As a result, the constraints on the data acquisition procedures and the methods used to process the data are different. The most common configuration for temperate marine refraction studies is a single stationary point receiver, such as an ocean bottom seismometer/hydrophone or sonobouy, and a source vessel criss-crossing the area to be studied [eg. Detrick and Purdy, 1980]. Alternatively, a towed hydrophone receiving array can be used while another source ship shoots very densely (50-200 m interval) with an air gun or explosives [Stoffa and Buhl, 1979]. Neither of these techniques are generally applicable to Arctic work since the use of an ice breaker in the same manner as a research vessel is impractical for many reasons, including its large self noise and most importantly, because sections of the ice are too thick for routine ice-breaking. As a result, the densely sampled travel time vs. offset distance curve upon which many inversion techniques are based is not available [Stoffa, et.al. 1981; Clayton and McMechan, 1981]. Since it is difficult to deploy acoustic sources or receivers at a large number of widespread locations in the Arctic, processing procedures and inversions using a minimum

of shots (and thus offsets), typically 5 to 20, instead of the hundreds for a standard line, are necessary. The schematic for a single shot is shown in figure 1.2a. The coverage for three of the lines shot during Fram 2 are shown in figure 1.2b. Obviously, the ability to resolve lateral structure will suffer, local inhomogeneities will be troublesome, and inversion techniques that make use only of detailed first arrival travel time curves are not applicable. However, improvements in interpretation beyond the classical time-term analysis for first arrival picks are both desirable and possible.

Array Data as a Partial Solution to the Difficulties in Arctic Work

Crustal structures in the Arctic can be determined by the use of a stationary array and a series of relatively widely spaced shots deployed by helicopter or small fixed wing aircraft. The ice cover, while impeding ship movement, does allow a stable platform for multi-channel seismic data acquisition. These data permit localized measurement of the phase velocity or horizontal slowness of an event, yielding an independent measurement of the slope of the travel time curve. Conditioning of the other observables such as travel time, offset, and various transformations of the two, on the slowness has become the standard data on which travel time inversion procedures operate [Johnson and Gilbert, 1972; Bessonova, et.al., 1974; Diebold and Stoffa, 1981; Clayton and McMechan, 1981; Dorman and Jacobson, 1981; Garmany, et.al. 1979; Phinney et.al., 1981]. The direct observation of the slowness datum thus enhances the quality of the data for subsequent inversion. The decomposition of the data by slowness is equivalent to a plane wave decomposition, since a broadband plane wave propagates with a constant horizontal slowness in a medium in which the elastic wave propagation velocities vary in only one dimension. In addition to direct measurement of the wave propagation parameters, time of arrival, slowness, offset, and spectral characteristics, the coherent processing util-

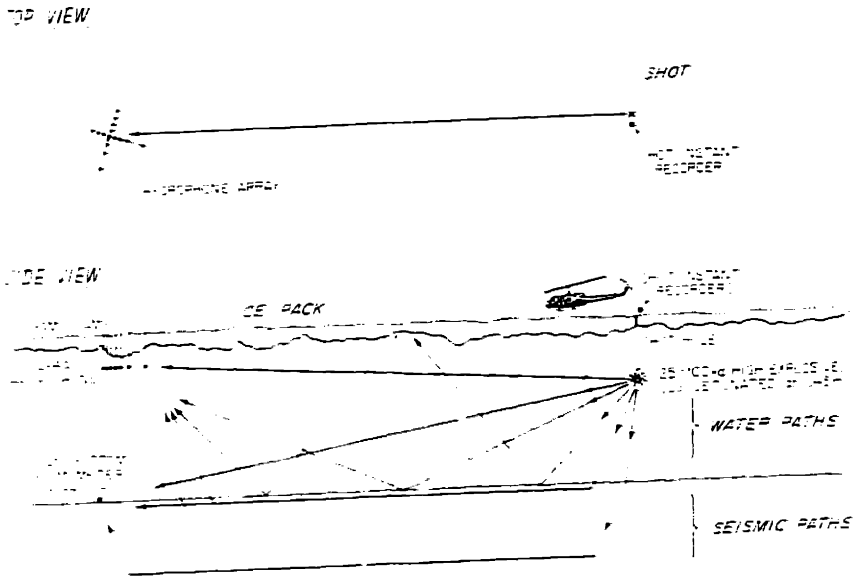

Fig. 1.2a) Experimental procedure for Fram 2 refraction shooting.

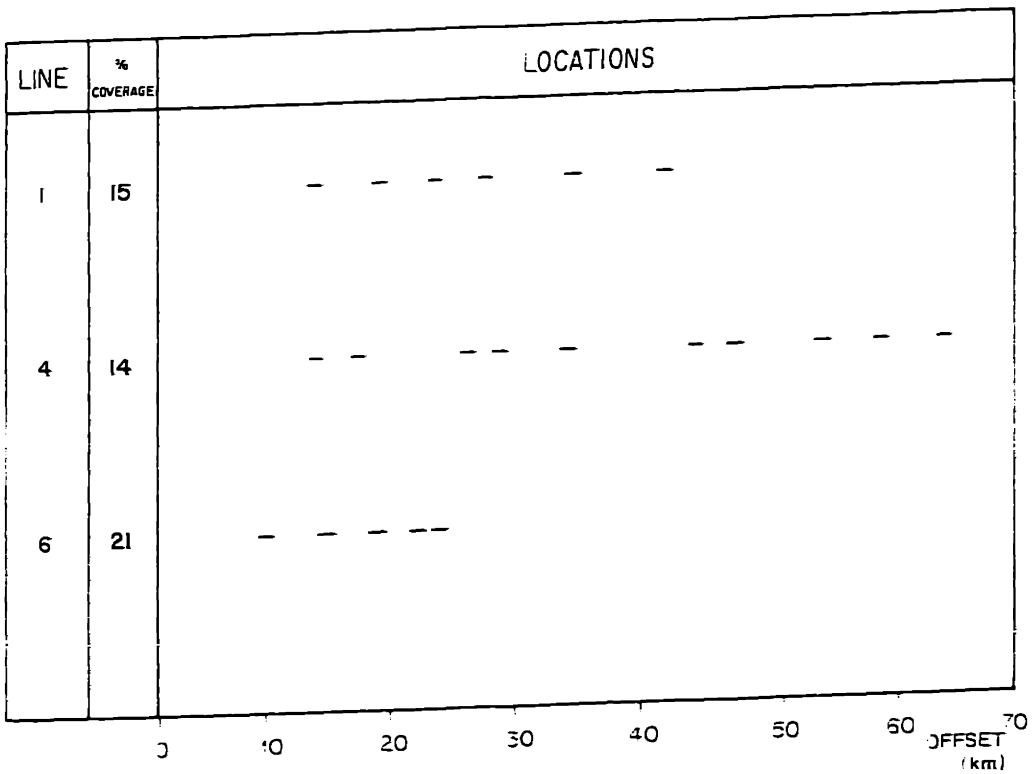

Fig. 1.2b) Refraction line coverage for Fram 2.

izes the array gain to increase the quality of the parameter estimates, and the detectability of weak, but important, arrivals such as multiples.

A BRIEF HISTORY OF REFRACTION EXPERIMENTATION IN THE ARCTIC

Background

Experimentation of any type in the Arctic are difficult and expensive to mount because of its remote location and harsh environment. This is especially true of seismic experiments in which large areas must be covered during the conduction of the actual data acquisition (e.g. for source/receiver offsets). Most experiments have been limited to point receivers, usually located near the ice camp, and a few (5-20) shots deployed at widely spaced offsets from the camp. This shooting geometry has constrained most analyses to parameterization of the earth by homogeneous layered models which allow correlation among arrivals in the observed time series on the basis of straight line headwave and wide angle reflection propagation interpretations. Experiments carried out in the deep Arctic of this type have included Fram 1 in the Eastern Arctic near Greenland [Jackson, et al., 1982], and a set of refraction lines in the Beaufort Sea during the AIDJEX program reported by Mair and Lyons [1981]. Current art in the refraction experiment dictates that coverage in offset should be continuous and dense so that the data may be easily decomposed into various fundamental components, typically plane waves. As mentioned earlier, this is regularly achieved in standard marine work using modern powerful, repeatable, and high duty cycle sources, such as air guns, and multichannel acquisition from long towed arrays [Stoffa and Buhl, 1979]. Deployment of large, dense arrays and tightly spaced shooting patterns, however, are rare in central Arctic work. On early experiments in which arrays were used for velocity determination, as in Hunkins, [1962], the small aperture and lack of a digital acquisition system enabled only rough slowness estimates to be

made. These values were then corrected for bias due to seafloor topography and interpreted as head wave arrivals from layers with the corresponding constant velocity. In many cases, such as the ARLIS II track, only normal incidence results are available [Ostenso and Wold, 1977], reflecting the non-standardness of the refraction measurements in Arctic work. A summary of the work carried out in the Arctic, and an extensive bibliography can be found in Baggeroer and Duckworth, [1983].

Historical Problems in Arctic Experimentation

Procedures and measurements regarded as trivial in temperate experiments are very often quite problematic in Arctic work. In reviewing the literature, many well conducted experiments suffer from ambiguities due to shot instant measurement problems [e.g. Hunkins, 1962]. Since the usual sound source is a remotely located explosion, the shot break must be detected by a geophone or hydrophone and either recorded along with a remote time base which is synchronized to the clock in the acquisition system, or relayed by radio link directly to the recording system. In general, radio links have not proven reliable over the ranges required*. Accurate knowledge of shot offset and initiation time is essential for successful refraction interpretation. Good measurements of the shot instants are required because direct calculation of the offset using the navigation systems in the base camp and aboard the deployment aircraft, such as the *Omega* system, do not perform adequately in the Arctic, even when synchronized with the satellite navigation receivers at the receiving (base) camp. The LORAN system does not cover these areas adequately. Attempts to use radar transponder ranging systems, such as the Decca *Mini-Ranger*, have also been rather problematic in the Arctic because of the need for

*Often the shots are deployed by small aircraft, leaving room for little more than the explosives and required personnel. The difficulty involved in the erection of an antenna sufficient for transmission of the shot break has typically been prohibitive. Our attempts during the Fram 4 experiment (1982) to establish radio links through a repeater in the helicopter also proved unsuccessful.

repeater stations at long range, and the requirement that the Helocopter be hovering at some altitude to make measurements at even moderate distances. However, when the water column velocity structure is known, a well determined direct water arrival travel time can be used for accurate ranging. [Mair and Lyons, 1981; Jackson, et al., 1982; Duckworth, et al., 1982] For the Fram 2 experiment, the upper water column sound speed profile was measured directly using an expendable sound velocimeter (XSV) system. The deeper regions were predicted using the standard formulae [Urick, 1975]. In addition, corrections to the average water column structure for large offsets over which significant dispersion takes place can be determined using the methods described in chapter 6. Ray tracing using the "known" water column structure gives ranges accurate to approximately 0.05 km (80 Hz bandwidth - model errors) over all ranges used for refraction studies in this work.

The first deployment of a large hydrophone array (12 channels, 600 m aperture) in the Arctic was during the CANBARX (1978) experiment in the Canadian Basin [Baggeroer and Falconer, 1982]. For this pilot experiment only one refraction line of 5 shots was carried out. Interpretations were done using homogeneous layered model travel-time fits in which the layer velocities were determined through their array estimated phase velocities. The array data were processed using the same method described and analysed in this thesis, and the measured arrival velocities were used to correlate the arrivals among the widely spaced shots.

Current History: The Fram 2 Refraction Experiment

For the Fram 2 experiment, a much more ambitious refraction program was carried out. Six lines with up to 15 shots/line were shot to a 0.8 by 0.8 km 2-dimensional non-uniformly sampled array of 24 hydrophones. The data were recorded digitally with a dynamic range exceeding 120 dB using a system described by Prada, et al. [1981]. The processing and inver-

sion of these data are a primary subject of this work and will be discussed in detail in chapters 2 through 5.

EXPERIMENTAL DESIGN OF THE LONG RANGE PROPAGATION EXPERIMENT

As source/receiver offsets increase beyond those typical for conventional refraction, the experiments become known as long range propagation experiments, or more recently as bottom interaction studies since the importance of the sea bottom to long range propagation as come to light. At distances greater than 100 km, deep crustal arrivals are highly attenuated by the intrinsic Q of the medium (typically 0.2 to 0.5 dB/km at 10 Hz). In addition, these ranges are beyond the geometrical offsets for primary crustal arrivals, and multiple reflection and transmission mechanisms introduce further propagation losses. As a result, in the long range propagation studies we are primarily interested in observing the effects of propagation on the more or less strictly water column arrival paths, which are multiply reflected and refracted. However, as longer arrays and lower frequencies become more common in ocean surveillance, it has become clear that bathymetry and composition of the ocean bottom is very important to these paths- in other words, the arrivals observed have significant interaction with the near bottom sediment structure. A schematic diagram of this type of experiment is shown in figure 1.3.

The arrivals can be separated into two primary groups. The first are the highly dispersive water column modes. The second are the paths that interact strongly with the seabottom sediments. These are indicated in figure 1.4. The use of array measurements allows the received data to be decomposed by arrival time (group velocity), phase velocity (slowness, or angle of arrival across the array), and frequency. After this finite set of observations is obtained, inverse techniques can be used to calculate the parameters (velocity structure) of the medium

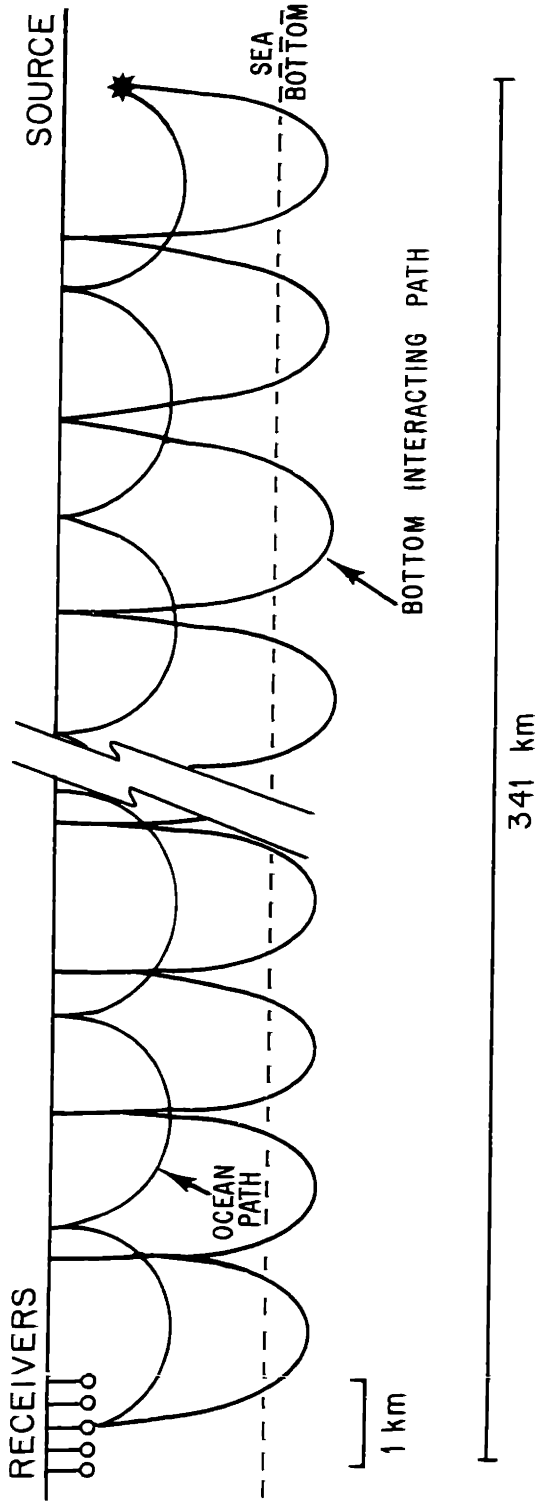

Fig. 1.3) Long-range propagation experimental geometry. The source was deployed at various depths to select the dominant modes at a given frequency.

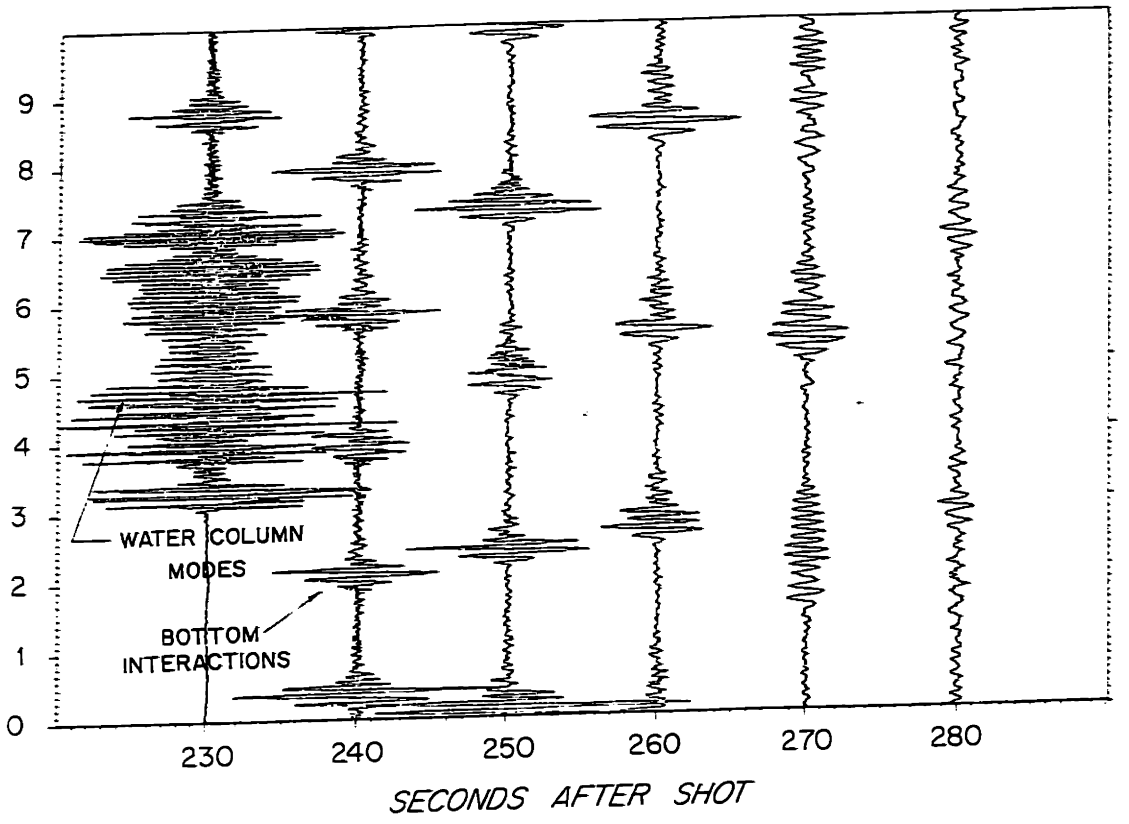

Fig. 1.4) A long-range propagation waveform received at a distance of 341.3 km. The water column and sediment interacting paths are indicated. Some sediment interacting paths are time coincident with the water arrivals and cannot be discerned on this plot.

through which the signal propagated. During Fram 2, explosive charges were detonated 341.3 km from the receiving array. Because of the limited amount of data of this type collected on this experiment, observation of the dispersion characteristics at one range, the detail of the model is necessarily restricted. This primarily manifests itself in the assumption of lateral homogeneity of the propagation path. Ordinarily, such data would not be useful for detailed seismic structural determination because of significant horizontal inhomogeneity in the upper crustal structure over such a distance. However, in this experiment both the source and the receiving points were located in the pole abyssal plain on a line approximately parallel to the spreading center at the Arctic Mid-ocean Ridge, and along the same magnetic anomaly (#25, $\approx$ 60 mybp.). In addition, there was no known bottom topography along the path*, and attenuation in the sediments was relatively low. The experiment also benefited from being located in the Arctic, which has a more stable and homogeneous lateral water column structure due to the ice cover and relatively isothermal boundary conditions [Mikhalevsky, 1981] and lack of major current systems. Because of the strong lateral homogeneity in the direction of the source from the array, the experiment closely approximated propagation of a broadband pulse in a layered waveguide, so a detailed analytical and numerical analysis of the system became possible. For the primarily water column borne arrivals, normal mode analysis allows prediction of the very dispersive arrivals. Inversion for perturbations to a trial water column velocity model are achieved through a linearized inversion scheme using numerically computed partial derivative matrices.

In addition to the highly dispersive first arrivals, for the Fram 2 data the water column reverberations interacting with the surface and near bottom sediments are present for approxi-

*Detailed bathymetry of the Arctic is not readily available and fracture zone locations have not yet been determined.

mately 60 sec. after the first arrival. Because of the lateral homogeneity, some 10-30 multiples (depending on frequency) can be constructed as a synthetic aperture wide angle reflection/refraction experiment with a densely spaced total aperture of some 35 km located at precisely the proper offsets to obtain the sediment arrivals. These data can be inverted for near bottom velocity structure in the same manner as the refraction data. The assumption of lateral homogeneity and lack of topography along this propagation path are supported by the adequate prediction of the amplitude structure of these multiple arrivals by simple ray trace and WKBJ techniques. (That is, this model is not inconsistent with the observed data.) Using prior knowledge of the structure, the multiplicity of the bottom interacting paths may be discerned. The bottom interacting paths are more easily modeled by ray and WKBJ techniques because each arrival that may be discerned in frequency, group velocity, and phase velocity space is a composite of several modes within the resolution of current processing techniques. For these arrivals, the dispersion of portions of the wavelet with significant amplitude is quite small, and that observed may be due to intrinsic attenuation of the sediment, not geometrical effects.*

A HISTORY OF LONG RANGE PROPAGATION EXPERIMENTATION IN THE ARCTIC

Background

The measurement and theoretical prediction of long range propagation characteristics is a problem that has long interested the naval community [Kutschale, 1961; 1969]. The most direct method used to characterize the sound channel is measurement of the response of the channel at various ranges from an explosive source. The first observations of the dispersive

*A personal communication with Dr. Henry Kutschale of the Lamont-Doherty Geological Observatory indicates that the work of his group has shown that the measured dispersion characteristics of the late sediment arrivals are, in fact, due to geometrical effects and P-wave propagation only, and not a result of attenuation or shear conversion. This work is contained in the Ph.D. thesis of Tai Lee, and should be completed in September of 1983.

characteristics of shallow water and SOFAR channel propagation [Ewing, 1936; Ewing and Worzel, 1948] were explained by Pekeris [1948] using a normal mode solution to the wave equation in a layered wave guide. Since then, a great deal of work has been expended in the development of theoretical results and numerical algorithms that allow efficient computation of the channel characteristics, such as propagation loss, and the waveforms that one would observe for a given experiment. These have followed two major tacks: i) ray theory, which works well for SOFAR propagation and for short ranges, but becomes inaccurate for low frequencies, and expensive for long ranges, and ii) full wave methods which attempt to solve the inhomogeneous wave equation under various assumptions about the velocity structure and boundary conditions. The major methods used are normal mode theory, the fast field method, and the parabolic equation method [Tolstoy and Clay, 1966; DeSanto, 1979; DiNapoli and Deavenport, 1979; Kuperman and Jensen, 1981].

In the Arctic, sound propagation centers around the surface ducting properties of the monotonically increasing velocity/depth profile. This profile is the result of the nearly isothermal temperature structure of Arctic waters [Kutschale, 1961] and is a unique property which makes long-range propagation in the Arctic different from that of more temperate oceans. One of the main results of the entirely surface ducted propagation is that higher frequencies are more highly attenuated than in open ocean due to interactions with the rough undersurface of the ever present pack ice [Kutschale, 1969; Urick, 1975]. Much current work in acoustics and ice science centers around characterization of the under ice roughness by acoustical and indirect remote sensing techniques. Knowledge of under-ice conditions would obviously be valuable in both active and passive sonar detection problems.

To be contrasted with the high frequency propagation characteristics, early work in the Arctic found that low frequency signals from small (2 lb.) charges dropped over 1000 km from the hydrophone and geophone receivers could be easily detected, and their group velocity dispersion curves for the first two modes determined by cycle counting or filter bank spectrogram (sonogram) techniques [Kutschale, 1961; 1969]. These were able to be matched quite well by normal mode analysis using the Thomson-Haskell matrix method for a velocity structure approximated by thin homogeneous layers. Early attempts at using geophone arrays for the direct measurement of mode phase velocities were unsuccessful. The main results, which confirm observations by sound velocimeter and bathythermographs, indicate that the canonical Arctic sound speed profile has an increasing velocity from surface to bottom, with the upper high gradient region a result of the rapid increase in temperature from a -2.0^{o}C surface boundary condition to about 0.5^{o}C at 350 to 450 m and a similarly steep positive halocline from 31 ppt. to 35 ppt. in the upper 400 m. Below this, the nearly isothermal (0.0^{o} to -0.5^{o}C) and isohaline water increases in sound velocity more slowly due to the increasing pressure. Anomalous transmission losses in early experiments indicated the need for inclusion of ice and bottom interaction effects in the propagation models. Subsequent work has centered on data gathering for the construction of empirical propagation loss curves in areas of complicated oceanography and bathymetry, such as the marginal ice zone, and the development of faster, more accurate, and more detailed modeling techniques [Kutschale, 1970; Gartrell and DiNapoli, 1976; DiNapoli and Powers, 1972; DiNapoli, 1971].

The Fram 2 Long Range Propagation Experiment

During the Fram 2 experiment, explosive charges of 55# were detonated at shallow depths (93 and 243 m) at a satellite camp 341.3 km from the receiving array. The analysis

reported here centers around the use of this high quality digital hydrophone array data to simultaneously measure group velocity and phase velocity dispersion curves, and the amplitude structure of the arrivals in a very well controlled experiment. The parameters measured from the received water column and bottom interacting signals from these shots are used to characterize the water column and near-bottom sediment structure in great detail. The necessary theoretical background is contained in chapter 2, and the analysis is in chapter 6.

REFERENCES

Baggeroer, A.B. and Falconer, R.K.H., "Array refraction profiles and crustal models of the Canada Basin," *Journal of Geophysical Research*, vol. 87, pp. 5461-5476, 1982.

Baggeroer, A.B. and Duckworth, G.L., "Seismic Exploration in the Arctic Ocean," in *Arctic Policy and Technology*, New York, NY: Hemisphere Publishing Co., in press, 1983.

Bessonova, E.N., Fishman, V.M., Ryaboyi, V.Z., and Setnikova, G.A., "The Tau Method of Inversion of Travel Times- I. Deep Sounding Seismic Data," *The Geophysical Journal of the Royal Astronomical Society*, vol. 36, pp. 377-398, 1974.

Chapman, C.H., "A New Method for Computing Synthetic Seismograms," *Geophysical Journal of the Royal Astronomical Society*, vol. 54, pp. 481-518, 1978.

Clayton, R. and McMechan, G., "Inversion of refraction data by wavefield continuation," *Geophysics*, vol. 46, no. 6, p. 860, 1981.

DeSanto, J.A., "Theoretical Methods in Ocean Acoustics," in *Topics in Current Physics: Ocean Acoustics*, ed. J.A. DeSanto, Berlin, BRD: Springer-Verlag, 1979.

Detrick, R.S. and Purdy, G.M., "The Structure of the Kane Fracture Zone from Seismic Refraction Surveys," *Journal of Geophysical Research*, vol. 85, pp. 3759-3777, 1980.

Diebold, J.B. and Stoffa, P.L., "The traveltime equation, tau-p mapping, and inversion of common midpoint data," *Geophysics*, vol. 46, no. 3, pp. 238-254, March, 1981.

DiNapoli, F.R., "Fast Field Program for Multilayered Media," NUSC Technical Report 4103, Naval Underwater System Center, Newport, RI, 1971.

DiNapoli, F.R. and Powers, M.R., "The Fast Field Program (FFP) and Attenuation Loss in Hudson Bay," NUSC Technical Report 4253, Naval Underwater System Center, New London, CT, 1972.

DiNapoli, F.R. and Deavenport, R.L., "Numerical Models in Underwater Acoustic Propagation," in *Topics in Current Physics: Ocean Acoustics*, ed. J.A. DeSanto, Berlin, BRD: Springer-Verlag, 1979.

Dorman, L. and Jacobson, R.S., "Linear Inversion of Body Wave Data; Part I: Velocity Structure From Travel Times and Ranges," *Geophysics*, vol. 46, no. 2, pp. 138-151, 1981.

Duckworth, G.L., Baggeroer, A.B., and Jackson, H.R., "Crustal Structure Measurements near FRAM II in the Pole Abyssal Plain," *Tectonophysics*, vol. 89, pp. 172-215, 1982.

Ewing, M., "Frequency of Water Waves," *U.S. Coast and Geodetic Survey Field Engineers Bulletin*, p. 65, 1936.

Ewing, M. and Worzel, J.L., "Long range sound transmission. Propagation of Sound in the Ocean," *Geological Society of America, Memoir*, vol. 27, pp. 1-35, 1948.

Garmany, J., Orcutt, J.A., and Parker, R.L., "Travel time inversion: A geometrical approach," *Journal of Geophysical Research*, vol. 84, pp. 3615-3622, 1979.

Gartrell, G. and DiNapoli, F.R., "Propagation Loss Model Assessment at Low Frequencies in a Bottom-Limited Region," NUSC Technical Report 5391, Naval Underwater System Center, New London, CT, 1976.

Hunkins, K., Herron, T., Kutschale, H., and Peter, G., "Geophysical Studies of the Chukchi Cap, Arctic Ocean," *Journal of Geophysical Research*, vol. 67, no. 1, pp. 235-247, 1962.

Jackson, H.R., Reid, I., and Falconer, R.K.H., "Crustal Structure Near the Arctic Mid-ocean Ridge," *Journal of Geophysical Research*, vol. 87, no. B3, pp. 1773-1783, 1982.

Johnson, L.E. and Gilbert, F., "A new datum for use in the body-wave travel time inverse problem," *Geophysical Journal of the Royal Astronomical Society*, vol. 30, pp. 373-380, 1972.

Kennett, B.L.N., "A Comparison of travel time inversions," *Geophysical Journal of the Royal Astronomical Society*, vol. 44, pp. 517-536, 1976.

Kuperman, W.A. and Jensen, F.B., "Propagation Modeling I: Fundamental Principles," in *Underwater Acoustics and Signal Processing*, ed. L. Bjorno, Dordrecht, Holland: D. Reidel Publishing Co., 1981.

Kutschale, H.W., "Long-Range Sound Transmission in the Arctic Ocean," *Journal of Geophysical Research*, vol. 66, no. 7, pp. 2189-2198, 1961.

Kutschale, H.W., "Arctic Hydroacoustics," *Arctic*, vol. 22, pp. 246-264, 1969.

Kutschale, H.W., "The Integral Solution of the Sound Field in a Multilayered Liquid-Solid Halfspace with Numerical Computations for Low-Frequency Propagation in the Arctic Ocean," Technical Report #1, Lamont-Doherty Geological Observatory, Palisades, NY, 1970.

Mair, J.A. and Lyons, J.A., "Crustal structure and velocity anisotropy beneath the Beaufort Sea," *Canadian Journal of Earth Science*, vol. 18, pp. 724-741, 1981.

Mikhalevsky, P.N., "Characteristics of CW signals propagated under the ice in the Arctic," *Journal of the Acoustical Society of America*, vol. 70, no. 6, pp. 1717-1722, 1981.

Ostenso, N.A. and Wold, R.J., "A Seismic and Gravity Profile Across the Arctic Ocean Basin," *Tectonophysics*, vol. 37, pp. 1-24, 1977.

Pekeris, C.L., "Theory of Propagation of Explosive Sound in Shallow Water," *Geological Society of America, Memoir*, vol. 27, p. 127, 1948.

Prada, K., VonderHeydt, K., and O'Brien, T.F., "A versatile multi-channel data acquisition system for seismic and acoustic applications," *Proceedings of the IEEE Conference Oceans '81*, pp. 43-47, 1981.

Stoffa, P.L. and Buhl, P., "2 Ship Multi-channel Experiment for Deep Crustal Studies: Expanded Spread and Constant Offset Profiles," *Journal of Geophysical Research*, vol. 84, no. B-13, December 10, 1979.

Stoffa, P.L., Diebold, J.B., and Buhl, P., "Inversion of seismic data in the tau-p plane," *Geophysical Research Letters*, vol. 8, no. 8, pp. 869-872, August, 1981.

Tolstoy, I. and Clay, C.S., *Ocean Acoustics*. New York, NY: McGraw Hill Book Co., 1966.

Urick, R.J., *Principles of Underwater Sound*. New York, NY: McGraw-Hill Book Co., 1975.

White, R.S. and Stephen, R.A., "Compressional to Shear wave conversion in oceanic crust," *Geophysical Journal of the Royal Astronomical Society*, vol. 63, pp. 547-565, 1980.

CHAPTER 2: The Plane Wave Decomposition and Modeling

INTRODUCTION

The Slant-stack and the Plane Wave Decomposition

In the current seismic literature much emphasis is placed on the plane-wave decomposition of wavefields measured at the surface as an intermediate step in the inversion of data for earth velocity and attenuation structure [Kennett, 1981]. One of its primary assets is that it projects the data into a domain where arrivals have both a clear organization and physical significance. For example, in earth models which vary only in the depth dimension the plane wave decomposition of surface data can be interpreted as the exact "generalized" reflection response of the earth [Phinney, et al. 1981]. After choosing some model framework for the medium, it is theoretically possible to invert this decomposition for a velocity and impedance model, although models this general have never been obtained practically. In most work, certain aspects of the estimated reflection response, or reflection coefficient at each slowness, p, are utilized to obtain only the impedance or velocity profiles separately. In general, large offset refraction experiments are used for velocity structure determination, and near normal incidence reflection experiments are used for impedance mapping. In its most simplistic interpretation, the organization of the data in the plane wave decomposition of slant stack and clearly defined relationships among the different classes of arrivals (e.g. refractions, post and pre-critical reflections, multiples) allows instant recognition of the gross features of the earth structure, including the extent of deviation from simple models. In addition, the plane wave itself is probably the most intuitive type of wave for physical understanding.

In the original development of slant-stacking formalisms [Chapman, 1978; Phinney, et al., 1981; McMechan and Ottolini, 1980] the 2-dimensional line source geometry was the primary

case considered. However, for this work we are concerned strictly with a point source in a 3-dimensional medium. For large offset work it will be seen that the operations required are similar, with some embellishments for the 3-D case. Because of the inertia of nomenclature I will continue to call the operations that are suitable for the line source case the slant-stack and the 2-D plane wave decomposition. For the point source geometry, they will be called the "proper" [Treitel, et al., 1982], or 3-D slant-stack, and the plane wave decomposition. The 2-D plane wave, or frequency-wavenumber, decomposition of a wavefield observed on the surface along a line radiating from the source will be defined as the two-dimensional Fourier transform over the 2-D surface offset, x, and time, t, variables [Chapman, 1978; Phinney, et al., 1981]:

$$U(\omega,k) = \int_{-\infty}^{\infty} dx \int_{-\infty}^{\infty} dt\ e^{i(\omega t - kx))}\phi(t,x) \qquad 2.1$$

where $\phi(t,x)$ is the wavefield at x and t. The inverse Fourier transform of a slice of this doubly transformed wavefield is also often called the plane wave decomposition [Phinney, et al. 1981]. To avoid confusion, in this work this quantity will be referred to as the slant-stack, $u(\tau,p)$:

$$u(\tau,p) = \frac{1}{2\pi}\int_{-\infty}^{\infty} U(\omega,\omega p)\, e^{-i\omega\tau}\, d\omega \qquad 2.2$$

where the parameter, p, may be interpreted as the slowness*, or inverse horizontal phase velocity of the plane wave component. The use of the horizontal slowness, p, instead of the wavenumber, $k = \omega p$, is often helpful to intuition because it has a clear interpretation as the propagation direction of a broadband plane wave in a horizontally stratified medium. Inserting equation 2.1 into equation 2.2 gives the Radon transform [Chapman, 1978; 1981] expression usually used for the slant-stack, and from which it derives its name:

*Slowness will always be construed to mean horizontal slowness unless otherwise modified.

$$u(\tau,p) = \int_{-\infty}^{\infty} \phi(\tau - px, x)\, dx. \qquad 2.3$$

This is simply a set of integrals over straight line, "slanted", trajectories across the wavefield data parameterized by τ and p. From fig. 2.1, it can be seen that the parameter τ can be interpreted as the vertical component of the travel time for a wave with slowness p. Readers with sonar signal processing backgrounds will recognize equation 2.3 as the expression for the delay and sum beamformer which is matched to planar wavefronts (far-field beamformer). In current practice, the generation of the plane wave decomposition or slant-stack of surface data has taken the form of discrete approximations to the transform operations one would carry out on a continuous and complete "paper" dataset, i.e. eqn 2.3. Some variations have been proposed to emphasize specific features, correct for approximations due to the discrete and experimental nature of the wavefield sampling and the fact that point sources, not line sources, are used, or for computational expedience [Stoffa, et al., 1981; Treitel, et al., 1982; Henry, et al. 1980].

Parameter Estimation vs. Wave-field Transforms

One of the hypotheses of this thesis is that the naive application of the theoretically required transform (2.3) or its 3-D point source equivalent, not only fails to generate an adequate estimate of the true plane wave response, but also, in trying to achieve this grandiose goal, fails to do as well as it could at extracting information that, while incomplete, is useful to a realistic inversion. This is especially true for the Arctic data to be dealt with because the small, non-uniformly sampled 2-D array aperture does not supply the integration interval required by eqn 2.3.

An example of this failure is the application of the Radon transform "slant stack" operator to a wavefield recorded on a large, sampled aperture. While this implements the desired

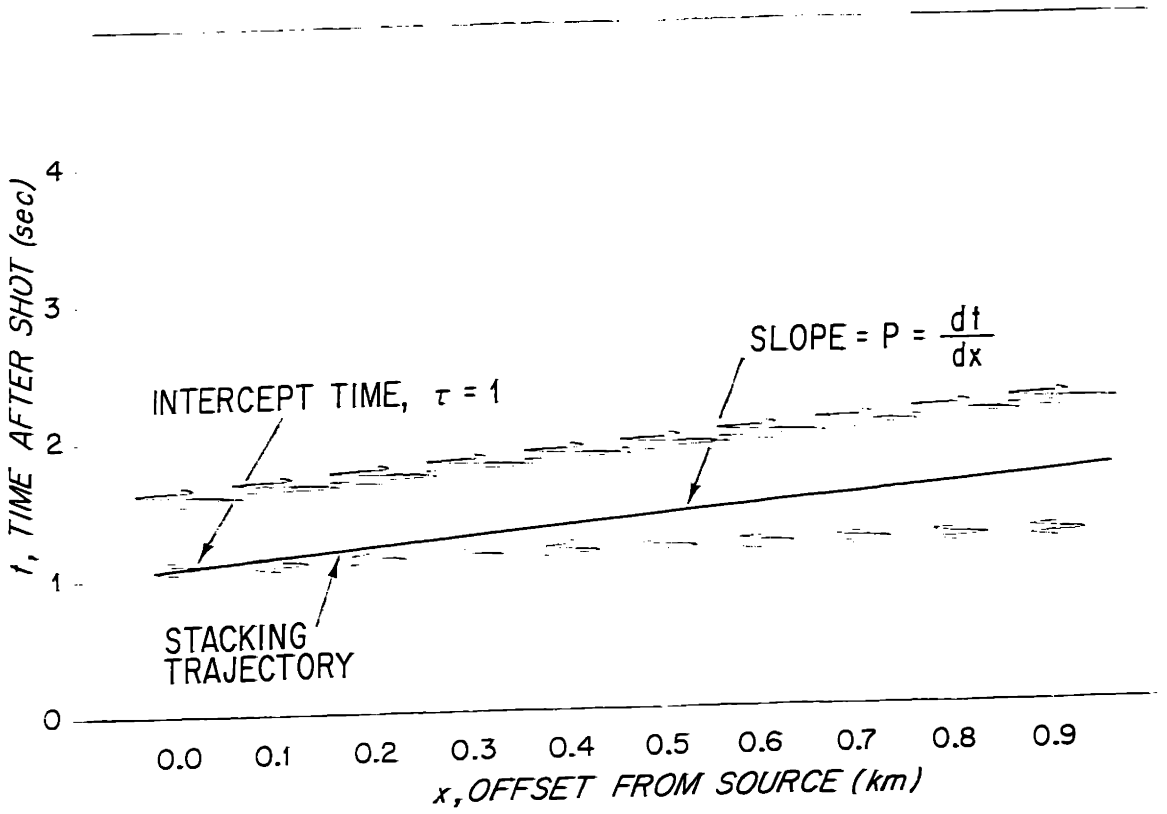

Fig. 2.1) Geometry and definitions of slant stack coordinates.

slant stack transform operator, it is corrupted by noise, finite aperture effects, and spatial aliasing which is practically unavoidable in experimental data due to the excessive cost of dense arrays. In addition, for most inversions the slant stack is not treated as the transform of a wavefield in which the linearity of operation 2.3 is important, but rather it is used as an intermediate step in the inversion from which features are extracted, e.g. wavelet arrival times, amplitudes, and phase shifts. These discrete data points are then used in least-squares or extremal inversion techniques [e.g. Dorman and Jacobsen, 1981; Orcutt, 1980].

To motivate how the Radon transform is sub-optimal in the extraction of these features or *parameters* we consider the following simple reasoning. It is desired to determine the arrival time, amplitude, and phase shift as a function of the angle (or equivalently the horizontal slowness, p) at which the wave strikes the boundary of a wide angle reflection from an interface with a strong velocity contrast. In the ray theoretic approximation, the reflection of the plane wave component of the source with parameter p will intersect the surface at a single distance, the geometrical offset, $x = x(p)$. To estimate the parameters of this local plane wave component with the best suppression of random sensor noise and interference effects from waves with different p values, it is desirable to use the data over as small an aperture in offset, x, as possible, since the other offsets (strictly) do not contain this arrival. However, it is necessary to average over enough aperture in which nearly coherent arrivals appear to suppress uncorrelated sensor noise, and, of course, to determine the slowness of the wave that is being observed through its local move-out. In practice, this directional or slowness decomposition is also necessary to isolate the desired arrival from others with different slownesses that may be arriving simultaneously due to multipath propagation. In general, for optimal parameter estimate performance the spatial and temporal extent of the data used in the estimator should be limited to the region in which parameters of the arrival are constant within the resolving power of the

decomposition algorithm. While the exact size of the spatial aperture would depend upon the amplitude, phase characteristics, and wavefront curvature specific to the given experiment, it would not be infinite except in the case of a true plane wave. Likewise, in the time dimension, the duration, bandwidth, and the spectral level of the wavelet with respect to the uncorrelated noise allow better estimation of the amplitude and arrival time through filtering and the use of a correlation receiver structure [van Trees, 1968] than the simplistic point-wise waveform estimate implied by a slant stack and first motion, or peak pick. In essence, the domain in which data should be used for a particular parameter estimate depends on the local signal structure, coherency, and signal to noise ratio. Chapter 3 deals with the signal processing which more fully utilizes the structure of the signal to obtain better parameter estimates.

Practical Aspects of Data Acquisition and Inversion Uniqueness

In experimental work most datasets are probably inadequate to admit complete treatment by large aperture stacking. For many experiments the aperture over which the coherent aspects of the processing may be carried out is limited by the navigational accuracy of the source (and receiver) ships. The fact that it doesn't really make much difference if widely separated traces are out of registration due to navigation errors is a reflection of the fact that the largest contribution to the slant stack integral (equation 2.3) comes from a limited region in offset for any given arrival. In practice, the data acquired in the Arctic which are the focus of this work are analysed by relatively small aperture processing over just the array fixed in the ice (<1 km aperture). The shot point location accuracy and source repeatability for this experiment are inadequate to allow a synthetic aperture to be constructed over multiple shots. From the short aperture slant stacks or plane wave decompositions of the data, the propagation parameters of the local plane wave components of the wave-field are estimated. The collection

of these local decompositions is not adequate for unique reconstruction of the wavefield everywhere when the collection was not computed from data taken over *all* offsets because the net transform generated does not reflect the true amplitude decay with range from the shot. If one tries to extrapolate the wavefield to unobserved offsets a local plane wave that appears over a limited range of offsets gets extrapolated to all offsets, i.e. it is interpreted as a true plane wave. From this it follows that the collection of short aperture stacks is also inadequate for unique inversion of an earth velocity structure model. However, the imposition of prior knowledge and physical constraints allows the construction of reasonable models from the available decompositions which predict the observed data. The methods used will be enumerated in chapter 4.

In this work the short aperture stacks are used to estimate the parameter needed most often for current travel time inversion procedures- delay time τ as a function of slowness, p. In addition, the use of a small aperture conditions the piecewise estimated $\tau(p)$ function on the nominal offset, x, for which the slant stack was carried out. The resulting $x(p)$ function has been shown to be a useful datum in inversion procedures on its own merits [Dorman and Jacobsen, 1981; Orcutt, et al., 1980], although chapter 4 will show that some care must be taken in its use. For most of the inversions carried out for this work, emphasis is placed on travel time and offset aspects of the data. For these travel time parameter inversions the estimation of the waveform of an event is clearly not necessary, but only its offset, arrival time, and slowness coordinates. In fact, it is desirable to implement an estimate of these quantities that is insensitive to such details as the phase shift of the arrival. In this and chapters 3 and 4 it is shown that the velocity spectrum, which is just a running short-time estimate of the plane wave decomposition, provides such an estimator.

PROPAGATION MODELS

Motivation

To understand what the plane wave decomposition does, the forward problem must first be solved. Since the point source is the only commonly used source* in most experimentation, analysis for the 3-D wave equation in a laterally homogeneous isotropic medium will be the prime focus of this work. Only the acoustic wave equation will be considered, since signal processing is the primary concern, and dealing with the elastic case would present needless notational complexity. This is not excessively restrictive for the work to be carried out because of two facts. First, the sources and receivers used are located in the water column, and thus only compressional waves (generated and detected by *pressure* devices) are supported at the source and receiver locations. Conversions to SV waves (vertically polarized shear- the only type of shear wave that can be excited in a laterally homogeneous medium by a compressional source) in the sediment, crust, and mantle can be adequately described by plane wave reflection/transmission coefficients. Second, because of the ability of the slant stacking/velocity spectral analysis algorithms to separate arrivals with different propagation paths, and the long wavelengths used *vis a vis* the possible layering in the sediments, a decomposition by individual "rays" is possible, and reflection conversion mechanisms are interpreted on a path by path basis. For this reason, it is natural to use the WKBJ synthetic seismogram method [Chapman, 1978] to generate synthetics for comparison with the data, to test algorithms, and to explain the actions of the various processing methods analytically.

*Line sources are currently used by the oil exploration industry, but have their major axis along lines in the radial direction, or measurement direction, not orthogonal to it, and are hardly infinite in length. The primary purpose of the line arrays is to provide velocity filtering, ie. additional weighting to the point source plane wave expansion to limit multiples. The small orthogonal extent of the arrays is used to diminish side-swipe somewhat.

To check the WKBJ method, and to model the effects of multiples due to the free surface reflections, both at the source and receiver, and for multiply turning rays, without having to exhaustively specify the required kinematic groups, an approximate normal mode method using a modification of the Bohr-Sommerfeld eigenvalue equation to get the required dispersion relations is used. This method leads to a relatively efficient method for computation of the complete acoustic field at the short ranges typical of a refraction experiment. It does not work as well for long-range propagation due to approximation errors for the lower order modes, and small phase velocity errors for the higher modes become appreciable at long ranges, thus giving poor results when the solution depends on having many modes superposed and interfering with each other correctly [Tolstoy and Clay, 1966].

For the long-range propagation analysis in a laterally homogeneous medium, the most expedient decomposition of the solution is not rays, but normal modes. For the low order modes of interest, a state variable technique for solution of the vertical wave equation with a general velocity-depth function is described later in this chapter. It will be shown how the modal decomposition can be used to solve for the medium properties when the dispersion curves of the highly dispersive lower order modes are measured by spectrogram and velocity analysis techniques. In this chapter the forward problem is presented, but the inverse problem is deferred to chapter 6.

Notation

For subsequent developments, the following notation and definitions will be used:

Fourier Transform (temporal)

$$F(\omega) = \int_{-\infty}^{\infty} f(t) e^{-i\omega t} dt$$

$$f(t) = \frac{1}{2\pi}\int_{-\infty}^{\infty} F(\omega)e^{-i\omega t}d\omega$$

Fourier Transform (spatial)

$$F(k) = \int_{-\infty}^{\infty} f(x)e^{-ikx}dx$$

$$f(x) = \frac{1}{2\pi}\int_{-\infty}^{\infty} F(k)e^{-ikx}dk$$

A progressive plane wave traveling in the $-x$ direction at frequency ω and wavenumber k_x is written:

$$e^{i(kx-\omega t)}$$

The Hilbert transform is defined by:

$$H^{-}[F(\omega)] = \bar{F}(\omega) = -isgn(\omega)F(\omega)$$

$$H^{-}[f(t)] = \bar{f}(t) = f(t) * \frac{-1}{\pi t}$$

where "*" denotes the convolution operation. The semi-standardized variables used in this thesis are given in table 2.1.

TABLE 2.1

VARIABLE	REPRESENTATION
Lame's constants	λ, μ
density	ρ
bulk modulus	$k = \frac{3\lambda+2\mu}{3} = \lambda$ (acoustic case)
Poissons ratio	$\sigma = \mu(3\lambda+2\mu)/\lambda+\mu$
displacement potential	ϕ
velocity potential	ψ
particle displacement	$\nabla\phi$
particle velocity	$-\nabla\psi$
pressure	$P = -\lambda\nabla^2\phi = \rho\frac{\partial\psi}{\partial t} = -\rho\frac{\partial^2\phi}{\partial t^2}$

TABLE 2.1 (continued)

VARIABLE	REPRESENTATION
spherical radius	R
cylindrical radius, offset	r
depth	z
turning point depth	z_r
wave speed	$c(z)$
compressional wave speed	$c(z) = ((\lambda+2\mu)/\rho)^{1/2}$
shear wave speed	$c(z) = (\mu/\rho)^{1/2}$
slant stack, 2-D	$u(\tau,p)$
2-D plane wave decomposition	$U(\omega,\omega p) = U(\omega,k_r)$
frequency, radians/s	ω
frequency, Hz	f
2-D surface offset	x
proper (3-D) slant stack	$u_{3D}(\tau,p)$
plane wave decomposition	$U_{3D}(\omega,\omega p) = U_{3D}(\omega,k_r)$
Heaviside step function	$H(t)$
time	t
intercept time	τ
horizontal slowness	p
vertical slowness	ν
radial wavenumber	k_r
free space wavenumber	k
Rayleigh reflection coeff.	$R_R(p)$
generalized reflection coeff.	$R(\omega,p)$ or $R(\omega,p,z)$
source depth	z_s
receiver depth	a_r
generalized plane wave imp. resp.	$R(\tau,p)$ or $R(\tau,p,z)$
normal mode expansion coeff.	a_m
sound speed at source	c_s
aperture amplitude distribution	$w_r(\omega,r)$
array response or beampattern	$W(\omega,p)$
spectral analysis window taper	$w_s(t)$

The Wave Equation

The inhomogeneous wave equation for displacement potential is given by:

2.4

$$\frac{\partial^2}{\partial t^2}\phi = c^2\nabla^2\phi + \frac{\Phi_s}{\rho}$$

where Φ_s is the source force potential, with the force being given by $\underline{f} = \nabla\Phi_s$.*

It is often very convenient to use the displacement potential, ϕ, as the field variable since generalizing to the elastic wave formulation is straightforward, and different receiver types are easily introduced (eg. pressure, velocity, displacement). However, for the rest of this work, the pressure itself will be dealt with since this is more physical for our application. All results shown for pressure can apply for the displacement potential after dividing the source function by the local density and integrating it twice with respect to time. Since pressure is given by:

2.5

$$P = -\rho\frac{\partial^2}{\partial t^2}\phi = -k\nabla^2\phi$$

it is seen that the pressure wave equation may be written:

2.6

$$\frac{\partial^2}{\partial t^2}P = c^2\nabla^2 P + P_s.$$

In most marine work, the source is characterized by the pressure function at some reference distance, $|\underline{R}_0|$, from the "source location", usually assumed to be delta-like in space. For explosive "point" sources in 3 dimensions, the pressure signature at the reference distance is nearly a string of impulses, so it is most natural to express the time evolution of the source function, P_s as an impulse (Dirac delta function). This is a result of the well known solution

---

*To see that the proper units for Φ_s are pressure, recall that in an acoustic medium: $P = -k\nabla^2\phi$. Φ_s/ρ must have the same dimensions as $c^2\nabla^2\phi = k/\rho\nabla^2\phi$. Thus Φ_s has the same dimensions as $k\nabla^2\phi$, which is pressure, and the source function should be expressed in terms of pressure when working with the displacement potential wave equation.

for eqn. 2.6 when the sound speed, c, is a constant in an infinite medium for $P_s = \delta(\underline{R})\delta(t)$:

$$P(t,\underline{R}) = \frac{1}{4\pi c^2|\underline{R}|}\delta(t-|\underline{R}/c|) \qquad |\underline{R}| = (x^2+y^2+z^2)^{1/2} \tag{2.7}$$

[Aki and Richards, 1980 p. 65]. From this it is seen that when specifying the displacement potential source, the time evolution must be two integrations higher than the pressure measured at some (nearby) reference offset.

To motivate the slant stacking operation for processing of seismic data from laterally homogeneous, but depth varying models, the solution of the wave equation (2.6) when $c=c(z)$ must be obtained. To do this we first consider $c(z)$ to be constant and the spatial and temporal Fourier transforms as defined above are taken of eqn. 2.6. In Cartesian coordinates this yields the representation of the point source:

$$P(\underline{R},\omega) = \frac{1}{4\pi c^2|\underline{R}|}e^{i\omega(|R|/c)} = \frac{1}{4\pi c^2}\frac{1}{2\pi^2}\int\int_{-\infty}^{\infty}\int\frac{e^{i\underline{k}\cdot\underline{R}}}{k^2-\frac{\omega^2}{c^2}}d\underline{k} \tag{2.8}$$

where $k = |\underline{k}|$ [Aki and Richards, 1980 p. 195]. This can be written as the Sommerfeld integral:

$$P(\omega,r,z)=\frac{i}{4\pi c^2}\int_0^{\infty}\frac{k_r J_0(k_r r)e^{ik_z|z|}}{k_z}dk_r \tag{2.9}$$

after changing variables $\underline{R} = (x,y,z) \Rightarrow (r,\theta,z) = ((x^2+y^2)^{1/2}, \tan^{-1}(y/x), z)$ from Cartesian to cylindrical coordinates and carrying out the integration over k_z. For this expression, the wavenumbers have been changed to k_r for the radial variable, r, and k_z for the depth variable, z. Note that the source has been located at $z=0$ and there is azimuthal, (θ), symmetry. The following branch definition is made:

$$k_z = \left(\frac{\omega^2}{c^2} - k_r^2\right)^{\frac{1}{2}} \qquad \mathrm{IM}[k_z] > 0. \tag{2.10}$$

In terms of the ray parameter, or horizontal slowness, p, usually used in vertically stratified problems:

$$k_r = \omega p \qquad k_z = \omega \nu \qquad \nu = (c^{-2} - p^2)^{\frac{1}{2}} \tag{2.11}$$

where ν is the vertical slowness. The Sommerfeld integral is rewritten:

$$\frac{1}{4\pi c^2 |\underline{R}|} e^{i\omega |R|/c} = \frac{i\omega}{4\pi c^2} \int_0^\infty \frac{p\, J_0(\omega p r)\, e^{i\omega \nu |z|}}{\nu} dp \tag{2.12}$$

where the ω integration contour needed to get back to the time domain has not yet been specified. In general, for real k_r and p integration paths, $arg(\omega) = -arg(p)$, and an absolute value on ω suffices [Chapman, 1978]. The key is to keep the integral conjugate symmetric so that the resulting time series are real.

The Reflectivity Method

To move to the depth varying case, we draw an analogy with Lamb's problem [Aki and Richards, 1980, chap. 4] for a point source and receiver in a homogeneous half space above a half space with different parameters. Once the field described by eqn. 2.12 is established in a region around the source point in which the medium is somewhat homogeneous, the response of the entire model to the point source function can be written as the superposition of the responses to each plane wave component. (The superposition is really of cylindrical waves, but I will go along with the established nomenclature.) This superposition is written as:

$$P(\omega, r, z) = \frac{i\omega}{4\pi c_s^2} \int_0^\infty \mathrm{R}(\omega, p, z) J_0(\omega p r)\, p\, dp \tag{2.13}$$

where for Lamb's problem:

$$R(\omega,p,z=h_r) = \frac{R_R(\omega,p)}{v(h_s,p)} e^{i\omega v(h_s-h_r)}$$

and $R_R(\omega,p)$ is the net Rayleigh reflection coefficient for the layered halfspace below the source/receiver region, h_r, h_s are the receiver and source heights above the layered halfspace, the exponential is due to the propagation delay in the vertical dimension to the boundary, and $v(h_s,p)$ is the weighting term due to the point source decomposition. The boundary between the half-spaces is located at $z=0$. So called "spectral" synthetic seismogram methods determine the $R(\omega,p)$ function using a model for the reflecting region and carry out the slowness integral first, then get the temporal response through the inverse Fourier transform of eqn. 2.13 [Fuchs and Muller, 1971; Kennett, 1974]. The "Rayleigh" reflection coefficient, R_R, is dependent upon frequency as well as slowness because of the layering. Note that the source directivity ($1/v$) factor is included in the reflection coefficient. Recovery of this net reflection coefficient can be used in inverse problem formulations that use a Gelfand-Levitan structure to recover the impedance profile of the layered medium when $R(k)$ is measured as in normal-incidence wideband experiments, or harmonic source, varying offset, experiments [Frisk, et al., 1981]. Formally, the velocity/depth and density/depth functions can both be recovered when $R(\omega,p)$ is measured with frequency and slowness being varied independently [Hooshyar and Razavy, 1983] although this has not been done practically.

The Ray Expansion

In many practical applications the reflection coefficient can be expressed as the sum over a dominant subset of the internal multiple reflections, or possible ray paths. In this case the reflection coefficient is expanded as:

$$R(\omega,p,z) = \sum_{i \in I} R_i(\omega,p,z) \qquad 2.14$$

where the members of the set I are the kinematic ray groups needed. Note that each term in the sum may be a product of many single interface reflection/transmission coefficients. The depth dependence of the receiver, z, has been included for generality. Instead of parameterizing the medium as many thin homogeneous layers and taking all possible internal multiples using the Thomson-Haskell propagator matrix formulation, as in the reflectivity method, only major interfaces are specified, and a more general gradient structure is used between the interfaces. Each possible ray path is included explicitly. This characterization is often more enlightening than the net Rayleigh reflection coefficient method because the medium often supports only a few of these paths sufficiently for the arrivals to be observed above the ever-present measurement noise. If the paths can be identified from the observed data it will be seen that much can be said about the structure of the medium. In addition, for synthetics, the response to each individual term, R_i, often has a very simple approximation which leads to efficient evaluation of the frequency or slowness integrals. Analytical evaluation of the frequency integral after using the WKBJ approximation for the reflection coefficient is the basis of the WKBJ synthetic seismogram method [Chapman, 1978], and will be outlined later in this chapter.

The Normal Mode Method

A third popular method for the solution of the wave equation (2.6) is to set up boundary conditions for the layered medium that lead to an eigenvalue problem in the z-direction for solutions of the homogeneous version of the equation. The homogeneous equation is separable for models which vary only with depth, and it can be shown that the homogeneous solutions, or modes, can be superposed to solve the inhomogeneous problem, eqn 2.6. The reflection coefficient can be expressed as:

$$R(\omega,p,z) = -4\pi c_s^2 i \sum_{m \in M} a_m(\omega,p)\phi_z^m(\omega,z) \qquad 2.15$$

where the a_m are the expansion coefficients for each mode, and are given by (see eqn 2.49):

$$a_m(\omega,p) = \frac{-1}{2\pi c_s^2} \frac{\phi_z^m(\omega,z_s)}{(k_m^2(\omega)-\omega^2 p^2)} \qquad 2.16$$

Where $k_m(\omega)$ and $\phi_z^m(\omega,z_s)$ are the eigenvalue and normalized eigenfunction for mode m at frequency ω evaluated at the source depth, z_s. The pole dependence of the a_m on p allows the slowness integral in eqn. 2.13 to be solved analytically, and leaves only the inverse temporal Fourier transform to be evaluated. This is exactly the opposite of the WKBJ method, a so-called "slowness" technique, which allows the frequency transform to be performed analytically, and leaves the slowness integral for numerical evaluation. In the following sections, the WKBJ and normal mode synthetic seismogram methods are discussed, and the signal processing needed to recover the various representations of the reflectivity function, $R(\omega,p,z)$, from observed data are derived. Again, estimation of these functions is an intermediate step in most inversion algorithms used for the recovery of the sound speed or density/depth profiles. It will turn out that the ray expansion of the WKBJ method is most useful for short range propagation in which dispersion effects are minimal, and that the mode analysis is better applied to long range propagation in which the geometrical dispersion characteristics of the medium can be exploited.

THE WKBJ METHOD AND THE PLANE WAVE DECOMPOSITION

The WKBJ Synthetic Seismogram Method

To motivate the use of the plane wave decomposition operation for estimation of $R(\tau,p,z)$ or $R(\omega,p,z)$, the WKBJ synthetic seismogram method is derived. To do this recall

the expression for the response to a harmonic pressure source, eqn. 2.13:

$$P(\omega,r,z) = \frac{i\omega}{4\pi c_s^2}\int_0^\infty R(\omega,p,z)J_0(\omega pr)\,p\,dp. \qquad 2.13$$

The time response is obtained by inverse Fourier transforming over the contour $arg(\omega) = -arg(p)$ since the k_r integration was real [Chapman, 1978]. To obtain a real time series, the conjugate symmetry of $P(\omega,r,z)$ is enforced.

$$P(\omega,r,z) = P^*(-\omega,r,z). \qquad 2.17$$

For high frequencies and large ranges ($\omega pr \gg 1$) eqn. 2.13 can be approximated. First, $J_0(\omega pr)$ is rewritten as:

$$J_0(\omega pr) = \tfrac{1}{2}[H_0^{(1)}(\omega pr)+H_0^{(2)}(\omega pr)] = \tfrac{1}{2}[H_0^{(1)}(\omega pr)-H_0^{(1)}(-\omega pr)]$$

[Abramowitz and Stegun, 1964, p. 361, eqn. 9.139] giving eqn. 2.13 as:

$$P(\omega,r,z) = \frac{i|\omega|}{4\pi c_s^2}\frac{1}{2}\int_{-\infty}^{\infty} R(\omega,p,z)H_0^{(1)}(\omega pr)\,p\,dp. \qquad 2.18$$

The absolute value must be used to keep $P(\omega,r,z)$ conjugate symmetric. If expressions valid only for $\omega>0$ are written under the implicit assumption that $P(\omega,r,z)$ is conjugate symmetric, then the absolute value may be dropped. The $H_0^{(2)}$ term, and thus the negative p integration region in eqn 2.18 represent waves that are converging on the point source. In evaluating 2.18 these give a negligible contribution and may be eliminated [Chapman, 1978]. The first term of the asymptotic expansion for the Hankel function is:

$$\tfrac{1}{2}H_0^{(1)}(\omega pr) \approx \frac{1}{(2\pi\omega pr)^{\frac{1}{2}}}e^{i(\omega pr-\pi/4)} \qquad 2.19$$

Inserting 2.19 into 2.18 yields:

$$P(\omega,r,z) = \frac{|\omega|\frac{e^{i\pi/4}}{\omega^{1/2}}}{4\pi c_s^2\sqrt{2\pi r}}\int_{-\infty}^{\infty} R(\omega,p,z)e^{i\omega pr}p^{1/2}dp \qquad 2.20^*$$

For a homogeneous medium, comparing 2.20 and 2.12, the reflection coefficient for the direct arrival should be given by:

$$R(\omega,p,z) = \frac{e^{i\omega\nu|z|}}{\nu} \qquad 2.21$$

where $\nu = (c^{-2}-p^2)^{1/2}$ is the vertical slowness [Aki and Richards, 1980, p. 199]. If the vertical component of the wave equation is solved using the WKBJ approximation (see appendix 1), then the generalized reflection coefficient is given by (A1.30):

$$\begin{aligned} R(\omega,p,z) &= \prod_j T_j(p)\frac{\nu^{1/2}(z_s)}{\nu(z_s)\nu^{1/2}(z)}e^{i\omega\int_{z_s}^{z}\nu(x)dx} \\ &= \prod_j T_j(p)\frac{1}{\nu^{1/2}(z_s)\nu^{1/2}(z)}e^{i\omega\int_{z_s}^{z}\nu(x)dx} \end{aligned} \qquad 2.22$$

for the direct wave. Note that this matches to the homogeneous solution for $\nu(z) = \nu$, constant. The $1/\nu(z_s)$ in the first equation of 2.22 comes from the weighting of the plane wave components for the source spherical wave from the Sommerfeld integral. The product of the $T_j(p)$ is the accumulated transmission/reflection coefficient effect for any discrete impedance interfaces through which the ray travels. For a ray which turns n times the reflection coefficient is given by (A1.42):

---

*Note that the definition $e^{i\pi/4}/\omega^{1/2} = e^{i\pi/4\,\mathrm{sgn}(\omega)}/|\omega|^{1/2}$ has been used, corresponding to the positive imaginary branch of $\omega^{1/2}$. This makes the function conjugate symmetric.

$$R(\omega,p,z) = \prod_j T_j(p) \frac{1}{v(z_s)} \left[\frac{v^{1/2}(z_s)}{v^{1/2}(z_t)} e^{i\omega \int_{z_s}^{z_t} v(x)dx} \right] (-isgn(\omega))^n \left[\frac{v^{1/2}(z_t)}{v^{1/2}(z)} e^{-i\omega \int_{z_t}^{z} v(x)dx} \right] \quad 2.23$$

$$= \prod_j T_j(p) \frac{(-isgn(\omega))^n}{v^{1/2}(z_s) v^{1/2}(z)} e^{i\omega \left(\int_{z_t}^{z_t} v(x)dx + \int_{z}^{z_t} v(x)dx \right)}$$

where formal cancellation of the zeros in the numerator and denominator is used. The depth z_t is the turning point depth of the ray where the horizontal slowness equals the medium slowness. For surface located source and receiver, 2.23 becomes:

$$R(\omega,p,z=0) = \prod_j T_j(p) \frac{(-isgn(\omega))^n}{v(0)} e^{i\omega\tau(p)} \quad 2.24$$

where $\tau(p)$ is the vertical component of the geometrical two-way travel time through the medium from source to receiver given by:

$$\tau(p) = t(p) - p\,x(p) = \int_{z_s=0}^{z_t} v(x)dx + \int_{z=0}^{z_t} v(x)dx \quad 2.25$$

where $t(p)$, $x(p)$ define the travel time curve, $t(x)$, parameterized by horizontal slowness, p. The term $R(\omega,p,z=0)$ in eqn 2.24 is an example of one of the R_i in equation 2.14.

To complete the WKBJ method as it appears in the literature [Chapman, 1978], equation 2.24 is substituted into 2.20:

$$P(\omega,r,z) = \frac{|\omega| \frac{e^{i\pi/4}}{\omega^{1/2}}}{4\pi c_s^2 \sqrt{2\pi r}} \int_{-\infty}^{\infty} B(\omega,p)\, e^{i\omega(pr - \tau(p))} p^{1/2} dp$$

with the definition:

$$B(\omega,p) = \prod_j T_j(p) \frac{(-isgn(\omega))^n}{v(0,p)}$$

in which the dependence of ν on p is noted. Weighting this by the source spectrum of the pressure at a reference distance and recognizing that [eg. Chapman, 1978]:

$$|\omega| = (i\omega)(-isgn(\omega)) \iff -\frac{d}{dt}\mathrm{H}^{-}[\,]$$

$$\pi^{1/2}\frac{e^{+i\pi/4}}{\omega^{1/2}} \iff \frac{H(t)}{t^{1/2}}$$

$$\pi^{1/2}\frac{e^{-i\pi/4}}{\omega^{1/2}} \iff \mathrm{H}^{-}\left[\frac{H(t)}{t^{1/2}}\right] = \frac{H(-t)}{(-t)^{1/2}}$$

gives:

$$P(t,r,z) = \frac{1}{4\pi^2 c_s^2\sqrt{2r}}\int_{-\infty}^{\infty} d\omega\pi^{1/2}\frac{e^{+i\pi/4}}{\omega^{1/2}}S(\omega)(-i\omega)(-isgn(\omega))\int_{-\infty}^{\infty}B(p)e^{i\omega(pr-\tau(p)-t)}\,p^{1/2}dp$$

$$= \frac{-d/dtS(t)}{4\pi^2 c_s^2\sqrt{2r}} * \frac{H(-t)}{(-t)^{1/2}} * \int_{-\infty}^{\infty} p^{1/2}B(p)\,\delta(\theta(p)-t)\,dp$$

where

$$\theta(p) = \tau(p) + pr \qquad 2.26a$$

is the "arrival time" of the wave with slowness p at range r. This equation is valid for $B(p)$ real. In general $B(p)$ will be complex and conjugate symmetric in ω due to turning point phase shifts, post-critical reflections, etc. and an analytic time series formulation is used. The complex B is denoted by $\bar{B}$. This results in:

$$P(t,r,z) = \frac{-d/dtS(t)}{4\pi^2 c_s^2\sqrt{2r}} * \qquad 2.26b$$

$$\left[\frac{H(-t)}{(-t)^{1/2}} * \int_{-\infty}^{\infty} p^{1/2}\mathrm{RE}[\bar{B}(p)]\,\delta(\theta(p)-t)\,dp + \frac{H(t)}{t^{1/2}} * \int_{-\infty}^{\infty} p^{1/2}\mathrm{IM}[\bar{B}(p)]\,\delta(\theta(p)-t)\,dp\right]$$

Making the change of variables $u = \theta(p)$ and evaluating the integral leads to:

$$P(t,r,z) = \frac{-d/dtS(t)}{4\pi^2 c_s^2\sqrt{2r}} * \mathrm{RE}\left\{\left[\frac{H(-t)}{(-t)^{1/2}} - i\frac{H(t)}{t^{1/2}}\right] * \sum_{\theta(p)=t} \frac{p^{1/2}\bar{B}(p)}{\left|d\theta(p)/dp\right|_r}\right\}. \qquad 2.26c$$

Chapman [1978] smooths over two sampling intervals, Δt, to avoid the singularity in $d\theta/dp$ at the geometrical arrivals, and obtains

$$\left|\frac{d\theta(p)}{dp}\right| \approx \frac{2\Delta t}{\Delta p_{2\Delta t}} \qquad 2.26$$

and writes the seismogram as:

$$P(t,r,z) = \frac{-d/dtS(t)}{4\pi^2 c_s^2\sqrt{2r}} * RE\left\{\left[\frac{H(-t)}{(-t)^{1/2}} - i\frac{H(t)}{t^{1/2}}\right] * \sum_{\theta(p)=t=\Delta t} p^{1/2}\bar{B}(p)\right\}. \qquad 2.26e$$

or

$$P(t,r,z) = \frac{-d/dtS(t)}{4\pi^2 c_s^2\sqrt{2r}} * RE\left\{\left[\frac{H(-t)}{(-t)^{1/2}} - i\frac{H(t)}{t^{1/2}}\right] * \sum_{\theta(p)=t} \frac{p^{1/2}\bar{B}(p)\Delta p_{2\Delta t}}{2\Delta t}\right\}. \qquad 2.26f$$

Common values of $\bar{B}(p)$ are:

$$\begin{aligned}
\bar{B}(p) &= \frac{\prod_j T_j(p)}{v(0,p)}(1+0i) && \text{Direct ray}\\
\bar{B}(p) &= \frac{\prod_j T_j(p)}{v(0,p)}(0-1i) && \text{Single turning ray}\\
\bar{B}(p) &= \frac{\prod_j T_j(p)}{v(0,p)}(1+0i) && \text{2 turns + 1 free surface reflection}\\
\bar{B}(p) &= \frac{\prod_j T_j(p)}{v(0,p)}(0+1i) && \text{3 turns + 2 free surface reflections}
\end{aligned} \qquad 2.26g$$

Note that the analytic time series formulation just replaces the Hilbert transform with the proper convolution. For any time, t, the sum is thus carried out by integrating the weighted reflection coefficient over the regions in slowness for which $\theta(p)$ is within Δt of t. There can be multiple p regions for which this is true at a given time, t. An example plot of a θ curve

and the integration interval is shown in fig. 2.2 for two arrival times. At time t_1, there are two arrivals and the sum in 2.26b is approximately:

$$\sum = p_{1a}^{-\frac{1}{2}} B(p_{1a}) \Delta p_{1a} + p_{1b}^{-\frac{1}{2}} B(p_{1b}) \Delta p_{1b}$$

At time t_2 there is only one arrival, but it is at an inflection in the θ curve, giving a much larger response:

$$\sum = p_2^{-\frac{1}{2}} B(p_2) \Delta p_2$$

as a result of the larger slowness interval, Δp_2, for an approximately fixed $B(p)$. The inflection corresponds to a geometrical arrival time, since

$$0 = \frac{d}{dp}\theta(p) = \frac{d}{dp}(\tau(p) + pr) = -x(p) + r$$

and thus $r = x(p)$, the geometrical offset. Chapman [1978] has shown that the WKBJ method reduces to the geometrical ray theoretic result at the inflection points.

The Plane Wave Decomposition and Slant Stacking

It can be seen from equation 2.24, that if $R(\omega,p)$ can be recovered, much can be said about the medium. Neglecting the phase shift effects due to the possible post-critical reflections and the turning point term, and assuming that the source can be deconvolved to obtain the impulse response, $R(\omega,p)$, the travel time can be obtained through $\tau(p)$, and this may be formally inverted by the Herglotz-Wiechert formula*:

$$z(p) = \frac{1}{\pi} \int_0^{\tau(p)} (p^2(\tau) - p^2)^{-\frac{1}{2}} d\tau \qquad 2.27$$

---

*This assumes that τ is a continuous and monotonically decreasing function of p. When low velocity zones are present this assumption breaks down. An analysis of this case is given by Gerver and Markushevich [1966].

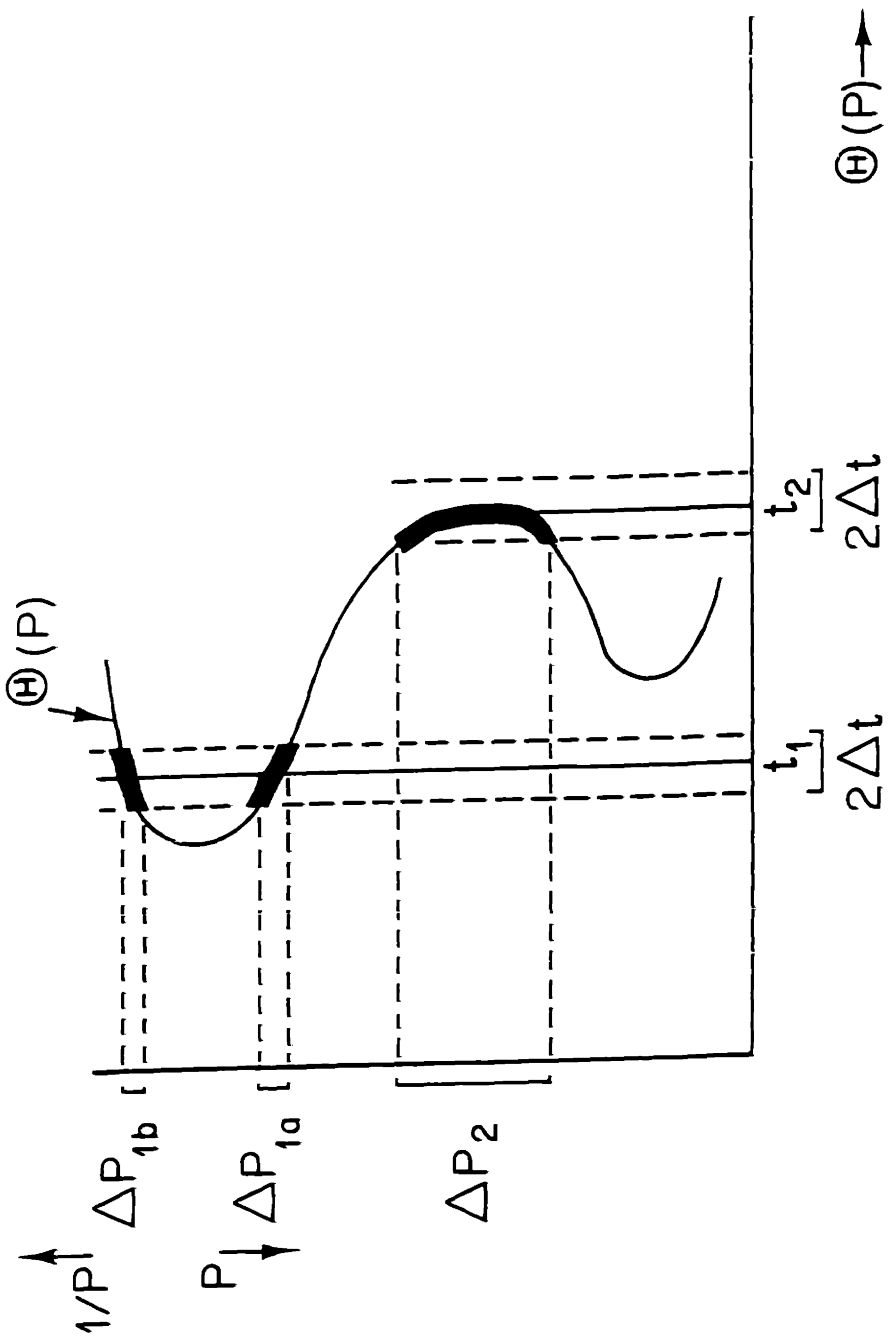

Fig. 2.2) The θ function used in the WKBJ synthetic seismogram method showing the smoothing regions.

[Aki and Richards, 1980, p.656], or by any number of the more numerically expedient methods outlined in chapter 4. The major difficulty in most travel time inversion schemes is removal of source effects, separation of the turning point and reflection/transmission phase shifts from the propagation phase, and identification of the travel path when the model and source/receiver geometries support multipath propagation. Note that the expressions 2.22-2.24 are not the net generalized reflection coefficients, but just one of the terms in the expansion 2.14. The net reflection coefficient is due to all kinematic groups that the model supports, and any observations will consist of the superposition of these responses.

Disregarding all the problems listed above, the inverse operation for equation 2.13 is needed to recover $R(\omega,p)$. Instead of inverting the approximate form, 2.20, the Fourier-Bessel transform (2.13) is dealt with directly. The transform relations:

$$\frac{\delta(r-r_0)}{r} = \int_0^\infty J_0(kr_0)J_0(kr)\,k\,dk$$
$$J_0(kr_0) = \int_0^\infty \frac{\delta(r-r_0)}{r} J_0(kr)\,r\,dr \qquad 2.28$$

lead to the fact that the Fourier-Bessel transform is its own inverse operation, thus:

$$x(r) = \int_0^\infty X(k)J_0(kr)\,k\,dk$$
$$X(k) = \int_0^\infty x(r)J_0(kr)\,r\,dr. \qquad 2.29$$

From this it is seen that the inverse operation for equation 2.13 is:

$$R(\omega,p,z) = \omega^2\frac{4\pi c_s^2}{i\omega}\int_0^\infty P(\omega,r,z)J_0(\omega pr)\,r\,dr$$
$$= -i\omega 4\pi c_s^2\int_0^\infty P(\omega,r,z)J_0(\omega pr)\,r\,dr \qquad \text{(proper slant stack)} \qquad 2.30$$

where the leading ω^2 term in the first equation comes from the change of variables, $k = \omega p$, and P is the Fourier transform of the pressure *impulse* response of the medium. Note that the time derivative ($-i\omega$ factor) of the "proper slant-stack" [Treitel, et al., 1982] embodied in the integral transform of eqn. 2.30 must be taken to obtain the generalized reflection coefficient*. As has been noted by many authors [Henry, et al., 1980; Phinney, et al. 1981; Treitel, et al., 1982], the slant stack defined in eqns. 2.2 and 2.3 is valid only for the 2-dimensional problem with a line source. The proper, 3-D, slant-stack requires a Fourier-Bessel, or Hankel transform if no approximations are to be made.

One of the key issues to note is that in general, $P(\omega,r,z)$ is sampled on an "r" or offset grid that is not well suited for direct evaluation of the Fourier-Bessel transform. The work by Henry, et al. [1980] is an interesting approach to the problem and solves the equivalent of equation 2.13 for $R(\omega,p,z)$ as a least squares inverse problem via a large matrix equation. For the Arctic data, the sampling in offset space is completely unsuited for any direct evaluation of 2.30, so a hybrid analytical/estimation theory approach is taken. What is available from the Arctic data is a sparse 2-D surface coverage with groups of approximately 24 dense samples ($\lambda/3$ to $\lambda/15$ spacings) covering an aperture of 20 λ to 4 λ with 2.5 to 10 km gaps between the groups (corresponding to 50−200 λ at the highest practical frequency, 30 Hz, and 10−40 λ at the lowest practical frequency, 6 Hz). As a result, this work will concentrate on relating the operations that can be performed on a small aperture to the desired transform, 2.30.

Since the standard slant-stack (eqn. 2.2, 2.3) has such a simple form, it is unfortunate that it is not the correct operation to perform. However, if the large argument expansion for the Bessel function is used again, the approximate expression for 2.30 in eqn. 2.32 can be

written which includes the standard (2-D) slant stack operation and a filtering operation. This is obtained by the following operations. In the frequency domain, the operations in equations 2.16 through 2.19 can be repeated, replacing the expansion of $J_0(\omega pr)$ by $\frac{1}{2}[H_0^{(1)}(\omega pr)-H_0^{(1)}(-\omega pr)]$ with $\frac{1}{2}[-H_0^{(2)}(-\omega pr)+H_0^{(2)}(\omega pr)]$. The principle asymptotic form of $\frac{1}{2}H_0^{(2)}(\omega pr)$ is:

$$\tfrac{1}{2}H_0^{(2)}(\omega pr) \approx \frac{1}{(2\pi\omega pr)^{\frac{1}{2}}} e^{-i(\omega pr-\pi/4)}.$$

Thus, 2.30 becomes:

$$R(\omega,p,z) = -i|\omega|4\pi c_s^2 \int_{-\infty}^{\infty} r\,dr\,P(\omega,r,z)\frac{1}{(2\pi\omega pr)^{\frac{1}{2}}} e^{-i(\omega pr-\pi/4)} \qquad 2.31$$

$$= \frac{-i|\omega|4\pi c_s^2}{\sqrt{2\pi p}} \frac{e^{+i\pi/4}}{\omega^{\frac{1}{2}}} \int_{-\infty}^{\infty} P(\omega,r,z)\,e^{-i\omega pr}\,r^{\frac{1}{2}}dr$$

where, again, the $|\omega|$ term is used to enforce conjugate symmetry. The usual expression, valid for $\omega>0$ only is:

$$R(\omega,p,z) = \frac{-i\omega 4\pi c_s^2}{\sqrt{2\pi p}} \frac{e^{+i\pi/4}}{\omega^{\frac{1}{2}}} \int_{-\infty}^{\infty} P(\omega,r,z)\,e^{-i\omega pr}\,r^{\frac{1}{2}}dr \qquad \omega>0 \qquad 2.32$$

where the definitions:

$$\pi^{\frac{1}{2}} \frac{e^{+i\pi/4}}{\omega^{\frac{1}{2}}} \Longleftrightarrow \frac{H(t)}{t^{\frac{1}{2}}} \qquad 2.33$$

$$-i\omega \Longleftrightarrow \frac{d}{dt}$$

$H(t) \equiv$ Unit Step Function

are used to evaluate the inverse temporal Fourier transform of the expression to obtain time domain results. It should be noted that the approximations 2.20 and 2.32 are exact inverse operators. In addition, if the stationary phase peak from 2.20 with $R(\omega,p,z)$ given by 2.21 is

*2.30 is really the temporal Fourier transform of the proper slant stack.

used for $P(\omega,r,z)$, then it is seen that the contribution in 2.31 to get back $R(\omega,p,z)$ comes from $r>0$. Thus, in the same manner that the negative p values (or the $H_0^{(2)}$ term) in 2.20 represent converging solutions at the reflector and are unimportant, the $-r$ region, corresponding to waves diverging from the observation point ($H_0^{(1)}$ term) in 2.31 are unimportant, and the negative r region in the integral is often neglected [Chapman, 1978].

To relate equation 2.31 or 2.32 to the standard slant stack operator, (2.2), one must first note that the observed data is:

$$P_{obs}(\omega,r,z) = S(\omega)P(\omega,r,z) \qquad 2.34$$

where $S(\omega)$ is the (conjugate symmetric) source spectrum. Thus, any operation on $P(\omega,r,z)$ must be on data that has already been deconvolved. It is seen in 2.32 that the data, $P(\omega,r,z)$ is weighted by $r^{\frac{1}{2}}$ to compensate for geometrical spreading effects in a layered waveguide, and then "stacked" over a plane wave trajectory by the Fourier integral:

$$U_{3D}(\omega,\omega p) = \int_0^\infty P(\omega,r,z=0)\, e^{-i\omega pr}\, r^{\frac{1}{2}} dr \qquad 2.35a$$

$$u_{3D}(\tau,p) = \int_0^\infty P(\tau+pr,r,z=0)\, r^{\frac{1}{2}} dr \qquad 2.35b$$

After the stacking operation, in the far-field approximation used, all that must be done is a filtering and scaling operation, where the scaling depends on the stacking parameter, the slowness p. This operation is simply:

$$R(\omega,p,z=0) = \frac{-i\omega 4\pi c_s^2}{\sqrt{2\pi p}} \frac{e^{+i\pi/4}}{\omega^{\frac{1}{2}}} U_{3D}(\omega,\omega p) \qquad \omega>0 \qquad 2.36$$

or in the time domain, the generalized reflection impulse response is:

$$R(\tau,p,z=0) = \frac{d}{d\tau}\frac{4c_s^2}{\sqrt{2p}}\frac{H(\tau)}{\tau^{\frac{1}{2}}} * \frac{1}{2\pi}\int_{-\infty}^{\infty} U_{3D}(\omega,\omega p)\, e^{-i\omega\tau} d\omega \qquad 2.37a$$

$$R(\tau,p,z=0) = \frac{d}{d\tau}\frac{4c_s^2}{\sqrt{2p}}\frac{H(\tau)}{\tau^{\frac{1}{2}}} * \int_0^\infty P(\tau+pr,r,z=0)\,r^{\frac{1}{2}}dr \qquad 2.37b$$

where the terms on the right are the 3-D analogs of equations 2.2 and 2.3.

In this section the operations needed to recover the generalized reflection coefficient, $R(\omega,p,z)$, from the observed pressure data have been derived (eqns. 2.35 and 2.36). Using the generalized reflection coefficient, $R(\omega,p,z=0)$, recovered from the data, equations 2.23, 2.24, and 2.27 indicate how to invert it for velocity/depth structure using the WKBJ approximation. In chapter 3 we will deal with methods for isolation of the $\tau(p)$ function from transmission effects and from responses that contain the source function, not the impulse response. It will be seen how the Fourier transform used to obtain the integrand in equation 2.35 can be more effectively carried out by a sequence of short-time Fourier transforms on each channel. This will lead to signal processing signal to noise ratio gains because each short-time Fourier transform will still contain the transient signal, but not a large window of noise. The offset, (r), integral will also be able to be carried out by the MLM method, giving higher resolution in slowness. All the analyses follow in the same manner as for the infinite time window case, except that the complete functions must then be pieced together in time. We will, in fact, be able to make the time window so short that the expression 2.36 will be able to be indexed on the window start time, t, and a time varying spectral characterization of the reflection coefficient will be obtained. It will be seen that by squaring the short-time estimated $R(\omega,p,z=0)$ function a smoothed time series of the arrival power as a function of frequency and slowness is obtained. This short time power estimate is called the velocity spectrum, $\tilde{S}^2(t,\omega,p)$, and yields a smoothed time series that will be shown to have some nice properties *vis a vis* the estimation of travel-times for inversions. Again, the underlying idea is to separate the components from the individual kinematic groups so that it is a relatively simple matter to

get the underlying model.

THE NORMAL MODE METHOD AND THE PLANE WAVE DECOMPOSITION

Normal Mode Theory

The pressure wave equation for a constant density and an impulsive point source is given by:

$$\ddot{P} = c^2\nabla^2 P + \delta(\underline{R}-\underline{R}_s)\,\delta(t) \qquad 2.38$$

For cylindrical symmetry, the harmonic wave equation obtained by Fourier transforming over time is:

$$-\omega^2 P = c^2\left[\frac{1}{r}\frac{\partial}{\partial r}\left(r\frac{\partial P}{\partial r}\right) + \frac{\partial^2 P}{\partial z^2}\right] + \frac{1}{2\pi}\frac{\delta(r)}{r}\delta(z-z_s)e^{-i\omega t} \qquad 2.39$$

where the source has been located at cylindrical radius $r=0$, and depth $z=z_s$. Defining $\omega^2/c^2 = k^2$:

$$\left[\frac{1}{r}\frac{\partial}{\partial r}r\frac{\partial}{\partial r} + \frac{\partial^2}{\partial z^2} + k^2\right]P = \frac{-1}{2\pi c_s^2}\frac{\delta(r)}{r}\delta(z-z_s)e^{-i\omega t} \qquad 2.40$$

If we consider the model to vary only with z, then $k^2 = k_r^2 + k_z^2(z) = \omega^2/c^2(z)$. This makes the solution to the homogeneous equation in which the right hand side of 2.40 is zero separable into radial and depth components, $P = P_r(\omega,r)P_z(\omega,z)$, with the radial function $P_r = P_r(\omega,r)$ satisfying the zeroth order Bessel Equation:

$$\frac{1}{r}\frac{\partial}{\partial r}r\frac{\partial}{\partial r}P_r + k_r^2 P_r = 0 \qquad 2.41$$

and the homogeneous depth solution, $P_z = P_z(\omega,z)$ satisfying:

$$\frac{\partial^2}{\partial z^2}P_z - (k^2-k_r^2)P_z = 0 \qquad 2.42$$

where k_r is the radial wavenumber and $k_z = (k^2 - k_r^2)^{1/2}$ is the vertical wavenumber. The linearly independent solutions to Bessels equation are:

$$P_r(r) = \begin{cases} J_0(k_r r)) \\ Y_0(k_r r) \end{cases} \qquad 2.43$$

Because the solution of the homogeneous equation is finite at the origin, the Y_0 solution is eliminated. When the boundary condition and model are specified for equation 2.42, k_z^2 assumes a set of discrete values when it is less than $k^2(z)$, the free space wavenumber, in all regions of the model, and a continuous spectrum for values greater than this value (corresponding to radial wavenumbers which are imaginary, and thus exponentially attenuating with range). Only the discrete spectrum is of great importance to typical refraction and long range propagation experiments. For the discrete values of $k_z(\omega)$, denoted γ_m, indexed on mode number, m, the discrete horizontal wavenumbers are $k_m = (k^2 - \gamma_m^2)^{1/2}$. The eigenvalue spectrum can be kept discrete by either assuming a rigid or free boundary at the surface, and a continuously increasing velocity with depth, or a rigid (or free) bottom boundary. In either case of the distribution of the γ_m, the modal solutions of the homogeneous equation,

$$P^m(\omega, r, z) = P_r^m(\omega, r) P_z^m(\omega, z) \qquad 2.44$$

can be scaled to form a complete orthonormal (CON) set. Thus, any particular solution can be represented as a superposition of these homogeneous solutions. This is the standard mode sum:

$$P(\omega, r, z) = \sum_m \int_0^\infty k_r \, dk_r \; a_m(k_r) P_r(\omega, r) P_z^m(\omega, z) \qquad 2.45$$

where

$$P_r(\omega, r) = J_0(k_r r) \qquad k_r = \omega p \qquad 2.46$$

and the k_z are all discrete. Note that the integration yields a superposition of terms that do not satisfy the homogeneous equation. It is from these that the source is synthesized. From 2.40 we want the particular solution for the source function $\frac{-1}{2\pi c_s^2}\frac{\delta(r)}{r}\delta(z-z_s)$. This is done by inserting the expansion (2.45) into 2.40 which yields:

$$\sum_m \int_0^\infty k_r\, dk_r\, a_m(k_r) J_0(k_r r) P_z^m(\omega,z)[k_m^2 - k_r^2] = \frac{-1}{2\pi c_s^2}\frac{\delta(r)}{r}\delta(z-z_s) \qquad 2.47$$

where $k_m = (k^2-\gamma_m^2)^{1/2} = (\omega^2/c^2(z)-\gamma_m^2)^{1/2}$ is the dispersion relation for the horizontal wavenumber at a depth z. To get the $a_m(k_r)$ coefficients, we use the orthonormality of the eigenfunctions; and the Bessel function identities:

$$\begin{aligned} &\int_0^\infty P_z^m(\omega,z) P_z^n(\omega,z)\, dz = \delta_{mn} \qquad \text{(Kronecker delta)} \\ &\int_0^\infty J_0(k'_r) J_0(k_r r)\, r\, dr = \frac{\delta(k'_r - k_r)}{k_r} \qquad \text{(Dirac delta)} \end{aligned} \qquad 2.48$$

Multiplying both sides of 2.47 by $J_0(k'_r r) P_z^n(\omega,z)$ and integrating in cylindrical coordinates yields:

$$\sum_m \int_0^\infty dk_r k_r a_m(k_r) \frac{\delta(k'_r - k_r)}{k_r}[k_m^2 - k_r^2]\delta_{mn} = \frac{-1}{2\pi c_s^2} P_z^n(\omega,z_s)$$

Thus:

$$a_m(k_r) = a_m(\omega,p) = \frac{-1}{2\pi c_s^2}\frac{P_z^m(\omega,z_s)}{(k_m^2 - k_r^2)} \qquad 2.49$$

are the expansion coefficients. This gives the solution as:

$$P(\omega,r,z) = \frac{-1}{2\pi c_s^2}\sum_m \int_0^\infty k_r dk_r \frac{P_z^m(\omega,z) P_z^m(\omega,z_s)}{k_m^2 - k_r^2} J_0(k_r r) \qquad 2.50$$

This integral can be carried out most easily by regarding k_r as a complex variable, representing $J_0(k_r r)$ as $\frac{1}{2}[H_0^{(1)}(k_r r) + H_0^{(2)}(k_r r)]$, and applying residue calculus. [c.f. Tolstoy and Clay,

1966, p. 82] Carrying out the integration yields:

$$P(\omega,r,z) = \frac{i}{2c_s^2}\sum_m P_z^m(\omega,z)P_z^m(\omega,z_s)H_0^{(1)}(k_m r). \qquad 2.51$$

Again, using the asymptotic expansion for $H_0^{(1)}$ for large arguments:

$$\tfrac{1}{2}H_0^{(1)}(k_m r) \approx \frac{1}{\sqrt{2\pi k_m r}} e^{i(k_m r - \pi/4)}$$

$$P(\omega,r,z) \approx \frac{e^{i\pi/4 sgn(\omega)}}{c_s^2\sqrt{2\pi r}}\sum_m \frac{P_z^m(\omega,z)P_z^m(\omega,z_s)}{k_m^{1/2}} e^{ik_m r} \qquad 2.52$$

$$P(t,r,z) \approx \frac{1}{2\pi}\int_{-\infty}^{\infty} d\omega S(\omega)\frac{e^{i\pi/4 sgn(\omega)}}{c_s^2\sqrt{2\pi r}}\sum_m \frac{P_z^m(\omega,z)P_z^m(\omega,z_s)}{k_m^{1/2}(\omega)} e^{i(k_m(\omega)r - \omega t)} \qquad 2.53$$

where $S(\omega) = S^*(-\omega)$ for a real time series, $P(t,r,z)$. In the next section we deal with the identification of each term of the mode sum in eqn. 2.53. This is useful because the eigenfunctions, $P_z^m(\omega,z)$, and dispersion curves, $k_m(\omega)$, are relatively easily related to the model that we are trying to estimate.

The Plane Wave Decomposition of Modal Data

In a previous section, slant stacking yielded a decomposition of the data that could be related by the WKBJ method to the $\tau(p)$ and amplitude functions that are useful for travel time inversions. In this section, we show that in some cases the modal description leads to terms that can be discriminated by practical analysis techniques, and that can be related to the underlying model in a simple fashion. The common point is that we want to utilize a decomposition for which individual terms in the synthesis sum or domain of integration can be extracted, since it is these individual terms that are just a step away from the model, or at least a part of it. For the normal mode case, we use the decomposition of eqn. 2.53.

Using array measurements from a broadband source, there are three main decompositions that can be carried out. One is to decompose by $k(\omega)$ and ω over a long observation interval, T, and the available spatial aperture. This is the plane wave decomposition and is frequently called the frequency-wavenumber decomposition in this context, and yields the wavenumber dispersion curves and the amplitude at each wavenumber and frequency from the sum of the observed modes. The group velocity for each mode, $d\omega(k_m)/dk_m$, may then be obtained if the $k_m(\omega)$ take unique trajectories by identifying the appropriate curve and differentiating. The problem with this method is that for small apertures, the resolution in k_m (or p_m) is very poor and the curves cannot be separated for mode identification. In addition, we are relying on obtaining group velocity by differentiating the measured curves, which is generally not a good thing to do. Figures 2.3 show the results of such an analysis on an array which is feasible for the Arctic. Figure 2.3a shows the synthetic data for a 341.3 km offset with a realistic water column and sediment structure. The model used will be treated in more detail in chapter 6, and the state-variable normal mode computation and synthesis technique that were used to compute the waveforms for modes 1-30 and frequencies 1-30 Hz are outlined later in this chapter. Since the transform operations are linear for conventional analysis, first the wavenumber integral was carried out, in this case via the slant stack on slowness given by eqn. 2.3. The offset has been reduced by 341.3 km, thus the first trace is at $r=x=0$. The results are shown in fig. 2.3b. Note that although the arrivals are propagating at specific slownesses dictated by $k_m(\omega) = \omega p_m(\omega)$, the small aperture and poor conventional beampattern of the array yield almost no slowness discrimination. A small decrease of about 5 dB in the amplitude of the low phase velocity complex due to modal propagation in the water column (first arrivals) can be seen at the highest phase velocity. Likewise, the higher phase velocity bottom arrival attenuates to the left. As could be predicted, the magnitude squared of the

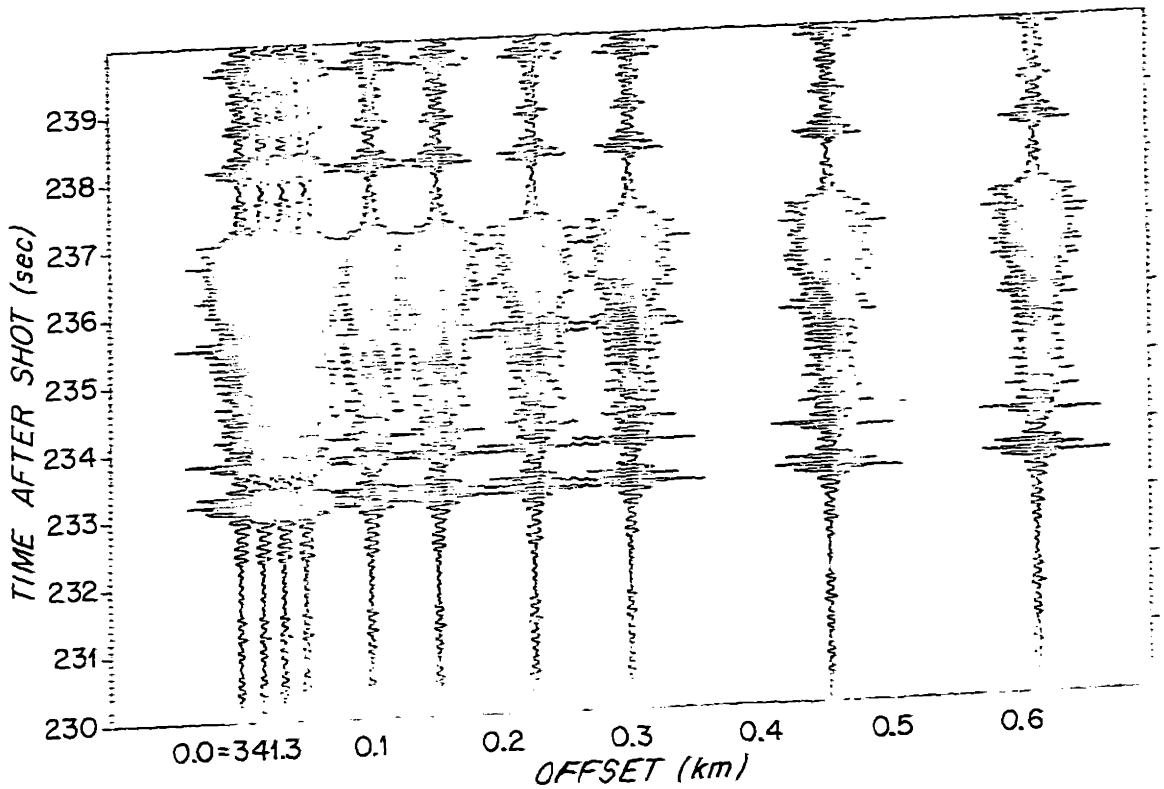

Fig. 2.3a) Synthetic long-range propagation waveforms generated by a normal mode code. The dispersive region is primarily due to water column paths, and the later discrete arrivals are due to bottom interactions. The precursors are numerical artifacts from the absolute band-limiting of the data.

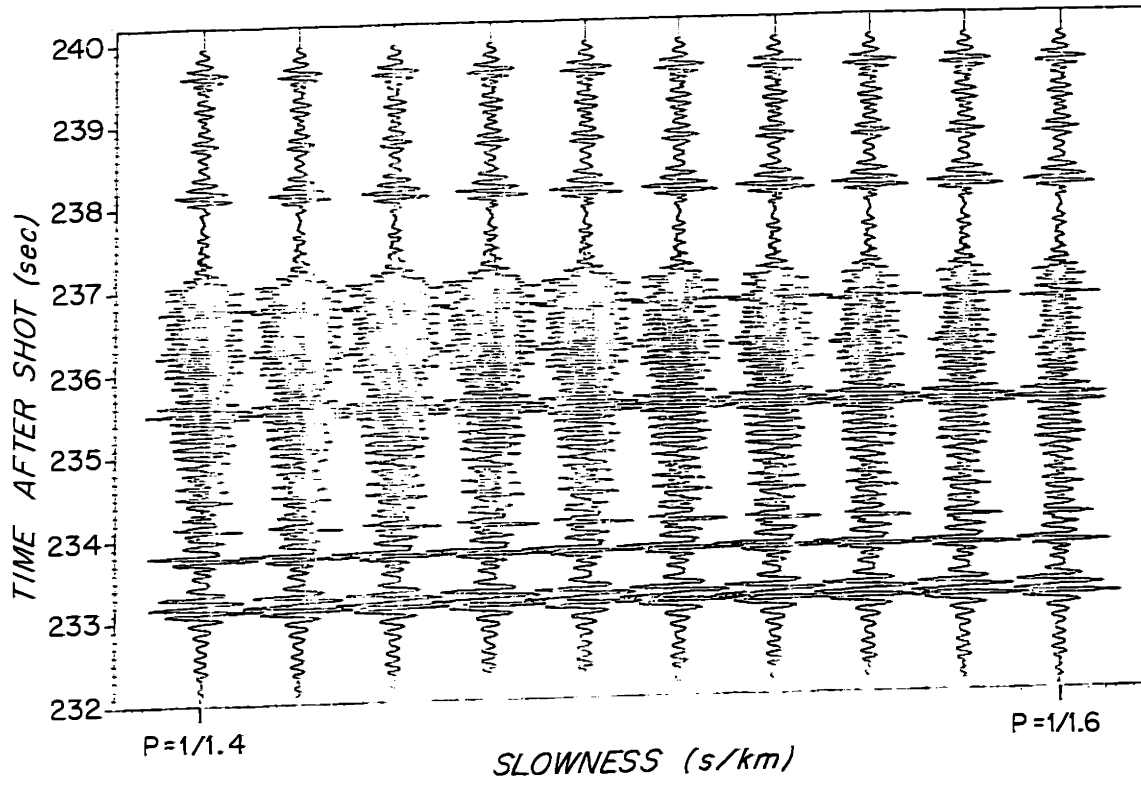

Fig 2.3b) Output of conventional slant stacking on the waveforms of figure 2.3a. Note the diminishing amplitude of the dispersive water column arrivals at smaller slowness, and the smaller amplitude of the later arrivals at larger slowness. The slowness resolution is certainly not dramatic.

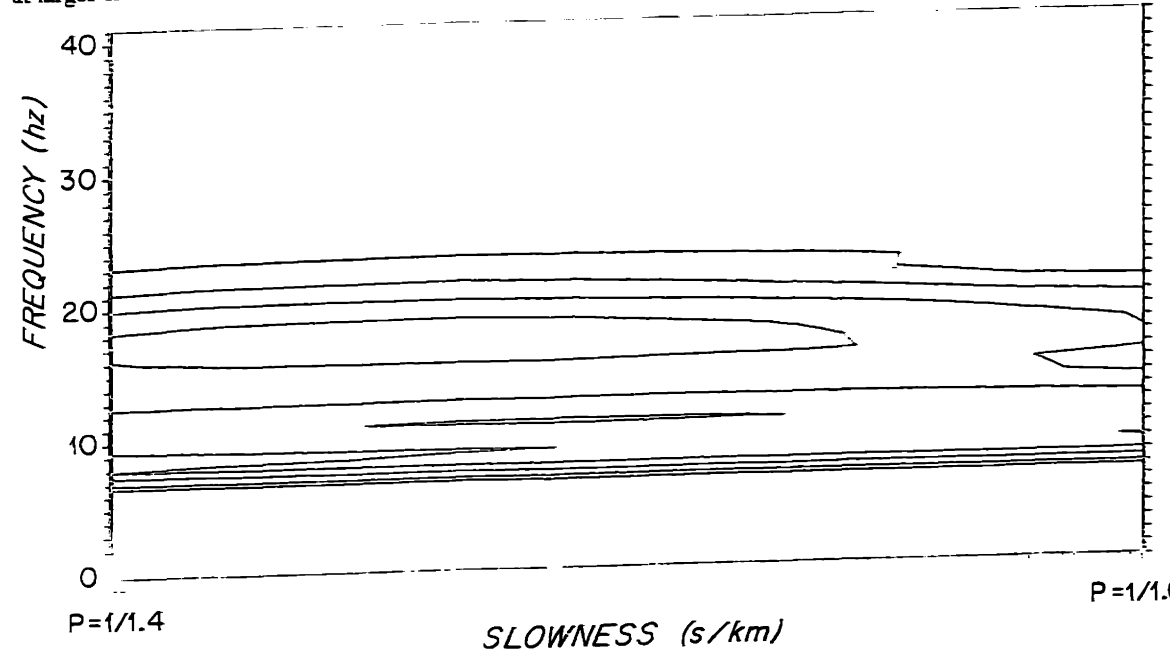

Fig. 2.3c) Temporal Fourier transform of the slant-stack output in figure 2.3b. The poor slowness resolution is again in clear evidence.

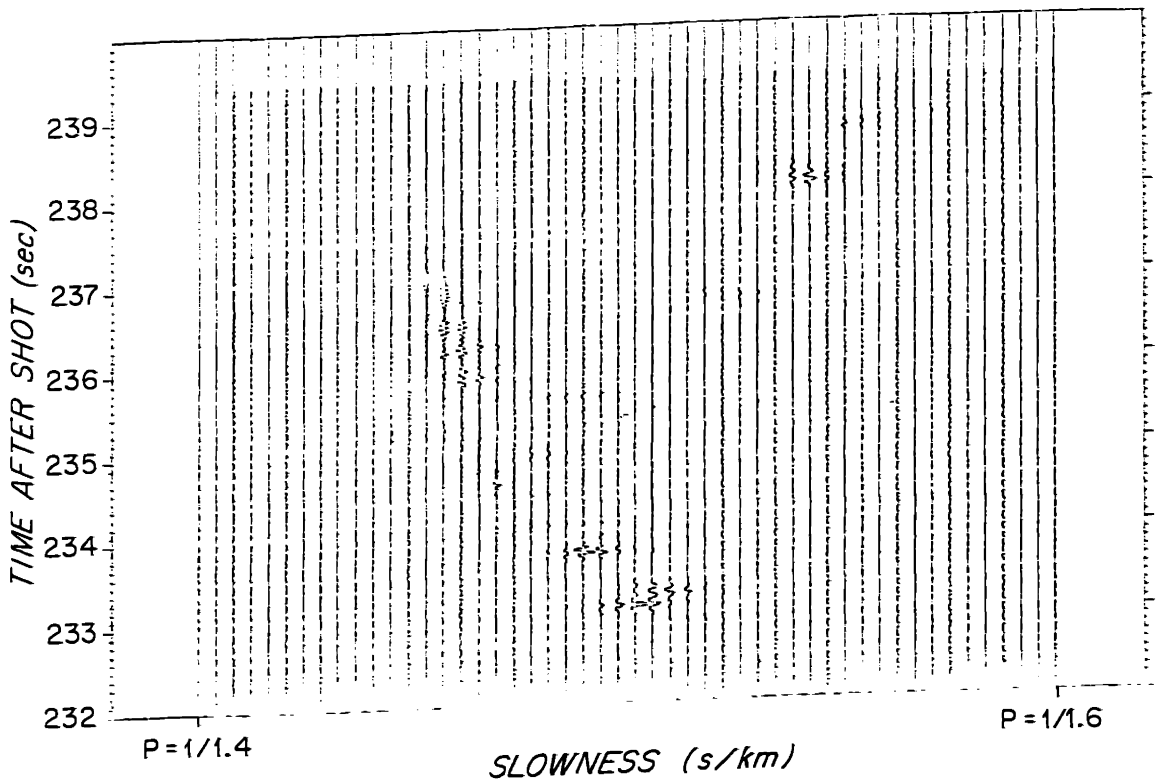

Fig. 2.3d) Output of the MLM slant-stacking algorithm described in chapter 3 after being applied to the waveforms in fig. 2.3a. Note the good slowness resolution of different parts of the waveform: the moderate slowness first arrivals, the low phase velocity mode 1 chirp, and the high velocity (small slowness) bottom interaction.

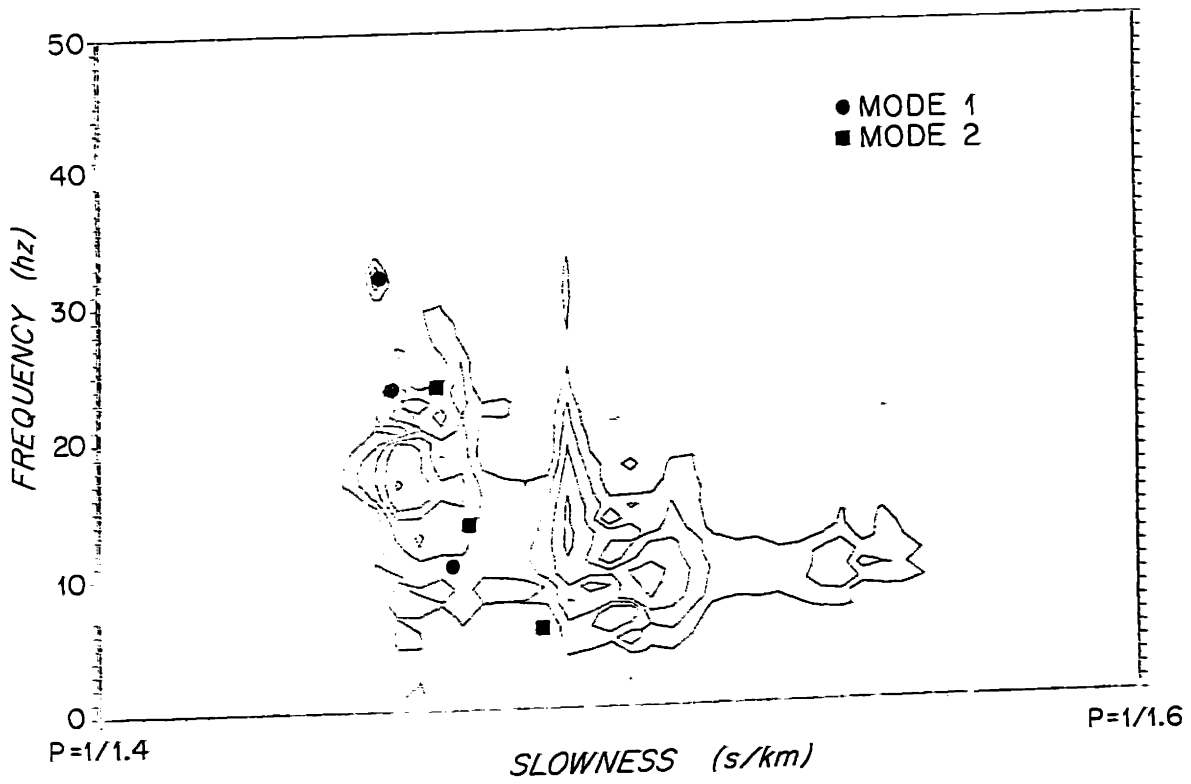

Fig. 2.3e) Temporal Fourier transform of the slant-stack output in figure 2.3d. The good slowness resolution almost allows parts of the dispersion curves for modes 1 and 2 to be discerned. The theoretical dispersion curve points are indicated on the plot by the circles and boxes.

Fourier transforms of the traces in fig. 2.3b, which give the $f-p$ decomposition (almost $\omega-k$) in fig. 2.3c are quite uninteresting since there is almost no slowness resolution. Even if there is better slowness resolution, the $f-p$ or $\omega-k$ representation is not very informative. For illustrative purposes, this resolution was obtained not by the use of a larger aperture, but through application of the short-time MLM slant-stacking technique to be described in chapter 3. The velocity filtered traces from this algorithm on the data of fig. 2.3a are shown in fig. 2.3d. Starting from the left (low phase velocity), the mode 1 and mode 2 "chirps" can be seen, then the superposition of higher order modes and the high velocity sediment refraction. The temporal Fourier transform is shown in fig. 2.3e, and indicates many more features, however the superposed dispersion curves for the true model show that they are not very clearly discerned.

Another tack, which is more successful and is conventionally applied due to the lack of array measurements, is to forget about phase velocity measurements, and to do a short-time spectrogram analysis on one channel. While this decomposition throws away phase velocity resolution, what is achieved through the time windowing is resolution of the group velocity as a function of frequency. This can be done because the wave packet from mode m with frequency ω travels with group velocity $c_g^m(\omega) = d\omega(k_m)/dk_m$. Thus, the spectrogram analysis, which decomposes the arrivals by time of arrival and frequency, $t_m(\omega)$, can be used to obtain the group velocity using the range between the source and the receiver, r:

$$c_g^m(\omega) = \frac{r}{t_m(\omega)} \qquad 2.54$$

after the multiple curves are identified and associated with their proper modes. Figure 2.4 shows a spectrogram of one channel of the data of figure 2.3a. The power in the signal is contoured as a function of arrival time and frequency. The solid lines are the true dispersion curves of the model used to generate the data. The circles and X# labels will be explained

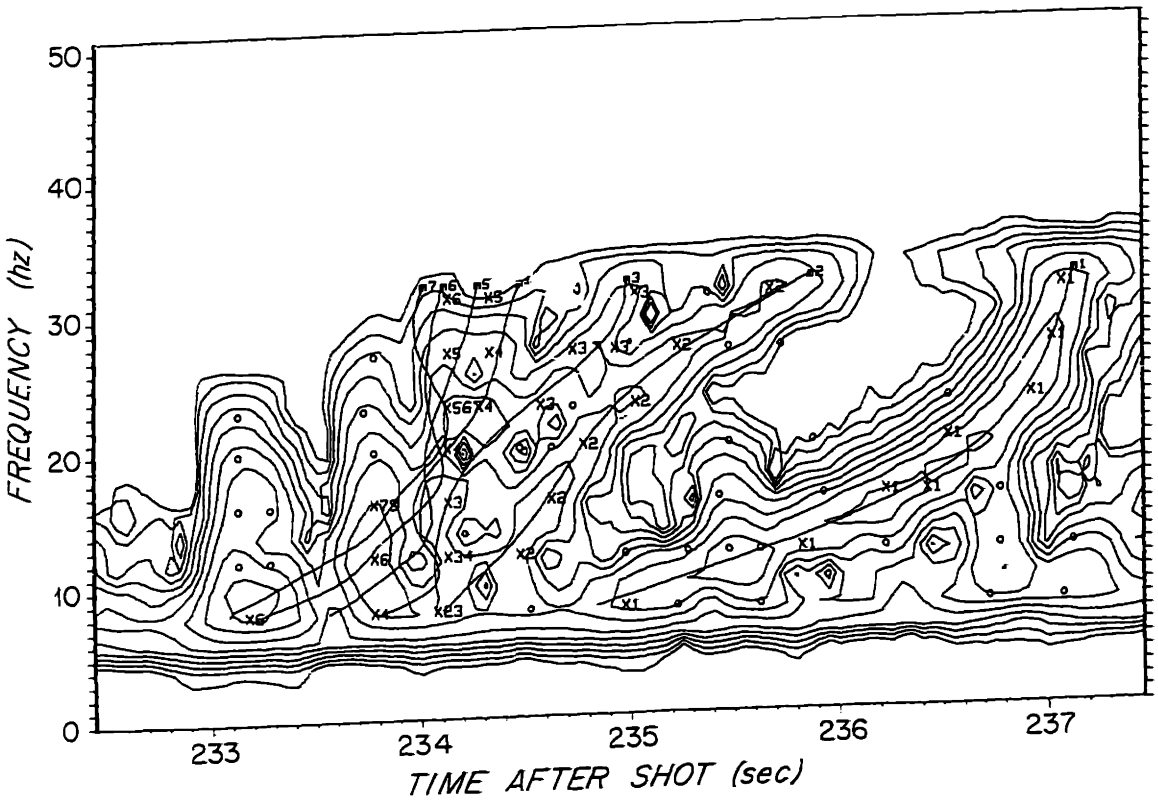

Fig. 2.4) The spectrogram of the first trace of the data shown in figure 2.3a. A tapered window of .25 seconds length was used to achieve the time resolution using a simple discrete Fourier transform spectral estimator. The lines and characters on the plot are described in the text.

later. The thing to note about this plot is that while the modes 1 and 2 are reasonably well delineated, in the areas where the mode curves cross each other the spectrogram becomes very difficult to interpret. It will be seen in chapter 6 that a lot of prior information must generally be used to associate the modes correctly on spectrogram analyses because the curves $c_g^m(\omega)$ or $t_m(\omega)$ cross each other and are highly intertwined. Chapter 6 will also show how the measured curves can be inverted for a model. It can also be seen from equation 2.53 that if a mode can be isolated in the $c_p - c_g - \omega$ domain, the product of the source and receiver mode amplitudes over the square root of $k_m(\omega)$ can be estimated.

The best method that we have found for analysis of dispersive arrivals is to do simultaneous decomposition of the power in the multichannel data by arrival time (or group velocity), phase velocity, and frequency. The two previous analyses can be seen in figures 2.5 to be projections of this most general decomposition onto one or the other of its coordinate planes. In this figure the locus of arrivals for a given mode are described by unique trajectories of peaks of the power of the 3-dimensional decomposition. One very helpful aspect of the complete decomposition is that, like the $f-p$ plots, the dispersion curves never intersect. The advantage of running the short-time frequency analysis simultaneously with the slowness decomposition rests in two facts: i) the group velocity is obtained directly, and ii) assuming a small ($< 1\%$ of the range) aperture, only a few modes may be arriving with appreciable energy in any short time window, and these will most often be of differing frequency. Using the data from this small window can help the slowness decomposition. Chapter 3 will expound on this matter endlessly, but, in short, the nonlinear MLM beamformer used to obtain the slowness performs much better, and achieves high slowness resolution, on limited amounts of data when the data contains arrivals at only one slowness at each frequency in the processing band. In addition, because of the structure of the phase velocity dispersion curves of fig. 2.5a, if arrivals are

Fig 2.5) Various wave-field characterizations and their relationship to the velocity spectrum.

a) Phase velocity (c_p) dispersion curves. The variable f is temporal frequency (Hz).

b) Frequency-wavenumber loci. ($k = f/c_p$)

c) Group velocity (c_g) dispersion curves.

d) Spectrograms ($t = x/c_g$), the standard method of group velocity dispersion curve estimation.

e) The complete decomposition by all variables.

f) The velocity spectrum as an implementation of the complete decomposition. The trajectory of the line in three-dimensions in (e) is indicated by the circled dots.

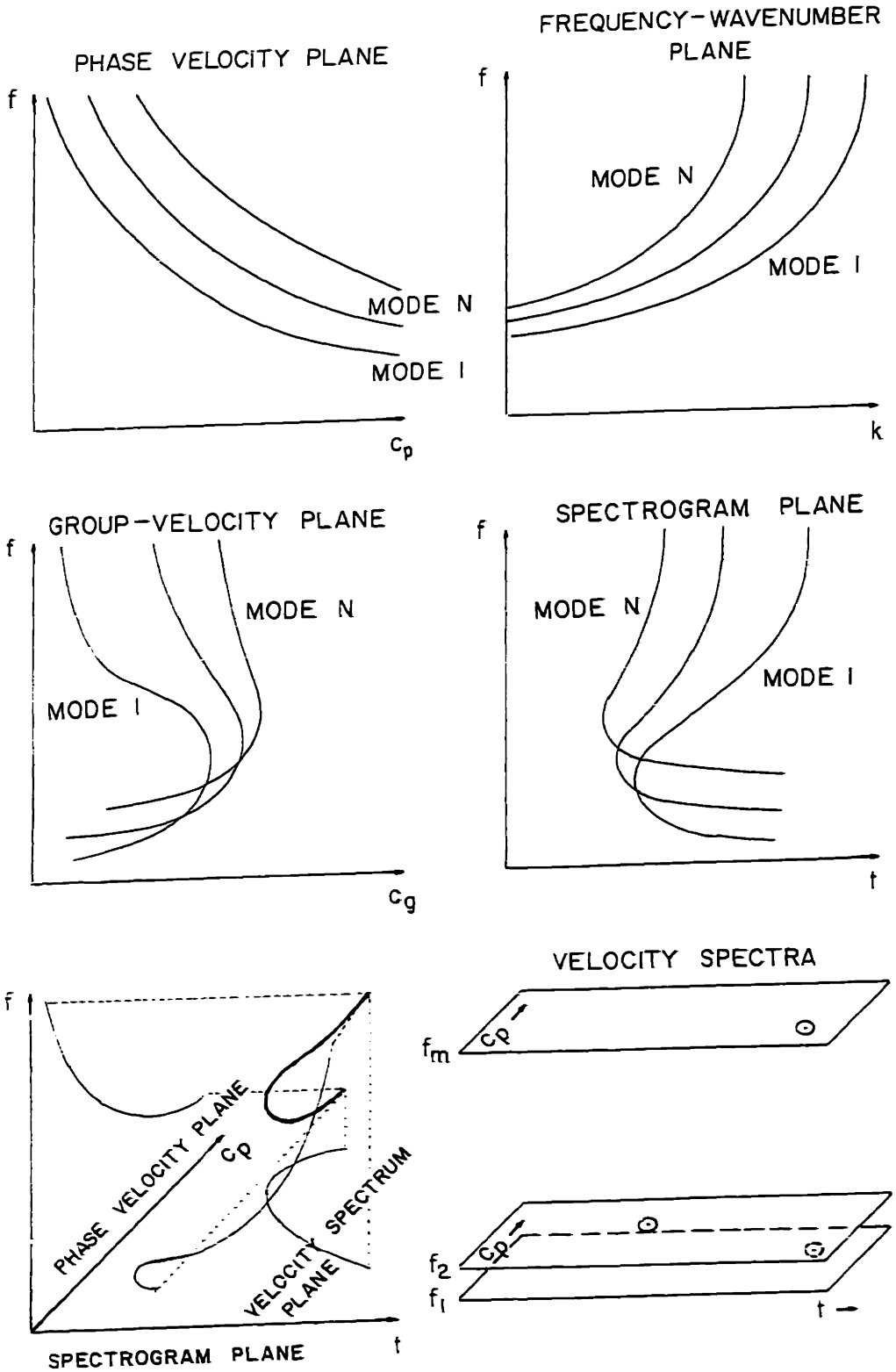
PHASE VELOCITY PLANE
f
MODE N
MODE I
c_p
FREQUENCY-WAVENUMBER PLANE
f
MODE N
MODE I
k
GROUP-VELOCITY PLANE
f
MODE N
MODE I
c_g
SPECTROGRAM PLANE
f
MODE N
MODE I
t
VELOCITY SPECTRA
f_m
cp
f_2
f_1
cp
t
f
PHASE VELOCITY PLANE
cp
VELOCITY PLANE
SPECTRUM
SPECTROGRAM PLANE
t

coincident in frequency but have different arrival times, the one with the highest phase velocity must be associated with the highest mode. Thus, less prior information is required for the mode identification. From figs. 2.5e&f, we see that the 3-D decomposition of the dispersive arrivals is done by the velocity spectral decomposition, $\hat{S}^2(t,\omega,p)$ or $\hat{S}^2(t,\omega,c_p)$. An example MLM velocity spectrum computed from the data of fig. 2.3a is shown in fig. 2.6. This plot is a slice in frequency of the 3-D structure in fig. 2.5e, and is one sheet of fig. 2.5f at 12 Hz. The peaks picked from this analysis are labeled X#, where # is the mode that they are associated with. Other peaks which are less powerful and have not been identified are labeled "o". The underlying dispersion curve points are labeled with m#, and are seen to agree with the estimates. The projection of the "X" points are also labeled on fig. 2.4 (along with the others at differing frequencies) and are shown to trace the underlying dispersion curves (solid lines on 2.4) quite well. It should be noted that this is the same velocity spectral analysis procedure that was mentioned in the interpretation of refraction data for the WKBJ "ray expansion".

In an earlier section it was seen that the slant stack and/or velocity spectral analysis yielded terms of the ray expansion of the reflection coefficient and could easily be related to relatively simple operations on the velocity-depth model, and thus inverted for the model. In this section it was seen that the identification of individual mode amplitudes and group velocity and phase velocity dispersion curves could also be done through velocity spectral analysis. Chapter 6 will give a method for inverting these measurements for the sound speed structure of the water or crust through which the dispersive energy propagated.

RELATING THE MODEL TO MODE AMPLITUDES AND DISPERSION CURVES

Introduction

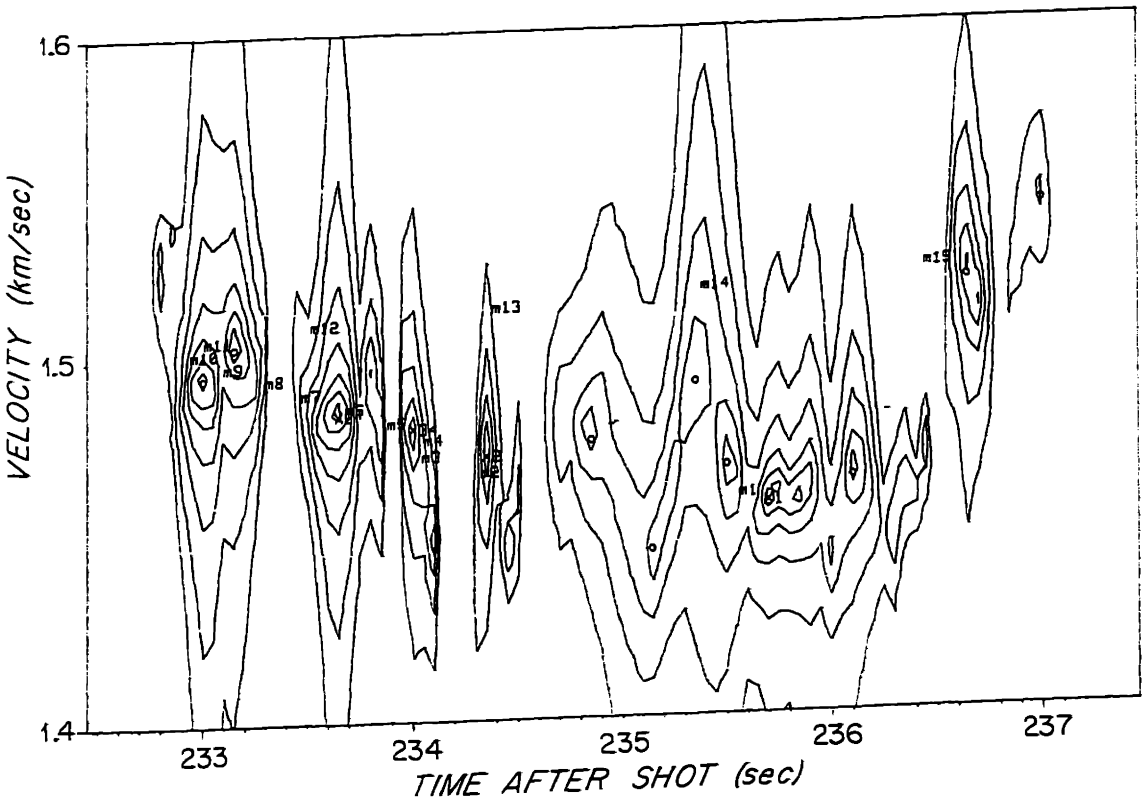

Fig. 2.6) 12 Hz velocity spectrum for the data shown in fig. 2.3a. This plot is one of the slices shown in fig. 2.5f. The labels are described in the text.

To relate the decomposition of the refraction data to the model velocity profile the WKBJ method and the Herglotz-Wiechert integrals were used. For long range acoustic propagation data no simple normal mode approximation works as well as the WKBJ technique does for refraction observations. A simple approximate technique that works well for high mode numbers is described in the latter part of this section. However, for moderate ranges (<1000 km), the velocity spectral decompositions do not have enough resolution to separate the individual contribution from the higher order modes, thus it does not really help in the solution of the inverse problem. A much more complicated, and more exact, method is necessary to solve for the lower order (1-5) modes dispersion curves and amplitudes to within the measurement capabilities of the array. This technique is outlined first because it will be used extensively in chapter 6 in the computations necessary for the inversion of the lower order mode dispersion curves for velocity structure.

After this, an approximate normal mode solution is presented that is useful because it provides some intuition about the relationship between ray and normal mode theory, and because it leads to an efficient technique for computation of the complete acoustic field for general gradient models over ranges that are typical in refraction experiments. The advantage over the standard WKBJ technique is that all kinematic groups do not need to be explicitly outlined, i.e. all multiples and surface ghosts are automatically taken care of.

Computing the Mode Eigenvalues and Eigenfunctions: a State Variable Technique

A number of methods have been proposed for solving the non-constant coefficient vertical wave equation (2.42). For some (usually non-realistic) sound-speed profiles, the equation can be solved analytically. However, in most cases it is done numerically. The most common methods seem to use a finely layered medium in which the solutions are known analytically

inside each layer. These are then matched at the boundaries to determine the eigenfunctions and the dispersion relation (eigenvalues). The most popular method uses homogeneous layers, in which case the Thomson-Haskell propagator matrices may be used. For the low-order mode calculations in this work, a method developed by Baggeroer [unpublished] which converts the second order equation (2.42) into two coupled first order equations and the usual "state space" representation is used. The non-constant coefficient first order equations have a coupling matrix in which only the diagonal elements are depth varying. The diagonal elements are just negatives of one another, and can be computed by solving a Ricatti equation. This must be done only once, and has been shown to have desirable numerical properties. Once the coefficient matrix has been calculated, trial solutions are "shot" by integrating upward from the bottom boundary condition. This is iterated until the top boundary condition (free surface) is satisfied. In practice, to improve the numerical properties of the solution, the state variables are transformed into a magnitude and phase representation. Since the phase is the important component for boundary condition matching, and does not have a large dynamic range, it can be intuited that this solution might have desirable properties.

In summary, the state variable method works well for low-order modes and accepts a pointwise parameterization of the medium sound speed with linear velocity gradients connecting the points. It is a computationally intensive technique, and practical densities of frequency sampling and bandwidth are 0.5 Hz over a 30 Hz bandwidth for the first 30 modes. For this problem, the computation of the eigenvalues and eigenfunctions takes 10 hours of CPU time on a mini-computer*.

---

*The program was implemented in the "C" language on a Digital Equipment Corporation PDP-11/45 with floating point hardware running the UNIX operating system.

The primary uses of the predicted dispersion curves and mode amplitude functions were to match curves measured from the data using the spectrogram and velocity spectral analysis codes. (These will be discussed later in this chapter.) They were also used to compute the partial derivatives of the dispersion curves with respect to the profile parameters so that the measured dispersion curves could be inverted for water column structure. The accuracy and sampling density in frequency was entirely adequate for these tasks. The analysis of this work will be found in chapter 6.

It is useful to make actual synthetic time series data in order to test the decomposition algorithms. However, the sparse specification of the dispersion curve (0.5 Hz intervals, for example) makes waveform synthesis through the frequency integral (2.53) awkward, since a dense frequency sampling is required to eliminate temporal aliasing in the discrete Fourier transform that is typically used to implement equation 2.53. In addition, the group velocity calculation which requires a derivative of $k_m(\omega)$ ($c_g(\omega) = d\omega/dk_m(\omega)$) is subject to error when the frequency sampling is too large.** However, even with the sparse frequency samples, it has proven reasonably adequate (that is, no overt artifacts are generated) to carry out the frequency integration (2.53) by first expanding $k_m(\omega)$ around ω_i as:

$$k_m(\omega) \approx k_m(\omega_i) + \dot{k}_m(\omega)|_{\omega_i}(\omega-\omega_i) + \frac{\ddot{k}_m(\omega)}{2}|_{\omega_i}(\omega-\omega_i)^2 \qquad 2.54$$

where the derivatives are calculated numerically. The integrals over the bandwidth intervals between frequency samples are done analytically, and then summed, yielding a effectively dense sampling in frequency, and no temporal aliasing was visible. The main artifact with

**Later examples in chapter 6 will show that it is best to interpolate sampled dispersion relations using linear interpolation. Since interpolation by a cubic spline can lead to ripple, and the first derivatives of this function yield the group velocity, the results can be quite odd- and lead to smearing and periodic artifacts in the time domain. Linear interpolation does not have this problem because for adequate sampling rates (in frequency), the first difference is bounded above and below by the true derivatives at the end points.

synthesis by this method was the absolute band-limiting of the spectrum necessitated by computational considerations. This led to the predictable convolution with a modulated *sinc* function in time. Replacement of the zero phase flat source spectrum with the phase response of the causal flat spectrum with -60 dB stop-bands led to a coda that was less acceptable than the precursor and coda due to the non-causal *sinc* convolution.

Computing the Mode Eigenvalues and Eigenfunctions: the WKBJ Approximate Technique

The main computation of the normal mode decomposition is in finding the eigenvalues and eigenfunctions of equation 2.42 that satisfy the boundary conditions. Replacing $(k^2-k_r^2)$ in equation 2.42 with $\omega^2\nu^2(z,p)$, we obtain:

$$\frac{\partial^2}{\partial z^2}P(\omega,z) + \omega^2\nu^2(z,p)P(\omega,z) = 0 \qquad 2.55$$

If the sound speed profile is smooth on the scale of a wavelength, then $\nu(z,p) = (c^{-2}(z)-p^2)^{1/2}$ will also be smooth. When this condition holds, and $\nu(z)$ is monotone non-increasing with z (which it will be for a monotone non-decreasing $c(z)$), then the solution to 2.55 is well approximated for large ω using the WKBJ approximation by equation A1.27 in the region above the turning point for the ray with slowness p at which $\nu(z) = \nu(z,p)$ is zero. More formal constraints on the behavior of $\nu(z)$ are given in equation A1.11. This solution is called the WKBJ solution [Budden, 1961] and is well known in many fields. The complete WKBJ solution, which is pieced together from solutions valid in (I) the propagating region above the turning point, where $\nu^2(z) > 0$, (II) near the turning point, z_t, where $\nu^2(z)$ is approximated by $-a(z-z_t)$, and (III) below the turning point where the solution is exponentially decaying and $\nu^2(z) < 0$. These solutions are (see Appendix 1 for derivations):

Region I) $$P_I(\omega,p,z) = \frac{2C}{v^{1/2}(z)} sin(\omega \int_z^{z_t} v(x)\,dx + \pi/4) \qquad 2.56a$$

Region II) $$P_{II}(\omega,p,z) = 2\sqrt{\pi}(\frac{\omega}{a})^{1/6} C\,Ai(\omega^{2/3}a^{1/3}(z-z_t)) \qquad 2.56b$$

$$a = -\frac{d}{dz}v^2(z)|_{z=z_t} = -2p(z)\frac{d}{dz}p(z)|_{z=z_t} \qquad Ai = \text{the Airy function}$$

Region III) $$P_{III}(\omega,p,z) = \frac{C}{(-v^2(z))^{1/4}} e^{-\omega \int_{z_t}^{z} +IM[v(x)]\,dx} \qquad 2.56c$$

Note that $v(z) = (c^{-1}(z)-p^2)^{1/2}$ depends on p, giving the solutions in 2.56 their dependence on p.

We now obtain the eigenfunctions and dispersion curves. For an earth or water column model, the surface, $z=0$, is a free boundary condition, $P(\omega,p,z=0) = 0$. The solution which is valid here is that of region I, and the eigenvalue equation for $k_m(\omega) = \omega p_m$ is obtained by setting the solutions equal to zero at the surface. This yields:

$$\sin(\omega_m \int_{z=0}^{z_t(p)} v(x,p)\,dx + \pi/4) = 0 \qquad 2.57a$$

or equivalently:

$$\omega_m \int_{z=0}^{z_t(p)} v(x,p)\,dx + \frac{\pi}{4} = m\pi \qquad m = 1,2,3,... \qquad 2.57b$$

giving the eigenvalue relation:

$$\omega_m(p) = \frac{\pi(m-1/4)}{\tau(p)/2}. \qquad 2.58$$

Thus, $k_m(\omega)$ is obtained by multiplying the inverse function of ω, $p_m(\omega)$, by ω: $k_m(\omega) = \omega p_m(\omega)$. The normalized eigenfunctions are obtained by evaluating P_I, P_{II}, and P_{III} in their appropriate regions of applicability, and dividing by the normalization factor

$$||P_p^m||^2 = \int_0^\infty [P^m(\omega_m, p, x)]^2 dx.$$

Following an analysis similar to that of Bender and Orzag [1978, p. 516] the approximate area in the squared eigenfunction can be found to be:

$$\begin{aligned} ||P_p^m||^2 &\approx 2C^2 \int_0^{z_t} \frac{1}{v(z,p)} dz - \frac{C^2}{\omega_m v^2(0,p)} \cos(2\omega_m \int_{z=0}^{z_t(p)} v(x,p)\, dx) \\ &= C^2 \left[\frac{x(p)}{p} - \frac{\cos(\omega_m \tau(p))}{v^2(0,p)} \right] \end{aligned} \qquad 2.59$$

This requires no more computation than the single ray trace to obtain $\tau(p)$, and another to obtain the geometrical offset function, $x(p)$, both of which are quite easy to do for very general sound speed profile parameterizations. For this work we consider both a linear slowness and a linear velocity gradient interpolation between specified velocity-depth points. For these cases, tracing rays within each gradient layer can be done by easy analytical integrations and closed form solutions written. The approximation in eqn. 2.59 has been found to agree well with trapezoidal integration of the eigenfunctions themselves using an adaptive sampling rate of 10 samples per vertical wavelength.

Equation 2.57b is the Bohr-Sommerfeld eigenvalue equation [Tolstoy, 1973, p. 124; Mitchell, 1977] originally used for the calculation of atomic energy levels. Note that in 2.58 we have identified the usual $\tau(p)$ function in 2.57:

$$\tau(p) = 2 \int_{z=0}^{z_t} v(x,p)\, dx. \qquad 2.60$$

Despite its simplicity, the approximate normal mode solution has some interesting interpretations. The group velocity dispersion curve is also easy to compute: by definition,

$$c_g^m(\omega_m) = \frac{d\omega_m}{dk_m} \qquad k_m = \omega_m p_m$$

and

$$dk_m = p_m d\omega_m + \omega_m dp_m$$

giving:

$$c_g^m(\omega_m) = \frac{d\omega_m}{p_m d\omega_m + \omega_m dp_m}.$$

Inverting this yields:

$$\frac{1}{c_g^m(\omega_m)} = p_m + \omega_m \frac{dp_m}{d\omega_m}$$

and thus:

$$c_g^m(\omega_m) = \frac{1}{p_m + \omega_m \dfrac{dp_m}{d\omega_m}}.$$

But from 2.58:

$$\frac{d\omega_m}{dp_m} = (dp_m/d\omega_m)^{-1} = \frac{d}{dp_m}\left[\frac{2\pi(m-1/4)}{\tau(p_m)}\right] = \frac{-\dot{\tau}(p_m)}{\tau(p_m)}\frac{2\pi(m-1/4)}{\tau(p_m)} = \frac{x(p_m)}{\tau(p_m)}\omega_m$$

and substituting this into the previous equation yields:

$$c_g^m(\omega_m) = \frac{1}{p_m + \tau(p_m)/x(p_m)} = \frac{x(p_m)}{\tau(p_m) + p_m x(p_m)} = \frac{x(p_m)}{t(p_m)} \qquad 2.61$$

where we have used the results from the Herglotz-Wiechert travel-time equations:

$$\tau(p) = t(p) - px(p) \qquad 2.62a$$

$$\tau(p) = 2\int_{x=0}^{x_t(p)} v(x,p)\,dx \qquad 2.62b$$

$$x(p) = -\frac{d\tau(p)}{dp} = 2\int_0^{x_t(p)} \frac{p}{v(x,p)}\,dx \qquad 2.62c$$

$$t(p) = 2\int_0^{z_t(p)} \frac{p(x)}{v(x,p)}\,dx \qquad 2.62d$$

$$p(z) = c^{-1}(z) \qquad 2.62e$$

$$v(z,p) = (p^2(z) - p^2)^{1/2} \qquad 2.62f$$

$$z_t(p) = z : p(z) = p. \qquad 2.62g$$

From 2.61 it is seen that we obtain the ray-theoretic results for the group velocity associated with a given phase velocity, just the geometrical offset divided by the geometrical arrival time. Note, however, that for a fixed mode, m, the arrival time at offset X of frequency ω is:

$$t_m(\omega) = \frac{X}{c_g^m(\omega)} = \frac{X}{x(p_m(\omega))} t(p_m(\omega)) \qquad 2.63$$

This is dispersive since for each mode, each ray parameter, p_m, has a unique frequency associated with it through equation 2.58. Thus, for a fixed mode, we re-interpret the geometrical travel-time not as a broadband travel-time, but as the travel-time of a single frequency component. In addition, the amount of energy in the mode at a given frequency depends on the source and receiver depths. Broadband non-dispersive arrivals are due to a dense "pile-up" of modes. All frequencies which satisfy 2.58 for $m = 1,2,3,...$ for a fixed p will arrive at X at the same time (see 2.63). This is illustrated in fig. 2.7 for the model in fig. 2.8. In fig. 2.7 it is seen that each mode contributes arrivals at the same time, but at different frequencies, i.e. the group velocity curves for the different modes are just scaled in frequency differently. Figure 2.9 shows the $t(p)$ function for this model at an offset of 20 km. This was calculated by:

$$t(p_m) = \frac{X}{c_g^m(p_m)} = \frac{X}{x(p_m)} t(p_m) \qquad 2.64$$

This curve is implicitly parameterized by frequency, and for the various modes, different regions of the curve are associated with differing frequencies, however the locus in $t-p$ space is the same. Along with the $t(p)$ function of 2.64 are plotted the "theta" curves associated with

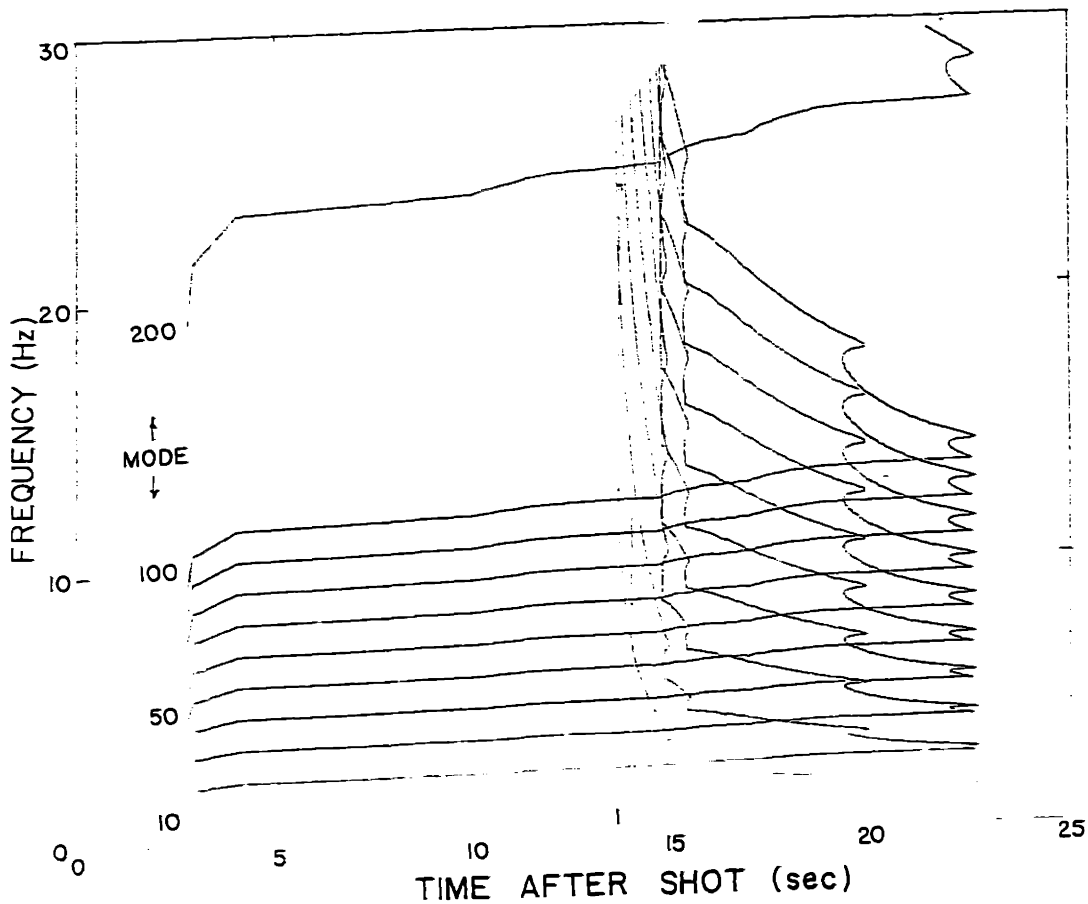

Fig. 2.7) Frequency vs. arrival time curves for various modes using the approximate dispersion relation. Note that for each mode, the arrival at any given time has a characteristic frequency. The model used to compute these curves is given in fig. 2.8.

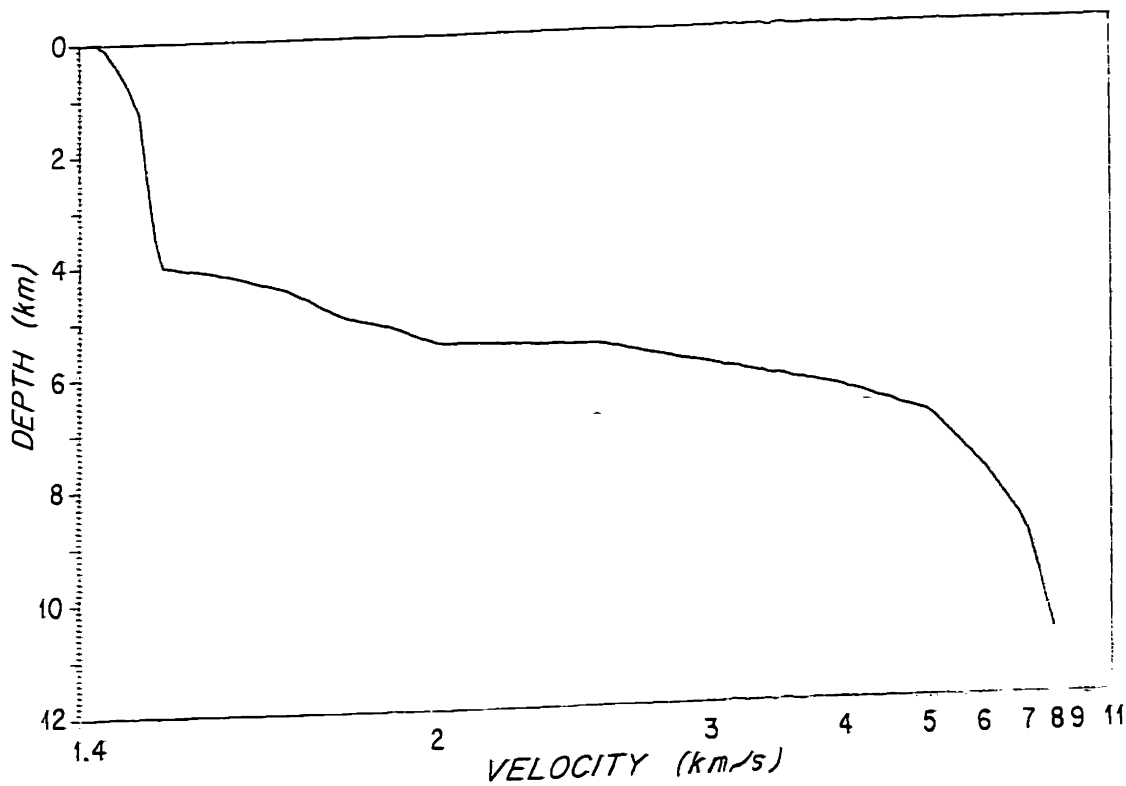

Fig. 2.8) Velocity-depth model used to compute the curves of figures 2.7, 2.9, and 2.10.

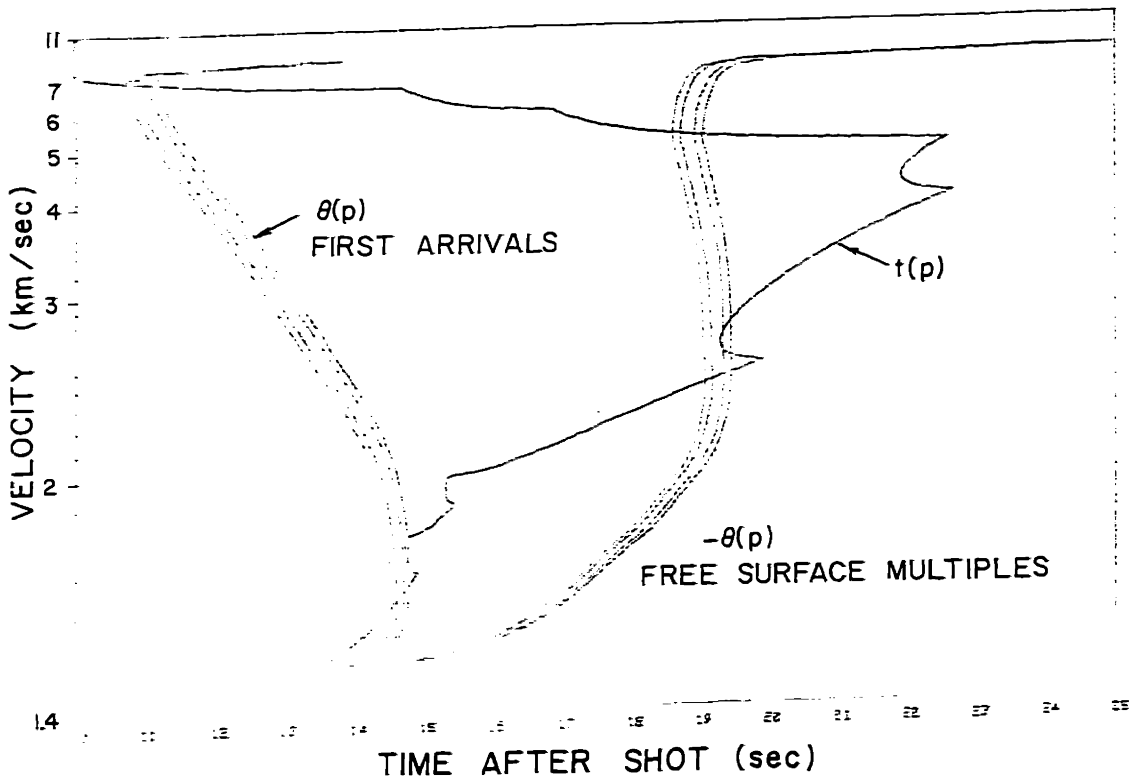

Fig. 2.9) Approximate normal mode and WKBJ arrival time curves. Note that the approximate normal mode arrival curves ($t(p)$) intersect the $\theta(p)$ curves for the WKBJ method at their inflections. The θ curves for the primary and first free surface multiple are shown. All near-source and near-receiver multipaths (surface ghosts) are also shown.

the WKBJ method (see eqn. 2.26a). Recalling the discussion in the section on the WKBJ method that indicated that the major contributions to the seismogram come from the inflection points where $d\theta/dp = 0$, we note that the $\tau(p)$ locus of the approximate mode method crosses the θ curves for the primary and first free surface multiple and their source and receiver surface ghosts at exactly these inflections. Figure 2.10 shows that for the profile of fig. 2.8 that the region in phase velocity space between 1.44 and 8 km/s and frequency between 2 and 25 Hz is well covered by the first 200 modes. Additional modes would only contribute to the higher frequency content of the waveforms. Unlike the WKBJ method, each type of ray (direct, refracted, reflected, multiple, ...) does not need to be specified and its $\tau(p)$ curve computed explicitly. Free surface multiples are included, and source/receiver surface ghosting is accounted for. For our refraction work, this has been the greatest advantage of this method. Though they have not been implemented, pre-critical reflection effects may possibly be accommodated by using $\tau(p)$ functions that are truncated before the turning point depth.

It has been suggested that the next higher order term in the WKBJ expansion be used to improve the accuracy and applicability of the solution. The analysis for this case has been carried out by Bender and Orzag [1978, p. 534]*. The eigenvalue equation equivalent to 2.58 is the quadratic:

$$\omega_m^2(\tau(p)/2) + \omega_m \pi(m-1/4) + \eta(p) = 0 \qquad 2.65$$

and the positive sign on the square root of the quadratic solution formula is taken to obtain the correct root:

$$\omega_m = \frac{\pi(m-1/4) + [\pi^2(m-1/4)^2 - 2\tau(p)\eta(p)]^{1/2}}{\tau(p)}. \qquad 2.66$$

*Alternatively, the Langer expansion can be used instead of the WKBJ expansion. This case was dealt with by Mitchell [1977].

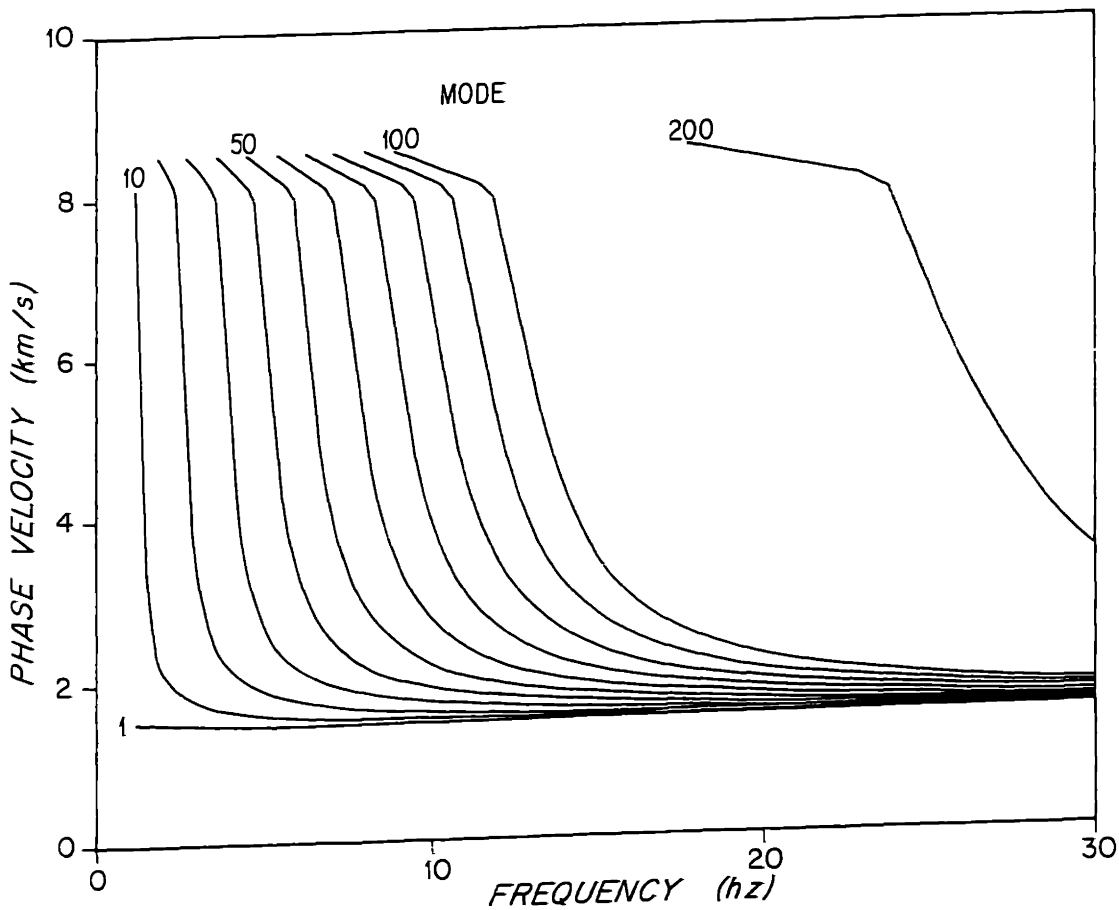

Fig. 2.10) Phase velocity dispersion curves for the model of fig. 2.8. These indicate that the first 200 modes are adequate to cover the synthetics below 20 Hz.

The function $\eta(p)$ is given by:

$$\eta(p) = -\left[\frac{5}{48}\frac{-d(v^2(z))/dz}{v^3(z)}\Big|_{z=0} - \frac{1}{48}\int_{z=0}^{z_t-\mu}\frac{-d^2(v^2(x))/dx^2}{v^3(x)}dx + \frac{ba^{-3/2}}{12\sqrt{\mu}}\right] \qquad 2.67$$

where

$$a = \frac{-d(v^2(z))}{dz}\Big|z=z_t$$

$$b = \frac{-d^2(v^2(z))}{dz^2}\Big|z=z_t$$

μ = constant chosen ensure convergence of the second term in 2.67

The integrals in 2.67 can be done analytically for a piecewise linear slowness gradient profile. Examples carried out have shown the dispersion curves of 2.66 to differ very little from those of the first order equation, 2.58. From equation 2.65, it is easy to see that as ω_m and m get large, the effect of $\eta(p)$ diminishes- a reflection of the fact that the first order WKBJ method is the high frequency approximation and gives a very good description of the physics in this region. For short ranges (< 100 km) the low order modes are only important at very low frequencies (< 5 Hz), and thus the first order calculation is sufficient. For long ranges (e.g. 341 km), the correction was small, and did not appreciably help the first order result. The approximate normal mode method has proven to be a useful tool for prediction of seismograms from range invariant models. For this thesis, the prime utility has been the calculation of the complexes associated with each major arrival due to surface ghosting at the source and receiver.

To compare the standard WKBJ synthetic seismogram method described earlier to the approximate normal mode synthetic seismogram we consider the model of fig. 2.11. A simple isovelocity water column overlays a high linear slowness gradient sediment layer. Energy which penetrates deeper than the 3.9 km/s basement is lost into the underlying homogeneous

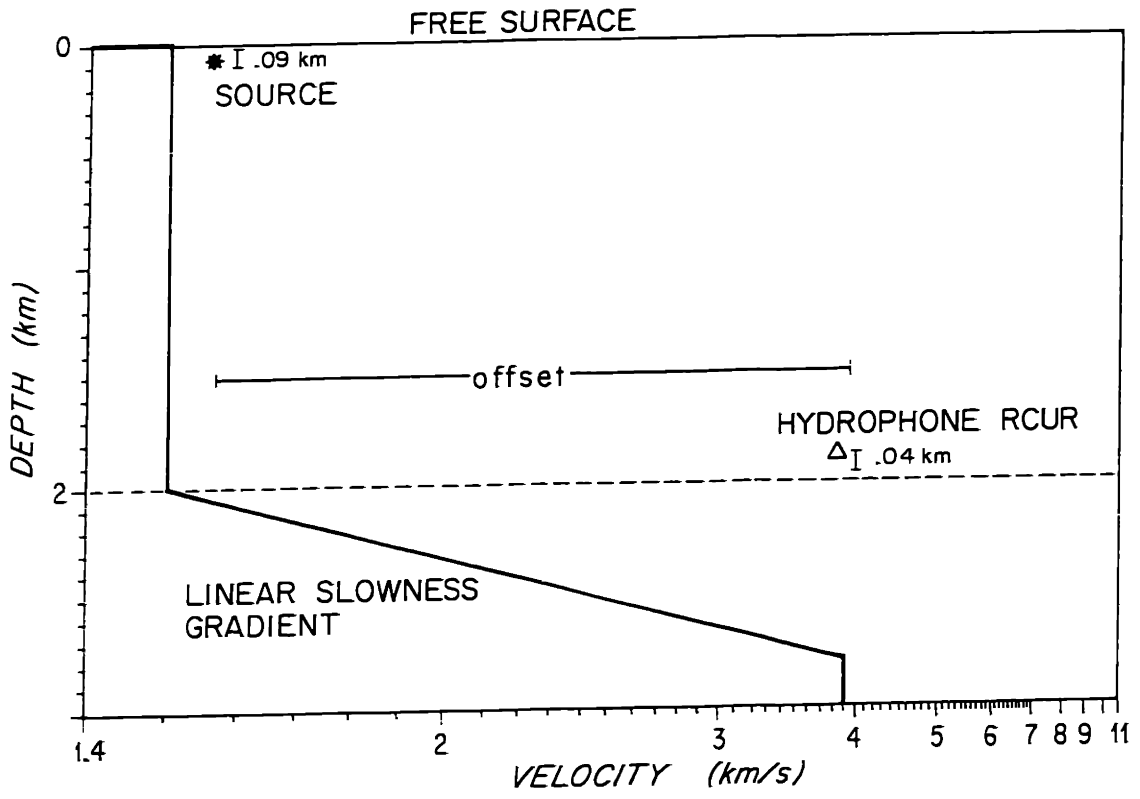

Fig. 2.11) Model used to compute the WKBJ and approximate normal mode synthetics of figures 2.12a&b. Note the locations of the source and receiver with respect to the surface and bottom.

halfspace. The explosive source and the seabottom receivers are located as indicated in fig. 2.11. For the WKBJ method, 4 rays are used, the direct and single loop refracted, and their surface ghosts. For the approximate normal mode method, 100 modes are used over the 1-10 Hz band. For the WKBJ method, 300 rays were traced for each kinematic group to define the $\tau(p)$ and amplitude curve. For the approximate normal mode method, 200 rays total were traced. For both methods, the impulse responses were perfectly (and thus, non-causally) band limited to 1-10 Hz. The seismograms for the region in which all dominant paths were traced for the WKBJ method are plotted in fig. 2.12a. The traces for the two methods are plotted on top of each other and are seen to be in good agreement. Figure 2.12b shows the approximate normal mode seismograms over the region in which the 2-loop refractions and the single loop plus a direct path from the surface are included. The travel time curves for the non-ghost arrivals are also plotted for these paths. As can be seen, the approximate normal mode method computes the complete acoustic field, with, in this instance, less computer time than the WKBJ method.

SUMMARY

This chapter has presented a synopsis of two methods for the solution of the 3-D acoustic wave equation for a point source in a laterally homogeneous medium. The solutions were seen to consist of integral transforms on reflection coefficients that were computed from the depth varying model and boundary conditions. It was then shown that operations on the observed data at the surface can recover terms in the reflection coefficient expansions that may be analytically or computationally related to the underlying velocity-depth model. In the next chapter, the details of the practical operations needed to recover parts (or all) of the reflection coefficient will be presented. The inversion of the recovered reflection coefficient for the

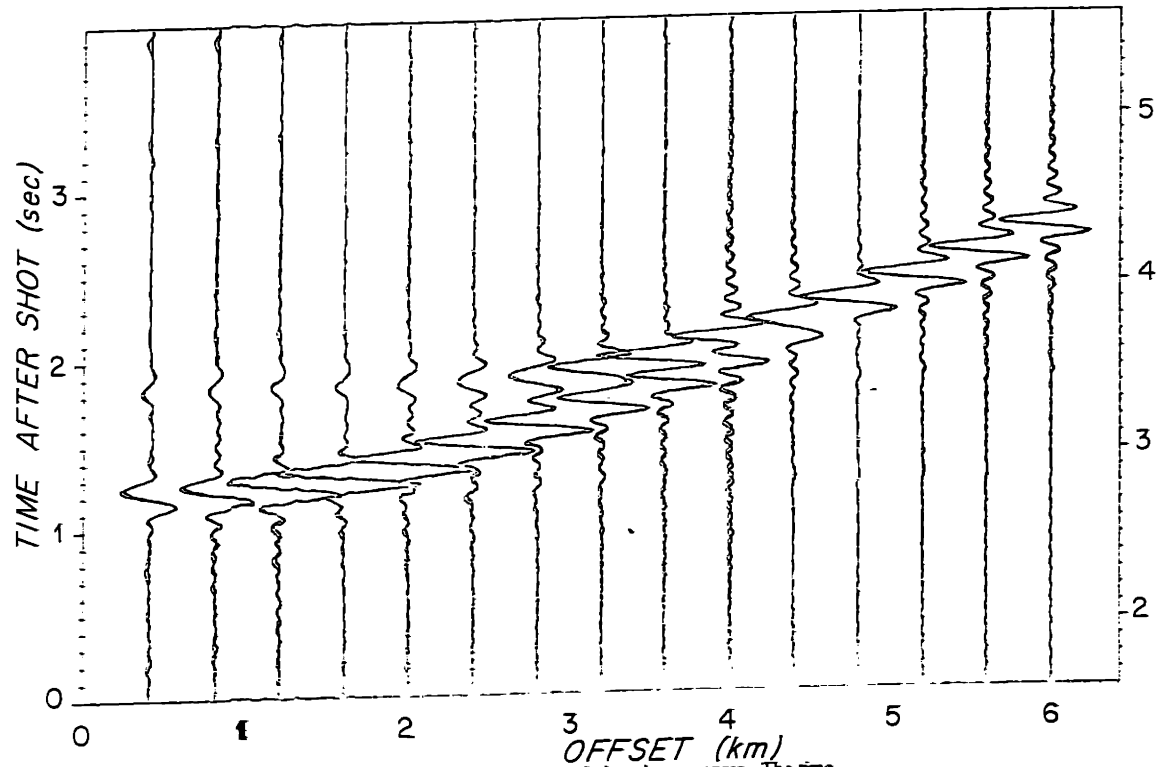

Fig. 2.12a) Comparison of WKBJ and approximate normal mode impulse responses. The time window is such that the water column multiples are not seen. The impulse responses for both methods are perfectly band limited to less than 10 Hz for comparison. The rays included in the WKBJ solution are discussed in the text. The plot is reduced on 4 km/s.

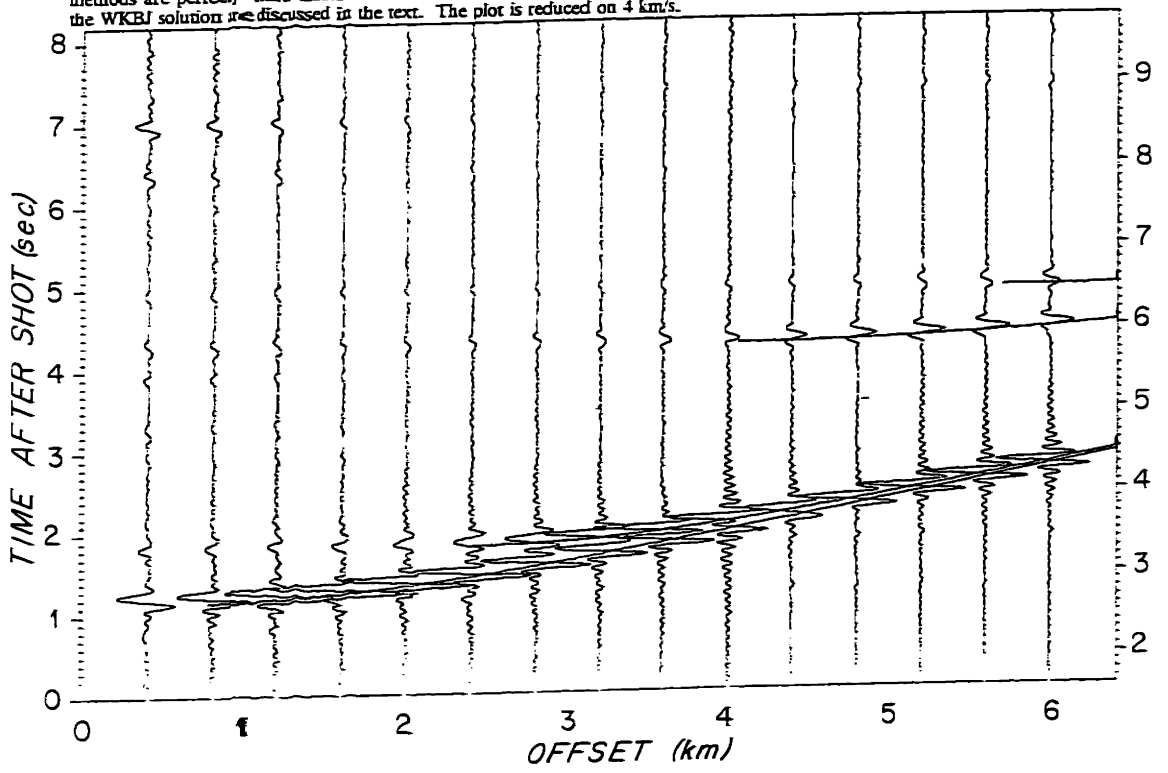

Fig 2.12b) The approximate normal mode synthetics for the model of fig. 2.11. Later sections of the waveform are plotted to show the inclusion of the water column multiples. The ray trace travel-time curves are also shown. The plot is reduced on 4 km/s.

velocity/depth model is treated in chapters 4,5, and 6.

REFERENCES

Abramowitz, M. and Stegun, I.A., *Handbook of Mathematical Functions*. Washington, D.C.: U.S. Bureau of Standards, U.S. Printing Office, 1964.

Aki, K. and Richards, P.G., in *Quantitative Seismology: Theory and Methods*, San Francisco: W.H. Freeman, 1980.

Budden, K.G., in *Radio Waves in the Ionosphere*, Cambridge, U.K.: Cambridge University Press, 1961.

Chapman, C.H., "A New Method for Computing Synthetic Seismograms," *Geophysical Journal of the Royal Astronomical Society*, vol. 54, pp. 481-518, 1978.

Chapman, C.H., "Generalized Radon Transforms and Slant Stacks," *Geophysical Journal of the Royal Astronomical Society*, vol. 66, pp. 445-453, 1981.

Dorman, L. and Jacobson, R.S., "Linear Inversion of Body Wave Data; Part I: Velocity Structure From Travel Times and Ranges," *Geophysics*, vol. 46, no. 2, pp. 138-151, 1981.

Frisk, G.V., Doutt, J., and Hays, E., "Bottom Interaction of Low-frequency Acoustic Signals at Small Grazing Angles in the Deep Ocean," *Journal of the Acoustical Society of America*, vol. 69, no. 1, 1981.

Fuchs, K. and Muller, G., "Computation of synthetic seismograms with the reflectivity method and comparison with observations," *Geophysical Journal of the Royal Astronomical Society*, vol. 23, pp. 417-433, 1971.

Gerver, M. and Markushevich, V., "Determination of seismic wave velocity from the travel time curve," *Geophysical Journal of the Royal Astronomical Society*, vol. 11, pp. 165-173, 1966.

Henry, M., Orcutt, J.A., and Parker, R.L., "A New Method fo Slant Stacking Refraction Data," *Geophysical Research Letters*, vol. 7, no. 12, pp. 1073-1076, December 1980.

Hooshyar and Razavy, "A method for constructing wave velocity and density profiles from the angular dependence of the reflection coefficient," *JASA*, vol. 73, no. 1, p. 18, 1983.

Kennett, B.L.N., "Reflections, Rays, and Reverberations," *BSSA*, vol. 64, pp. 1685-1696, 1974.

Kennett, B.L.N., "Slowness techniques in seismic interpretation," *Journal of Geophysical Research*, vol. 86, no. B12, pp. 11575-11584, 1981.

McMechan, G.A. and Ottolini, R., "Direct Observation of a Tau-P curve in a Slant Stacked Wavefield," *Bull. BSSA*, vol. 70, pp. 775-789, 1980.

Mitchell, S.K., "An Extension of Langer's Asymptotic Solution with Applications to Ocean Acoustics," Applied Research Laboratories, U.T. Austin #ARL-TR-77-13, March 1, 1977.

Orcutt, J.A., Mackenzie, K., and McClain, J., "The role of X(p) constraints in linear, extremal inversion of explosion profile data," *Bulletin of the Seismological Society of America*, vol. 20, pp. 2103-2116, 1980.

Orcutt, J.A., "Joint Linear, Extremal Inversion of Seismic Kinematic Data," *Journal of Geophysical Research*, vol. 35, no. B5, pp. 2649-2660, 1980.

Stoffa, P.L., Diebold, J.B., and Buhl, P., "Inversion of seismic data in the tau-p plane," *Geophysical Research Letters*, vol. 8, no. 8, pp. 869-872, August, 1981.

Tolstoy, I. and Clay, C.S., *Ocean Acoustics*. New York, NY: McGraw Hill Book Co., 1966.

Treitel, S., Gutowski, P.R., Hubral, P., and Wagner, D.E., "Plane wave decomposition of seismograms," *Geophysics*, vol. 47, no. 10, pp. 1375-1401, 1982.

VanTrees, H.L, *Detection, Estimation, and Modulation Theory: Part I*. New York, NY: John Wiley and Sons, 1968.

CHAPTER 3: Velocity Spectral Analysis

INTRODUCTION

Logistical considerations and data acquisition procedures do not often allow large aperture coherent processing to be practically implemented. As a result, it is impossible to compute the true plane wave decomposition or proper slant stack defined in Chapter 2. However, this does not adversely effect most practical inversion procedures because the decomposition itself is not used, but rather parameters estimated from it. The primary reason for the use of parameters is that the wavefield transform itself contains both too much and too little information. The waveform and spectral details carry effects of propagation through structures that are more complicated than the simple model structures usually assumed can represent, and therefore cannot be predicted, no matter how the model parameters are varied. That the transform contains too little information is shown by the fact that even if a continuous set of seismograms along a radial line on the surface were obtained, this data would not uniquely specify a model of complexity sufficient to match the data, such as one that allowed lateral inhomogeneities. A classical solution to this ambiguity in the inverse problem has been to throw out measurements that cannot be predicted from models that are more or less uniquely* specified from the limited dataset. The remaining data are those parameters which are robust to the phenomena that the assumed model framework cannot predict. Thus, the parameters of the simplified model are observable from the remaining measurement parameters which, in turn, are predictable from the model specification.** It should be noted that unless information is removed intelligently from the data, then features that are inconsistent with one another using the given model framework will cause grave difficulties in the inversion. A simple example of this would

*I allow the "more or less" phrase because prior information and other physical constraints can often augment the uniqueness of the inverse problem in the face of sparse data.

**Excluding the effects of observation noise.

be the use of the arrival times of every event on the seismograms as data parameters without allowing the model to know about the existence of multiples. For the seismic inverse problem, the standard dividing lines are laterally homogeneous versus inhomogenous models and kinematic versus dynamic measurements. The restrictions on data acquisition and the computational burden for 3-D modeling and processing are such that laterally inhomogeneous models have only just recently been approached by the large budgeted oil companies, even though recent years have brought advances in forward problem solutions for laterally varying media [Cerveny, 1972; 1983; Chapman and Drummond, 1982; Alterman and Loewenthal, 1972; Boore, 1972; Kelley, et al., 1976] Similarly, kinematic, or travel time, measurements have just recently been augmented by dynamic, or amplitude and phase measurements in practical inversion procedures [Jobert, 1982; Garmany, 1982; Brocher and Phinney, 1981; Jurkevics, et al., 1980]. This beginning has become possible through both advances in theory which allow efficient computation of amplitudes from forward models [e.g. Chapman's WKBJ synthetics [1978]], and the advent of wide dynamic range multichannel digital recording systems. The use of laterally varying models and dynamic measurements are intimately linked because small changes in the model can cause very large changes in the amplitude structure of arrivals, while leaving travel times relatively unperturbed.

To return to the issue at hand, it is possible to estimate travel times and even arrival amplitudes on a scale at which they are useful as constraints on the model without carrying out the impossible plane wave decomposition. The main purpose of this chapter is to describe and quantify an algorithm for estimating these parameters from coherent processing over a short and discretely sampled spatial aperture. This work will concentrate on new methods for carrying out the parameter estimates and the necessary separation of multipath contributions both in refraction and long-range propagation data so that observables which are easily related to the

model can be obtained.

The structure of this chapter will be to first present a simple model which will allow the effects of practical acquisition and processing to be quantified. After declaring certain aspects (parameters) of the observed data to be important, a "velocity spectral analysis" algorithm for their estimation will be defined. This algorithm is analysed in terms of arrival time, slowness, and amplitude estimation performance, and examples are given to justify the choices of parameters used within the algorithm for use on the real data of chapters 5 and 6. Finally, an extension of the velocity spectral analysis algorithm is presented which allows the waveforms, or slant-stack itself to be generated. This method is demonstrated on synthetic and real data and shown to be superior to conventional slant stacking on short aperture data.

DETERMINISTIC PROPAGATION AND APERTURE EFFECTS

The Model

Chapter 2 outlined a procedure for obtaining the reflection coefficient from the pressure field measured at the surface and indicated how the reflection coefficient was related to the model. The inversion problem was motivated for regions where the WKBJ solution was adequate, and for situations where the more complete normal mode method was required, but the waves were adequately dispersed to allow measurement of individual dispersion curves. In this section we use the WKBJ synthetic seismogram method to show just what can be practically estimated from finite bandwidth observations of refraction data on a short aperture.

Following an analysis similar to that of Chapman [1978], eqn. (2.26) leads to the geometric arrival for a single turning ray when $dx(p)/dp\,|_{p_0} < 0$ (low gradient refraction, forward branch of the travel time curve) as:

$$P(t,r_0,z=0) = \frac{p_0^{\frac{1}{2}}}{4\pi c_s^2 \nu(0,p_0) r_0^{\frac{1}{2}}} \frac{\left|\prod_j T_j(p_0)\right|}{\left|dx(p)/dp\right|_{p_0}^{\frac{1}{2}}} \cdot \qquad 3.1$$

$$\left[s(t-T(r_0)) \cos(\arg \prod_j T_j(p_0)) + \bar{s}(t-T(r_0)) \sin(\arg \prod_j T_j(p_0)) \right]$$

This can be extended to a high gradient refraction reversed branch ($dx(p)/dp > 0$), by an additional Hilbert transform. This leads to $s(t) \Rightarrow \bar{s}(t)$, and $\bar{s}(t) \Rightarrow -s(t)$in the above equation. For a wide angle reflection reversed branch ($dx(p)/dp > 0$, no "turning point"), equation 3.1 holds. For both refraction cases, each additional turning point simply introduces an additional Hilbert transform. For a small region around the nominal offset, r_0, the terms in eqn. 3.1 can be expanded as:

Slowness:

$$p = p_0 \qquad 3.2a$$

Reflection/Transmission Coefficient Magnitude:

$$\left|\prod_j T_j(p)\right| = \left|\prod_j T_j(p_0)\right| = A(p_0) = A_0 \qquad 3.2b$$

Reflection/Transmission Coefficient Phase Shift:

$$\arg \prod_j T_j(p) = \phi(r) = \phi_0 + \dot{\phi}_0(r-r_0) \qquad 3.2c$$

(critical angle) $0 > \phi(r) > -180$ (grazing)

$$\dot{\phi}_0 \equiv \frac{d\phi_0(r)}{dr}\Big|_{r_0}$$

Time of Arrival:

$$T(r) = T(r_0) + p_0(r-r_0) + \frac{\dot{p}_0}{2}(r-r_0)^2 \qquad 3.2d$$

$$= T_0 + p_0(r-r_0) + \frac{\dot{p}_0}{2}(r-r_0)^2$$

$$\equiv \tau_0 + p_0 r + \frac{\dot{p}_0}{2}(r-r_0)^2$$

$$\dot{p}_0 \equiv \left.\frac{d^2T(r)}{dr^2}\right|_{r_0}$$

Geometrical Spreading Factor:

$$dx(p)/dp = dx(p)/dp\,|_{p_0} \qquad 3.2e$$

For the small apertures that are of practical interest ($\approx$ 1 km), the amplitude functions are well approximated by constants; however, the phases and times of arrival must be expanded to first and second order to approximate realistic data. This is the usual pattern for wave problems; a smooth envelope function with rapid modulation. The wavefield near r_0 becomes (dropping the $z=0$ dependence):

$$P(t,r) = \frac{p_0^{1/2}}{4\pi c_s^2 \nu(0,p_0)} \frac{A_0}{|dx(p)/dp\,|_{p_0}|^{1/2}} \frac{1}{r^{1/2}} \cdot \qquad 3.3a$$

$$Q_\tau \Big[\, s(t-T(r))\cos(\phi_0 + \dot{\phi}_0(r-r_0)) + \tilde{s}(t-T(r))\sin(\phi_0 + \dot{\phi}_0(r-r_0)) \,\Big]$$

$$P(\omega,r) = \frac{p_0^{1/2}}{4\pi c_s^2 \nu(0,p_0)} \frac{A_0}{|dx(p)/dp\,|_{p_0}|^{1/2}} \frac{1}{r^{1/2}} \cdot \qquad 3.3b$$

$$Q_\omega S(\omega) e^{i\omega[\tau_0 + p_0 r + \frac{\dot{p}_0}{2}(r-r_0)^2]}\, e^{i(\phi_0 + \dot{\phi}_0(r-r_0))sgn(\omega)}$$

where

$$Q_\tau = \begin{cases} [\mathrm{H}^-]^{n-1} & \text{for low gradient refraction} \quad dx(p)/dp < 0 \\ [\mathrm{H}^-]^{n} & \text{for high gradient refraction} \quad dx(p)/dp > 0 \\ 1 & \text{for wide angle reflection} \quad dx(p)/dp > 0 \end{cases}$$

and Q_ω is the frequency domain representation of Q_τ. In equation 3.3b, $e^{i\omega\tau_0}$ is the vertical propagation term , $e^{i\omega p_0 r}$ is the planar movement term, $e^{i\omega\dot{p}_0/2(r-r_0)^2}$ is the wavefront curvature, $e^{i\phi_0}$ is the nominal reflection/transmission coefficient phase shift, and $e^{i\dot{\phi}_0(r-r_0)}$ is the change in reflection/transmission phase due to the change in p with the change in r across the aperture. The $[H^-]$ terms in Q_τ and Q_ω take into account n turning points at depth. In other words, the order of the multiple is n. For travel time inversions the primary interest lies in estimating $\tau(p)$, or in this case τ_0 and p_0. As an additional bonus, the use of a short aperture also gives us a good estimate of the geometrical offset, r_0, which is accurate enough to be of use in inversion procedures defined on $x(p)$. We will also be concerned with retaining amplitude linearity. Although it is highly dependent upon medium details, it can be used as a constraint, if not a primary datum.

Using the expressions 3.3a and b, we want to determine the effects of the short aperture, the wavefront curvature $\dot{p}_0$, the reflection/transmission coefficient and turning point phase shifts, and the band limitation of the source spectrum on the estimated τ_0 and p_0. In practice, the effective source spectrum as measured at the receiver is unknown. Even though explosive signatures are known theoretically and can be measured experimentally with a source monitor hydrophone, the poor signal to noise ratio, and the effects of intrinsic attenuation, scattering along the propagation path, and multipath propagation disallow determination at the receiver. The spectrum will change for each ray-path, due to the differing medium, and among kinetic groups because of differing interactions with rough interfaces, such as the water/ice/air boundary. Autoregressive spiking filters for time delay estimation which supposedly work on data with unknown spectral characteristics have not been tried in this work. The spiking filter would have to be designed on one channel and then applied to all the others in order to ensure that the phase structure of the signals were changed uniformly so as not to degrade later

slowness estimates. For these reasons, it is not generally possible to deconvolve the data. The analyses will be carried out for the bandlimited spectrum, and then a discussion of how to recover the intercept time $\hat{\tau}_0$ and slowness $\tilde{p}_0$ estimates will be given.

The Finite Aperture

To examine the effects of limiting the r integration of eqn. 2.35 to $r_0=L/2$, the analysis will be broken into the cases for planar, $\tilde{p}_0=0$ and curved, $\tilde{p}_0\neq 0$ wavefronts. For the planar case we formally separate $\tilde{p}_0$ and its inverse, $dx/dp\,|_{p0}$, for obvious reasons. Since the spreading factor amplitude, $|dx(p)/dp\,|_{p0}|^{1/2}$, does not change across the aperture, we define the constant:

$$C \equiv \frac{p_0^{1/2} A_0 Q}{4\pi c_s^2 \nu(0,p_0)\,|dx(p)/dp\,|_{p0}|^{1/2}}$$

which will appear in many equations. Q is taken as Q_τ or Q_ω, whichever is appropriate. The aperture weighting function $w_L(r)$ is positive and symmetrical about zero, has an area of one, and is zero outside $\pm L/2$.

Case 1) $\tilde{p}_0 = 0$, no wavefront curvature:

From 2.35a,

$$\hat{U}_{3D}(\omega,\omega p) = \int_0^\infty w_L(r-r_0) P(\omega,r) e^{-\omega p r} r^{1/2} dr \qquad 3.4a$$

$$= CS(\omega)\, e^{[\phi_0 sgn(\omega) + \omega\tau_0]} \int_{-L/2}^{L/2} w_L(r) e^{i\omega(p_0 + \frac{\tilde{\omega}_0}{|\omega|} - p)r}\, dr$$

$$= CS(\omega)\, e^{i\omega(\tau_0 - \frac{\omega_0}{|\omega|})} W_L(\omega(p-\tilde{p}_0(\omega)))$$

where:

$$W_L(\omega,p) = \mathrm{FT}_r[w_L(r)] \quad \text{and} \quad \hat{p}_0(\omega) = p_0 + \frac{\dot{\phi}_0}{|\omega|}.$$

This leads to the proper slant-stack (before filtering):

$$\hat{u}_{3D}(\tau,p) = C[s(\tau-\tau_0)\cos\phi_0 + \bar{s}(\tau-\tau_0)\sin\phi_0] * FT_\omega^{-1}[W_L(\omega(p-\hat{p}_0(\omega)))] \qquad 3.4b$$

From 3.4a we see that when $W_L(\omega p)$ has its peak at $\omega p = 0$, the estimated slowness, i.e. the slowness at which $\hat{U}_{3D}$ has its maximum, will be biased:

$$\hat{p}_0(\omega) = p_0 + \frac{\dot{\phi}_0}{|\omega|} \qquad 3.5$$

and change as a function of frequency. When $\dot{\phi}_0 \neq 0$, the inverse temporal Fourier transform of W_L is quite complicated, and in the time domain the arrival peak will be smeared over a slowness interval. An example will be given later to show how much effect this has in typical problems.

When $\dot{\phi}_0$ can be neglected, the expression becomes

$$\hat{u}_{3D}(\tau,p) = C[\, s(\tau-\tau_0)\cos\phi_0 + \bar{s}(\tau-\tau_0)\sin\phi_0 \,] * \frac{1}{|p-p_0|} w_L(\tau/|p-p_0|). \qquad 3.6$$

It is interesting to note that the time domain convolutional filter in 3.6 is just a scaled version of the aperture taper. For example, if the uniform taper:

$$w_L(r) = \frac{1}{L}\mathrm{RECT}_L(r) \equiv \begin{cases} 1/L & |r|<L/2 \\ 0 & \text{elsewhere} \end{cases}$$

is used then:

$$w_L(\tau)|_p = \frac{1}{L|p-p_0|}\mathrm{RECT}_{L|p-p_0|}(\tau) \qquad 3.7a$$

which limits to an impulse as $p \to p_0$, leaving the wave undistorted, but lowpass filters with a boxcar of length $L|p-p_0|$ and amplitude $1/(L|p-p_0|)$ for slownesses $p \neq p_0$. For a uniform aperture weight the beampattern of the system is:

$$W_L(\omega,p) = \frac{\sin(\omega pL/2)}{\omega pL/2} = \mathrm{sinc}(\omega pL/2) \qquad 3.7b$$

and the unfiltered frequency wavenumber function is seen to limit to:

$$\hat{U}_{3D}(\omega,\omega p) = CS(\omega)e^{i\omega(\tau_0 + \frac{\phi_0}{|\omega|})}\,\delta(\omega(p-p_0)) \qquad 3.8$$

as $L\to\infty$, since $\lim_{L\to\infty} \mathrm{sinc}(Lx) = \delta(x)$, which it should, since it is a plane wave by assumption.

Case 2) $\dot{p}_0 \neq 0$, wavefronts with curvature:

This case occurs for reversed branches of the travel-time curve due to wide angle reflections or high gradient refractions for which $\dot{p}_0 = d^2T(r)/dr^2|_{r_0} > 0$ or $dx(p)/dp\,|_{p_0} > 0$, and for forward branches; $\dot{p}_0 = d^2T(r)/dr^2|_{r_0} < 0$ or $dx(p)/dp\,|_{p_0} < 0$ from low to moderate velocity gradient refractions. The analysis for this case is slightly more complicated than that for $\dot{p}_0 = 0$, and to simplify it somewhat the phase shift terms are neglected for the moment. Starting with relation 2.35b, we obtain:

$$\hat{u}_{3D}(\tau,p) = C\int_0^\infty w_L(r-r_0)\, s(\tau+pr-\tau_0-p_0r-\frac{\dot{p}_0}{2}(r-r_0)^2)\, dr \qquad 3.9$$

using 3.3a and the previous definitions. Changing variables $(r-r_0) = x$ yields:

$$\hat{u}_{3D}(\tau,p) = C\int_{-L/2}^{L/2} w_L(x)s(\tau-\tau_0+(p-p_0)(r_0+x)-\frac{\dot{p}_0}{2}x^2)\, dx. \qquad 3.10$$

Changing variables again, letting $u = \frac{\dot{p}_0}{2}x^2$ and assuming $\dot{p}_0 > 0$ yields:

$$\hat{u}_{3D}(\tau,p) = C\left[\frac{2}{|\dot{p}_0|}\right]^{1/2} \int_0^{\frac{\dot{p}_0}{2}(L/2)^2} w_L[(\frac{2}{|\dot{p}_0|}u)^{1/2}]\, \frac{s(\tau-\tau_0+(p-p_0)(r_0+(2u/|\dot{p}_0|)^{1/2}) - u)}{\sqrt{u}}\, du \qquad 3.11$$

This is messy to interpret for $p \neq p_0$, and we shall shortly see using the frequency domain representation that the value of p at which it peaks is still p_0, giving the same slowness estimate

as for the planar case, although with a degraded beampattern. At $p = p_0$, 3.11 is seen to be the convolution:

$$\hat{u}_{3D}(\tau, p_0) = C\left[\frac{2}{|\dot{p}_0|}\right]^{1/2} s(\tau - \tau_0) * \frac{[H(\tau) - H(\tau - \frac{\dot{p}_0}{2}(L/2)^2)]\, w_L[(2\tau/|\dot{p}_0|)^{1/2}]}{\sqrt{\tau}} \qquad 3.12$$

For the uniform aperture weight, $1/L$, the wave shape is seen to be the time response convolved with a $\frac{1}{L}\frac{H(\tau)}{\tau^{1/2}}$ function truncated at $\tau = \frac{\dot{p}_0}{2}(L/2)^2$. Note that the area in this function is $\left[|\dot{p}_0|/2\right]^{1/2}$, and thus cancels the leading constant. For a forward branch the operator is simply reversed and becomes anti-causal, but truncated at a negative τ. In equations 3.18 and 3.19 it will be seen that as $L \to \infty$, the convolution, 3.12, becomes

$$\hat{u}_{3D}(\tau, p_0) - C\, s(\tau - \tau_0) * \frac{H(\tau)}{\tau^{1/2}} = u_{3D}(\tau, p_0) \qquad \dot{p}_0 > 0 \quad \text{(reversed)} \qquad 3.13a$$

$$\hat{u}_{3D}(\tau, p_0) - C\, s(\tau - \tau_0) * \frac{H(-\tau)}{(-\tau)^{1/2}} = u_{3D}(\tau, p_0) \qquad \dot{p}_0 < 0 \quad \text{(forward)} \qquad 3.13b$$

when the aperture weight is 1, not $1/L$, and is equal to the infinite aperture result for a non-attenuating wave with wavefront curvature.

It remains to be seen that the largest response is at $p = p_0$ for the case in which $\phi_0 = \dot{\phi}_0 = 0$ but the wavefronts are curved. To do this, recall the frequency representation $P(\omega, r)$ from 3.3b and insert it into eqn. 2.35a. Using the same redefinition of the constant terms, C, as before this yields:

$$\hat{U}_{3D}(\omega, \omega p) = C\, S(\omega) \int_0^\infty w_L(r - r_0)\, e^{i\omega(\tau_0 + (p_0 - p)r + \frac{\dot{p}_0}{2}(r - r_0)^2)}\, dr \qquad 3.14$$

and changing variables, $x = (r - r_0)$ obtains:

$$\hat{U}_{3D}(\omega,\omega p) = C\,S(\omega)\, e^{i\omega(\tau_0+(p_0-p)r_0)} \int_{-L/2}^{L/2} w_L(x) e^{i\omega((p-p_0)x+\frac{\dot{p}_0}{2}x^2)}\, dx. \qquad 3.15$$

The integrand $w_L(x)$ is symmetric and real, and only the cosine term in the transform is nonzero. We are interested in the magnitude of $\hat{U}_{3D}$, and thus maximizing the integral with respect to p is all that is necessary. Setting the derivative to zero yields:

$$0 = \frac{d}{dp} \int_{-L/2}^{L/2} w_L(x) \cos(\omega(p-p_0)x + \frac{\dot{p}_0}{2}x^2)\, dx \qquad 3.16$$

$$= -\int_{-L/2}^{L/2} w_L(x)\,(\omega x) \sin(\omega(p-p_0)x + \frac{\dot{p}_0}{2}x^2)\, dx.$$

For $w_L(x)$ symmetric and $\omega \neq 0$, this is only zero when the sine term is completely symmetric in x, which occurs for $p = p_0$. Thus, the slowness estimate is unbiased in the presence of wavefront curvature. Note also, from eqn. 3.15, that the bulk travel time delay outside the integral is also unbiased, and is τ_0 at $p = p_0$. It can also be shown that the phase shift and phase shift change due to ϕ_0, $\dot{\phi}_0 \neq 0$ again lead to a quadrature sum of the source waveform and its Hilbert transform, as in eqn. 3.4b, and the same phase velocity estimate bias as eqn. 3.5.

At this point, we have determined the output of expressions 2.35a and b, the 2-D slant-stack operations, in the face of a finite aperture for point source data, but the estimation of the reflection coefficient $R(\omega,p)$ and the response $R(\tau,p)$ requires a further filtering operation, as given in eqns. 2.36 and 2.37a and b. The change in the reflection coefficient phase due to $\dot{\phi}_0$ manifests itself only as a slowness estimation error in the frequency domain given by 3.5. It has not been proven, but it is felt that the time domain convolution with the operator of eqn. 3.4b leads to very little distortion of the waveform in time domain implementations, though the peak, and thus estimated slowness, will be more diffuse on the 3-D slant stack $\hat{u}_{3D}(\tau,p)$ than on the plane wave decomposition, $\hat{U}_{3D}(\omega,\omega p)$. Note that the change in measured slowness

across frequency (eqn. 3.5) allows the plane wave decomposition to determine the $\dot{\phi}_0$ parameter if the statistical stability of the slowness estimate is adequate in the face of measurement noise.

The primary distortion in the reflection coefficient estimate will be due to wavefront curvature. To see what this distortion is, we insert the expression for the 3-D unfiltered slant stack $\hat{u}_{3D}(\tau,p_0)$ from eqn. 3.12 into expression 2.37b:

$$\hat{R}(\tau,p_0) = \frac{d}{d\tau}\frac{4c_s^2}{\sqrt{2p_0}}\frac{H(\tau)}{\tau^{1/2}} * \frac{p_0^{1/4}A_0Q_\tau[\cos\phi_0 + \sin\phi_0 H^-]s(\tau-\tau_0)}{4\pi c_s^2 v(0,p_0)\,|dx(p)/dp\,|_{p_0}|^{1/2}} sgn(\dot{p}_0) \qquad 3.17a$$

$$* \left[\frac{2}{|\dot{p}_0|}\right]^{1/2} \frac{[H(\tau) - H(\tau - \frac{\dot{p}_0}{2}(L/2)^{1/2})]}{\tau^{1/2}} w_L\left(\left[\frac{2}{|\dot{p}_0|}\right]^{1/2}\tau^{1/2}\right) sgn(\dot{p}_0)$$

or:

$$\hat{R}(\tau,p_0) = \frac{d}{d\tau}\frac{H(\tau)}{\tau^{1/2}} * \frac{[H(\tau) - H(\tau - \frac{\dot{p}_0}{2}(L/2)^{1/2})]}{\tau^{1/2}} w_L\left(\left[\frac{2}{|\dot{p}_0|}\right]^{1/2}\tau^{1/2}\right) \qquad 3.17b$$

$$* \left[\frac{2}{|\dot{p}_0|}\right]^{1/2} \frac{A_0Q_\tau[\cos\phi_0 + \sin\phi_0 H^-]s(\tau-\tau_0)}{\sqrt{2}\pi v(0,p_0)\,|dx(p)/dp\,|_{p_0}|^{1/2}}.$$

For a short aperture there are two main distortions, i) the amplitude "spreading" factor $|dx(p)/dp\,|_{p_0}|^{1/2}$ is present, and ii) the derivative and first convolution are not an identity as they would be for the infinite aperture. For the infinite $L\to\infty$ aperture with a uniform weighting of $w_L=1$, not $1/L$,

$$\lim_{L\to\infty} \frac{[H(\tau) - H(\tau - \frac{\dot{p}_0}{2}(L/2)^{1/2})]}{\tau^{1/2}} w_L \left(\left[\frac{2}{|\dot{p}_0|} \right]^{1/2} \tau^{1/2} \right) = \frac{H(\tau)}{\tau^{1/2}} \qquad 3.18a$$

and

$$\frac{d}{d\tau}\left[\frac{H(\tau)}{\tau^{1/2}} * \frac{H(\tau)}{\tau^{1/2}}\right] = \frac{d}{d\tau}\pi H(\tau) = \pi\delta(\tau). \qquad 3.18b$$

Thus the top line of 3.17b becomes $\pi\delta(\tau)$. For the infinite aperture, the $\left[\frac{2}{|\dot{p}_0|}\right]^{1/2}$ term is not canceled by the area in the difference of step functions and the $w_L = 1/L$ weighting, and thus removes the effect of the spreading term, since

$$\dot{p}_0 = \frac{dp}{dr}|_{r_0} = \frac{dp}{dx(p)}|_{r_0} = [dx(p)/dp\,|_{p_0}]^{-1} \qquad 3.18c$$

For the infinite aperture, with $w_L = 1$,

$$\hat{R}(\tau, p_0) = \frac{A_0 Q_\tau [\cos\phi_0 + \sin\phi_0 H^-] s(\tau - \tau_0)}{v(0, p_0)} \qquad 3.19a$$

$$= FT_\omega^{-1}\left[\frac{\prod_j T_j(p_0)(-i\,sgn(\omega))^n}{v(0, p_0)} e^{-i\omega\tau_0} S(\omega)\right] \qquad 3.19b$$

since

$$A_0[\cos\phi_0 + \sin\phi_0 H^-] \iff \prod_j T_j(p_0)$$

from eqn. 3.2 and

$$Q_\omega \Longleftrightarrow (-i\,sgn(\omega))^n \qquad Q_\tau \Longleftrightarrow [H^-]^n$$

from 3.3b. Thus, the infinite aperture result gives the correct reflection coefficient (eqn. 2.24) when the source, $S(\omega)$, is deconvolved.

The finite aperture result, on the other hand, is distorted. It turns out that for arrays that are shorter than 10 wavelengths long, the duration of the truncated $\frac{H(\tau)}{\tau^{1/2}}$ function for a

typical wavefront curvature is so short as to be unimportant. (A later example will show this.) If this is assumed, and because of the way the aperture window has been normalized, the area in the second line of equation 3.17a is one. Thus the short aperture reflection coefficient estimate is:

$$\hat{R}(\tau,p_0) = \frac{d}{d\tau}\frac{H(\tau)}{\tau^{\frac{1}{2}}} * \frac{A_0 Q_\tau[\cos\phi_0 + \sin\phi_0 H^-]s(\tau-\tau_0)}{\sqrt{2\pi\nu(0,p_0)}\,|dx(p)/dp\,|_{p_0}|^{\frac{1}{2}}} \qquad 3.20a$$

$$= \mathrm{FT}_\omega^{-1}\left[\frac{-i\omega\frac{e^{i\pi/4}}{\omega^{\frac{1}{2}}}}{|dx(p)/dp\,|_{p_0}|^{\frac{1}{2}}}\frac{\prod_j T_j(p)(-i\,sgn(\omega))^n e^{i\omega\tau_0}}{\sqrt{2\pi\nu(0,p_0)}}S(\omega)\right] \qquad 3.20b$$

and there is the distortion of a derivative, the spreading factor, and a filter relative to the correct reflection coefficient in 2.24.

To get a feeling for the effects of the wavefront curvature on the length of the truncated $\frac{H(\tau)}{\tau^{\frac{1}{2}}}$ convolutional operator we consider the simple example of a wide angle reflection from the homogeneous layered model of fig. 3.1a. For the wide angle reflection in the upper layer with sound speed c from the first interface at depth d, the geometrical arrival functions are:

$$T(p_0) = \frac{2d}{c\sqrt{1-(p_0c)^2}}$$

$$T(r_0) = \frac{\sqrt{(2d)^2+r^2}}{c}$$

$$r_0 = x(p_0) = \frac{2dp_0c}{\sqrt{1-(p_0c)^2}}$$

$$p_0(r_0) = \frac{r_0}{c\sqrt{(2d)^2+r_0^2}}$$

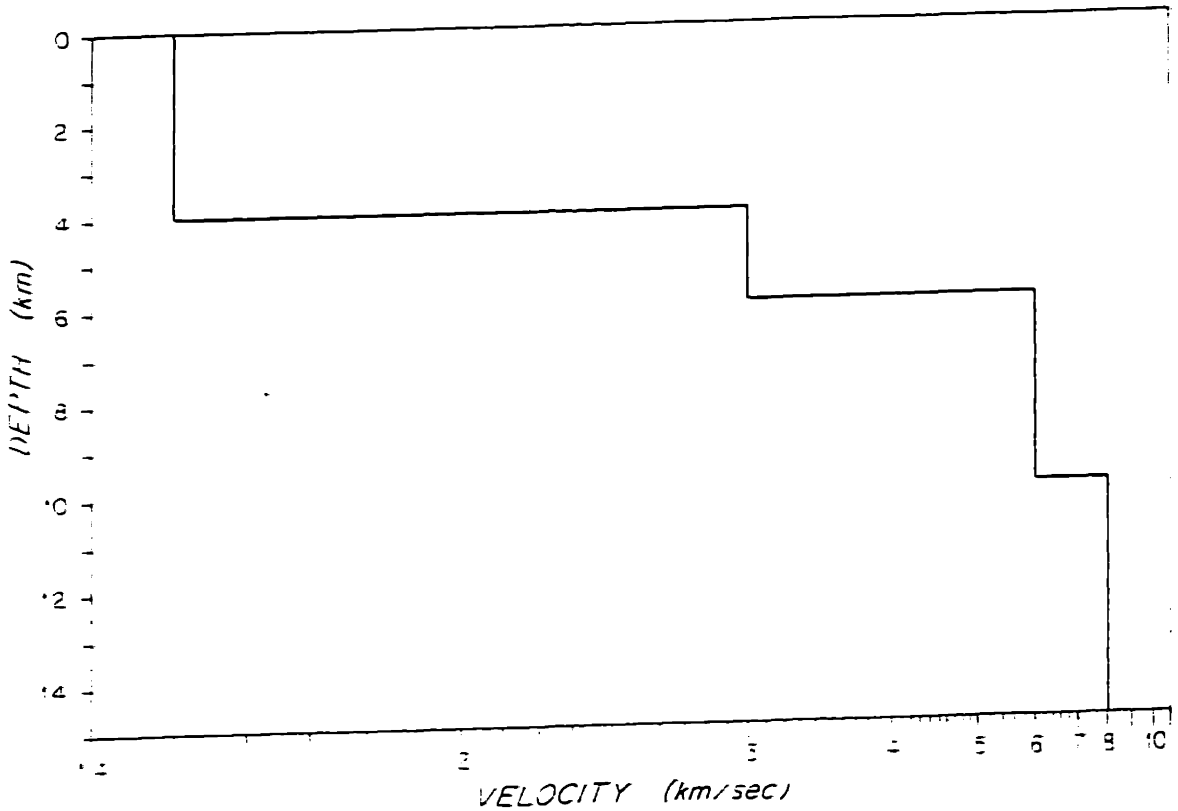

Fig. 3.1a) Homogeneous layered velocity-depth model used for the calculation of the reflection coefficient phase shifts of fig. 3.1b.

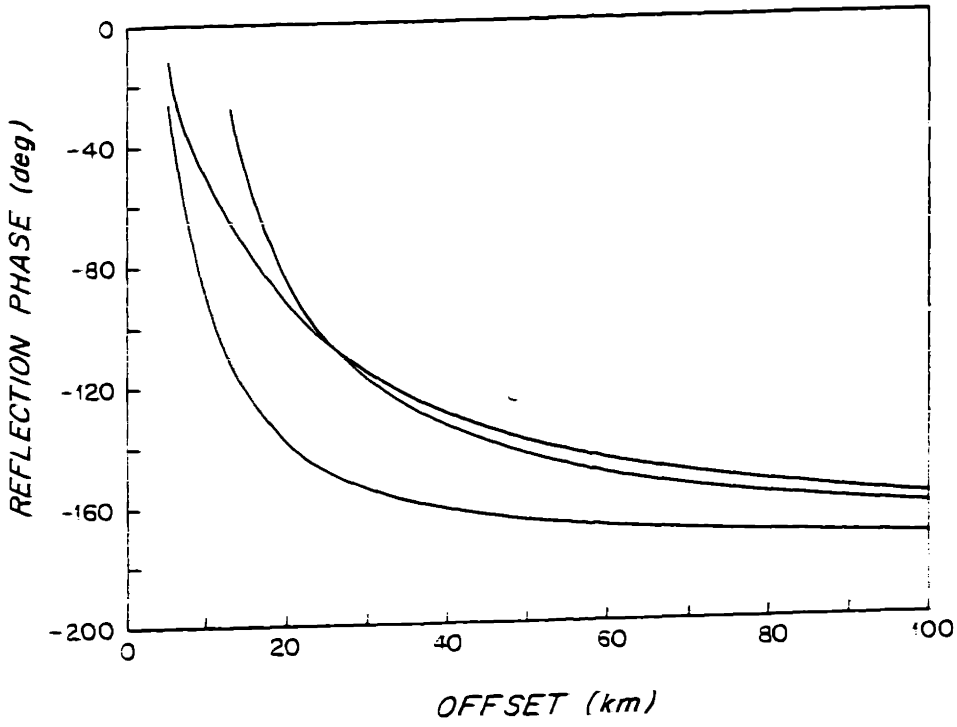

Fig. 3.1b) Reflection coefficient phase shifts as a function of offset for the homogeneous layered model of fig. 3.1a. The three curves correspond to the 3 interfaces which would cause wide angle reflections.

$$dx(p)/dp\,|_{p_0} = \frac{2dc}{\sqrt{1-(p_0c)^2}} + \frac{2dp^2c^3}{(1-(p_0c)^2)^{3/2}}$$

$$\dot{p}_0 \equiv \left.\frac{d^2T(r)}{dr^2}\right|_{r_0} = \left.\frac{dp_0(r)}{dr}\right|_{r_0} = \frac{1}{c\sqrt{(2d)^2+r_0^2}} - \frac{r_0^2}{c((2d)^2+r_0^2)^{3/2}}$$

An example with reasonably high curvature would be:

$d = 4$ km

$c = 1.5$ km/s

$r_0 = 10$ km

$p_0 = 1/1.92 = .521$ s/km

$\dot{p}_0 = 1/49.22 = .02$ s/km^2

$dx(p)/dp\,|_{p_0} = 49.22$ km^2/s

$L = 1$ km

Thus the length of the convolutional operator would be:

$$\frac{\dot{p}_0}{2}(L/2)^2 = .0025 \text{ seconds.}$$

This would obviously not affect low frequencies very much, and:

$$\hat{u}_{3D}(\tau,p_0) \approx P(\tau - p_0 r_0, r_0). \qquad 3.21a$$

$$= \frac{p_0^{1/2}A_0Q_\tau[\cos\phi_0 + \sin\phi_0 H^{-}]s(\tau-\tau_0)}{4\pi c_s^2 \nu(0,p_0)\,|dx(p)/dp\,|_{p_0}|^{1/2}} \qquad 3.21b$$

is the finite aperture 3-D slant stack without filtering.

The Finite Aperture 3-D Slant-stack and Plane Wave Decomposition

The conclusion from the above analysis is that the short aperture processing can recover the reflection coefficient multiplied by the source function and the spreading factor. To do this, the derivative and $\frac{H(\tau)}{\tau^{1/2}}$ filter should be omitted and the output of the stacker, $\hat{u}_{3D}$, or

$\hat{U}_{3D}$, should then be scaled by:

$$\frac{4\pi c_s^2}{p_0^{\frac{1}{2}}}. \tag{3.22}$$

This yields the short aperture slant stack formulae:

$$\hat{R}(\tau,p_0) = \frac{4\pi c_s^2}{p_0^{\frac{1}{2}}}\,\hat{u}_{3D}(\tau,p_0) \tag{3.23a}$$

$$\hat{R}(\omega,p_0) = \frac{4\pi c_s^2}{p_0^{\frac{1}{2}}}\,\hat{U}_{3D}(\omega,\omega p) \tag{3.23b}$$

and:

$$\hat{R}(\tau,p_0) = \frac{R(\tau,p_0) * s(\tau)}{|dx(p)/dp\,|_{p_0}|^{\frac{1}{2}}} = \frac{A_0 Q_\tau[\cos\phi_0 + \sin\phi_0 H^-]s(\tau-\tau_0)}{v(0,p_0)\;|dx(p)/dp\,|_{p_0}|^{\frac{1}{2}}} \tag{3.23c}$$

$$\hat{R}(\omega,p_0) = \frac{R(\omega,p_0)S(\omega)}{|dx(p)/dp\,|_{p_0}|^{\frac{1}{2}}} = \left[\frac{\prod_j T_j(p_0)(-i\,sgn(\omega))^n}{v(0,p_0)\;|dx(p)/dp\,|_{p_0}|^{\frac{1}{2}}}\,e^{-i\omega\tau_0}\,S(\omega)\right] \tag{3.23d}$$

using the approximate arrival from eqn. 3.1. Thus, with short aperture stacks we cannot get the correct magnitude of the impulse response, but only the local magnitude.

For the same wide angle reflection example it is useful to see the magnitude of the phase velocity estimation errors predicted by eqn. 3.5. The model in 3.1a gives the reflection coefficient phase shifts shown in fig. 3.1b. As a worst-case example, the lower curve in 3.1b (the shallow interface) has a phase rate of change $\dot{\phi}_0$ of $-\pi/30$ at 10 km. The results in table 3.1 are obtained and show that the bias is fairly small. In a later section of the chapter we will see whether or not this is within the error bounds on the estimates due to measurement noise.

TABLE 3.1		
$f=\omega/2\pi$ Hz	$1/p_0$ km/s	$1/\hat{p}_0$ km/s
6	1.45	1.456
24	1.45	1.452
6	8.0	8.18
24	8.0	8.04

APERTURE SAMPLING EFFECTS

In any practical implementation, the continuous integrals discussed in the previous section must be replaced by sums over data sampled in space and time. Problems involving time sampling are generally straightforward, since adequate sample rates and uniform sampling intervals are easy to achieve, with the major difficulty involving the need for interpolation of the time series in time domain implementations of the slant stack, eqn. 2.35b. The aperture sampling issue is more problematic, since cost and logistics considerations as well as the experimental goals can determine the density and positions of the sensors. In a later section of this chapter we deal with the effects of sampling locations within the aperture. The problem is essentially one of either array design for a good intrinsic beampattern, as in eqn. 3.7, or the use of adaptive processing techniques which weight the sensors of an array in an optimal fashion to synthesize a good pattern. For the arctic work, requirements on the slowness resolution needed for adequate inversions, the bandwidth over which the array needed to operate without aliasing, the two-dimensional coverage required and the limited number of channels in the acquisition system precluded the use of uniform 2-D sampling, and thus provided a relatively poor intrinsic beampattern. One of the main advantages of the application of the MLM method (discussed in the section of this chapter entitled *Velocity Spectral Analysis*) to the slowness decomposition is that the weights $w_L(\omega,r_n)$ are computed adaptively and form an

"optimal" window for each slowness, frequency, and spatial signal and noise structure to reject both independent sensor noise and interfering propagating signals. This will be seen to allow both higher apparent resolution in the slowness domain, and output that is relatively free of artifacts, even when using arrays with sparse, non-uniformly sampled sensor locations that have quite poor "conventional beampatterns", $W_L(\omega,p)$. Note that $W_L(\omega,p)$ is just the beampattern familiar to all array processing applications, where in terms of angle of incidence, θ, measured from broadside to the plane of the array, $p = \sin(\theta)/c_0$, and c_0 is the sound velocity in the medium immediately around the array.

The major problem in any sampled system in which the number of sensors is limited is aliasing. For a uniformly sampled aperture with N sensors spaced Δr and weighted by $1/N$, making an aperture of total length $L=(N-1)\Delta r$, the response equivalent to eqn. 3.7b is:

$$W_L(\omega p) = \frac{1}{N}\frac{\sin(\omega p N \Delta r/2)}{\sin(\omega p \Delta r/2)}. \qquad 3.24a$$

The slowness aliasing period, δp, is seen to be

$$\delta p = \frac{1}{f\Delta r} \qquad \text{where} \qquad f = \frac{\omega}{2\pi}. \qquad 3.24b$$

The time response of the filter is the sampled equivalent to eqn. 3.7a and is given for the above example as:

$$w_L(\tau,p) = \frac{1}{N}\sum_{n=-N/2}^{N/2-1}\delta\left(\frac{2\tau}{(p-p_0)\Delta r} + 2n + 1\right) \qquad 3.24c$$

and the response is seen to be undistorted for $p=p_0$ since the range of t over which $w_L(\tau,p)$ is nonzero becomes infinitely small, and the total area is one.

The region of influence of the sidelobes of the finite aperture stacker can be easily pictured. Figure 3.2a shows a hypothetical wave-field with two plane waves of slowness p_0 = 1/6 s/km with intercept τ_0 = 2s, and slowness p_0 = 1/1.5 s/km and intercept τ_0 = 1s, respectively.

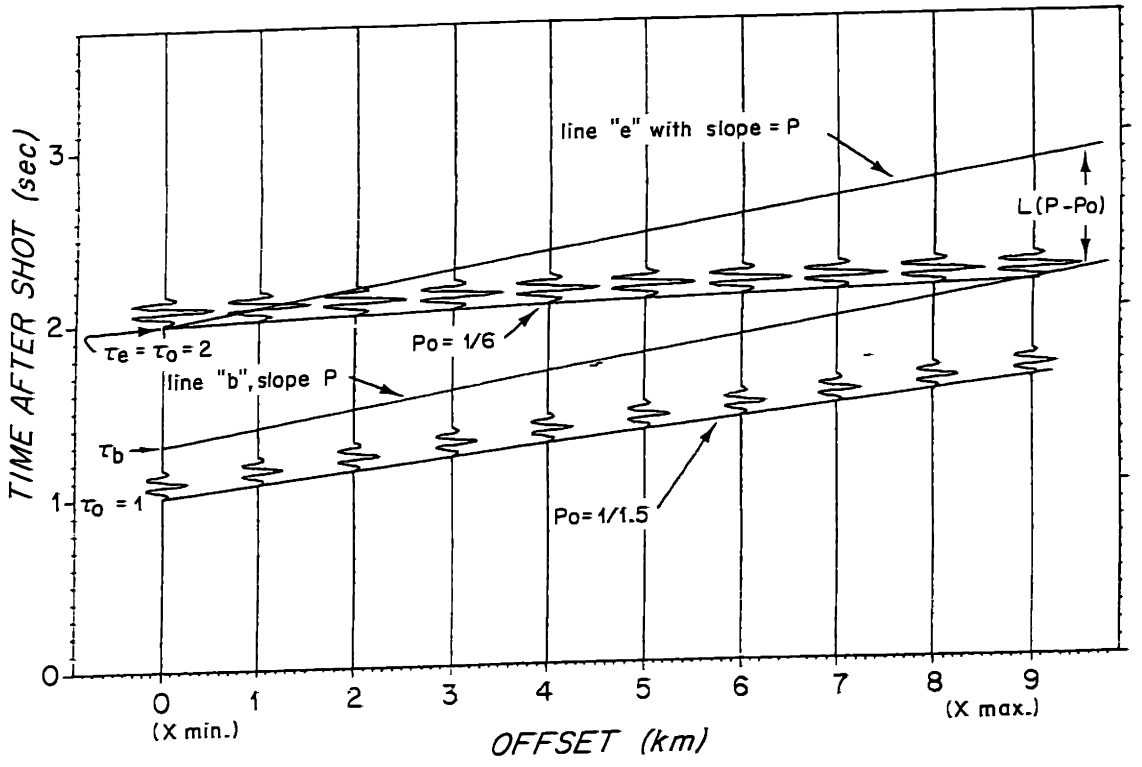

Fig. 3.2a) Coordinates for artifact generation. wave-field domain.

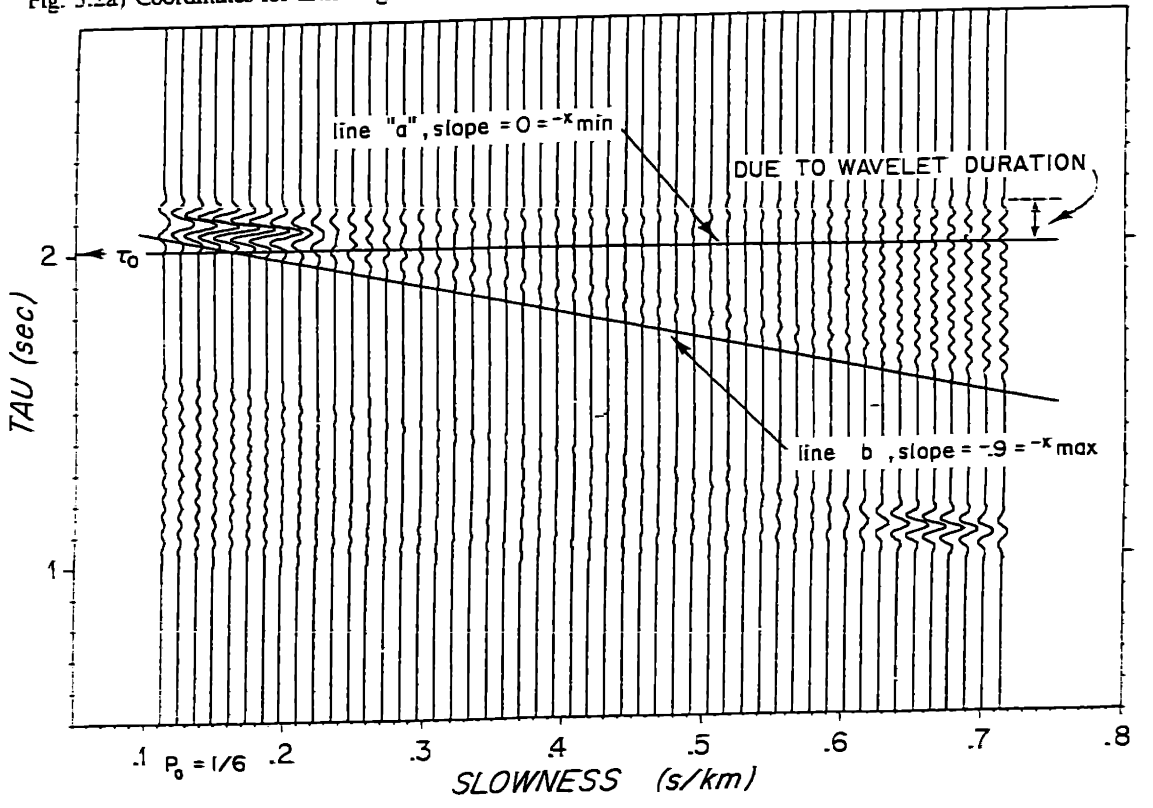

Fig. 3.2b) Slant-stack artifacts, $\tau(p)$ domain.

The line "b" with slowness p first intersects the wave at 6 km/s at $\tau_b - px_{max} = \tau_0 - p_0 x_{max}$ giving its equation as:

$$\tau_b = \tau_0 - x_{max}(p - p_0)$$

Similarly, line "e", where the stacking trajectory last hits the onset of the arrival, is given by:

$$\tau_e = \tau_0 - x_{min}(p - p_0).$$

Note that the distance between the lines defining the affected area is

$$\tau_e - \tau_b = (x_{max} - x_{min})(p - p_0) = L(p - p_0)$$

which is the length of the operator in eqns. 3.7a and 3.24c. Figure 3.2b is a $\tau - p$ plot and shows the affected region between these lines of slope $-x_{max}$ and $-x_{min}$ with intercepts τ_0 at p_0. The effects of aperture sampling are also evident from this plot. The sample interval was $\Delta r = 0.1$km, and the peak frequency of the wavelet was 15 Hz, yielding an aliasing distance in slowness of $\delta p = 1/f\Delta r = 1/1.5 = \overline{.6}\ s/km$. The rising amplitude at the opposite end of the slowness plot for each wavelet shows the aliasing.

RANDOM PROPAGATION AND APERTURE EFFECTS

In addition to cost and logistics difficulties, there are other reasons for limiting the aperture over which coherent processing is carried out. One has been mentioned already, the fact that small aperture plane wave decomposition allows the offset function, $x(p)$, to be estimated directly. Two others are the effects of errors in sensor locations and that of small but random inhomogeneities in the medium. In addition, if parameter estimation is the goal of the decomposition and the parameters change with offset, then only the aperture in which the parameters are constant within the resolution of the decomposition should be used. Another way to look at this phenomenon is that as the signals become less matched to the assumed structure (a

plane wave), the coherent processing gain decreases because a matched filter is no longer implemented, and a broader ambiguity function results. The flatter the ambiguity function for a given signal to noise ratio, the poorer the stability of the estimate will be.

To first deal with the issue of sensor location error, one reasonable model would be to assume increasing errors in location with distance away from a reference sensor. This situation could arise when the locations are surveyed from a baseline near the reference receiver. A deterministic way of looking at it would be to realize that when the offset errors, R, lead to phase errors in the pass-band of greater than some cutoff value, say $\pi/4$, then the gain from the coherent processing will degrade. This gives a bound on the aperture length as the distance, L, to the sensor at which the error in location is:

$$R(L) > \frac{\pi}{4\omega p} = \frac{1}{8fp} \qquad 3.25$$

and is seen to depend on the highest frequency of interest and the largest slowness, or correspondingly the shortest projected wavelength on the horizontal array.

Another way to treat the effects of errors in sensor location is to model the location estimates as having some probabilistic distribution about their true locations. This situation might occur when the sensors were located by an acoustic pinger location system using triangulation. To assess the effect of location errors in such a system, consider the following simple plane wave signal model:

$$P(\omega,r) = Ae^{i\omega pr}$$

and describe the sensor location error, R, as normally distributed with zero mean and variance σ_R^2, and independent from sensor to sensor. The error in the measurement due to a location error of R is:

$$\epsilon(r_0) \approx \frac{dP(\omega_0,r)}{dr}\Big|_{r_0} \cdot R(r_0)$$

This has an expected value of zero, and correlation function:

$$\begin{aligned} K(r_0,r) &= E[\epsilon(r_0)\epsilon^*(r)] \\ &= (\omega_0 pA)^2 e^{i\omega_0 p(r_0-r)}\, E[R(r_0)R(r)] \\ &= (\omega_0 pA)^2\, \sigma_R^2\, \delta(r_0-r). \end{aligned}$$

Thus, the measurement errors lead to an effective uncorrelated measurement noise level that is dependent upon the signal power, frequency, and slowness. The limiting signal to noise ratio at the sensor in the presence of no ambient noise is:

$$SNR = [\omega_0 p\, \sigma_R]^{-2} \qquad 3.26a$$

An example might be:

$$\left.\begin{array}{l} \omega_0 = 2\pi \cdot 15 \text{ radians/s} \\ p = .5 \text{ s/km} \\ \sigma_R = .005 \text{ km} \end{array}\right\} \Rightarrow SNR = 18 \quad (+13 \text{ dB})$$

From this one can see that relatively small sensor location errors can increase the effective noise level for coherent processing considerably. Even more unfortunate is the fact that if multiple signals are present, the noise power level tracks the total incoherent signal power in the band:

$$N_0(\omega) = \sigma_R{}^2 \omega_0^2 \sum_i (A_i p_i)^2 \qquad 3.26b$$

and thus the signal to uncorrelated noise ratio for any one wave is:

$$SNR_i = \frac{A_i}{N_0(\omega_0)} \leq SNR \qquad 3.27$$

and the spatial structure of the interfering coherent arrivals can no longer be used in their suppression when looking at the arrival of interest.

The issue of decorrelation distances in ocean acoustic propagation is a problem of historic and continued interest in sonar applications. Characterization of propagation in random media, be they the dynamic ocean or the static crust and sediments, is certainly beyond the scope of this work. We shall just have to assume that it occurs. Gammelsaeter, [1981], has shown how the coherent processing gain can decrease with increasing aperture and that the resolution in slowness (bearing in the sonar application for which that paper was written) plateaus and even decreases with increasing aperture for coherency degraded signals. The coherency degradation in terms of multichannel processing (vs. 2-sensor time delay estimation problems) is caused by both the uncertainty in the sensor locations and stochastic propagation effects due to inhomogeneities in the medium.

In summary, one advantage of short aperture acquisition stems from signal to noise coherent processing gains due to the use of only highly coherent arrivals. These are a result of the smaller array allowing more accurate sensor location, and sampling of the spatial signal before it decorrelates due to medium inhomogeneities. The advantage of the small aperture is the lack of compromise in the accuracy of the estimated slowness parameter, p, [Gammelsaeter, 1981], and the direct estimation of $x(p)$, the geometrical offset function.

ELIMINATION OF PHASE SHIFT EFFECTS

Introduction

For the moment, assume that a slant stack has been carried out on an infinite or finite aperture, and the results of either 3.19 or 3.23 have been obtained. Note that for the finite aperture stack, 3.23, the derivatives and filter have not been applied, but the correct scale factor 3.22 has been used. If we are interested in travel time inversion, then $\tau_0=\tau(p_0)$ must be

estimated. From 3.19a or 3.23a it can be seen that even if the signal shape, $s(t)$, is known, one cannot use a peak or first motion pick to estimate τ_0 plus a bias because of the unknown distortion due to the Q_τ and ϕ_0 phase shifts. (The amplitude factors do not matter since they only provide a scaling.) There are several methods for attempting to remove the effects of the phase shift. These will be outlined in this section and used to motivate the velocity spectral analysis algorithm.

Deconvolution

Because of spectral variability, low signal to noise ratio, and poor modeling of the return sequence (the net reflection coefficient) as a white noise process, the standard methods of blind deconvolution that are often used in reflection seismology cannot be applied to refraction data. Event detection algorithms [c.f. Dove, 1980] applied to the slant-stack output may be of use in determination of arrival times, however, this has not been tried in this work. These algorithms often require high signal to noise ratios and work best on detecting "first" events emerging from white noise backgrounds. After the first arrival, a typical refraction trace is a mass of multipath events with a very wide dynamic range. It is felt that the interpretation of the event detector output in this environment would be as complicated as interpreting the data trace itself.

Envelope, Matched Filter, and Spectral Detection

In this section it is assumed that the spectrum of the source, $S(\omega)$, is only changed by reflection and turning point phase shifts, not by intrinsic attenuation or random scattering, and thus maintains a constant magnitude structure. Using the estimate from the stacking equations 3.19a (infinite aperture) or 3.23c (finite aperture), the stacked arrivals have the wavelet struc-

ture:

$$a(\tau) = Q_\tau[\cos\phi_0 - \sin\phi_0 H^-]s(\tau-\tau_0) \qquad 3.28$$

where $Q_\tau = [H^-]^n$ is some number of Hilbert transforms. We desire some function of 3.28 that is independent of both Q_τ and ϕ_0. In the time domain, this is obviously the envelope function, $e(\tau)$, defined by:

$$e^2(\tau) = a^2(\tau) + \bar{a}^2(\tau) \qquad 3.29a$$

where the overbar denotes Hilbert transformation. To see this, insert 3.28 into 3.29 to obtain:

$$\begin{aligned} e^2(\tau) &= [(\cos^2\phi_0 + \sin^2\phi_0)(Q_\tau s)^2(\tau-\tau_0) - (\cos^2\phi_0 - \sin^2\phi_0)\overline{(Q_\tau s)}^2(\tau-\tau_0)] \\ &= [(Q_\tau s)^2(\tau-\tau_0) + \overline{(Q_\tau s)}^2(\tau-\tau_0)] \\ &= [s^2(\tau-\tau_0) + \bar{s}^2(\tau-\tau_0)] \end{aligned} \qquad 3.30$$

which is independent of Q_τ and ϕ_0. If the wavelet shape is known, then the envelope is known, and a point on the waveform $e^2(\tau)$ can be picked and related through some bias to τ_0. It will be seen that this method only works when the signal to noise ratio is quite large and thus filtering before detection is required.

The optimal filter to use when the random sensor noise is white and only one signal is present is the matched filter or correlation receiver for the wavelet $s(\tau)$ followed by envelope detection [van Trees, 1968]. The arrival time is then related to the time of the peak in the output of the envelope detector by some fixed bias. The classical result for the standard deviation of the arrival time estimate when the signal to noise ratio at the output of the matched filter, E/σ_N^2, is high ($\approx$>5 dB for low time-bandwidth products, BT <5) is:

$$\sigma_{\tau m} = \frac{1}{\beta\left[\frac{E}{\sigma_N^2}\right]^{1/2}} \qquad 3.31a$$

where

$$E = \frac{1}{2\pi} \int_{-\infty}^{\infty} |S_e(\omega)|^2 d\omega \qquad 3.31b$$

is the total energy in the envelope signal,

$$\beta = \left[\frac{1}{2\pi E} \int_{-\infty}^{\infty} \omega^2 |S_e(\omega)|^2 d\omega \right]^{1/2} \qquad 3.31c$$

is the rms bandwidth of the envelope of the signal in radians/sec, and the variance of the white noise at the input to the matched filter is σ_N^2. The input noise, σ_N^2 is usually reduced by the array gain from the sensor noise variance, σ^2, $\sigma_N^2 = \sigma^2/N$. The problem with this method is that it requires accurate knowledge of the signal shape, $s(t)$, to implement correctly. However, for small time-bandwidth products, BT, it will be seen that accuracy sufficient for inversion work can be achieved with a filter which is only roughly matched to the signal. Examples using Monte Carlo simulation techniques will be given later in this chapter.

A particularly easy filter to implement which is independent of knowledge of the modulation frequency of the signal and that utilizes the fact that the proper slant stack (2.35a) can be carried out in the frequency domain is the velocity spectral processor. We delay defining the actual processor for a moment, but note that the spectral processor is equivalent to running a short-time power spectral density estimator on slant-stacked data in terms of travel-time estimation. In this method, the arrival time, τ_0, is estimated by sliding a short spectral analysis window over the slant-stacked time series and choosing as τ_0 the start time of the window for which the magnitude of the Fourier transform of the tapered time series at a given frequency is a maximum plus a bias, b_s. This bias is dependent on the wave shape, $s(t)$, and the window shape, $w_s(t)$.

$$\hat{\tau}_0(\omega : p_0) = (\tau_0 - b_s) : [|\hat{S}(\tau_0,\omega,p_0)|^2 \geq |\hat{S}(\tau,\omega,p_0)|^2] \qquad \text{for all } \tau \tag{3.32a}$$

where

$$\hat{S}(\tau,\omega,p_0) = \int_{\tau}^{\tau+T} w_s(t-\tau-T/2)\, u(t,p_0)\, e^{i\omega t}\, dt. \tag{3.32b}$$

What this processor does is guess that the waveform has the envelope shape $w_s(t)$ with duration T, and then scan over the modulation frequencies, ω, tallying the power at each frequency for each window start time, τ. The window shape and duration can be adjusted to make the processor bandwidth around each trial center frequency approximately match the spectral characteristics and duration of the suspected wavelet. It is clear that this is equivalent to the matched filter and envelope detector when $w_s(\tau)$ is the envelope of the signal, $e(\tau)$, (see eqn. 3.30) and ω is the modulation center frequency.

The velocity spectral processor is an alternative method for carrying out eqns. 3.32 a and b which takes advantage of the multichannel nature of the data. The processor computes the short-time windowed Fourier transforms directly on the data, and then uses the frequency domain implementation of the slant-stack (eqn. 2.35a) to obtain $\hat{S}(\tau,\omega,p)$. This processor is defined by:

$$\hat{P}(\tau,\omega,p_0,r) = e^{i\omega p_0 r} \int_{\tau}^{\tau+T} w_s(t-\tau-T/2)\, P(t+p_0 r, r)\, e^{i\omega t}\, dt \tag{3.32c}$$

$$\hat{S}(\tau,\omega,p,r_0) = \int_{\substack{\text{aperture } L \\ \text{centered on } r_0}} w_L(r-r_0)\, \hat{P}(\tau,\omega,p_0,r)\, e^{-i\omega p r}\, r^{1/2}\, dr \tag{3.32d}$$

where the short aperture nature of the processing has been noted explicitly. Clearly, what this processor does is stack a short interval of the data in the frequency domain along some nominal trajectory, p_0. We will see later that the p parameter in 3.32d can be deviated a small amount from p_0 depending on the actual duration of the signal and the window length, T.

The major caveat with this implementation is that in order for the stack in 3.32d to be carried out successfully, the window shape and the duration must be chosen so that the frequency components around the center frequency, ω, in $\hat{P}(\tau,\omega,p_0,r)$ do not deviate so far from ω that the exponential kernel $e^{-i\omega pr}$ in 3.32d is no longer matched to the data in the short-time spectra, $\hat{P}$. In other words, the stack is only truly valid for the center frequency, ω, but the finite length of the aperture allows other frequencies to be nearly matched. If the bandwidth of $\hat{P}(\tau,\omega,p_0,r)$ is too large then waves with slowness p_0 and frequency $\omega_1 = \omega \mp \Delta\omega$ will look like they are arriving with slowness:

$$\hat{p}_0 = p_0 \frac{\omega}{\omega_1} = p_0 \frac{\omega}{\omega \mp \Delta\omega}. \qquad 3.33a$$

If the allowable slowness deviation in one direction is Δp then:

$$\Delta\omega = \omega \left[\frac{-\Delta p}{p_0 \mp \Delta p} \right] \qquad 3.33b$$

is the allowable half-bandwidth of the transform $\hat{P}(\tau,\omega,p_0,r)$. This means that the allowable width of the main lobe of the Fourier transform of the window $w_s(t)$ is approximately $2\Delta\omega$. An absolute upper bound on Δp is the half-width of the main lobe of the conventional beampattern of the array used. For an array of length L with no aperture taper this is given by $\Delta p = 1/(fL) = 2\pi/(\omega L)$ (see eqn. 3.7b). and:

$$|\Delta\omega| = \frac{\omega}{\frac{p_0 \omega L}{2\pi} + 1} \qquad 3.33c$$

Recalling the discussion after equation 2.37b in chapter 2, the utility of doing the short-time transforms on the data lies in the fact that the stack, 2.35a, can be carried out by the MLM algorithm to increase the slowness resolution and to decrease the interference effects of other propagating signals. This allows separate arrival time estimates when two signals are

arriving nearly simultaneously, but with different slownesses. This is important because the matched filter structure is only optimal for a signal in white noise, which would not be the case when two (possibly different) signals are present due to the sidelobes of one signal interfering with the other.

Before continuing, we should note again that the time of arrival estimated by eqn. 3.32a is free of bias due to phase shifts. To show that this estimate does not depend on Q_τ or ϕ_0, we first include the phase shifts from Q_τ into ϕ_0:

$$\phi = \phi_0 - n\frac{\pi}{2}$$

when $Q_\tau \equiv [\mathrm{H}^-]^n$. The signal is now given by:

$$u_{3D}(\tau,p_0) \quad \alpha \quad s(\tau-\tau_0)\cos\phi + \mathrm{H}^-[s(\tau-\tau_0)]\sin\phi. \qquad 3.34$$

Putting 3.34 into 3.32b and evaluating for the window centered on the wavelet ($\tau = \tau_0+T/2$):

$$|\hat{S}(\tau_0,\omega,p_0)|^2 = |\,[(I(\omega)+iQ(\omega))\cos\phi_0 - sgn(\omega)(Q(\omega)-iI(\omega))\sin\phi_0] * W_s(\omega)|^2 \qquad 3.35$$

where $S(\omega) = I(\omega)+iQ(\omega)$ and I and Q are the quadrature components of the spectrum and the window length, T, is greater than or equal to the signal duration. The phase shift is seen to cancel as in 3.30 when the squared magnitude is taken. In most practical cases the bandwidth of the signal is greater than that of the window, and the convolution with the window transform is nearly a unity operation. Thus, the spectral arrival time detector is not influenced by a constant phase shift, as would be introduced to a plane wave upon wide angle reflection. As an example, if the window is symmetric about τ=0, and if $S(\omega) = 1$, then the response will be maximized at $\tau = \tau_0+T/2$ and $b_s = T/2$.

Because of the restriction on the allowable bandwidth of $\hat{P}(\tau,\omega,p_0,r)$, it is not always possible to obtain the performance of the optimal matched filter time of arrival estimates given in 3.31 for any trial center frequency. This would occur when the bandwidth of the signal is

much greater than $1/T$, in other words for large BT. When the spectral processor is used and the center frequency is ω, the standard deviation of the arrival time estimate is given by a relation similar to 3.31, but with the optimal output signal to noise ratio, E/σ_N^2, diminished.

$$\sigma_{\tau s}(\omega) \approx \frac{1}{\beta_\omega \left[\frac{E_\omega}{\sigma_\omega^2}\right]^{1/2}} \tag{3.36a}$$

where

$$E_\omega = \left| \frac{1}{2\pi} \int_{-\infty}^{\infty} S(\omega' - \omega) W_s(\omega') d\omega' \right|^2 \tag{3.36b}$$

is the total energy of the signal in the pass band of the processor around frequency ω,

$$\sigma_\omega^2 = \sigma_N^2 \frac{1}{2\pi} \int_{-\infty}^{\infty} |W_s(\omega')|^2 d\omega' \tag{3.36c}$$

is the noise power out of the processor, and

$$\beta_\omega = \left[\frac{\int_{-\infty}^{\infty} \omega^2 E_\omega(\omega) d\omega}{\int_{-\infty}^{\infty} E_\omega(\omega) d\omega} \right]^{1/2} \tag{3.36d}$$

is the rms bandwidth in the passband of the processor. The standard deviation, $\sigma_{\tau s}$, in 3.36a is always greater than or equal to $\sigma_{\tau m}$ of eqn. 3.31a.

To compare the performance of the envelope detector, filtered envelope detector, matched-filter envelope detector, and spectral detector we consider a simple example. The wavelet, $s(t)$, is the modulated truncated Gaussian pulse:

$$s(t) = \begin{cases} e^{-\left[\frac{\omega(t-d/2)}{\gamma}\right]^2} \cos(\omega(t-d/2)) & 0 < t < d \\ 0 & \text{elsewhere} \end{cases} \qquad 3.37$$

where:

$$\gamma = 15$$

$$f = 15$$

$$\omega = 2\pi f = 2\pi \cdot 15$$

$$d = 5\frac{\pi}{\omega} = .167 \text{ seconds}$$

The spectrum of this function is shown in figure 3.3a, along with the white noise levels used in the example plots*. Figure 3.3b has the signal and noise spectra after using the spectral window function:

$$w_s(t) = \begin{cases} \sin^2\left(\frac{\pi}{T}(t-T/2)\right) & -T/2 < t < T/2 \qquad T = .25 \text{ sec} \\ 0 & \text{elsewhere} \end{cases} \qquad 3.38$$

when the window is centered on the wavelet ($t=d/2$). As can be seen this yields a window bias on a flat spectrum of - 4 dB. Since the signal is concentrated in the center of the interval, the window loss for the signal is 3 dB, thus slightly enhancing the output signal to noise ratio of the spectral processor. Figure 3.4 shows the results of four types of processing. Trace 1 is the noisy data trace, with an "in band" signal to noise ratio of about +10 dB ($\sigma_N=1$). The signal (3.37) is centered about 1.083 seconds (τ_a) and starts at 1 second into the trace (the middle). Trace 2 is the matched filter output, and trace three is its squared envelope. Because

*Because of time windowing, the spectrum can be expressed analytically only with a convolutional operation included.

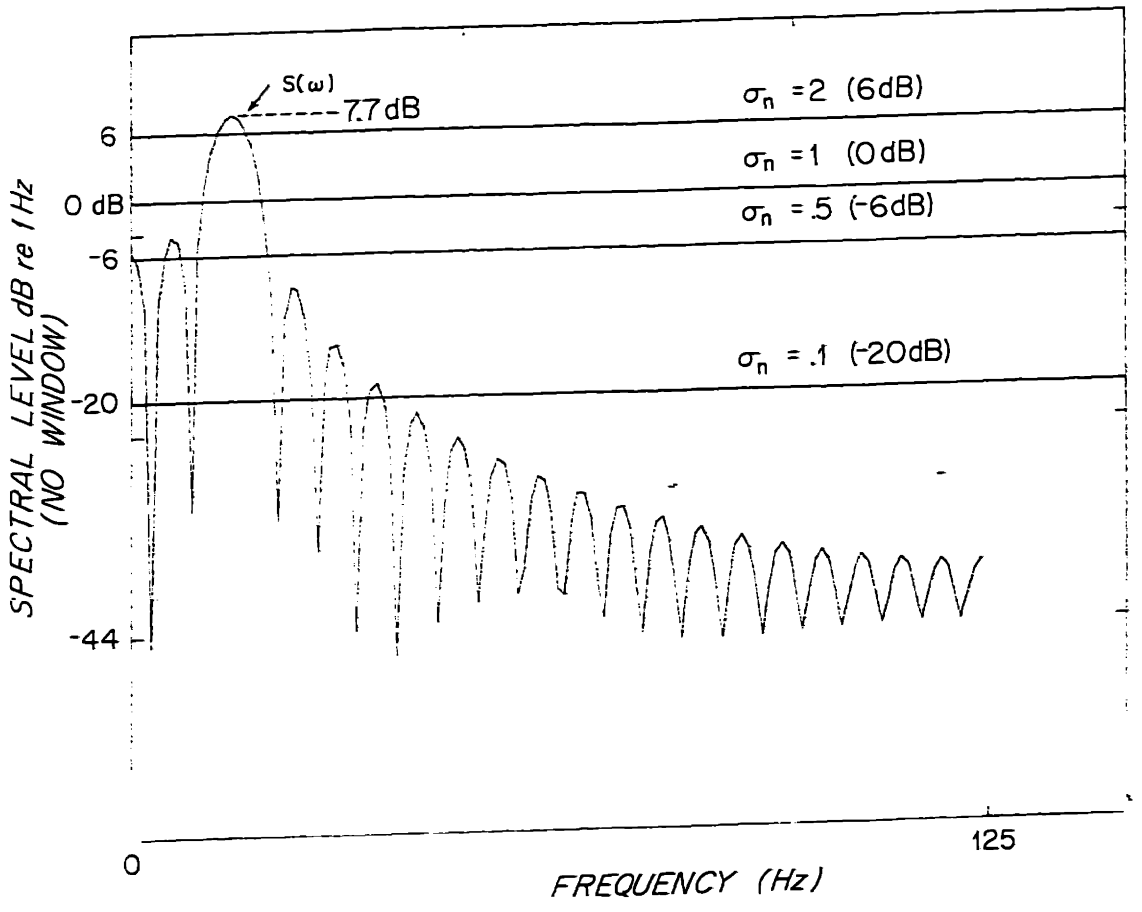

Fig. 3.3a) Signal and noise spectral levels, no spectral analysis window tapering function used.

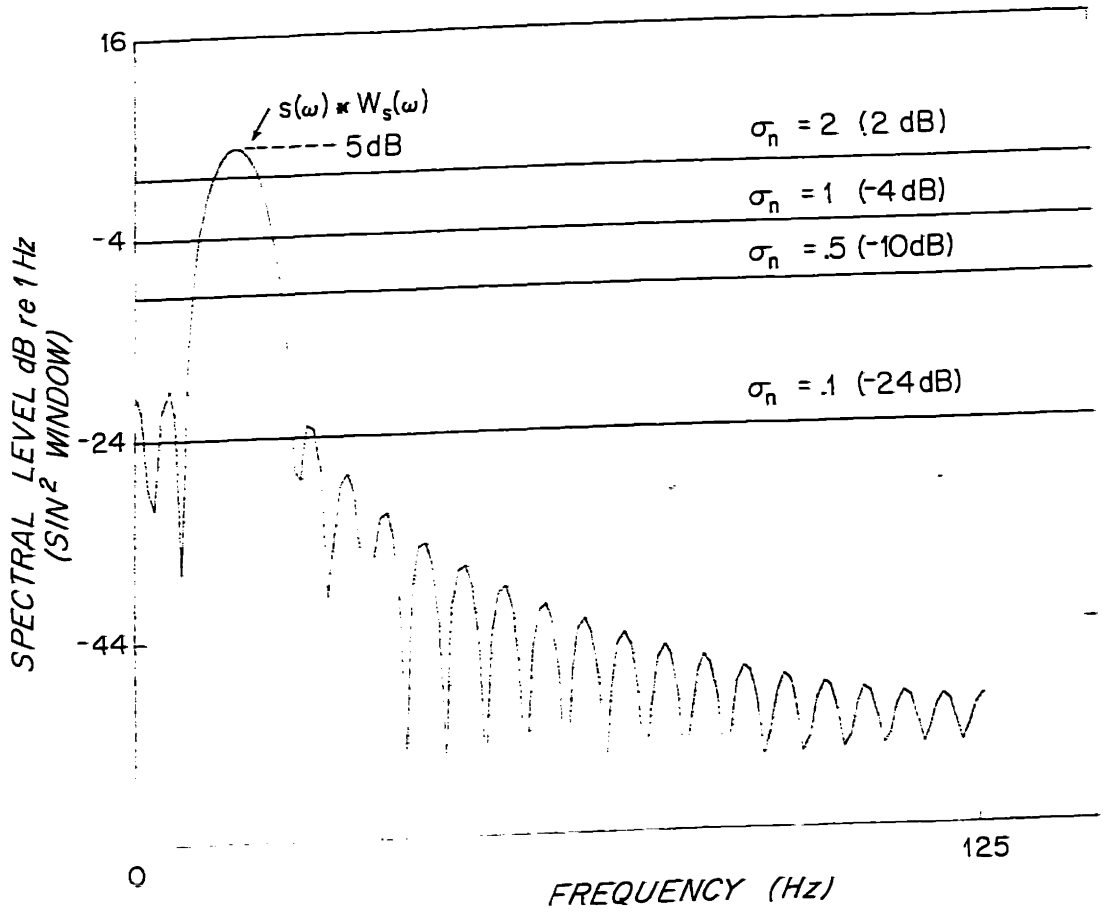

Fig. 3.3b) Signal and noise spectral levels. the spectral analysis window tapering function is given by eqn. 3.38.

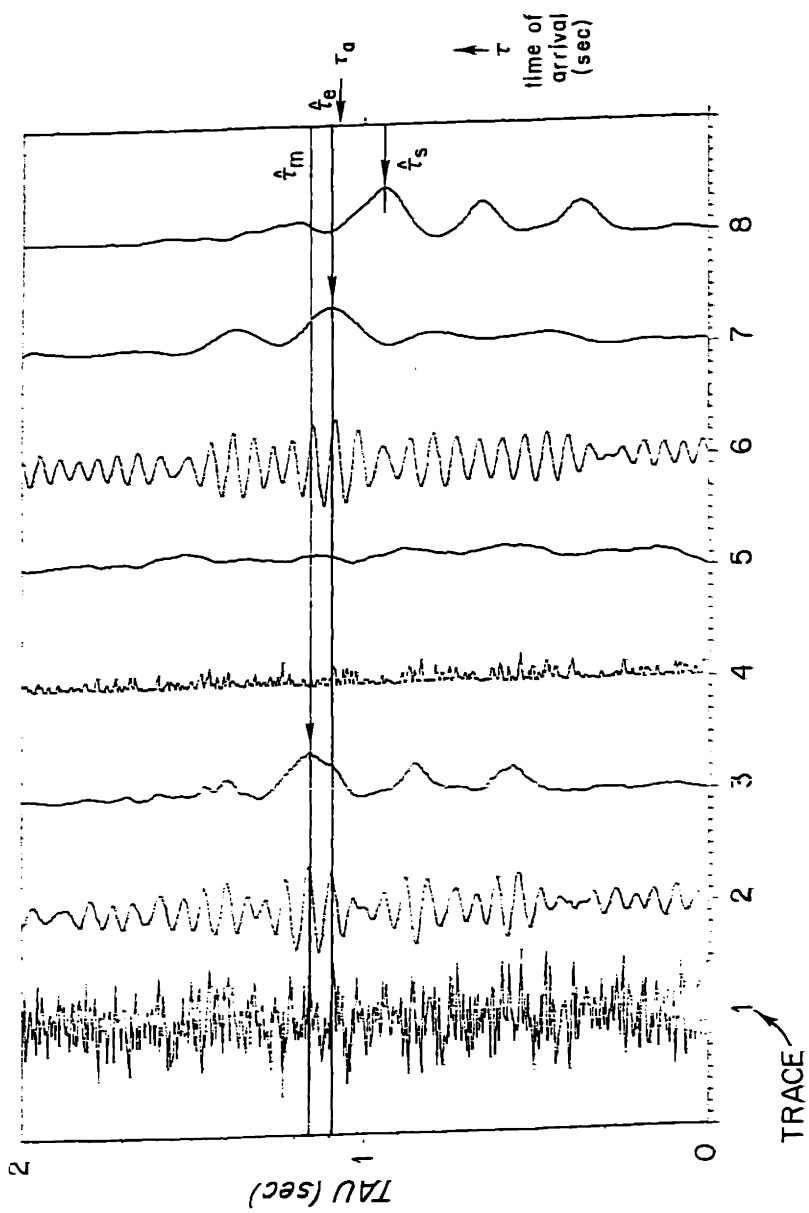

Fig. 3.4) Comparison of arrival time detector outputs. Trace 1 is the noisy data and τ_a is the centroid of the wavelet. Trace 3 is the matched filter output and $\hat{\tau}_m$ is the correct matched filter arrival time. Trace 7 is the bandpass filter/envelope detection output and $\hat{\tau}_e$ is the correct filter/envelope detect arrival time. Trace 8 is the spectral processor output and $\hat{\tau}_s$ is the correct spectral processor arrival time.

of the assumption that the matched filter is causal, there is an additional delay in the output of the filter of $d/2$. Thus the peak, $\hat{\tau}_m$, is detected near 1.167 sec ($1.083+d/2$). Trace 4 is the squared envelope of the noisy data, and trace 5 is the output of the baseband (envelope squared) matched filter. This method did not yield a peak anywhere near the correct arrival time. Because of the small BT of the signal, the result of the 4 Hz (13-17) wide ideal (non causal) band-pass filter gives an output in trace 6 that looks similar to the matched filter output in trace 2. The envelope squared of the filtered data is in trace 7 and is seen to have a peak, $\hat{\tau}_e$, very near the correct arrival time, and a correlation (ambiguity) function curvature similar to the matched filter, thus giving approximately the same performance (3.31a). Trace 8 is the result of the spectral processor at $f=15$ Hz using the window of eqn. 3.38 with duration $T=.25$ s (-10 dB bandwidth $\approx$ 10 Hz vs. 8.5 Hz for the rectangular window). Since the wavelet and window are symmetric and center-weighted, the expected window bias is $b_s=-T/2=$ -.125 sec, and the peak arrival, $\hat{\tau}_s$ is near τ = .958 sec. Note that the matched filter envelope (trace 3) and the output of the spectral processor are quite similar, supporting the near optimality of the spectral method for low time-bandwidth product signals.

Fig. 3.5 compares the data envelope processor, the filtered data envelope processor, and the spectral processor for various signal to noise ratios. Fig 3.5a contains the noiseless wavelet (trace 1), its squared envelope (trace 2) and the spectral processor output using the same parameters as the previous example (trace 3). After filtering with the ideal 13-17 Hz non-causal filter (trace 1), fig. 3.5b compares the envelope processor (trace 2) to the spectral processor on the unfiltered data (trace 3). Note that the spectral processor seems to show slightly better curvature of the ambiguity function, giving a higher quality estimate. Figures 3.5c and 3.5d show the same sequence, but with a noise standard deviation of σ_N = 0.1. Trace 2 of fig. 3.5c shows that the unfiltered envelope makes a very poor estimator. Figures 3.5e and

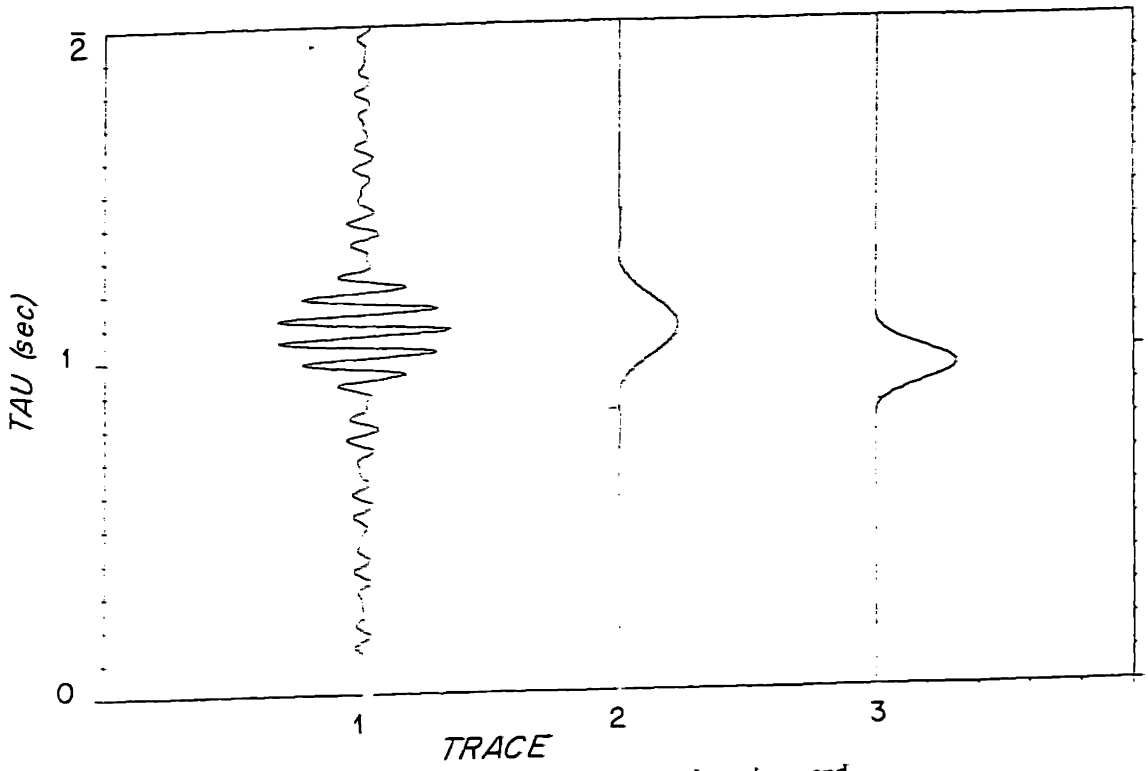

Fig. 3.5a) σ=0. Trace 1 is the wavelet, Trace 2 its squared envelope, and Trace 3 the spectral processor output.

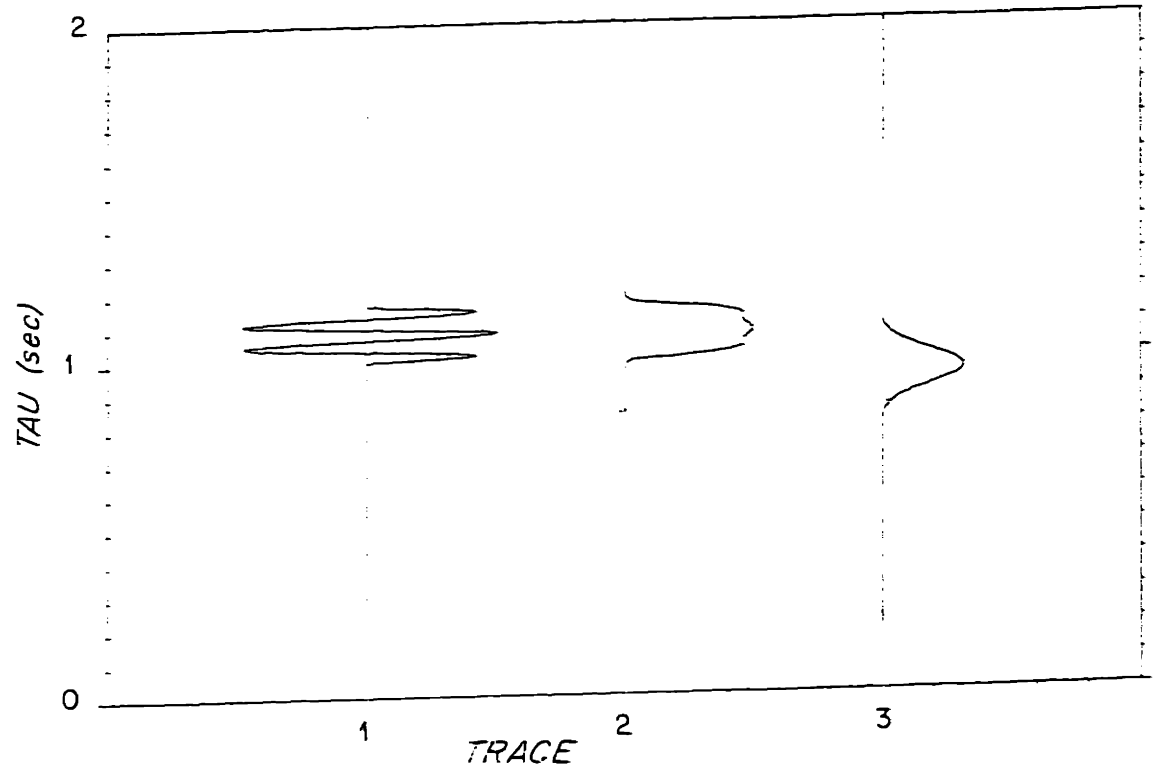

Fig. 3.5b) σ=0. Trace 1 is the filtered wavelet. Trace 2 its squared envelope, and Trace 3 the spectral processor output.

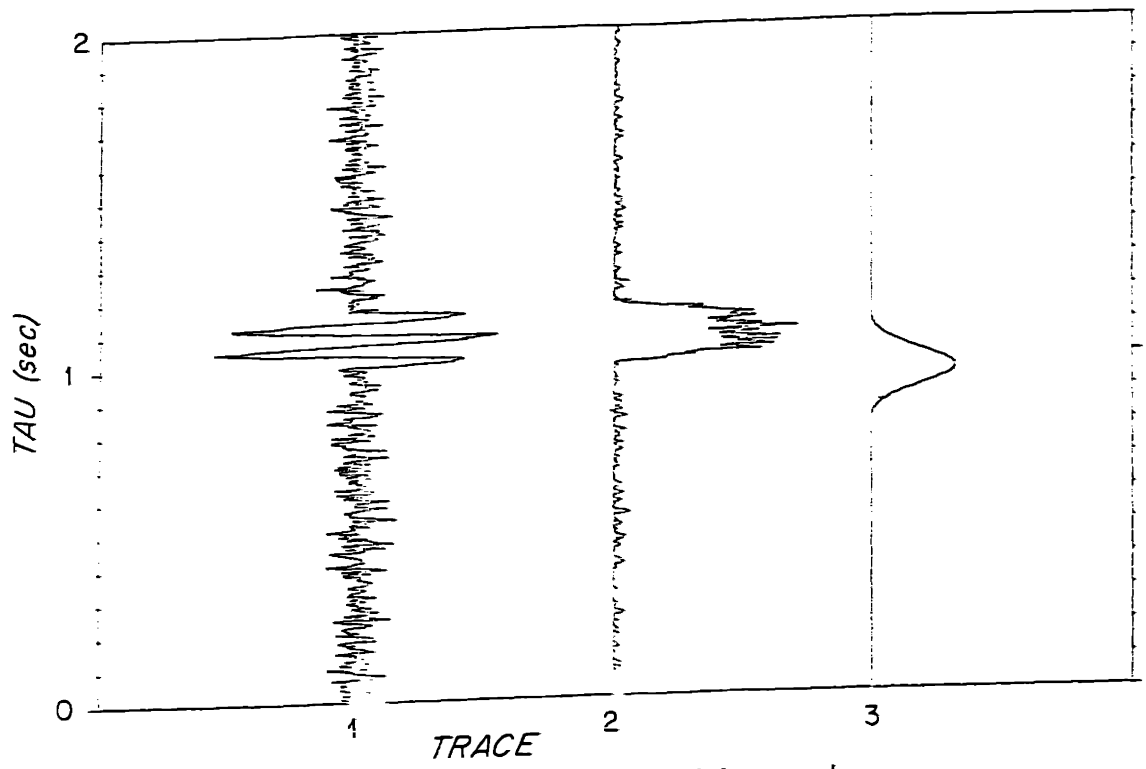

Fig. 3.5c) $\sigma = .1$. Trace 1 is the noisy wavelet. Trace 2 its squared envelope, and Trace 3 the spectral processor output.

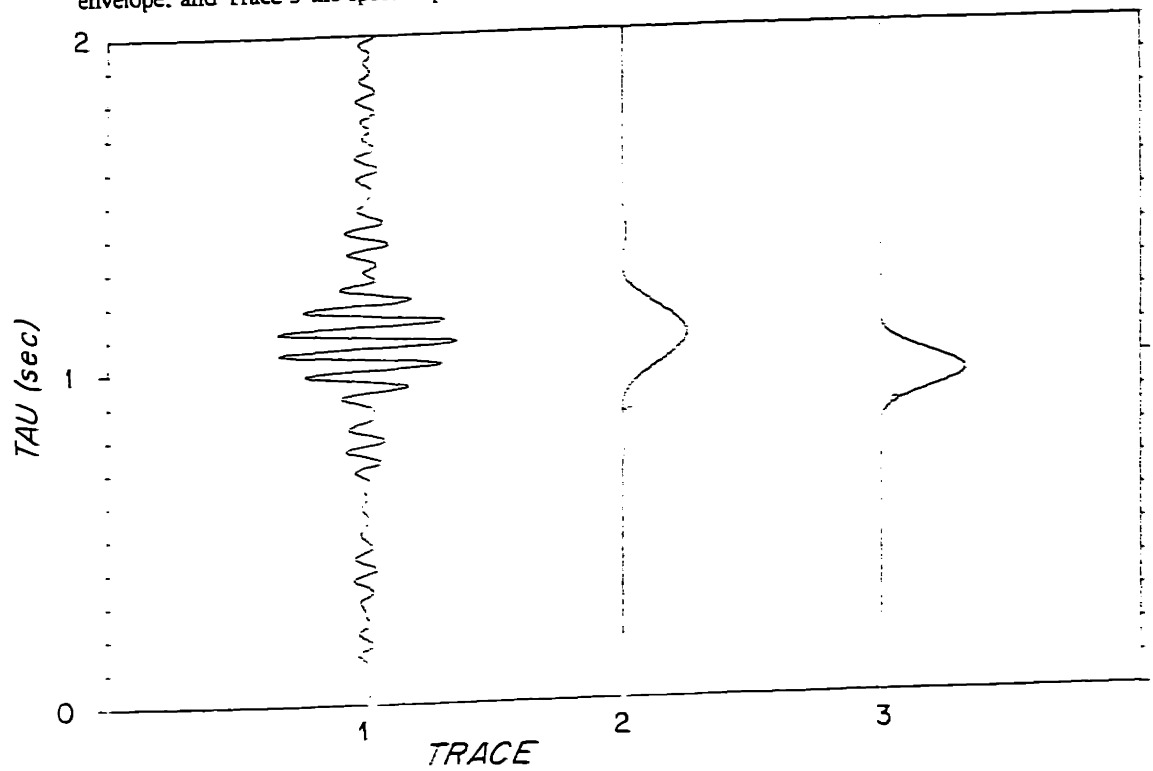

Fig. 3.5d) $\sigma = .1$. Trace 1 is the noisy wavelet after filtering, Trace 2 its squared envelope, and Trace 3 the spectral processor output.

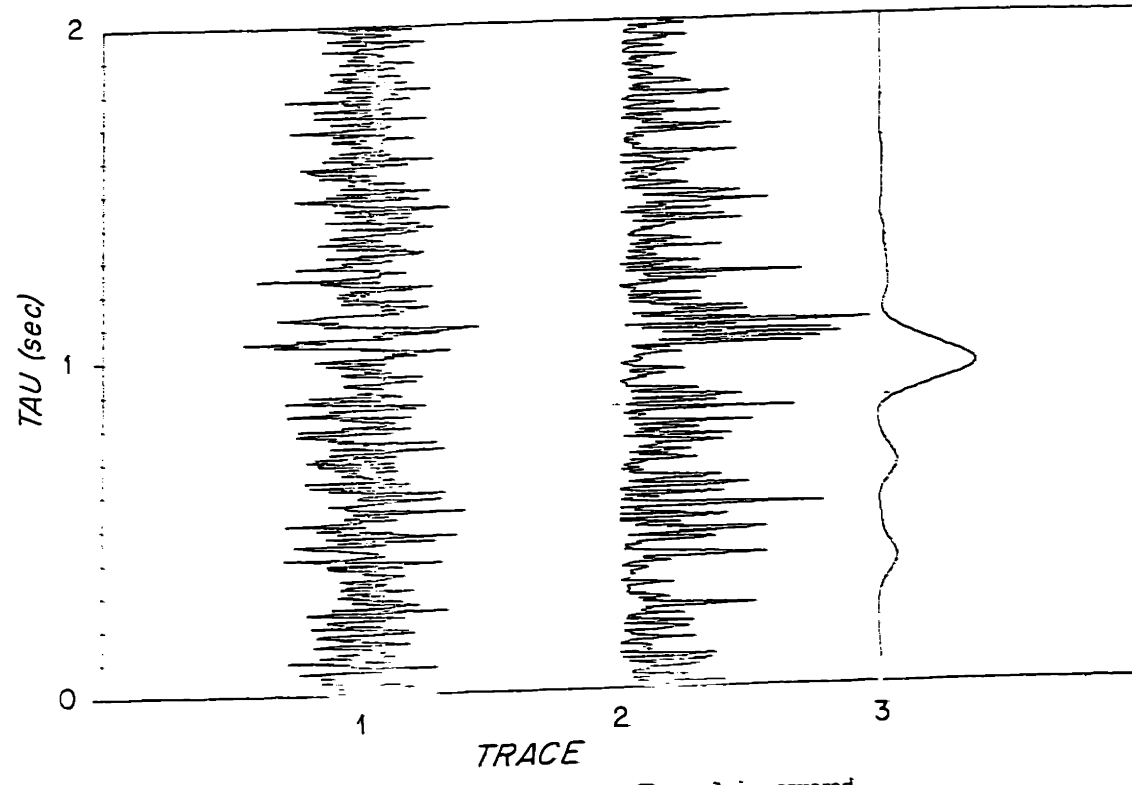

Fig. 3.5e) $\sigma=.5$. Trace 1 is the noisy wavelet. Trace 2 its squared envelope, and Trace 3 the spectral processor output.

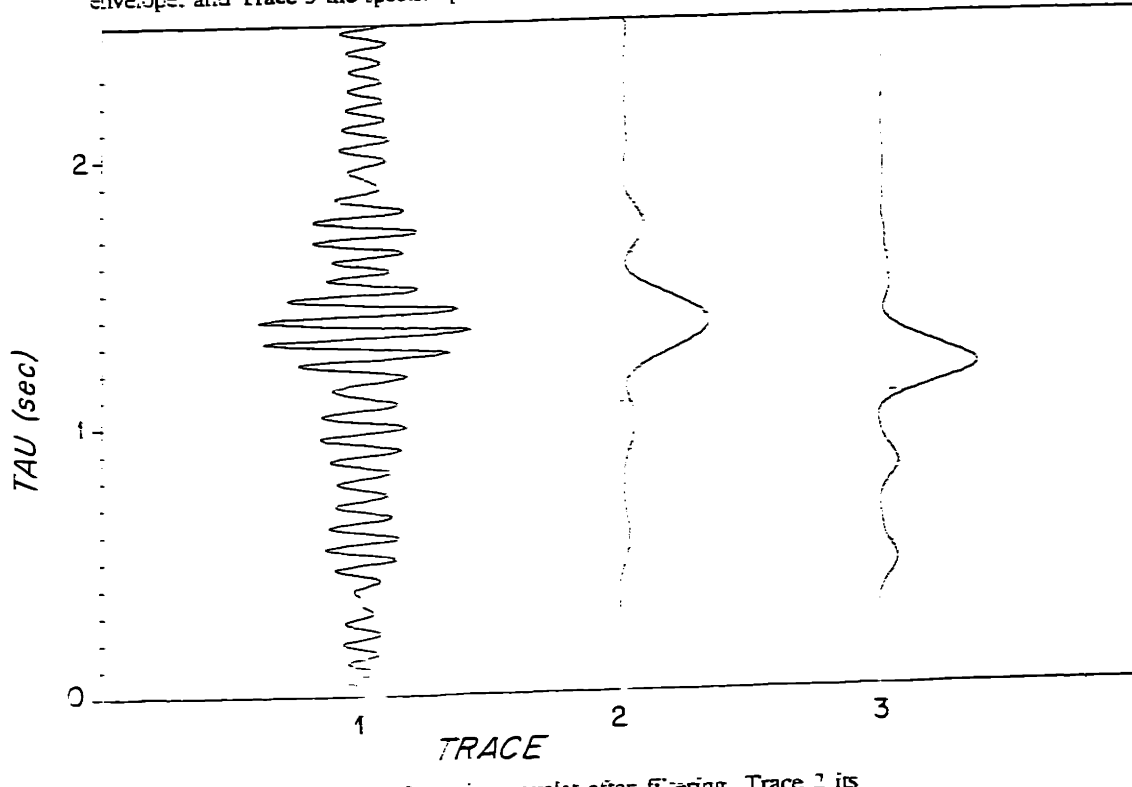

Fig. 3.5f) $\sigma=.5$. Trace 1 is the noisy wavelet after filtering. Trace 2 its squared envelope, and Trace 3 the spectral processor output.

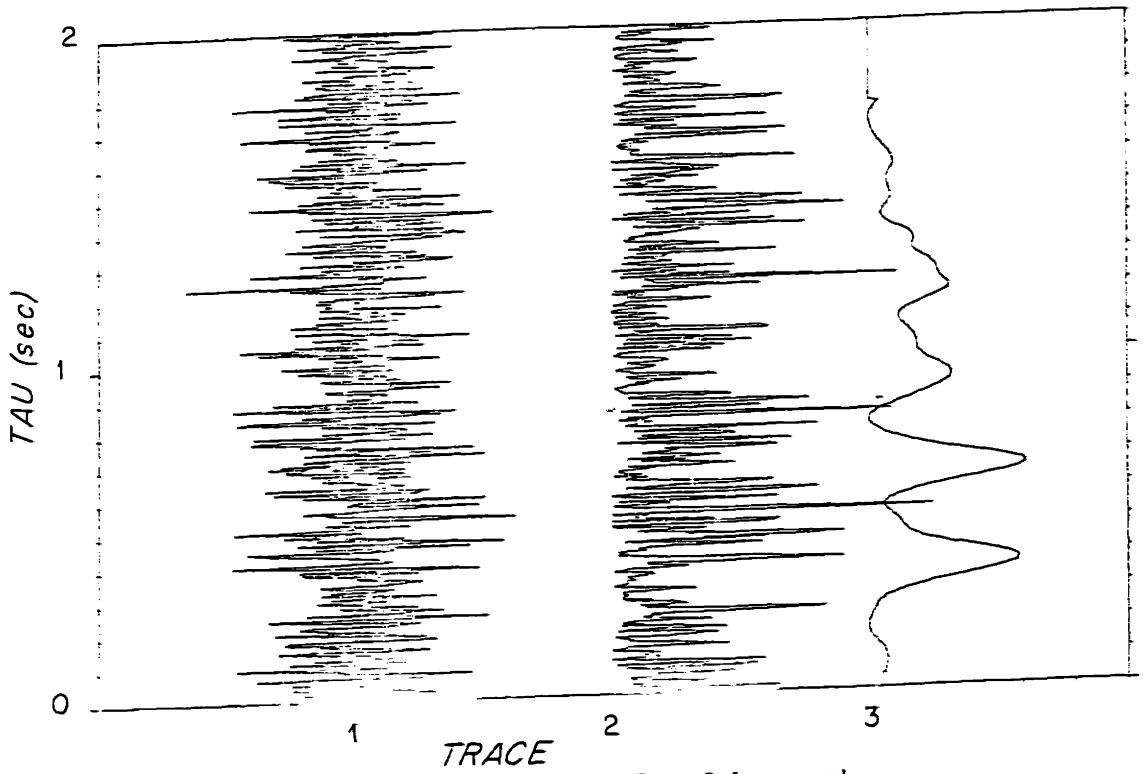

Fig. 3.5g) σ=2.. Trace 1 is the noisy wavelet. Trace 2 its squared envelope. and Trace 3 the spectral processor output.

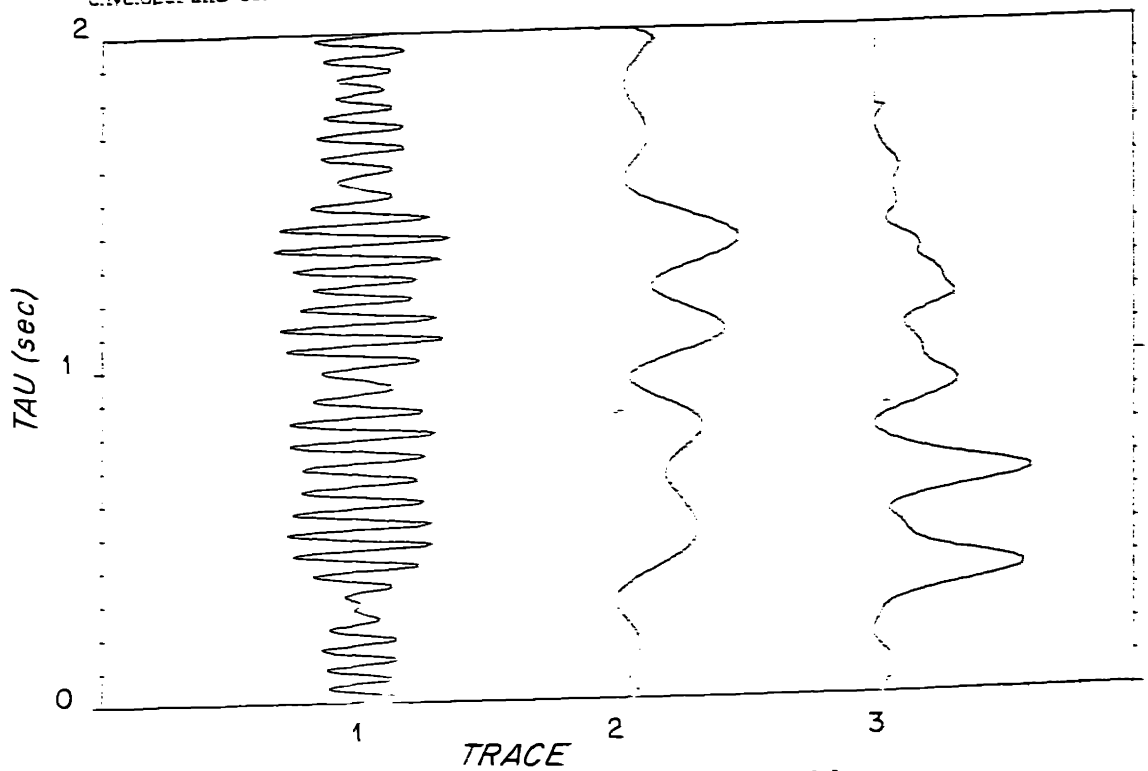

Fig. 3.5h) σ=2.. Trace 1 is the noisy wavelet after filtering. Trace 2 its squared envelope. and Trace 3 the spectral processor output.

3.5f show the same sequence for $\sigma_N = .5$, a 14 dB higher noise level. The output of the spectral processor looks slightly superior to the filter-envelope method. The unfiltered envelope is obviously useless. Figs 3.5g and 3.5h with $\sigma_N = 2$, or a 12 dB worse signal to noise ratio than fig. 3.5e&f show that this is below the threshold SNR for which the error can be modeled as perturbations around the central peak of the correlation function, and spurious peaks leading to global errors occur. In this region, the linearized error analysis of eqns. 3.31 and 3.36 do not hold, and more complicated error bounds, such as the Ziv-Zakai bound must be used [Weinstein, et al., 1983]. Comparing this to figure 3.4 for which $\sigma_N = 1$, or 6 dB better, we establish that the threshold for reasonable time of arrival estimates is somewhere between a +2 dB and −8 dB in-band, post-stacking signal to noise ratio. Figure 3.6 indicates the importance of the window taper, $w_s(\tau)$, to the ambiguity function. Trace 3 of this plot was generated for the rectangular window with a duration of .25 sec. Comparing this to trace 3 of fig. 3.5a shows that the tapered window has a much better ambiguity function, in fact the lack of curvature of trace 3 of fig. 3.6 yields $\sigma_{\tau s} = \infty$ using the linearized analysis! The "flat top" is due to the window duration being longer than the signal. A quantitative performance comparison of the matched filter and spectral processors is reserved until the velocity analysis algorithm has been defined, and Monte Carlo simulation results are compared to the predicted performance later in this chapter.

VELOCITY SPECTRAL ANALYSIS

Introduction

In the previous section short aperture velocity spectral analysis was all but derived in an effort to motivate it (see eqns. 3.32c,d). In this section it is presented in more detail and improved methods for carrying out the range integral or plane wave decomposition using the

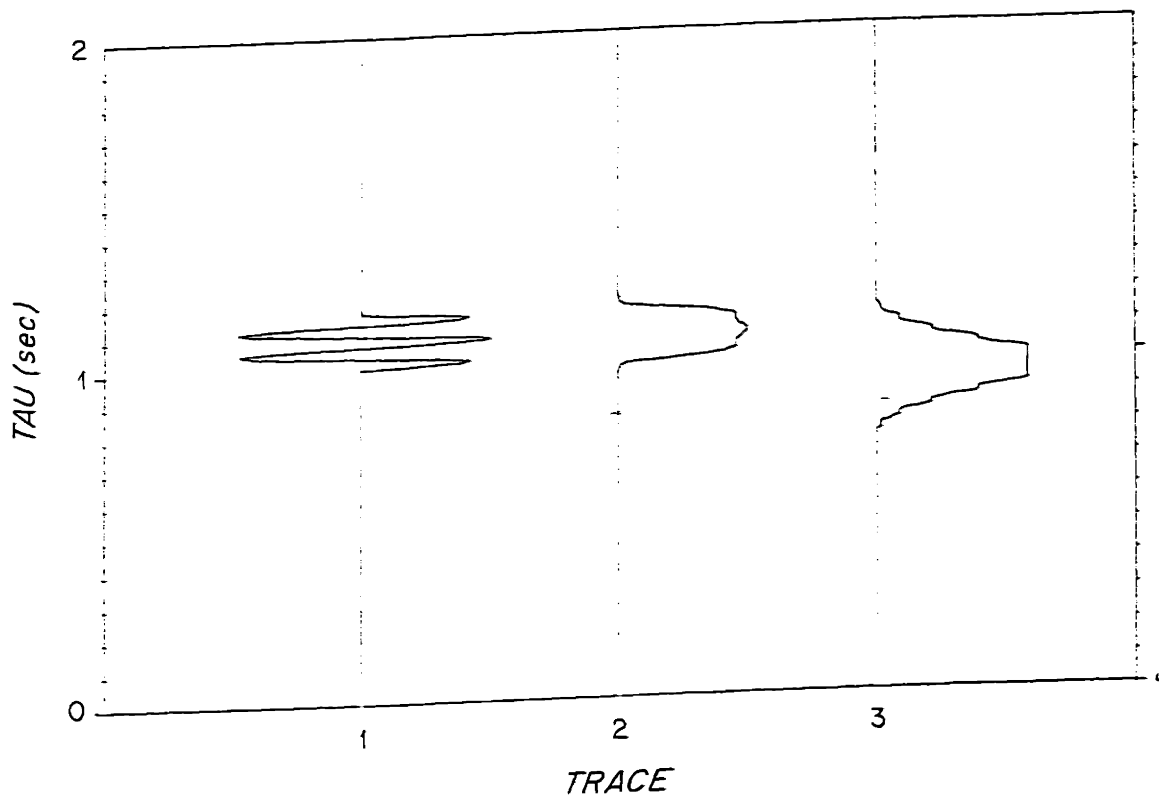

Fig. 3.6 This figure shows the effect on the spectral processor ambiguity function of omission of the spectral analysis window. Trace 1 is the signal wavelet. Trace 2 is its squared envelope, and Trace 3 is the spectral processor ambiguity function when no spectral analysis window is used. This should be compared to the ambiguity function in Trace 3 of fig. 3.5a which was computed using the $\sin^2$ tapering function and a .25 second window length.

MLM algorithm are given and analysed*.

Derivation

The first step in the velocity spectral analysis procedure is to compute the windowed and move-out corrected short-time amplitude spectral estimates on each of the channels:

$$\hat{P}(\tau,\omega,p_0,r) = e^{i\omega p_0 r} \int_{\tau}^{\tau+T} w_s(t-\tau-T/2)\, P(t+p_0 r, r)\, e^{i\omega t}\, dt \qquad 3.39a$$

where r is the channel location (discrete in the sampled case), and the fact that surface data has been used (z=0) is implicit. The important thing to note is that $\hat{P}$ is a function of both the input and output transform variables at the same time, i.e. t and ω, r and p. This is due to the short-time nature of the estimate. From fig. 3.7a we see that the fact that the window length, T, is comparable to the signal duration, d, requires that the spectral analysis window be move-out corrected in order not to vignette the signal wavelet at the ends of the array. Leverette [1977] has given an analysis of the effects of the window being mismatched to the arrival slowness. The density of the required move-out corrections, or "time-steers" of the array obviously increases with L, the closeness of d to T, and the shape of the spectral analysis window, $w_s(\tau)$ (a more center weighted window requires a greater density). In a later section the effects of the vignetting will be illustrated by examples. In equation 3.39a the $e^{i\omega p_0 r}$ term outside the integral restores the proper phase to the time shifted transforms. After the data are short-time Fourier transformed over the move-out corrected trajectories, the short-time transforms are put into what has been variously called the stacking, plane wave decomposition, or beamforming integral:

*Other researchers are working to extend the MEM family of high resolution spectral analysis techniques to non-uniformly sampled multi-dimensional data. The current state of the art has algorithms that can solve the problem, but present such a large computational burden as to be infeasible as standard processing techniques. [eg. Lang, 1981; McClellan, 1982; Lim and Malik, 1981]

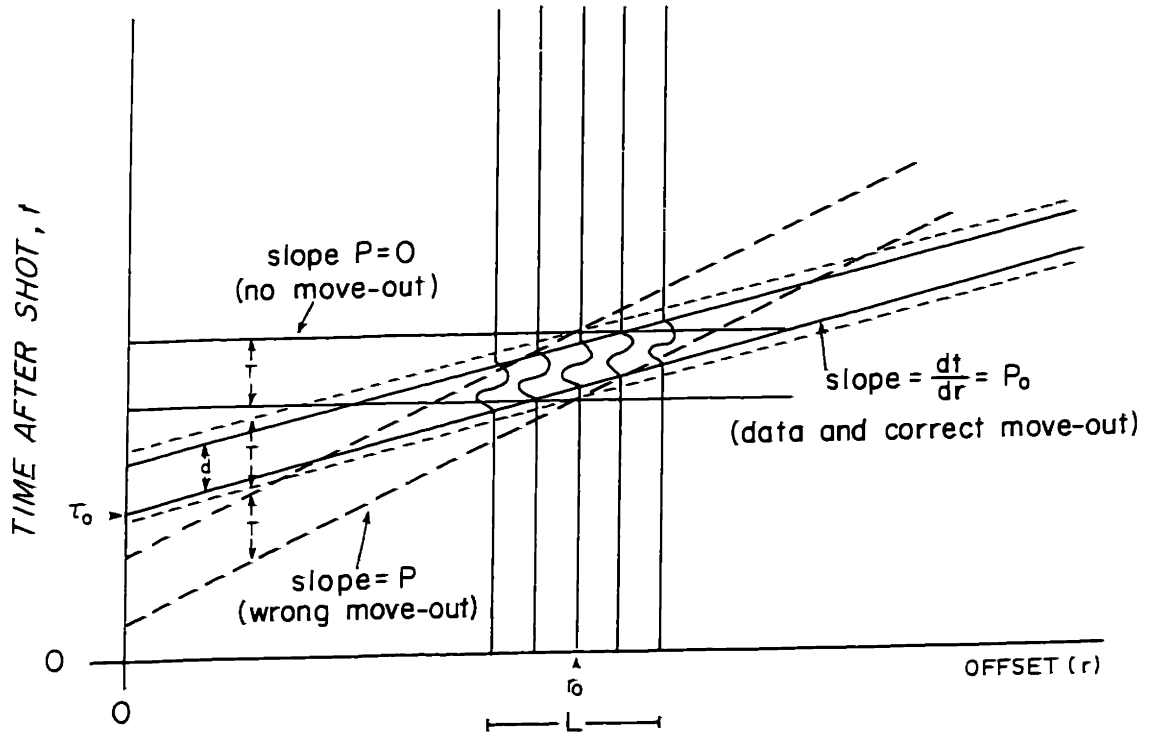

Fig 3.7a) Velocity spectral analysis window length and orientation effects.

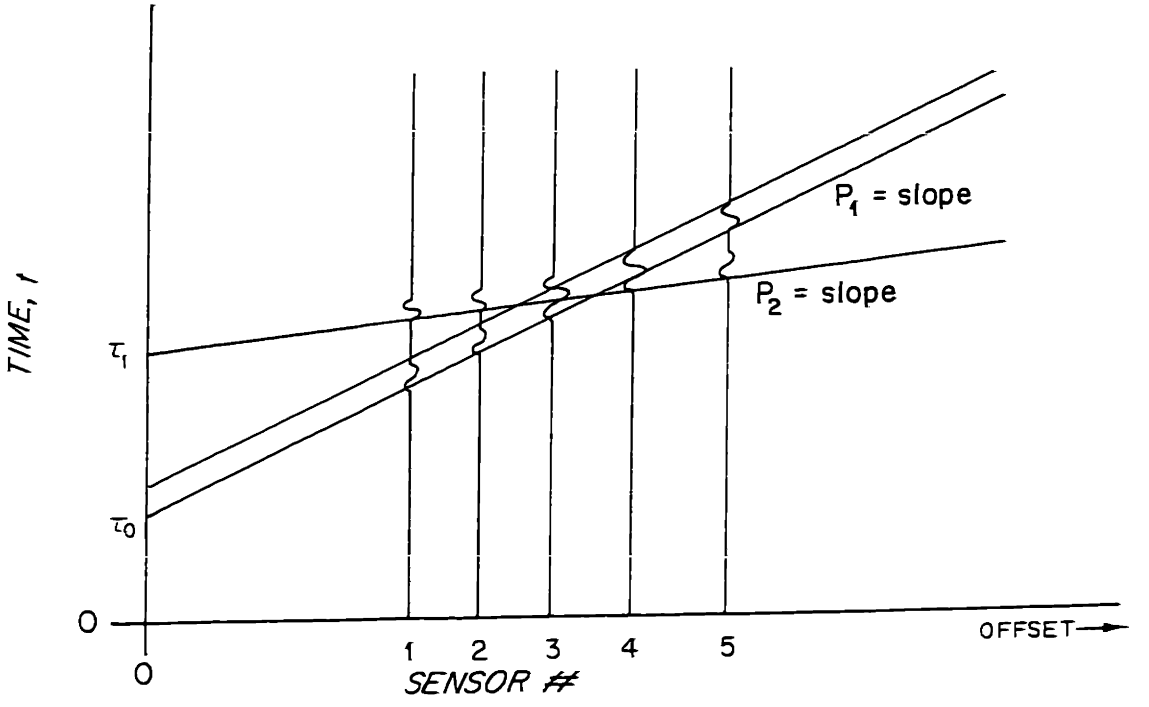

Fig 3.7b) Velocity spectral analysis window length and interfering wavelet effects.

$$\hat{S}(\tau,\omega,p,r_0) = \int_{\substack{\text{aperture } L \\ \text{centered on } r_0}} w_L(r-r_0)\,\hat{P}(\tau,\omega,p_0,r)\,e^{-i\omega pr}\,r^{\frac{1}{2}}dr \qquad 3.39b$$

In this expression we have allowed the output transform variable, p, to differ from the move-out trajectory, p_0, used for the short-time spectra. Since the window may be sightly larger than the wavelet duration, some amount of "slop" is possible, and some "phase steering" around p_0 is possible without seriously degrading the output. The ratio of time-steering to phase-steering obviously requires a performance/computational load trade-off decision to be made. The aperture taper or windowing function, W_L, has been included for generality, and is made different from $1/L$ for sidelobe control.

Equations 3.39 define the "conventional" velocity spectral processor for a continuous aperture. The usual velocity spectrum is the magnitude squared of the amplitude spectrum, $\hat{S}$, with $\hat{S}^2 \equiv |\hat{S}|^2$. The conventional velocity spectral processor for data from a sampled array simply implements the offset transform of 3.39b by a discrete transform sum on the observed sample offsets. The sample locations and the weights, $w_L(r_i-r_0)$ determine the array response, or beampattern of the system which is convolved with the true spectrum to yield the estimated velocity (slowness) spectrum. The sampled aperture conventional velocity spectrum is given by:

$$\hat{S}^2(\tau,\omega,p,r_0) = \left|\sum_{r_j} r_j^{\frac{1}{2}} w_L(r_j-r_0)\,\hat{P}(\tau,\omega,p_0,r_j)\,e^{-i\omega pr_j}\right|^2 \qquad 3.40$$

$\tau-p$ vs. $t-p$ Processing

Because it will turn out to be important in terms of the interpretability of the velocity spectra, there is a small twist that should be noted before introducing the maximum likelihood processor. In all the developments so far, the true offset values have been used in the stacking or plane-wave decomposition integrals and sums. If instead the offset is reduced by some

reference offset, say r_0, at the middle of the array, then instead of representing the intercept time, the variable τ becomes the arrival time itself, $\tau=t(r_0)=t(p_0)$. The advantage of this reduction to an array centered about zero is twofold. First, the data may be processed without knowledge of the actual offsets, except with reference to r_0, then warped when the value of r_0 is known by the usual mapping, $\tau(p_0) = t(p_0) - p_0 r_0$. The second advantage is that the sidelobe and aliasing artifacts shown in figure 3.2b cut across the stack or velocity spectrum with small slope, that is they remain at almost a constant time for each true arrival peak. For a large reference offset they would cut a diagonal fan shaped swath across the plot centered around slope = $-r_0$. Using the equations presented later in the chapter for the sidelobe structure and other properties of the stacking algorithm, this simple non-diagonal structure allows easy application of simple image processing algorithms to get rid of the sidelobe artifacts when zero-offset processing is used.

The Maximum Likelihood Method

As discussed earlier, (see eqns. 3.4-3.7), processing data via equation 3.40 with a short, sampled aperture yields poor slowness resolution spectra with artifacts due to sidelobes and aliasing. In the last 15 years spectral analysis and array processing (usually called beamforming in this context) algorithms have been proposed to ameliorate some of the undesirable effects of short data sequences or small arrays. The most common of these are autoregressive, "maximum entropy" (MEM), and "maximum likelihood" (MLM) methods [Lacoss, 1971]. For array processing applications in which the apertures are non-uniformly sampled and 2-dimensional no really satisfactory autoregressive or MEM techniques have been developed. The autoregressive methods yield non-unique spectra due to the problem of defining causality in multiple dimensions. The MEM techniques that have been proposed either require iterative

algorithms which have trouble converging, or non-linear optimizations which are computationally intensive and put constraints on the data that are often not met on applications to real data [Lim and Malik, 1981; Lang, 1981; McClellan, 1982]. On the other hand, the MLM algorithm which was originally popularized for non-uniform 2-D arrays [Capon, 1968] is a closed form, easy to apply, and computationally reasonable technique. Extensive applications have been made to all types of array data with good results, and though the algorithm makes more assumptions about the characteristics of the data, and is more sensitive to deviations from these assumptions (i.e. less robust) than the conventional method of equations 3.39b and 3.40, the properties are well understood and can be compensated for. [Duckworth, 1980; 1980] In this section the application of the MLM algorithm to the velocity spectral analysis problem is outlined.

The MLM, or unbiased minimum mean square estimate of the amplitude of the uncorrelated plane wave component of the signal vector:

$$\mathbf{d} = \begin{bmatrix} \cdot \\ \cdot \\ \cdot \\ d_j \\ \cdot \\ \cdot \\ \cdot \end{bmatrix} = \begin{bmatrix} \cdot \\ \cdot \\ \cdot \\ r_j^{\mu} P(\tau,\omega,p_0,r_j) \\ \cdot \\ \cdot \\ \cdot \end{bmatrix} \qquad 3.41a$$

at slowness p is obtained by finding the weighting vector (or function in the continuous case), $w(p)$, which yields an unbiased estimate of the amplitude of the component of $\mathbf{d}$ propagating with slowness p and frequency ω, while minimizing the expected total power out of the processor. In this case, we want the filter $w(p)$ which estimates a unity amplitude for the hypothesized monochromatic plane wave:

$$\mathbf{e}(p) = \begin{bmatrix} \cdot \\ \cdot \\ \cdot \\ e_j \\ \cdot \\ \cdot \\ \cdot \end{bmatrix} = \begin{bmatrix} \cdot \\ \cdot \\ \cdot \\ e^{i\omega p r_j} \\ \cdot \\ \cdot \\ \cdot \end{bmatrix} \qquad 3.41b$$

using the constraint equation:

$$1 = \mathbf{w}^H(p)\,\mathbf{e}(p) \qquad 3.41c$$

which also minimizes the expected total power out of the processor:

$$\min_{\mathbf{w}(p)} \mathrm{E}\left\{\mathbf{w}^H(p)\,\mathbf{d}\,\mathbf{d}^H\mathbf{w}(p)\right\} = \hat{S}^2_{MLM}(p) \qquad 3.41d$$

The weighting vector can be obtained by taking derivatives with respect to the real and imaginary parts of the elements in $\mathbf{w}(p)$ and using the Lagrange multiplier method for the constrained minimization. [Gammelsaeter, 1981; Duckworth, 1980; 1980] The resulting set of weights is given by:

$$\mathbf{w}(p) = \frac{\mathbf{R}^{-1}\mathbf{e}(p)}{\mathbf{e}^H(p)\,\mathbf{R}^{-1}\mathbf{e}(p)} \qquad 3.41e$$

where:

$$\mathbf{R} \equiv \mathrm{E}\{\mathbf{d}\,\mathbf{d}^H\} \qquad 3.41f$$

is the covariance matrix of the data. Note that the quadratic form inside the expectation of equation 3.41d is simply the operation in 3.40 where the weight vectors include both the aperture tapering function and the steering exponential. Thus for each p value the weighting vector changes and the concept of a fixed beampattern $W_L(\omega,p)$ disappears. Interpretations of this estimate appear in many places [Capon, 1969; Leverette, 1977; Aki and Richards, 1980; Duckworth, 1980; Gammelsaeter, 1981] and would be redundant to repeat here. Suffice it to say that the weighting function "adapts" to the data through the covariance $\mathbf{R}$ to optimally

suppress both uncorrelated sensor noise and coherent arrivals from other sources which are uncorrelated with one another and with the signal of interest. Duckworth [1980] has shown that the MLM method also works to suppress propagating signals from distributed sources, such as isotropic noise, which can be modeled as a dense distribution of independent radiators.

Spectral Covariance Estimation

From equation 3.41f it is seen that the second order statistics of the data are required to design the optimal weighting filter. Since we obviously do not know the statistics of the data (if we did, the problem would be solved), the covariance matrix, R, must be estimated. Because the data consists of transient arrivals propagating with different slownesses (p) at different times, the data are nonstationary in time.* It is this fact that requires the data vector Fourier transforms to be carried out in a short-time fashion. To estimate the covariance matrix** we assume that the data are stationary over the spectral analysis interval, T. To implement the expectation in 3.41f several methods may be used. The best would be to acquire data by multiple shots at the same nominal offset distance, r_0. These would be decomposed and then averaged:

$$\hat{\mathbf{R}} = \frac{1}{N} \sum_{N \text{ shots}} \mathbf{d}\mathbf{d}^H \qquad \text{(ensemble average)} \qquad 3.42$$

This method, which is used extensively in sonar and radar processing, is not really practical in seismic work because of logistical considerations. A more reasonable method is to utilize the fact that disjoint spectral bands of a stationary random process are statistically independent. Thus, the covariance at a nominal frequency could be formed by the standard method of spec-

*They are also inhomogeneous in space— the second order statistics of the spatial data are not shift invariant. It is this fact that necessitates the need for short aperture parameter estimates.

**Often called the spectral covariance matrix because it is a function of ω.

tral smoothing:***

$$\hat{\mathbf{R}}(\omega_0) = \int_{\omega_0 - B/2}^{\omega_0 + B/2} \mathbf{d}(\omega)\mathbf{d}^H(\omega)\, dw \qquad 3.42$$

If this method is used, the same consideration must be given to the size of the averaging bandwidth, B, as was given to the bandwidth of the original spectral decomposition in equation 3.33 using $B/2=\Delta\omega$. Again, if too large a bandwidth is averaged, the slowness estimate will be smeared. However, in most cases, the bandwidth, $2\Delta\omega$, of the spectral processor has already been chosen by fixing the window shape, $w_s(\tau)$, and duration, T, from a guess at the signal model, $s(t)$. For transient signals, this bandwidth is usually already pushing the slowness-smearing limit in order to obtain good time resolution, and no spectral averaging is possible. In addition, since the signals are transient and the time location of the transient is of interest, no temporal averaging can be carried out.* This leaves only one choice for the covariance estimate, the single outer product, plus a stabilizing uncorrelated noise matrix with power ϵ^2 to make it invertible:

$$\hat{\mathbf{R}} = \mathbf{d}\mathbf{d}^H + \epsilon^2\mathbf{I} \qquad 3.43$$

This formulation makes the MLM velocity power spectral output particularly easy to compute:

$$\begin{aligned} \hat{S}^2_{exact}(p) &= |\mathbf{w}^H\mathbf{d}|^2 = \mathbf{w}^H\mathbf{d}\mathbf{d}^H\mathbf{w} \\ &= \frac{\mathbf{e}^H\hat{\mathbf{R}}^{-1}}{\mathbf{e}^H\hat{\mathbf{R}}^{-1}\mathbf{e}}\,(\hat{\mathbf{R}} - \epsilon^2\mathbf{I})\,\frac{\hat{\mathbf{R}}^{-1}\mathbf{e}}{\mathbf{e}^H\hat{\mathbf{R}}^{-1}\mathbf{e}} \\ &= \frac{1}{\mathbf{e}^H\hat{\mathbf{R}}^{-1}\mathbf{e}} - \epsilon^2\,\frac{\mathbf{e}^H\hat{\mathbf{R}}^{-2}\mathbf{e}}{\mathbf{e}^H\hat{\mathbf{R}}^{-1}\mathbf{e}^2} \end{aligned} \qquad 3.44$$

***The dependence of the covariance matrix, R, and data vector, d, on time, frequency, and time steering slowness, p_0, is implicit and is obtained through equation 3.41a.

*Temporal averaging is common for the quasi-stationary signals in passive CW source location problems [c.f. Lacoss et al., 1978-83].

In practice, the stabilizing noise level, ϵ^2, is chosen to keep the condition number of the matrix $\hat{\mathbf{R}}$ within some limit dependent upon the precision of the machine being used to invert the matrix, or for reasons of estimator amplitude bias (discussed in a later section of this chapter). The largest eigenvalue of $\hat{\mathbf{R}}$ from 3.43 is $\mathbf{d}^H\mathbf{d}+\epsilon^2$ and the smallest is ϵ^2. Thus, to keep the condition number below γ

$$\epsilon^2 \geq \frac{|\mathbf{d}|^2}{(\gamma-1)} \qquad 3.46$$

For small ϵ^2, the last term of 3.44 is negligible** and the MLM power estimate used is:

$$\hat{S}^2_{MLM}(p) = \frac{1}{\mathbf{e}^H(p)\hat{\mathbf{R}}^{-1}\mathbf{e}(p)} \qquad 3.47$$

where:

$$\hat{\mathbf{R}} = \mathbf{d}\mathbf{d}^H + \epsilon^2\mathbf{I}$$

It is easy to see that the "conventional" estimate of equation 3.40 when $w_L(r) = 1/L$ ($1/N$ in sampled case) is:

$$\hat{S}^2_{CONV}(p) = \frac{1}{N^2}\,|\mathbf{e}^H(p)\mathbf{d}|^2 = \frac{1}{N^2}\,\mathbf{e}^H(p)(\hat{\mathbf{R}} - \epsilon^2\mathbf{I})\mathbf{e}(p) \approx \frac{1}{N^2}\mathbf{e}^H(p)\hat{\mathbf{R}}(p)\mathbf{e} \qquad 3.48$$

where the "stabilizing factor" $\epsilon^2\mathbf{I}$ is not needed in $\hat{\mathbf{R}}$ because the matrix is not inverted.

MLM Power Bias due to Interfering Signals

The major problem with the MLM filter and estimator of equations 3.41f and 3.47 is that with the *estimated* covariance matrix of 3.43, they are highly biased in amplitude due to uncorrelated noise and the presence of other propagating signals. The uncorrelated noise

---

**It is of order ϵ^2/N and thus corrects for the bias in a noiseless plane wave estimate since $\mathbf{d} = a\mathbf{e}$ – $\hat{S}^2_{MLM} = a^2 - \epsilon^2/N$ and $\hat{S}^2_{corr} \approx a^2$. The removal of the bias is not usually necessary because calculating ϵ^2 by 3.46 yields $\epsilon^2 = Na^2/(\gamma-1)$, and the fractional bias is on the order of the inverse of the condition number when $\gamma \gg 1$.

causes a bias because it appears in the cross-spectral or off-diagonal components of $\hat{\mathbf{R}}$. This occurs because no averaging is done to cancel the uncorrelated terms off the diagonal, as would happen in the ensemble averaging case. For example, $\epsilon^2\mathbf{I}$ is just the ensemble spectral covariance matrix of uncorrelated sensor noise with power in the passband of ϵ^2. Later it will be seen that the bias from this "off diagonal" sensor noise is quite predictable and can be compensated for.

However, before dealing with noise issues, the propagating signals with other slownesses and the same spectrum that appear in $\hat{\mathbf{R}}$ are much more problematic. This is because the lack of averaging, or single "snapshot" acquisition structure, forces any two propagating signals in the moved-out window of equation 3.39a to appear correlated, which violates the assumptions under which the MLM was derived. The estimated spectral covariance matrix will look like

$$\hat{\mathbf{R}} = (\mathbf{d}_1+\mathbf{d}_2)(\mathbf{d}_1+\mathbf{d}_2)^H + \epsilon^2\mathbf{I} = \mathbf{d}_1\mathbf{d}_1^H + \mathbf{d}_2\mathbf{d}_2^H + \epsilon^2\mathbf{I} + 2\mathrm{RE}[\mathbf{d}_1\mathbf{d}_2^H] \qquad 3.49$$

where $\mathbf{d}_1$ and $\mathbf{d}_2$ are two separate propagating components of $\mathbf{d}$. The cross term $2\mathrm{RE}[\mathbf{d}_1\mathbf{d}_2^H]$ is the false correlated term that would go away with averaging because of the assumption that $\mathbf{d}_1$ and $\mathbf{d}_2$ are independent. The effects of these cross terms are shown in detail by Duckworth [1980, p. 103]. However, in the transient array processing case we are considering, the use of the short time-steered moveout window for the calculation of the vector $\mathbf{d}$ helps this problem. The short duration of the window removes arrivals with vastly different slownesses on all but a few sensors when the array is long and the window is short. Figure 3.7b shows this effect. The wave at slowness p_0 is interfered with by the wave at slowness p for only the sensors 3 and 4. Because of this, the cross term appears only for isolated elements of the covariance matrix.

To evaluate this bias in the power out at the correct slowness, p_0, we write the expression for the power out of the MLM estimator as a function of the powers in the two signals, the

conventional beampattern of the array, and the uncorrelated sensor noise power which appears only on the diagonal of the spectral covariance matrix. The signal model is

$$\mathbf{d} = \mathbf{d}_1 + \mathbf{d}_2 = a\mathbf{e}_1 + b\mathbf{e}_2 \qquad 3.50a$$

where $\mathbf{d}$, $\mathbf{e}_1$ and $\mathbf{e}_2$ are vectors of length N, and a^2 and b^2 are the powers in the two signals in the bandwidth of the processor. The array responses are defined as

$$B_{ij} \equiv \mathbf{e}_i^H \mathbf{e}_j \qquad 3.50b$$

The maximum values of B_{ij} are N when $i=j\neq 2$ and M when $i=j=2$, which corresponds to M sensors having the interfering wavelet #2 present. In general, the resolution for the beampattern with i or $j=2$ will also be degraded because the effective array is shorter, and because the window move-out is not matched to the wavelet with slowness p_2. The general expression for $\hat{S}^2_{MLM}$ is

$$\hat{S}^2_{MLM}(p_0) = \frac{\epsilon^2[\epsilon^2 + a^2B_{11} + b^2B_{22} + 2abB_{12}]}{N\epsilon^2 + a^2NB_{11} + b^2NB_{22} + 2abNB_{12} - a^2B_{01}^2 - b^2B_{02}^2 - 2abB_{01}B_{02}} \qquad 3.51a$$

The expression for a single wave, ($b=0$), is:

$$\hat{S}^2_{MLM}(p_0) = \frac{\epsilon^2[\epsilon^2 + a^2B_{11}]}{N\epsilon^2 + a^2NB_{11} - a^2B_{01}^2} = \frac{\epsilon^2[\epsilon^2 + a^2N]}{N\epsilon^2 + a^2(N^2 - B_{01}^2)} \qquad 3.51b$$

These should be compared to obtain the bias. For $p_0=p_1\neq p_2$ and $B_{12}=B_{02}=0$, $B_{11}=N$, $B_{22}=M$, corresponding to the power estimate at p_1 when the interfering wave is far enough away in slowness and present on enough sensors so that the array response with term $2=j$ is zero, the approximate expression is:

$$\hat{S}^2_{MLM}(p_1) \approx \frac{\epsilon^2[\epsilon^2 + Na^2 + Mb^2]}{N\epsilon^2 + NMb^2} \qquad 3.52a$$

and is diminished from the correct estimate 3.51b primarily by the denominator term, MNb^2. This expression is plotted by the solid lines of Fig. 3.8 for $a=1$, $N=24$, $\epsilon^2=.1$ (10 dB sensor

SNR) for various values of signal 1 to signal 2 ratio, and M. Note that this expression is not valid for small M (except 0) because as the effective array length over which signal 2 is received diminishes, $B_{02}=B_{12}$ cannot be zero since the main lobe gets very wide. The small M case is better approximated by $B_{22}=B_{02}=B_{12}=M$, and the approximate expression is:

$$\hat{S}^2_{MLM}(p_1) = \frac{\epsilon^2[\epsilon^2 + a^2N + b^2M + 2abM]}{N\epsilon^2 + NMb^2 - b^2M} \qquad 3.52b$$

This is plotted by the dotted lines of Figure 3.8. Note that since the signal of interest has power=1, the plot represents the power output bias in dB. As may be seen from this plot, for equivalent powers (horizontal axis 0 dB) the bias is large--approximately 10 to 20 dB for 1 to 5 sensors affected. For this case we also note that the output noise power away from the source p values would be $\epsilon^2/N \Rightarrow -24$ dB, so the output dynamic range is grossly compressed when an interfering source is present.

One way to decrease the bias due to interfering sources is to "normalize" the spectral covariance estimate 3.43. This normalized matrix is given by

$$\hat{\mathbf{R}}_{norm} = \left[\hat{\mathrm{R}}_{ij}\right] = \left[\frac{\mathrm{K}_{ij}}{(\mathrm{K}_{ii}\,\mathrm{K}_{jj})^{1/2}}\right] \left(\prod_{i=1}^{N} \mathrm{K}_{ii}\right)^{1/N} - \epsilon^2\mathbf{I} \qquad 3.53a$$

where:

$$\mathbf{K} = \mathbf{d}\mathbf{d}^H \qquad \mathrm{K}_{ij} = \mathrm{d}_i\mathrm{d}_j^*$$

and $\hat{\mathrm{R}}_{ij}$ is the i,j^{th} element of $\hat{\mathbf{R}}_{norm}$. The geometric mean (or average dB value) of the diagonal elements is used to restore the overall power to the estimated matrix because it is less sensitive than the arithmetic average to extreme values from constructive interference between the two waves. This normalization forces the covariance matrix to look as though it is from a homogeneous process (the spatial equivalent of stationarity) in which there is no interference on the average, and all the diagonal elements are equal (in fact, all the elements are equal for

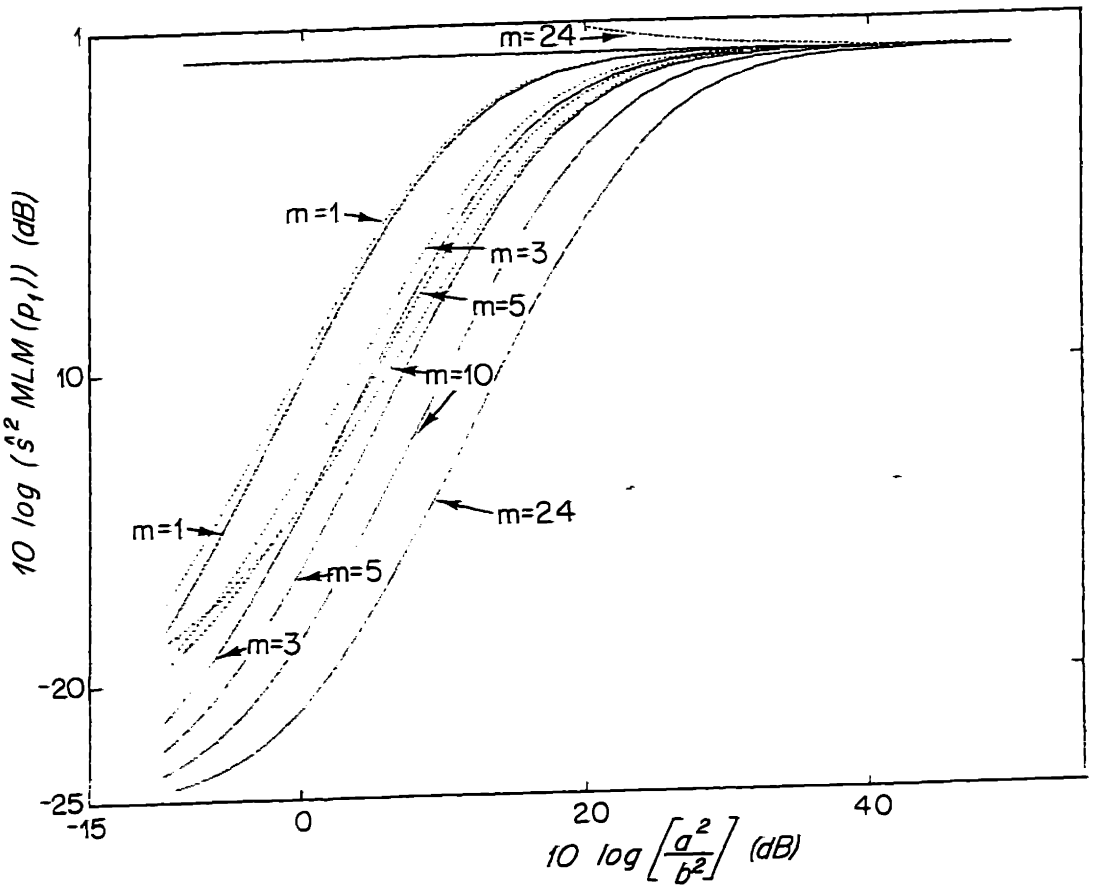

Fig 3.8) MLM power output bias as a function of number of overlapping wavelets within the analysis window (m), and the ratio of the power in the desired wavelet (a^2) and the interfering wavelet (b^2). The differing models used for the dotted and solid lines are described in the text.

the single outer-product covariance estimate of 3.43). The evaluation of the output power after normalization is messy, and it is left to the reader to use equation 3.51a to carry this out.

MLM Power Bias due to Independent Sensor Noise

When very little averaging is used in the estimate of the spectral covariance matrix the amplitude of the MLM estimator is biased even when only one source term is present. This bias is due to the presence of uncorrelated sensor noise terms off the diagonal of the matrix. By using Monte Carlo simulations, Scheer [1982] developed empirical formulas for the bias as a function of the true noise level σ^2, the required inversion noise, ϵ^2, the signal level a^2 and the number of outer products averaged to form the covariance matrix. Leverette [1977] developed an analytical formula for the bias as a function of these variables when a single outer product is used to estimate the spectral covariance matrix. Because the single data vector case is the one of primary concern to this work in which we are trying to get the best arrival time resolution possible (and thus the bandwidth $1/T$ reaches the p-smearing limit), this formula was tested by Monte Carlo simulations. The reason for interest in quantifying the bias is that if the variance of the biased value is low enough, then it is possible to "invert" the biased power outputs for a^2 using the bias expression, the known value of ϵ^2, and the noise level, σ^2, measured from a signal-free region of the data or processor output.

The usual spectral covariance estimate using one outer product is:

$$\hat{\mathbf{R}} = \mathbf{d}\mathbf{d}^H + \alpha \frac{\mathbf{d}^H\mathbf{d}}{N}\mathbf{I} \qquad \gamma = \frac{N}{\alpha} + 1 \qquad \gamma = \text{condition number} \tag{3.54}$$

where ϵ^2 has been replaced by $\alpha\mathbf{d}^H\mathbf{d}/N$ to track the signal power and keep the condition number of the covariance matrix constant. The data vector, $\mathbf{d}$, is given by:

$\mathbf{d} = a\mathbf{e}(p_0) - \mathbf{n}$ $\qquad\qquad$ $\mathbf{n} = N(0,\sigma^2\mathbf{I})$

The signal to noise ratio at the sensor is a^2/σ^2 and the term $\alpha\mathbf{d}^H\mathbf{d}/N$ adds α times the average (signal power ÷ noise power) to the diagonal for stabilization. Leverette [1977] shows that the expected MLM and convention velocity spectral estimates at the slowness, p_0, corresponding to the data vector slowness are:

$$\hat{S}^2_{MLM}(p_0) = \frac{\alpha(a^2 + \sigma^2)}{N} + \frac{a^2 + \frac{\sigma^2}{N}}{1 + \frac{\sigma^2[N-1]}{\alpha(a^2+\sigma^2)}} \qquad 3.55a$$

$$\hat{S}^2_{CONV}(p_0) = \frac{\alpha(a^2 + \sigma^2)}{N} + a^2 + \frac{\sigma^2}{N} \qquad 3.55b$$

A slight extension to Leverette's work shows that the complete array responses for all slownesses for these parameters are given by:

$$\hat{S}^2_{MLM}(p) = \frac{\alpha(a^2 + \sigma^2)}{N} + \frac{a^2\frac{B^2(p-p_0)}{N^2} + \frac{\sigma^2}{N}}{1 + \frac{N[a^2(1-B^2(p-p_0)/N^2) + \sigma^2(1-1/N)]}{\alpha(a^2+\sigma^2)}} \qquad 3.56a$$

$$\hat{S}^2_{CONV}(p) = \frac{\alpha(a^2 + \sigma^2)}{N} + a^2\frac{B^2(p-p_0)}{N^2} + \frac{\sigma^2}{N} \qquad 3.56b$$

when the signal is propagating with slowness p_0 and $B(p-p_0)$ is the conventional array response, $B(p-p_0)=\mathbf{e}^H(p)\mathbf{e}(p_0)$. Far from the signal slowness ($B(p-p_0) = 0$) 3.56a and b evaluate to:

$$\hat{S}^2_{MLM} = \frac{\alpha(a^2 + \sigma^2)}{N} - \frac{\frac{\sigma^2}{N}}{1 + \frac{N[a^2 + \sigma^2(1-1/N)]}{\alpha(a^2+\sigma^2)}} \approx \begin{cases} \alpha\frac{a^2}{N} & \text{for } a^2 \gg \sigma^2 \\ \alpha\frac{\sigma^2}{N} & \text{for } \sigma^2 \gg a^2 \end{cases} \qquad 3.57a$$

$$\hat{S}^2_{CONV} = \frac{\alpha(a^2 + \sigma^2)}{N} + \frac{\sigma^2}{N} \approx \frac{\sigma^2}{N} \qquad 3.57b$$

A final set of useful expressions is the power out of the processors when the signal power is zero. From 3.55a and b, these are

$$\hat{S}^2_{MLM} \approx \alpha \frac{\sigma^2}{N} \qquad 3.58a$$

$$\hat{S}^2_{CONV} \approx \frac{\sigma^2}{N} \qquad 3.58b$$

Figure 3.10 shows the MLM and conventional array responses for a uniform and a non-uniform array, each with $N=10$ sensors. The parameters and predictions from the above formulae are given in Table 3.2.

TABLE 3.2

Parameters				Figs. 3.10 a&c		Figs. 3.10 b&d	
a^2	σ^2	SNR (dB)	α	$\hat{S}^2_{MLM}$ peak	$\hat{S}^2_{MLM}$ noise	$\hat{S}^2_{CONV}$ peak	$\hat{S}^2_{CONV}$ noise
1	0.0	∞	.002	0 dB	-37 dB	0 dB	-37 dB*
1	0.01	+20	.002	-16.5	-37	0	-37*
1	1.	0	.002	-30.5	-33.25	0.4	-10
1	100.	−20	.002	-16.5	-16.5	10.4**	+10**

The sensor distributions are given in table 3.3 and are plotted in figure 3.9.

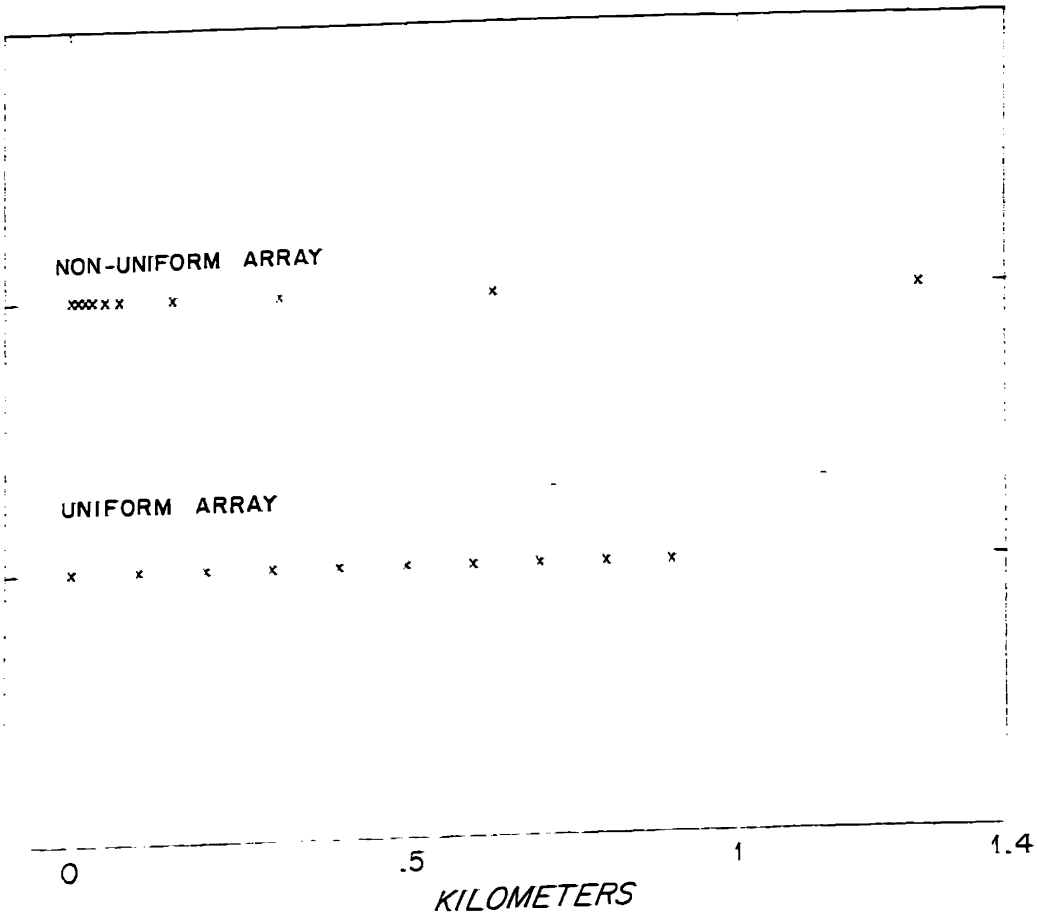

Fig 3.9) The uniform and non-uniform array distributions used for the examples in figure 3.10.

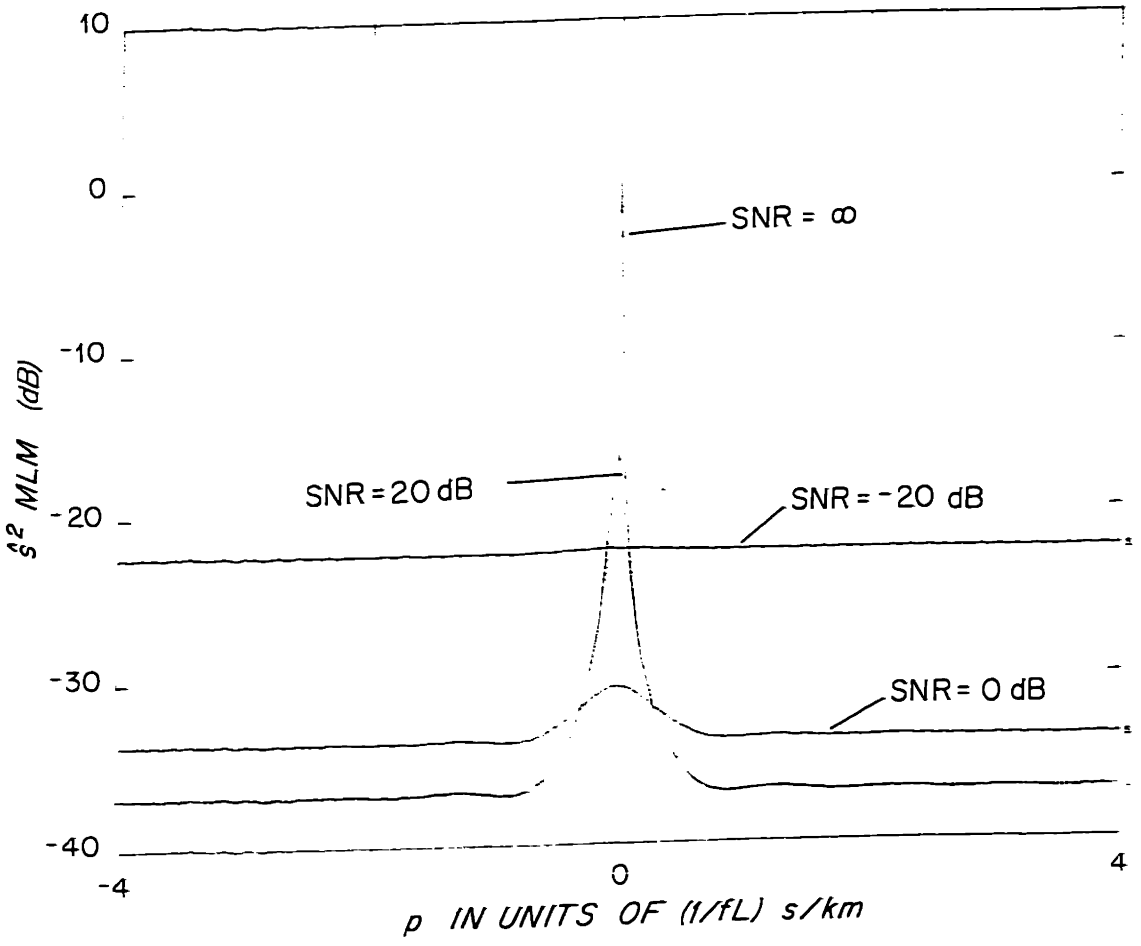

Fig 3.10(a) MLM response as a function of SNR for a single source received on the uniform array of fig. 3.9.

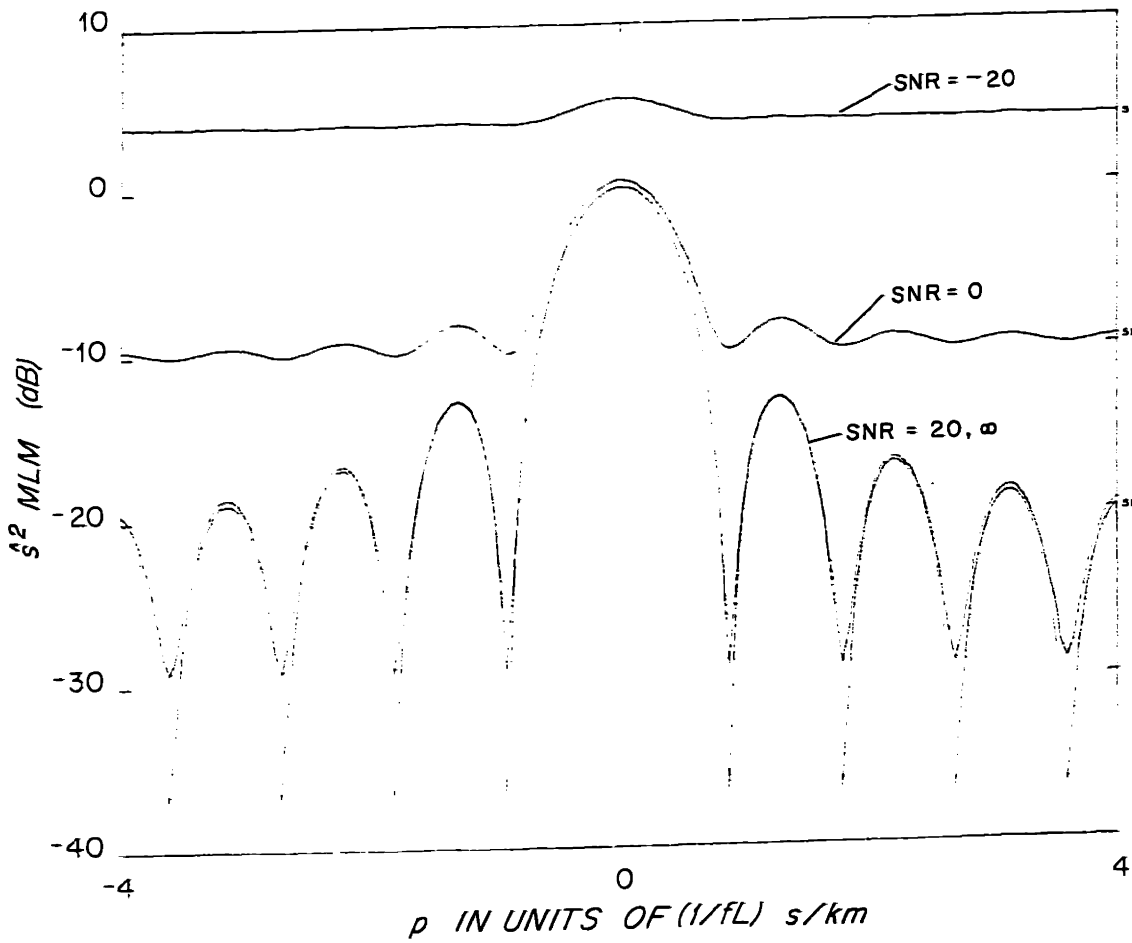

Fig 3.10b) Conventional response as a function of SNR for a single source received on the uniform array of fig. 3.9. The response for a noise level of +10 dB has been shifted down by 6 dB.

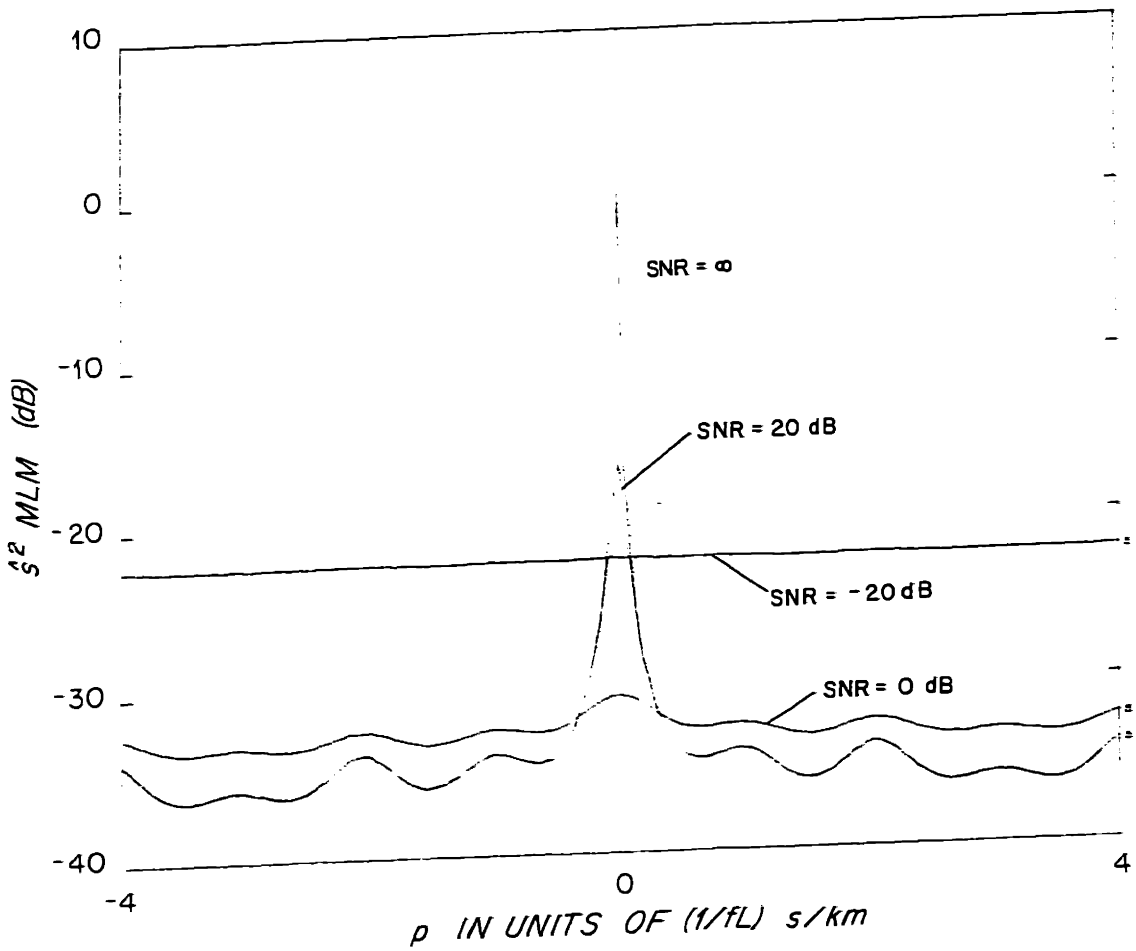

Fig 3.10c) MLM response as a function of SNR for a single source received on the non-uniform array of fig. 3.9.

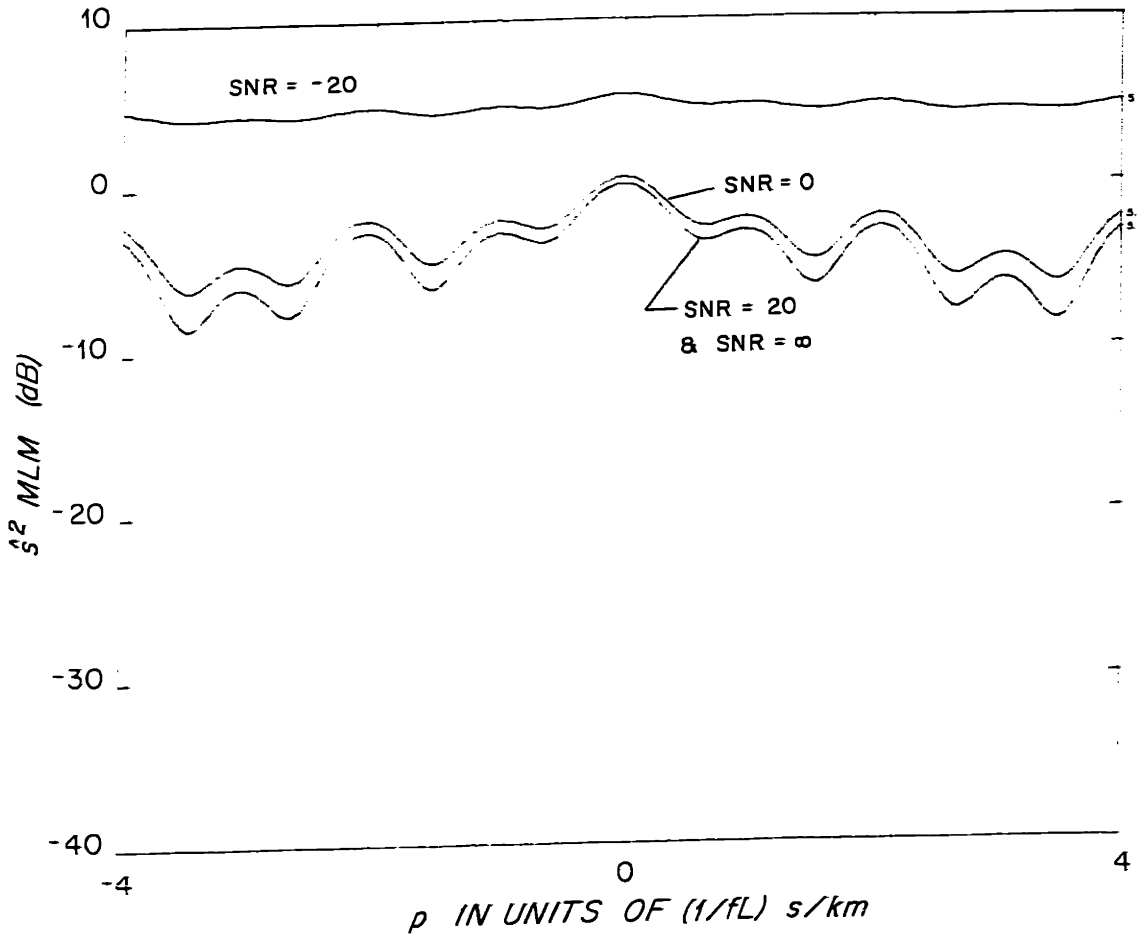

Fig 3.10d) Conventional response as a function of SNR for a single source received on the non-uniform array of fig. 3.9. The response for a noise level of +10 dB has been shifted down by 6 dB.

TABLE 3.3	
Uniform Array	Non-uniform Array
0.	0.
.1	.01
.2	.02
.3	.03
.4	.05
.5	.07
.6	.15
.7	.31
.8	.63
.9	1.27

From these plots we can see that while the MLM method is highly biased, the array response is much better and its width is independent of the noise level, σ^{2***}. In the single source case the good sidelobe structure of the MLM algorithm allows correct estimation of the background noise levels without the interference of the sidelobes of the conventional array response. The reader will recall that if α, σ^2, and N are known, the true source power can be estimated from the biased output power through the bias prediction formulae (eqns. 3.55). Thus, if the biased power estimator estimator is stable enough, the results can be "de-biased". Note also that while the MLM works just as well on the uniform and non-uniform arrays, the conventional estimate is almost useless on the non-uniform array, even for high SNR.

A Monte Carlo simulation was run to test the power bias using the processing programs on a simple test example similar to that used for the time of arrival estimator comparisons. All parameters were the same except that the γ parameter for the Gaussian envelope was 5 instead

---

*This noise level is not observable because the sidelobes of the beampattern are too large.

**These levels should be off the plot scale and have been shifted down by 6 dB for visibility.

***It is not, however, independent of α or any noise that properly appears only on the diagonal of the covariance matrix. As the diagonal increases relative to the cross-spectra, the MLM beampattern converges to the conventional beampattern.

of 15, leading to a more peaked pulse (see equations 3.37 and 3.38 for the wavelet and window parameters). The power estimates at 15 Hz and the peak in arrival time and slowness were chosen* to obtain the Monte Carlo data for varying signal to noise ratios (a^2/σ^2 in band) and varying values of α. The results of the Monte Carlo simulations are compared to the predictions of equations 3.55a and b in Figure 3.11 and are seen to agree quite well. Figures 3.11a and b parameterize the curves by in-band signal to noise ratio at the sensor and the abscissa is the stabilizing fraction, α. Figures 3.11c and d parameterize the curves by the stabilizing fraction α, and the abscissa is the in band signal to noise ratio. $N=10$ channels were used on the uniform array of table 3.3 for these computations. For the plots the in-band power in the signal has been normalized to one so that the bias can be read from the ordinate directly. From these figures it is clear that the MLM estimator is quite biased, while the conventional one is not. However, the previous plots in fig. 3.10 show that the MLM does have advantages vis a vis resolution, sidelobes, and performance on non-uniform arrays. For this simulation, 50 trials were used for each SNR and α value and the standard deviations of the peak power dB values were always less than 2 dB. The good stability of the biased peak power estimate and the agreement of the simulations with equation 3.55, indicate that "undoing" the bias is possible.

The bias removal or amplitude correction procedure is demonstrated on an example. Two plane waves with the parameters listed in Table 3.4 were simulated using the wavelet in the last example. The sensor noise power was -4 dB in the processor band using the $\sin^2$ window which has a 4 dB window loss yielding $\sigma = .631$, the stabilizing fraction was $\alpha=.002$, and there were $N=10$ channels. (See also table 3.5.)

*Note, these were not necessarily the correct time and slowness due to estimation error.

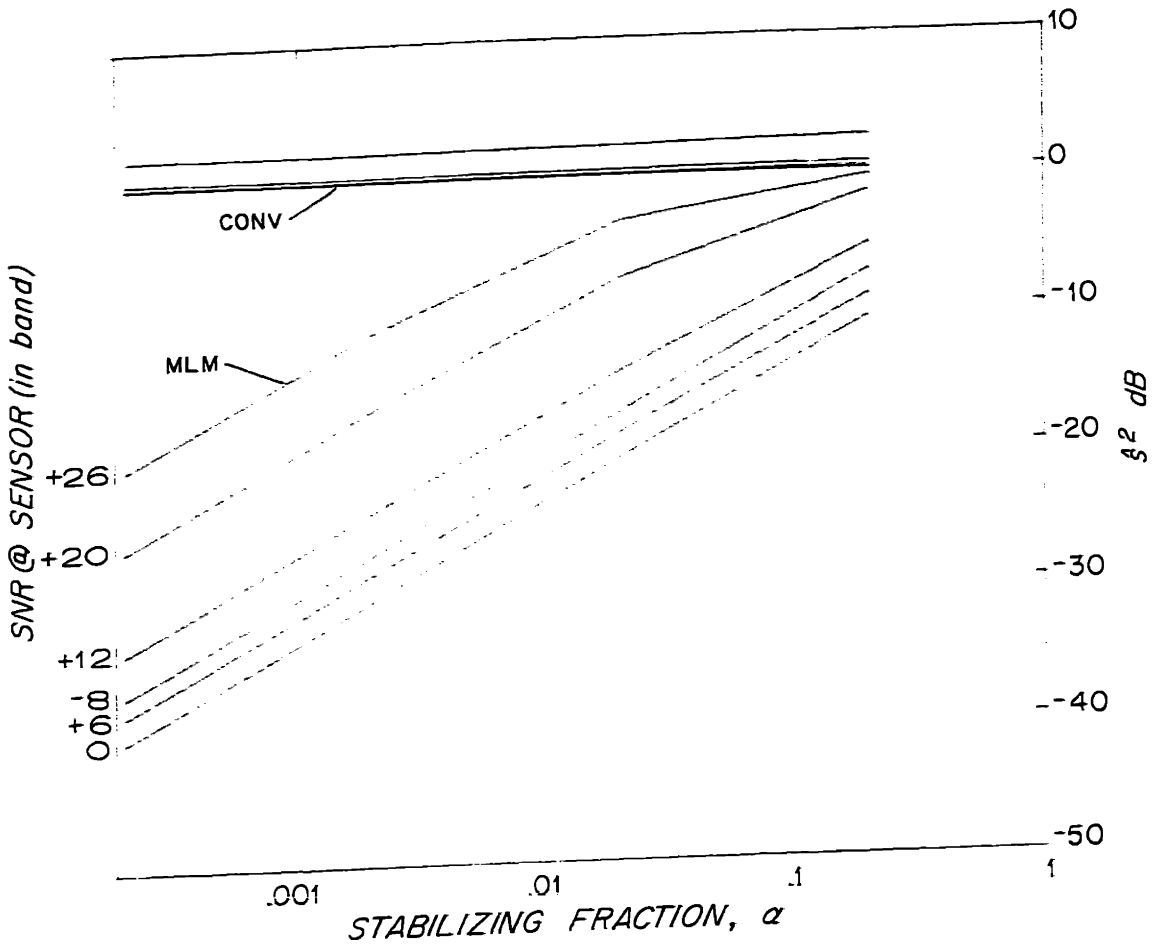

Fig. 3.11a) Predicted power bias as a function of stabilizing fraction, α, and in-band sensor signal to noise ratio. The 10 element uniform array of fig. 3.9 was used for the calculation. (No bias corresponds to 0 dB.)

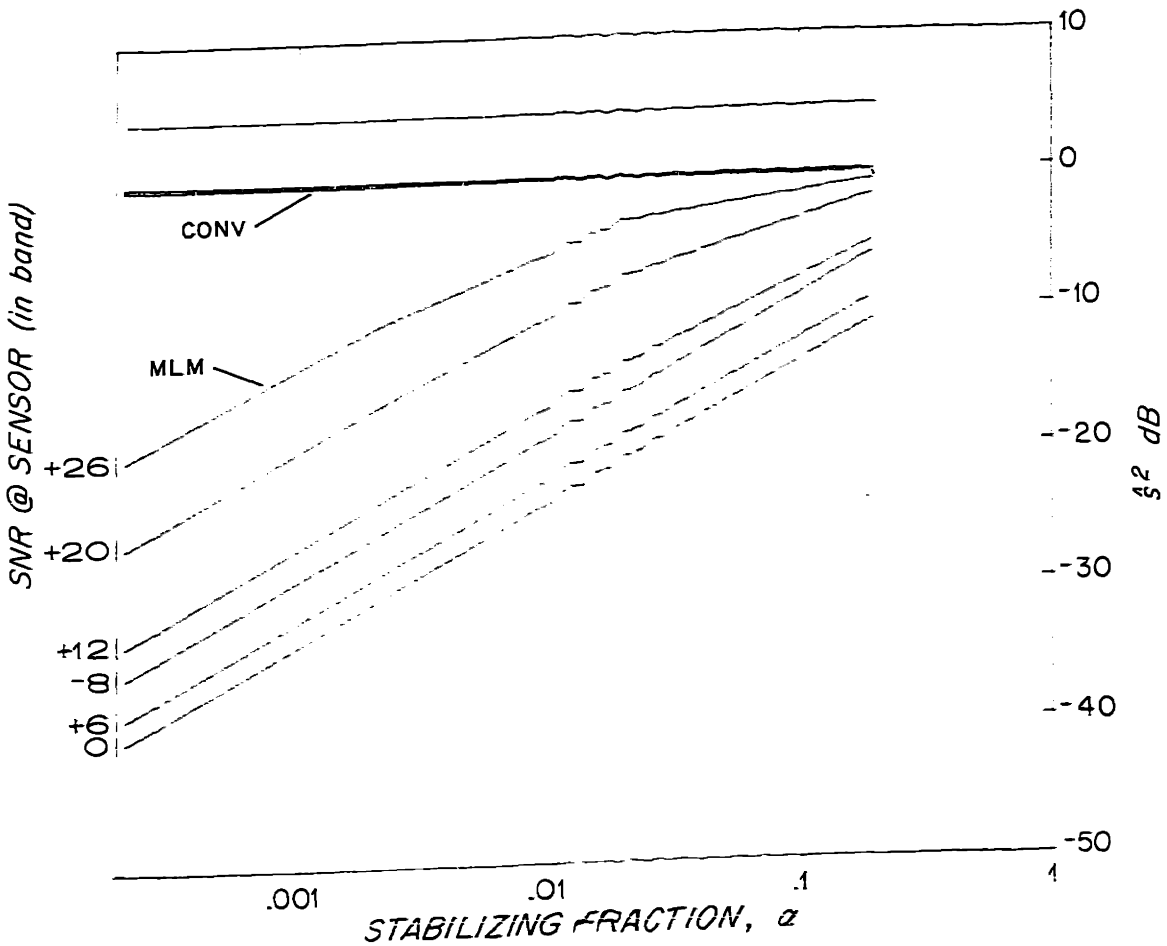

Fig. 3.11b) Measured power bias as a function of stabilizing fraction, α, and in-band sensor signal to noise ratio from Monte Carlo simulation. The 10 element uniform array of fig. 3.9 was used for the simulation.

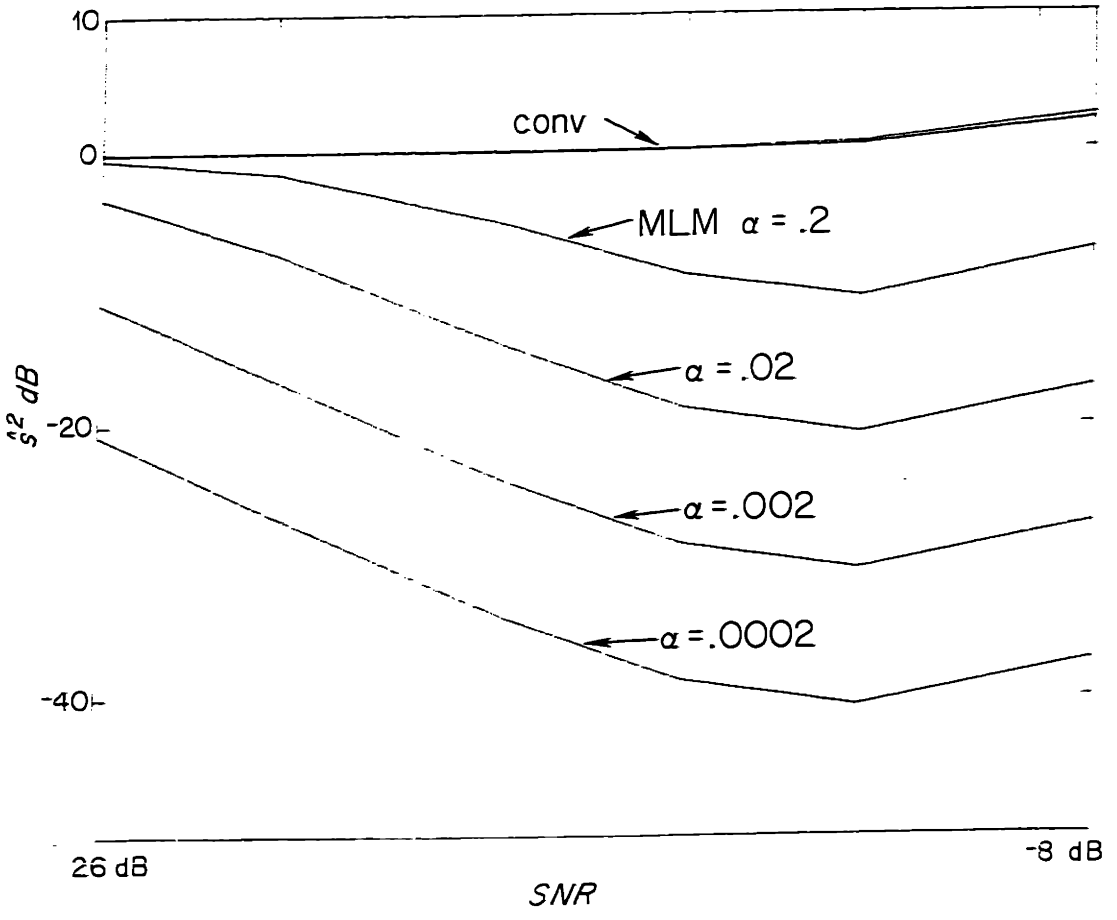

Fig. 3.11c) Predicted power bias as a function of stabilizing fraction, α, and in-band sensor signal to noise ratio. This is the same data as in figure 3.11a just parameterized by the stabilizing fraction, α, instead of the SNR.

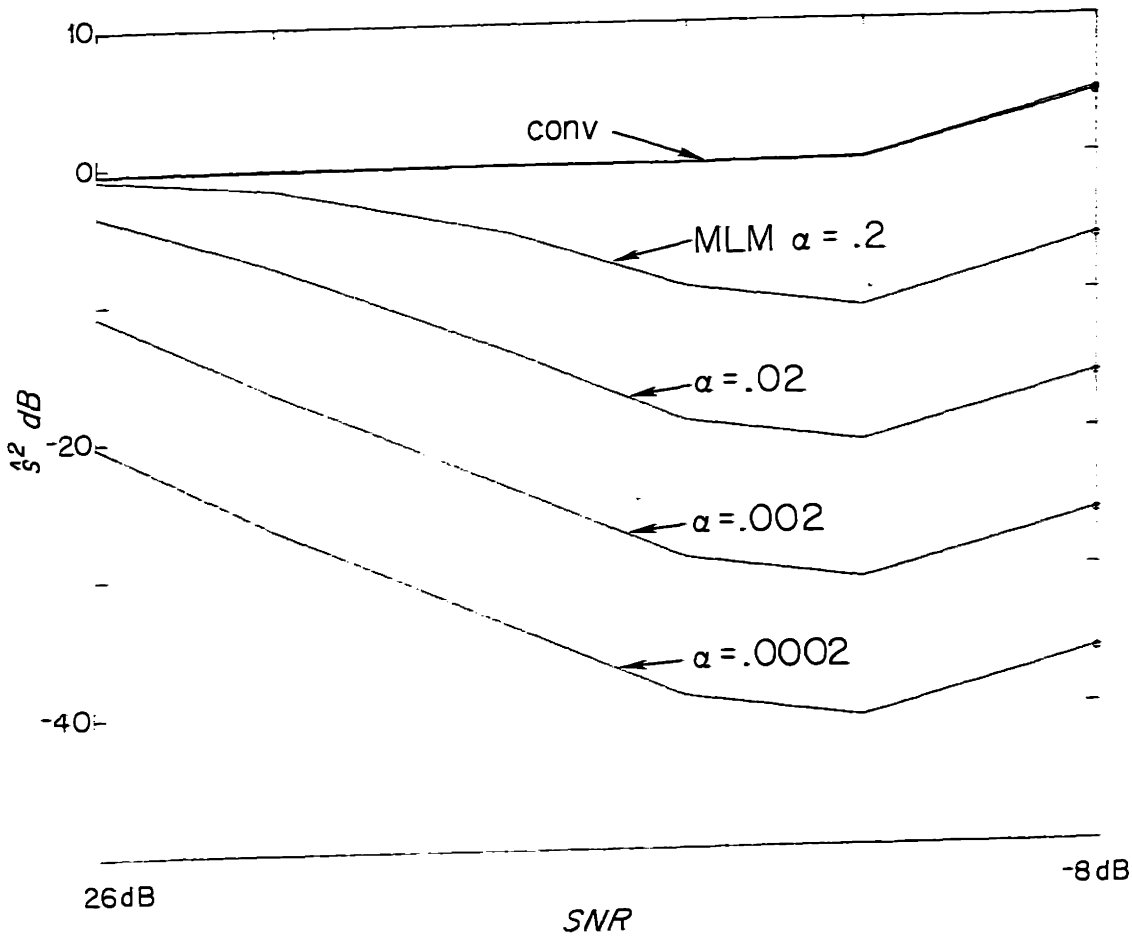

Fig. 3.11d) Measured power bias as a function of stabilizing fraction, α, and in-band sensor signal to noise ratio from Monte Carlo simulation. This is the same data as in figure 3.11b just parameterized by the stabilizing fraction, α, instead of the SNR.

TABLE 3.4

wave #	arrival time (sec)	phase vel (km/sec)	(dB) level in band around 15 Hz	biased predicted level (dB)	biased observed level (dB)	corrected level (dB)
1	1	1.5	2	-26.7	-25.3	2.9
2	2	6	8	-16.2	-18.3	6.8

The output of the MLM velocity spectral processor is shown in Figure 3.12. The predicted and measured biased power values for the peaks are given in Table 3.4. To correct the plot, first the noise level must be estimated. Using relation 3.58a, we see that the noise level can be computed from a signal-free region of the velocity spectrum by:

$$\sigma^2 \approx \frac{N}{\alpha}\hat{S}^2_{MLM} \qquad 3.59a$$

$$\sigma^2 \approx \frac{N}{\alpha}10^{(\hat{S}^2_{MLM}(dB)/10)} \qquad 3.59b$$

The average value of the background is $\hat{S}^2_{MLM}(dB) = -40$ dB on the first time slice out of the estimate in Figure 3.12. This leads to an estimated σ of .7071 (versus .631 and -41 dB in reality). To correct the plot, at each time slice the peak in slowness is picked and assumed to be due to a signal. The unbiased signal power corresponding to this measured power, $\hat{S}^2_{MLM}$, $N=10$, $\alpha=.002$, and $\sigma=.631$ is then found by a table lookup for a^2 as a function of $\hat{S}^2_{MLM}$ using a table calculated from equation 3.56a with true amplitude, a, varied over the required range of values. Once the true a is found, the MLM array response is calculated for all other values of p_0 using 3.51b with p_1 taking the peak location using $\epsilon=\sigma=.631$, and a^2 = power obtained from the table lookup. This procedure essentially calculates the MLM estimate as if an ensemble covariance matrix was available. (The uncorrelated noise, σ^2, has been removed from the off diagonal elements and placed strictly on the diagonal, as it would be in the infinite average case.) The results of this "correction" or bias removal are shown in Figure 3.13,

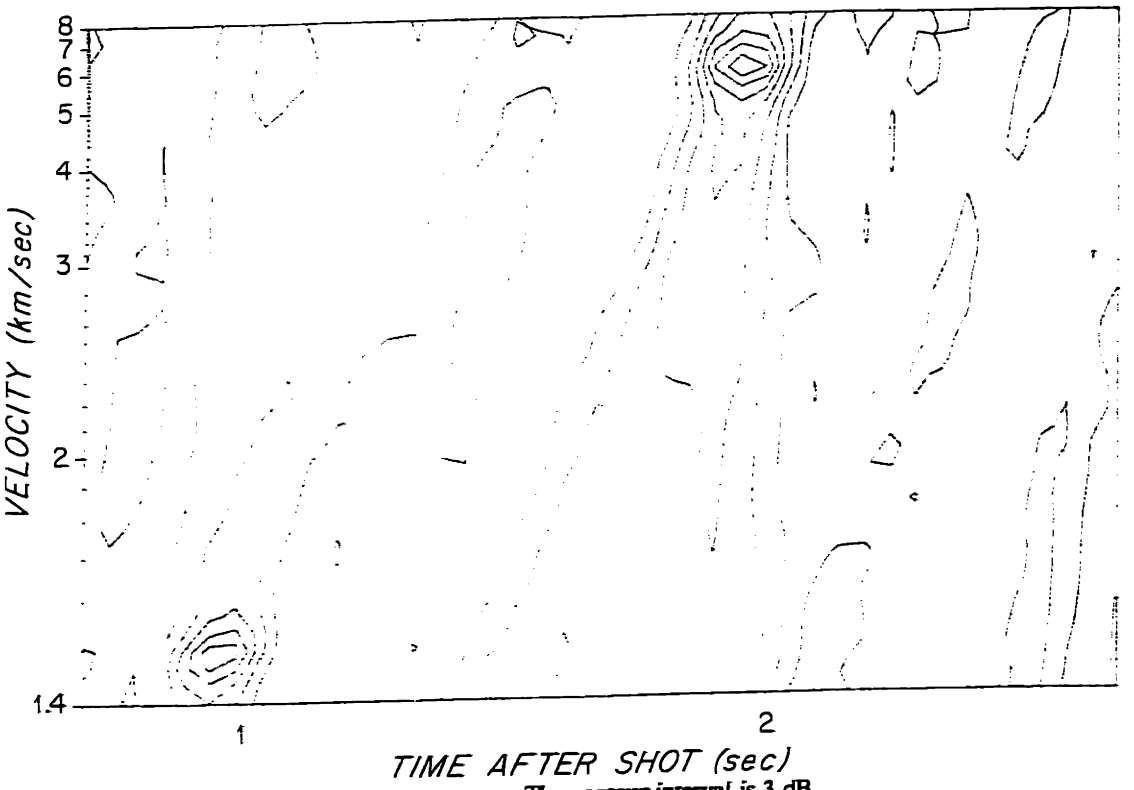

Fig. 3.12) Biased MLM velocity spectrum. The contour interval is 3 dB.

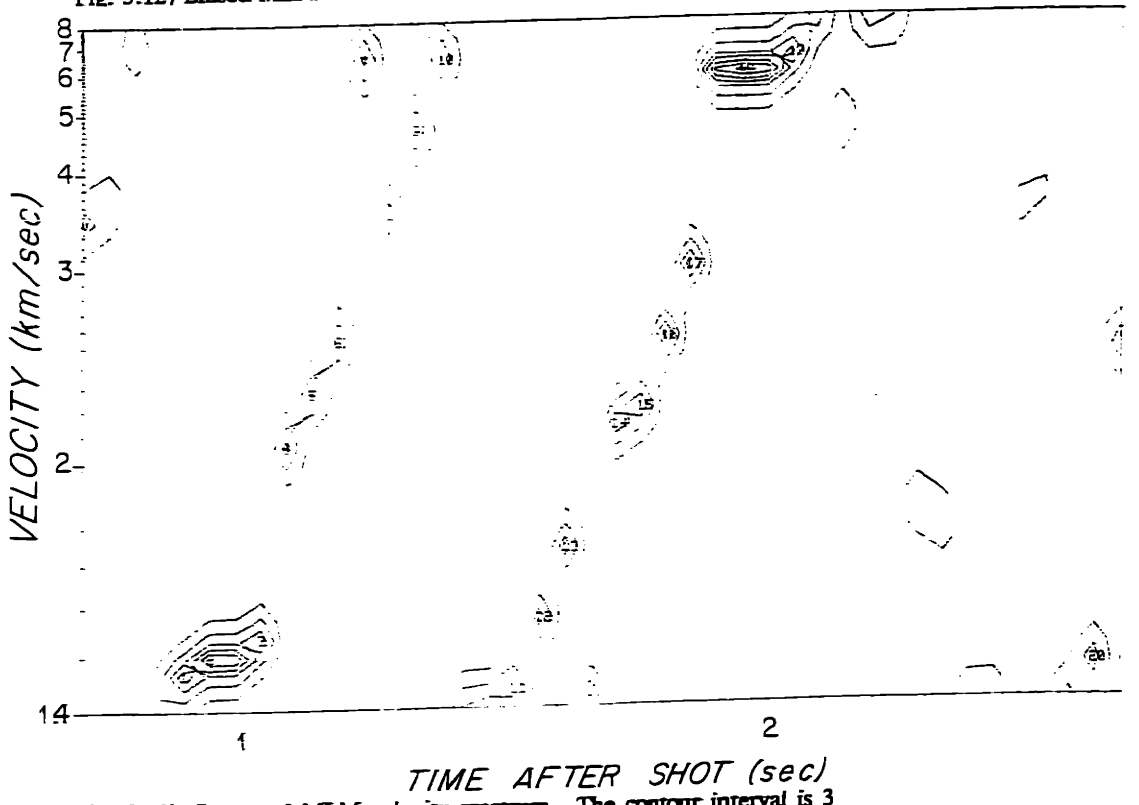

Fig. 3.13) Corrected MLM velocity spectrum. The contour interval is 3 dB.

and the corrected peak values tabulated in Table 3.4. The plot generally has the correct background level of $\sigma^2/10 \Rightarrow -13$ dB (1 dB off from the -14 dB correct value, see eqn. 3.51b with $B_{01}=0$). and the corrected peaks are about 1 dB from their proper values. The only problem with the use of this method is that because of the arbitrary choice of the largest value at any time step as signal, spurious peaks are generated due to sidelobes and random noise variability of the background. These can be seen in Figure 3.13 but are not too obtrusive at these reasonable sensor signal to noise ratios. This does not, however, diminish the utility of correcting the peaks themselves, which can be picked by 2-D gradient calculations and thresholding on the original velocity spectrum, 3.12. and then "de-biased" individually.

The Velocity Spectral Analysis Algorithm- Explicit Details

To summarize the velocity spectral analysis procedure it will be presented with its full regalia of indices and variables using data sampled in space and time.

Step 0: Set up region of estimate and parameters

i) Fix T, $w_s(\tau)$, N channels

ii) Choose τ, ω, p_0 for estimate; these must be scanned over space of interest

Step 1: Short-time Fourier transform move-out and offset corrected and windowed data

$$\mathbf{d}(\tau,\omega_k,p_0) = \begin{bmatrix} \cdot \\ \cdot \\ \cdot \\ \mathrm{d}(\tau,\omega_k,p_0,r_j) \\ \cdot \\ \cdot \\ \cdot \end{bmatrix} \qquad 3.60a$$

where

$$\mathbf{d}(\tau,\omega_k,p_0,r_j) = r_j^{\frac{1}{2}} e^{i\omega_k(p_0 r_j - \tau + n_0\Delta t)} \sum_{n=n_0}^{n_0+N_T-1} w_s(n\Delta t - T/2) P(n\Delta t, r_j) e^{i\omega_k n\Delta t} \qquad 3.60b$$

$$n_0 = \left[\frac{\tau - p_0 r_j}{\Delta t}\right]^- \qquad N_T = \left[\frac{T}{\Delta t}\right]^- \qquad [\ ]^- \equiv \text{floor function} \qquad 3.60c$$

The sum may be carried out by the FFT algorithm for all frequencies simultaneously after padding the data with zero to make the transformed sequence length a power of 2 N_2. The window is maintained at length T, the frequency coefficient for ω_k will be $k = \omega_k N_2 \Delta t/2\pi$. The index k on ω is used because in practice the exact ω samples are not chosen, but set by the FFT length, N_2 and sampling interval, Δt. The phase correction term $e^{i\omega p_0 r_j}$ restores the phase to the data removed by the window shift of $p_0 r_j$. The $e^{-i\omega(\tau - n_0\Delta t)}$ corrects for the timing error due to discrete time sampling, and is equivalent to, but easier to implement, than the bandlimited interpolation of the time series needed for time domain slant stacking.* The $r_j^{\frac{1}{2}}$ compensates for the cylindrical spreading of the layered medium.

Step 2: Form covariance matrix with optional bandwidth average

$$\hat{\mathbf{R}}(\tau,\omega_k,p_0) = \sum_{\omega_i=\omega_k-B/2}^{\omega_k+B/2} \mathbf{d}(\tau,\omega_i,p_0)\mathbf{d}^H(\tau,\omega_i,p_0) \qquad 3.60d$$

Note that no re-normalization by the bandwidths has been done in this or the previous step; the final output power will therefore be expressed as the power in the processor band, not per Hertz.

Step 3: Add stabilizing noise term and do optional normalization.

*Usually linear interpolation is adequate.

i) optional normalization:

$$P_{ave}(\tau,\omega_k,p_0) = \left[\prod_{j=0}^{N} \hat{R}_{jj}(\tau,\omega_k,p_0,r_j)\right]^{1/N} \quad 3.60e$$

$$\hat{R}(\tau,\omega_k,p_0) - P_{ave}(\tau,\omega_k,p_0)\left[\frac{\hat{R}_{ij}}{(\hat{R}_{ii}\hat{R}_{jj})^{\frac{1}{2}}}\right] \quad 3.60f$$

ii) add stabilizing fraction

$$\hat{R}(\tau,\omega_k,p_0) - \hat{R}(\tau,\omega_k,p_0) + \frac{d^H(\tau,\omega_k,p_0)d(\tau,\omega_k,p_0)}{\gamma-1} I \quad 3.60g$$

where γ is the desired condition number.

Step 4: Beamforming: (phase scanning over an interval around p_0 can be done)

Conventional method:

$$\hat{S}^2_{CONV}(\tau,\omega_k,p\,p_0) = \frac{1}{N} e^H(\omega_k,p)\hat{R}(\tau,\omega_k,p_0)e(\omega_k,p) \quad 3.60h$$

MLM:

$$\hat{S}^2_{MLM}(\tau,\omega_k,p\,p_0) = \frac{1}{e^H(\omega_k,p)\hat{R}^{-1}(\tau,\omega_k,p_0)e(\omega_k,p)} \quad 3.60i$$

where**

$$e(\omega_k,p) = \begin{bmatrix} \cdot \\ \cdot \\ \cdot \\ e^{i\omega_k p r_j} \\ \cdot \\ \cdot \\ \cdot \end{bmatrix} \quad 3.60j$$

is the steering vector. The slowness, p, is in some small interval around p_0. (The range and reason will be discussed later.)

**For a 2-D array the radii, r_j, from the source to each sensor must be determined from their surface x-y components.

Computational Tricks

A few tricks can be used to cut computation time:

[1] If the $\hat{\mathbf{R}}$ matrix is not to be normalized, then the Woodbury identity can be used to calculate the inverse in $O(n^2)$ operations instead of $O(n^3)$ via a general Gaussian elimination inversion. This identity is:

$$[\mathbf{x}\mathbf{x}^H + \sigma^2\mathbf{I}]^{-1} = \frac{1}{\sigma^2}\left[\mathbf{I} - \frac{\mathbf{x}\mathbf{x}^H}{\sigma^2 + \mathbf{x}^H\mathbf{x}}\right] \qquad 3.61a$$

or more generally (needed for update in bandwidth average):

$$[\mathbf{A} + \mathbf{BDC}]^{-1} = \mathbf{A}^{-1} - \mathbf{A}^{-1}\mathbf{B}[\mathbf{D}^{-1} + \mathbf{CA}^{-1}\mathbf{B}]^{-1}\mathbf{CA}^{-1}. \qquad 3.61b$$

[2] The covariance matrix does not need to be recomputed (and inverted) for each output slowness--thus saving lots of FFT's and the associated averaging and covariance formation. For practical window lengths, the covariance matrix $\hat{\mathbf{R}}(\tau,\omega_k,p_0)$ is valid for a slowness region around p_0. Later simulations examples will show the effects of this time steer (p_0 scan) versus phase steer (p scan) tradeoff.

[3] For repetitive computation, the most efficient way to evaluate the plane steer (equivalent to equation 3.40) is to store the steering vectors $\mathbf{e}(\omega_k,p)$. However, if uniform slowness increments are used, a set of phase steering vectors:

$$\begin{aligned} &\{\, \mathbf{e}(\omega_k,(m-n_p/2)\delta p)\,\} \qquad m=0,1,\ldots,n_p-1 \quad n_p \text{ even} \\ &\{\, \mathbf{e}(\omega_k,(m-(n_p-1)/2)\delta p)\,\} \qquad m=0,1,\ldots,n_p-1 \quad n_p \text{ odd} \end{aligned} \qquad 3.62a$$

can be used, where:

$$\begin{aligned} \Delta p &= \text{difference between adjacent time steers, or moveout corrections, } p_0 \\ \delta p &= \frac{\Delta p}{n_p} = \text{phase steering slowness increment} \end{aligned} \qquad 3.62b$$

when the move-out phase restoration term in $e^{i\omega p_0 r_i}$ is eliminated from equation 3.54b. Thus only n_p phase steering vectors must be stored for each frequency to scan over $\pm\frac{n_p-1}{2}\delta p$ around p_0. What this effectively does is create a broadside array for each slowness, p_0, and phase steer incrementally around it.

Estimation Statistics of the Velocity Spectral Analysis Algorithm

An obvious bound on Δp, the slowness time steering increment, is the value that would move the start time of the analysis window one window length, T, at the extreme end of the array. If Δp were larger than this, all the data would not be used. A more conservative bound and one that considers the use of the tapering function, $w_s(\tau)$, would be the Δp that moves the window start time by $\zeta<T$. This value is clearly

$$\Delta p = \frac{\zeta}{L} \qquad 3.63$$

In this section we quantify the performance of the velocity spectral analysis algorithm described in the previous section in terms of its power, time, and slowness estimation performance on noisy data. In particular, we examine the effects of the trade-off between time steers and phase steers.

To quantify the performance, a Monte Carlo simulation was carried out using a single arrival of 1.5 km/s ($.\bar{6}$ s/km) in varying levels of uncorrelated sensor noise. Three frequency bands were used corresponding to adjacent Fourier coefficients for a 64 point FFT on .25 seconds of data with a sampling interval of $\Delta t = .004$sec. No frequency averaging was done in the spectral covariance estimate at the three frequencies shown in Table 3.5. This table gives the in-band signal and noise powers and signal to noise ratios for the three frequencies for the trial noise levels. All three frequencies were used to illustrate that there is little bias in the

slowness estimates due to spectral leakage with the window function used. The differing frequencies also serve to illustrate the effects of the beampattern or ambiguity function peak curvature on the performance of the slowness estimate, since the higher frequencies will give more curvature with their narrower beam-width for a fixed array length. The array used for all tests had $N=10$ elements spaced by .1 km for a total aperture of $L=.9$ km. The signal wavelet used was given by:

$$s(t) = \begin{cases} e^{-\left[\frac{\omega(t-d/2)}{\gamma}\right]^2} \cos(\omega(t-d/2)) & 0 < t < d \\ 0 & \text{elsewhere} \end{cases} \qquad 3.64$$

where:

$$\gamma = 5$$

$$f = 15$$

$$\omega = 2\pi f = 2\pi \cdot 15$$

$$d = 5\frac{\pi}{\omega} = .167 \text{ seconds}$$

and the velocity analysis processor window was given by:

$$w_s(t) = \begin{cases} \sin^2(\frac{\pi}{T}(t-T/2)) & -T/2 < t < T/2 \qquad T = .25\ sec \\ 0 & \text{elsewhere} \end{cases} \qquad 3.65$$

TABLE 3.5

σ	σ (dB) @ sensor re 1 Hz	σ_N (dB) after array re 1 Hz	σ_ω^2 noise power (dB) (in band) re 1 Hz	E_ω, in band signal energy (dB) re 1 Hz		
				f=11.7 0 dB	f=15.6 2 dB	f=19.5 -1 dB
				SNR (in band, at sensor)		
.1	-20	-30	-34	24	26	23
.2	-14	-24	-28	18	20	17
.5	-6	-16	-20	10	12	9
1	0	-10	-14	4	6	3
2	6	-4	-8	-2	0	-3
5	14	4	0	-10	-8	-11

The processing algorithm described in equations 3.60 was used without normalizing the spectral covariance matrix, and the stabilization fraction used was α=.002, corresponding to a condition number of γ=5001. The density of time of arrival scans, δt, was 0.01 secs (2.5 samples) and the search interval for the peak was adapted to the expected arrival time variance and set large enough to make an outlier probability negligible (<.01) assuming a Gaussian distribution of arrival time errors. At large signal to noise ratios the standard deviation of the arrival time, σ_τ, was less than the scanning interval, δt, and Bernoulli trials were relied upon. For computational considerations, the slowness scanning density, δp, and search intervals were also adapted to the expected slowness standard deviation, σ_p. The slowness scanning density was on the order of the expected standard deviation at high signal to noise ratios and Bernoulli statistics were again used. At extremely low signal to noise ratios the probability of outliers was allowed to reach 0.2, so the standard deviations are actually slightly larger than those computed. For sensor signal to noise ratios greater than 0 dB, however, the outlier probability was less than 0.01. For all tests, 50 trials were used for each set of parameters and the following table of error bounds and 95% confidence intervals was obtained.

TABLE 3.6

Estimate	Standard Deviation of Estimate	95% Confidence Interval
mean $\hat{M}$	$\hat{\sigma}/\sqrt{N} = \hat{\sigma}/7.07$	$\lvert m-\hat{m}\rvert < 0.287\hat{\sigma}$
variance $\hat{\sigma}^2$	$\hat{\sigma}^2\sqrt{2/N} = \hat{\sigma}^2/5$	$.7\hat{\sigma}^2 < \sigma^2 < 1.5\hat{\sigma}^2$
standard deviation $\hat{\sigma}$	$\hat{\sigma}/\sqrt{2N} = \hat{\sigma}/10$	$.84\hat{\sigma} < \sigma < 1.22\hat{\sigma}$

Sample statistics were computed for the arrival time performance, slowness estimate performance, and power output (dB) from both the conventional and MLM estimators. The tested time steer scanning intervals are tabulated below:

TABLE 3.7

Scan Density Label	Time steers in the interval 1.4-11. km/s	Time steering slowness increment, Δp, s/km	ζ at $L = .9$ km (sec)	fraction of window ζ/T, $T = .25$
"a"	125	.005	.0045	1/55
"b"	50	.0125	.0113	1/22
"c"	25	.025	.0225	1/11
"d"	10	.0623	.056	1/4.5

Figure 3.14a shows the mean values of the slowness estimate as a function of signal to noise ratio for both the MLM and conventional estimators and for all time steering densities. All three frequencies have been composited and indicate that there is no bias with frequency or signal to noise ratio within the 95% confidence interval of the estimate.* However, the oscillations of the curves show that at low SNR the estimated slownesses are slightly biased toward the direction that 15 Hz leakage into the 11 and 19 Hz bins would give- i.e. the 19 Hz estimate is generally slightly high, and the 11 Hz estimate is slightly low. Note that the number of time steers makes no difference within the error bars of the mean estimate, and the "a"-"d" curves are not labeled. In fact, the one large deviating point is for the densest scan on the conven-

*I have shown the confidence interval around the true value instead of the sample value for clarity.

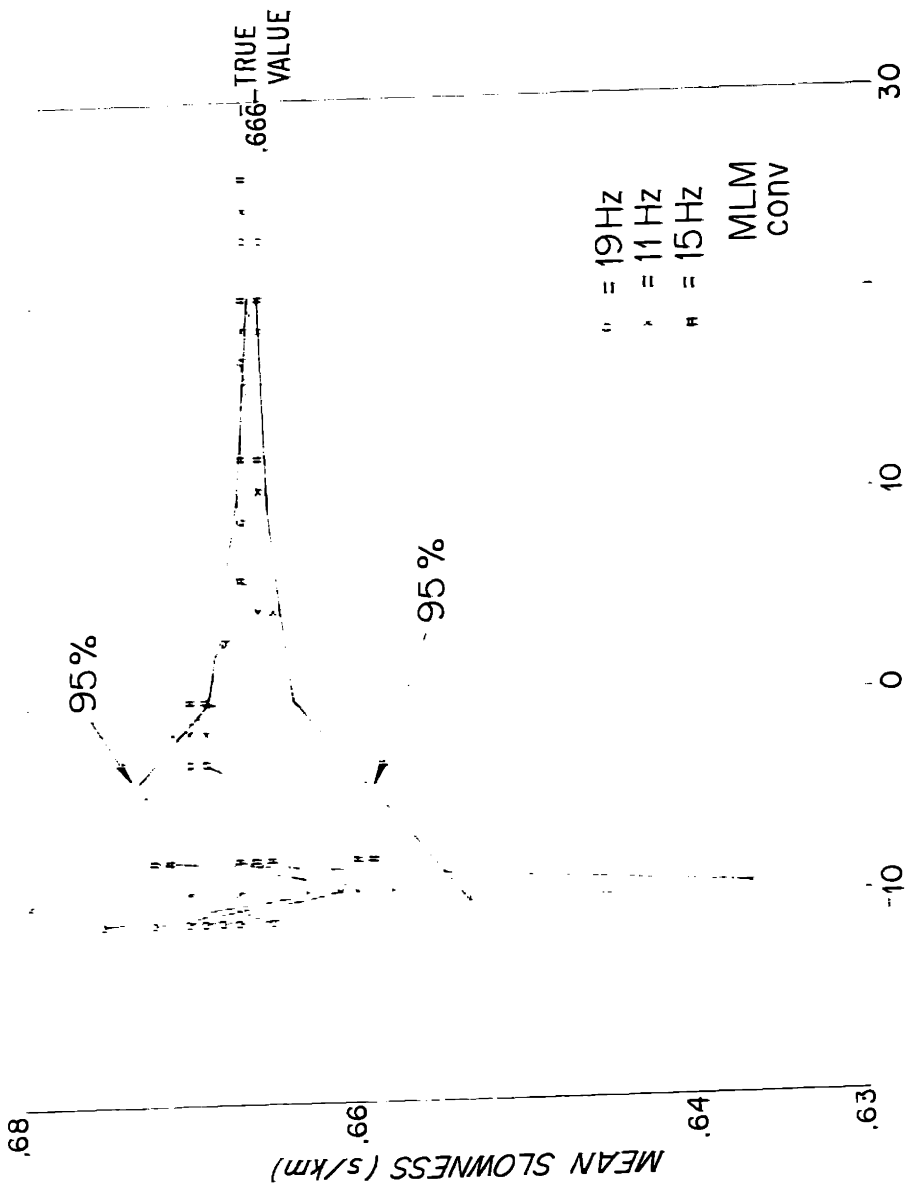

Fig. 3.14a) Mean slowness estimates as a function of sensor SNR from the Monte Carlo simulations.

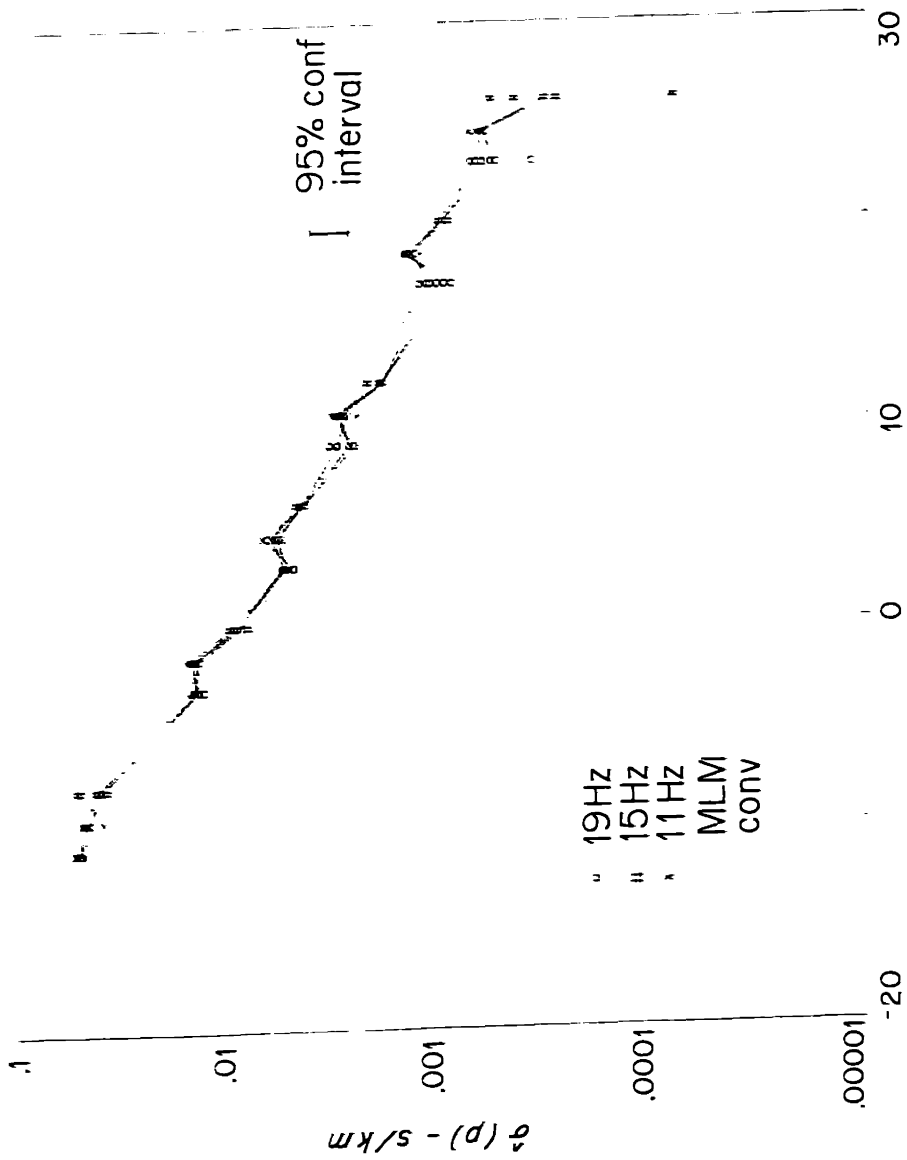

Fig. 3.14b) Slowness standard deviation estimates as a function of sensor SNR from the Monte Carlo simulations.

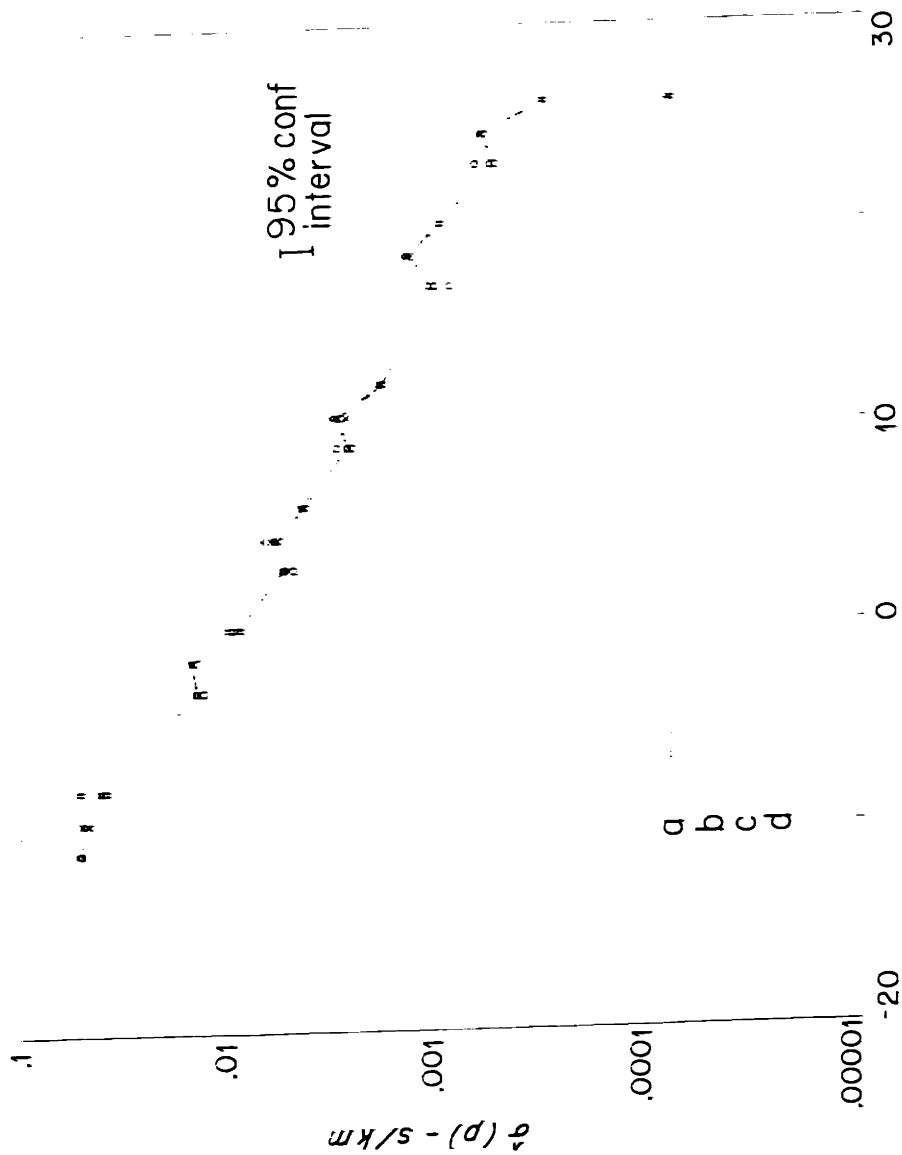

Fig. 3.14c) Slowness standard deviation estimates for the MLM processor as a function of sensor SNR from the Monte Carlo simulations. The different time-steer/phase-steer scan densities are labeled and are described in table 3.7.

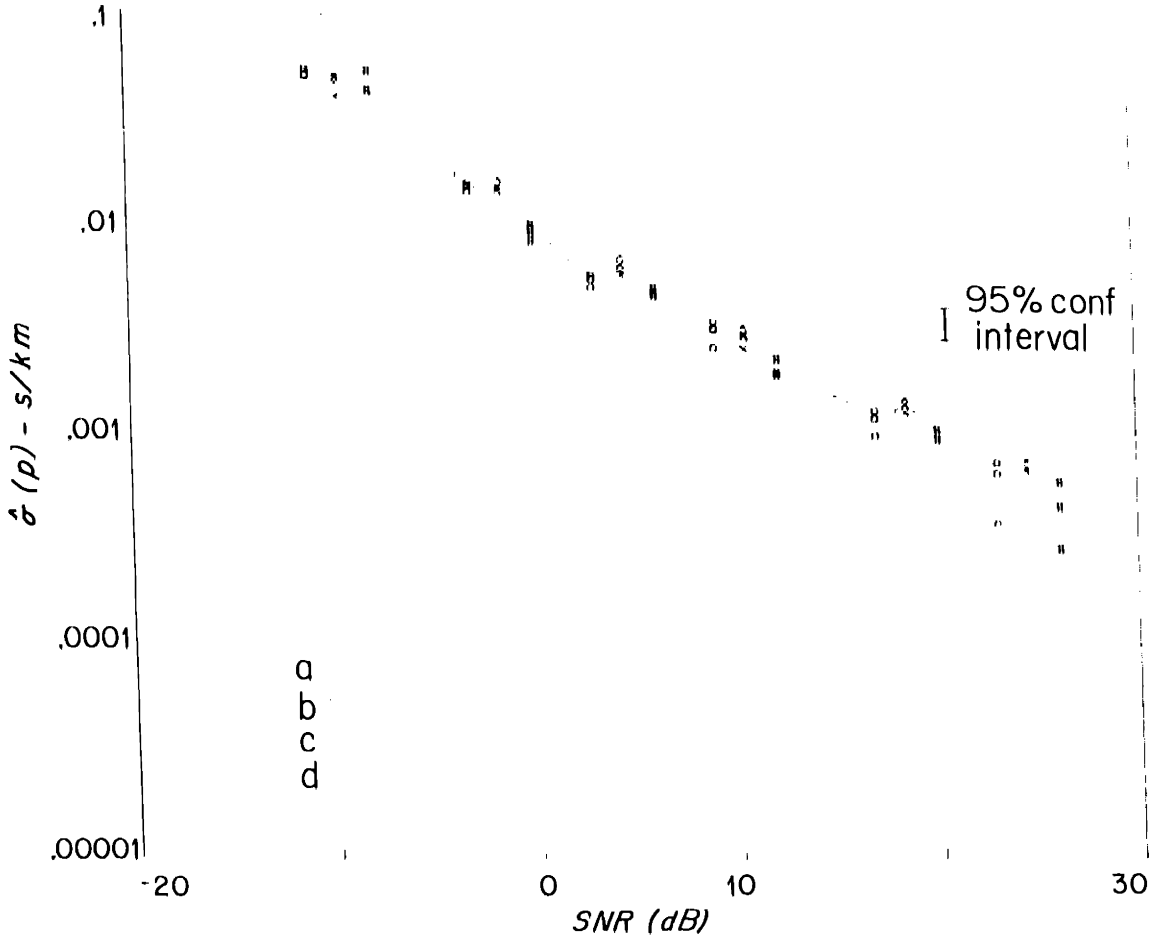

Fig. 3.14d) Slowness standard deviation estimates for the conventional processor as a function of sensor SNR from the Monte Carlo simulations. The different time-steer/phase-steer scan densities are labeled and are described in table 3.7.

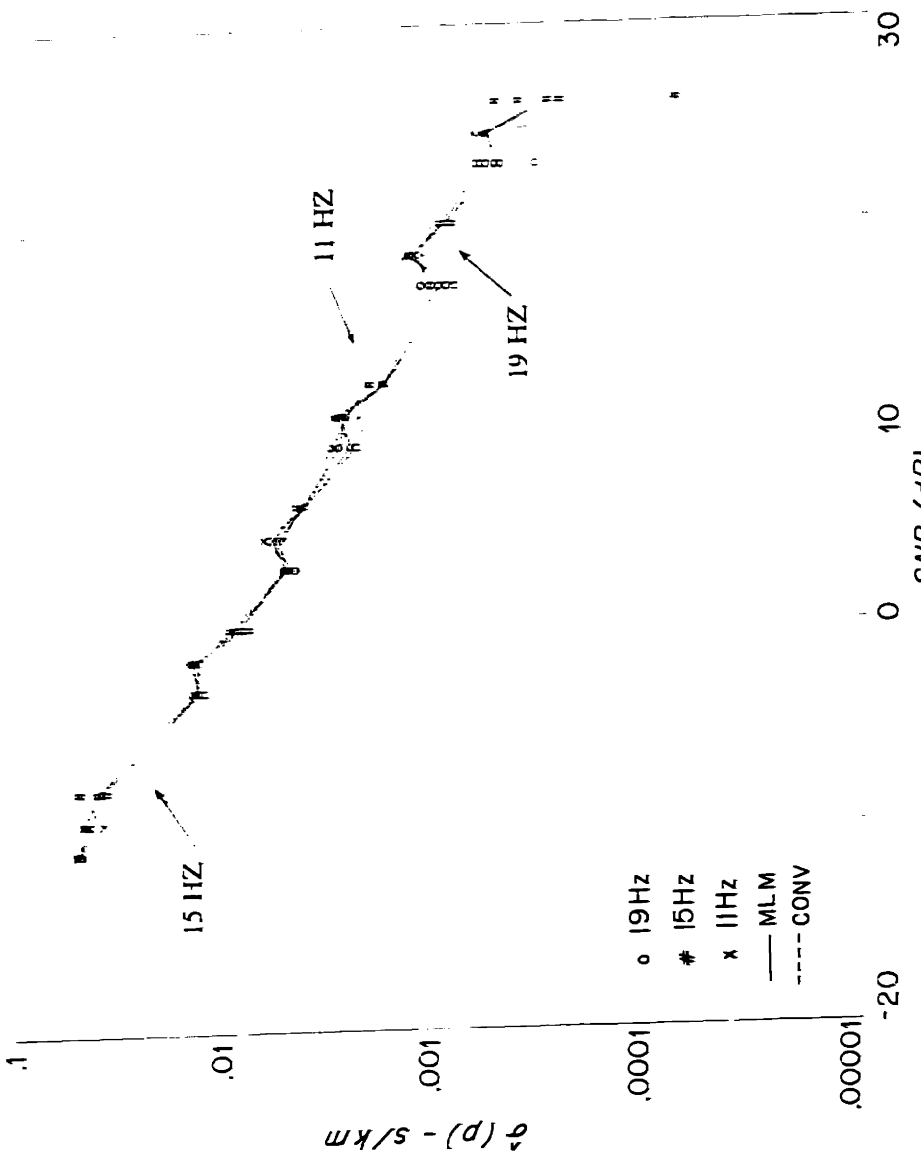

Fig. 3.14e) Predicted and measured slowness estimate standard deviation. The labeled solid lines are the theoretical predictions.

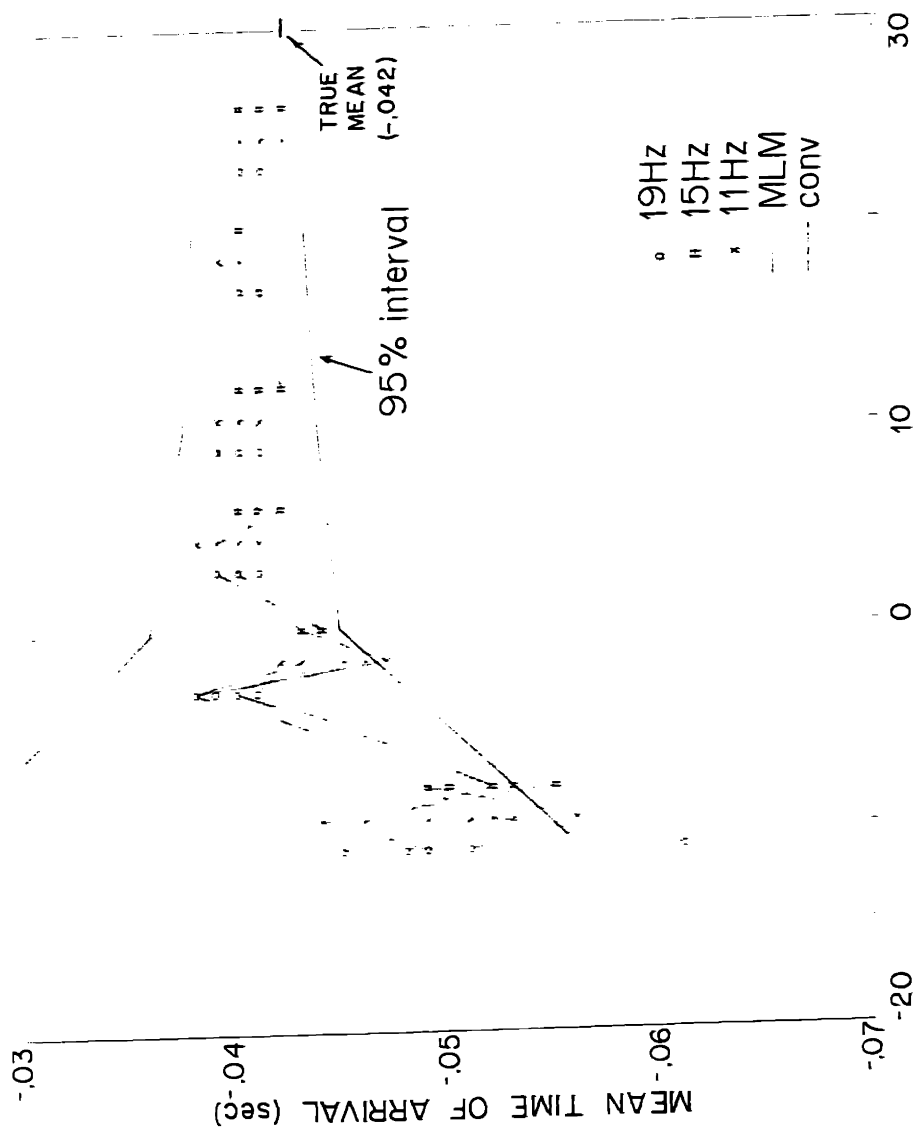

Fig. 3.14f) Mean time of arrival estimates as a function of SNR, frequency, and processor.

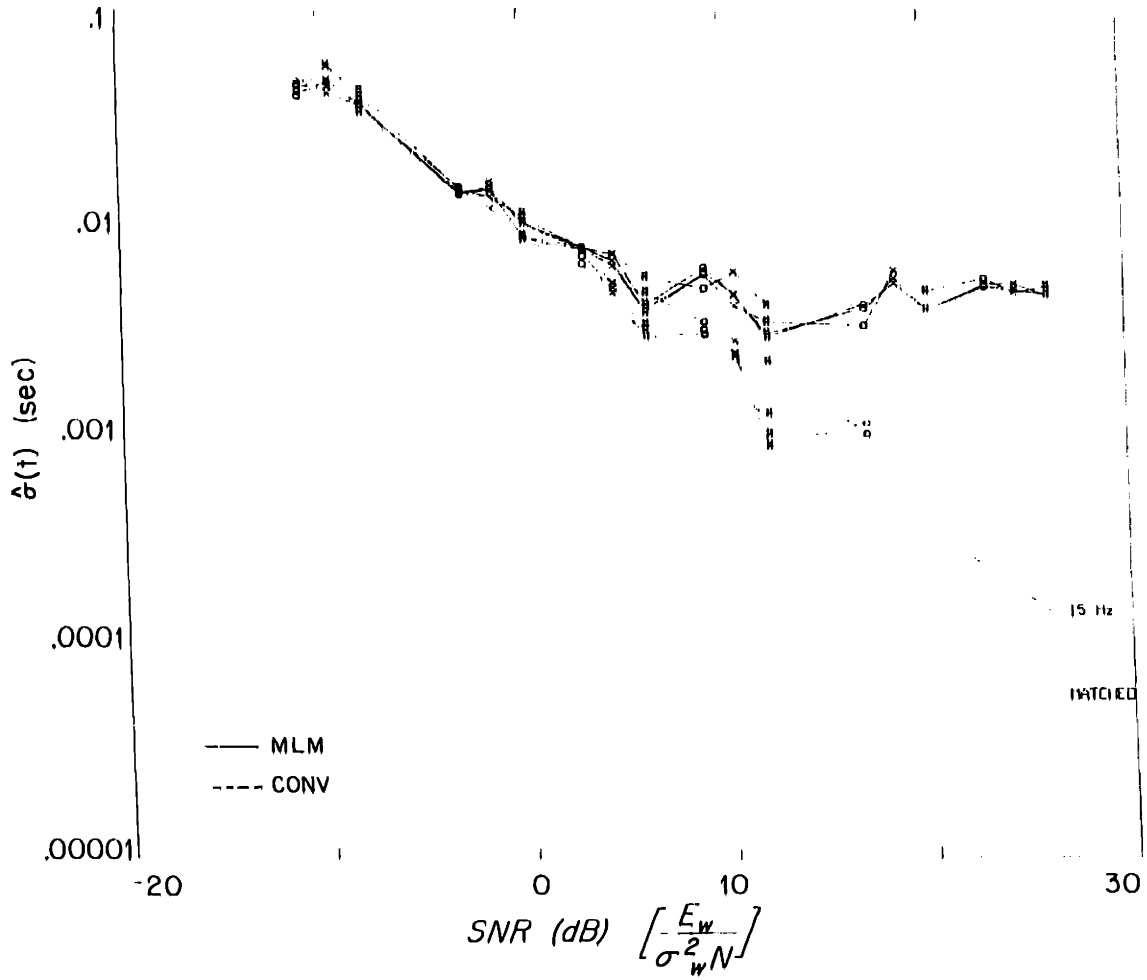

Fig. 3.14g) Comparison of predicted and measured time of arrival estimate standard deviation. The solid lines give the predicted standard deviation of the matched filter (MATCHED), and the theoretical prediction for the spectral processor derived in the text (15 Hz).

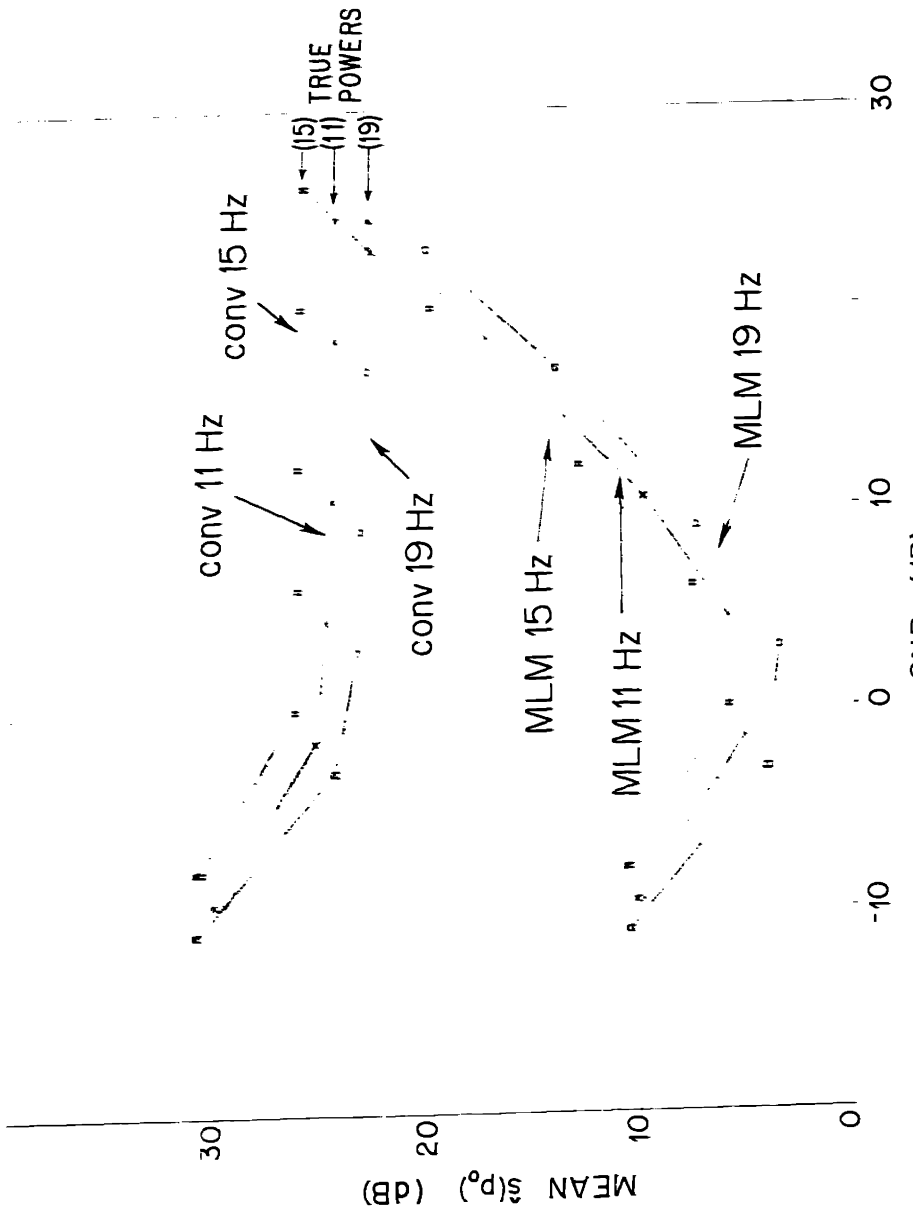

Fig. 3.14h) Mean values of conventional and MLM power estimates as a function of SNR.

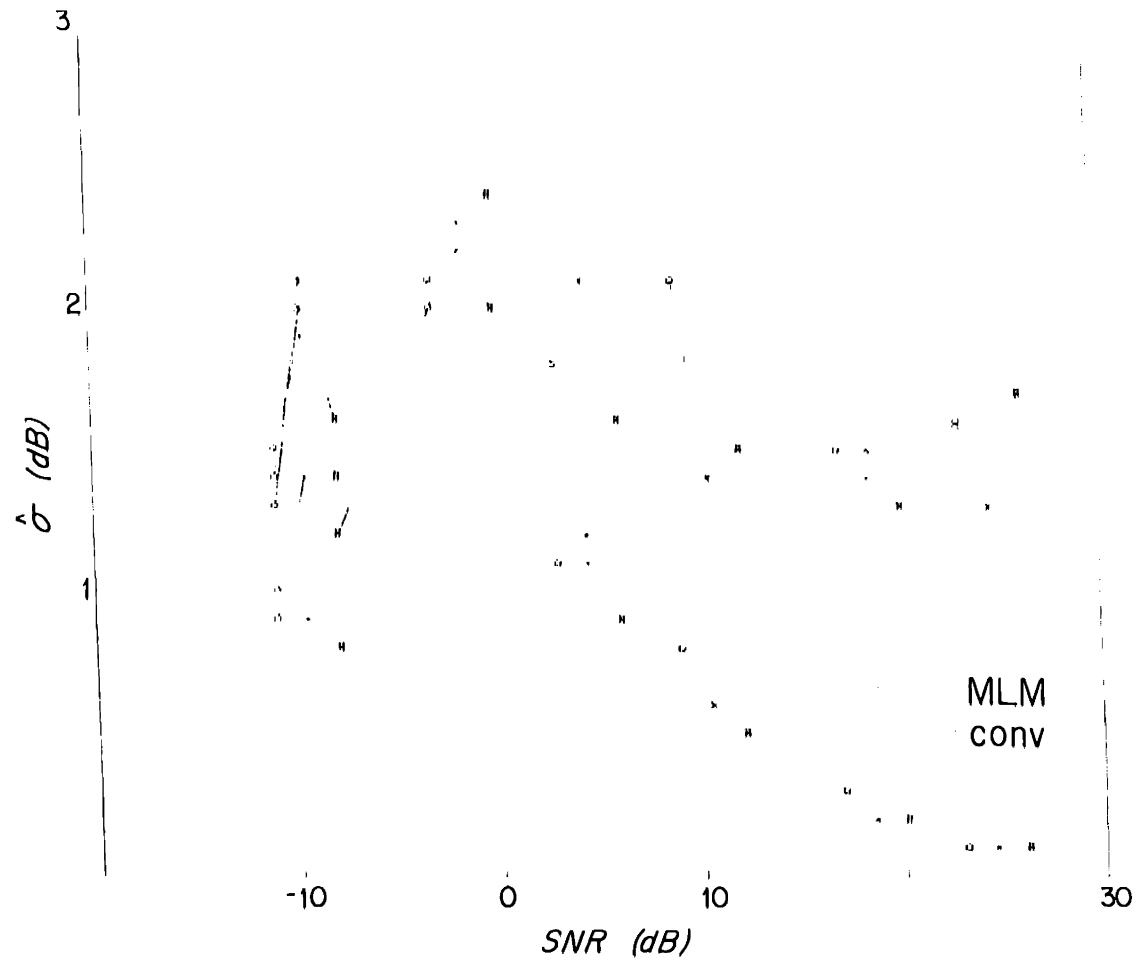

Fig. 3.14) Estimated standard deviations of conventional and MLM power estimates as a function of SNR.

tional estimate.

The estimated standard deviation of the slowness estimate as a function of SNR is given in figure 3.14b. The confidence interval length is constant in this log plot and is shown on the figure. The interesting features on this graph are the ripples which are due to the compositing of the error estimates of the three frequencies on the same plot, each with a slightly different SNR sample point (see table 3.5). The performance differences are due to the differing ambiguity function at each frequency. The 19 Hz data consistently shows the lowest standard deviation, and the 11 Hz data the highest. Within the confidence interval of the estimate, neither the MLM or conventional method appears to have better error performance. The results for the MLM processor only are shown in figure 3.14c. The different time steer densities (see table 3.7) are coded by line type and no significant difference in performance is found between them. A similar result is shown for the conventional estimator in fig. 3.14d.

To compare the estimated slowness errors with theory, we use the classical result from Steinberg [1976, p. 193]:

$$\sigma(p) = \frac{B_p}{\sqrt{2}(a^2/\sigma_N^2)^{1/2}} \qquad 3.66$$

where B_p is some measure of the beamwidth, and a^2 and σ_N^2 are the powers in the signal and noise in the bandwidth of the processor at the output of the beamformer, $\sigma_N^2 = \frac{\sigma^2}{N}$. This is completely analogous to the time domain result in eqn. 3.31 where the aperture weighting function, $w_L(r)$ is substituted for the spectrum, $S(\omega)$, and $B_p = 1/\beta$. For the single signal in uncorrelated sensor noise case both the MLM and conventional beampattern are given by:

$$W_L(\omega(p-p_0)) = \frac{\sin(\omega(p-p_0)L/2)}{\omega(p-p_0)L/2}$$

when looking at the slowness of the signal, p_0. Thus the aperture weighting function, $w_L(r)$, is the constant $1/L$. Using the duality between $t \Longleftrightarrow f$ and $p \Longleftrightarrow r/f$ yields

$$\beta = \frac{\pi f L}{\sqrt{3}} \qquad\qquad B_p = \frac{\sqrt{3}}{\pi f L}.$$

Thus, the predicted $\sigma(p)$ function is:

$$\sigma(p) = \frac{1}{1.81 f L \sqrt{2N}\,[a^2/\sigma^2]^{1/2}} \qquad 3.67$$

since $\sigma_N^2 = \sigma^2/N$ results from the array gain of the N channel array. The predictions are compared to the simulation results in fig. 3.14e. The simulation data curves are the same as those in fig. 3.14b, and the straight solid lines are the predictions of eqn. 3.67. Note that the simulation error is starting to become worse than the predicted value for beamformer output signal to noise ratios below -5 dB. This is due to the failure of the prediction when global errors start to be made, and not just perturbations on the main lobe of the ambiguity function.

The mean arrival time from the simulations is graphed in fig. 3.14f as a function of sensor signal to noise ratio. Although the 95% confidence intervals (which again have been placed around the true mean, not the sample mean) embrace the true mean, there is apparently a bias toward underestimation of the time of arrival as the signal to noise ratio gets small. There is no significant bias due to frequency or time steering density. The true mean arrival time is -.042 seconds because the time of arrival estimate is taken as the window start time. For a symmetric wavelet, $s(t)$, with a peak energy arrival at $d/2 = .083$ seconds, and a symmetric, center weighted window, $w_s(t)$, of length $t = .25$ seconds, the arrival time bias, b_s, (see eqn. 3.32a) should be:

$$b_s = \frac{d}{2} - \frac{T}{2} = -.042 \text{ seconds.}$$

The standard deviation of the arrival time estimator is given in fig. 3.14g for both the MLM and conventional estimators. No vast differences are observed due to center frequency of time steering density. There does, however, appear to be a difference between the MLM and conventional estimators. The errors for the conventional estimator continued to decrease as the signal to noise ratio increased. The results from the MLM processor plateaued at the simulation output time of arrival scanning density of δt = .01 sec. The sample size of 50 did not allow the Bernoulli statistics to be used for the conventional estimate above a signal to noise ratio of 17 dB using this δt value. It is unclear whether the error of the time estimate of the MLM processor would also have continued decreasing, and the plateau is, in fact, an artifact of the simulation. To determine this, a more accurate simulation must be carried out. The predicted error performance using equations 3.31 and 3.36 is shown by the straight lines in figure 3.14g. The matched filter of eqn. 3.31 had E=18, β=20, and N=10. The noise levels are given in table 3.5. The spectral processor for center frequency $\omega=2\pi\cdot15.6$ is predicted by equations 3.36. Using the parameters for this simulation yields the E_ω and σ_ω figures in table 3.5. The spectral window diminished the sensor noise by about 4 dB, and the array gain diminished it another 10 dB. The rms bandwidth was calculated to be β_ω=22, or 3.5 Hz. The curve marked 15 Hz shows that this prediction matches the observed 15 Hz data very well.

Figure 3.14h shows the mean power estimate from the MLM and conventional processors. As discussed before, the MLM output is highly biased, however, neither processor shows any change in mean output power as a function of time steering density over the range tested (the curves are virtually on top of one another). The standard deviation of the (dB) power levels out of the processors is shown in figure 3.14i. The processors are virtually identical for low signal to noise ratios, with the conventional processor being slightly better at high SNR.

EXAMPLES OF VELOCITY SPECTRA

In previous sections of this chapter a velocity spectral analysis algorithm has been motivated, developed, and analysed. In this section, example velocity spectra on a real data set will be compared using different parameters and methods. This will serve to illustrate some of the phenomena described in earlier sections, and to justify the choices of parameters chosen for the data analysis of chapter 5.

The data used for these examples are 22 hydrophone channels from a 25 kg TNT refraction shot. The explosive was detonated at a depth of 243 m and at a range of 19.4 km (Fram 2, reel 3044) from the receiving array, which was the 800 by 800 m cross shown in figure 3.16 with sensors deployed at 93 meters. For these parameters, the bubble pulse and dominant frequency of the source is 15.5 Hz. The figures to be discussed and their important parameters are summarized in table 3.8. This table is organized in order of performance, with the best performance at the top and to the left. The parameters used are defined as:

T	processing window duration
N_T	number of sample points in a window of length T
δt	processing window advance (output sample interval)
N_t	number of time steers (move-out corrections) in the total slowness scanning interval, equally spaced in slowness
N_p	number of slowness phase steers between time steers, equally spaced in slowness
N_r	number of channels
f_0	center frequency of processing
BW	bandwidth over which frequency averaging was done (independent of window smearing) in Hz

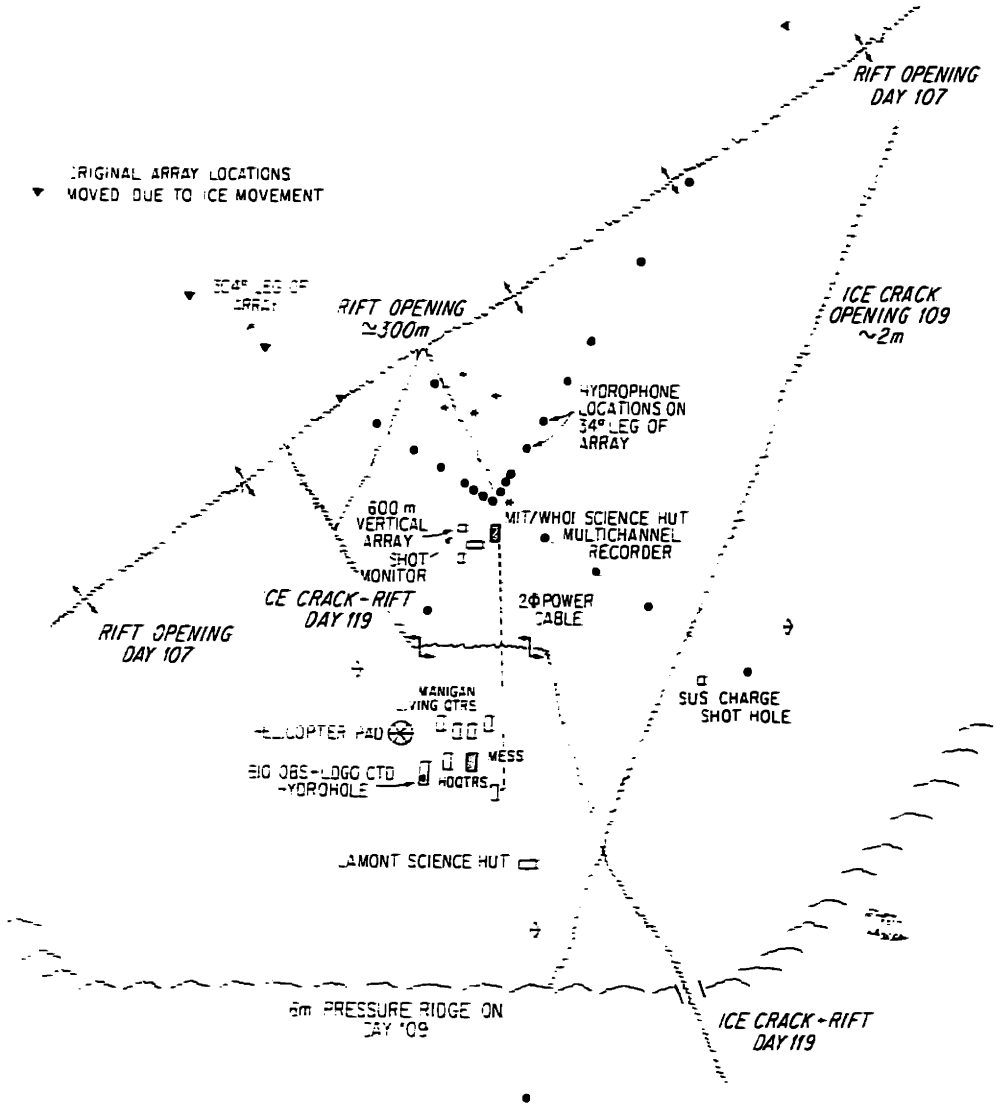

Fig. 3.16) Camp plan and array layout for ice station Fram 2.

ave number of Fourier transform coefficients averaged to make *BW*

TABLE 3.8

T	δt	N_t-N_p	f_0	*BW/ave*	MLM Fig 3.15	TIME Fig 3.15	CONV Fig 3.15
.25	.05	60-2	12	4/1	a	d*	f
.25	.05	25-5	12	4/1	b	e*	
.25	.05	12-10	12	4/1	c		
.5	.1	60-2	12	4/2	g		
.5	.1	25-5	12	4/2	h		j
.5	.1	12-10	12	4/2	i		k
1.	.1	60-2	12	4/4	l		
1.	.1	25-5	12	4/4			
1.	.1	12-10	12	4/4	m		

The data were sampled at .004 seconds, and the Fourier transforms were done by the shortest power of 2 length FFT possible. All data were windowed with a $\sin^2(\pi(t-T/2)/T)$ window, even for the time domain processing. This processing was done by the average stack and semblance measures on data that had been pre-filtered to 6-30 Hz. The average stack and semblance processors were defined by [Neidell and Taner, 1971]:

Average Stack:

$$S_{stk}(\tau_0,p_0) = \frac{1}{N_T}\sum_{i=1}^{N_T} w_T(i)\,\frac{1}{N_r}\left[\sum_{j=1}^{N_r} P(i\Delta t-\tau_0-p_0 r_j, r_j)\right]^2$$

*Plot "e" is the time domain averaged stack, and plot "d" is the average semblance. For both of these, $N_t=125$, $N_p=1$.

Average Semblance:

$$S_{sem}(\tau_0,p_0) = \frac{S_{stk}(\tau_0,p_0)}{\frac{N_r}{N_T}\sum_{i=1}^{N_T} w_T(i)\left[\frac{1}{N_r}\sum_{j=1}^{N_r} P^2(i\Delta t+\tau_0-p_0 r_j, r_j)\right]}$$

$$= \frac{\sum_{i=1}^{N_T} w_T(i)\left[\sum_{j=1}^{N_r} P(i\Delta t+\tau_0+p_0 r_j, r_j)\right]^2}{N_r \sum_{i=1}^{N_T} w_T(i)\sum_{j=1}^{N_r} P^2(i\Delta t+\tau_0-p_0 r_j, r_j)}$$

The MLM and average stack plots have been plotted with 3 dB power contours over a 70 dB dynamic range from the largest power on the plot. The semblance was plotted from .2 to 1.0 in increments of .05, and the conventional processing plots span a 90 dB interval in 3 dB increments downward from the peak. For the rest of this section I will refer to the figures as a,b,c,... and suppress the reference to fig. 3.15.

Figure a shows that with a short .25 sec window, individual arrivals are well resolved in both phase velocity and arrival time. The monotonic sidelobe structure of the MLM processor gives the smooth vertical tails for this zero-offset processing. The corresponding fan-shaped artifacts shown in figure 3.2b become more linear because of the bias of the MLM algorithm. For much of the "fan" only a few sensors have windows containing the arrival, and the output is further diminished by the MLM bias properties. Figure b shows the same data processed with a less dense time steer density. (See tables 3.8 and 3.7) The visible differences between this and the previous plot are minimal, supporting the performance similarities observed on the Monte Carlo simulations. Even at the very low number of time steers used for fig. c, the plot is not substantially different from a or b. Some increased angularity is observed in the sidelobes, but again, not enough to appreciably decrease estimator performance.

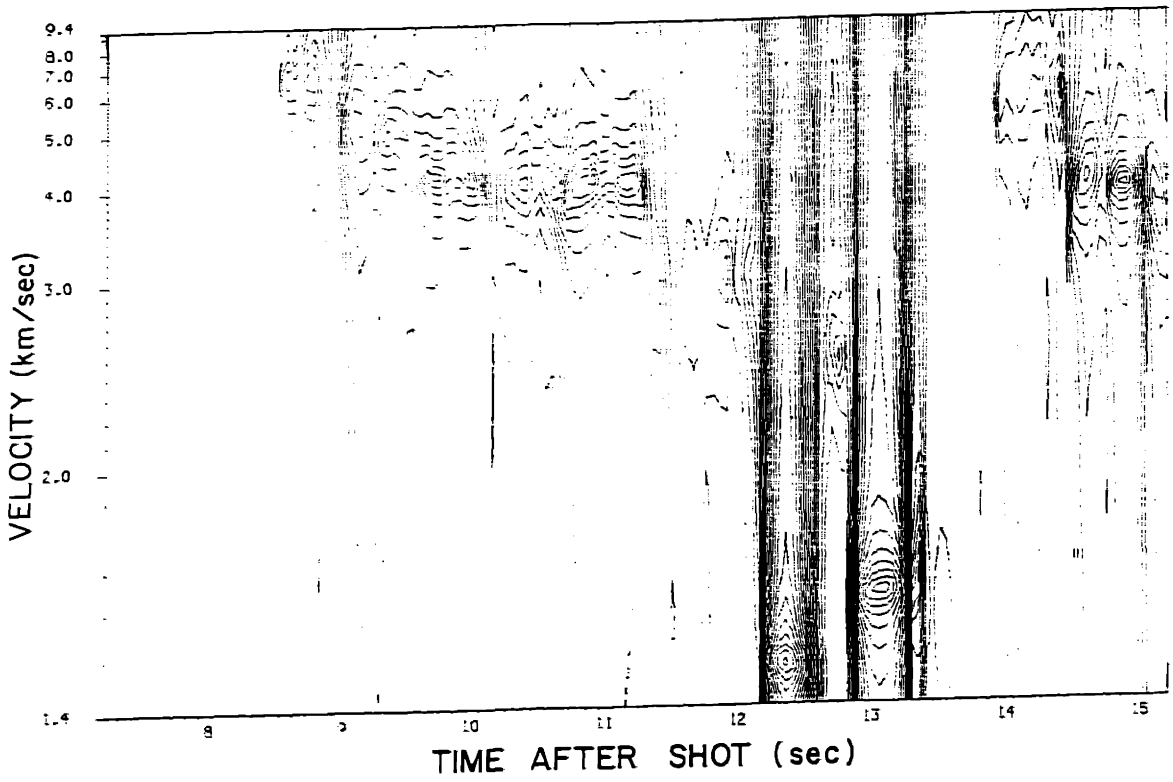

Fig. 3.15a) MLM velocity spectrum: $T = .25$ sec, $\delta t = .05$ sec, $N_t = 60$.

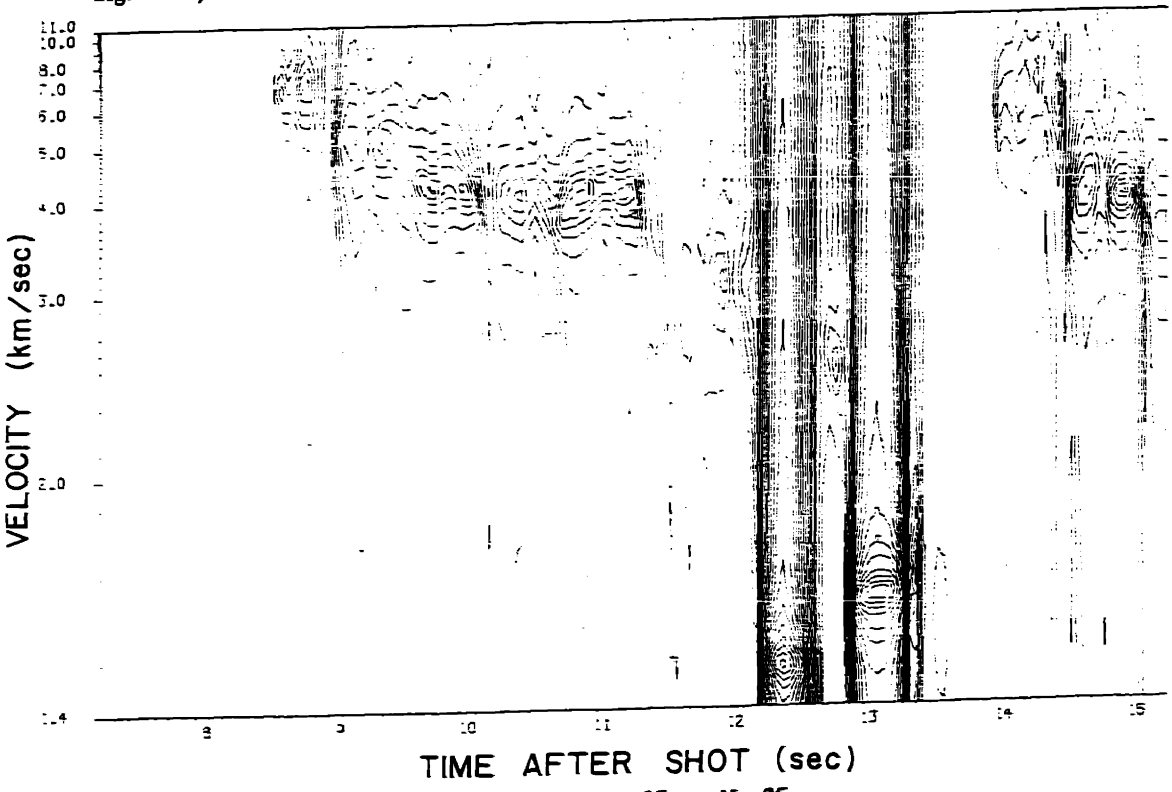

Fig. 3.15b) MLM velocity spectrum: $T = .25$ sec, $\delta t = .05$ sec, $N_t = 25$.

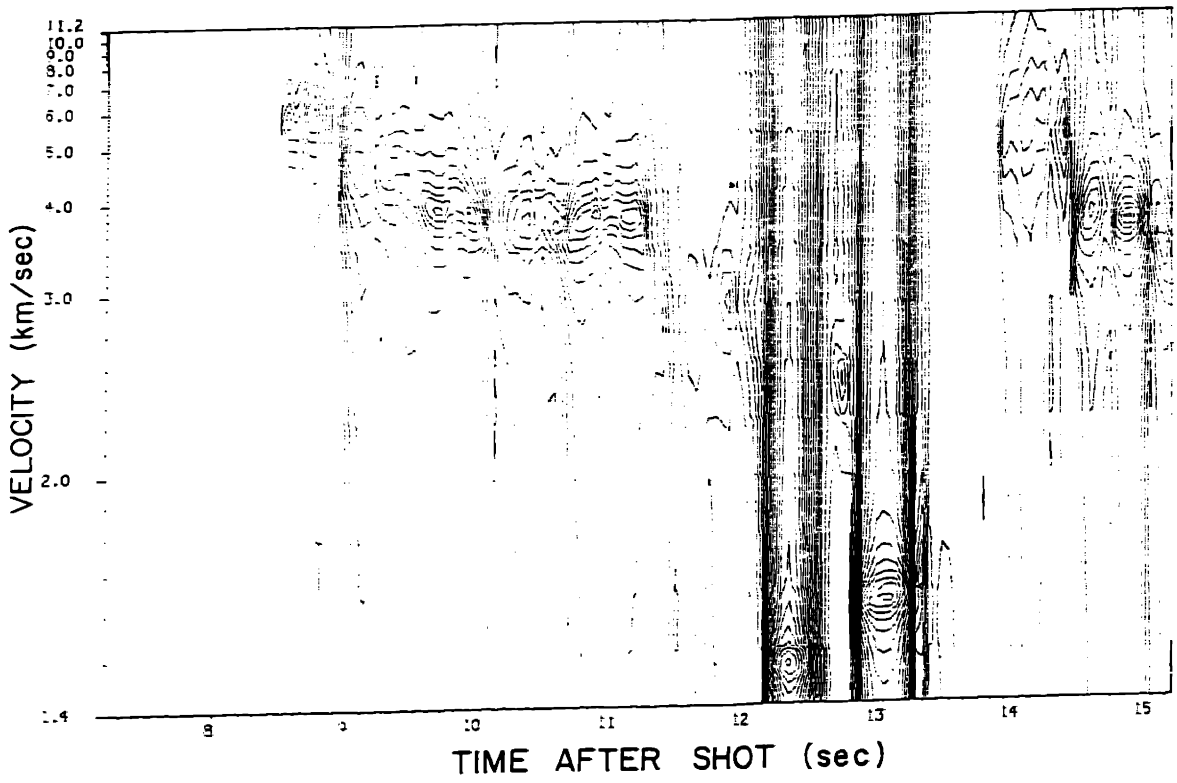

Fig. 3.15c) MLM velocity spectrum: $T = .25$ sec. $\delta t = .05$ sec, $N_t = 12$.

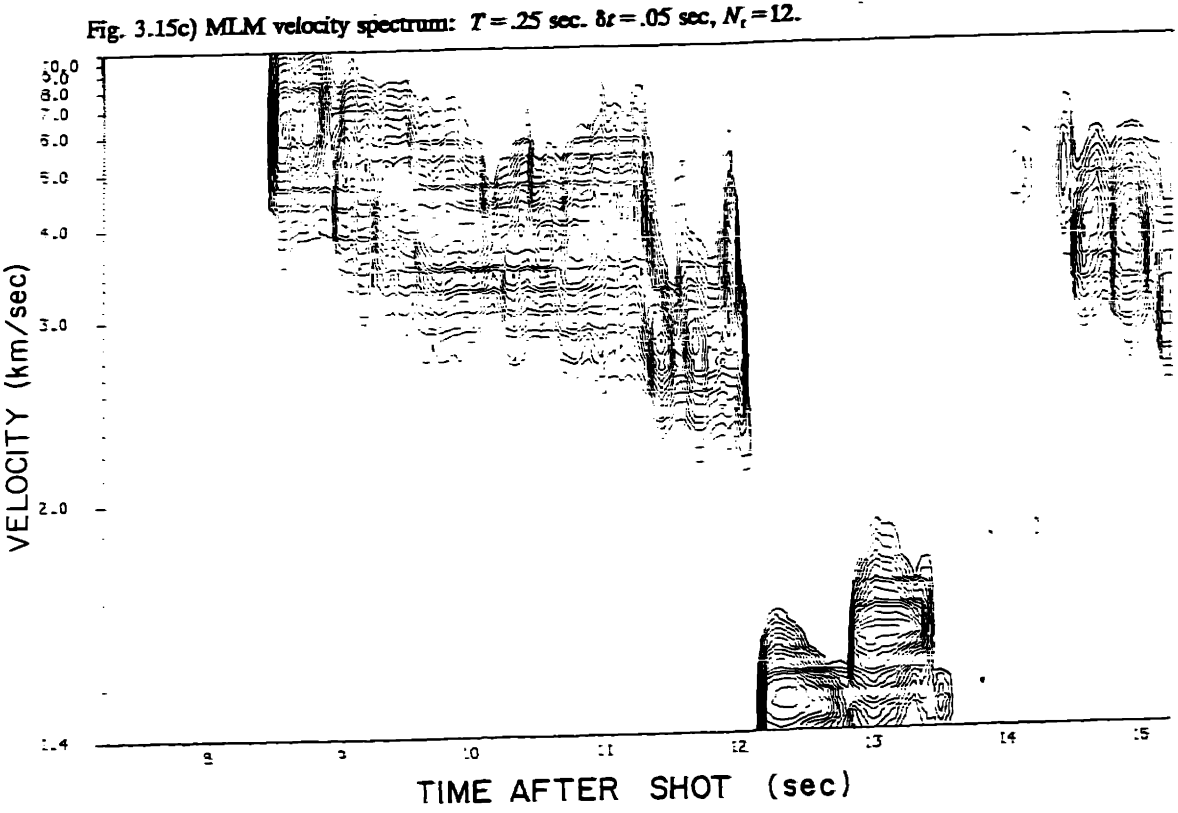

Fig. 3.15d) Average Semblance: $T = .25$ sec, $\delta t = .05$ sec, $N_t = 125$.

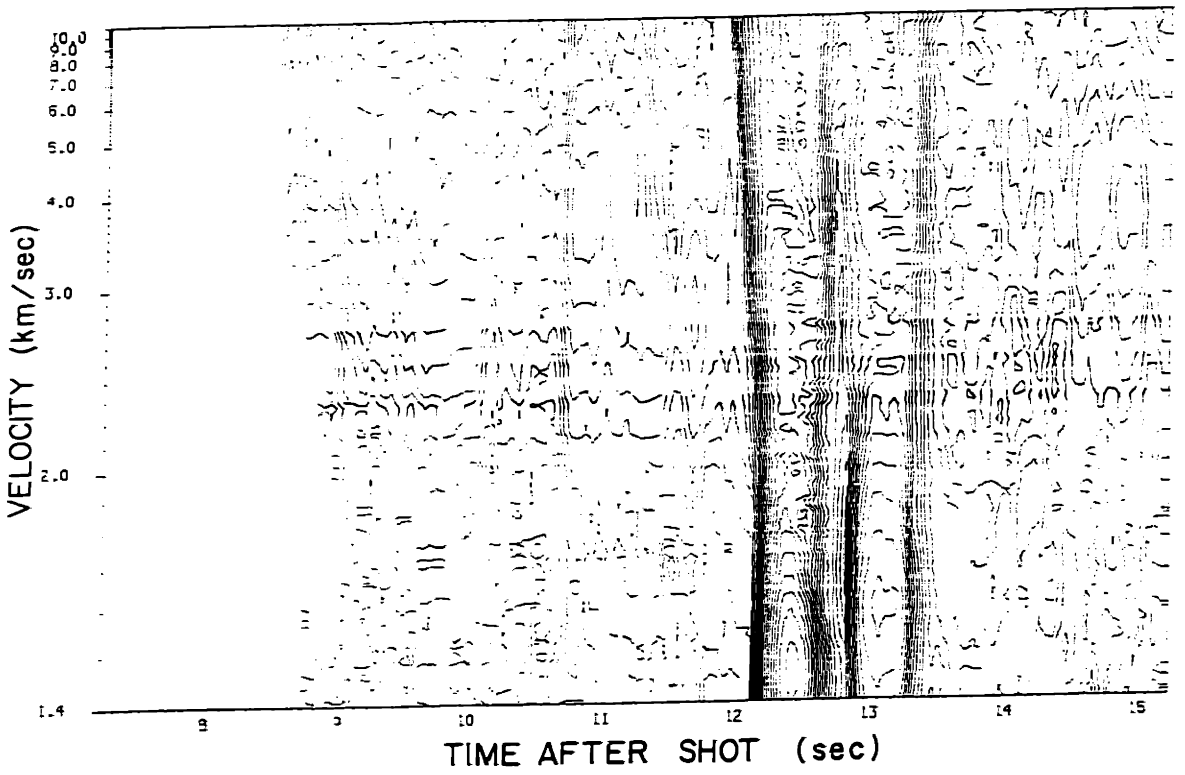

Fig. 3.15e) Average Stack: $T = .25$ sec, $\delta t = .05$ sec, $N_t = 125$.

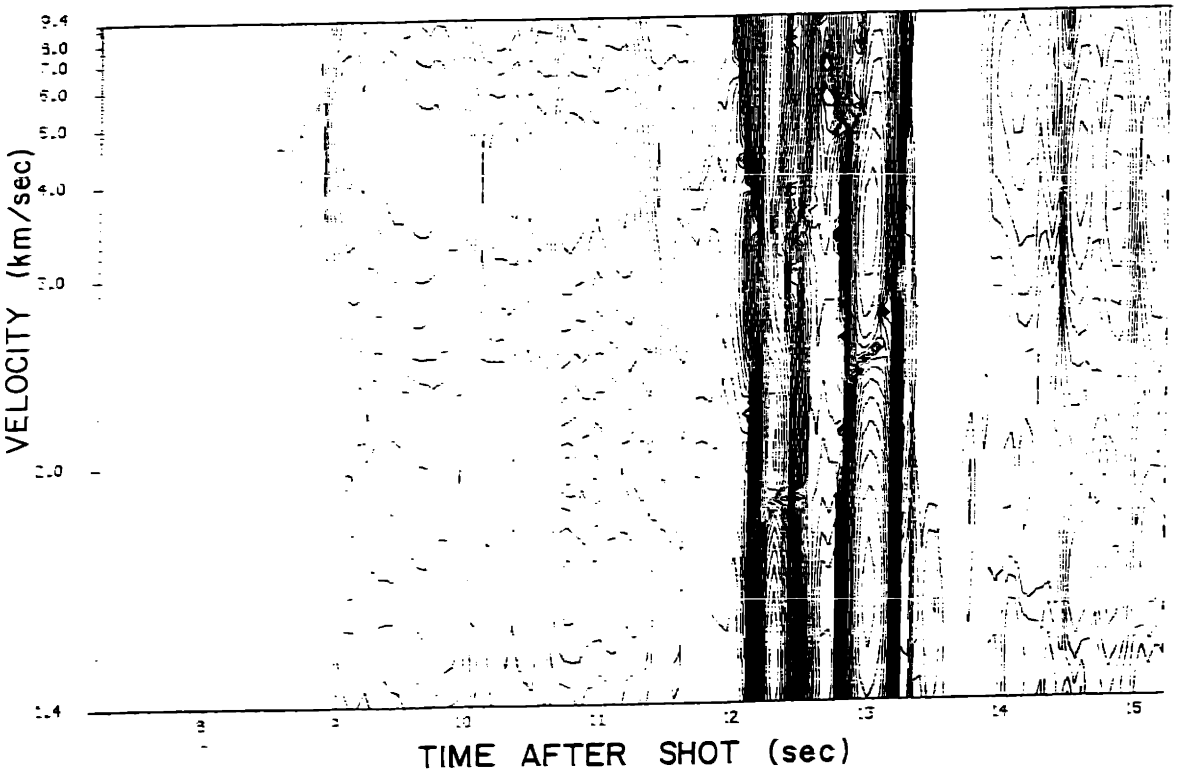

Fig. 3.15f) CONV velocity spectrum: $T = .25$ sec, $\delta t = .05$ sec, $N_t = 60$.

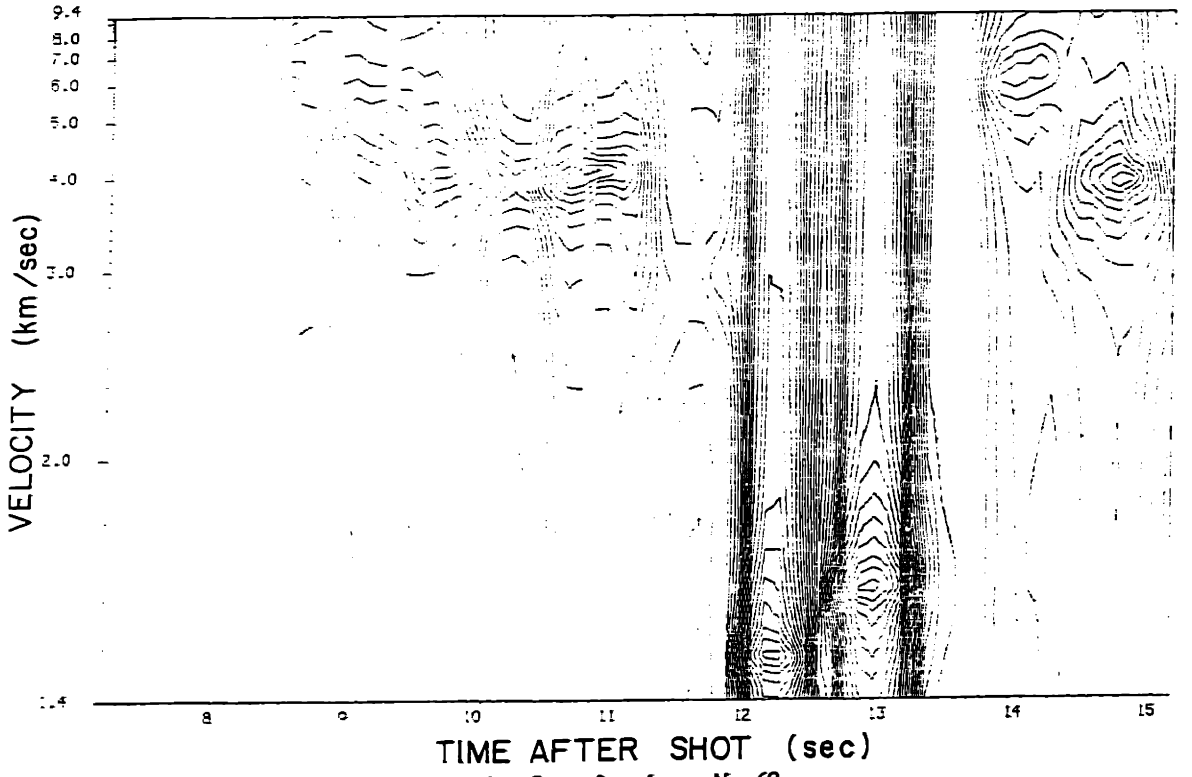

Fig. 3.15g) MLM velocity spectrum: $T=.5$ sec, $\delta t=.1$ sec, $N_t=60$.

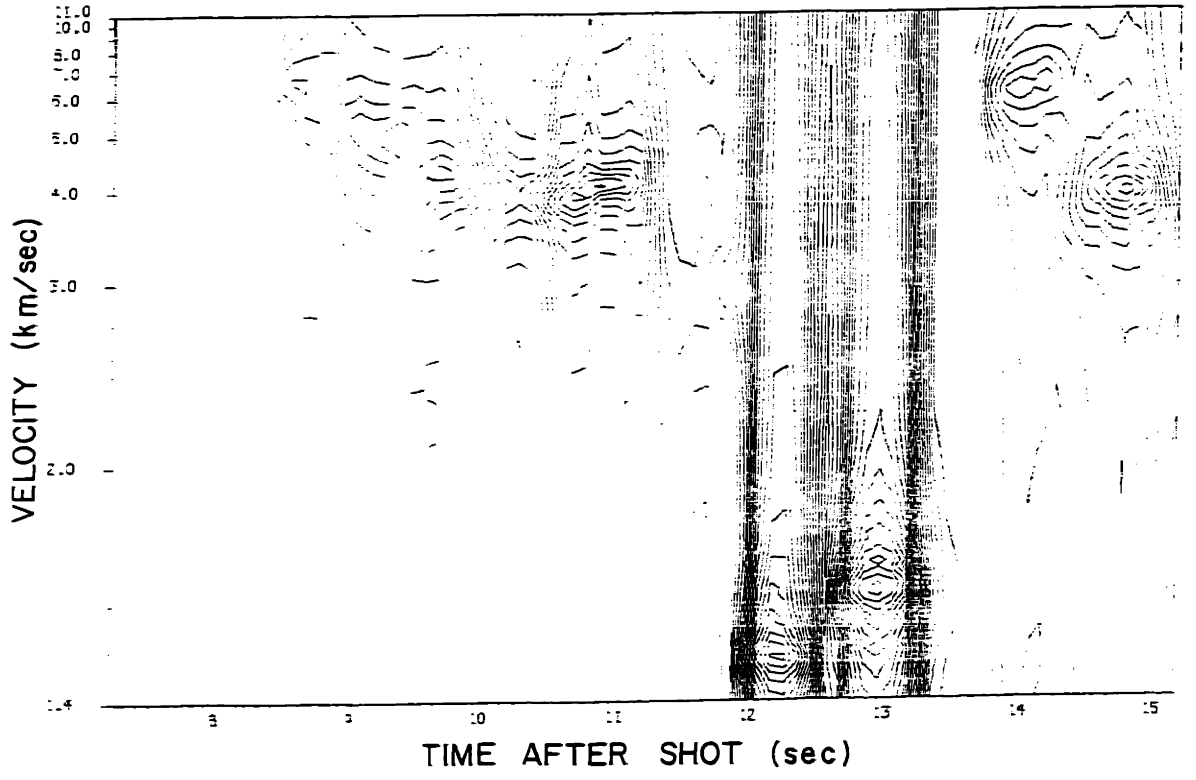

Fig. 3.15h) MLM velocity spectrum: $T=.5$ sec, $\delta t=.1$ sec, $N_t=25$.

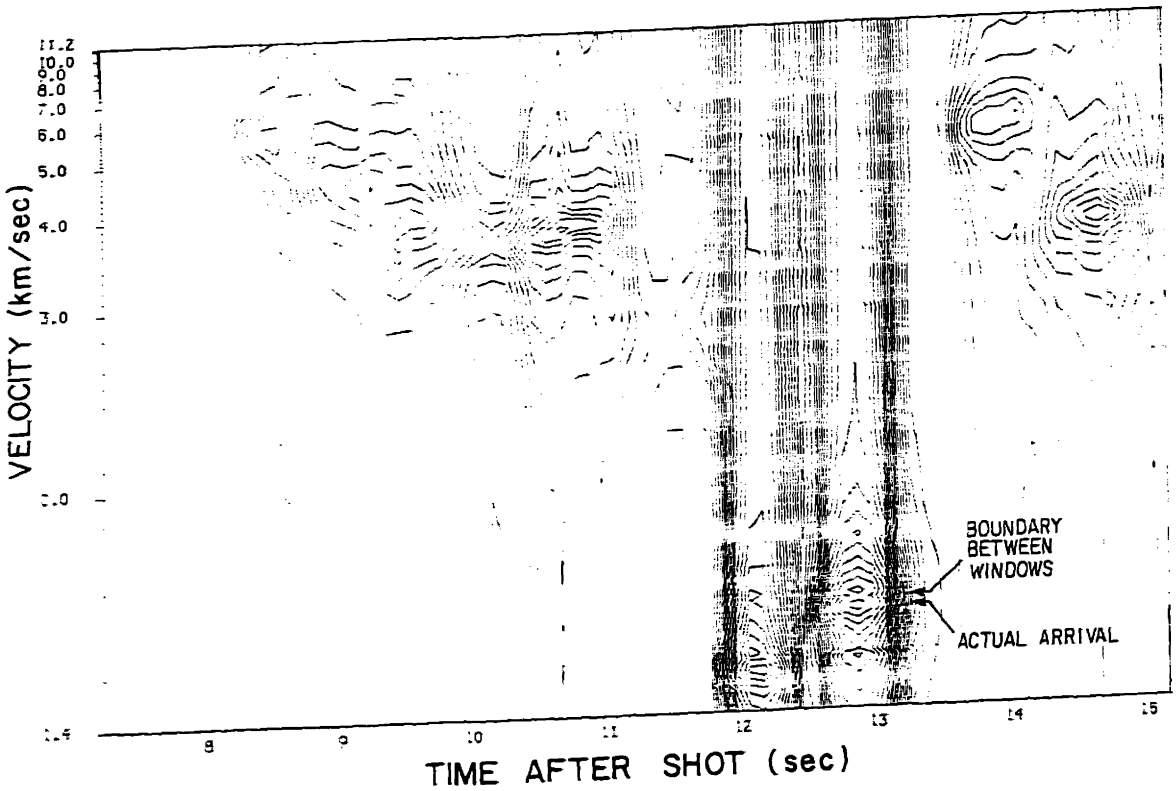

Fig. 3.15i) MLM velocity spectrum: $T = .5$ sec, $\delta t = .1$ sec, $N_t = 12$.

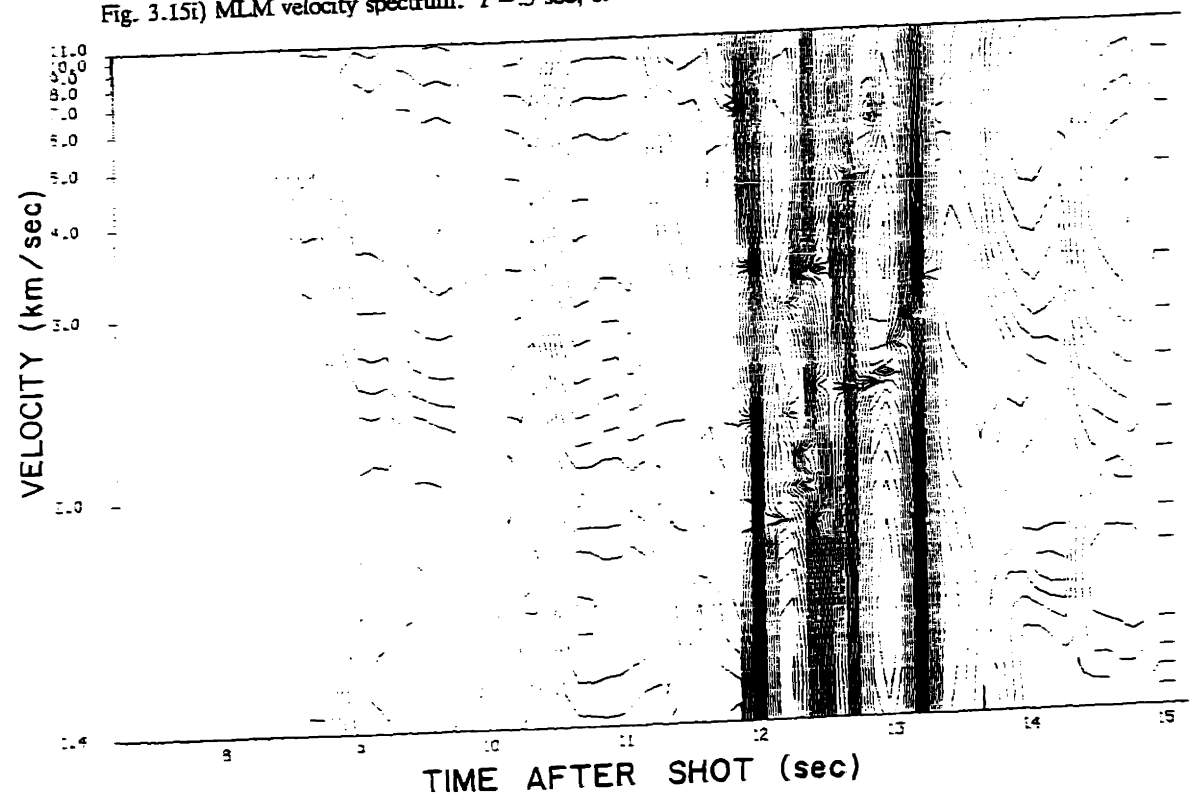

Fig. 3.15j) CONV velocity spectrum: $T = .5$ sec, $\delta t = .1$ sec, $N_t = 25$.

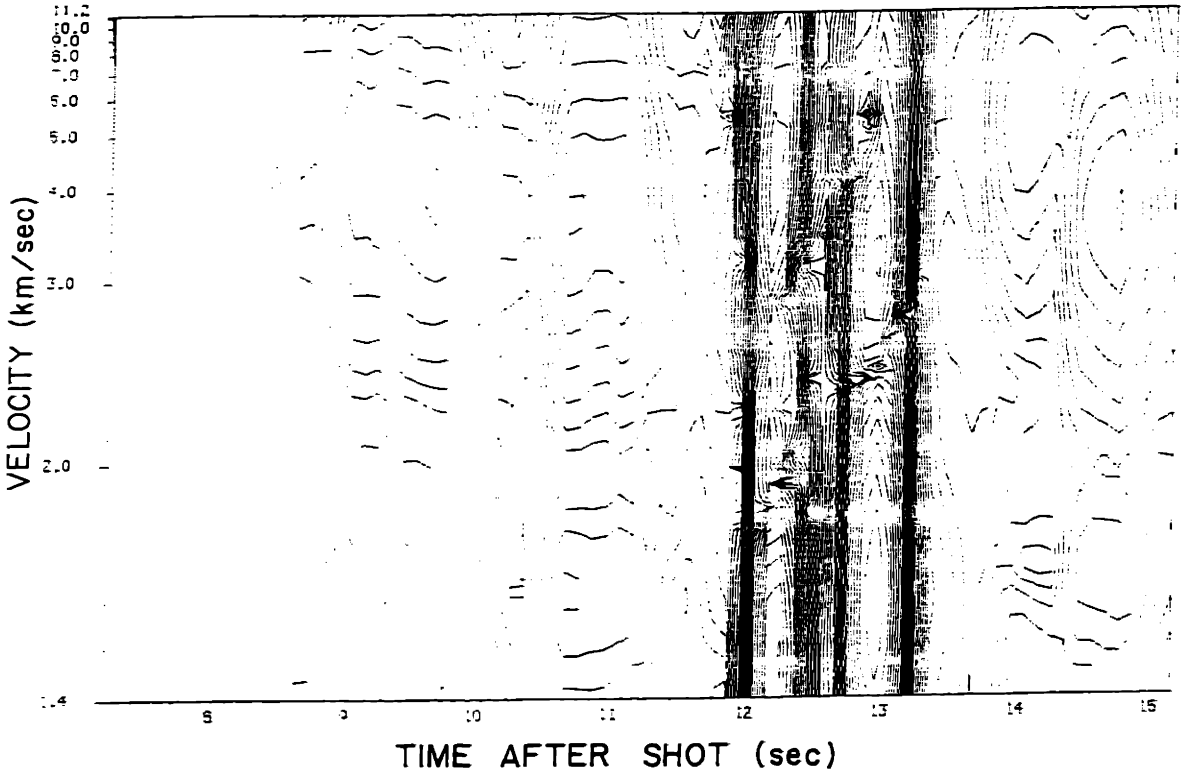

Fig. 3.15k) CONV velocity spectrum: $T = .5$ sec, $\delta t = .1$ sec, $N_r = 12$.

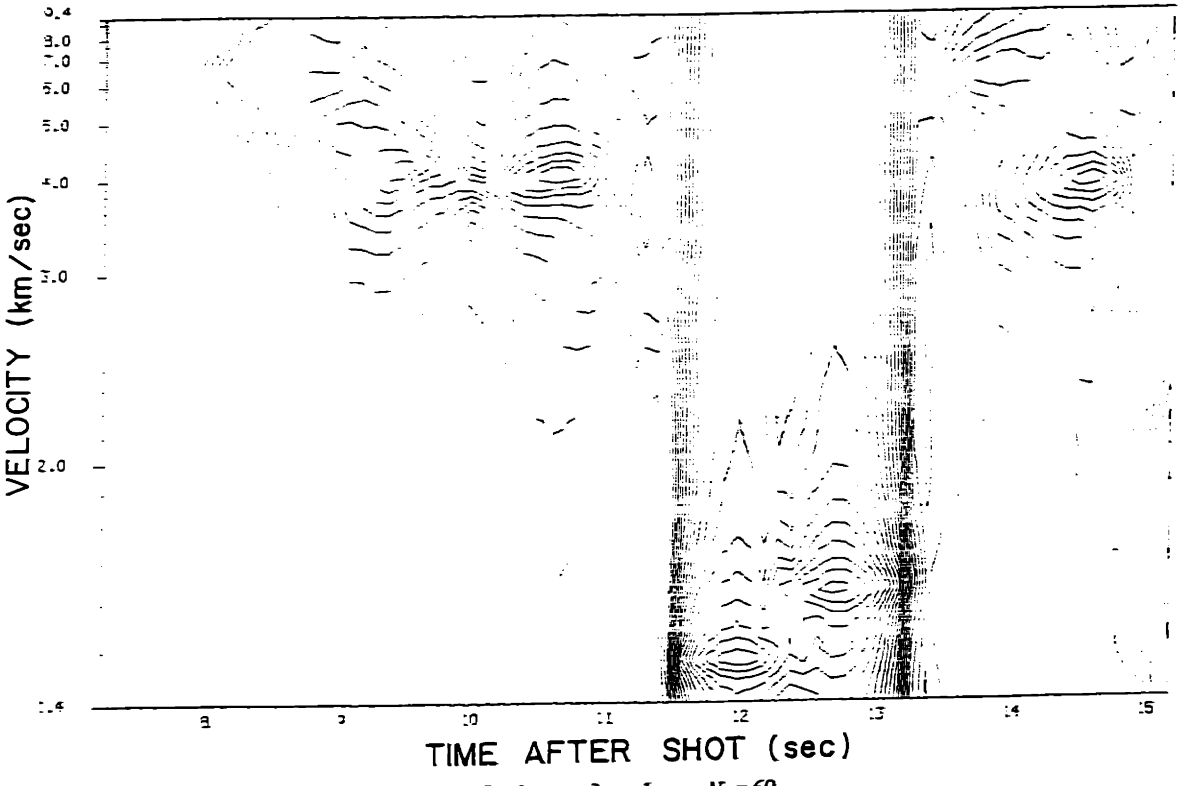

Fig. 3.15l) MLM velocity spectrum: $T = 1.$ sec, $\delta t = .1$ sec, $N_r = 60$.

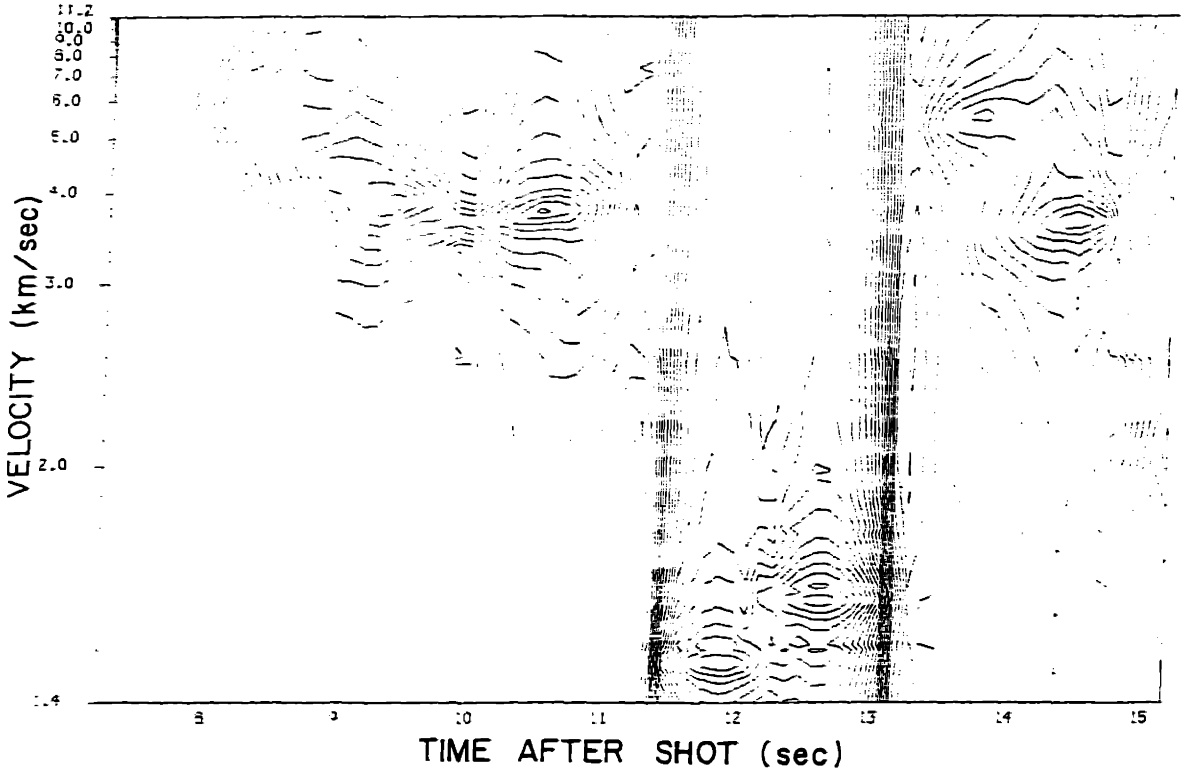

Fig. 3.15m) MLM velocity spectrum: $T = 1.$ sec, $\delta t = .1$ sec, $N_t = 12$.

Figure d shows the average semblance results for the same window length used in the previous figures. The time resolution for this method seems better than for the spectral technique, mostly due to the larger bandwidth of the time domain processor. The averaged semblance and stack methods have been used for comparison because they too implement a relatively phase shift independent detector. Note that the weak arrival between the strong water-wave and sedimentary arrival detected on the MLM plots a, b, and c is not detected on the semblance plot, nor are the high phase velocity multiples at 13-14 seconds discerned. The time domain averaged slant-stack of fig. e is very difficult to interpret, has poor dynamic range compared to the MLM plots, and shows the expected strong fan-shaped sidelobes. The sidelobes are, however, relatively monotonic because of the broadband nature of the time domain stack.

The conventional estimator results in fig. f should be compared to those of fig. a. The large sidelobes of the array (approx -9 dB) are quite evident on this narrowband processing output. These, combined with the lack of sharpness of the peaks, make the plot f much more difficult to interpret than the MLM result a.*

Figures g, h, and i show the results of MLM processing when a longer window is used. The time resolution is clearly not as good in these plots as in figs. a-c. In addition, we see that the longer window leads to a "scalloping" effect when the number of time steers used is decreased. For the low time steering density of fig. i, two peaks have appeared for the arrival at 12.6 seconds and 1.6 km/s, where on the more accurate plot, g, only one exists. This scalloping problem is primarily confined to low phase velocity, highly multipathed events in which the effective signal duration is quite long, and the individual contributions are beyond the time

*Although the actual peak location stability is the same for the conventional and MLM methods for the single outer product spectral covariance estimate.

resolution capabilities of the system. The "splitting" is most pronounced when the true arrival velocity lies in the middle of two true time steer slownesses. Longer windows suffer the effect more than shorter ones because the estimated covariance matrices for adjacent time steers are more nearly alike, especially when the signal duration is long. Figures j and k for the conventional processor with a .5 second window show that the scalloping effect is less important on this lower resolution estimator. The elimination of scalloping effects is important when velocity spectral analysis is used for the interpretation of waveforms in long range normal mode propagation experiments. These will be dealt with in chapter 6.

For the very long (1 sec.) windows of figs. l and m, the scalloping is quite dramatic, as is the lack of time resolution. This is clearly not a suitable parameter choice.

The conclusions that we draw from these examples are that the $T = .25$ s window, with 25 time steers and 5 phase steers in the 1.4-11 km/s range is the best combination to use. The lack of variability in the adjacent time slices of fig. b indicates that the .05 s output sampling interval is adequate in terms of lack of undersampling. From the Monte Carlo tests in the previous section, it was seen that the standard deviation of the time of arrival and slowness estimates were less than these time and slowness scanning densities, and thus it would seem that all the performance possible is not being exploited. The answer to this lies in the fact that the shape of the wave is not known well enough for the "arrival" time to be related to the peak detected time sufficiently accurately to make denser time sampling worthwhile. Similary, the variability in the slowness estimate due to noise is far less than that due to medium lateral inhomogeneities, such as unknown bathymetry at the source and receiver points, making it pointless to obtain the exact peaks more accurately.

SHORT-TIME FOURIER TRANSFORM SLANT-STACKS

Discussion

Up to this point we have considered only parameter estimation from short-time, short-aperture velocity spectral analysis. There is also interest in analysis of the waveforms themselves, since their details can give information about density changes or attenuation properties of the medium. One of the main drawbacks of conventional slant-stacking over short apertures is that the sidelobes of the array response cause a great deal of interference between waves of differing slowness (see figs. 3.2). The examples in the previous section showed that the maximum likelihood method is useful for reducing the sidelobe interference from other sources in estimates of the individual frequency component magnitudes, i.e. the velocity spectra. In light of this it seems reasonable that the MLM filters for each frequency from equation 3.41e could be used to "stack" or steer the data vectors at each frequency, yielding the Fourier coefficients for each steering slowness. An inverse transform of these steered Fourier coefficients would then yield the optimally filtered waveform at the particular slowness. In fact, this procedure was among the first uses of the MLM algorithm. The task was the isolation of waves from a particular earthquake from interfering seismic events [Capon, et al., 1969]. However, in that application, the signal and interference directions, θ, and slownesses, p, were known, and the matrix $\mathbf{R} = \mathbf{R}(\omega,p,\theta)$ used in equation 3.41e could be constructed analytically. In the refraction data case, no prior knowledge of the arrival parameters exists, and because of the transient nature of the signals, the parameters change with time after the shot initiation. For this reason, the short-time *estimates* of the MLM filters must again be used. To lend continuity to the waveforms, and because the spectral analysis window is tapered, only a small section of the waveform at the center of the window is "reconstructed" from the inverse

Fourier transform of the MLM filtered or "steered" coefficients as the analysis window of length T is moved along the data for various intercept times and move-outs. These sections are pieced together to form the complete time series at each slowness. Henceforth, this method of piecing together the short time waveform estimates from their steered Fourier transforms will be called the Short-time Fourier transform Slant-stack (STFTSS).

The Short-time Fourier Transform Slant-stack Algorithm (STFTSS)

There are a number of variables to define before making the computation:

Δt time sampling interval

T short-time Fourier transform analysis window length

N_T $= \frac{T}{\Delta t}$ is the number of data points per window

$w_s(\tau)$ window tapering function

τ_{min}, τ_{max} start and end times for reconstruction

δt window advance between covariance estimates

N_τ $= \frac{\tau_{max} - \tau_{min}}{\delta t} - 1$ is the number of windows in the output time range of interest

n_τ $= \frac{\delta t}{\Delta t}$ is the number of points reconstructed for each window

n_s $= \frac{N_T - n_\tau}{2}$ is the start point in the steered short-time inverse Fourier transform of the desired portion of the sequence. This sequence will end at $n_s - n_\tau - 1$.

N_2 is the smallest power of 2 that is greater than or equal to N_T

Δp slowness increment between estimates (δp is zero, all steering is done by time shifting)

p_{min}, p_{max} minimum and maximum slownesses of interest

N_p $= \frac{p_{max}-p_{min}}{\Delta p}+1$ is the number of slowness scans

N number of channels used

ω_k frequencies over which to reconstruct waveform, $k \in \{k_{min},...,k_{max}\}$

$F(\omega_k)$ is the frequency response of the filter to apply to the data for temporal filtering

γ is the condition number of the inverse covariance matrix

STFTSS Algorithm

start:

$p \leftarrow p_{min} \quad \tau \leftarrow \tau_{min}$

loop over p for $p \leq p_{max}$:

loop over τ for $\tau \leq \tau_{max}$:

compute data transforms

$$n_0 = \left\lceil \frac{\tau + pr_j}{\Delta t} \right\rceil^{-} - n_s$$

$$d(\tau,\omega_k,p,r_j) = r_j^{\frac{1}{2}} e^{i\omega(pr_j - \tau + n_0\Delta t)} \sum_{n=n_0}^{n_0+N_T-1} w_s(n\Delta t - T/2) P(n\Delta t, r_j) e^{i\omega_k n\Delta t}$$

done by an FFT for $\omega_k = 2\pi k/N_T\Delta t$

$$\mathbf{d}(\tau,\omega_k,p) = \begin{bmatrix} \cdot \\ \cdot \\ \cdot \\ \mathrm{d}(\tau,\omega_k,p,r_j) \\ \cdot \\ \cdot \\ \cdot \end{bmatrix}$$

loop over frequencies of interest

$k = k_{\min}$

loop over k for $k \le k_{\max}$:

estimate the spectral covariance matrices

$$\hat{\mathbf{R}}(\tau,\omega_k,p) = \mathbf{d}(\tau,\omega_k,p)\mathbf{d}^H(\tau,\omega_k,p) + \frac{\mathbf{d}^H(\tau,\omega_k,p)\mathbf{d}(\tau,\omega_k,p)}{\gamma-1}\,\mathbf{I}$$

or

$$\hat{\mathbf{R}}^{-1} = \frac{\gamma-1}{\mathbf{d}^H(\tau,\omega_k,p)\mathbf{d}(\tau,\omega_k,p)}\left[\mathbf{I} - \frac{\mathbf{d}(\tau,\omega_k,p)\mathbf{d}^H(\tau,\omega_k,p)}{\frac{\mathbf{d}^H(\tau,\omega_k,p)\mathbf{d}(\tau,\omega_k,p)}{\gamma-1} + \mathbf{d}^H(\tau,\omega_k,p)\mathbf{d}(\tau,\omega_k,p)}\right]$$

compute the MLM filter (if MLM is to be used)

$$\mathbf{e}(\omega_k,p) = \begin{bmatrix} \cdot \\ \cdot \\ \cdot \\ e^{i\omega_k p r_j} \\ \cdot \\ \cdot \\ \cdot \end{bmatrix}$$

$$\mathbf{w}(\tau,\omega_k,p) = \frac{\hat{\mathbf{R}}^{-1}(\tau,\omega_k,p)\,\mathbf{e}(\omega_k,p)}{\mathbf{e}^H(\omega_k,p)\hat{\mathbf{R}}^{-1}(\tau,\omega_k,p)\mathbf{e}(\omega_k,p)}$$

compute the steered Fourier coefficients

Conventional Method:

$$S_{CONV}(\tau,\omega_k,p) = \frac{1}{N}\mathbf{e}^H(\omega_k,p)\mathbf{d}(\tau,\omega_k,p)$$

MLM:

$$S_{MLM}(\tau,\omega_k,p) = \mathbf{w}^H(\tau,\omega_k,p)\mathbf{d}(\tau,\omega_k,p)$$

next k: $k \leftarrow k+1$

compute the current segment reconstructed sequence at slowness p after [optionally] temporal frequency filtering with filter $F(\omega)$*

$n \leftarrow n_s$

loop over n for $n \le n_\tau$:

$$\hat{S}(n\Delta t+\tau,p) = \frac{1}{N_2}\sum_{k=k_{min}}^{k=k_{max}} F(\omega_k)S(\tau,\omega_k,p)\,e^{-i\omega_k n\Delta t}$$

where

$$\omega_k = \frac{2\pi k}{N_2\Delta t} \quad \text{for inverse FFT}$$

and S is one of S_{CONV} or S_{MLM}

next n: $n \leftarrow n+1$

next τ: $\tau \leftarrow \tau+1$

next p: $p \leftarrow p+1$

---

*The Wiener filter would be good to use here if prior knowledge of the signal and noise spectra is available. For the MLM technique biases in the output due to noise effects can also be corrected here by the method described earlier in this chapter.

end:

The output, $\hat{S}$, should be scaled by:

$$\frac{4\pi c_{source}^{2}}{p^{\frac{1}{2}}}$$

in accordance with equations 3.22 and 3.23a to yield the estimate of the short aperture slant-stack when pressure data and a pressure source, such as an explosive or air-gun, are used.

Examples

It was seen earlier in this chapter that the magnitudes of the Fourier coefficient estimates from the MLM velocity spectral analysis procedure are biased in the presence of independent sensor noise and interfering signals.* Similarly, the amplitudes of the reconstructed signals will be biased unless the steered Fourier coefficients used to reconstruct the short-time segments of the signal are corrected before inverse transformation. Since different coefficients will have differing signal to noise ratios, depending upon the signal and noise spectral characteristics, the relative biases will introduce a waveform distortion, not just a scaling. A procedure for computing these corrections was given in the section of this chapter entitled *MLM Power Bias due to Independent Sensor Noise*. For the example given there, the wavelet was relatively narrow-band and had three dominant Fourier coefficients, 11.7, 15.6, and 19.5 Hz. Table 3.9 shows the change in the relative levels for two signals with 6 dB different powers when the in-band noise spectral level is -4 dB.

*When the poor, but only available, estimate of the spectral covariance matrix in eqn. 3.42 is used.

TABLE 3.9						
amplitude	true spectral levels (dB re 1 Hz)			biased spectral levels (dB re 1 Hz)		
	f=11.7	f=15.6	f=19.5	f=11.7	f=15.6	f=19.5
1	0	2	-1	-29.2	-26.7	-31.3
2	6	8	5	-19.1	-16.2	-21.8

From this table, it can be seen that 2-3 dB relative changes can occur. These can, however, be corrected using the bias formulae presented, and the correct wave shapes and levels recovered. Since this work has no immediate use for the waveforms themselves, no extensive testing or correction applications were carried out. However, a few uncorrected examples on synthetic and real data will serve to illustrate the possible utility of the MLM beamformer in the STFTSS algorithm.

Figures 3.17 show the data used for the examples. The parameters of the two plane waves simulated are given in table 3.10.

TABLE 3.10				
signal #	arrival time (s)	velocity (km/s)	slowness (s/km)	amplitude (units)
1	1	1.5	.6	1
2	2	6.0	.16	2

Figure 3.17a shows the noiseless data on the uniform 10 sensor array. In fig. 3.17b, the noise level is σ=.1, and in fig. 3.17c, the noise level is σ=1. The noiseless non-uniform array data is shown in figure 3.17d. Noisy traces would be similar to those of the uniform array. The actual sensor distributions for these two arrays are given in table 3.3. The in-band signal to noise ratios are given as a function of σ in table 3.5 for the wave with amplitude 1. The amplitude 2 case will be 6 dB better everywhere. Note that in this table, σ^2 is the noise spectral level at the sensor, σ_N^2 is the noise spectral level diminished by the array gain, 10 dB, and

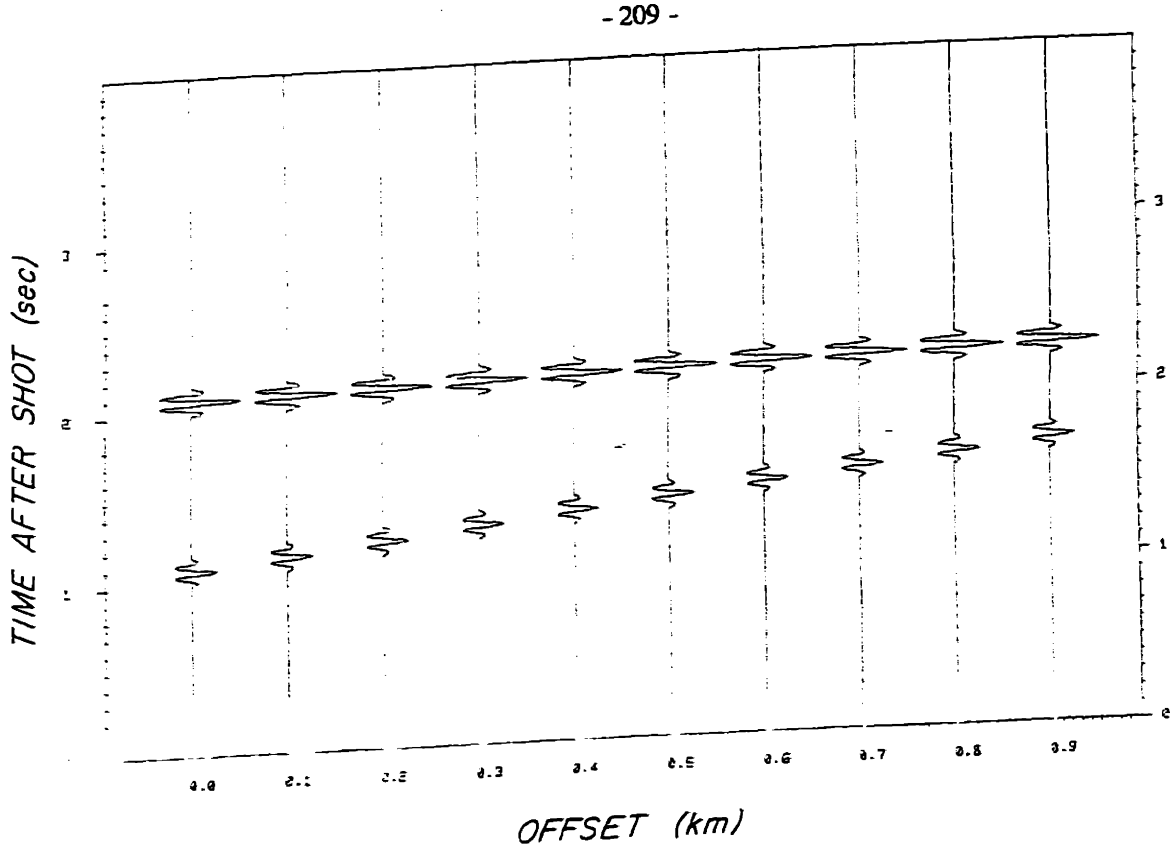

Fig. 3.17a) Synthetic wave-field data. σ=0. (no noise).

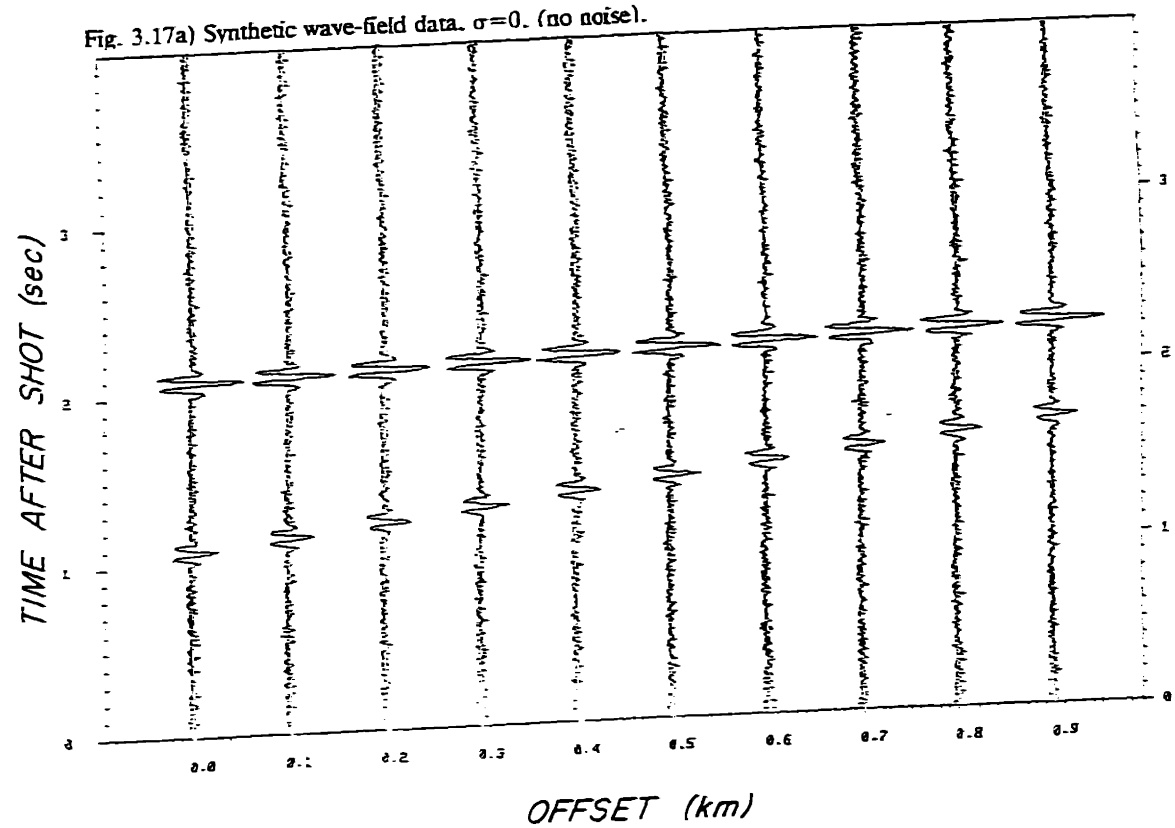

Fig. 3.17b) Synthetic wave-field data. σ=0.1.

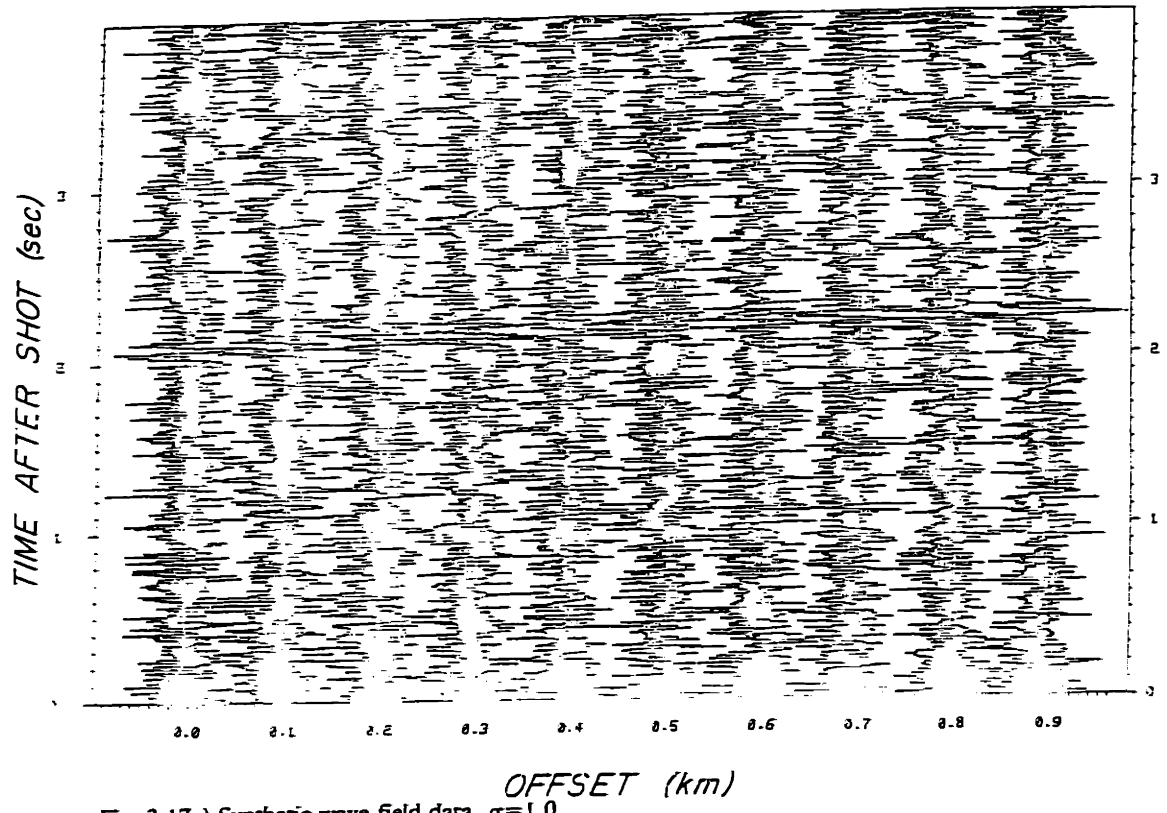

Fig. 3.17c) Synthetic wave-field data, σ=1.0.

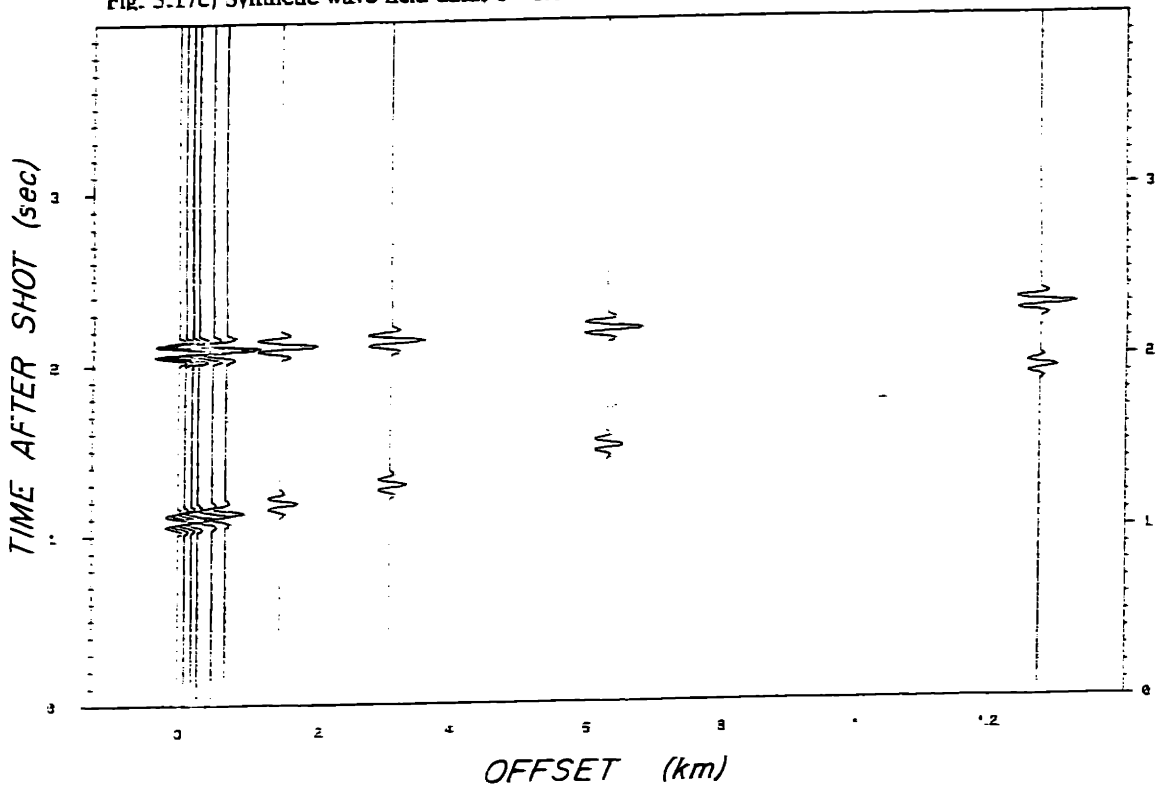

Fig. 3.17d) Synthetic wave-field data (non-uniform array), σ=0. (no noise).

σ_ω^2 is the noise spectral level in the processor band (re 1 Hz) after the array gain. The signal to noise ratios in that table are $10\log_{10}(E_\omega/10\sigma_\omega^2)$, which is the sensor signal to noise ratio in the processor band. The array gain has not been figured in, but the effect of the spectral analysis window function has, for both the signal (-1.5 dB over the the true spectral level) and noise (-4 dB over the true spectral level). Table 3.11 lists the examples to be discussed for ease of reference. In the processing entry of the table, T-stack denotes the usual implementation of the Radon-transform slant-stack of equation 2.3. No temporal filtering is done for this operation. MLM and CONV denote the use of the STFTSS algorithm just described, using the MLM or conventional spatial filter respectively. The parameters for the examples are $T=.248$ seconds, $\Delta t=.004$ seconds, and $\delta t=.048$ seconds. The $\sin^2$ window is used for all STFTSS processing.

TABLE 3.11

Fig.	Array	σ	Processing	Gain factor on plot
3.18a,b	uniform	0	T-stack	.1/.5
3.18c,d	uniform	0	T-stack	.1/.5
3.19a,b	uniform	.1	CONV	.1/.5
3.20a,b	uniform	.1	MLM	1/5
3.21a,b	uniform	1	T-stack	.1/.5
3.21c	uniform	1	T-stack,filtered	.5
3.22a,b	uniform	1	CONV	.1/.5
3.22c,d	non-uniform	1	CONV	.1/.5
3.23a,b	uniform	1	MLM	10/50
3.23c,d	non-uniform	1	MLM	10/25
3.24	uniform	1	MLM,post-filtered	50

Figures 3.18 show the time domain stack results on noiseless data for reference. The sidelobes and aliasing noted earlier for the uniform array are clearly visible in 3.18a&b. The non-uniform array trades aliasing for sidelobes as evidenced by figs. 3.18c&d. This picture shows that for any arrival complexity, the interpretability of time domain stacks on the short, non-

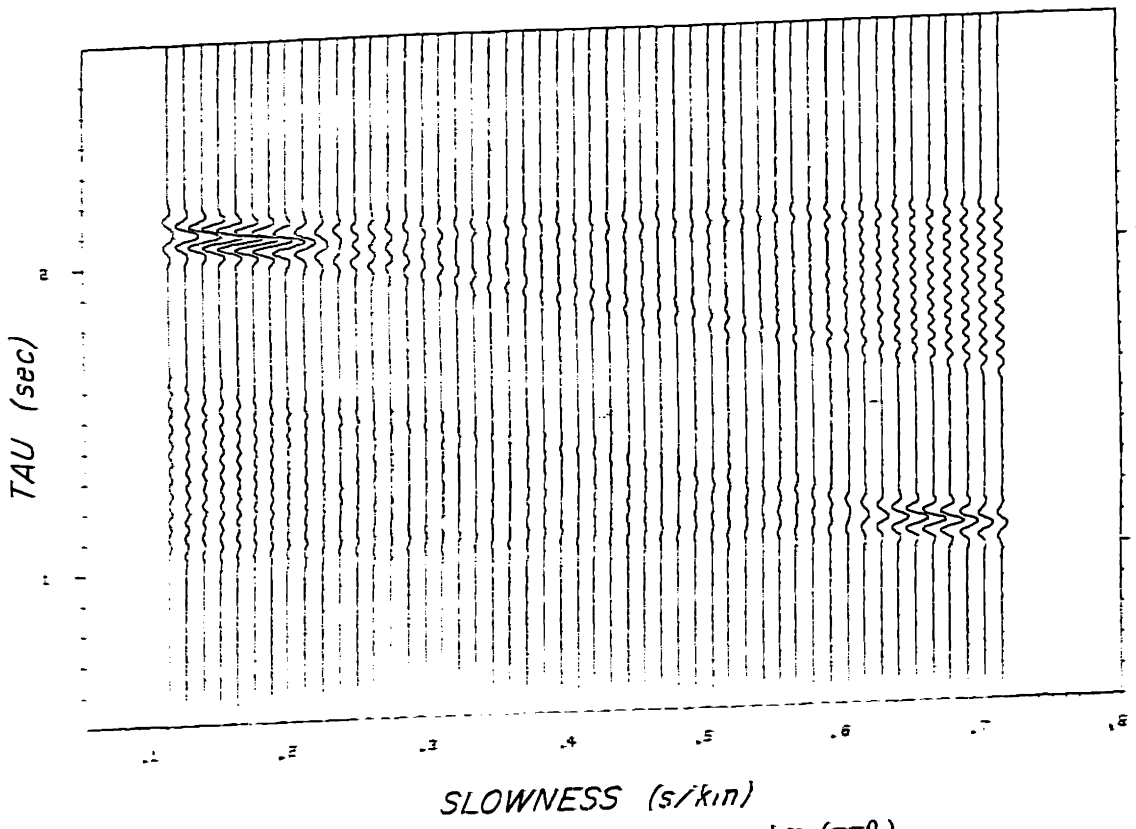

Fig. 3.18a) Conventional time-domain slant-stack of uniform array data. (σ=0.)

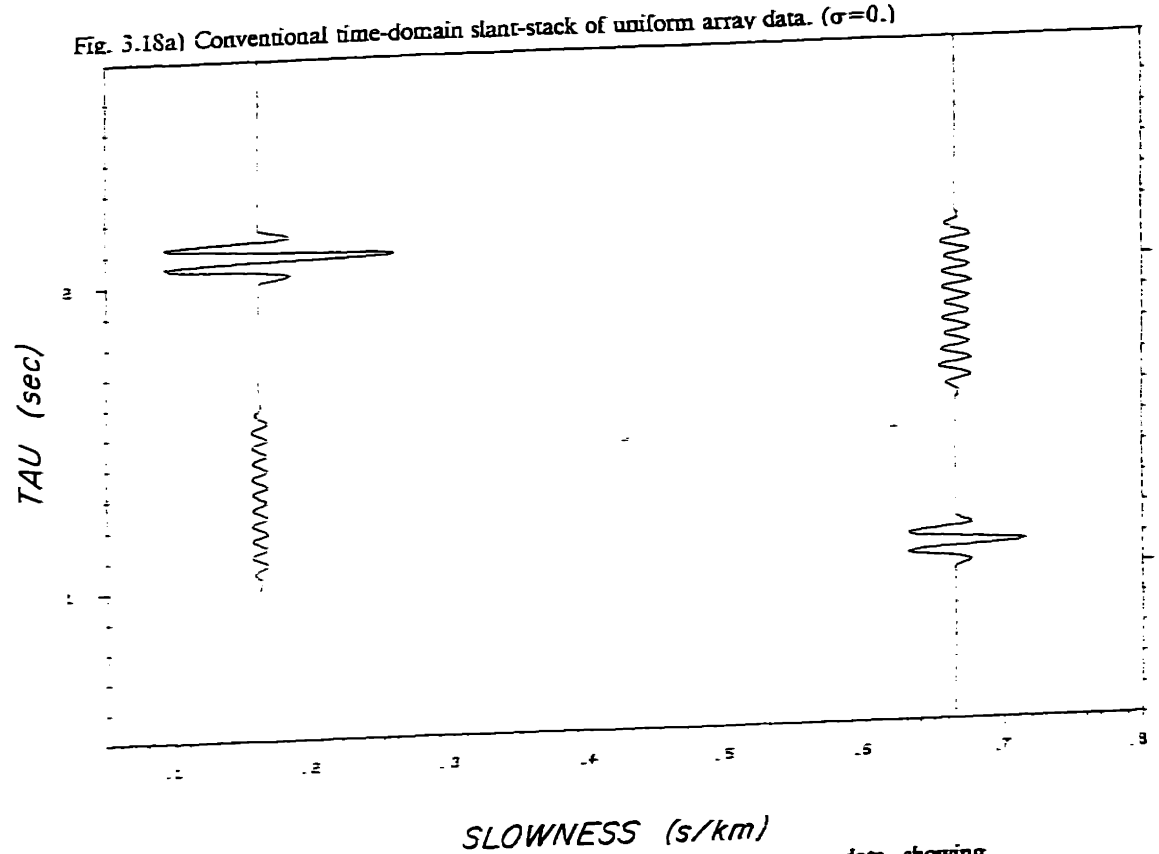

Fig. 3.18b) Conventional time-domain slant-stack of uniform array data showing waveforms at the true slowness values. (σ=0.)

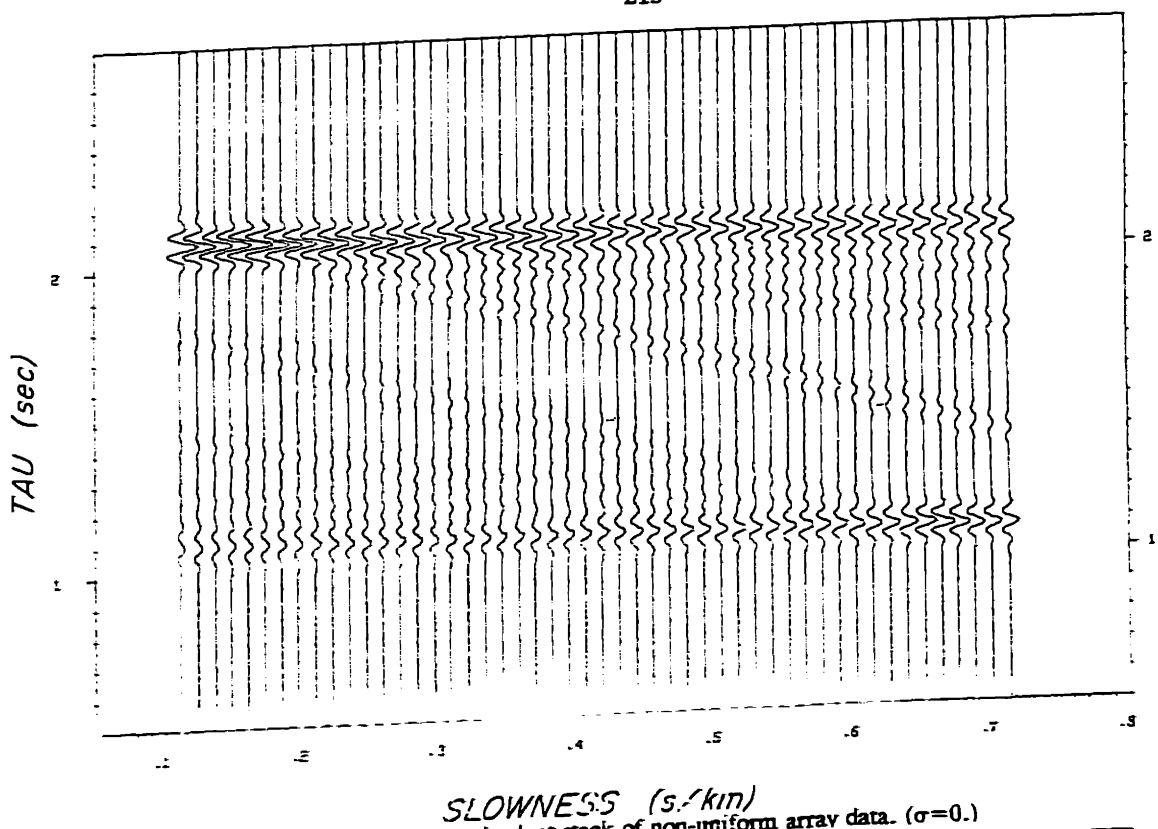

Fig. 3.18c) Conventional time-domain slant-stack of non-uniform array data. (σ=0.)

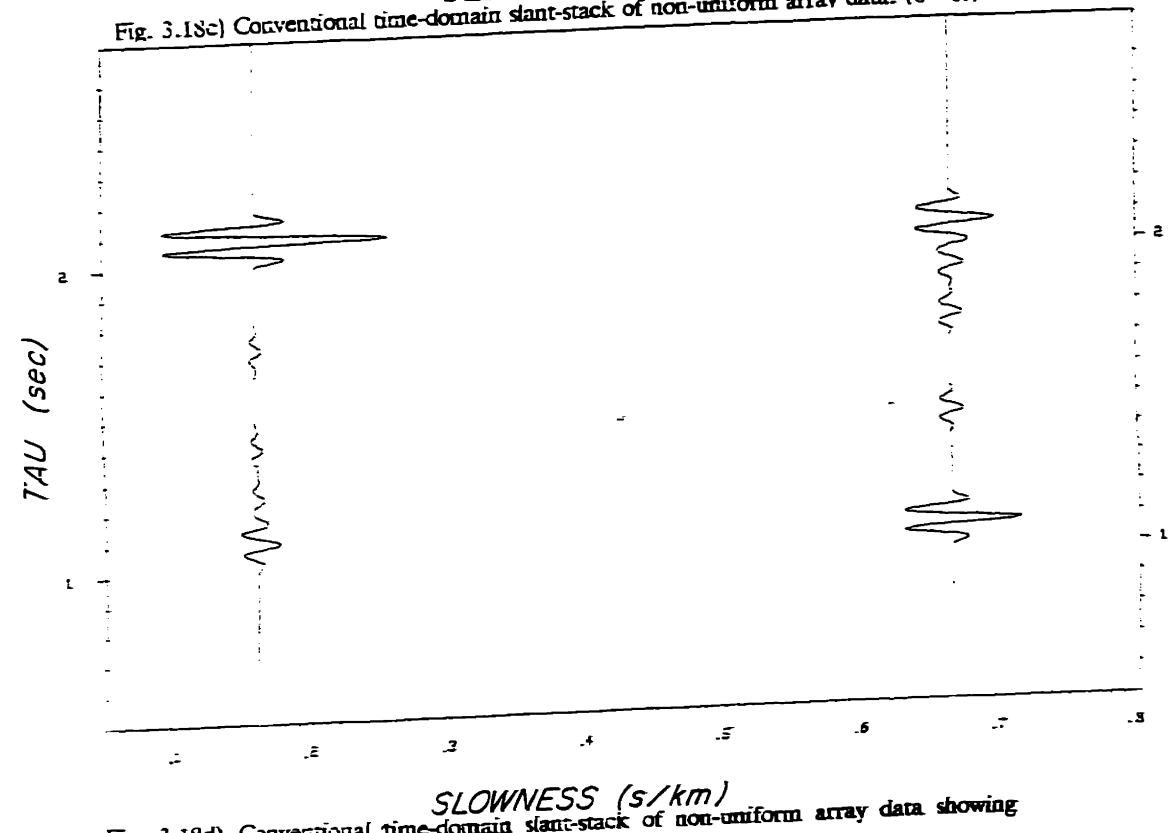

Fig. 3.18d) Conventional time-domain slant-stack of non-uniform array data showing waveforms at the true slowness values. (σ=0.)

uniformly sampled aperture would be poor due to interference effects. Figures 3.19 a&b show that the short-time Fourier transform slant-stack (STFTSS) with the conventional processor gives results that are quite similar to the time domain slant-stack. Comparing fig. 3.18b and 3.19b we see that some amplitude is lost due to the un-normalized window function ($\approx$1.5 dB) and some is lost to filtering (only 3 Fourier coefficients, or 12 Hz of bandwidth, were used to reconstruct fig. 3.19). The thing to note is that piecing the waveforms together leaves very few artifacts at the joints between the sections.* For the same amount of noise as in fig. 3.19, fig. 3.20 shows the results of the STFTSS with the MLM processor. The wave shapes are slightly more jagged, due to the bias of the MLM algorithm, however, this can be removed by post filtering the reconstructed signals back to the reconstruction bandwidth (12 Hz), thus eliminating the "joints". In figure 3.20 there is an apparent bias that makes the larger signal (6 km/s) look smaller than the 1.5 km/s signal. This is because the resolution in slowness at this signal to noise ratio is so large that the observed wave amplitude is highly dependent upon how close the scanned slowness is to the true signal slowness. The 1.5 km/s signal is almost exactly sampled by the scanning shown; however, the 6 km/s signal falls directly between the sampled slowness values. Clearly, the resolution of the MLM at large signal to noise ratio values is much higher than the conventional frequency domain method and standard time domain slant stacks.

Figures 3.21 a&b show that when a realistic amount of broadband noise is introduced, the unfiltered time domain slant stack is very poor. Temporal filtering from 10-20 Hz, shown in fig. 3.21c, helps, but the sidelobes are undiminished. The STFTSS with conventional processing in figs. 3.22 a&b gives results almost exactly the same as the filtered time domain

*The reconstruction in 3.19 is also in the presence of a small amount of sensor noise, and should not look quite as clean as 3.18.

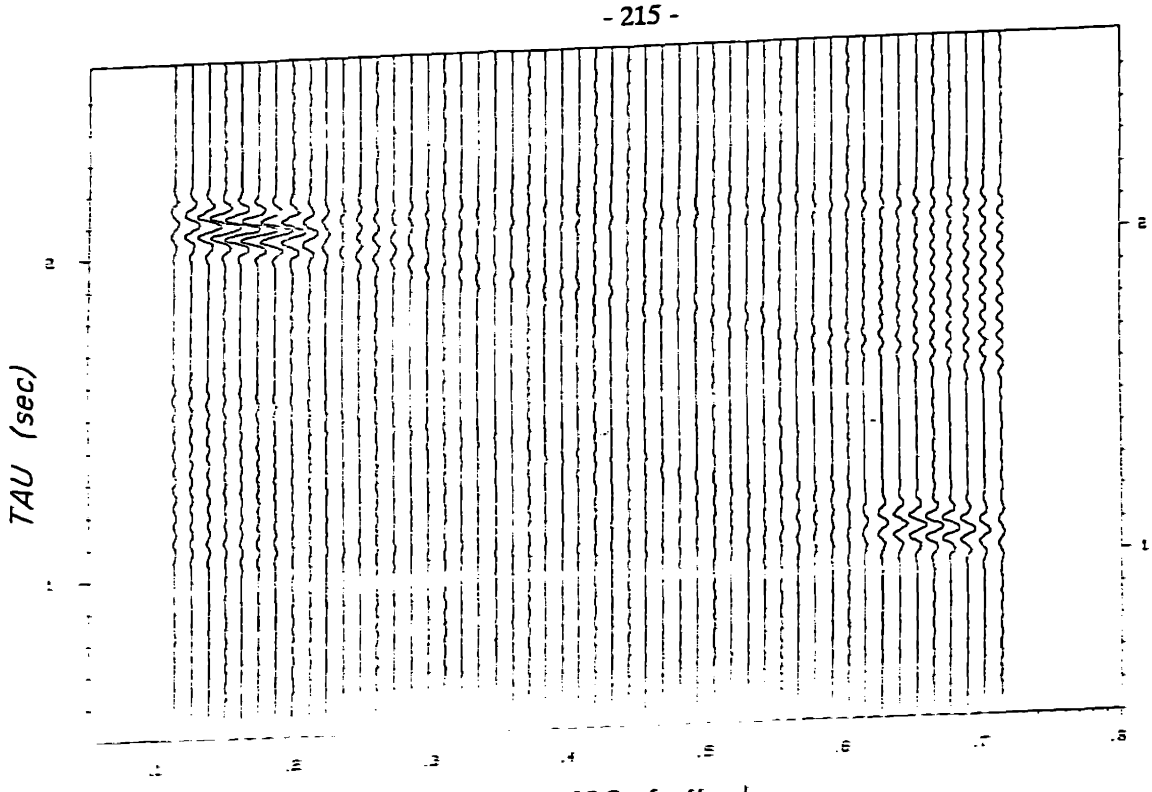

Fig. 3.19a) Conventional STFTSS of uniform array data. (σ=.1)

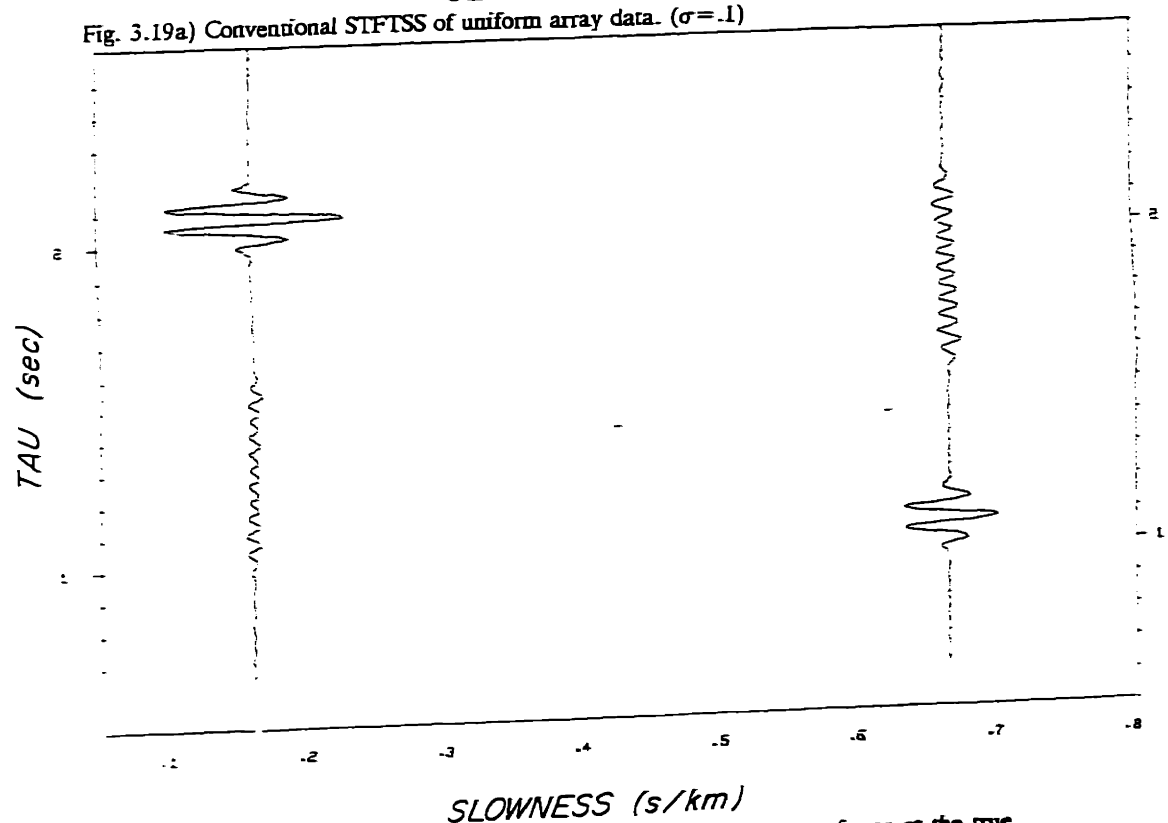

Fig. 3.19b) Conventional STFTSS of uniform array data showing waveforms at the true slowness values. (σ=.1)

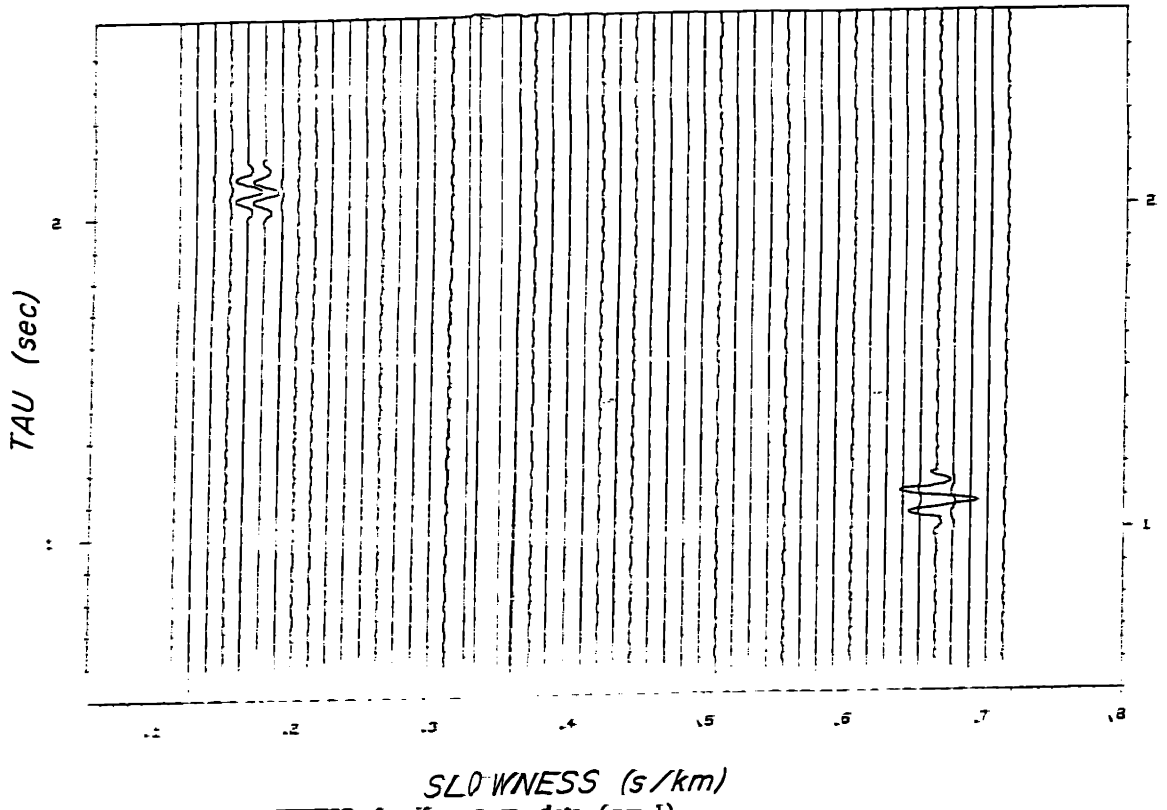

Fig. 3.20a) MLM STFTSS of uniform array data. (σ=.1)

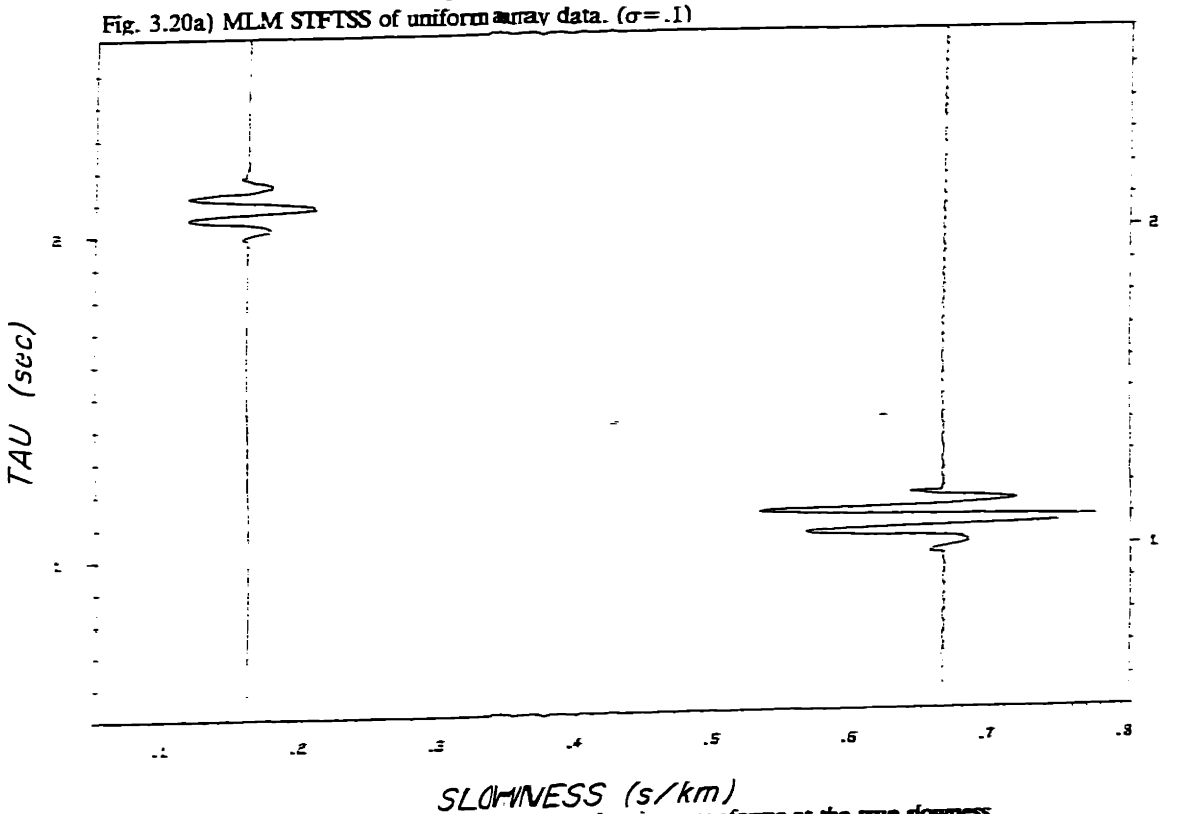

Fig. 3.20b) MLM STFTSS of uniform array data showing waveforms at the true slowness values. (σ=.1)

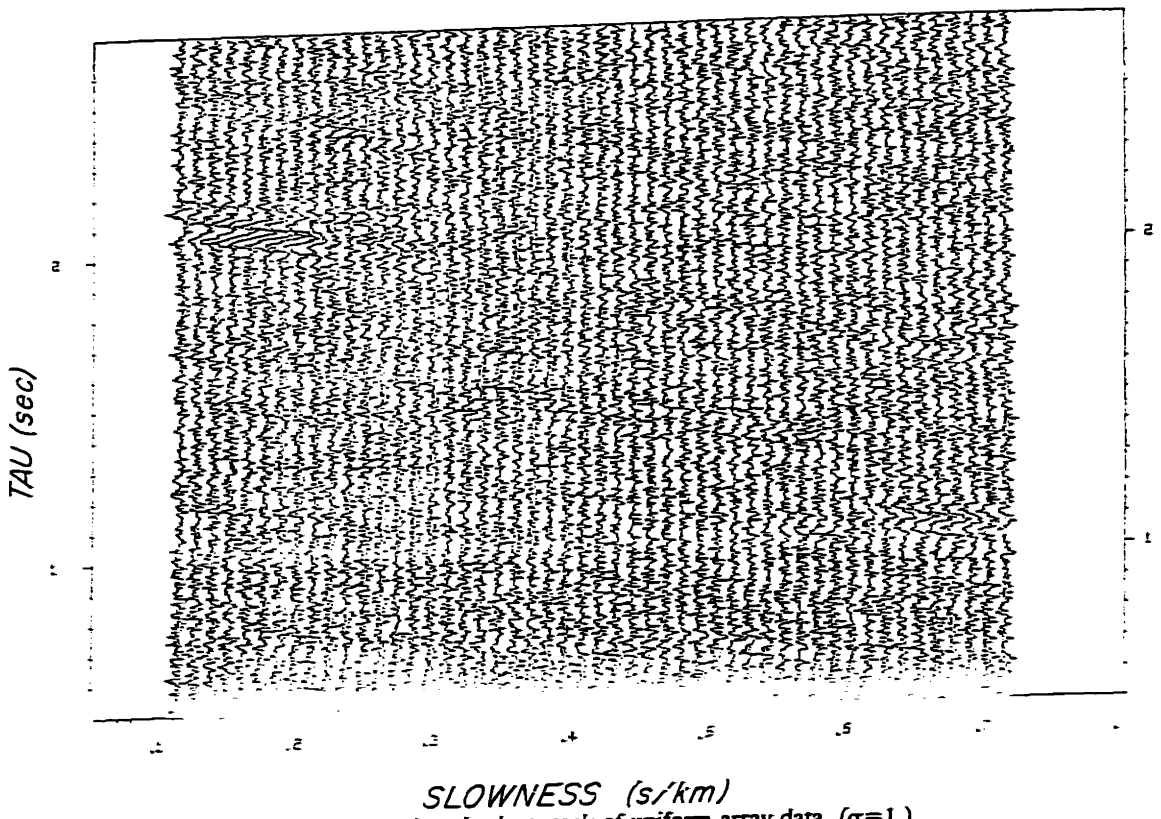

Fig. 3.21a) Conventional time-domain slant-stack of uniform array data. (σ=1.)

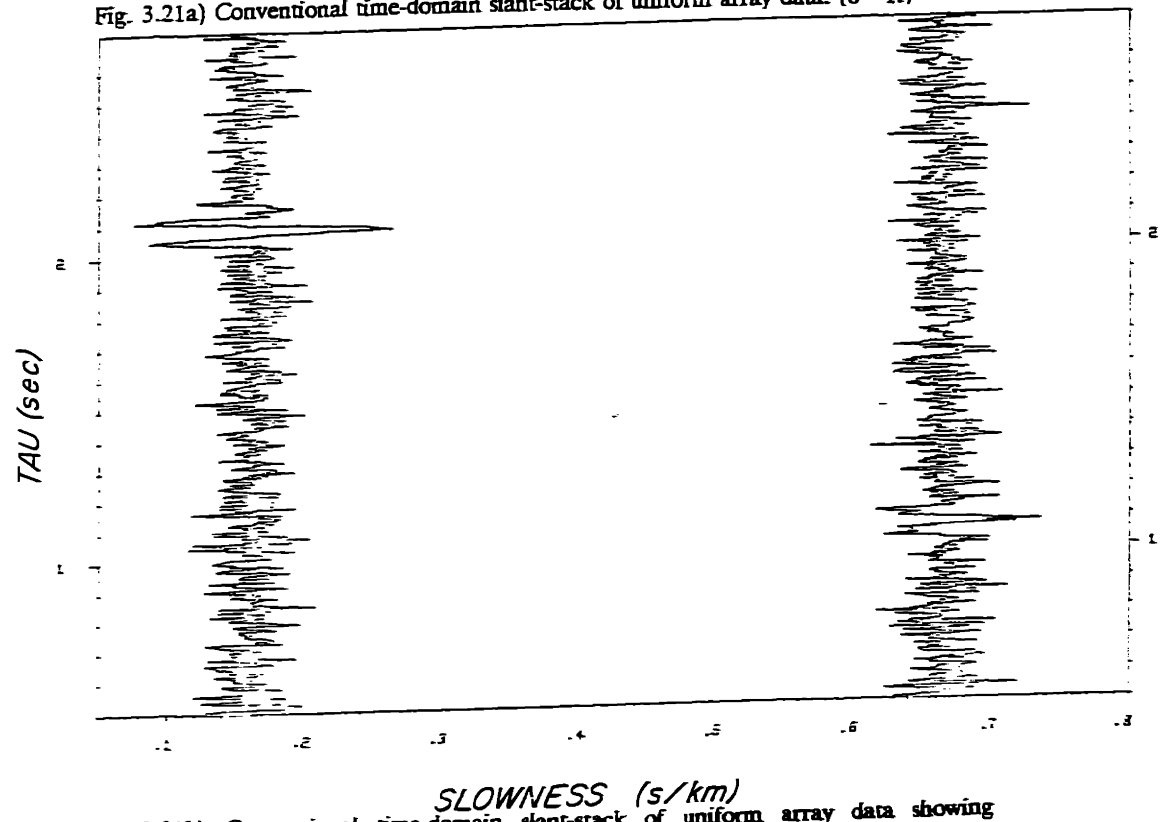

Fig. 3.21b) Conventional time-domain slant-stack of uniform array data showing waveforms at the true slowness values. (σ=1.)

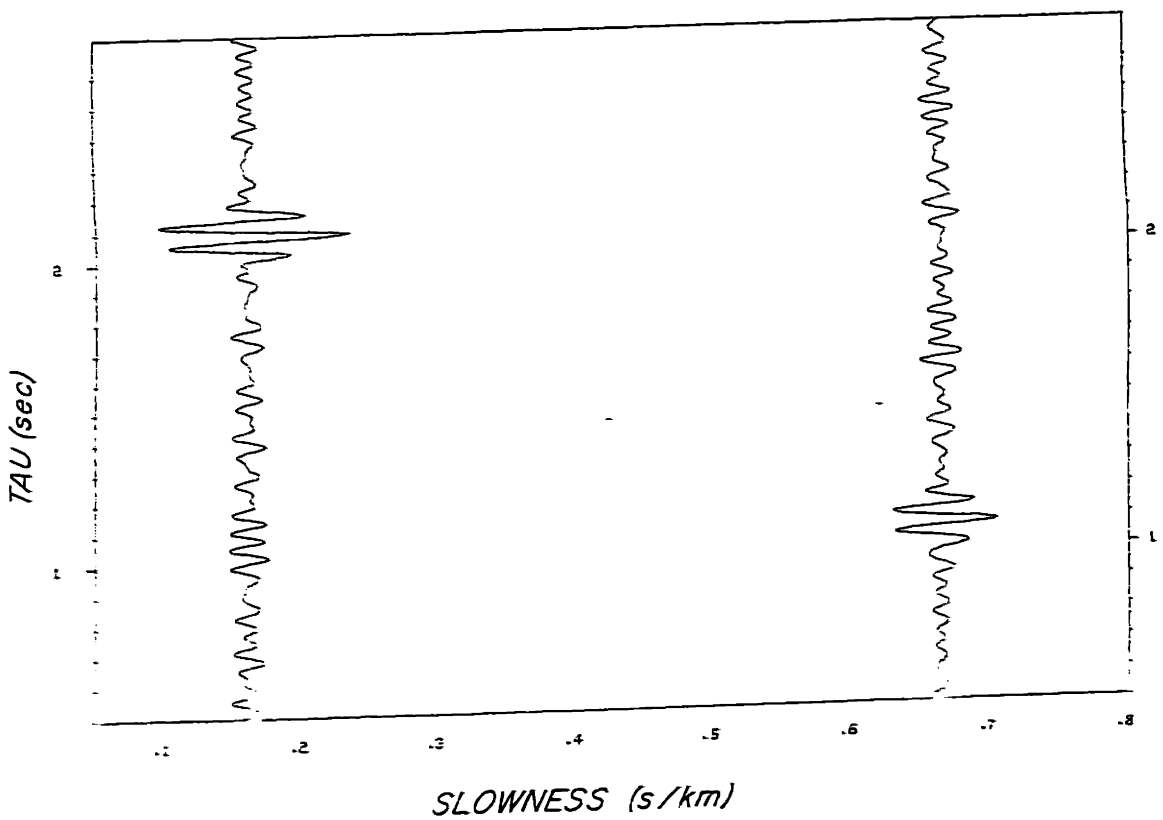

Fig. 3.21c) Conventional time-domain slant-stack of uniform array data after filtering. This plot shows the waveforms at the true slowness values. (σ=1.) (This plot is just a filtered version of fig 3.21b.)

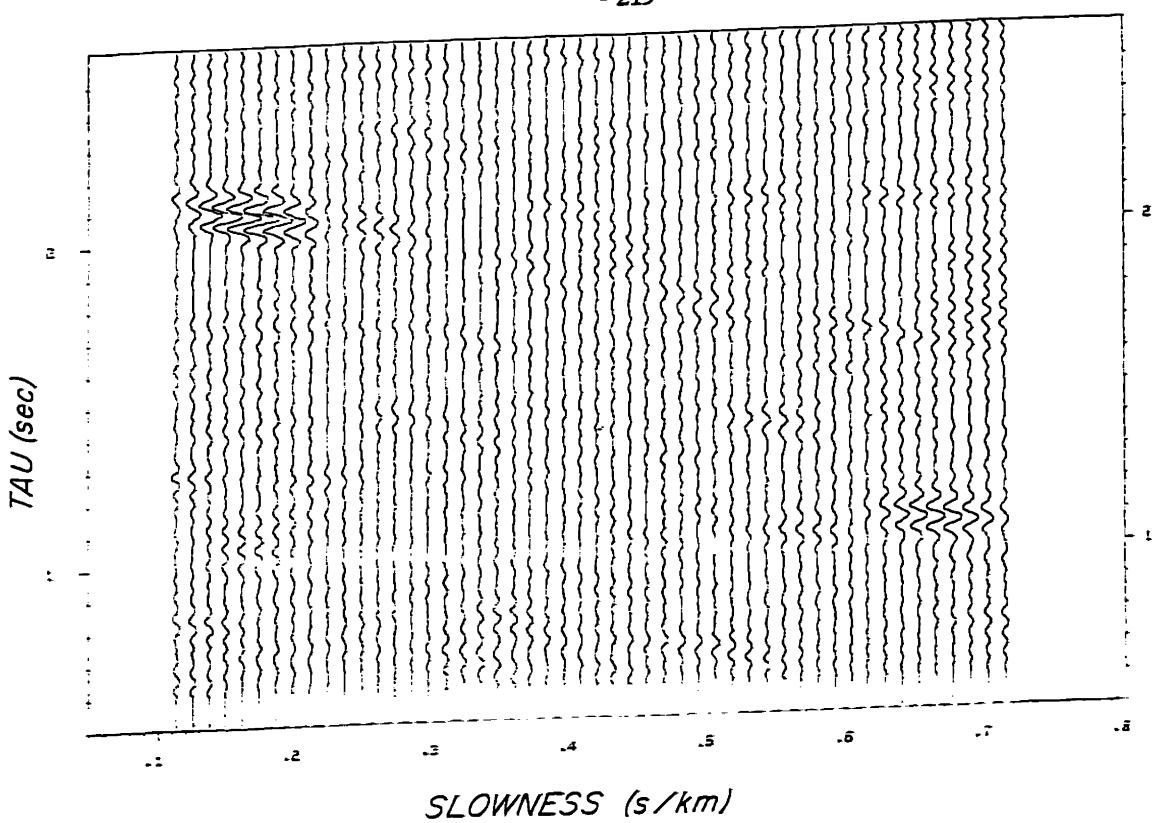

Fig. 3.22a) Conventional STFTSS of uniform array data. (σ=1.)

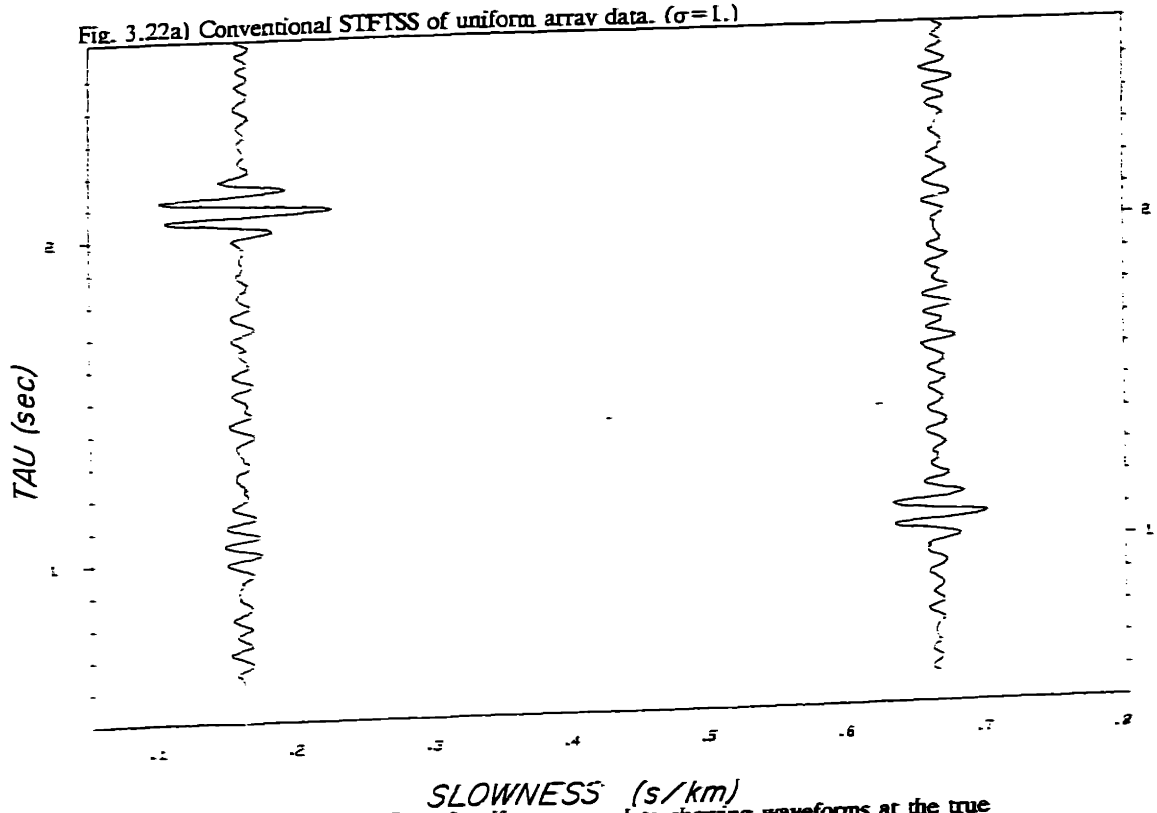

Fig. 3.22b) Conventional STFTSS of uniform array data showing waveforms at the true slowness values. (σ=1.)

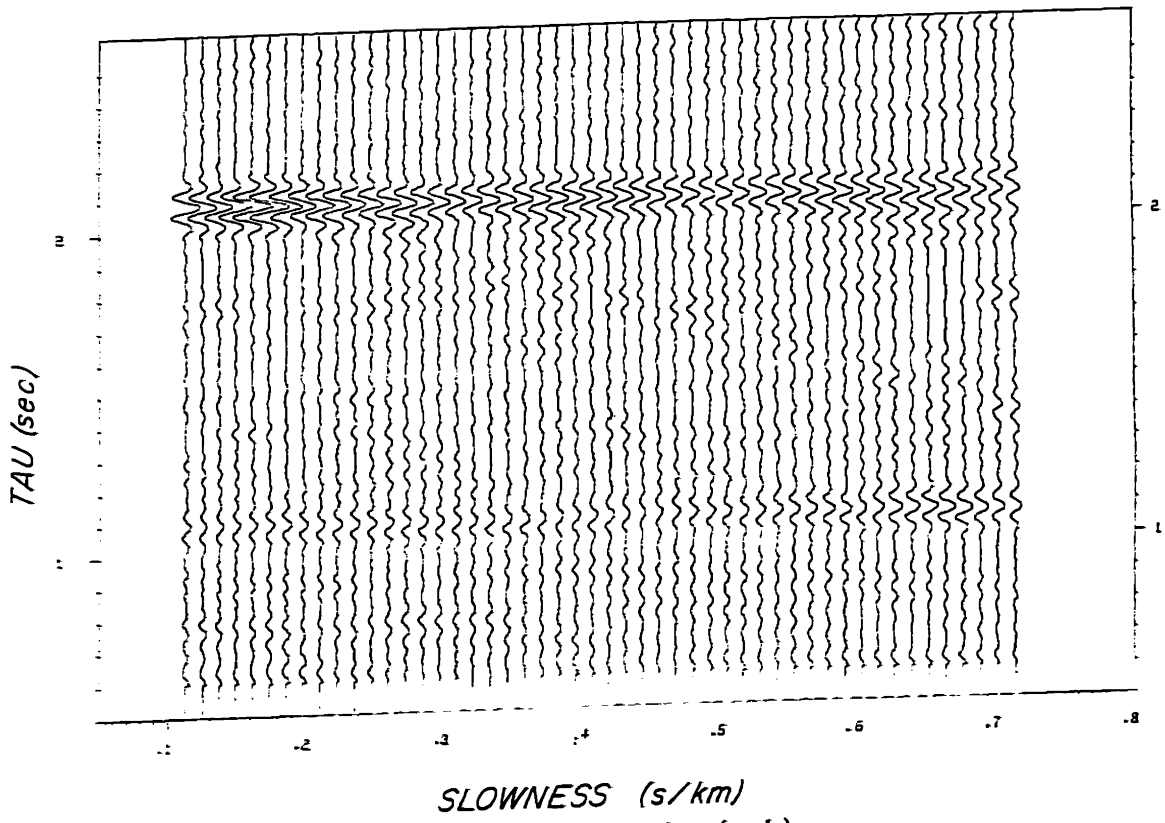

Fig. 3.22c) Conventional STFTSS of non-uniform array data. (σ=1.)

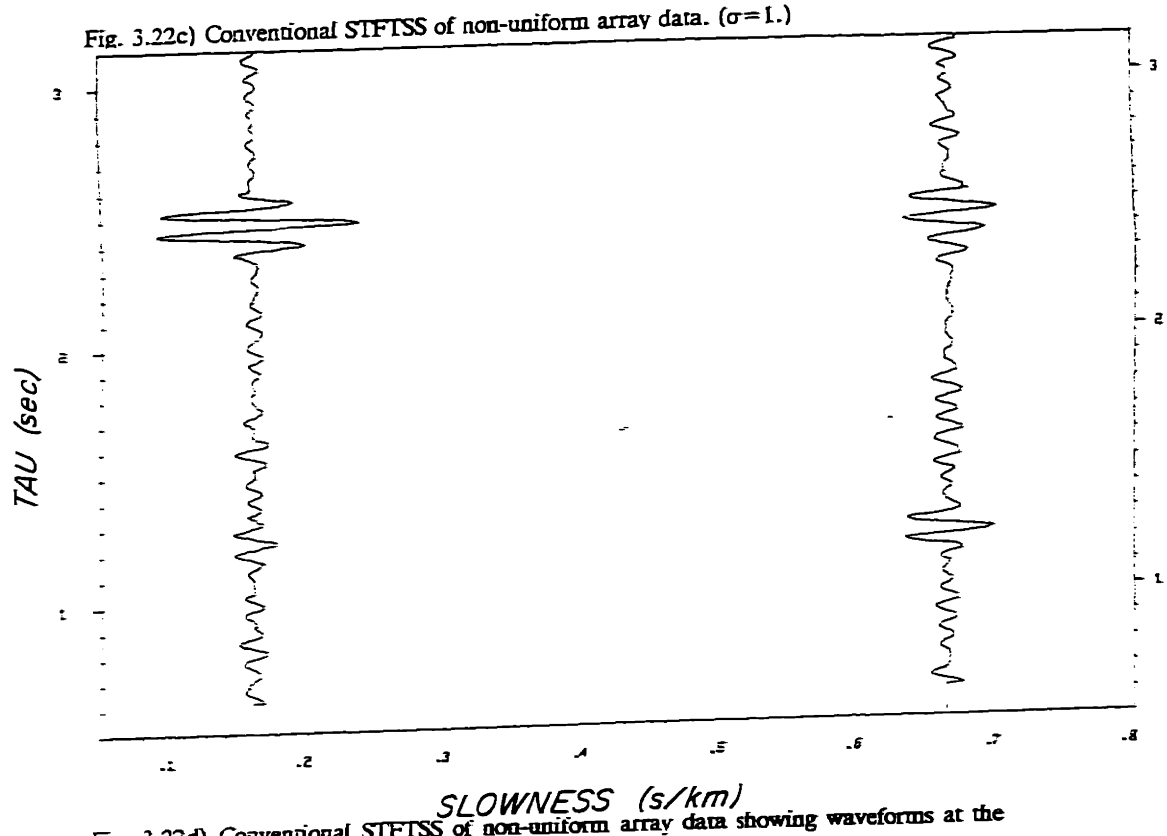

Fig. 3.22d) Conventional STFTSS of non-uniform array data showing waveforms at the true slowness values. (σ=1.)

slant-stack (compare 3.21c and 3.22b.) when reconstructed over the same bandwidth as the filtered time domain slant-stack. The performance of the STFTSS with the conventional processor on non-uniform array data is again poor, as seen in figures 3.22 c&d.

At a realistic noise level and on a uniform array, the STFTSS with MLM processing in figs. 3.23 a&b still shows significantly better sidelobes and aliasing suppression than the conventional processor (compare 3.23b and 3.22b). The output levels are highly biased, however the distortion of the waveforms due to the relative bias among the Fourier coefficients of about 3 dB is not significant. The relative bias between waves with 6 dB different power has increased to 9.5 dB. Recall that in table 3.4 the power bias for this same example was predicted to be 10.5 dB. The small amount of "jaggedness" in fig. 3.23 from piecing together the waveforms can be removed by post filtering to the reconstruction bandwidth. Figure 3.24 illustrates the effect of 10-20 Hz bandpass filtering on the data in fig. 3.23b.

Figures 3.23 c&d show the result of the STFTSS processor with MLM filtering on the non-uniform array data at the realistic noise level. The sidelobe artifacts are worse than those obtained from the uniform array; however, the results are far superior to those of the conventional processor in fig. 3.22 c&d.

A final test of the algorithm is re-inversion of the slant-stacked waveforms to obtain the wave-field. Since short aperture stacking was done, it is only valid to "extrapolate" the wave-field back to the original aperture. The re-inversion was done by:

$$P(t,r) = \int_{p_{min}}^{p_{max}} \hat{S}(\tau+pr,p)\,dp$$

since for these examples pure plane waves have been used and the $r^{\frac{1}{2}}$ cylindrical spreading factors have been dropped. Fig. 3.25a shows the wave-field that is obtained from the convention-

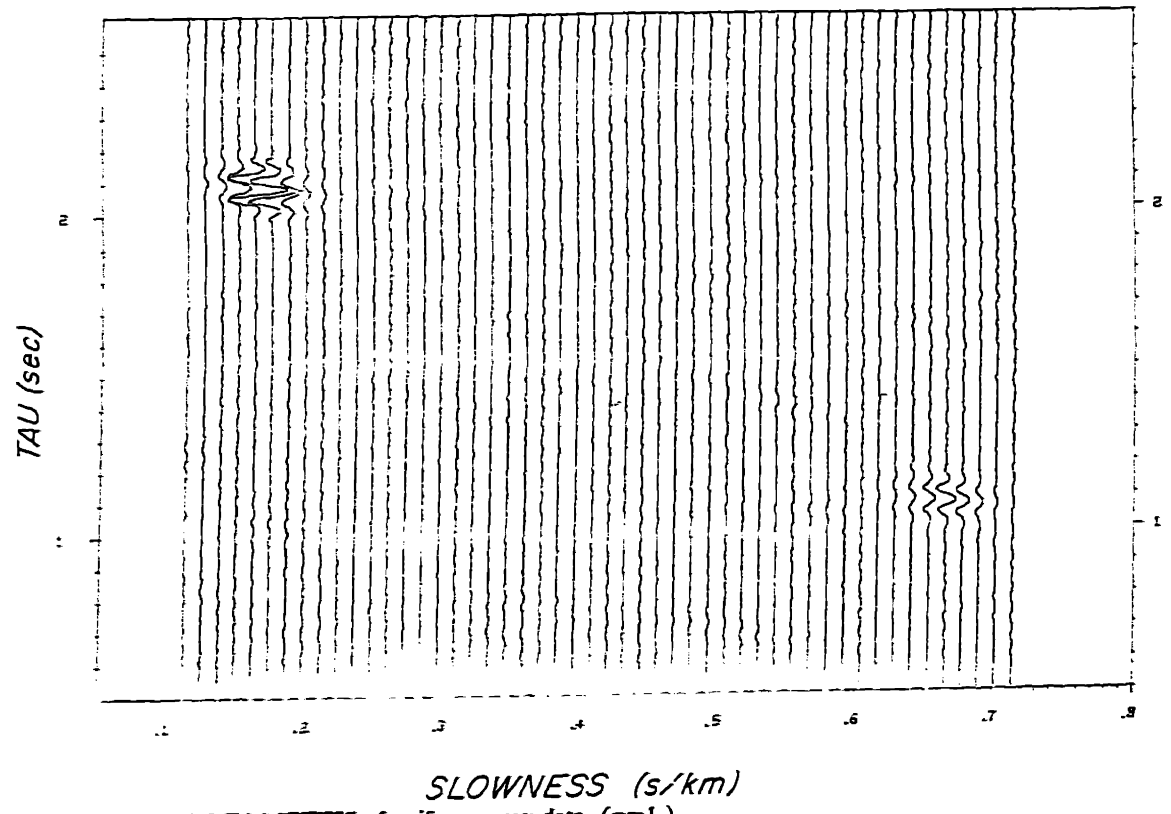

Fig. 3.23a) MLM STFTSS of uniform array data. (σ=1.)

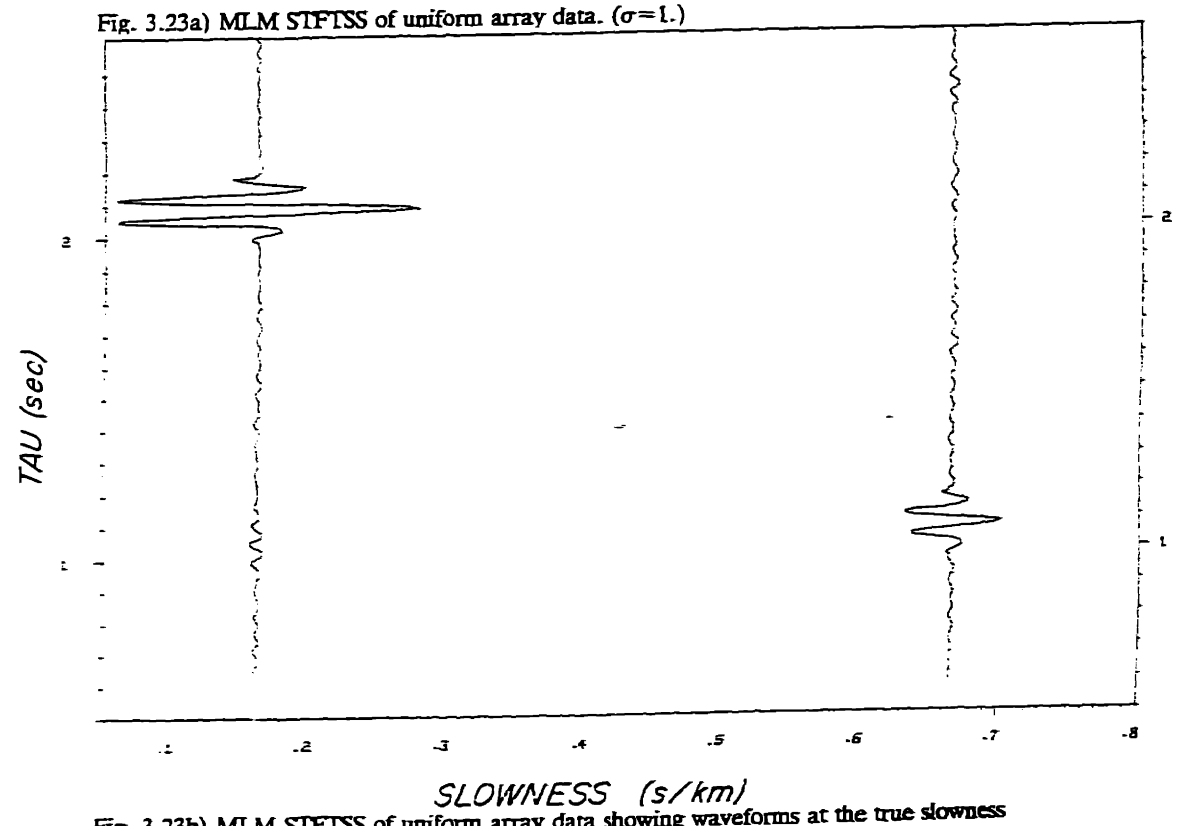

Fig. 3.23b) MLM STFTSS of uniform array data showing waveforms at the true slowness values. (σ=1.)

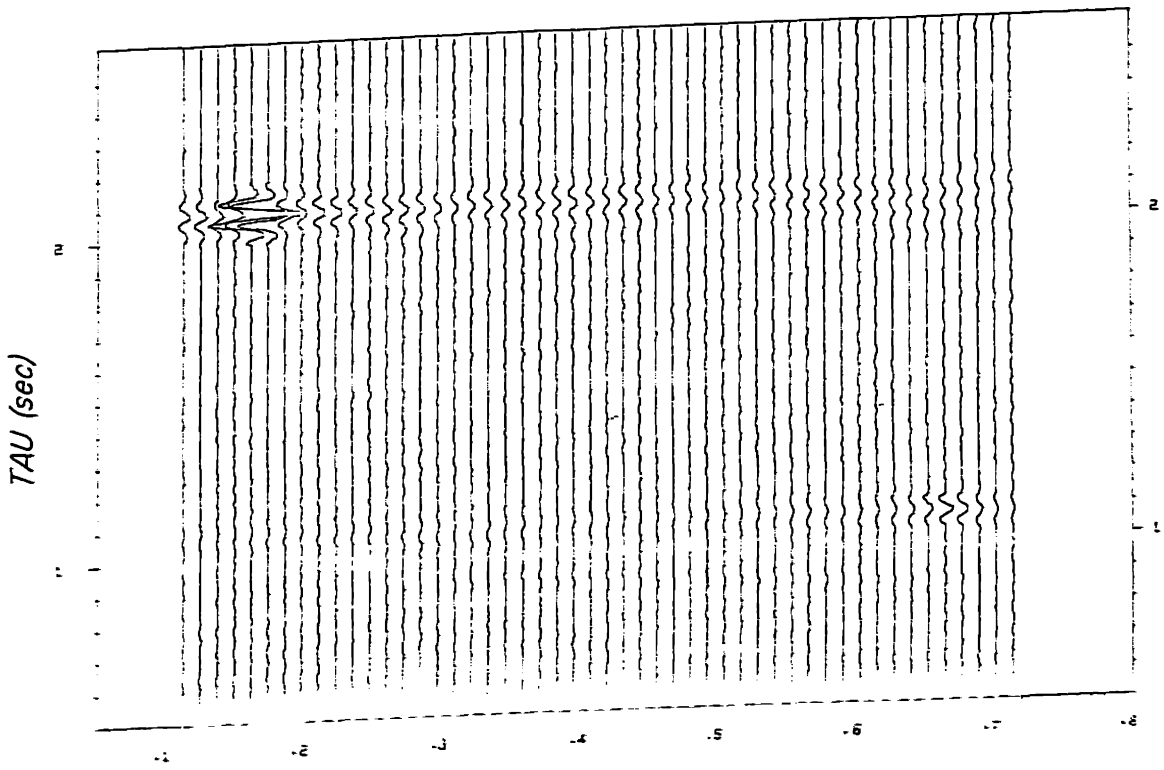

Fig. 3.23c) MLM STFTSS of non-uniform array data. (σ=1.)

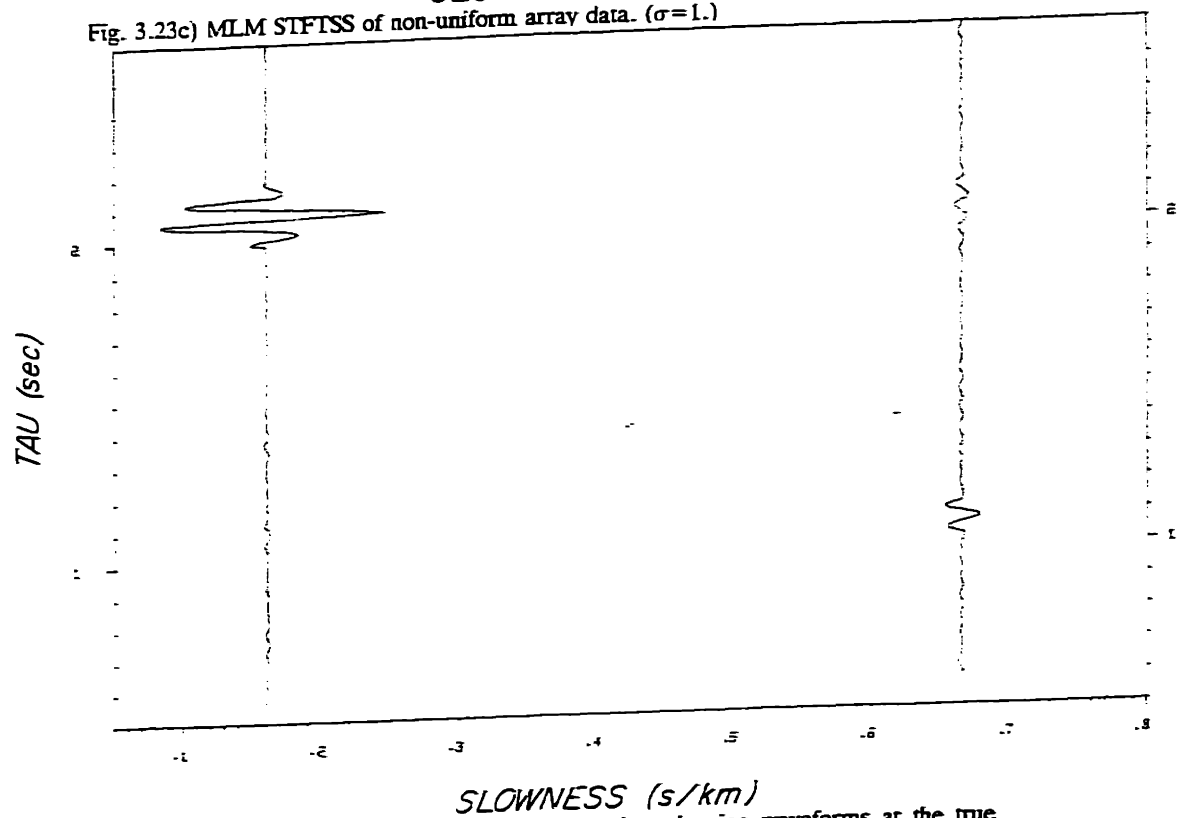

Fig. 3.23d) MLM STFTSS of non-uniform array data showing waveforms at the true slowness values. (σ=1.)

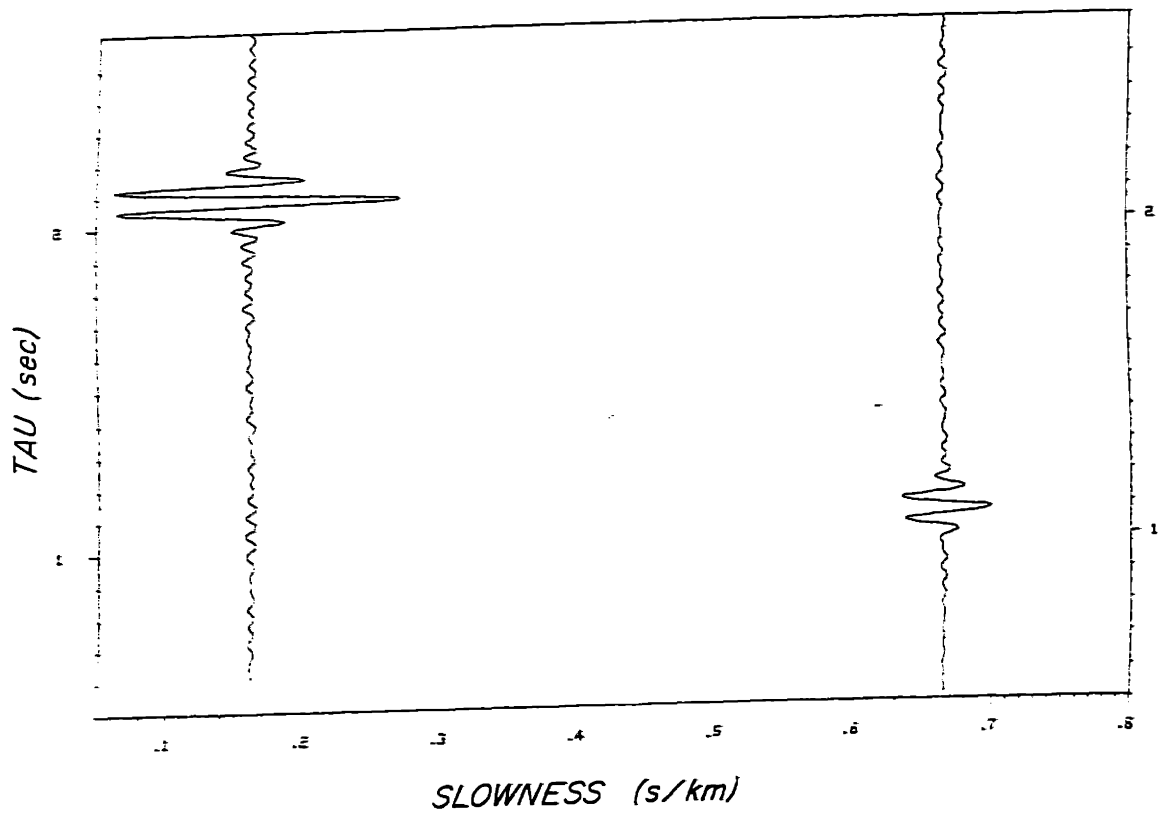

Fig. 3.24) MLM STFTSS of uniform array data showing waveforms at the true slowness values. (σ=1.) The waveforms of fig. 3.23b have been post filtered to the reconstruction bandwidth to eliminate the "joints" or discontinuities between the adjacent segments.

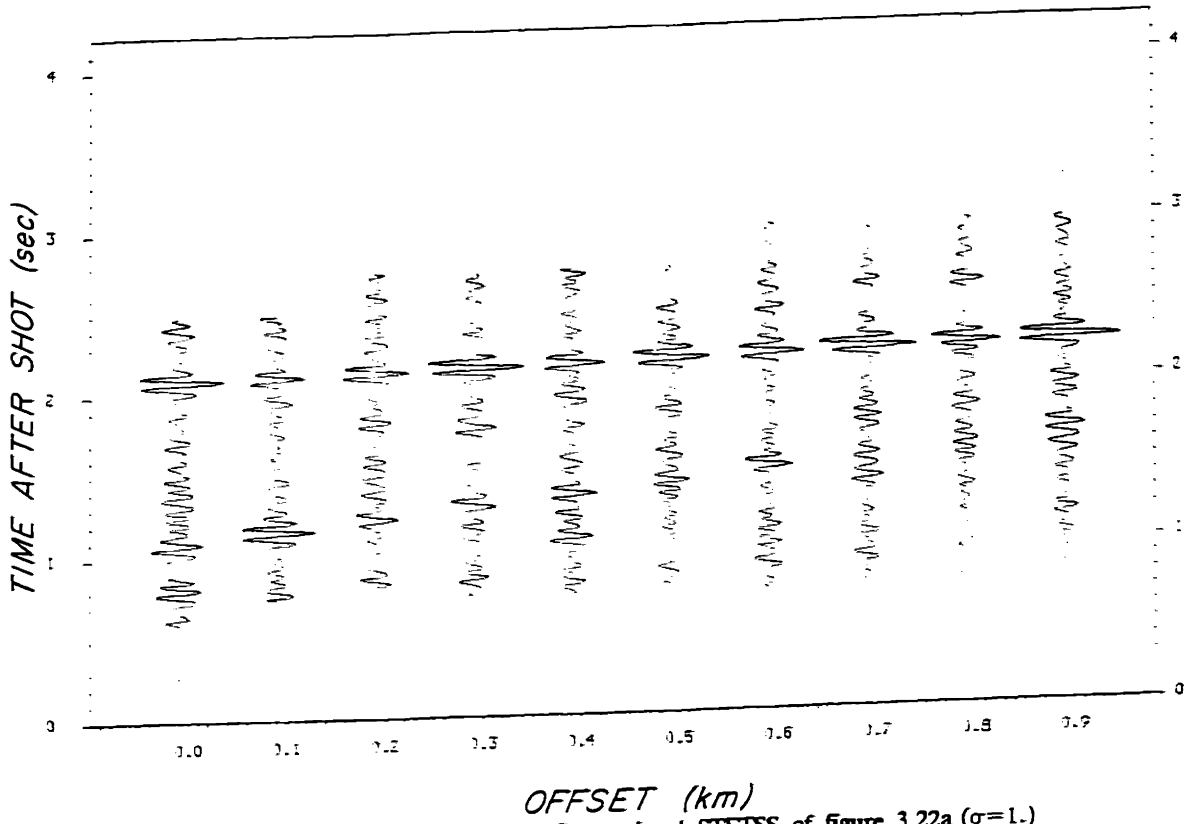

Fig. 3.25a) Reconstructed wave-field from the Conventional STFTSS of figure 3.22a (σ=1.)

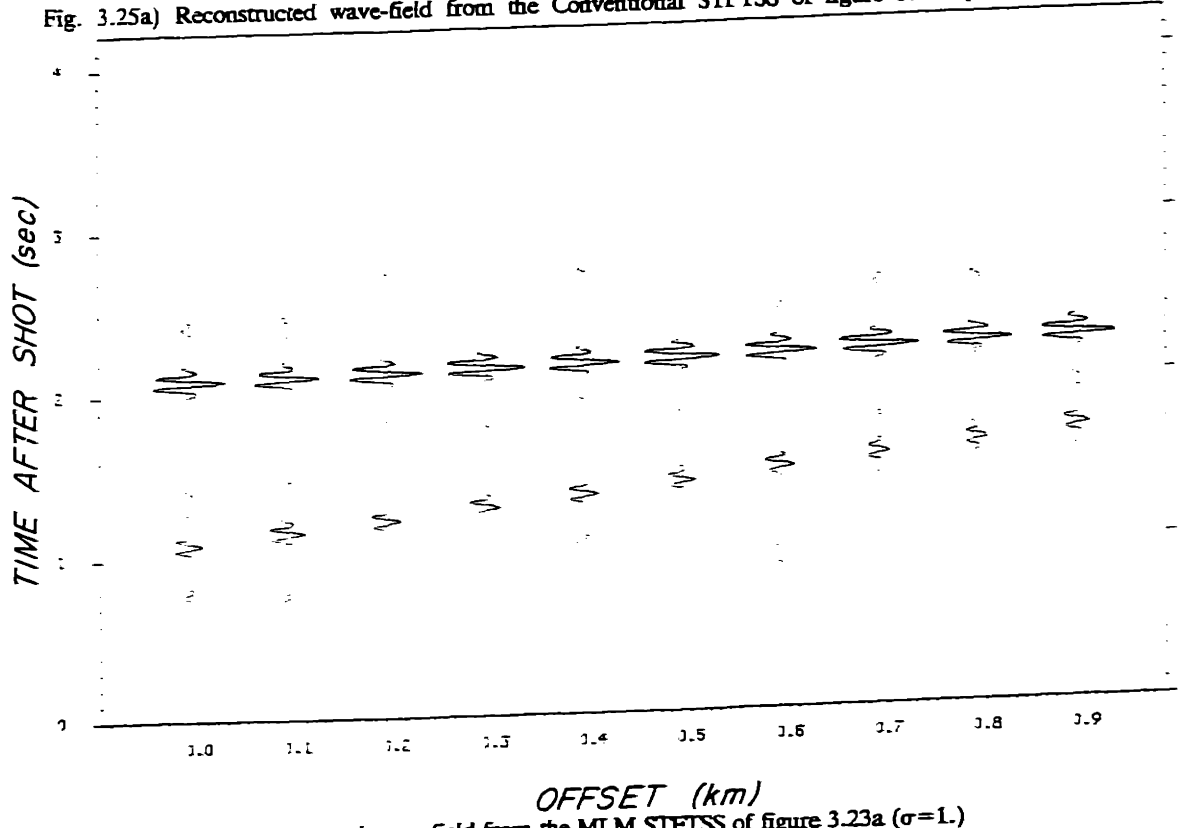

Fig. 3.25b) Reconstructed wave-field from the MLM STFTSS of figure 3.23a (σ=1.)

ally processed results of fig. 3.22a. Note that the interfering side lobes cause a great deal of waveform variation across the section (it should ideally look like fig. 3.17a since the noise has been reduced by the array gain and the temporal filtering.) The low-amplitude arrival is very poorly reconstructed. Figure 3.25b shows the result of re-inversion of the MLM processed data of fig. 3.23a. The lack of sidelobes and higher noise suppression give a reconstruction that is much more similar to the original noiseless data. (Note the vast improvement over the noisy data themselves in fig. 3.17c.) This shows that the STFTSS with MLM processing can be a very effective method for implementing velocity filters.

A final test of the algorithm is on real data taken on the Fram 2 experiment. The raw data are plotted in figs. 3.26 a&b. The data are positioned correctly for the projection of the 22-channel 2-D surface array onto the propagation direction, i.e. the equivalent radial linear array. The data are from a 25 kg explosive detonated at 243 m at the distances from the sensors shown on the plot. Figure 3.26a is plotted at a gain of 30 with respect to fig. 3.26b and the powerful water column arrivals have been clipped for the plot. This is the same dataset that was processed to obtain the velocity spectra of figs. 3.15, using a nominal offset of 19.4 km. The standard time domain slant stack results from "zero-offset" processing are shown in figures 3.27 a&b. Fig 3.27a shows the direct water wave and first sediment arrivals. The sidelobe and aliasing artifacts are clearly visible at the smaller slownesses. The higher velocity deep crustal arrivals are not well resolved in slowness on the higher plotting gain plot, fig. 3.27b. Figures 3.28 contain the same data processed with the STFTSS using MLM beamforming. For these examples, the window length was $T = .248$ sec, and the reconstruction subsequence length for each window was $\delta t = .084 = T/3$ seconds. The Fourier coefficients at 7.8, 11.7, 15.6, and 19.5 Hz were used for the reconstruction. Figure 3.28a shows the direct water and first sediment arrival. Note that the response is very sharp in slowness compared to the

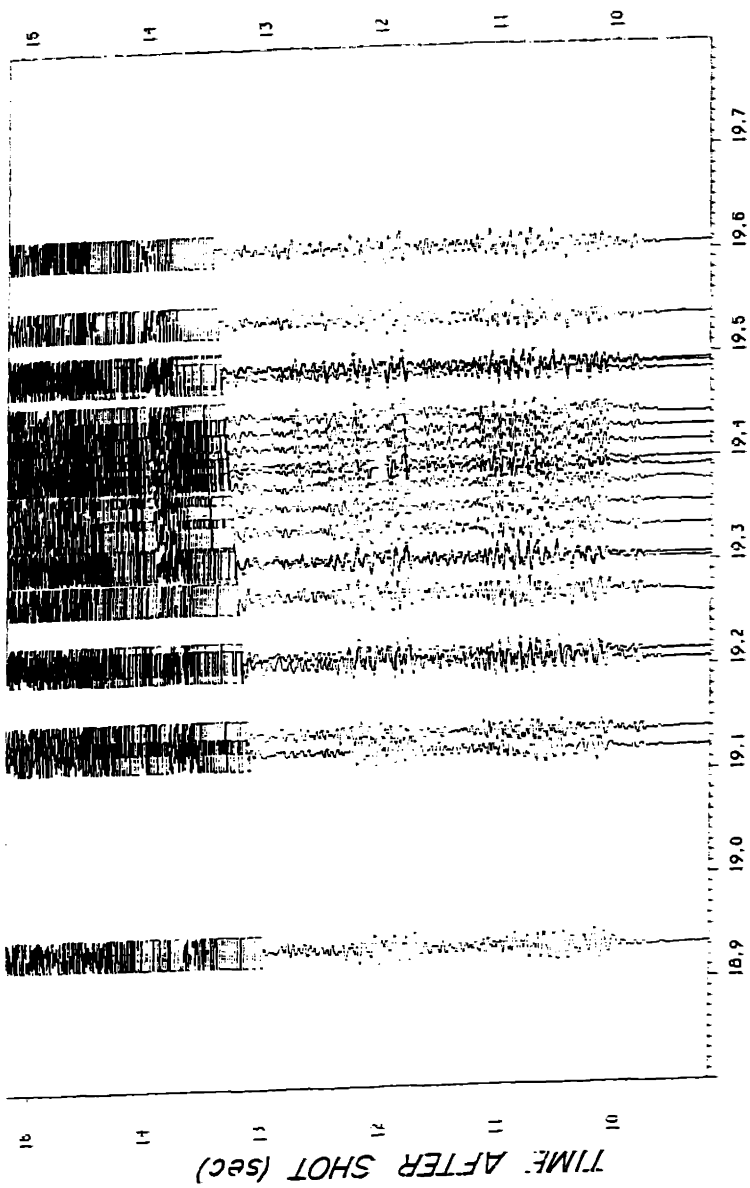

Fig. 3.26a) Refraction data from Fram 2, reel 3044 (18.9 km), 55# charge. The 2-D array has been projected onto the direction of propagation to show the equivalent linear array configuration. The plotting scale factor is .3.

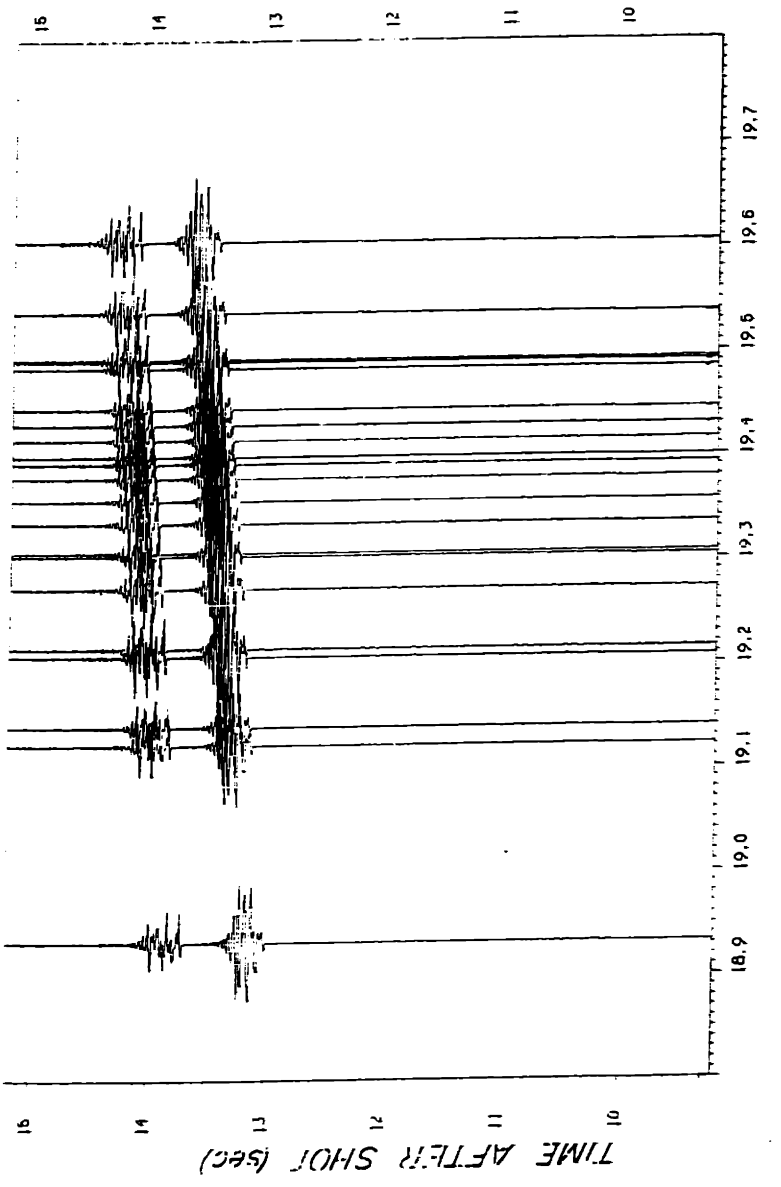

Fig. 3.26b) The same data as in fig. 3.26a, but plotted with a scale factor of 0.01 to linearly plot the direct water arrival.

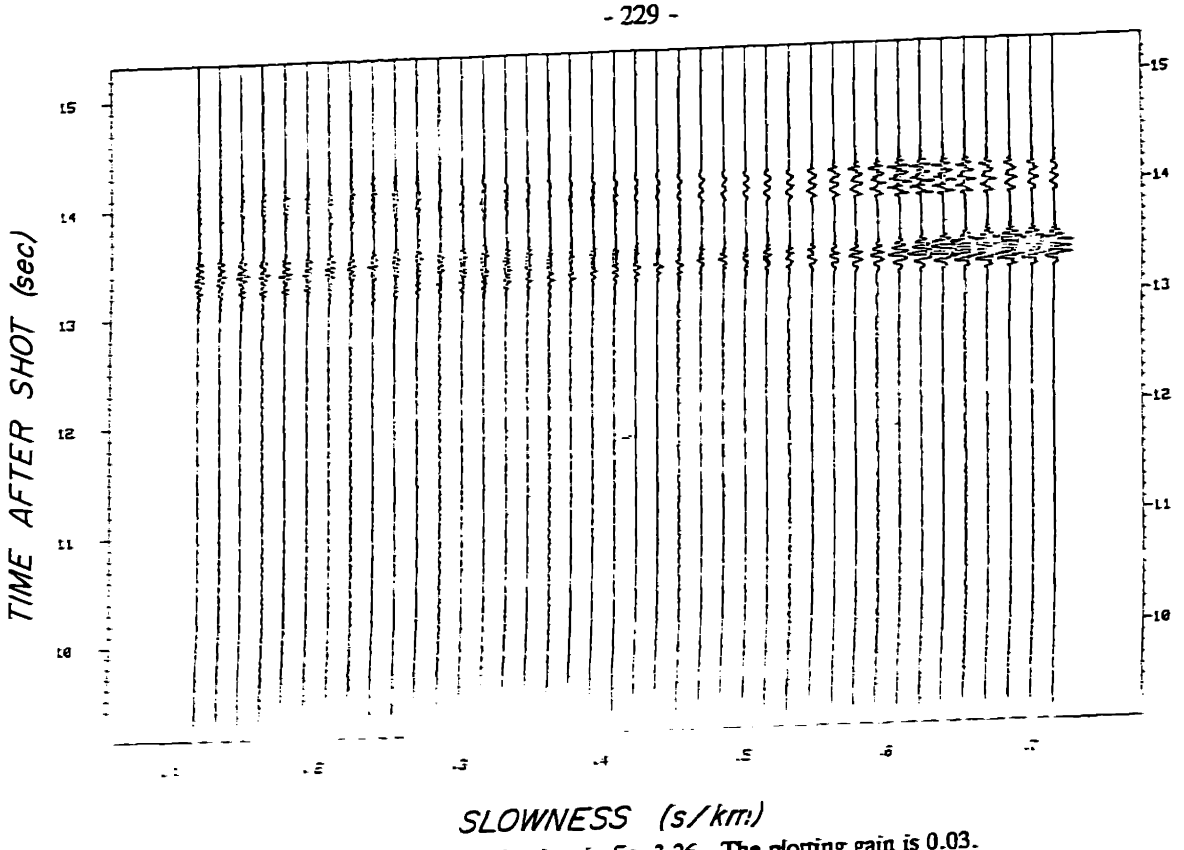

Fig. 3.27a) Conventional STFTSS of the data in fig. 3.26. The plotting gain is 0.03.

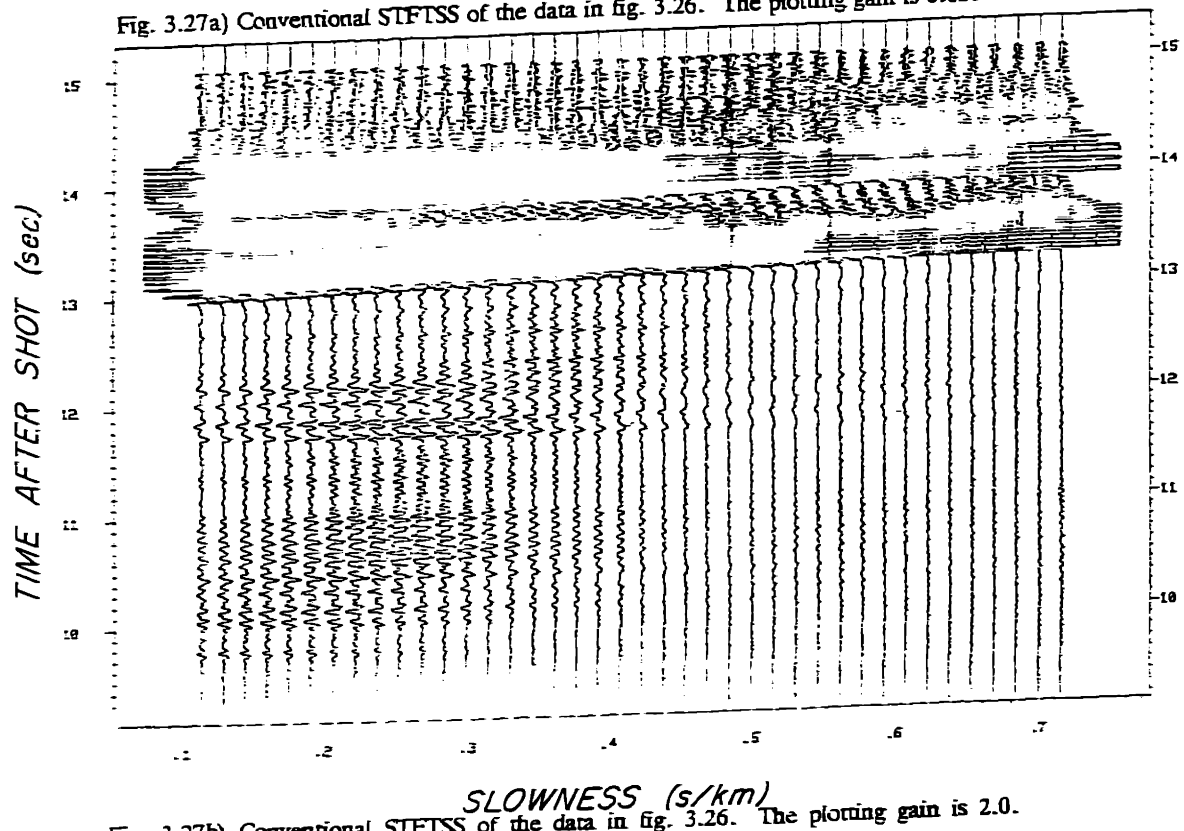

Fig. 3.27b) Conventional STFTSS of the data in fig. 3.26. The plotting gain is 2.0. (Same data as fig. 3.27a)

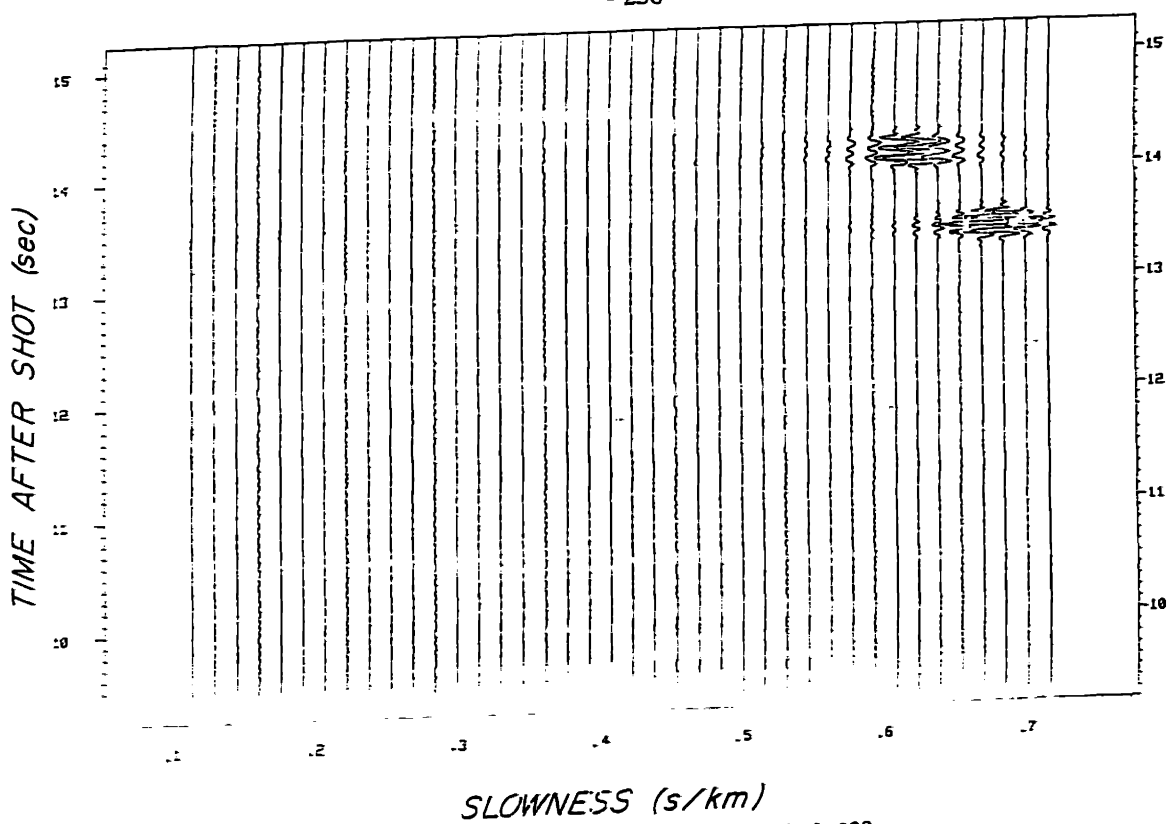

Fig. 3.28a) MLM STFTSS of the data in fig. 3.26. The plotting gain is 100.

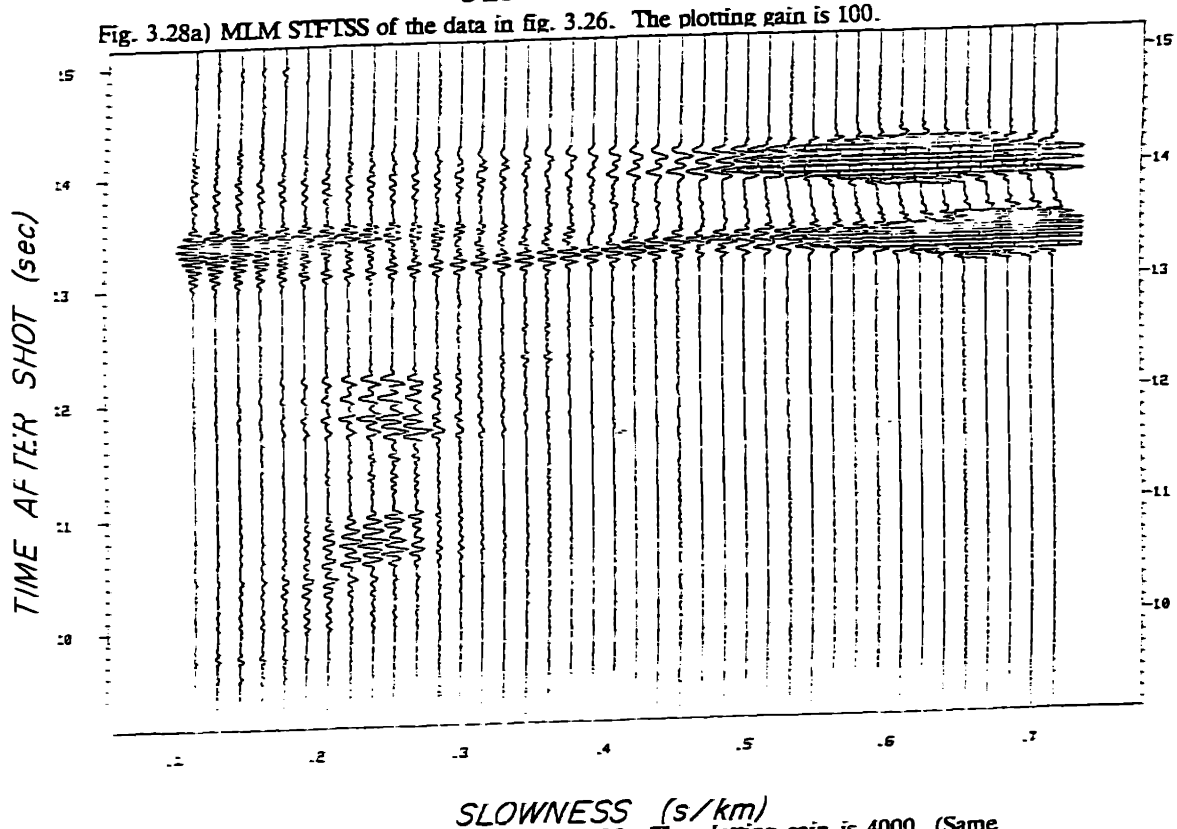

Fig. 3.28b) MLM STFTSS of the data in fig. 3.26. The plotting gain is 4000. (Same data as fig. 3.28a)

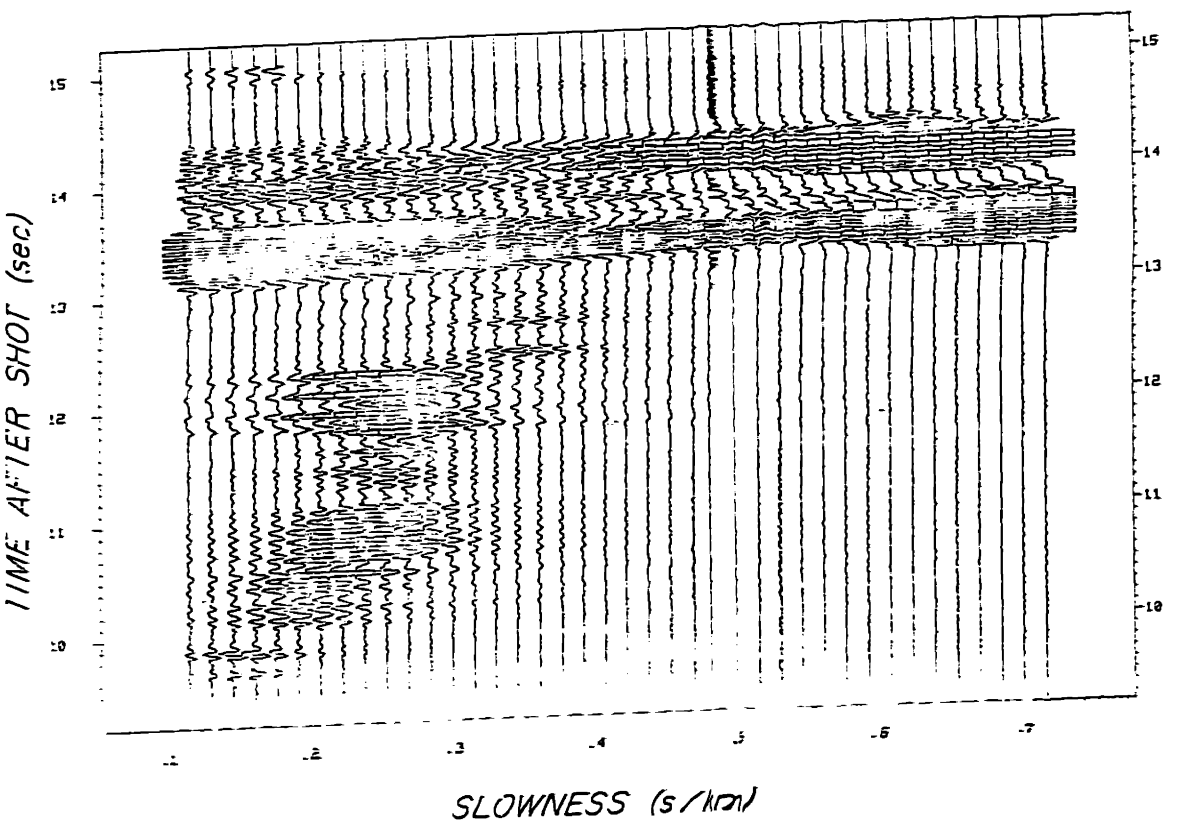

Fig. 3.28c) MLM STFTSS of the data in fig. 3.26. The plotting gain is 20000. (Same data as fig. 3.28a)

figure 3.27a, and the aliasing and sidelobes are suppressed. Fig. 3.28b shows the result when the plotting gain has been increased by a factor of 40. The sediment and shallow crustal arrivals are well constrained in slowness, and the effects of aliasing are noticeable, but highly suppressed when compared to the time domain results. The 2 distinct regions of aliasing from the direct water arrival at about 13.4 seconds and .1-.3 s/km are due to the few widely separated sensors for this array. This effect is visible on the noiseless slant stack comparisons of the uniform and non-uniform arrays of figures 3.18. Increasing the plotting gain by another factor of 5 gives fig. 3.28c. The weaker arrivals, such as the layer-3 arrival at $p = .15$ s/km are visible. Note by comparison with the time domain stack that the individual wavelets are relatively undistorted, the main difference being due to some additional band limiting on the STFTSS results.

SUMMARY

In this chapter I have presented a detailed analysis of the properties of velocity spectral analysis on short aperture data. The effects of various causes of non-planarity of the waves and some of the effects of non-ideal propagation and experimental conditions were examined. One important result of this work is that it was shown that the velocity spectral analysis estimate of arrival times is not influenced by wavelet phase shifts. This will be shown to be helpful in the use of the arrival time data for inversion for crustal structure in chapter 4.

The velocity spectral analysis algorithm using the Maximum Likelihood Method was presented in great detail, and the effects due to violation of the assumptions used to derive the algorithm were examined. The statistics of the arrival time, slowness, and amplitude estimator performance were characterized by Monte Carlo simulations, and shown to agree with theoretical predictions.

Finally, the STFTSS (Short-Time Fourier Transform Slant-stack) algorithm for high resolution velocity filtering of short aperture data was presented and examples of its performance were given. This algorithm uses the Maximum Likelihood filters computed using statistical estimates from short segments of the data to compute the time evolution of the plane wave from a given direction with optimal rejection of uncorrelated sensor noise and propagating signals from other directions. The advantage of the algorithm is that it obtains slant-stacks over small apertures that are less influenced by the sampling pattern and dimensions of the array than conventional slant stacks or beamforming. The difference between this algorithm and standard adaptive beamforming lies in the fact that the filters used change with time evolution of the data, thus acommodating transient signals.

REFERENCES

Aki, K. and Richards, P.G., in *Quantitative Seismology: Theory and Methods*, San Francisco: W.H. Freeman, 1980.

al., R.T. Lacoss et, *Distributed Sensor Network Semi-Annual Reports*. MIT Lincoln Laboratory, 1978-1983.

Alterman, Z. and Loewenthal, D., "Computer generated seismograms," in *Methods in Computational Physics*, ed. B.A. Bolt, New York, NY: Academic Press, 1972, pp. 35-164.

Boore, D.M., "Finite difference methods for seismic waves," in *Methods in Computational Physics*, ed. B.A. Bolt, New York, NY: Academic Press, 1972, pp. 1-35.

Brocher, T.M. and Phinney, R.A., "Inversion of slant stacks using finite-length record sections," *Journal of Geophysical Research*, vol. 86, no. B8, pp. 7065-7072, 1981.

Capon, J., "High Resolution Frequency-Wavenumber Analysis," *Proceedings of the IEEE*, vol. 57, no. 8, August 1969.

Capon, J., Greenfield, R.J., and Lacoss, R.T., "Long period signal processing results for the large aperture seismic array," *Geophysics*, vol. 34, pp. 305-329, 1969.

Cerveny, V., "Seismic rays and ray intensities in inhomogeneous anisotropic media," *Geophysical Journal of the Royal Astronomical Society*, vol. 29, pp. 1-13, 1972.

Cerveny, V., "Synthetic body wave seismograms for laterally inhomogeneous media by the Gaussian beam method," *Geophysical Journal of the Royal Astronomical Society*, vol. 73, pp. 389-426, 1983.

Chapman, C.H., "A New Method for Computing Synthetic Seismograms," *Geophysical Journal of the Royal Astronomical Society*, vol. 54, pp. 481-518, 1978.

Chapman, C.H. and Drummond, R., "Body-wave seismograms in inhomogeneous media using Maslov asymptotic theory," *BSSA (in press)*, 1982.

Dove, W.P., "Event Compression Using Recursive Least Squares Signal Processing," MIT Research Laboratory of Electronics Technical Report 492, Cambridge, MA, July, 1980.

Duckworth, G.L., *Adaptive Array Processing for High Resolution Acoustic Imaging*. S.M. and E.E. Thesis, Massachusetts Institute of Technology; Department of Electrical Engineering and Computer Science, February, 1980.

Duckworth, G.L., "Array Processing for High Resolution Acoustic Imaging," *Acoustical Imaging, Vol. 9*, Plenum Press, 1980.

Gammelsaeter, O.B., "Adaptive Beamforming with Emphasis on Narrowband Implementation," in *Underwater Acoustics and Signal Processing*, ed. L. Bjorno, Dordrecht, Holland: D. Reidel Publishing Co., 1981.

Garmany, J., "Amplitude constraints in linear inversion of seismic data," *Journal of Geophysical Research*, vol. 87, no. B10, pp. 8426-8434, 1982.

Jobert, G., "Linear formulation of the inverse problem for the amplitude of seismic waves," *Geophysical Journal of the Royal Astronomical Society*, vol. 69, pp. 841-844, 1982.

Jurkevics, A., Wiggins, R., and Canales, L, "Body-wave inversion using travel time and amplitude data," *Geophysical Journal of the Royal Astronomical Society*, vol. 63, pp. 75-93, 1980.

Kelley, K.R., Ward, R.W., Treitel, S., and Alford, R.M., "Synthetic Seismograms: a finite-difference approach," *Geophysics*, vol. 41, pp. 2-27, 1976.

Lacoss, R.T., "Data Adaptive Spectral Analysis Methods," *Geophysics*, vol. 36, pp. 661-675, 1971.

Lang, S.W., "Spectral Estimation for Sensor Arrays," *Ph.D. Thesis*, Massachusetts Institute of Technology, Aug. 1981.

Leverette, S., *Data Adaptive Velocity/Depth Spectra Estimation in Seismic Wide Angle Reflection Analysis*. Ph.D. Thesis, Joint Program in Ocean Engineering, Massachusetts Institute of Technology and Woods Hole Oceanographic Institution, October, 1977.

Lim, J.S. and Malik, N., "A New Algorithm For Two-Dimensional Maximum Entropy Power Spectrum Estimation," *IEEE Trans. ASSP*, pp. 401-413, June 1981.

McClellan, J.H., "Multidimensional Spectral Estimation," *Proceedings of the IEEE*, vol. 70, no. 9, pp. 1029-1039, 1982.

Neidell, N.S. and Taner, M.T., "Semblance and other Coherency Measures for Multichannel Data," *Geophysics*, vol. 36, no. 3, pp. 482-497, June 1971.

Scheer, E., Cambridge, MA: S.M. thesis, Joint Program of the Massachusetts Institute of Technology and the Woods Hole Oceanographic Institution, 1982.

Steinberg, B.D., in *Principles of Aperture and Array System Design*, New York, NY: John Wiley and Sons, 1976.

VanTrees, H.L, *Detection, Estimation, and Modulation Theory: Part I*. New York, NY: John Wiley and Sons, 1968.

Weinstein, E., Ianiello, J.P., and Weiss, A, "A comparison of the Ziv-Zakai lower bound on time delay estimation with correlator performance," *Proceedings of the ICASSP '83*, IEEE Press, 1983.

CHAPTER 4: Inversion Methods for Refraction Data

INTRODUCTION

Chapter 3 was prefaced with some remarks that argued for the omission of observations from the data to be inverted which are most sensitive to aspects of the earth that are not accounted for by the model. For example, with data sparsely sampled in offset, lateral variation is very difficult to quantify. For this reason, only laterally homogeneous models have been considered in this work. Purdy [1981] has shown that seemingly minor lateral changes, such as seabottom topography, can markedly influence observed surface amplitude structure, while leaving travel-times relatively unaffected. Since the amplitude observations are, in effect, almost decoupled or independent of the model parameters in the assumed layered structure, there is often little advantage to their inclusion in the data to be inverted. Similarly, if shear conversions are not accounted for in the amplitude modeling energy balance, the compressional model indicated will be biased. One may, of course, ascribe a high degree of variability to these measurements, and consider the data weighted by one's confidence in them; however, some inversion structures cannot easily accommodate this. Other inversion methods are unsuited to inclusion of amplitude data from their formulation. For all these reasons, we will be concerned primarily with inversion of the robust travel-time data.

One of the advantages of velocity spectral analysis is that it smooths waveform details that are in large part unpredictable using simplified layered models. Waveform phase shifts, attenuation filtering, and scattering effects are removed, and as was seen in Chapter 3, arrival times, offsets, and the waveform envelope power are estimated. These data are precisely what are most useful for travel-time inversions. (Envelope power can be useful for amplitude studies, subject to the caveat above.) In addition, it is possible to efficiently compute predictions

of the velocity spectral analysis output using modifications to currently existing synthetic seismogram techniques. This points to a possible linearized least squares joint travel-time and amplitude inversion algorithm in which the velocity spectra are the error domain. The problems with such complete techniques are threefold. First, most datasets are inadequate to provide a single global solution for which the error is significantly lower than the multitude of local minima. The algorithms thus tend to get stuck on local minima with the wrong model parameters. Second, for sparse data, and fairly general models (i.e. nearly overdetermined), the local minima are often quite deep. The formulation of algorithms that can get "unstuck" in these conditions is quite difficult. Finally, algorithms that do tend to approach global minima usually do so because of liberal application of prior information or the use of very simple model parameterizations (e.g. laterally homogeneous, few degrees of freedom). In these cases, the prior information, and data which are not predictable, but remain included in the dataset, serve to wrongly bias the inversion result.

In the writer's experience, the most severe problem is the inability of simplified models to predict all arrivals. For this reason it is necessary to selectively remove data to achieve datasets that *could* be measured if the earth had the model structure, and then to choose the parameters in the model structure that cause the predicted data to best agree with the observations. The situation is exactly analogous to the matched filtering problem, and can be interpreted in terms of ambiguity functions and noise levels. The assumed model structure is equivalent to the waveform shape. (By model structure, I mean the choice of whether to use homogeneous layers or gradients, elastic or acoustic formulations, whether to allow lateral homogeneity or not, etc.) The parameters to be estimated are the layer velocities, gradients, densities,...,etc., depending on the complexity of the assumed model. These are equivalent to the trial arrival times in the time delay estimation via a matched filter problem discussed in Chapter 3. The

(multidimensional) ambiguity function is the output of the system shown in figure 4.1 as a function of changes in the trial earth parameters when there is no observation noise. Note that the source parameters and acquisition parameters remain as variables, since the shape of the ambiguity function depends on them, and they should be optimized to yield the desired ambiguity function shape with respect to the earth model parameters. These parameters are not really in the same category as the earth model parameters because, ostensibly, they are known, and are not part of the search space in the inverse problem. The diagram in figure 4.1 defines a very general inversion structure, and figure 4.2 shows the output for a 2-trial earth parameter system.* The experiment must first be designed to exhibit good curvature of the ambiguity function peaks, so that good earth parameter resolution in the presence of noise will be achieved. The other local maxima should be small with respect to the "main lobe," or outside the region of feasible models so that they need not even be considered, such as the peak at (x_2,y_2) in figure 4.2. All this could be done if only the true earth model structure were known; however, it is not. As a result, the ambiguity function typically becomes quite multimodal, with no guarantee that the model parameters which yield the global peak yield a model which is close to the true model. In addition, the lack of "matching" will cause the peak curvature and processing gain to be very low, leading to poor statistical stability of the estimated parameters at the peak when noise is present. An extremely simple example is illustrated in figure 4.3. The 2-layered true earth model, a ray diagram for a particular offset, and the observations are shown in figure 4.3a. The assumed earth model is a single layer, and the

---

*Since the parameter space is large, most inversion schemes start with an initial model, then compute the change in parameters that moves the model to a point which minimizes the error between predictions of the model and the observed data, instead of exhaustively searching all of the parameter space. However, the qualitative features are the same, the error is multimodal, and local minima (analogous to the local maximum at (x_1,y_1) in figure 4.2) can be reached, from which the model will not move.

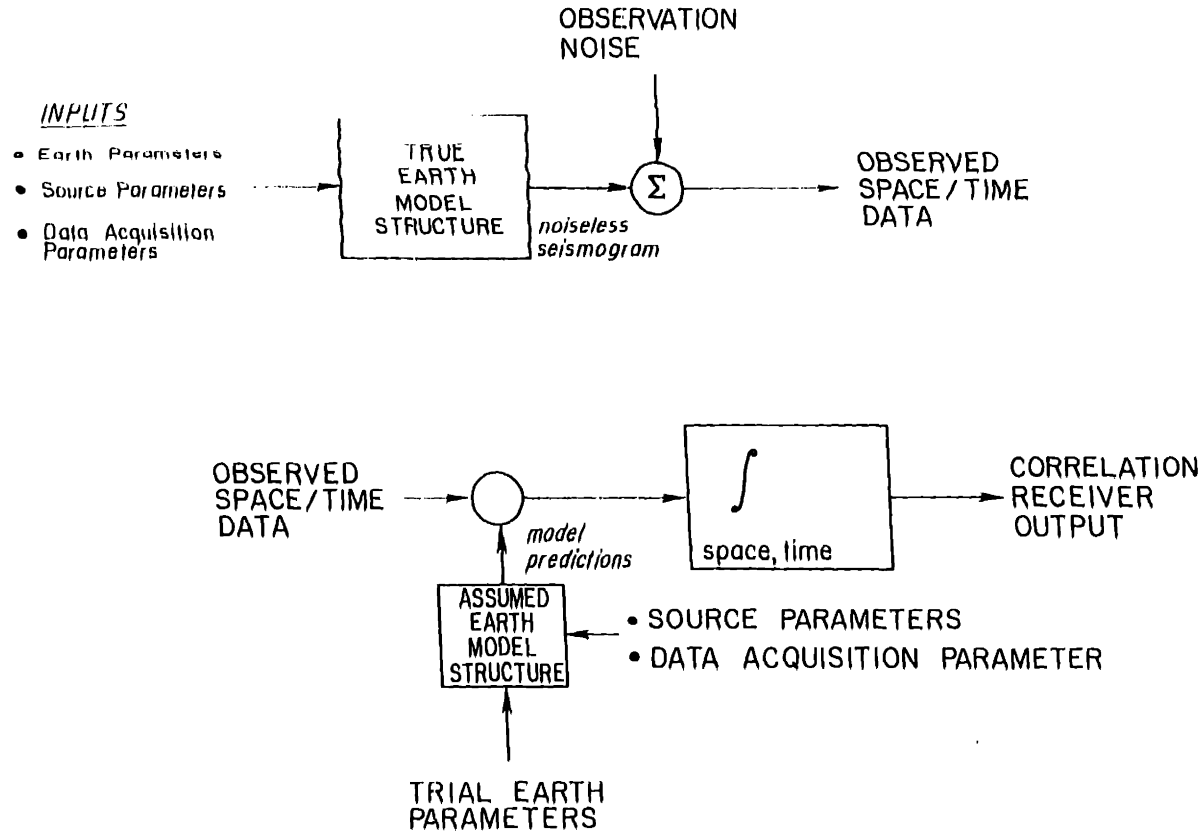

Fig. 4.1) Interpretation of the inversion problem in terms of ambiguity functions.

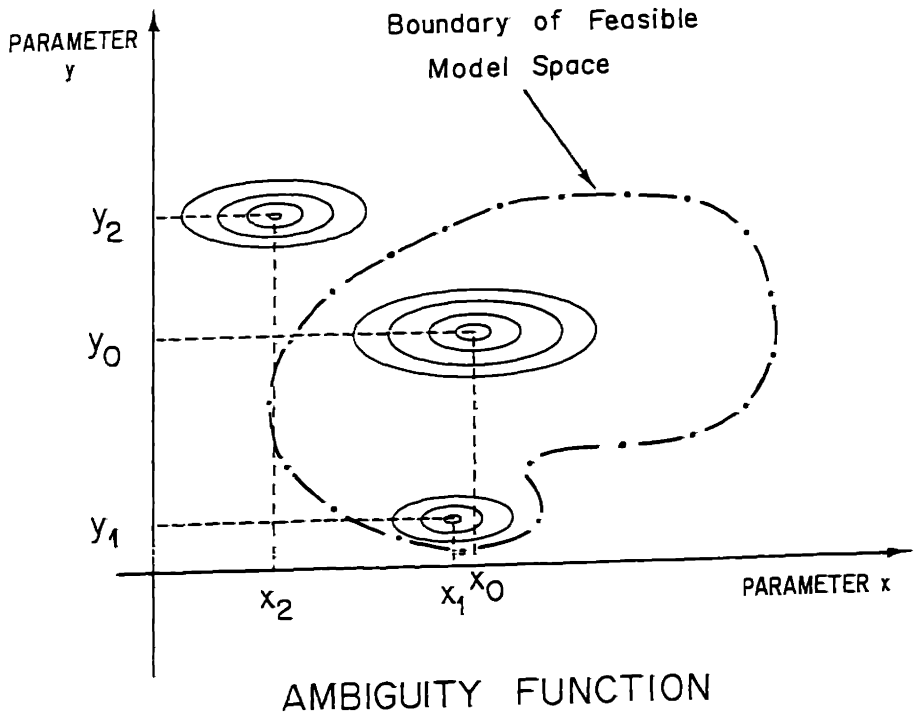

Fig. 4.2) An ambiguity function for a possible inversion problem.

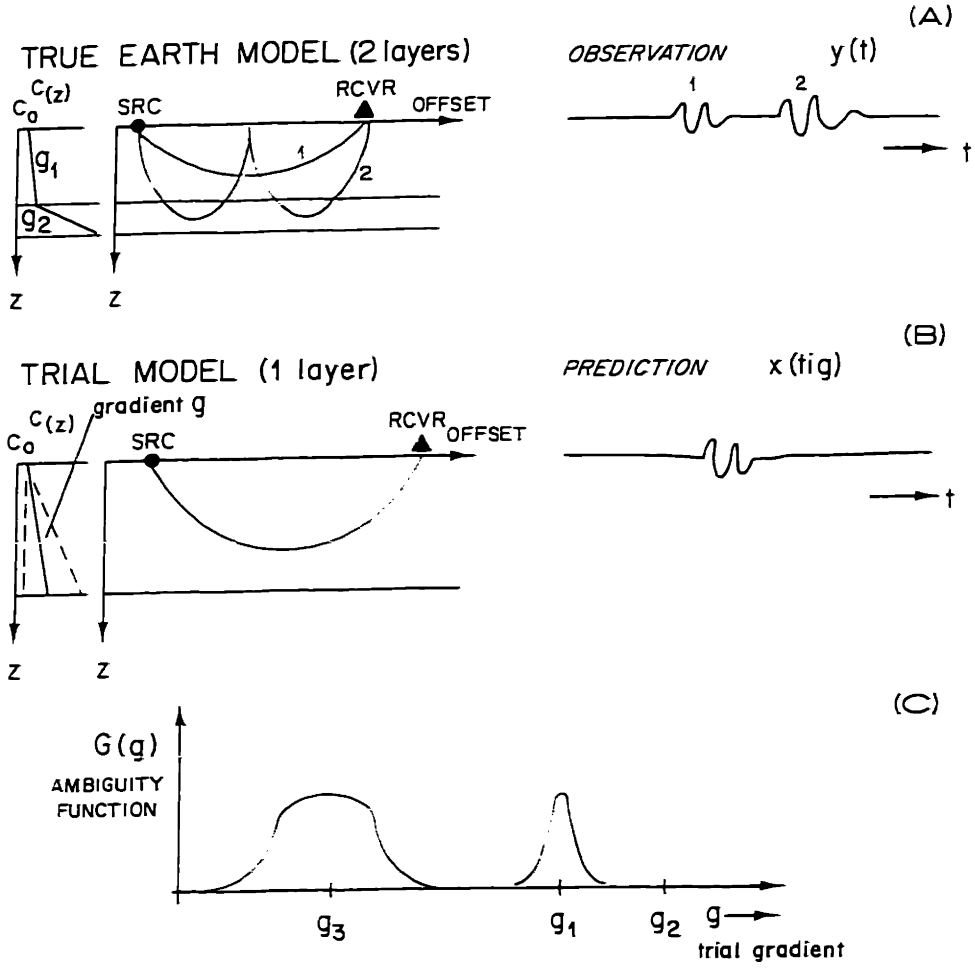

Fig. 4.3) Example of a multi-modal ambiguity function.

free parameter is the velocity gradient. This model and a typical prediction are shown in figure 4.3b. The ambiguity function is shown in figure 4.3c, and is given by:

$$G(g) = \left| \int_0^\infty x(t;g)\, y(t)\, dt \right|.$$

In this example, there is a peak which matches the upper layer and has good characteristics, but at some lower gradient, the second peak is matched, and another gradient, g_3, is obtained, which is completely wrong. One would obviously not use a single layered model for a piece of data which has two peaks, but this example serves to illustrate the importance of matching the assumed and true model structure in obtaining interpretable correlation receiver outputs, or useful ambiguity functions. One way to make the output in figure 4.3c more useful would be to eliminate arrival 2 from the data. This would allow unique determination of the upper layer gradient, but would, of course, make layer 2 unobservable. It is a procedure similar to this that must be carried out in all travel-time inversions. Prior information about the model is used to associate a given arrival with a general path, or kinetic group. Arrivals which don't seem to fit in anywhere are tossed out as being due to effects that the assumed model does not take into account. This laborious, and often full of guesswork method must be used to make the ambiguity function have a unique maximum which is close to the true model. In addition, there is always the possibility that through poor editing of the data one ends up with a globally wrong answer!

In this work, three main travel time inversion methods are used, the "tau-sum" method [Diebold and Stoffa, 1981], a linear least squares method, similar to that of Dorman and Jacobson [1981], and the velocity depth migration technique of Clayton and McMechan [1981], with extensions to enable its use on sparse datasets. In the first two methods, the decisions as to the paths of the arrivals must be made in data space, and the result leaves little indication of

the quality of the fit of the model to the data, other than the error,* or the generation of physically unrealizable model. The migration method takes its error directly from the model space, and thus the effects of application of prior knowledge and elimination of particular data points are much more clear. In fact, the ambiguity function of the data can be mapped directly into model space, and thus gives the interpreter a clear indication of how much confidence should be put in the model.

OUTLINE

The overall goal of this chapter is to summarize the inversion methods used. It is the author's feeling that while tedious to write and, certainly, to read, the details are important to anyone who wants to use the techniques or to refute the author's work. Overly general exposes require almost as much work to be done by the user of the work as was originally done by the author. Because of this philosophy, this chapter will begin with the nitty-gritty of datum corrections, the methods for handling multiples, the method for correcting amplitude bias of the MLM power output, and the removal of artifacts from the short aperture processing. This will be followed by the method used to quickly compute velocity spectra from trial models using the WKBJ synthetic seismogram technique. The tau-sum method and the linear least squares inversion are summarized. Finally, an extensive discussion of the velocity-depth migration technique will be given in which a new method for inclusion of offset data will be presented.

TRAVEL-TIME AND AMPLITUDE CORRECTIONS

*The error must be normalized the the degree of overdeterminanion because for a sufficiently general model, the noisy data can be predicted exactly.

Datum correction

Since the sources and receivers are at some depth into the water column, it is necessary to reduce (or extrapolate) the measured data parameters to a common datum for convenience. The geometry is pictured in figure 4.4. In general, the velocity profile of the water column is known quite accurately, and travel times of rays within the water column can be computed quite accurately. To extrapolate observations to the surface datum, we use the following relations:

$$\tau_s = \tau - \tau_a + \tau_b \tag{4.1a}$$

$$x_s = x - x_a - x_b \tag{4.1b}$$

$$t_s = \tau_s - px_s = t + \tau_a + \tau_b - p(x_a + x_b) \tag{4.1c}$$

$$\tau_a = \int_0^{z_s} v(z)\,dz \qquad \tau_b = \int_0^{z_r} v(z)\,dz$$

$$x_a = \int_0^{z_s} p/v(z)\,dz \qquad x_b = \int_0^{z_r} p/v(z)\,dz \tag{4.1d}$$

$$v(z) \equiv (c^2(z) - p^2)^{\frac{1}{2}}$$

where the data τ, x, p, t are related by $\tau = t - px$.*

To reduce to the sea bottom datum:

$$\tau_{bot} = \tau - \tau_c - \tau_d \tag{4.2a}$$

$$x_{bot} = x - x_c - x_d \tag{4.2b}$$

$$t_{bot} = \tau_b + px_b = t - \tau_c - \tau_d - p(x_c + x_d) \tag{4.2c}$$

$$\tau_c = \int_{z_s}^{z_b} v(z)\,dz \qquad \tau_d = \int_{z_r}^{z_b} v(z)\,dz$$

$$x_c = \int_{z_s}^{z_b} p/v(z)\,dz \qquad x_d = \int_{z_r}^{z_b} p/v(z)\,dz \tag{4.2d}$$

*We measure only one of τ, t, depending on whether zero offset processing is used.

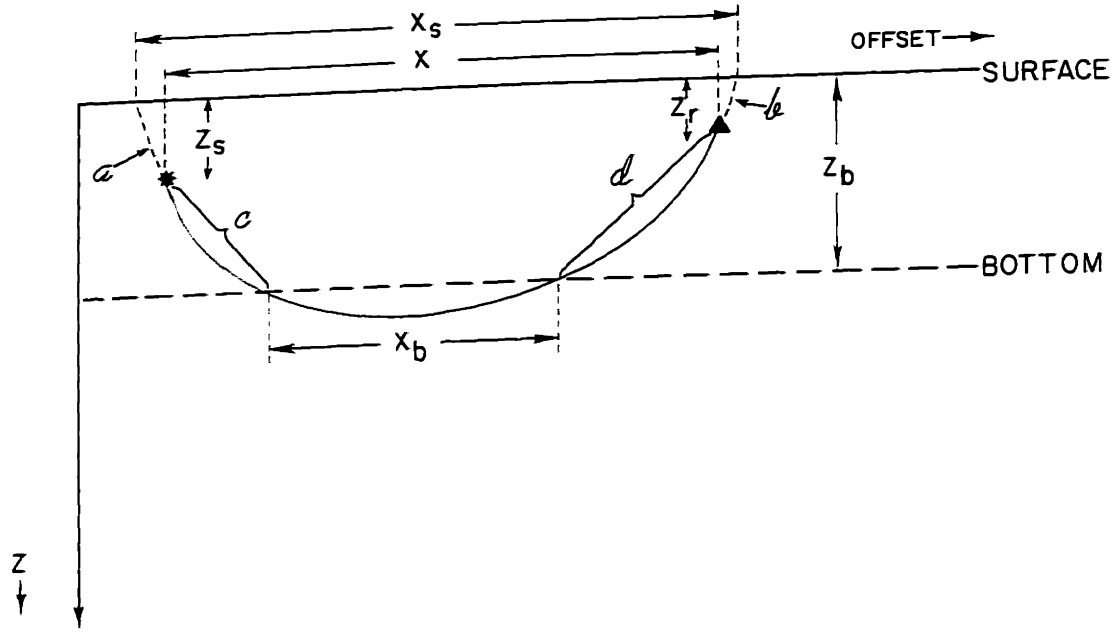

Fig. 4.4) Coordinate definitions for datum corrections of eqn. 4.1.

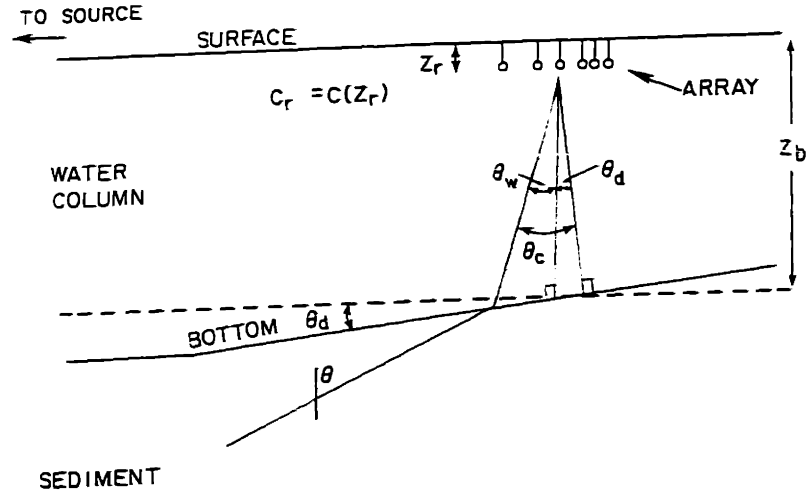

Fig. 4.5) Coordinate definitions for dip corrections of eqn. 4.3.

Free surface multiple reduction

For a laterally homogeneous medium, free surface multiples can be reduced to equivalent first arrivals. This is done by correcting to the (free) surface, as in eqn. 4.1, then dividing all the corrected data values, t, τ, x, by the order of the multiple, defined as the number of surface-to-surface "loops" the ray makes. The datum correction must be done to the surface so that all loops are the same before dividing by the number of loops. If arrivals can be ascribed to other paths, such as the common seabottom peglegs, they can also be reduced to the primary curve using the known water column velocity structure and bathymetry.

Dip correction

To account for bathymetric dip under the array (see fig. 4.5), the observed phase velocity or slowness must be corrected for the change in apparent slowness due to the sloped ocean bottom interface. The angle θ_w is calculated from the apparent slowness across the array, p_w, by:

$$\theta_w = \sin^{-1}(p_w c_r) \qquad 4.3a$$

The true slowness is given by:

$$p = \frac{\sin\theta}{c_0} = \frac{\sin\theta_c}{c_r} = \frac{\sin(\theta_w - \theta_d)}{c_r} \qquad 4.3b$$

where θ_d is the dip of the bottom, measured positive for bottoms sloping downward away from the receiver toward the source (as in figure 4.5).

Power bias corrections

When single outer product covariance estimation of the form in eqn. 3.54 is carried out with stabilizing fraction α, on N channels of data, the in-band uncorrelated noise level on a signal-free portion of the velocity spectrum is given by:

$$\sigma^2 = \frac{N}{\alpha}\hat{S}^2_{MLM} \qquad 4.4a$$

where $\hat{S}^2_{MLM}$ is the power measured in the signal-free region (see eqn. 3.58a). The true signal power, a^2, is computed using eqn. 3.55a,

$$\hat{S}^2_{MLM}(p_0) = \frac{\alpha(a^2 + \sigma^2)}{N} + \frac{a^2 + \frac{\sigma^2}{N}}{1 + \frac{\sigma^2[N-1]}{\alpha(a^2+\sigma^2)}} \qquad 4.4b$$

This is most easily done by a table lookup on $\hat{S}^2_{MLM}$ after calculating a set of pairs of $(\hat{S}^2_{MLM}, a^2)$ using a^2, N, α, and σ^2.

Sidelobe artifact removal

In the previous chapter, the finite length of the array was shown to lead to sidelobes in slowness centered around the line $\tau_0 - r_0(p - p_0)$, where r_0 is the nominal array offset, and (τ_0, p_0) are the arrival coordinates. For zero offset processing, $r_0 \equiv 0$, and the sidelobes are virtually at the same time as the peak. Because of this, they may be easily removed while still preserving the signal power, by finding the peak power value in slowness, p_0, at each arrival time sample, and attenuating the powers at slownesses away from this value. To preserve the size of the peak for resolution evaluation, another method would be to attenuate power starting at some value below the peak power. These procedures are demonstrated in figures 4.6. Figure 4.6a shows the original velocity spectrum, and figure 4.6b its corresponding $\tau - p$ spectrum obtained through the usual transformation $\tau(p) = t(p) - px(p)$. For this example, $x(p) = r_0 = 19.6$ km. Figure 4.6c shows the velocity spectrum after attenuating the power by

$$\hat{S}^2_{MLM}(p) = \hat{S}^2_{MLM}\frac{(p)}{\beta(p - p_0)} \qquad 4.5$$

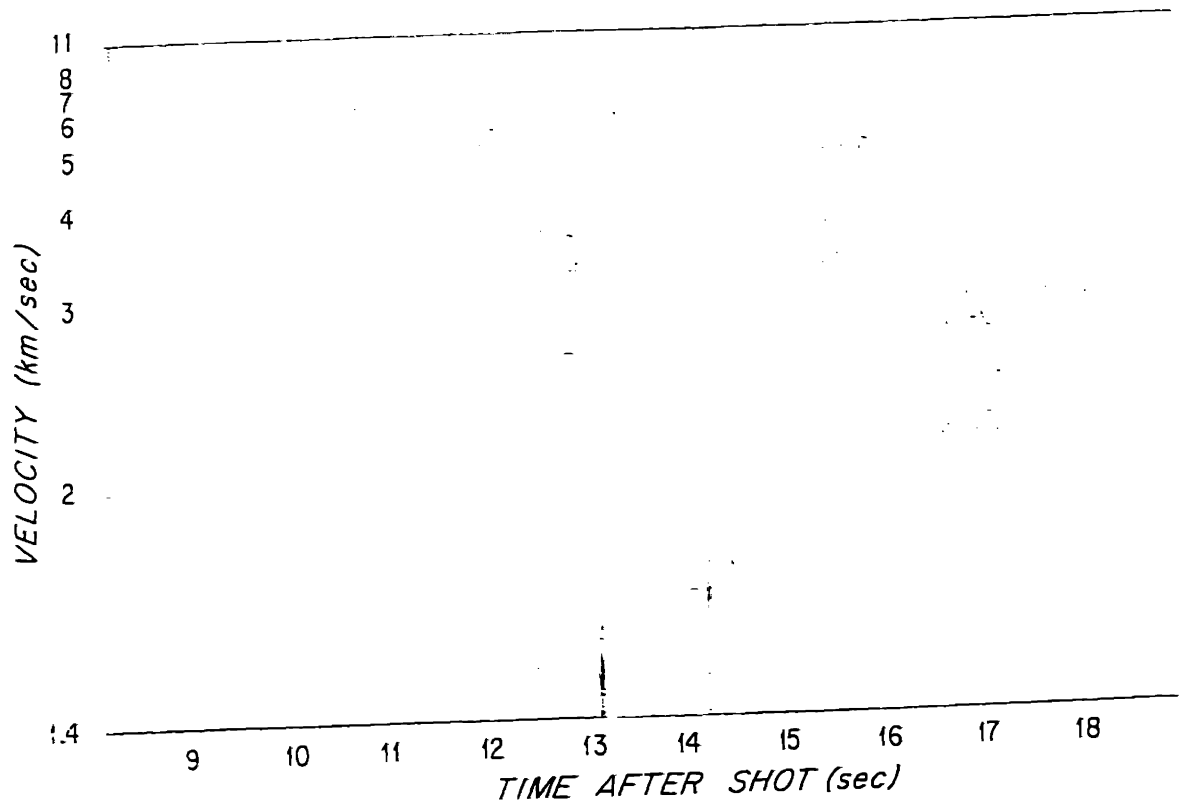

Fig. 4.6a) Original MLM velocity spectrum for an offset of 19.6 km. The contour intervals are 5.0 dB.

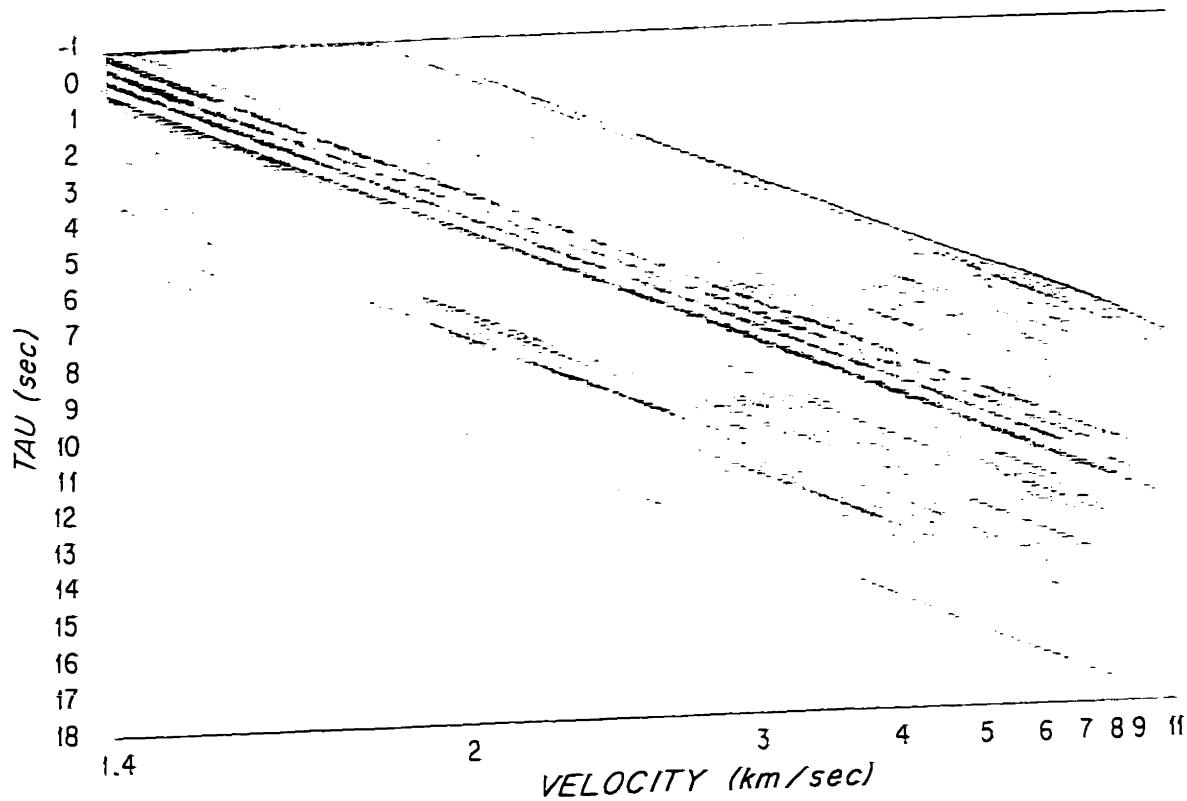

Fig. 4.6b) $\tau - p$ spectrum corresponding to the velocity spectrum of fig. 4.6a. Note the rotation of the sidelobes of the velocity spectral peaks to lines with slope $-x = -19.6$.

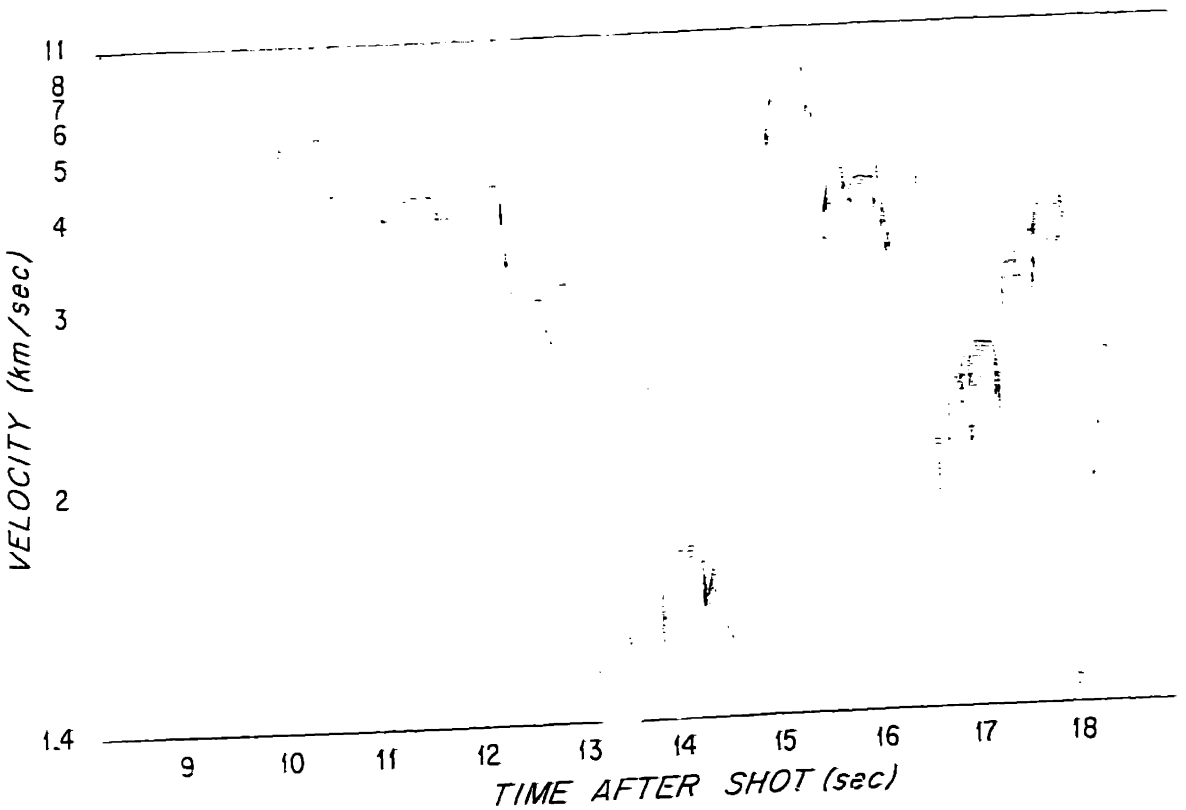

Fig. 4.6c) Enhanced MLM velocity spectrum for an offset of 19.6 km. The sidelobes were attenuated smoothly away from the phase velocity peak at each time by the expression given in text. The original spectrum is in fig. 4.6a. The contour intervals are 5.0 dB.

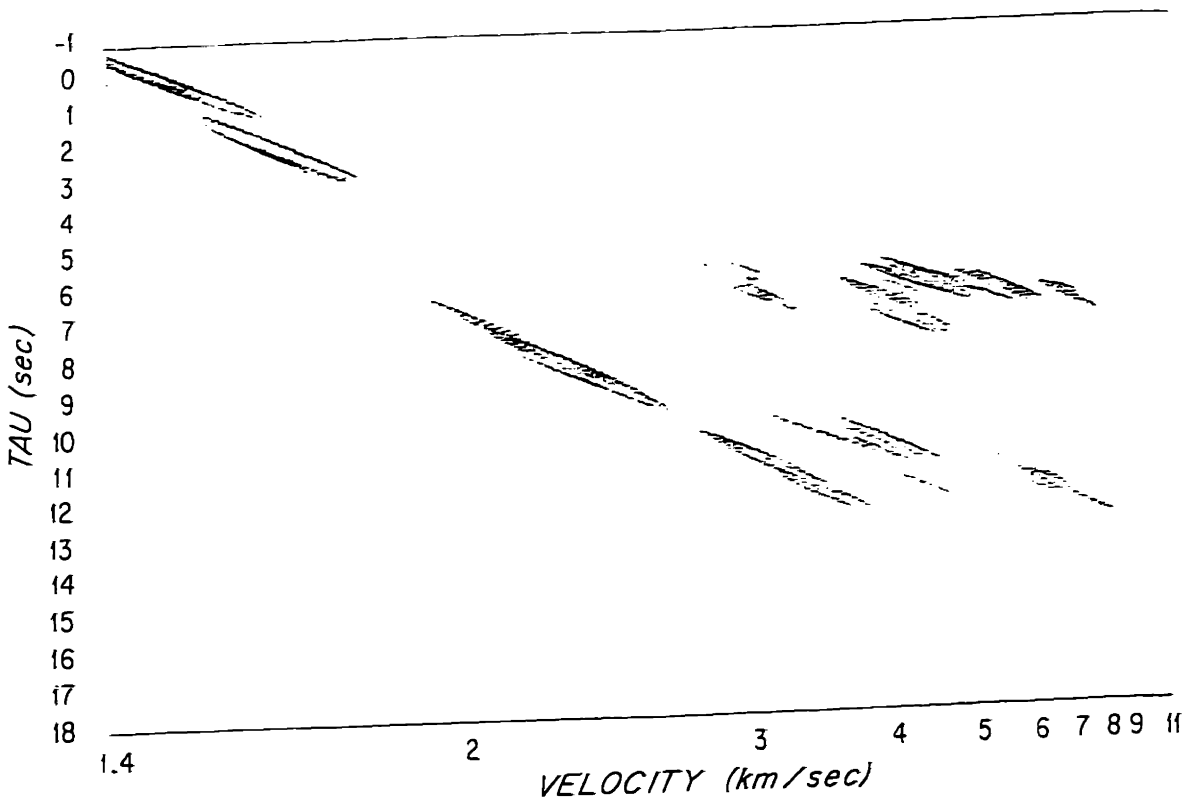

Fig. 4.6d) $\tau-p$ spectrum corresponding to the velocity spectrum of fig. 4.6c. The artifacts seen in fig 4.6b have been eliminated. The contour intervals are 5.0 dB.

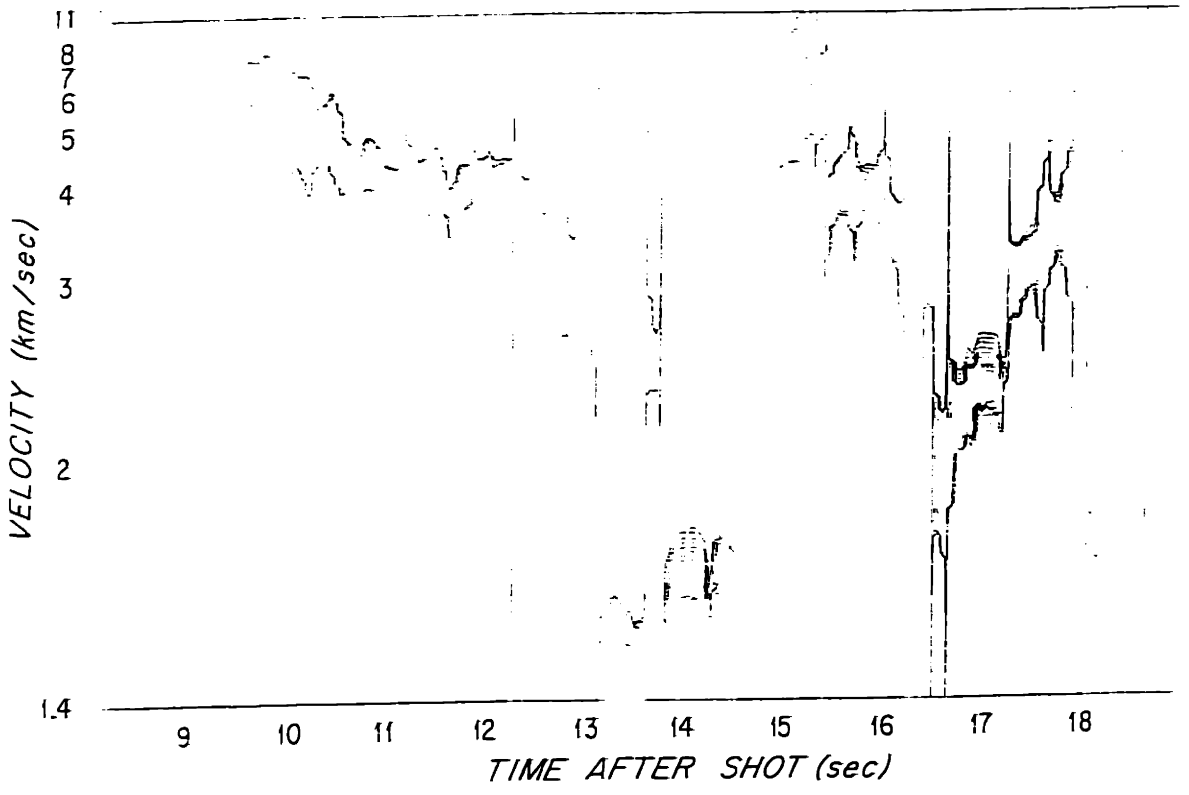

Fig. 4.6e) Enhanced MLM velocity spectrum for an offset of 19.6 km. The peak structure was maintained to the - 6 dB level, then the sidelobes were attenuated smoothly away from the phase velocity peak at each time by the expression given in text. The original spectrum is in fig. 4.6a. The contour intervals are 5.0 dB.

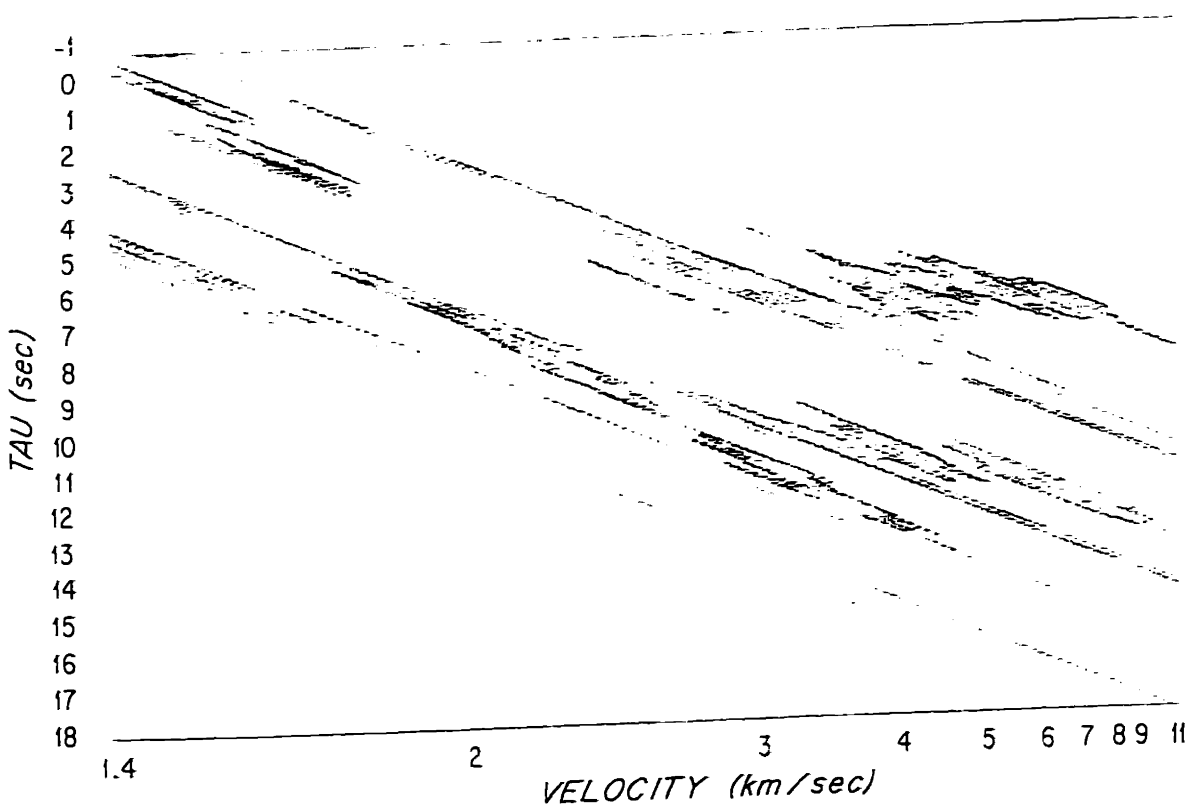

Fig. 4.6f) $\tau-p$ spectrum corresponding to the velocity spectrum of fig. 4.6e. The contour intervals are 5.0 dB.

with $\beta=60$. The corresponding $\tau-p$ spectrum is shown in figure 4.6d, and is greatly improved. If the velocity spectrum is kept linear for the top 6 dB around each peak, the results are in figure 4.6e&f. The attenuation beyond this is the same as that of figures 4.6c&d. All plots in figure 4.6 are contoured in 5 dB increments over a 70 dB dynamic range downward from the peak value in the plot.

WKBJ VELOCITY SPECTRA

In the introduction, the smoothing and decomposition operation carried out by velocity spectral analysis was justified in terms of: i) removal of information that is not predictable by simple models, ii) enhancement of information that is useful in inversions, and robust to model simplification over the true earth. To check models resulting from inversion of the data, it is useful to generate synthetic data from the model and compare it to the observations which were inverted. Since the important and predictable features of the data are preserved by the velocity spectral analysis transformation, it seems logical that the synthetics be compared to the data in this domain. One method for comparison would be to generate waveform synthetics at the offsets actually measured by the array, and then process them with the velocity spectral analysis algorithm used on the real data. This method has the advantage of putting the synthetic data through *exactly* the same transformation as the real data. Unfortunately, is also has the disadvantage of requiring a lot of computer effort. A less exact, but faster method is to use the known properties of the velocity spectral analysis algorithm, and the WKBJ synthetic seismogram technique to construct approximate velocity spectra directly.

Recalling the development of eqn. 2.26 (Chapter 2), it was seen that contributions for a given kinematic group observed at the offset r lay along the path

$$\theta(p) = \tau(p) - p\,r \tag{4.6a}$$

as a function of p. At each point (θ,p), the amplitude was given by:

$$\frac{p^{1/2}\bar{B}(p)}{\left|\frac{d\theta(p)}{dp}\Big|_r\right|} \approx \frac{p^{1/2}\bar{B}(p)}{\left|\frac{2\Delta t}{\Delta p_{2\Delta t}}\right|} \tag{4.6b}$$

In this equation, $\bar{B}(p)$ is the product of the transmission/reflection coefficients encountered along the path, the source directivity factor, and a turning point factor (see eqn. 2.26g). The factor $\Delta p_{2\Delta t}$ is illustrated in figure 2.2, and is discussed in Chapter 2 after eqn. 2.26. Thus, to construct the synthetic velocity spectra, the hypothesized response of the velocity spectral analysis algorithm to a wave with power given by the square of eqn. 4.6b at $(t=\theta(p),p)$ is "convolved" in $t-p$ space with the "lines":

$$\frac{p\,|\bar{B}(p)|^2}{\left|\frac{2\Delta t}{\Delta p_{2\Delta t}}\right|^2} \cdot \delta(t-\theta(p)) \tag{4.6d}$$

computed for each important kinematic group. Note that this is not a linear convolution for MLM processing because the velocity spectral analysis response at a given point on the line is a function of the power in the wave (see eqn. 3.56, with p in eqn. 4.6d equal p_0 in eqn. 3.56). Figure 4.7a illustrates the result of processing actual synthetic seismic records with the velocity analysis processor. The noiseless data for this example were computed using the approximate normal mode technique described in Chapter 2. Figure 4.7b shows the approximate technique of eqn. 4.6 using a Gaussian response function

$$e^{-\frac{1}{2}[t^2/\sigma_t^2 - p^2/\sigma_p^2]} \qquad \sigma_t = 0.05\ s \qquad \sigma_p = 0.0005\ s/km$$

linearly convolved with the equation 4.6d. The "theta" curves for the 4 dominant surface ghosts are shown for the source located at 243 m, and the receiver located at 93 m. The plots

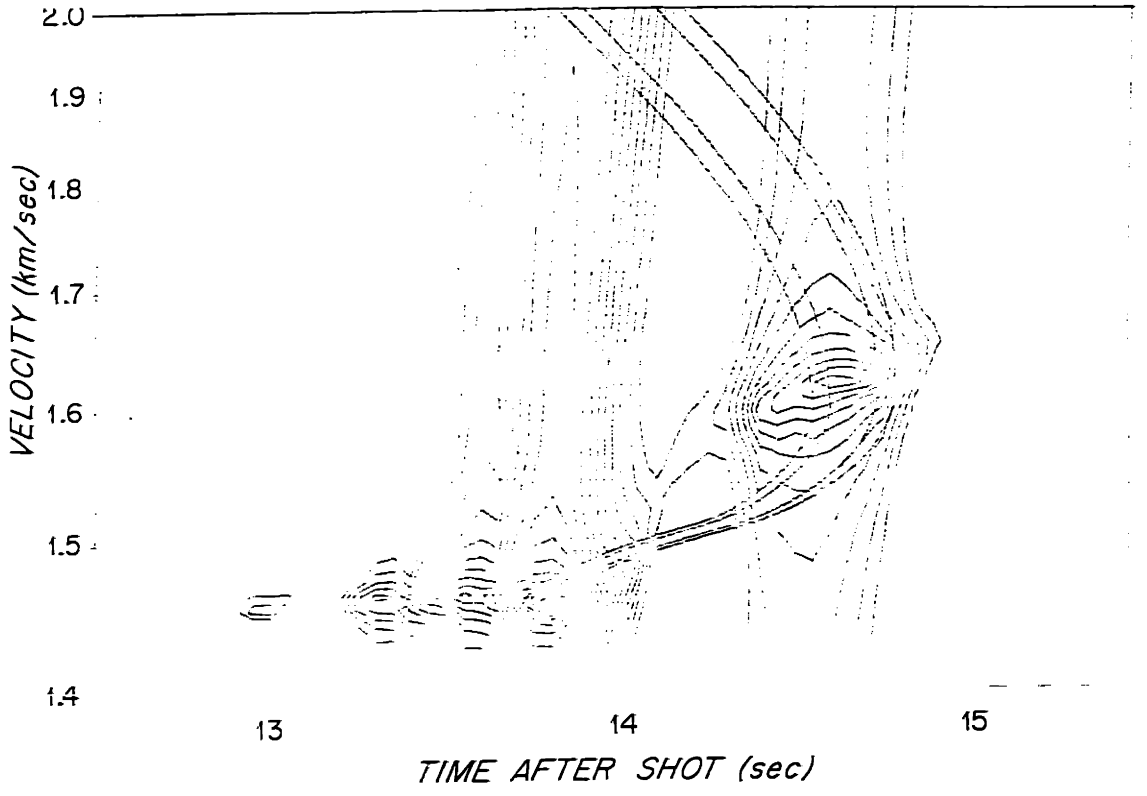

Fig. 4.7a) Velocity spectrum obtained by processing synthetic waveform data with the MLM velocity spectral analysis program. The contour intervals are 3.0 dB.

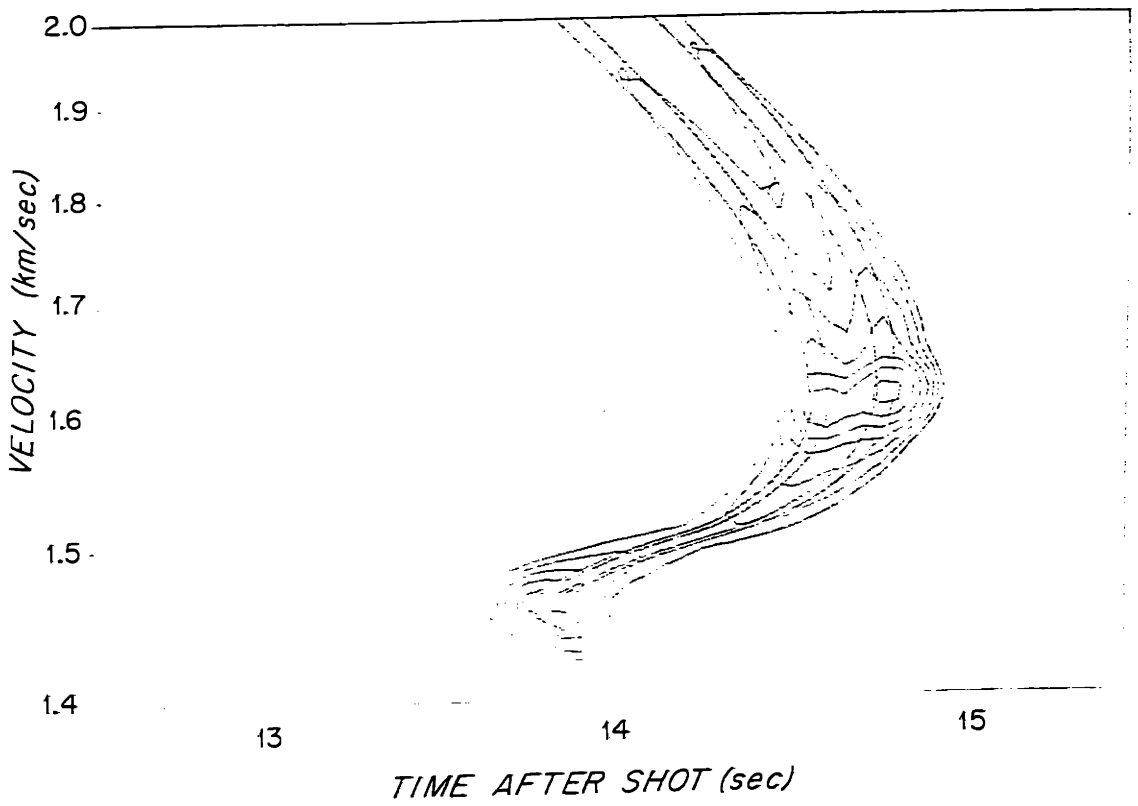

Fig. 4.7b) Velocity spectrum obtained by convolving the WKBJ theta curves (with predicted amplitudes) with a Gaussian smoothing function to approximate the velocity spectral analysis resolution. The contour intervals are 3.0 dB.

show the same features even though the modeling of the velocity analysis response as a simple Gaussian is a vast oversimplification.

THE TAU-SUM METHOD

The tau-sum method [Diebold and Stoffa, 1981] is a useful method for inverting $\tau-p$ data when the $\tau-p$ curve is densely sampled. The most commonly used form strips the data layer by layer using homogeneous layers with slownesses chosen by the $\tau-p$ curve slowness sample points. The formulation used first orders the $\tau(p_i)$ data in order of decreasing slowness samples, p_i. The first layer is chosen to have slowness p_0, the datum slowness, and is defined to have intercept time $\tau(p_0)=0$. The homogeneous layer slownesses are given by p_i, $i=0,1,\ldots,n$, and have thicknesses:

$$d_i = \frac{\tau(p_{i+1})/2 - \sum_{j=0}^{i-1} d_i (p_j^2 - p_{i+1}^2)^{1/2}}{(p_i^2 - p_{i+1}^2)^{1/2}} \qquad i=0,1,2,\ldots,n-1 \qquad 4.7$$

As a result of noise or the use of precritical reflection $\tau-p$ points, some layer thicknesses may be computed to be negative. The standard practice for this work is to set negative thicknesses to zero. This causes the $\tau(p)$ function of the resulting model to upperbound (in τ) the data $\tau(p)$ curve. (The model will be a little slower.) Departures of the predicted $\tau(p)$ curve from the data usually indicate that the data which cannot be predicted are from precritical reflections. For sparsely sampled $\tau(p)$ functions, as are obtained from shooting at relatively few offsets, it is often difficult to determine the exact intersection point of 2 postcritical ellipses, and precritical reflection can be accidently included in the picked $\tau-p$ curve.

The tau-sum method can also be formulated to peel off linear slowness gradient layers. A surface slowness, p_0, is chosen, and p_i are the slownesses at the bases of the succeeding

layers. This formulation assumes that $\tau(p_i)$ comes from a ray which turns exactly at the base of a slowness gradient layer which runs from p_{i-1} to p_i in slowness. For this method, the layer thicknesses are:

$$d_i = \frac{\tau(p_{i-1})/2 - \sum_{j=0}^{i-1} \hat{\tau}_j^{(i-1)}}{\hat{\tau}_i^{(i-1)}/d_i} \qquad 4.8$$

where

$$\hat{\tau}_j^{(i-1)} = \int_0^{d_j} v_j(z, p_{i-1})\,dz = \int_0^{d_j} (p_j^2(z) - p_{i-1}^2)^{-1/2}\,dz = \int_0^{d_j} ((\alpha_j + \beta_j z)^2 - p_{i-1}^2)\,dz \qquad 4.9$$

When $\alpha_j + \beta_j d_j = \alpha_{j+1} = p_{j+1}$ (no first order discontinuities), we have:

$$\hat{\tau}_j^{(i-1)} = d_j \left[(p_{j+1}^2 - p_{i-1}^2)^{1/2} + \frac{p_j}{p_{j+1} - p_j} [(p_{j+1}^2 - p_{i-1}^2)^{1/2} - (p_j^2 - p_{i-1}^2)^{1/2}] \right.$$
$$\left. - \frac{p_{i-1}^2}{(p_{j+1} - p_j))} \ln \left(\frac{(p_{j+1}^2 - p_{i-1}^2)^{1/2} + p_{j+1}}{(p_j^2 - p_{i-1}^2)^{1/2} + p_j} \right) \right] \qquad 4.10$$

There is again a problem of negative layer thicknesses. For this case, this is circumvented by assuming the negative layer thickness, d_i, should be zero, then modifying the previous layer thickness to make d_i evaluate to zero, or correspondingly, to make the predicted value $\hat{\tau}(p_{i+1})$ equal the data value $\tau(p_{i+1})$. This is done by setting

$$d_{i-1} - d_{i-1} - \frac{\sum_{j=0}^{i-1} \hat{\tau}_j^{(i-1)} - \tau(p_{i+1})}{\hat{\tau}_{i-1}^{(i-1)}/d_{i-1}}. \qquad 4.11$$

This method only seems to work when the data are quite densely sampled in slowness. For this work, densely sampled $\tau(p)$ functions are not available. When it was desired to use this formulation, my usual practice was to cubic spline the data points in an over-determined fashion using the picked peaks from all frequencies simultaneously to enhance the stability of

the estimate.

LINEAR LEAST SQUARES INVERSION

Background and Philosophy

The tau-sum methods are very simple inversion techniques which generally generate a model "point" for each data point. Except for the removal of negative thickness layers, the model could be inverted again for the exact (noisy) data values. More sophisticated inversion methods differ from this method in 3 primary ways:

[1] Different types of data and prior information may be combined to determine the model.

[2] The model may be over- and/or underdetermined by the available data. The algorithms therefore must decide which data to use (overdetermined) and how to allocate the excess degrees of freedom (underdetermined). The error norms chosen and the methods used to express the reliability of a given datum determine which data get used. The use of model norm constraints or prior information helps to allocate the excess degrees of freedom. A problem may be under- and overdetermined at the same time if more data points than model parameters are present, but the data say nothing about some of the parameters [Parker, 1977 has a good discussion on these matters].

[3] Primary outputs of the inversion include information on the uniqueness and reliability of the model, in addition to the model itself.

*Linearization**

The (nonlinear) inverse problem for finite model parameterization and finite sampled data sets consists of solving the equation

$$F(x) + w = y \tag{4.12}$$

for the model, x, from the measurement data, y, which is obtained from the model through the nonlinear transformation F( ) and the additive noise process, w. Most inversion schemes assume that w is independent of the model, x, and the experimental setup, F( ), and that F( ) is known. The last assumption is probably the most erroneous in most cases, but will not be dealt with any further in this work. Because nonlinear equations are difficult to solve, the first task is usually the linearization of F( ), so that matrix algebra can be used to solve for x. Because the linearization is only valid locally, the usual method is to iterate on "linearized" inversions around an updated trial model. This yields the algorithm:

i) Choose $\hat{x}$, the starting model

ii) Expand about $\hat{x}$

$$F(x) = F(\hat{x}) + A\Delta x \tag{4.13a}$$

$$A \equiv \nabla_x F \mid_{\hat{x}} \tag{4.13b}$$

$$\Delta x \equiv (x - \hat{x}) \tag{4.13c}$$

$$\Delta y \equiv (y - \hat{y}) \equiv y - F(\hat{x}) \tag{4.13d}$$

iii) Solve for $\Delta\hat{x}$:

$$\Delta\hat{x} \equiv \{A\}^{-1}\,\Delta y \tag{4.13e}$$

iv) Update $\hat{x}$

$$\hat{x} \Leftarrow \hat{x} - \Delta\hat{x} \tag{4.13f}$$

This relinearization and solution is repeated until the change in $\hat{x}$ at each iteration is below some level, and the iteration is stopped. No more will be said about the properties or convergence problems with the linearization; we just assume it can be done. The breakdown of eqn.

---

*The material in this section is primarily background for chapter 6.

4.13 is also useful for the case in which we regard the model, x, the noise, w, and the data, y, as stochastic processes. In this case $\hat{\mathbf{x}}$ is the mean value of x, obtained from the a priori probability density of x. w is always assumed to be zero mean, and thus y has mean $\hat{\mathbf{y}} \equiv \mathbf{F}(\hat{\mathbf{x}})$ and $\Delta\mathbf{y}$ and $\Delta\hat{\mathbf{x}}$ are zero mean. What must be concentrated on is eqn 4.13e. I have placed braces around the matrix A to indicate that this is not always just a simple matrix inversion, and often is modified to account for the a priori statistics of x, y, and w. Indeed, it can't possibly be when the dimension of the model vector $\Delta\mathbf{x}$ is greater than the data vector, $\Delta\mathbf{y}$. Several approaches to the inversion of A are popular and will be summarized here for completeness, and to document the methods used to invert the data of chapters 5 and 6.

The generalized inverse:

The first, and most simple inverse for A is the standard generalized inverse. The A matrix is decomposed into its representation by the product of the data eigenvector (columns of U), the model eigenvector (rows of $\mathbf{V}^T$), and the eigenvalues in the diagonal matrix, $\mathbf{\Lambda} = [\lambda_i]$.

$$\mathbf{A} = \mathbf{U}\mathbf{\Lambda}\mathbf{V}^T \qquad 4.14$$

For over- or underdetermined systems, some eigenvalues will be zero. In this case, the generalized inverse operator is given by

$$\{\mathbf{A}\}^{-1} \equiv \mathbf{A}_g^{-1} = \mathbf{V}\{\mathbf{\Lambda}\}^{-1}\mathbf{U}^T \qquad 4.15a$$

where $\{\mathbf{\Lambda}\}^{-1}$ has as its diagonal elements λ_i^{-1} for $\lambda_i \neq 0$ and 0 for $\lambda_i = 0$. The generalized inverse estimate is given by:

$$\Delta\hat{\mathbf{x}}_g = \mathbf{A}_g^{-1}\Delta\mathbf{y} \qquad 4.15b$$

The interpretation of this inverse is that the aspects of the data which are not within the capability of the model to generate are eliminated from consideration for model determination, as

are components of the model which are not specified by the data, because the eigenvectors corresponding to the zero eigenvalues are not used. This inverse has the property of minimizing the error norm $|\Delta \mathbf{y} - \mathbf{A}\Delta\hat{\mathbf{x}}_g|^2$ of the data and, in the event of undetermination, minimizing the norm of the model, $|\Delta\hat{\mathbf{x}}_g|^2$. Other properties of the generalized inverse are available in any linear algebra text.

The performance of any inversion algorithm can be determined by examining the resolution, information, and model covariance matrices. There are discussions in detail in Aki and Richards [1980, Chapter 12], and by Franklin [1970] and Wiggins [1972]. The resolution matrix indicates how the resulting model, $\hat{\mathbf{x}}$, is related to the true model for the given inverse operator $\{\mathbf{A}\}^{-1}$. In general, the resolution matrix, R, is given by $\mathbf{R} = \{\mathbf{A}\}^{-1}\mathbf{A}$ and $\hat{\mathbf{x}} = \mathbf{R}\mathbf{x}$. From 4.14 and 4.15, this yields a resolution matrix, $\mathbf{R}_g$, for the generalized inverse:

$$\Delta\hat{\mathbf{x}} = \mathbf{R}_g\Delta\mathbf{x} \qquad 4.16a$$

where

$$\mathbf{R}_g = \mathbf{V}_p\mathbf{V}_p^T \qquad 4.16b$$

and $\mathbf{V}_p$ is the matrix obtained by keeping only the eigenvectors in V that correspond to nonzero eigenvalues. The complete V matrix is often written as [Lanczos, 1961]

$$\mathbf{V} = \left[\, \mathbf{V}_p \;\; \mathbf{V}_0 \,\right] \qquad 4.16c$$

where $\mathbf{V}_0$ are the eigenvectors with zero eigenvalues. Similarly, the left-hand eigenvector, or data eigenvectors of A, are divided as

$$\mathbf{U} = \left[\, \mathbf{U}_p \;\; \mathbf{U}_0 \,\right] \qquad 4.16d$$

where the matrix $\mathbf{U}_p$ consists of the eigenvector with nonzero eigenvalues, and $\mathbf{U}_0$ are those with zero eigenvalues. To keep consistent with this notation, the diagonal eigenvalue matrix is

often represented as

$$\Lambda = \begin{bmatrix} \Lambda_p & 0 \\ 0 & \Lambda_0 \end{bmatrix}.$$

The information matrix relates the observed data to the data calculated by the resulting model. The general expression is $E = A\{A\}^{-1}$ and $\hat{y} = Ey$. Again, from 4.14 and 4.15, the information matrix for the generalized inverse, E_g, defined by

$$\Delta\hat{y}_g = E_g \Delta y \qquad 4.17a$$

is given by

$$E_g = U_p U^T{}_p. \qquad 4.17b$$

Finally, no solution is complete without a measure of the reliability of the solution. In general, a covariance matrix for the data, R_{yy}, is defined, and the linear operation of $\{A\}^{-1}$ simply propagates the errors.

$$R_{\hat{x}\hat{x}} = E[\{A\}^{-1}\Delta y\ [\{A\}^{-1}\Delta y]^T] = \{A\}^{-1} R_{yy} [\{A\}^{-1}]^T. \qquad 4.18a$$

For the generalized inverse this results in

$$R_{\hat{x}_g \hat{x}_g} = A_g^{-1} R_{yy} A_g^{-T} * \qquad 4.18b$$

The maximum likelihood inverse:

The standard generalized inverse does not take into account possible differing reliability of the various data components, nor correlations among them. We will not discuss the aspect of correlation among the data values, but intuitively one can see that independent, but not identically reliable data should not be weighted equally in determining the model. Likewise, if prior information about the model exists, then it is reasonable that its distance from the prior mean, with each component weighted by the confidence in the prior value, should be minim-

ized. These considerations led to the use of the "maximum likelihood inverse" by Wiggins [1972] and Jackson [1972]. In this method the data are characterized by their mean, y_0, and covariance, $\mathbf{R}_{yy} = E[\Delta\mathbf{y}\Delta\mathbf{y}^T]$, and the model by its prior mean, x_0, and covariance, $\mathbf{R}_{xx} = E[\Delta\mathbf{x}\Delta\mathbf{x}^T]$. The important thing to note about this formulation is that the dependence of the probability density of y on x is neglected, and it is assumed that the statistics of each are known and specified separately. In essence, the observation noise term, w, is absorbed in the given statistics of y. The name "maximum likelihood" stems from the fact that if the data are assumed to be Gaussian distributed, then the solution, $\hat{\mathbf{x}}_{ML}$, which minimizes:

$$\Delta\mathbf{y}^T\mathbf{R}_{yy}^{-1}\Delta\mathbf{y} \qquad \Delta\mathbf{y} = \mathbf{y} - \mathbf{A}\hat{\mathbf{x}}_{ML} \tag{4.19}$$

is the usual maximum likelihood estimate familiar in estimation theory (Van Trees, 1968, p. 74). Jackson and Wiggins showed that the generalized inverse applied to the normalized data, $\Delta\mathbf{y}'$, and normalized model, $\Delta\mathbf{x}'$, deviations given by:

$$\Delta\mathbf{y}' = \mathbf{R}_{yy}^{-T/2}\Delta\mathbf{y} = \Lambda_{yy}^{-1/2}\mathbf{Y}^T\Delta\mathbf{y} \tag{4.20a}$$

$$\Delta\mathbf{x}' = \mathbf{R}_{xx}^{-T/2}\Delta\mathbf{x} = \Lambda_{xx}^{-1/2}\mathbf{X}^T\Delta\mathbf{x} \tag{4.20b}$$

$$\mathbf{A}' = \mathbf{R}_{yy}^{-T/2}\mathbf{A}\mathbf{R}_{xx}^{1/2} = \Lambda_{yy}^{-1/2}\mathbf{Y}^T\mathbf{A}\mathbf{X}\Lambda_{xx}^{1/2} \tag{4.20c}$$

where

$$\mathbf{R}_{yy} = \mathbf{R}_{yy}^{1/2}\mathbf{R}_{yy}^{T/2} = \mathbf{Y}\Lambda_{yy}\mathbf{Y}^T \tag{4.20d}$$

$$\mathbf{R}_{xx} = \mathbf{R}_{xx}^{1/2}\mathbf{R}_{xx}^{T/2} = \mathbf{X}\Lambda_{xx}\mathbf{X}^T \tag{4.20e}$$

gave the desired result, 4.19. In addition, because of the minimum model norm property mentioned in the section on the generalized inverse, the generalized inverse on the primed coordinates also minimizes the weighted model deviation norm**:

---

*The exponent symbol $-T$ signifies taking the inverse transpose.

**This aspect is usually not included in true maximum likelihood parameter estimates. It is generally assumed that nothing is known about the model. For inversion work, however, the norm minimization property is often useful to cause non-uniqueness in the inversion to "default" to reasonable models, some prior mean x_0. This is often better than minimizing the norm, or total length of a model for which one doesn't expect to obtain a zero

$$\Delta\hat{\mathbf{x}}^T \mathbf{R}_{xx}^{-1} \Delta\hat{\mathbf{x}}$$

The effects of these weightings is clearly seen when the individual components of the vectors x and y are independent. The contribution to the total error by each component Δy_i^2 or Δx_i^2 is weighted by the inverse of its variance, $\sigma_{y_i}^2$ or $\sigma_{x_i}^2$, causing highly reliable data to be more important. Note that this weighting also eliminates the effects of data units and scale factors, thus allowing sensible blending of many types of data into one complete inversion. (As long as the probability densities of the different data are of the same type.)

In summary, the maximum likelihood inverse is simply implemented by the generalized inverse on the transformed data of eqn. 4.17. In terms of the singular value decomposition, eqn. 4.14, the maximum likelihood inverse is given by:

$$\begin{aligned} \{\mathbf{A}\}^{-1} = \mathbf{A}_{ML}^{-1} &= \mathbf{R}_{xx}^{1/2}[\mathbf{A}']_g^{-1}\mathbf{R}_{yy}^{-T/2} \\ &= \mathbf{R}_{xx}^{1/2}\mathbf{V}'\{\Lambda'\}^{-1}[\mathbf{U}']^T\mathbf{R}_{yy}^{-T/2} \\ &= \mathbf{R}_{xx}^{1/2}\mathbf{V}'_p[\Lambda'_p]^{-1}[\mathbf{U}'_p]^T\mathbf{R}_{yy}^{-T/2} \end{aligned} \qquad 4.21a$$

since

$$[\mathbf{A}'_g]^{-1} = \mathbf{V}'\{\Lambda'\}^{-1}[\mathbf{U}']^T \qquad 4.21b$$

from eqn. 4.15a. The estimate in normalized coordinates is

$$\Delta\hat{\mathbf{x}}'_g = [\mathbf{A}'_g]^{-1}\Delta\mathbf{y}' \qquad 4.21c$$

This assumes an especially computationally simple form when the components of the vectors x and y are uncorrelated--X and Y in 4.20 are identity matrices, and Λ_{xx} and Λ_{yy} are diagonal matrices with diagonal elements equal to the variances of the corresponding vector elements. The final vector model in non-normalized coordinates is recovered by:

$$\Delta\hat{\mathbf{x}}_{ML} = \mathbf{A}_{ML}^{-1}\Delta\mathbf{y} = \mathbf{R}_{xx}^{1/2}\Delta\hat{\mathbf{x}}'_g \qquad 4.22$$

---

value.

Analogously to the generalized inverse, the resolution, information, and model covariance matrices are obtained. The resolution matrix of the normalized system is:

$$\mathbf{R}' = \mathbf{V}'_p[\mathbf{V}'_p]^T \qquad 4.23a$$

where

$$\mathbf{A}' = \mathbf{U}'\mathbf{\Lambda}'[\mathbf{V}']^T \qquad 4.23b$$

The resolution matrix in the original (real) coordinate system is

$$\mathbf{R}_{ML} = \mathbf{R}_{xx}^{1/2}\mathbf{R}'\mathbf{R}_{xx}^{-T/2}. \qquad 4.23c$$

The information matrix in the normalized system is

$$\mathbf{E}' = \mathbf{U}'_p[\mathbf{U}'_p]^T \qquad 4.24a$$

where $\mathbf{U}'$ is obtained from 4.23b.

The information matrix in the real coordinate system is

$$\mathbf{E}_{ML} = \mathbf{R}_{yy}^{1/2}\mathbf{E}'\mathbf{R}_{yy}^{-T/2}. \qquad 4.24b$$

The covariance matrix of the estimated model is given by:

$$\mathbf{R}_{\hat{\mathbf{x}}_{ML}\hat{\mathbf{x}}_{ML}} = \mathbf{R}_{xx}^{1/2}\mathbf{V}'_p[\mathbf{\Lambda}']^{-2}[\mathbf{V}'_p]^T\mathbf{R}_{xx}^{T/2}. \qquad 4.25$$

The stochastic inverse

The last linear least squares inversion method used for this thesis is the stochastic inverse [Franklin, 1970; Jackson, 1979]. This is equivalent to the linear least squares Bayes estimate well known in estimation theory. In this method, the observation equation 4.12 is assumed, and the probability density of $\mathbf{x}$ and the conditional probability of $\mathbf{y}$ given $\mathbf{x}$ are assumed to be known. In most cases, these are specified through the second order statistics:

$$E[\mathbf{x}] = \mathbf{x}_0 \qquad E[(\mathbf{x}-\mathbf{x}_0)(\mathbf{x}-\mathbf{x}_0)^T] = \mathbf{R}_{xx}$$

$$E[\mathbf{w}] = 0 \qquad E[\mathbf{w}\mathbf{w}^T] = \mathbf{R}_{ww}$$

and the statistics of y are calculated using 4.12. After reduction to zero mean observations and model $\Delta\mathbf{y}$, $\Delta\mathbf{x}$, the linear* estimate which minimizes the expected error between the true model, x, and the estimated model, $\hat{\mathbf{x}}$, is given by calculating the estimated deviation, $\Delta\hat{\mathbf{x}}_s$, by [Aki and Richards, 1980, p. 695]:

$$\{\mathbf{A}\}^{-1} = \mathbf{A}_s^{-1} = \mathbf{R}_{xy}\mathbf{R}_{yy}^{-1} \qquad 4.26$$
$$\Delta\hat{\mathbf{x}}_s = \mathbf{A}_s^{-1}\Delta\mathbf{y}$$

For the linearized system of equation 4.12 and 4.13,

$$\Delta\mathbf{y} = \mathbf{A}\Delta\mathbf{x}+\mathbf{w} \qquad 4.27$$

is the observation equation with measurement noise vector w, linearized system for propagating the model to the data, A, and data and model deviations $\Delta\mathbf{y}$, $\Delta\mathbf{x}$. Assuming that the model and noise are independent, this equation yields

$$\Delta\hat{\mathbf{x}}_s = \mathbf{R}_{xx}\mathbf{A}^T(\mathbf{A}\mathbf{R}_{xx}\mathbf{A}^T+\mathbf{R}_{ww})^{-1}\Delta\mathbf{y} \qquad 4.28a$$

or

$$\{\mathbf{A}\}^{-1} = \mathbf{A}_s^{-1} = \mathbf{R}_{xx}\mathbf{A}^T(\mathbf{A}\mathbf{R}_{xx}\mathbf{A}^T+\mathbf{R}_{ww})^{-1} \qquad 4.28b$$

since

$$\mathbf{R}_{xx} = E[\Delta\mathbf{x}\Delta\mathbf{x}^T] \qquad 4.29$$
$$\mathbf{R}_{ww} = E[\mathbf{w}\mathbf{w}^T]$$
$$\mathbf{R}_{yy} = E[\Delta\mathbf{y}\Delta\mathbf{y}^T] = \mathbf{A}\mathbf{R}_{xx}\mathbf{A}^T+\mathbf{R}_{ww}$$
$$\mathbf{R}_{xy} = E[\Delta\mathbf{x}\Delta\mathbf{y}^T] = \mathbf{R}_{xx}\mathbf{A}^T$$

from eqn. 4.27 and 4.26.

---

*For data and model that are Gaussian random variables, the linear estimate is also the best nonlinear estimate.

Aki and Richards [1980, p. 696] point out that if the normalized variables of equation 4.20 are used, with $\mathbf{R}_{xx}$ and $\mathbf{R}_{yy}$ as in eqn. 4.29, then the expressions in transformed coordinates for those of 4.28a&b are:

$$\Delta\hat{\mathbf{x}}'_s = [\mathbf{A}']^T\Delta\mathbf{y}' \qquad \{\mathbf{A}'\}^{-1} = [\mathbf{A}'_g]^{-1} = [\mathbf{A}']^T \tag{4.30}$$

and the deviations to the real coordinates are:

$$\Delta\hat{\mathbf{x}}_s = \mathbf{R}_{xx}^{1/2}\Delta\hat{\mathbf{x}}'_s = \mathbf{X}\Lambda_{xx}^{1/2}\Delta\hat{\mathbf{x}}'_s \tag{4.31}$$

The resolution, information, and covariance matrices for the stochastic inverse are straightforward:

resolution

$$\begin{aligned}\mathbf{R} &= \{\mathbf{A}\}^{-1}\mathbf{A} = \mathbf{R}_{xx}\mathbf{A}^T(\mathbf{A}\mathbf{R}_{xx}\mathbf{A}^T+\mathbf{R}_{ww})^{-1}\mathbf{A} \\ &= \mathbf{R}_{xx}^{1/2}[\mathbf{A}']^T\mathbf{A}'\mathbf{R}_{xx}^{-T/2}\end{aligned} \tag{4.32a}$$

information

$$\begin{aligned}\mathbf{E} &= \mathbf{A}\{\mathbf{A}\}^{-1} = \mathbf{A}\mathbf{R}_{xx}\mathbf{A}^T(\mathbf{A}\mathbf{R}_{xx}\mathbf{A}^T+\mathbf{R}_{ww})^{-1} \\ &= \mathbf{R}_{yy}^{1/2}\mathbf{A}'[\mathbf{A}']^T\mathbf{R}_{yy}^{-T/2}\end{aligned} \tag{4.32b}$$

model covariance

$$\begin{aligned}\mathbf{R}_{\Delta x} &= \mathbf{R}_{xx}-\mathbf{R}_{xx}\mathbf{A}^T(\mathbf{A}\mathbf{R}_{xx}\mathbf{A}^T+\mathbf{R}_{ww})^{-1}\mathbf{A}\mathbf{R}_{xx}^T \\ &= \mathbf{R}_{xx}^{1/2}[\mathbf{I}-[\mathbf{A}']^T\mathbf{A}']\mathbf{R}_{xx}^{T/2} \\ &= [\mathbf{I}-\mathbf{R}]\mathbf{R}_{xx}\end{aligned} \tag{4.32c}$$

The stochastic inverse can easily be carried out by a small modification to the maximum likelihood inverse defined in the previous section. We interpret the $\mathbf{R}_{yy}$ matrix input to the ML algorithm as $\mathbf{R}_{ww}$ instead of $\mathbf{R}_{yy}$. Using these matrices, we normalize the coordinates as before,

$$\mathbf{A}' = \mathbf{R}_{ww}^{-T/2}\mathbf{A}\mathbf{R}_{xx}^{1/2} \qquad 4.33$$

$$\Delta\mathbf{x}' = \mathbf{R}_{xx}^{-1/2}\Delta\mathbf{x} \qquad \Delta\mathbf{y}' = \mathbf{R}_{ww}^{-1/2}\Delta\mathbf{y}$$

In the normalized system, the stochastic inverse operator is obtained by inserting $\mathbf{A} = \mathbf{R}_{ww}^{1/2}\mathbf{A}'\mathbf{R}_{xx}^{-T/2}$ into 4.28b.

$$\begin{aligned}
\mathbf{A}_s^{-1} &= \mathbf{R}_{xx}\mathbf{R}_{xx}^{-1/2}[\mathbf{A}']^T\mathbf{R}_{ww}^{T/2}[\mathbf{R}_{ww}^{1/2}\mathbf{A}'\mathbf{R}_{xx}^{-T/2}\mathbf{R}_{xx}\mathbf{R}_{xx}^{-1/2}[\mathbf{A}']^T\mathbf{R}_{ww}^{T/2} - \mathbf{R}_{ww}^{1/2}\mathbf{R}_{ww}^{T/2}]^{-1} \\
&= \mathbf{R}_{xx}^{T/2}[\mathbf{A}']^T\mathbf{R}_{ww}^{T/2}[\mathbf{R}_{ww}^{1/2}(\mathbf{A}'[\mathbf{A}']^T + \mathbf{I})\mathbf{R}_{ww}^{T/2}]^{-1} \\
&= \mathbf{R}_{xx}^{T/2}[\mathbf{A}']^T\mathbf{R}_{ww}^{T/2}\mathbf{R}_{ww}^{-T/2}(\mathbf{A}'[\mathbf{A}']^T + \mathbf{I})^{-1}\mathbf{R}_{ww}^{-1/2} \\
&= \mathbf{R}_{xx}^{T/2}[[\mathbf{A}']^T[\mathbf{U}'\Lambda'[\mathbf{V}']^T\mathbf{V}'\Lambda'[\mathbf{U}']^T + \mathbf{I}]^{-1}]\mathbf{R}_{ww}^{-1/2} \\
&= \mathbf{R}_{xx}^{T/2}[[\mathbf{A}']^T[\mathbf{U}'(\Lambda')^2[\mathbf{U}']^T + \mathbf{I}]^{-1}]\mathbf{R}_{ww}^{-1/2} \\
&= \mathbf{R}_{xx}^{T/2}[[\mathbf{A}']^T[\mathbf{U}'[(\Lambda')^2 + \mathbf{I}][\mathbf{U}']^T]^{-1}]\mathbf{R}_{ww}^{-1/2} \\
&= \mathbf{R}_{xx}^{T/2}[\mathbf{V}'\Lambda'[\mathbf{U}']^T[[\mathbf{U}']^T]^{-1}[(\Lambda')^2 + \mathbf{I}]^{-1}[\mathbf{U}']^{-1}]\mathbf{R}_{ww}^{-1/2} \\
&= \mathbf{R}_{xx}^{T/2}[\mathbf{V}'\Lambda'[(\Lambda')^2 + \mathbf{I}]^{-1}[\mathbf{U}']^{-1}]\mathbf{R}_{ww}^{-1/2}
\end{aligned}$$

but $\mathbf{U}'$ is a unitary matrix, $[\mathbf{U}']^T = [\mathbf{U}']^{-1}$, thus

$$\mathbf{A}_s^{-1} = \mathbf{R}_{xx}^{1/2}\mathbf{V}'\left[\frac{\lambda'_i}{\lambda'^2_i+1}\right][\mathbf{U}']^T\mathbf{R}_{ww}^{-T/2} \qquad 4.34a$$

and

$$[\mathbf{A}'_s]^{-1} = \mathbf{V}'\left[\frac{\lambda'_i}{\lambda'^2_i+1}\right][\mathbf{U}']^T$$

Thus, the normalized system maximum likelihood formulation, eqn. 4.21a, is used, but the elements of $\{\Lambda'\}^{-1} = [\Lambda'_p]^{-1}$,

$$\begin{cases} \lambda'^{-1}_i & \lambda'_i \neq 0 \\ 0 & \lambda'_i = 0 \end{cases} \qquad 4.35a$$

are replaced by:

$$\frac{\lambda'_i}{\lambda'^2_i - 1} \qquad 4.35b$$

This is a useful relationship for using the same computer code to do the stochastic as well as maximum likelihood inverse.

The model

Following Dorman [1979] and Dorman and Jacobson [1981], this work uses the parameterization of the model, x, as linear velocity gradient between a fixed partition of velocity points. Integration of the gradient model obtains the usual velocity-depth relation. The advantage of this parameterization over that of the velocity-depth points themselves is that a linear relation between the travel-time data and the gradients can be obtained [Garmany, 1979]. This vastly simplifies the inversion by eliminating the need to iterate on linearized systems.

Dorman and Jacobson chose as their data values the $\tau(p)$ and $\zeta(p)$ functions. $\tau(p)$ is the usual intercept time variable

$$\tau(p) = t(p) - p\,x(p) \qquad 4.36a$$

and $\zeta(p)$ is the more artificial variable:

$$\zeta(p) = t(p) + p\,x(p) \qquad 4.36b$$

where $t(p)$ is the geometrical travel time, and $x(p)$ the geometrical offset as a function of ray parameter, p. The justification of this use of the τ and ζ transformations over the t and x values directly is that the error covariance matrix for τ and ζ is diagonal. This is important for the original application because x and t were correlated due to the measurement method used--arrival time picks were made directly in $x-t$ space and a smoothed travel-time curve fit to them using least squares techniques. The slowness was then obtained by differentiating the

smoothed travel time curve. This is not the case in our work, since p, $t(p)$, and $x(p)$ are measured independently by the array processing methods. In addition, we prefer the use of the maximum likelihood or stochastic inverse formulation which automatically diagonalize and normalize all the datum values into a coordinate system in which all the data are uncorrelated and equal in variance. In fact, Dorman and Jacobson show that because $\tau(p)$ is independent to first order of errors in the estimated slowness, p, any other datum will lead a diagonal covariance matrix with respect to p when paired with τ.

One very important point is brought up by Dorman and Jacobson, which I feel to be the key to the whole misconception about results from inverse theory: The effective error in the measurements is primarily due to modeling error, not estimation error. The modeling error stems from departures of the real earth from the assumed structure, such as lateral inhomogeneity. For any finite data set, we can construct a model with enough degrees of freedom in the wrong parameterization which will predict noisy data from a completely different model perfectly. It is enough to make one quite cynical.

The use of the Dorman-Jacobson parameterization is straightforward. The A matrix on which the inversion structures outlined previously operate has elements $a_{ij} = \partial y_i/\partial x_j$. These elements are calculated through the relations originally derived by Slotnick [1959] through a change of variables from the Herglotz-Wiechert equations:

$$x(p) = np \int_{c_{min}}^{1/p} (c^{-2}-p^2)^{-1/2} \frac{dz(c)}{dc} dc \qquad 4.37a$$

$$t(p) = n \int_{c_{min}}^{1/p} c^{-2}(c^{-2}-p^2)^{-1/2} \frac{dz(c)}{dc} dc \qquad 4.37b$$

$$\tau(p) = n \int_{c_{min}}^{1/p} (c^{-2}-p^2)^{1/2} \frac{dz(c)}{dc} dc \qquad 4.37c$$

$$\zeta(p) = n \int_{c_{min}}^{1/p} [(c^{-2}-p^2)^{1/2} - p^2 c^2(z)(c^{-1}-p^2)^{1/2}] \frac{dz(c)}{dc} dc \qquad 4.37d$$

where c_{min} is the surface velocity, and n is the number of times the ray with parameter p traverses the model. To form a linear inverse problem, the medium is partitioned into layers with velocity bounds given by the set

$$\{\alpha_i\} \qquad i = 0,1,2,\ldots,n.$$

The inverse velocity gradients, $\frac{dz}{dc}$, are made constant between these partition points. For example, the offset function becomes

$$x(p_i) = \sum_{j=0}^{n-1} [dz/dc]_j \, n_j \int_{\alpha_j}^{\alpha_{j+1}} p\,(c^{-2}-p^2)^{-1/2} dc \qquad 4.38a$$

$$a_{ij} = n_j \int_{\alpha_j}^{\alpha_{j+1}} p\,(c^{-2}-p^2)^{-1/2} dc \qquad 4.38b$$

$$x_j = [dz/dc]_j \qquad 4.38c$$

$$y_j = x(p_i) \qquad 4.38d$$

where n_j is the number of times the ray traverses layer j. The other matrix elements follow similarly, and evaluation of the integrals in 4.37 for the linear velocity gradient leads to the kernel elements:

offset:

$$a_{ij} = dx(p_i)/dx_j = \frac{n_j}{p}[(1-p^2\alpha_j^2)^{1/2} - (1-p^2\alpha_{j+1})^{1/2}] \qquad 4.39a$$

arrival time:

$$a_{ij} = dt(p_i)/dx_j = n_j[\ln(\frac{\alpha_{j+1}}{\alpha_j}\frac{1+(1-p^2\alpha_j^2)^{1/2}}{1+(1-p^2\alpha_{j+1}^2)^{1/2}})] \qquad 4.39b$$

intercept time:

$$a_{ij} = d\tau(p_i)/dx_j = n_j[\ln(\frac{\alpha_{j+1}}{\alpha_j}\frac{1+(1-p^2\alpha_j^2)^{1/2}}{1+(1-p^2\alpha_{j+1}^2)^{1/2}}) + (1-p^2\alpha_{j+1}^2)^{1/2} - (1-p^2\alpha_j^2)^{1/2}] \quad 4.39c$$

zeta:*

$$a_{ij} = d\zeta(p_i)/dx_j = n_j[\ln(\frac{\alpha_{j+1}}{\alpha_j}\frac{1+(1-p^2\alpha_j^2)^{1/2}}{1+(1-p^2\alpha_{j+1}^2)^{1/2}}) - (1-p^2\alpha_{j+1}^2)^{1/2} - (1-p^2\alpha_j^2)^{1/2}] \quad 4.39d$$

These equations are valid for all layers j, except that for which $\alpha_j<1/p<\alpha_{j+1}$. For this layer, the turning point layer, $\alpha_{j+1}=1/p$ must be substituted into eqn. 4.39.

To recover the velocity-depth model from the inverse gradient dz/dc, an integration must be carried out. For the sampled inverse gradient solution, $x=[x_i]$, this is done by:

$$z(\alpha_i) = \sum_{j=0}^{i-1}[dz/dc]_j(\alpha_{j+1}-\alpha_j) = \sum_{j=0}^{i-1}x_j(\alpha_{j+1}-\alpha_j) \quad 4.40a$$

or, in matrix notation,

$$z = Tx \quad 4.40b$$

$$z = \begin{bmatrix} . \\ . \\ z_i \\ . \\ . \end{bmatrix} = \begin{bmatrix} . \\ . \\ z(\alpha_i) \\ . \\ . \end{bmatrix} \quad 4.40c$$

$$T = \begin{bmatrix} \Delta\alpha_0 & 0 & \cdot\ \cdot & 0 \\ \Delta\alpha_0 & \Delta\alpha_1 & \cdot\ \cdot & 0 \\ . & . & \cdot\ \cdot & . \\ . & . & \cdot\ \cdot & . \\ \Delta\alpha_0 & \Delta\alpha_1 & \cdot\ \cdot & \Delta\alpha_{n-1} \end{bmatrix} \qquad \Delta\alpha_j = (\alpha_{j+1}-\alpha_j) \quad 4.40d$$

The transformation matrix, T, is also used to obtain the resolution, information, and covariance matrices for the integrated model z from the inverse gradient model, x.

*The corresponding equation, Number 33 in Dorman and Jacobson's [1981] paper, is in error.

resolution:

$$\mathbf{R}_{\tilde{\tau}} = \mathbf{T}\mathbf{R}_{\tau}\mathbf{T}^{-1} \qquad 4.41a$$

information:

$$\mathbf{E}_{\tilde{\tau}} = \mathbf{E}_{\tau} \qquad 4.41b$$

covariance:

$$\mathbf{R}_{\tilde{\tau}\tilde{\tau}} = \mathbf{T}\mathbf{R}_{\tau\tau}\mathbf{T}^{T} \qquad 4.41c$$

While Dorman and Jacobson [1981] show that including the $x(p)$ data through $\zeta(p)$ in the inversion can improve the stability of the resulting model, the inversion is poor if non-geometrical arrivals are used. This was not a problem in their work because tracing the first arrival curve in $x-t$ space guarantees that only geometrical arrivals will be used. This can be seen by examining the $\theta(p)$ curves used in the WKBJ method (eqn. 4.6a). Being the first arrival at $\theta(p_0)$ implies that other arrivals are later, thus, $\theta(p_0)$ is a minimum of the $\theta(p)$ curve. If $\theta(p_0)$ is a minimum, then $d\theta(p)/dp\,|_{p0} = 0$, which is the condition for a geometrical arrival, since

$$0 = \frac{d}{dp}\theta(p)|_{p0} = \frac{d}{dp}[\tau(p) - pX]|_{p0} = -x(p_0) = X$$

and $X = x(p_0)$, the geometrical offset. However, using slant stacking or any of the methods of coherent processing described in Chapter 3 will pick up significant late breaking arrivals not predicted by ray theory, along with later breaks due to triplications, etc. If the WKBJ method is again used for illustrative purposes, we know that all arrivals will appear on the $\theta(p)$ locus for a given offset and kinematic group of interest. It doesn't matter to the $\tau(p)$ datum whether or not the arrival is at an inflection of $\theta(p)$, corresponding to a geometrical arrival. The measurements made by the short aperture zero offset velocity analysis processor centered at X will be $\theta(p)$, p, X. The estimate of $\tau(p)$, $\tilde{\tau}(p)$, is obtained from these (noiseless) measurements

by:

$$\hat{\tau}(p) = \theta(p) - pX.$$

Since in the WKBJ approximation $\theta(p) = \tau(p) + pX$,

$$\hat{\tau}(p) = \tau(p).$$

On the other hand, the estimated value of $\zeta(p)$, $\hat{\zeta}(p)$, is obtained by:

$$\hat{\zeta}(p) = \theta(p) - pX = \tau(p) - pX - pX.$$

The true value of $\zeta(p)$ which is assumed in the matrix kernel of eqn. 4.39d is:

$$\zeta(p) = \iota(p) + px(p) = \tau(p) + px(p) + px(p)$$

and is not equal to $\hat{\zeta}(p)$ unless $X = x(p)$, and a geometrical arrival is obtained. Thus, if valuable late breaks are to be used, it must be determined if they are geometrical arrivals due to triplication, and not non-geometric (e.g. shadow zone) arrivals before including them in the $\zeta(p)$ data. This caution is true of all parameterizations except $\tau(p)$, which was seen to map all arrivals predicted by the WKBJ method onto the proper geometrical $\tau(p)$ curve.

To illustrate this problem, noisy synthetic data were generated for arrays at offsets of 5, 10, 15, 20, 25, and 30 km using the WKBJ synthetic seismogram method. To keep the example simple, the sources and receivers were located at the surface, and 3 free surface multiples were included. The synthetic-array data were velocity analysed with zero-offset processing to yield estimates of arrival time and offset as a function of slowness from the peaks of the velocity spectra. These data were then converted into $\tau(p)$ and $\zeta(p)$ using the required transformations, and all arrivals, including multiples from the 6 offsets were inverted simultaneously using the maximum likelihood formulation of the linear least squares inversion technique. For these simple examples, the velocity partition used was the same as the true model. Figure 4.8a shows the model $\tau(p)$ curves for each multiple (solid lines) and the sample points (letters and

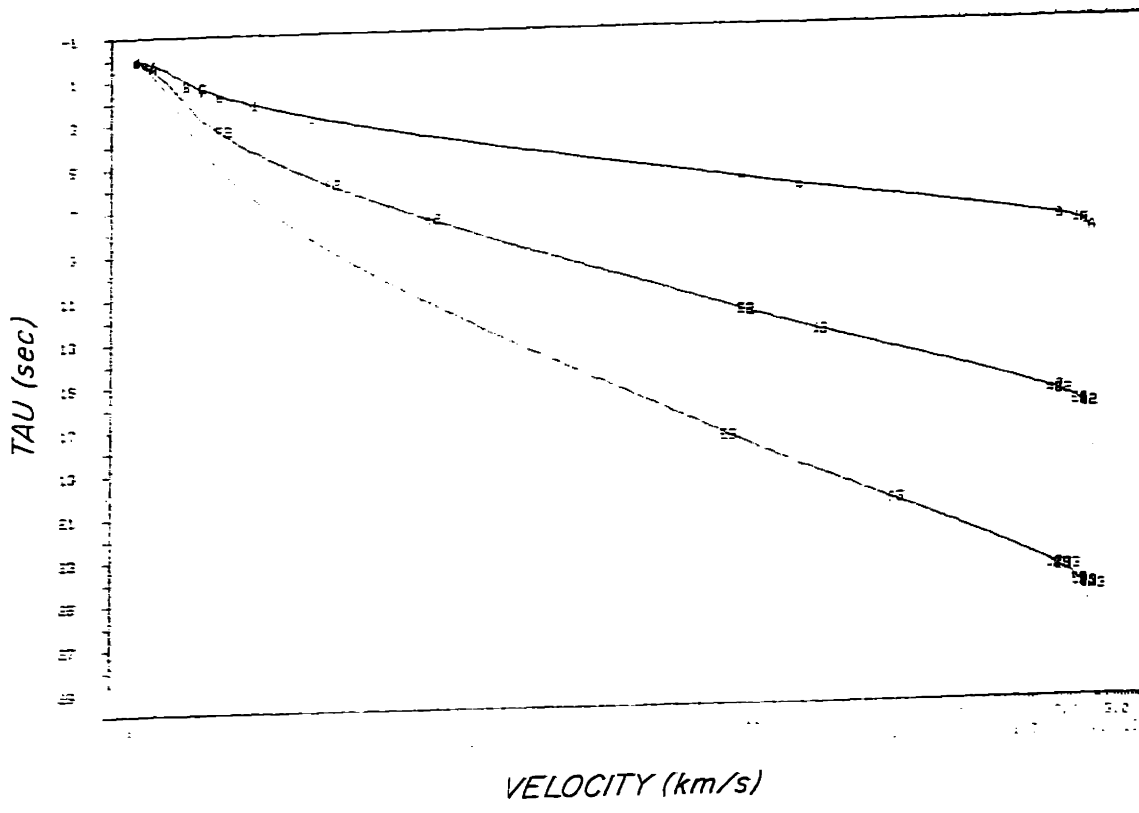

Fig. 4.8a) $\tau(p)$ data (letters) and ray trace $\tau(p)$ curves (solid lines) for the primary and first 2 free surface multiples.

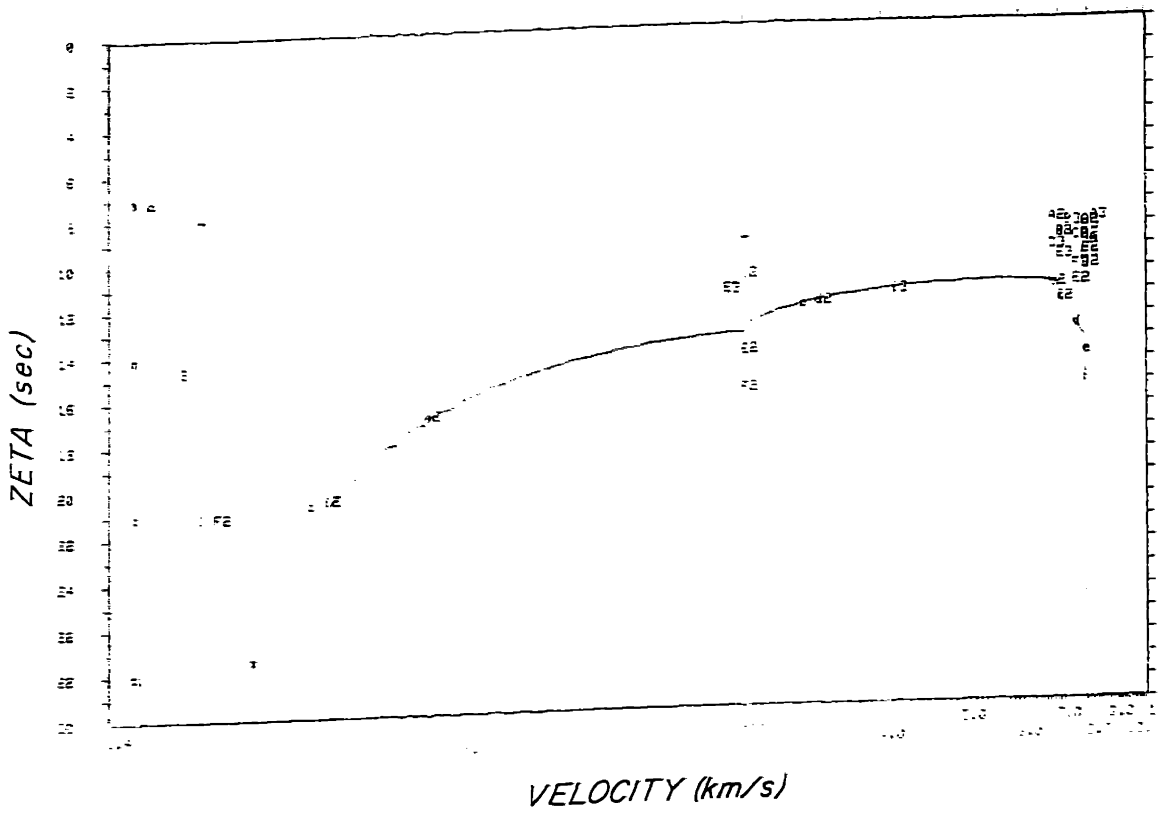

Fig. 4.8b) $\zeta(p)$ data (letters) and ray trace (geometrical) $\zeta(p)$ curve (solid lines) for the primary and first 2 free surface multiples. The multiple data have been "condensed" to their equivalent primary curve by the method given in the second section of this chapter. The upper case data points are non-geometrical arrivals.

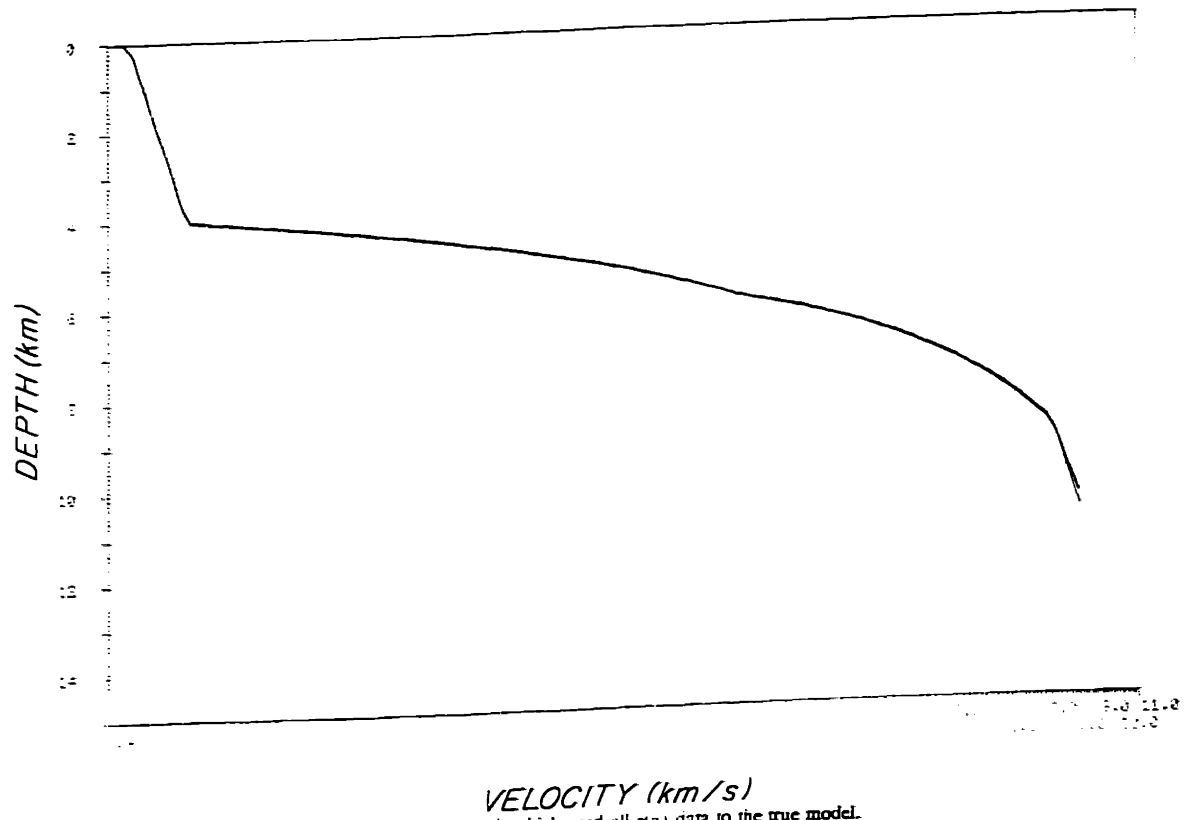

Fig. 4.8c) Comparison of the $\tau(p)$ inversion result which used all $\tau(p)$ data to the true model. The curves are nearly identical.

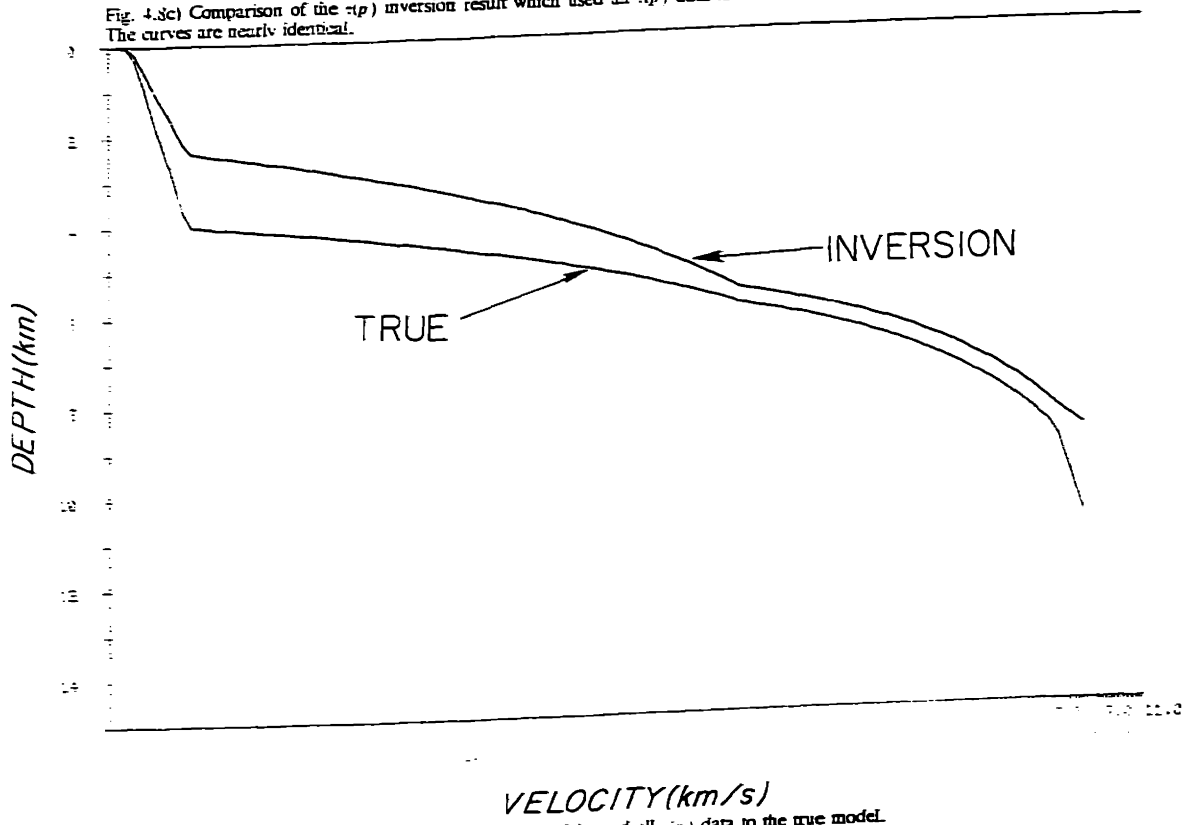

Fig. 4.8d) Comparison of the $\tau(p)$ inversion result which used all $\tau(p)$ data to the true model. The inversion result is grossly in error due to the inclusion of the non-geometrical data.

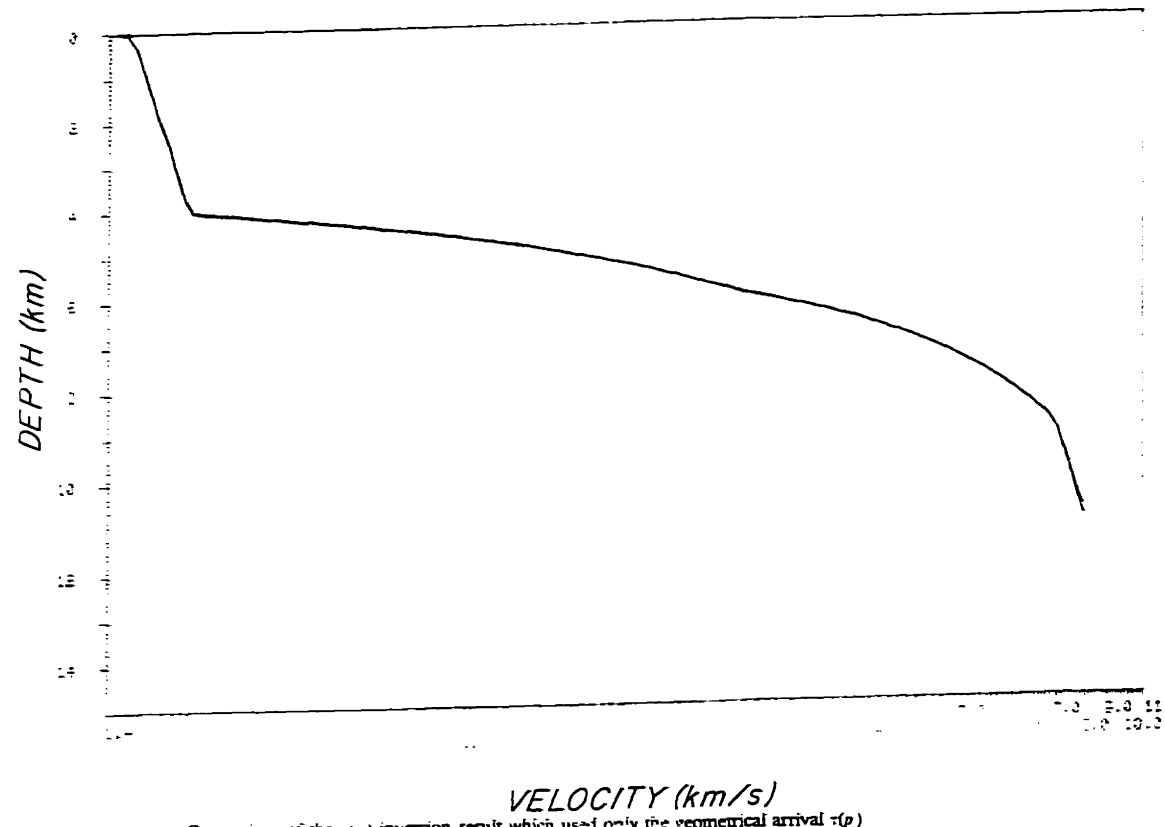

Fig. 4.8e) Comparison of the $\tau(p)$ inversion result which used only the geometrical arrival $\tau(p)$ data to the true model. The curves are nearly identical.

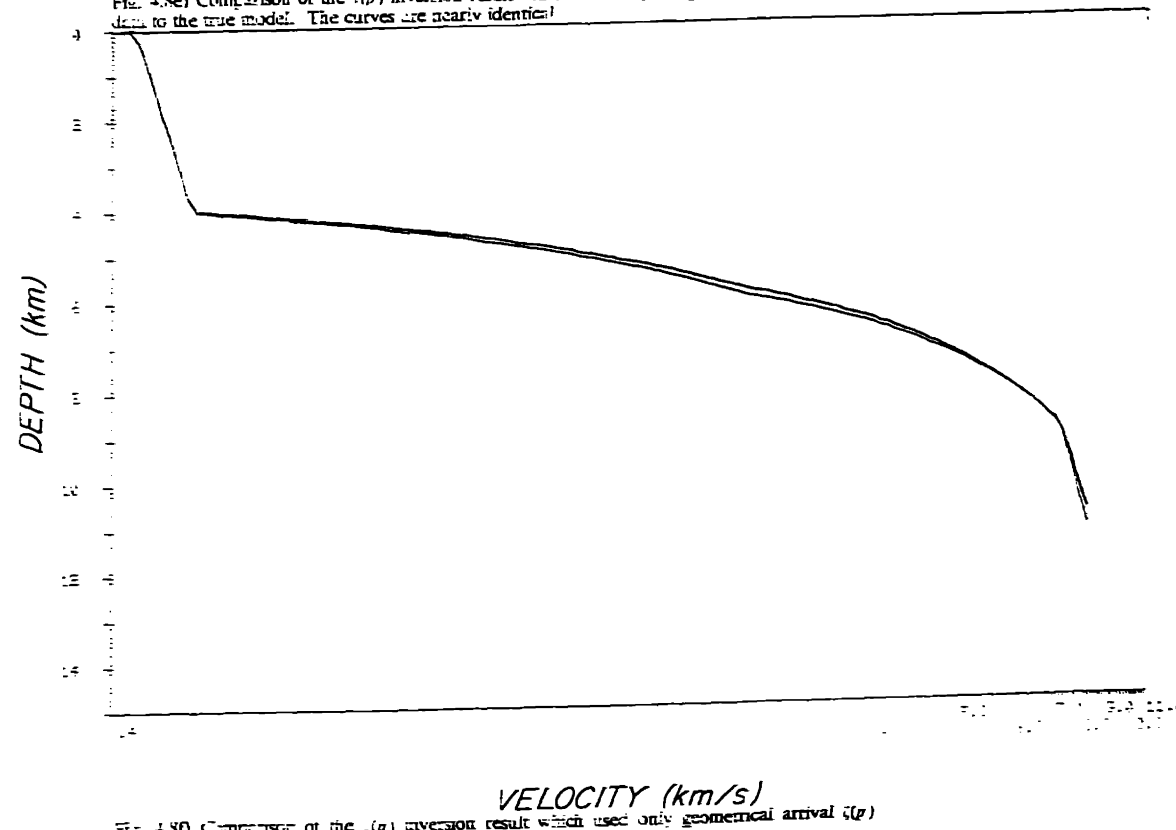

Fig. 4.8f) Comparison of the $z(p)$ inversion result which used only geometrical arrival $z(p)$ data to the true model. The curves are nearly identical.

numbers) from the 6 offsets. The letters $a,b,c,...$ indicate the offset, 5, 10, 15, ... , and the numbers the order of the free surface multiple. Upper case letters are from non-geometrical arrivals, and lower case letters are from geometrical arrivals.* Note that all $\tau(p)$ arrivals, geometrical and non-geometrical, fall on the geometrical $\tau(p)$ curves.

Figure 4.8b shows the true first arrival geometrical $\zeta(p)$ curve (solid line) and the letters are the $\zeta(p)$ values determined from the data. The multiples have been reduced by their multiplicity, as described in an earlier section, to convert all to their equivalent first arrival values. Note that the geometrical arrivals (lower-case letters) generally fall on the solid curve,** while the non-geometrical arrivals (upper-case) do not. Figure 4.8c shows the true model and the result of inverting just the $\tau(p)$ data. The models are in such close agreement as to be undifferentiable. Figure 4.8d shows the true model, and the result of inverting the $\zeta(p)$ data including all arrivals. The inversion result is not close at all to the true model because of the inclusion of the non-geometrical arrivals. Figure 4.8e is the $\tau(p)$ inversion result for geometrical data only. This result is identical to the result of Figure 4.8c. Figure 4.8f is the result of inverting the geometrical $\zeta(p)$ data only. A nearly correct model has resulted, comparing the true (bottom) and result (top) curves. The deviation that is seen is probably due to the fact that I left a $\zeta(p)$ value that was not quite geometrical in the dataset that was inverted.

---

*Whether or not the arrivals are geometrical can be determined on the synthetic data since the $\theta(p)$ curves are available.

**The seismograms did have noise added, so there is some estimation error.

INVERSION BY WAVE-FIELD IMAGING (MIGRATION)

Introduction

The final method used to invert refraction/wide angle reflection data in chapter 5 is a modification of the method proposed by Clayton and McMechan [1981]. In their method, the slant stacked data in $\tau-p$ space is downward continued in depth-slowness space by an approximation to the wave equation using a trial model. They showed that when the migrated data agreed with the trial model that the trial model was correct, and that an algorithm which converged to this solution could be constructed by choosing the results of the previous migration as the next trial model.

The advantages of this method over those previously described are:

[1] The error between the trial model and the migrated data is viewed in model space, thus giving a direct indication of regions where the model is either unspecified by the data, or in error.

[2] Decisions regarding data editing are done in model space, again making it clear what the ramifications of a given choice are.

[3] The observed wavefield data themselves are transformed, thus allowing the inherent bandwidth (or width of the ambiguity function) to be propagated to the model domain, thus directly giving an indication of the resolution of the inversion.

[4] For sparse data any interpolation is done in model space, and is thus directly operator controlled. (Interpolation of a $\tau-p$ curve leads to effects on the model resulting from the inversion of the interpolated $\tau-p$ data which are difficult to control.)

[5] Association of a given peak in the data [$\tau-p$ space] with the incorrect kinematic group is easily detected and corrected. This makes this method more similar to an " L1 " or robust inversion than the usual " L2 " or least squares type.

For this work, the algorithm has been modified to work with data processed by velocity spectral analysis and which is not densely sampled in offset, thus leading to gaps in the slowness coverage. In the original development of the algorithm, the slant stacked waveforms themselves were migrated. In general, the slant stacks were computed on the entire data section, and one $\tau-p$ representation was obtained. In this work, we have carried out short-aperture slant stacking (similar to Diebold and Stoffa, [1981]), and the many $\tau(p)$ spectra (one for each shot and frequency for which coherent processing over the sensor array was carried out) must be combined for the inversion. The differing offset samples will sample different regions of the infinite aperture $\tau(p)$ section, and thus no coherent addition can be done once in the $\tau(p)$ domain. For this reason I have chosen to composite the short offset velocity spectra by choosing as the output value at any $\tau(p)$ the largest value on any of the short aperture velocity spectra (after conversion of the velocity spectra to $\tau(p)$ coordinates.

Another major change that is sometimes used consists of replacement of the migration of the entire velocity analysis output after conversion to $\tau-p$ coordinates with inversion of peaks picked from velocity analysed data and expressed as $\tau(p)$ and $x(p)$ points. This method was chosen because it was much more computationally expedient, and because the complexity of the arrivals due to surface multipaths can yield very difficult to interpret raw $\tau-p$ representations. The width of the peaks is retained, however, in order to indicate the resolution of the result. The migration of both the $\tau(p)$ and $x(p)$ data is useful because of the sparse and variable density of the slowness sampling due to the sparse offset acquisition. The use of the $x(p)$

data constrains the derivative of the $\tau(p)$ curve, and thus allows tighter constraints on the model between measured $\tau(p)$ points.

In this section I will give a derivation of the original formulation by Clayton and McMechan that is more complete than theirs, and also give the extension of the migration to $x(p)$ data. It will also be shown that the wavelet phase independent nature of velocity spectral analysis and envelope detection removes the phase shift problems encountered in migration of the slant-stacks themselves. The propagation of the ambiguity functions associated with $\tau(p)$ and $x(p)$ data will be discussed. Finally, convergence properties on densely and sparsely sampled data curves with and without measurement noise will be demonstrated and an algorithm for stabilizing and increasing the convergence rate of the migration method will be introduced.

Original Formulation

The wave-field measured at the surface of a laterally homogeneous medium is given by $P(t,r)$. This data is slant stacked, either by the standard or proper slant stack*. Assuming that the simple 2-D Radon transform slant stack is used,

$$u(\tau,p,z=0) = \int_{-\infty}^{\infty} P(\tau+pr,r,z=0)\,dr \qquad 4.42$$

we have a representation of the observed surface data, $P(t,r)=P(t,r,z=0)$, in terms of the vertical component of its travel time, τ, and the ray parameter, p. Transforming over τ into the frequency domain using the sign definition in chapter 2 gives the Fourier transform of the slant stack as a slice through the 2-D Fourier transform over surface offset and time of the wave field.

*It doesn't matter which method is used to carry out the stack. The migration algorithm is approximate, and only migrates travel times correctly, not amplitude or wave shapes. The travel times are the same no matter what the dimensionality.

$$U(\omega,p,z=0) = \int_{-\infty}^{\infty} d\tau \int_{-\infty}^{\infty} P(t,r,z=0)e^{i\omega(t-pr)}dr = P(\omega,\omega p,z=0) \qquad 4.43$$

Recalling that both the 2-D and 3-D wave equation are separable in a layered medium (see eqn. 2.40) with separation constant $k_r = \omega p$ gives the vertical wave equation as:

$$\left[\frac{\partial^2}{dz^2} - k_z^2(z)\right] P_z(\omega,\omega p,z) = 0 \qquad 4.44a$$

$$k_z^2(z) = k^2(z) - k_r^2 = (\omega p(z))^2 - (\omega p)^2$$

Thus each component with fixed p can be migrated or extrapolated separately. For a homogeneous medium, $k_z(z) = k_z$, the downward continued or migrated solution to equation 4.44 at depth z subject to the boundary condition at the surface being given by $P(\omega,\omega p,z=0)$, and the field satisfying the radiation condition as $z \Rightarrow \infty$ is:

$$P(\omega,\omega p,z) = P(\omega,\omega p,0)e^{-ik_z z} \qquad 4.45$$

The minus sign in the exponent shows that though z is increasing and k_z is positive, we are running time backwards, so back-propagation requires decreasing the phase. Claerbout [1976, Chapter 10] indicates that for non-constant vertical wavenumbers the surface wave-field may be approximately downward continued** if terms involving the logarithmic gradient of the velocity with respect to depth are small compared to the gradients of the wave field itself. In any case, the travel time aspects of the approximate continuation are still correct, though the amplitude is approximate when the formula:

$$P(\omega,\omega p,z) = P(\omega,\omega p,0)\, e^{-i\omega\Psi(p,z)} \qquad 4.46$$

is used, with the phase factor given by:

$$\Psi(p,z) = \int_{\Gamma} [p^2(y) - p^2]^{1/2}\, dy \qquad 4.47$$

**Back-propagation would be more appropriate terminology, because we will actually run the wave equation backwards to the source, which requires both downward and upward propagation.

where Γ is the total vertical path from source to the receiver taken to a maximum depth of z. Thus, back-propagating the slant-stacked wave field:

$$\hat{U}(\omega,p,z) = U(\omega,p,z=0)e^{-i\omega\Psi(p,z)} \qquad 4.48a$$

or

$$\hat{u}(\tau,p,z) = \int_{-\infty}^{\infty} U(\omega,p,z=0)e^{-i\omega[\Psi(p,z)+\tau]}d\omega \qquad 4.48b$$

through the turning point can be used to image the source function as a function of z and the assumed profile, $p(z)$. To image the velocity depth profile, each plane wave component must be back-propagated to the source through the depth z at which it turns. After this operation, the $\tau=0$ value is the source value itself. Thus, the image of the source function is obtained by carrying out 4.48b with $\tau=0$, yielding

$$\hat{u}(p,z) = u(\tau=\Psi(p,z),p,z=0) \qquad 4.49$$

Thus, if the profile, $p(z)$, is the correct one for the data, the $\Psi(p,z=z_{turn})$ value will be $\tau(p)$, and the $\tau(p)$ curve in the slant-stacked wavefield will be imaged to $\hat{u}(p,z)$. If this image falls onto the trial curve $z(p)$, then the trial curve agrees with the data, and the correct solution has been obtained.

To get a qualitative feel for how the slant-stack is imaged when the trial $p(z)$ is correct we consider a simple case. If $z<z_{turn}$ then $\Psi(p,z)$ will be too small and points with smaller τ will be imaged to z. The magnitude of the τ difference, $\Delta\tau$, will depend on how much additional time the extra propagation distance, Δz, to z_{turn} would take. If z_{turn} is in a high velocity region, then for a given Δz, $\Delta\tau$ will be small, thus large changes in z away from the correct turning point selects points only slightly away from the correct $\tau(p)$ value, and the bandwidth of the slant stack is reflected in the "peakiness" in depth of the imaged wave-field. Similarly, for slower velocity regions, the spatial resolution is better. It is important to note that because

we are scanning z independently of the $p(z)$ and p values, the quantity inside the absolute values of eqn 4.47 can become negative. This problem is fixed by using an absolute value inside the square root, so z values which are below the trial model turning point simply continue to accumulate larger and larger τ values.

To motivate the convergence properties of the algorithm which uses the results of the previous image as the next trial model we consider what happens when the trial model, $z_i(p)$, is not the correct model, $z(p)$. If $z_i(p)$ is too fast, i.e. $z_i(p) < z(p)$ or $p_i(z) < p(z)$, then the accumulated τ at the correct turning depth, $z(p)$, will be too small. Thus, not until a larger (deeper) z will enough τ accumulate to pick up the data $\tau(p)$ point. This will indicate that z should be deeper at that p, or $z_{i+1}(p) > z(p) > z_i(p)$. Thus, the next trial model will err on the slower side of the true model. It is not obvious that this algorithm is convergent, and difficult to prove analytically*. Examples showing convergence properties will be given in a later section.

Migration of $x(p)$ data

The imaging of the $\tau(p)$ curve onto $z(p)$ done above does not need to be regarded as an operation on a wave-field, but simply as a method for inverting a function ($\tau(p)$) of the unknown model ($z(p)$) to obtain the model. The Herglotz-Wiechert equations give a formula for the direct inversion of $\tau(p)$ or $x(p)$ data for $z(p)$, and this has been realized using discrete approximations to the integral by the inversion methods outlined earlier in the chapter. As mentioned, the major problems with these methods are that the data curves are sparsely sampled in slowness, and that the correct trajectories must be identified and separated from artifacts and multipaths in the data space before the inversion can proceed. The slant stack

transformation greatly aids this procedure by giving a simple structure to the data (vis a vis the $x-t$ format), however, the migration method essentially takes this simplification one step further and allows picking to be done in the model space. In addition, the interpolation between sample points must be pre-specified by the model parameterization, and may or may not be correct. In their formulation, Clayton and McMechan deal only with $\tau(p)$ slant stack data, the usual format. Because of the short aperture used in our processing, the $x(p)$ datum is directly available. Because of the large distance between the short aperture estimates, however, the $\tau(p)$ curve is not sampled as densely in p as could be desired. This places a heavy burden on the model parameterization to interpolate between points specified by the measured $\tau(p)$ data. But, because the $x(p)$ datum is more dependent upon gradients in the velocity-depth profile, and less on the cumulative effects of the profile [Dorman and Jacobson, 1981], correct matching of the $x(p)$ curve is useful for interpolation of the model between points specified by matching of the $\tau(p)$ curve. The $x(p)$ data are also easily imaged by a modification to the migration algorithm. Instead of regarding the method as an operation on a wavefield, is should be thought of as simply using a trial model to pick up $\tau(p)$ or $x(p)$ data at points specified by the trial model and the image z value. When the trial model is consistent with the true model, the large amplitude peaks in $\tau(p)$ and $x(p)$ will be deposited on the trial model. Thus, the algorithm is just an iterative scheme for inverting a (multidimensional) function of the model for the model. Although the Herglotz-Wiechert equations give explicit inverse functions, we may motivate the use of this method because of the sparsely sampled (and thus non-invertible) nature of the data, and because of the inability to correctly pick the appropriate data points until they are already in model space. In this work, we have found the addition of $x(p)$ migration to help the operator more quickly converge on models which are

*I could not do it.

consistent with both the observed $\tau(p)$ and $x(p)$ data.

The method: The migration computer program

For complete transformation of the output of the velocity spectral analysis to imaged velocity depth sections the following steps are taken:

[1] The velocity spectral outputs are processed to remove the sidelobe artifacts by the simple image processing algorithm discussed earlier. The peaks of the velocity spectrum in (t,x,p) space are picked and stored.

[2] The image processed velocity spectral outputs are transformed to their surface datum $\tau-p$ representations using the measurement offset, x, and the source and receiver depths, z_s, z_r, by mapping the points (t,x,p) into (τ,p) using equations 4.1. When free surface multiples are to be migrated along with the direct arrivals, the regions on the velocity spectrum which contained multiples are identified and the value of the surface corrected τ is divided by the order of the multiple, as described in an earlier section of this chapter.

[3] The $\tau-p$ transformations of data at different offsets are superposed using the rule that the value of the superposition is the largest of the corresponding points on the individual offset $\tau-p$ spectra. This rule was used because the different offsets contained different samples of the $\tau-p$ curve, and thus the noise would continue to add, while the signals would not if a simple additive superposition was used. (See earlier discussion.)

[4] The superposed (or single offset) sections are imaged by an interactive computer program that displays the migrated section and/or picked peaks on a graphics device. The next trial model is then obtained by: i)picking from the display using the cursor on the graphics device to specify sample points along the curve, ii) entered via a terminal, iii) read

from a previously stored file, iv) automatically picked from the peak locus of the migrated section, or v) any combination of the above methods. In addition to the display of the migrated section, the program can display the $\tau-p$ (slant-stack) section and the trial $\tau-p$ curve computed from the model*, the picked $\tau(p)$ or $x(p)$ points from the velocity spectra (input data to the program, as well as the $\tau-p$ spectrum) and the $x(p)$ curve predicted by the trial model. Finally, to quickly check or match the arrival amplitude pattern to that of the model, the program can compute the predicted output of the velocity spectral analysis procedure on synthetic data generated at the observed offsets using the WKBJ method on the trial model. The predicted arrivals from the synthetics could be compared to those actually observed to further deviate the model to agree with the data, or to use the amplitude data to constrain ambiguous regions of the model.

After sufficient understanding of the velocity spectra of the real data was developed it was found that the primary arrival peak could be picked from the multipath complex with good reliability. This understanding was obtained through extensive analyses of detailed synthetics which included all the near-source/receiver multipaths. With this ability, it was found to be much more computationally expedient to migrate the picked $\tau(p)$ and $x(p)$ sections. This removed the need for each point on the $\tau-p$ spectrum to be migrated, and the extensive interpolation and contour plotting computations to be carried out. Instead, a reasonably fast search algorithm was used to find the $z(p)$ value that corresponded to the picked $\tau(p)$ and $x(p)$ data points. More will be said about this algorithm in the subsection on convergence. The picking was done in the non-datum corrected velocity spectral domain, and the surface datum and free

*The points specified by any of the above methods were interpolated by assuming linear slowness gradients with no first order discontinuities. This is not restrictive because an arbitrary density of velocity-depth points can be specified, thus effectively synthesizing any profile.

surface multiple corrected $\tau(p)$ and $x(p)$ data obtained through the (t,x,p) transformations of eqn. 4.1. The usual problem of picking without really knowing what one was picking was still prevented; any peak that might be an arrival was picked, and the multipath structure associated with it was determined later, after the $\tau-p$ transformation, or as the migration progressed. Both the $\tau(p)$ and $x(p)$ data can be imaged, though because of its "less simple" relation to the model and gradients, the $x(p)$ migration was usually used to determine the interpolation between sample $\tau(p)$ points, not to carry out the main migration. Results of the use of both these computer codes for inversion of real and synthetic data will be seen later in this chapter, and in chapter 5.

Phase shift effects

One of the major problems encountered by users of the migration technique for inversion of refraction/wide angle reflection data is the effects of variable phase shifts due to forward and reversed branch refractions and wide angle reflections. In the original work on the issue, Clayton and McMechan [1981] showed that an average phase shift could generally be satisfactorily used to bring the peak locus of migrated synthetic data to nearly the true velocity depth function. From there, the operator could often compensate for the phase shift by varying the picking criterion. This is not necessary when using the velocity spectral analysis processor. As was shown in chapter 3, this processor is insensitive to phase shifts, and thus once corrected for the window length effects, the arrival time detections are unbiased. This is illustrated in figures 4.9-4.14. Figure 4.9 shows the homogeneous layered model used to calculate the synthetic wide angle reflection data used in the examples. The reflection phases are shown in figure 4.10 for each of the layers. The theoretical slant stack of a modulated non-causal Gaussian pulse with peak located at the correct travel time is shown in figure 4.11, along with the

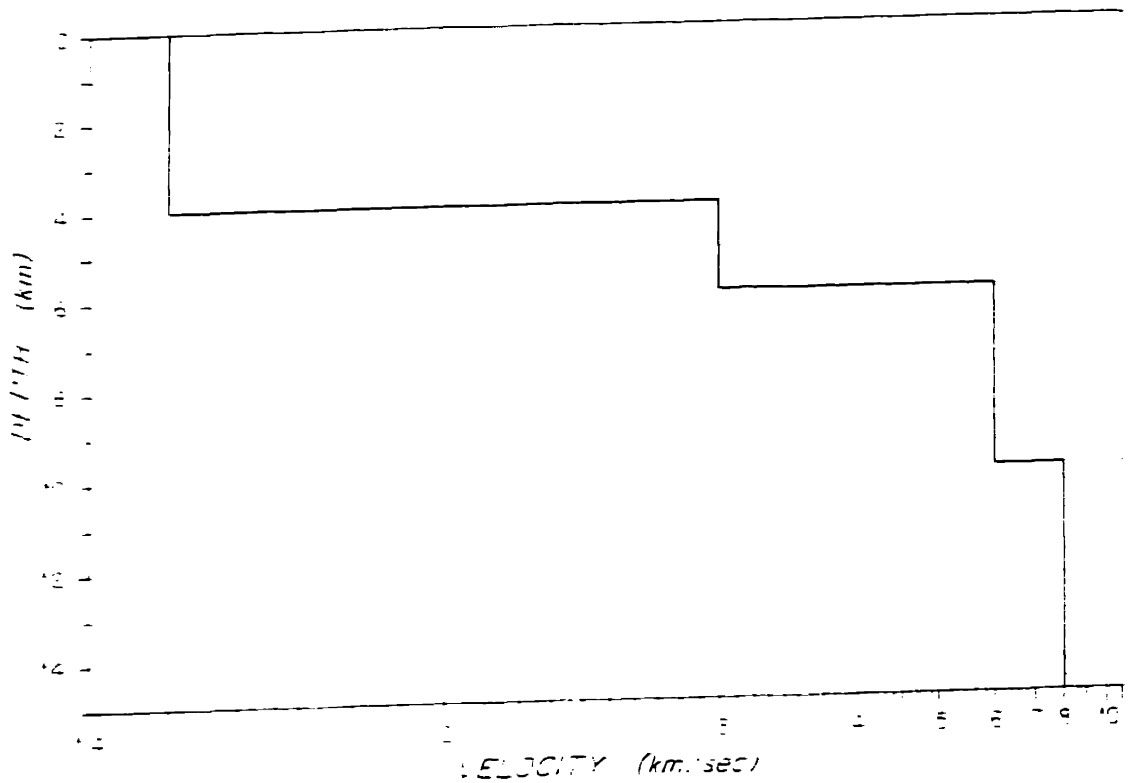

Fig. 4.9) Homogeneous layered velocity-depth model used for the calculation of the reflection coefficient phase shifts of fig. 3.1b.

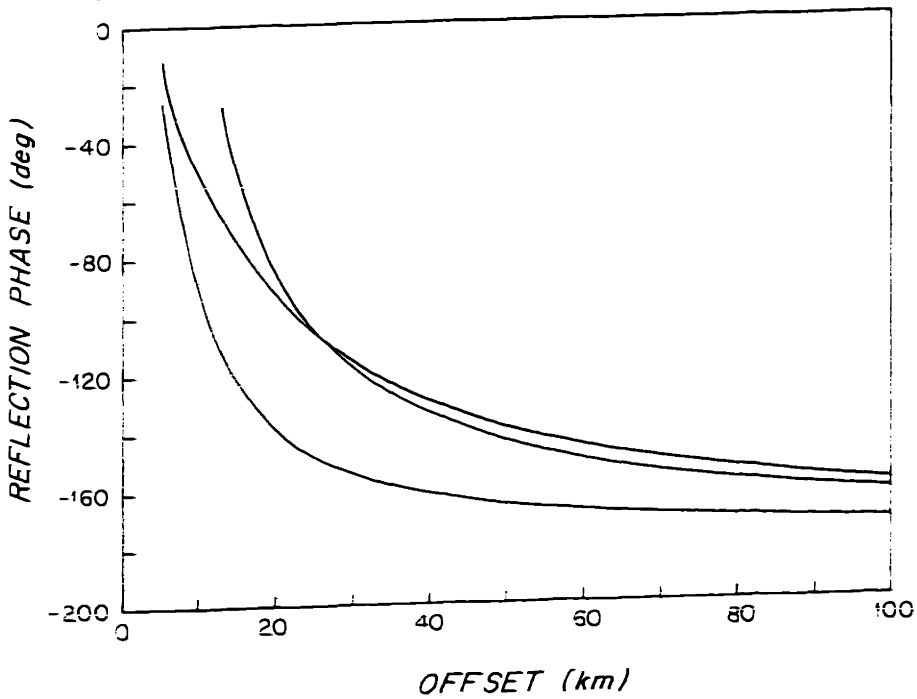

Fig. 4.10) Reflection coefficient phase shifts as a function of offset for the homogeneous layered model of fig. 3.1a. The three curves correspond to the 3 interfaces which would cause wide angle reflections.

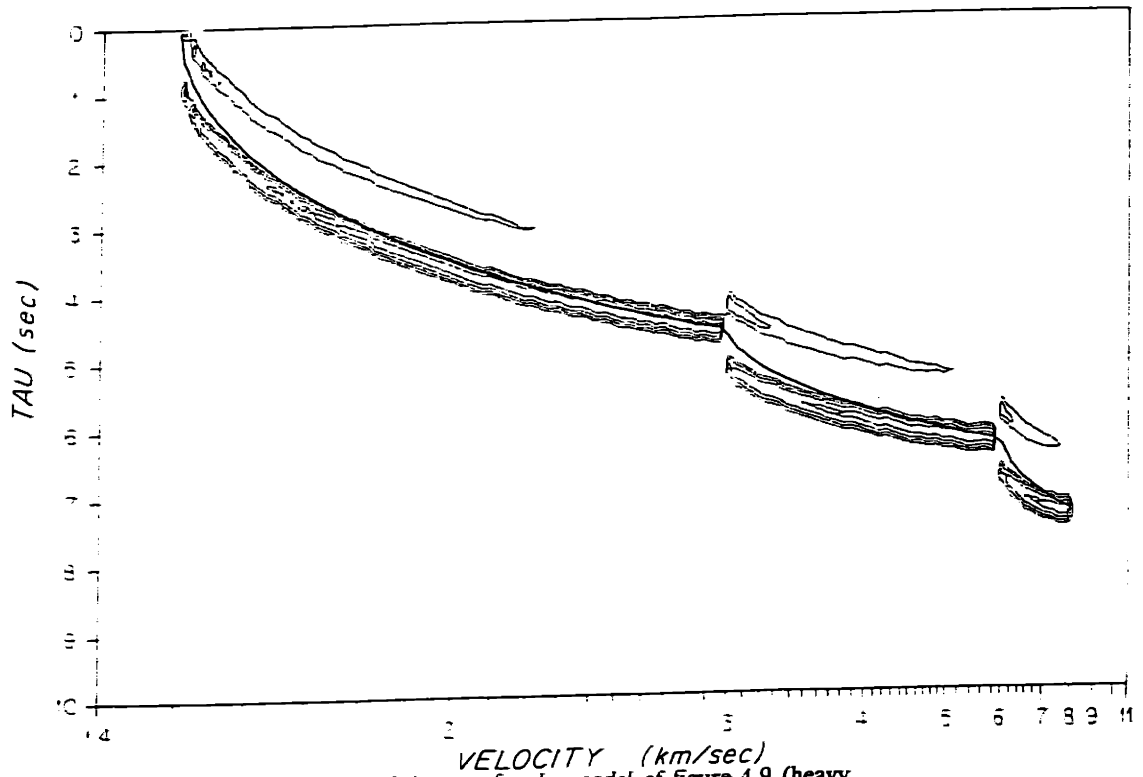

Fig. 4.11) The geometrical $\tau(p)$ curve for the model of figure 4.9 (heavy solid line) and the locus of the peak of the Gaussian pulse data (contours).

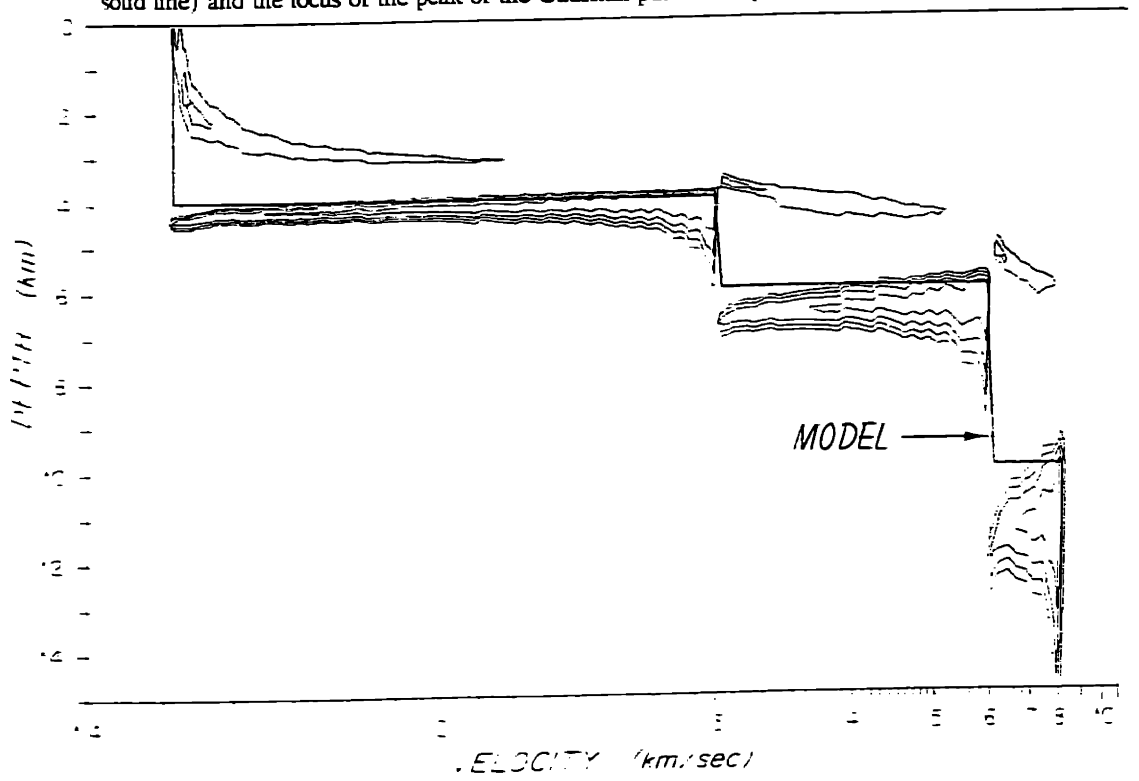

Fig. 4.12) The correct trial model (heavy solid line) and the image of the Gaussian pulse data of fig. 4.11 (contours). Note the discrepancy between the two in regions of large phase shift.

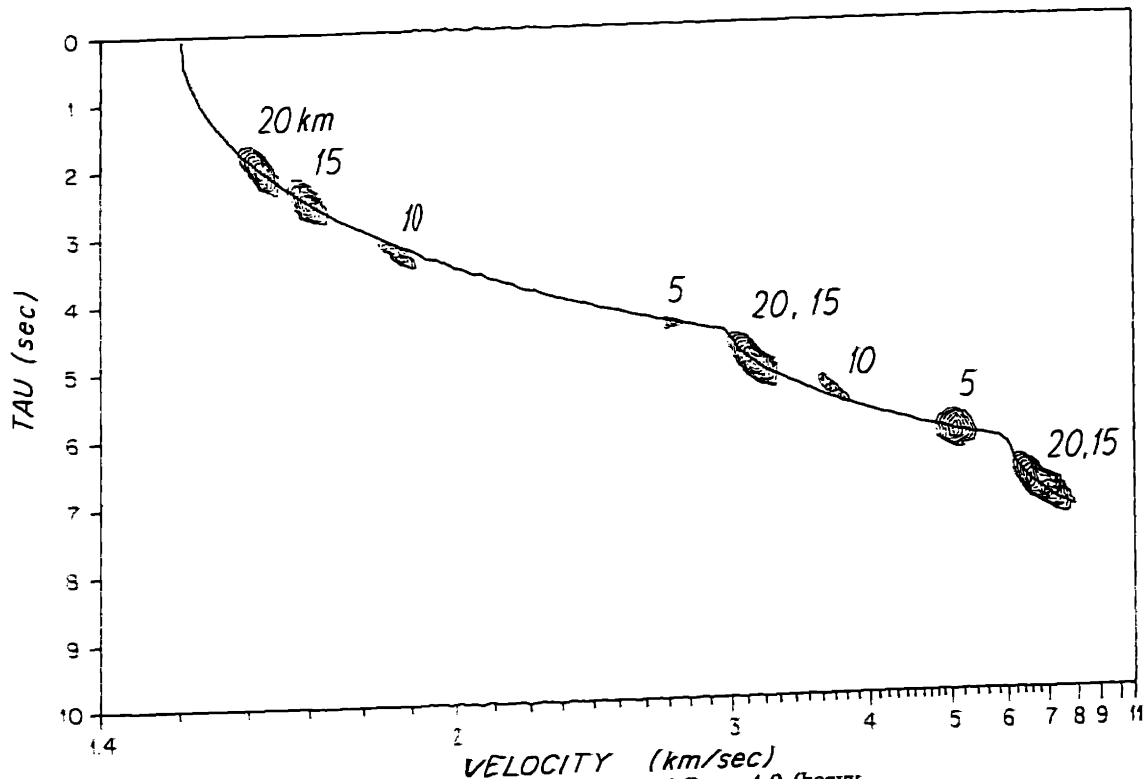

Fig. 4.13) The geometrical $\tau(p)$ curve for the model of figure 4.9 (heavy solid line) and the locus of the $\tau(p)$ estimates obtained from the velocity spectral analysis algorithm on synthetic array data centered around offsets of 5,10,15, and 20 km (contours).

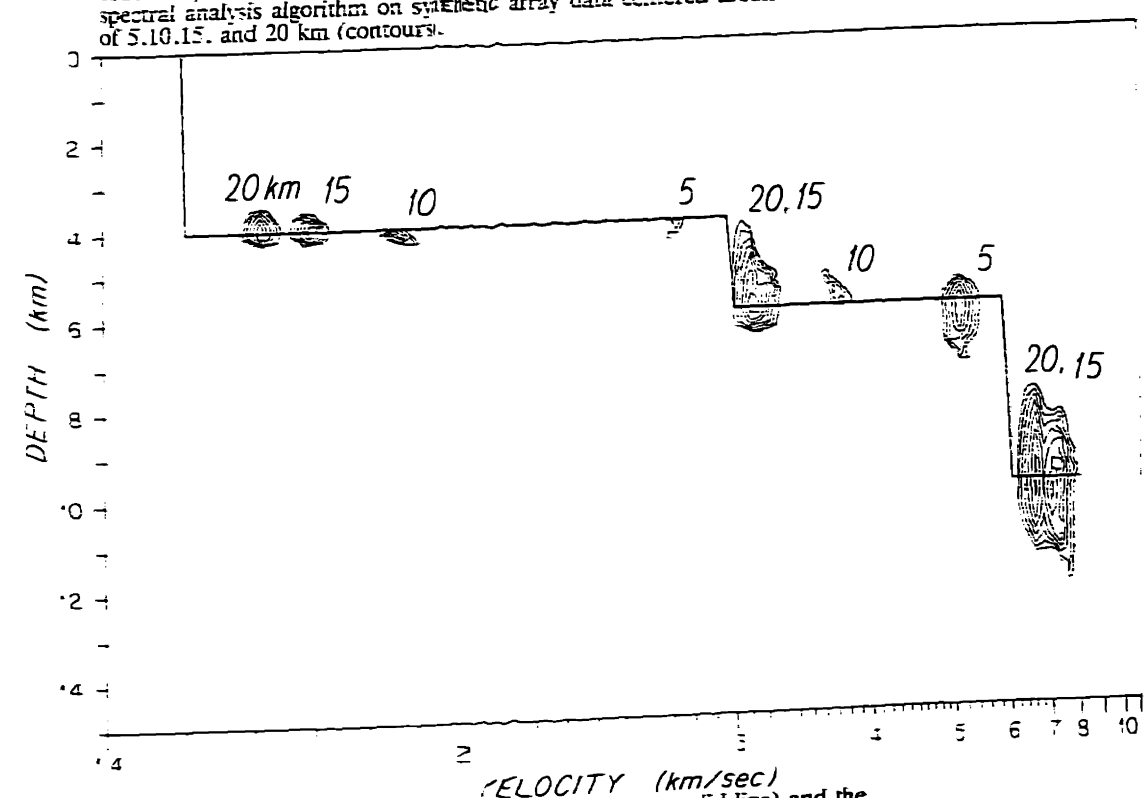

Fig. 4.14) The correct trial model of figure 4.9 (heavy solid line) and the locus of imaged $\tau(p)$ estimates from fig. 4.13 (contours).

true $\tau(p)$ curve for the model. A low frequency (1 Hz) modulation of the Gaussian was used to emphasize the phase shift. Note that the slant stack does not image the $\tau(p)$ curve correctly in figure 4.11 nor does the migration of the data fall on the correct profile in fig. 4.12. On the other hand, the output of the velocity spectral processor at 5, 10, 15, and 20 km. offsets is shown in figure 4.13, along with the model $\tau(p)$ curve. After imaging with the correct model, the velocity spectral results are shown in figure 4.14. Note that there is no consistent bias in the peak location, thus confirming that the velocity spectral analysis method is phase shift independent.

Properties and Examples of Velocity/Depth Migration

Resolution properties

Before using the migration inversion algorithm it is useful to examine its properties on synthetic data. The first issue is that of ambiguity function propagation. The imaging of the velocity spectra directly in the velocity depth plane allows the width of the peaks due to finite bandwidth to reflect the resolution of the inversion. Instead of imaging the spectra themselves, the effects are more clearly seen by imaging the synthetic data, and error bounds around the data. Figure 4.15 shows the $\tau(p)$ (solid lines) and $x(p)$ (dotted lines) curves (letters connected by lines) and the ± 0.1 sec and ± 2.0 km error bounds (lines only). Figure 4.16 gives the profile used to generate the data, "A", and two incorrect profiles used to migrate the data in some of the examples to show the relative utilities of $\tau(p)$ and $x(p)$ data. One model, "B", has gradients identical to those of the true model, but is 1 km too deep at each velocity. The other model, "C", has the wrong profile in the sedimentary region, but has the same deep layers as "A" and the accumulated τ and x for small p nearly correct. Figure 4.17a shows how the $\tau(p)$ data and error bounds are imaged by the trial model "A", which is the correct model. These

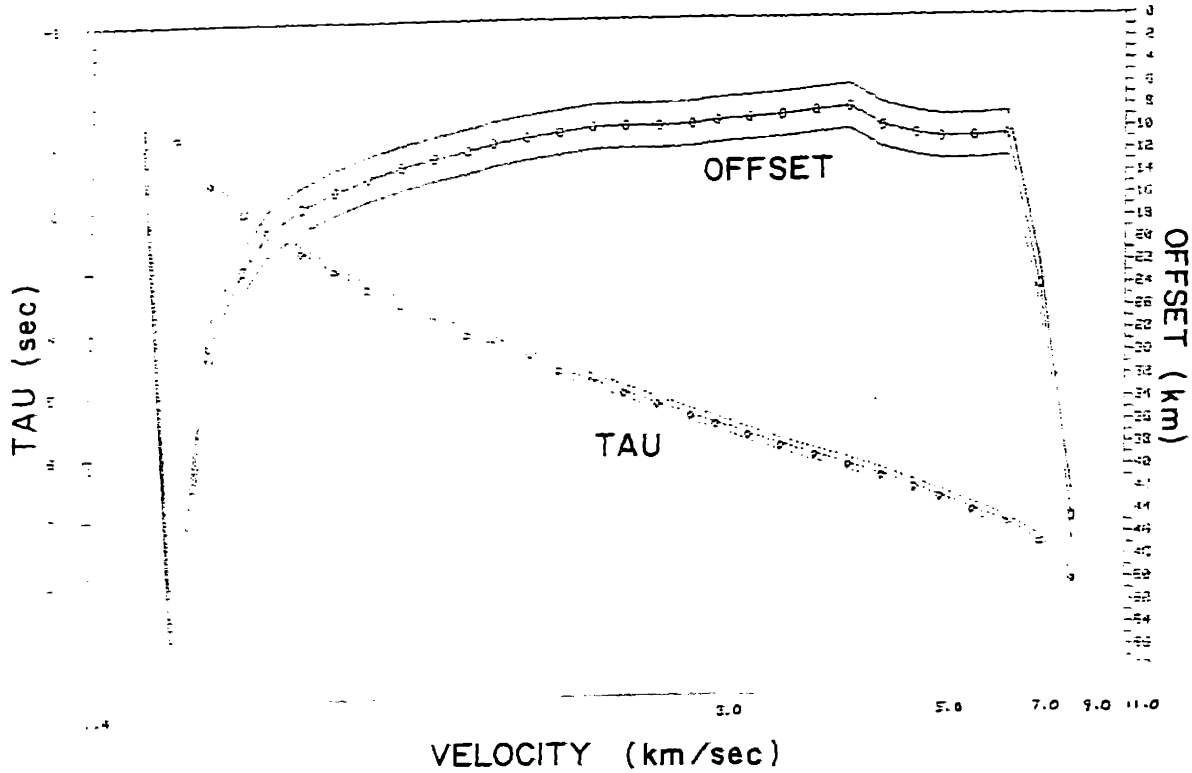

Fig. 4.15) $\tau(p)$ curve and $\pm.1$ sec error bounds (dotted) and $x(p)$ curve and $\pm 2.$ km error bounds (solid) for model "A" of fig. 4.16.

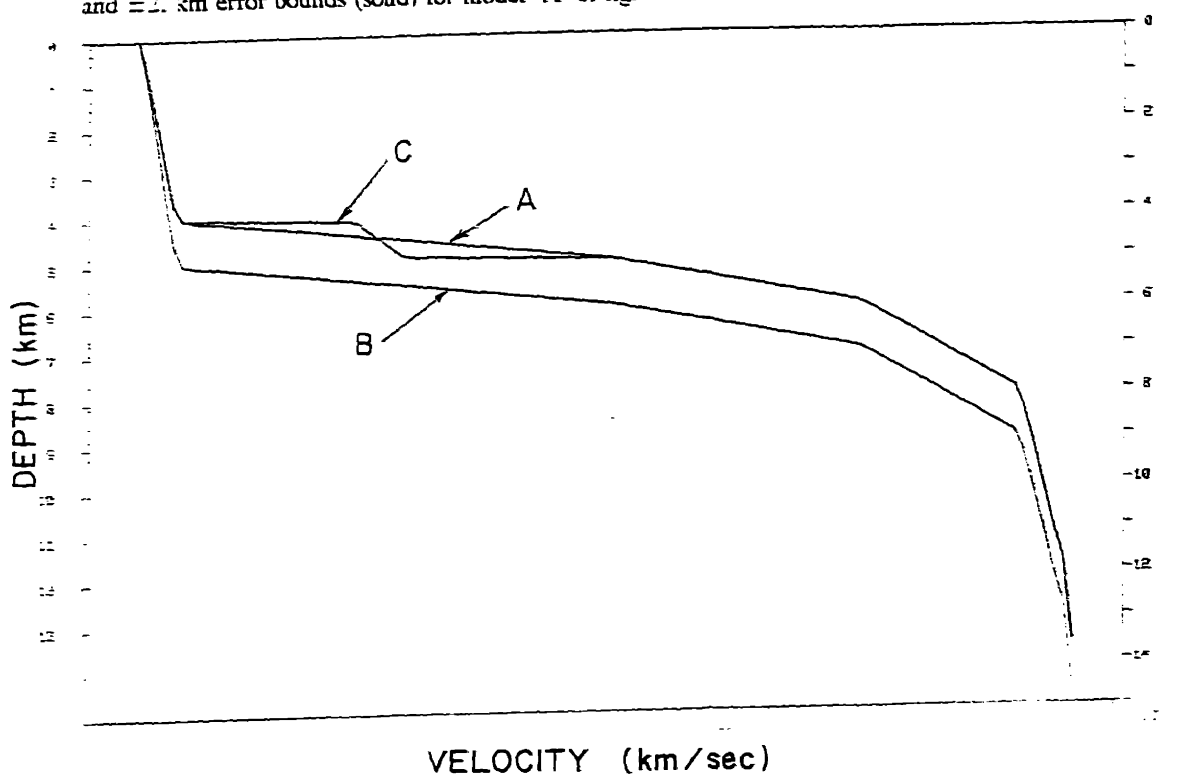

Fig. 4.16) Velocity-depth models used for examples in the text.

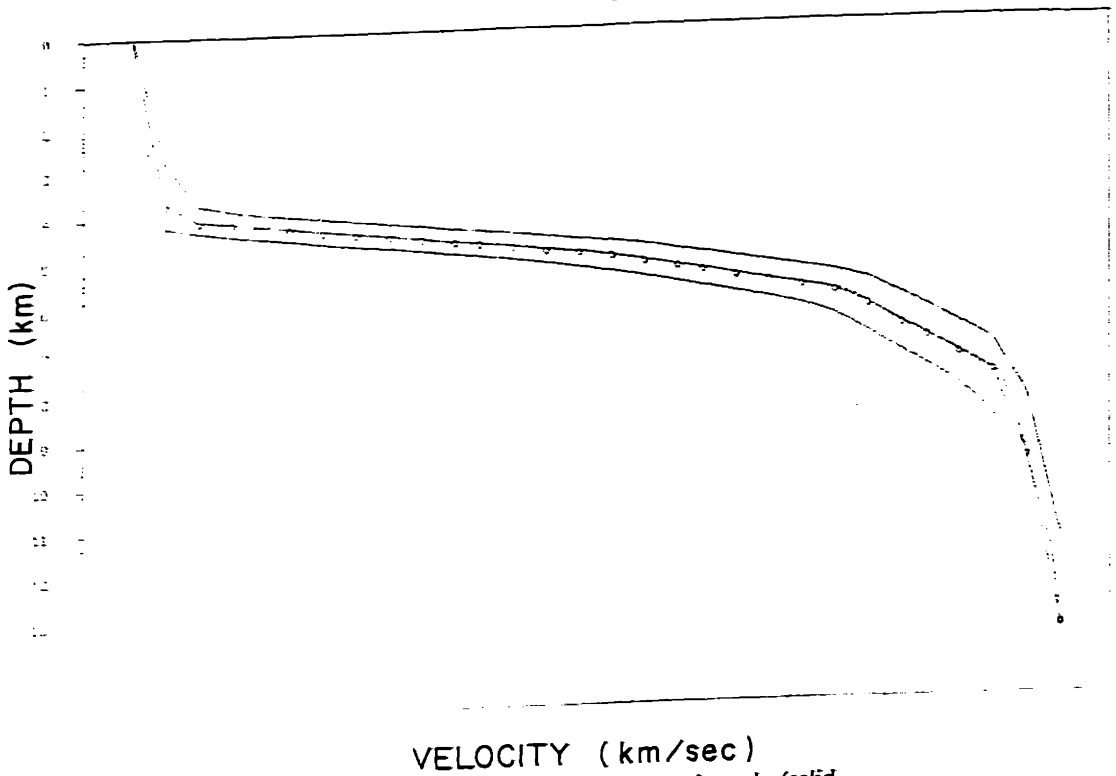

Fig. 4.17a) $\tau(p)$ data (solid line with circles) and error bounds (solid lines) imaged by correct model ("A" of fig. 4.16 given by the dotted line on this plot).

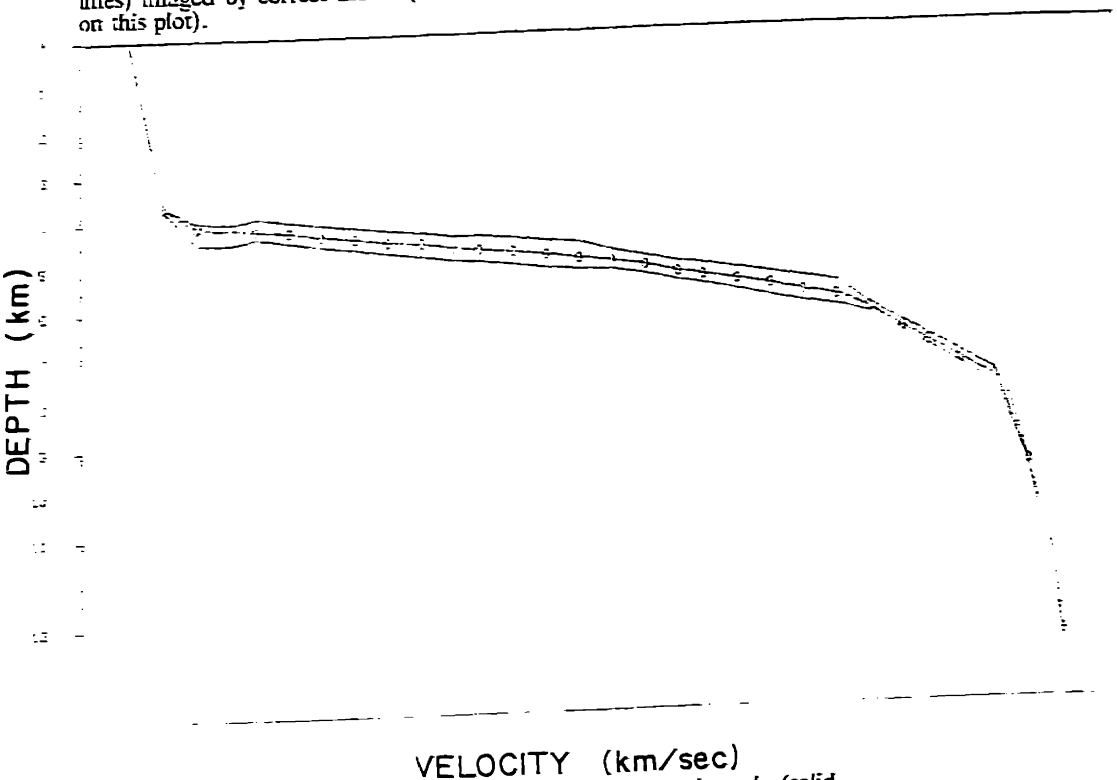

Fig. 4.17b) $x(p)$ data (solid line with circles) and error bounds (solid lines) imaged by correct model ("A" of fig. 4.16 given by the dotted line on this plot).

are given by the solid lines, and when compared to the profile "A" (dotted line) show that the trial model is correctly imaged. The imaged error bounds on the $\tau(p)$ data show the resolution of the model when the τ error is ± 0.1 second. Fig 4.17b shows how the $x(p)$ curve and error bounds are imaged by the trial model "A". Again, these are given by the solid lines, and fall onto the trial $x(p)$ curve (dotted line). Whereas the $\tau(p)$ data indicates increasing uncertainty with depth, as might be expected, the imaged $x(p)$ bounds show that a wide range of values for the $x(p)$ datum are mapped to the trial curve when it is, in fact, the correct model. The spread in the correctly imaged bounds seems to depend on the gradient at the imaging slowness. For large gradients, the bounds are large, corresponding to a large change in z necessary to move the very flat $x(p)$ curve.

We now consider the case when the data is imaged by an incorrect trial model. Figure 4.18a shows how the $\tau(p)$ data and error bounds are migrated by the trial model "C". These are given by the dotted lines, and when compared to the trial profile "C" (solid line) show that the trial model is not quite correctly imaged within the error bounds on the $\tau(p)$ data. The peak locus (center dotted line with data points marked "o") shows that the model is too fast initially because it is imaged below the trial model. This indicates qualitatively why the migration algorithm which uses the imaged $\tau(p)$ curve as the next trial model tends to converge. Note, however, that the region of significant deviation of the imaged $\tau(p)$ curve from the trial model is limited to regions where significant travel time differences have *accumulated*. This will be contrasted to the offset image, which immediately indicates that the gradient is wrong. The region for comparison will be right at the base of the water column, in which the τ error only accumulates slowly. Fig 4.18b shows how the $x(p)$ curve and error bounds are migrated by the trial model "C". Again, these are given by the dotted lines, and do not migrate onto the trial $x(p)$ curve (solid line). Some interesting features of the $x(p)$ migration are shown by this

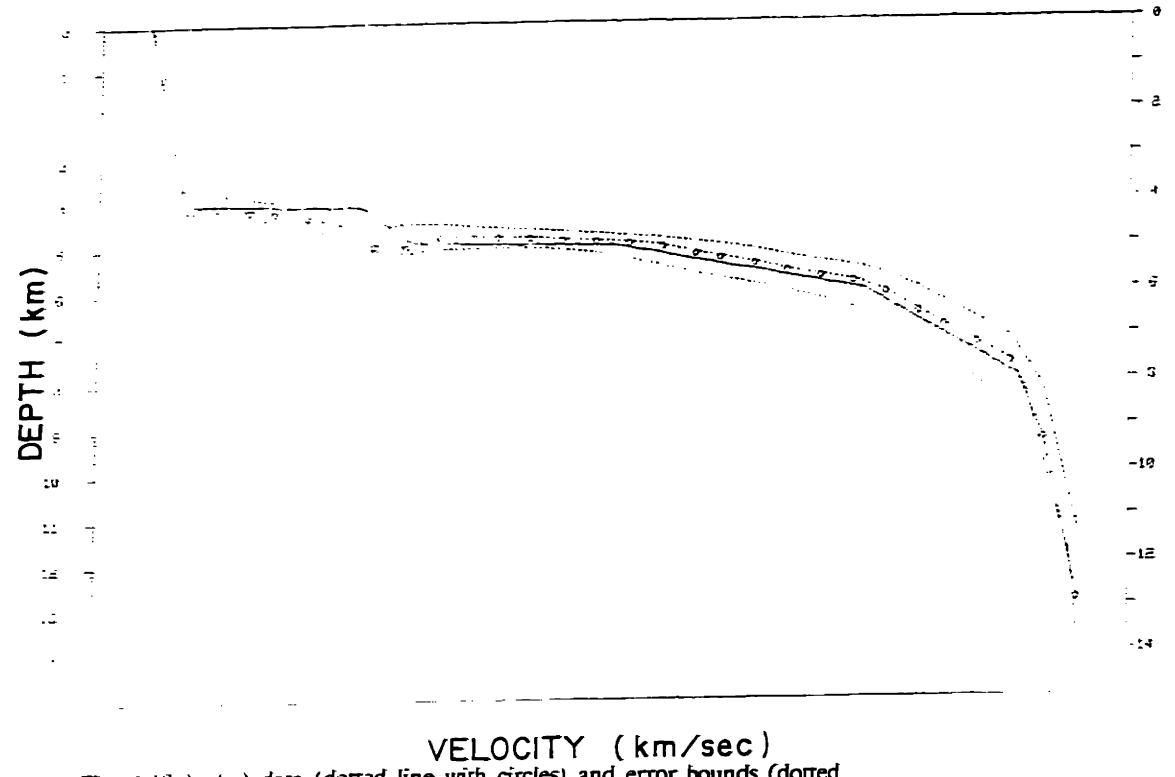

Fig. 4.18a) $\tau(p)$ data (dotted line with circles) and error bounds (dotted lines) imaged by incorrect model ("C" of fig. 4.16 given by the solid line on this plot).

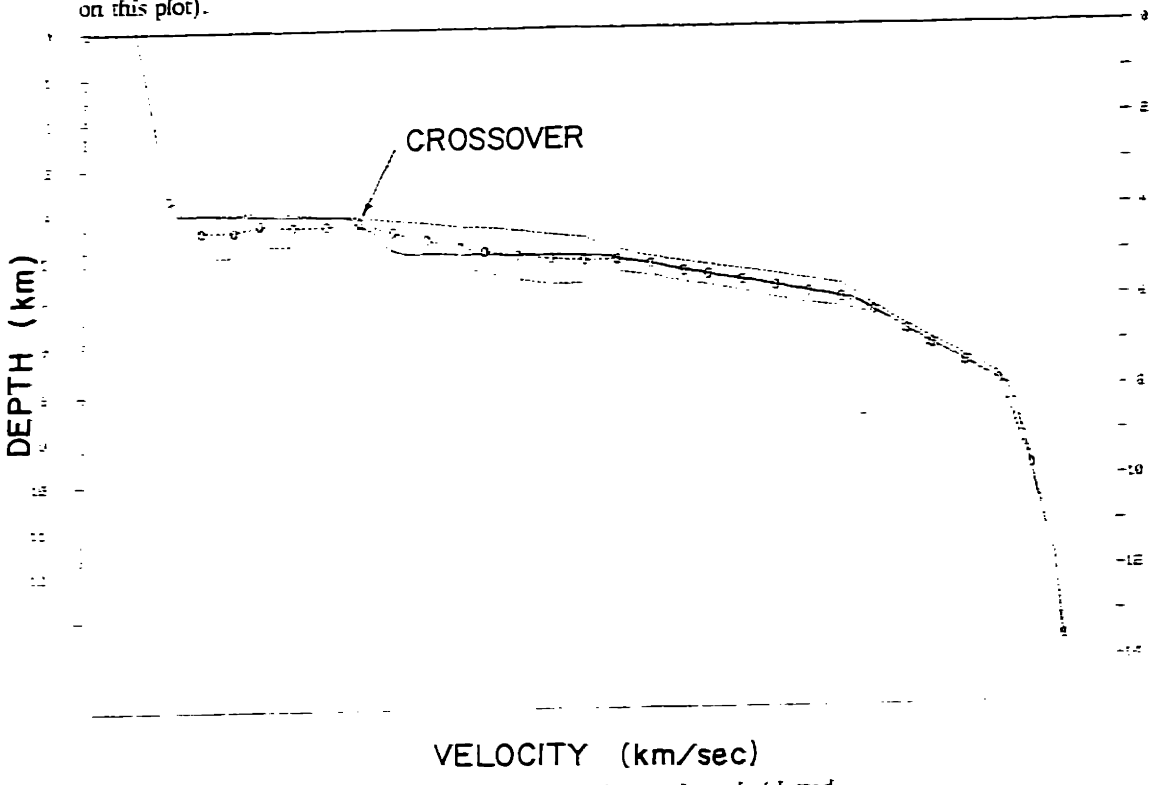

Fig. 4.18b) $x(p)$ data (dotted line with circles) and error bounds (dotted lines) imaged by incorrect model ("C" of fig. 4.16 given by the solid line on this plot).

plot. When the trial model and true $x(p)$ curves cross-over and the gradient of the trial model is low, then the imaged $x(p)$ bounds waist in, as indicated on the plot. That this is the cross-over point can be seen from fig 4.19, in which the solid lines are the curves for the true model, "A", and dotted lines are for the trial model, "C". Note, however, that in other regions in which the gradient is wrong, the imaged $x(p)$ bounds are spread. Thus, the variability in the bound separation indicates that the predicted and data $x(p)$ curves are crossing over each other, which in turn indicates that the trial model gradients must be wrong. In general, when the trial model gradients are correct, the imaged bounds for offset will be the tightest, and will be at a relatively constant separation from the peak (center) curve. Note too, that the incorrect gradient in the trial model at the top of the sediments is indicated immediately by the "too deep" image of the $x(p)$ data points (circles on the dotted line). Because it required extra depth to image the offset data, this indicates that the gradient assumed in the trial model is too high, and the predicted offsets are too small.

The next example will show how trial models which are incorrect in absolute depth, but which have correct gradients, still image offset data onto themselves. This indicates that the $x(p)$ data contains much more information about gradients at the turning point than about depth itself. This feature was pointed out in the context of least squares inversion by Dorman and Jacobson [1981]. For this example, the trial model "B" in fig. 4.16 has been used. Fig. 4.20a shows the trial model (lower solid curve), the true model (upper solid curve), and the imaged $\tau(p)$ data and bounds (solid and dotted curves with circles). The image clearly indicates that the trial model is too deep. Fig. 4.20b shows the trial model (lowest solid curve), the true model (upper solid curve), and the imaged offset data and bounds (solid and dotted curves with circles). Even though the trial model is grossly in error in overall depth, the offset data is ultimately imaged onto it, thus indicating that the gradients are correct. As pointed out

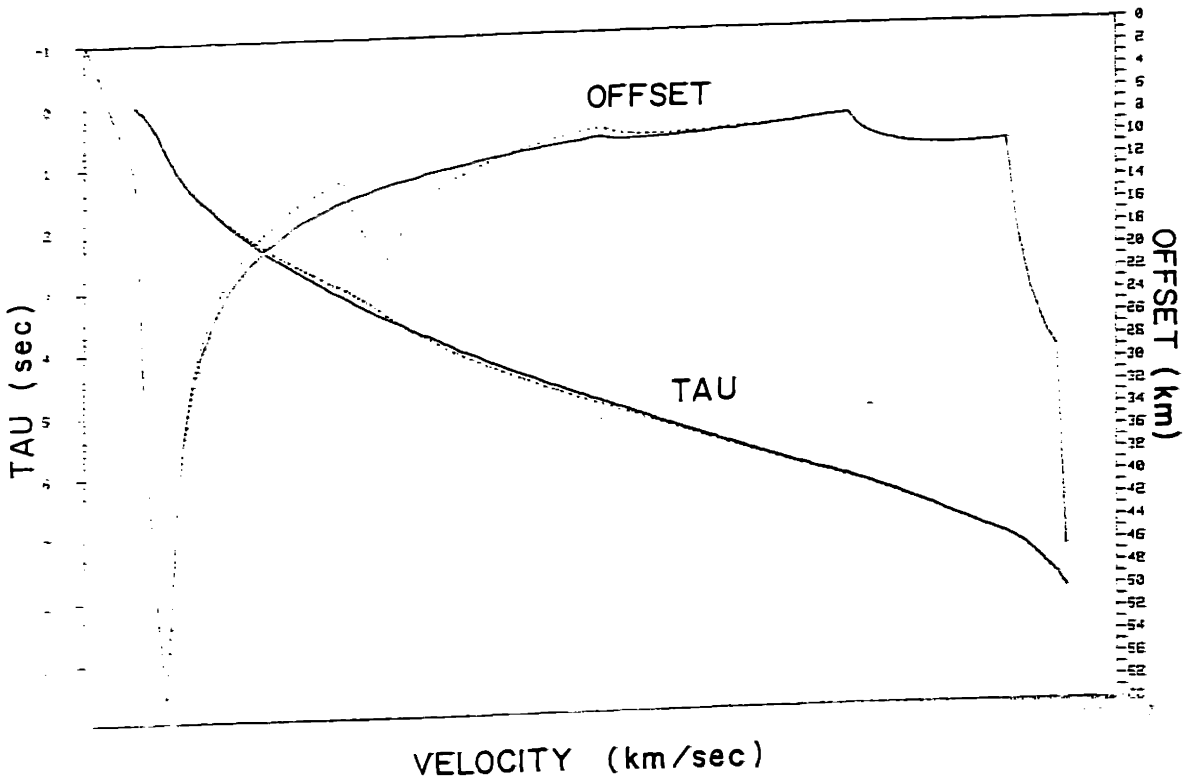

Fig. 4.19) $\tau(p)$ and $x(p)$ curves for model "A" of fig. 4.16 (solid lines) and $\tau(p)$ and $x(p)$ curves for model "C" of fig. 4.16 (dotted lines).

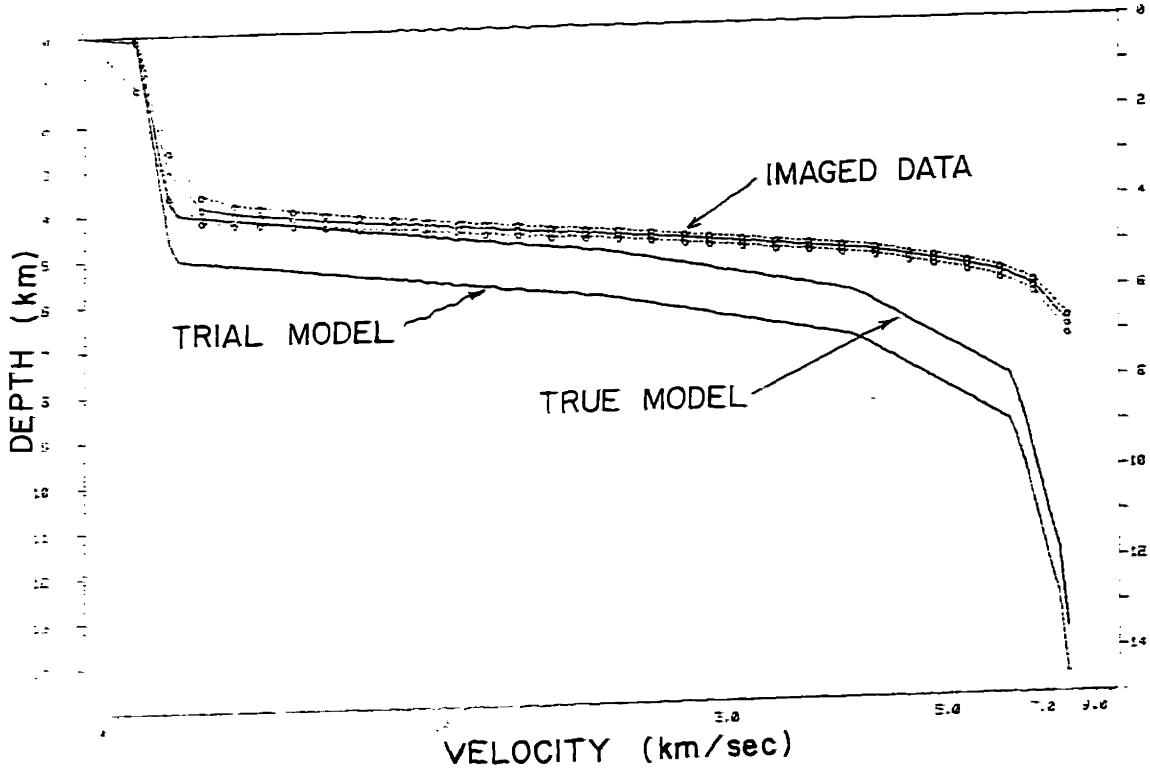

Fig. 4.2(a) $\tau(p)$ data (solid line with circles) and error bounds (dotted lines) imaged by incorrect model ("B" on fig. 4.1a given by the lower heavy solid line on this plot). The correct model ("A") is given by the upper heavy solid line.

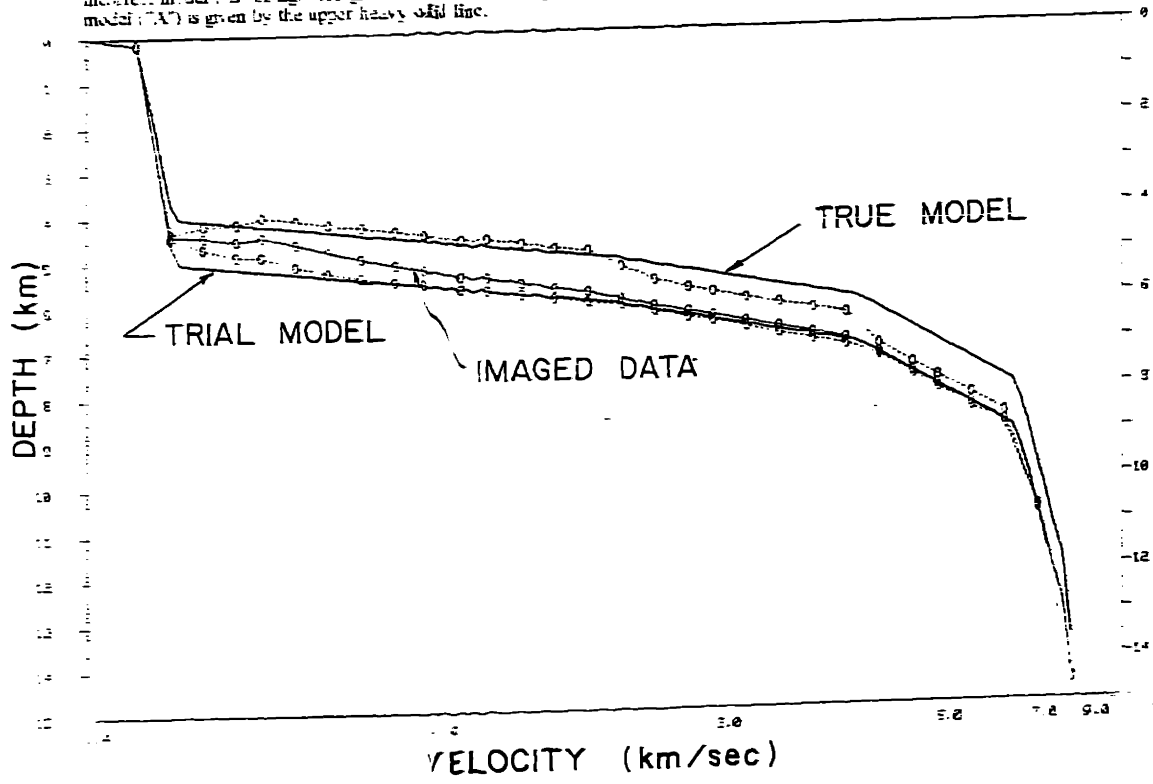

Fig. 4.2(b) $\tau(p)$ data (solid line with circles) and error bounds (dotted lines) imaged by incorrect model ("B" on fig. 4.1a given by the lower heavy solid line on this plot). The correct model ("A") is given by the upper heavy solid line.

above, for this example in which the gradients are correct and the true and predicted offset curves do not cross, the spread in the error bounds is approximately constant over regions with constant gradient, changing only when the gradient itself changes.

Convergence properties

In their paper, Clayton and McMechan [1981] claim that the algorithm for migration described above converges to the correct model within the resolution inherent in the bandwidth of the data. As you will recall, this algorithm used the peak locus of the slant-stack imaged with a trial model into the velocity-depth plane as the next trial model. In the examples carried out in that work, however, they noticed that the use of a uniform picking criterion led not to a single converged model, but to two quasi-stable models, for which the choice of one as the trial model imaged the data onto the other, and vice versa. They attributed this to the use of a uniform picking criterion, such as the largest peak of the waveform, because this method does not pick out the correct geometrical $\tau(p)$ curve when variable phase shifts are present in the data for different slownesses. This postulate seemed to be confirmed by the fact that a human operator exercising an adaptive picking criterion from iteration to iteration could come up with a model which imaged the data (nearly) onto itself, thus satisfying the convergence criterion. The work done for this thesis indicates that the algorithm described does not converge to a single correct model when operating on sampled $\tau(p)$ data, and that this is due not to picking problems, but to numerical properties of the algorithm. However, a slight modification can be made to the algorithm which will cause it to converge to a single model on noiseless data which is densely sampled in slowness, and to exhibit limit cycles which form tighter bounds on the velocity depth curve than the two "psuedo-stable" states observed with the standard algorithm in other cases. In addition, this simple modification also causes the iteration to converge more

quickly.

To first motivate why the "oscillations" are not due to picking problems, we consider the following argument. At each iteration a uniform picking criterion will always pick the same $\tau(p)$ curve from the slant stack*. Even if this curve is not the same as the true geometrical $\tau(p)$ curve due to slowness variable phase shifts, it still describes a valid $\tau(p)$ curve for *some* $\tau(p)$ curve due to slowness variable phase shifts, it still describes a valid $\tau(p)$ curve for *some* model as long as it is monotonic. For a noiseless and infinitely densely sampled curve this model could be computed by the Herglotz-Wiechert relations. Thus, if the algorithm is convergent, it should converge to this model.

To show that the limit cycles are due to numerical properties of the algorithm, we consider a few simple examples which use noiseless $\tau(p)$ data straight from a ray tracing program using the same interpolation between slowness values as the migration, linear slowness. The first set of examples will show that using the correct model as the initial trial model, the trial models will diverge from the correct model and will develop the two quasi-stable limit cycles. The shape and spread of the limit cycles will be seen to be relatively independent of the density of sampling of the $\tau(p)$ curve. The second set of examples will show that different initial models lead to the same set of limit cycles for a given $\tau(p)$ sampling, and thus are unique. To carry out the migration of the continuous time $\tau(p)$ curve a set of $\Psi(p,z) = \tau(p,z)$ values is computed using eqn. 4.47 on a grid of uniformly spaced z samples. The value of z between the grid points is then obtained by linear interpolation of these samples. The standard grid is spaced at $\Delta z = 0.05$ km, thus the quantization noise is somewhat better than this due to the interpolation. It is hypothesized that the limit cycles are due to numerical noise from this, or any algorithm, causing the peaks not to image exactly back onto the curve. Some of this noise

*For example, consider the peak locus. This will not change as a function of trial model using the simple algorithm described which only images the travel time aspects of the data, and does not affect the amplitudes.

is due to the grid/linear interpolation scheme, and some is due to the fact that the sample slowness values will not be the same as the vertices of the original model used to calculate the ray trace $\tau(p)$ curve, thus the trial models, which use the measured slowness points as the vertices, cannot be exactly the same as the true model**. Any practical velocity-depth migration algorithm will suffer from similar problems. Even if the slant stacked waveforms are migrated exactly using a frequency domain implementation, the image is necessarily sampled in depth. Thus, if the peaks of the imaged data are picked, there a quantization noise of $\Delta z/2$.

Figures 4.21 show the image trajectories as a function of the number and location of the data samples using a migration grid of Δz = 0.05 km. The migration algorithm used the image of the previous model as the next trial model, except for the water column. Because the water column velocity differs so greatly from the earth, and is often well known in velocity and depth, the correct water column was used in each trial model.

Fig. 4.21a shows the iteration trajectory for a set of 7 data points with vertices approximately equal in slowness to the true model vertices. The algorithm diverged from the correct model and exhibited limit cycles corresponding to the observed maximum and minimum profiles after 15 iterations.

Fig. 4.21b shows the iteration trajectory for a set of 10 data points equally spaced in slowness. The algorithm again diverged from the correct model and exhibited limit cycles corresponding to the observed maximimum and minimum profiles after 15 iterations. The migration results are necessarily poor in the higher velocity regions where the uniform slowness sampling is inadequate to specify the model details.

** And certainly not the same as some arbitrary real model!

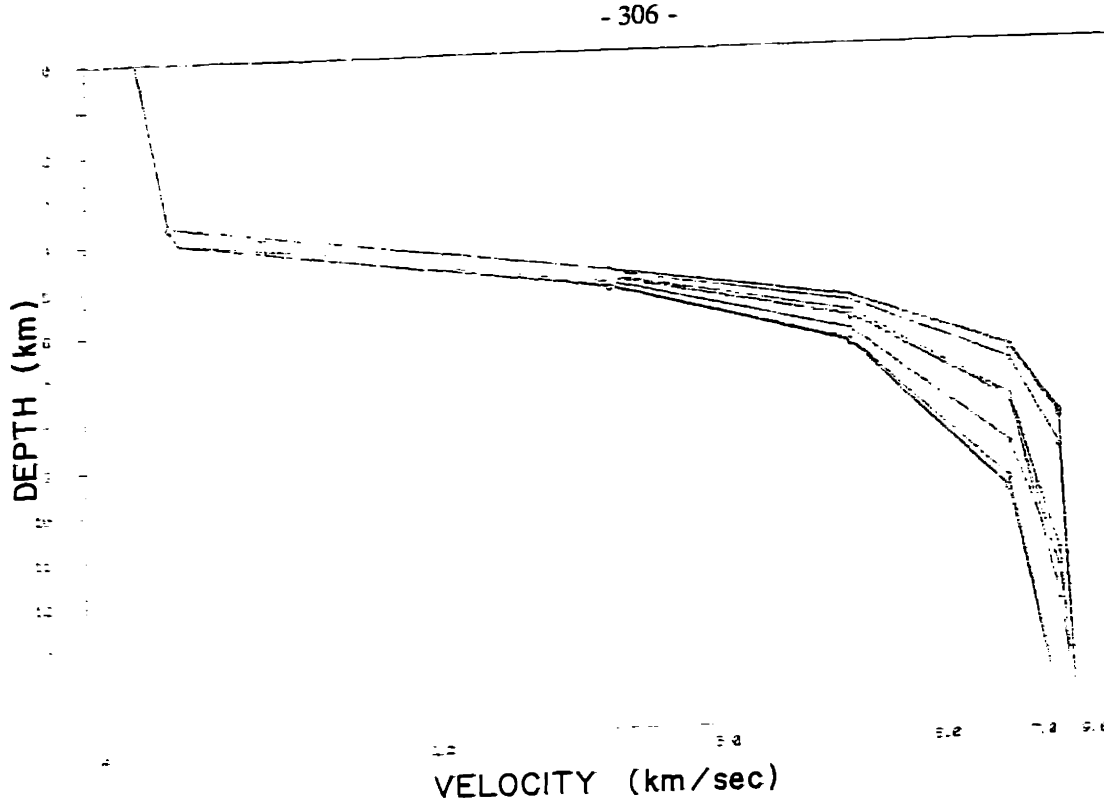

Fig. 4.21a) Migration iteration trajectory for 7 data points at the true vertices of the model. ($\Delta z = .05$ km)

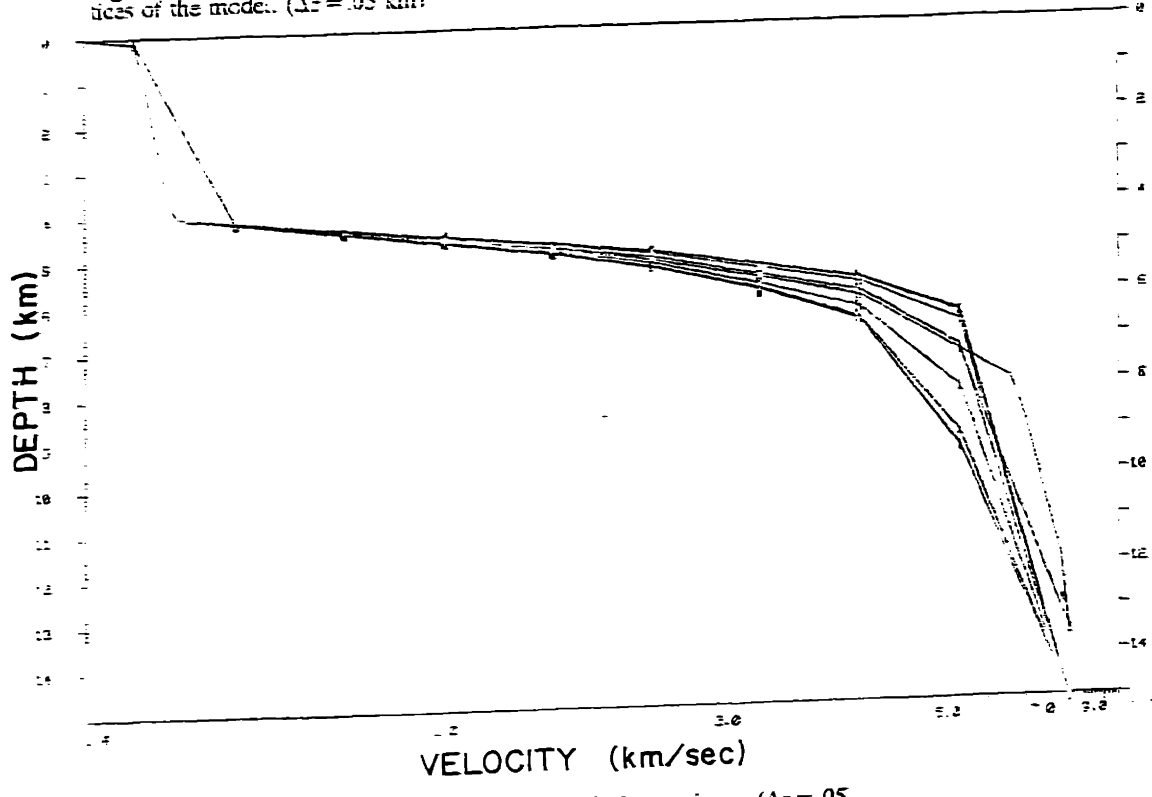

Fig. 4.21b) Migration iteration trajectory for 10 data points. ($\Delta z = .05$ km)

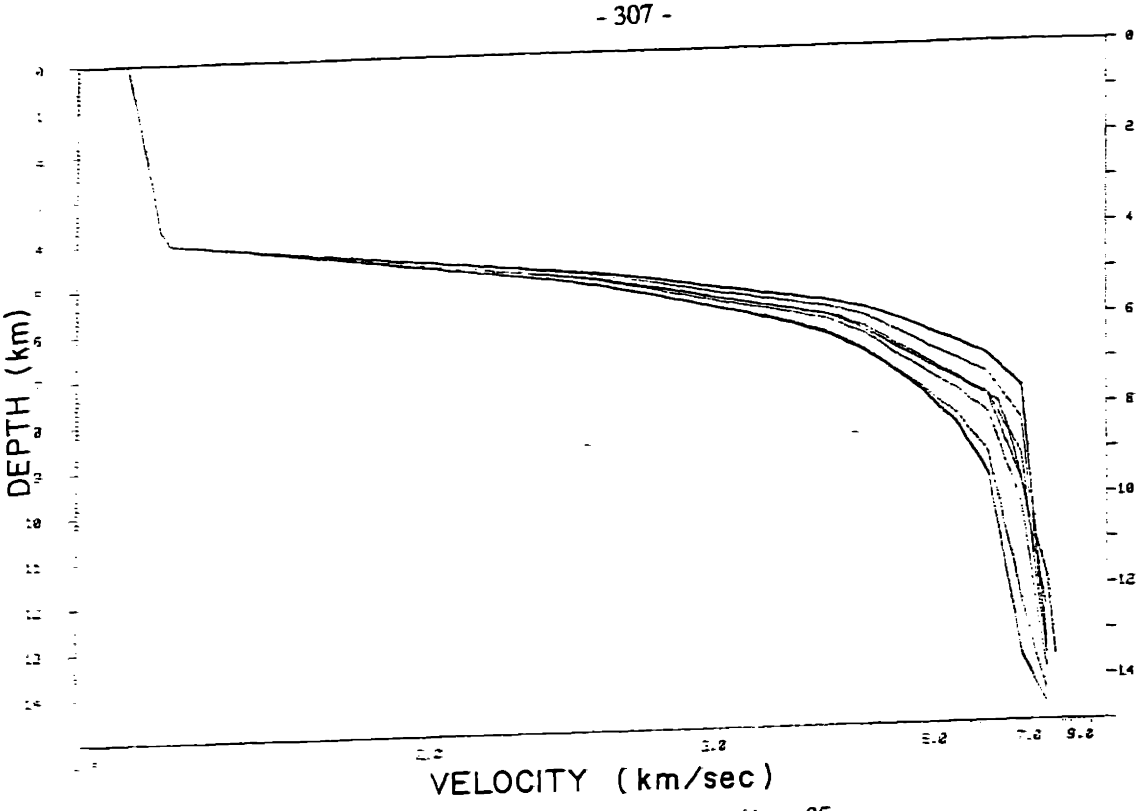

Fig. 4.21c) Migration iteration trajectory for 30 data points. ($\Delta z = .05$ km)

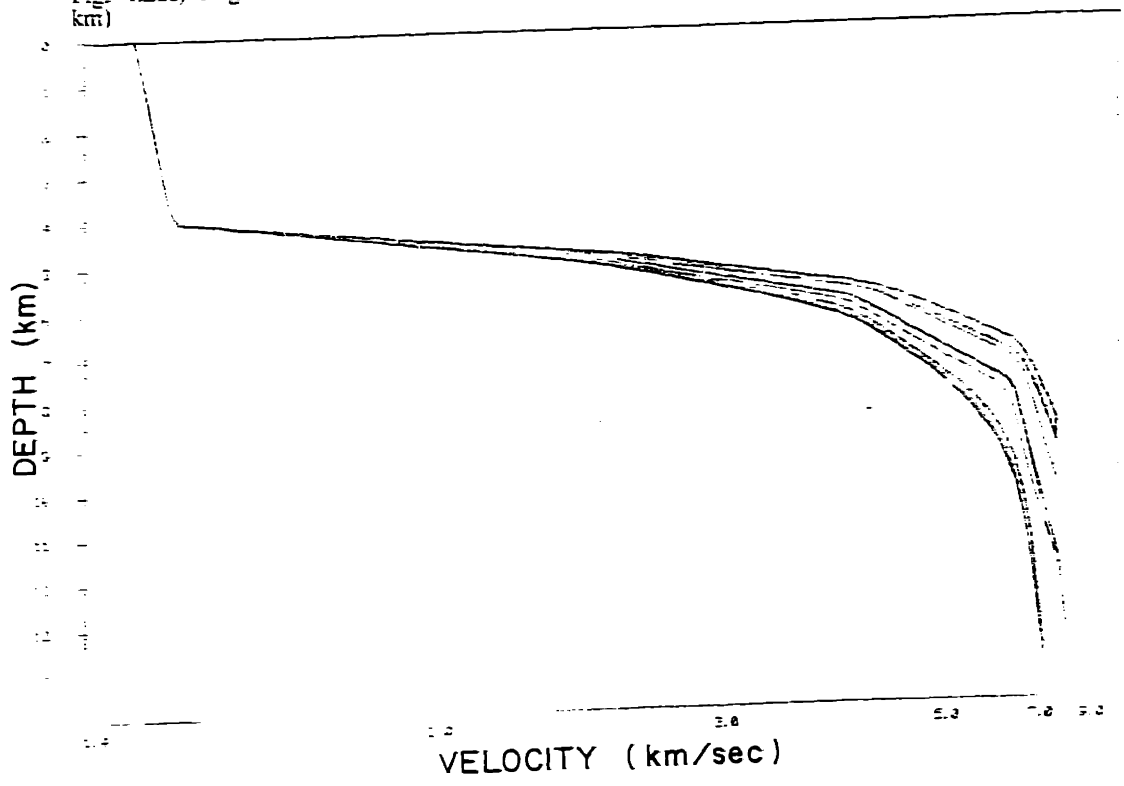

Fig. 4.21d) Migration iteration trajectory for 100 data points. ($\Delta z = .05$ km)

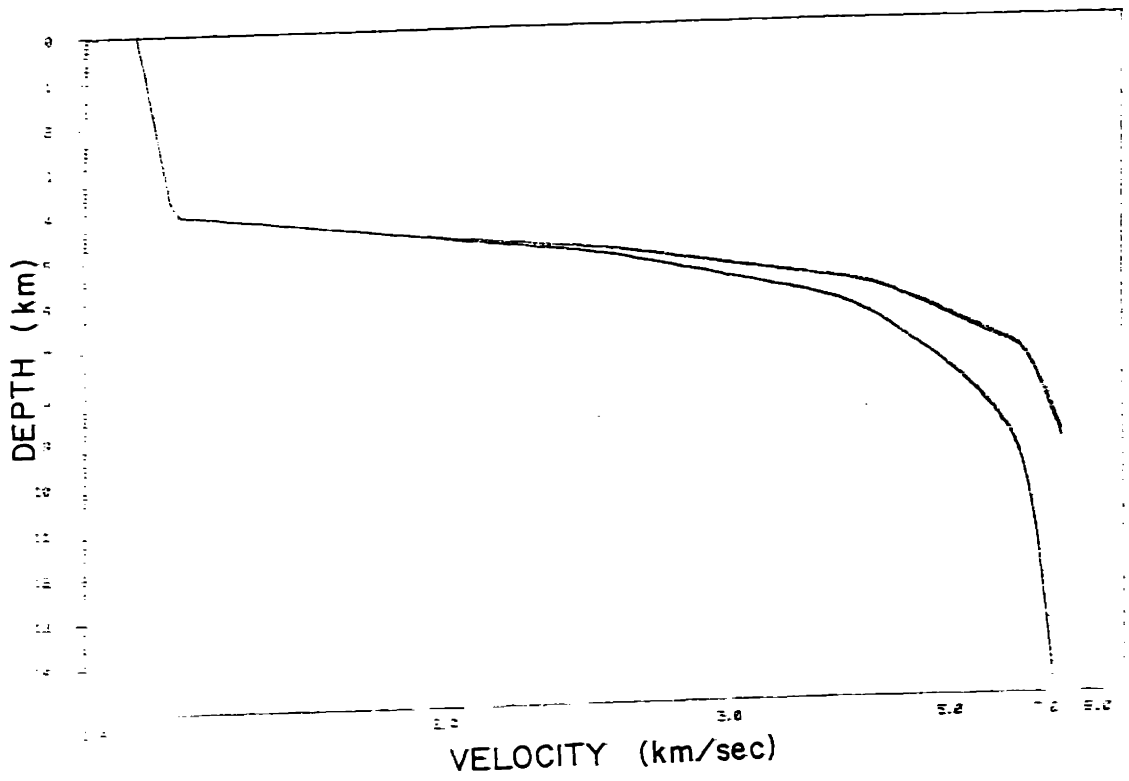

Fig. 4.21e) Limit cycles (iterations 26-39) for 100 data points with $\Delta z = .05$ km.

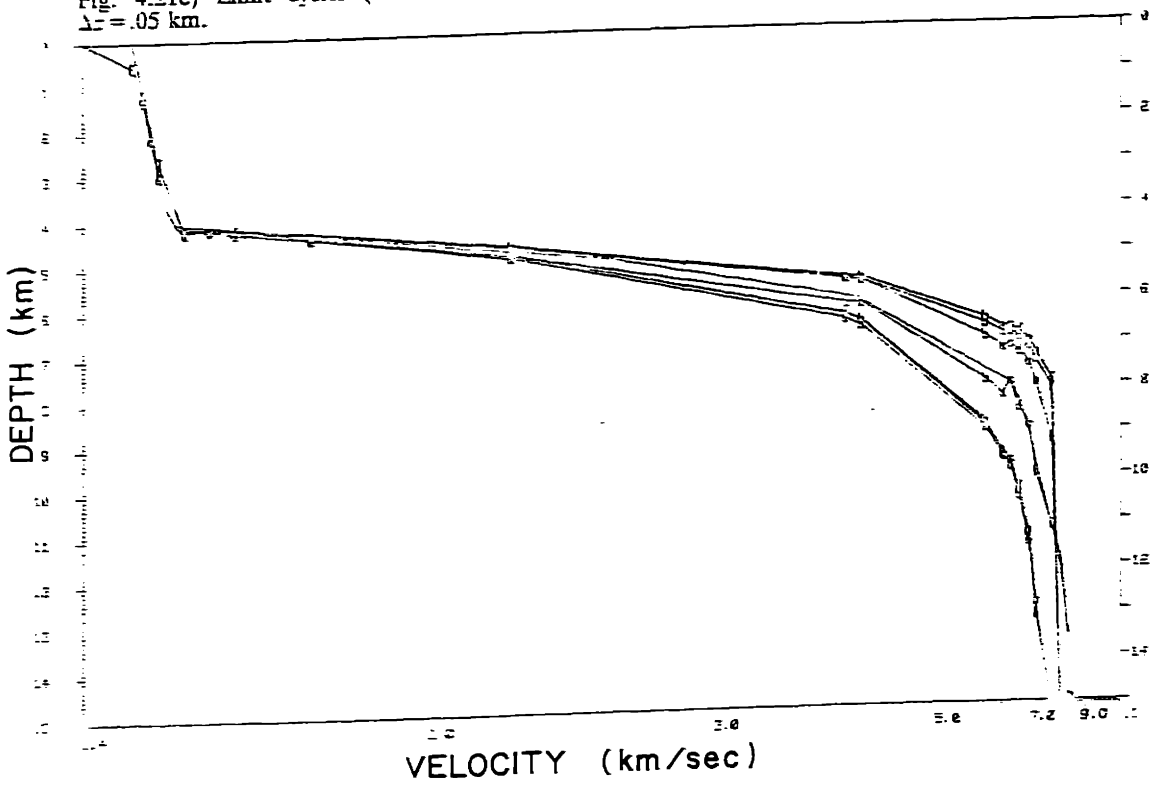

Fig. 4.21f) Migration iteration trajectory for data points from WKBJ synthetics. ($\Delta z = .05$ km)

Fig. 4.21c contains the iteration trajectory for a set of 30 data points equally spaced in slowness. The actual points have been omitted for clarity. The algorithm again diverged from the correct model and exhibited limit cycles corresponding to the observed maximimum and minimum profiles after 15 iterations. The spread in the limit cycles is similar to the spread observed for the two previous slowness sampling densities, perhaps being a little smaller.

Fig. 4.21d contains the iteration trajectory for a set of 100 data points equally spaced in slowness. The actual points have again been omitted for clarity. The migration algorithm diverged from the correct model to the extremes of the heavy dark lines (actually a collection of thin lines) in 6 iterations. After this, the "limit cycles" slowly seemed to be converging toward each other. Fig 4.21e shows the set of curves for iterations 26-39. The algorithm was run only to 51 iterations, at which time the limit cycles were still closer, but it is not known what the ultimate limit cycles are. It is suspected that the curves would continue to converge for some time, possibly reaching a unique single limit. A discussion of why this might occur for this sampling density, and why the spread in the limit cycles decreases slightly for greater slowness sampling density will be given shortly.

Finally, we show that the convergence properties similar to those for uniformly sampled curves are obtained for data that are realistically sampled in slowness for Arctic experiments. To do this, the $\tau(p)$ data of significant peaks predicted by the WKBJ method calculated at 7 offsets (every 5 km from 5 to 35 km) were used. The migration trajectories in figure 4.21f are similar to the initial example (Fig. 4.21a) and exhibit the same limit cycles after 15 iterations.

To show that the limit cycles observed are independent of the initial trial model, we consider the examples pictured in figures 4.22. Fig. 4.22a shows the complete trajectory of images after initializing with model "B" (see fig 4.16). Fig 4.22b shows the trajectory when model "C"

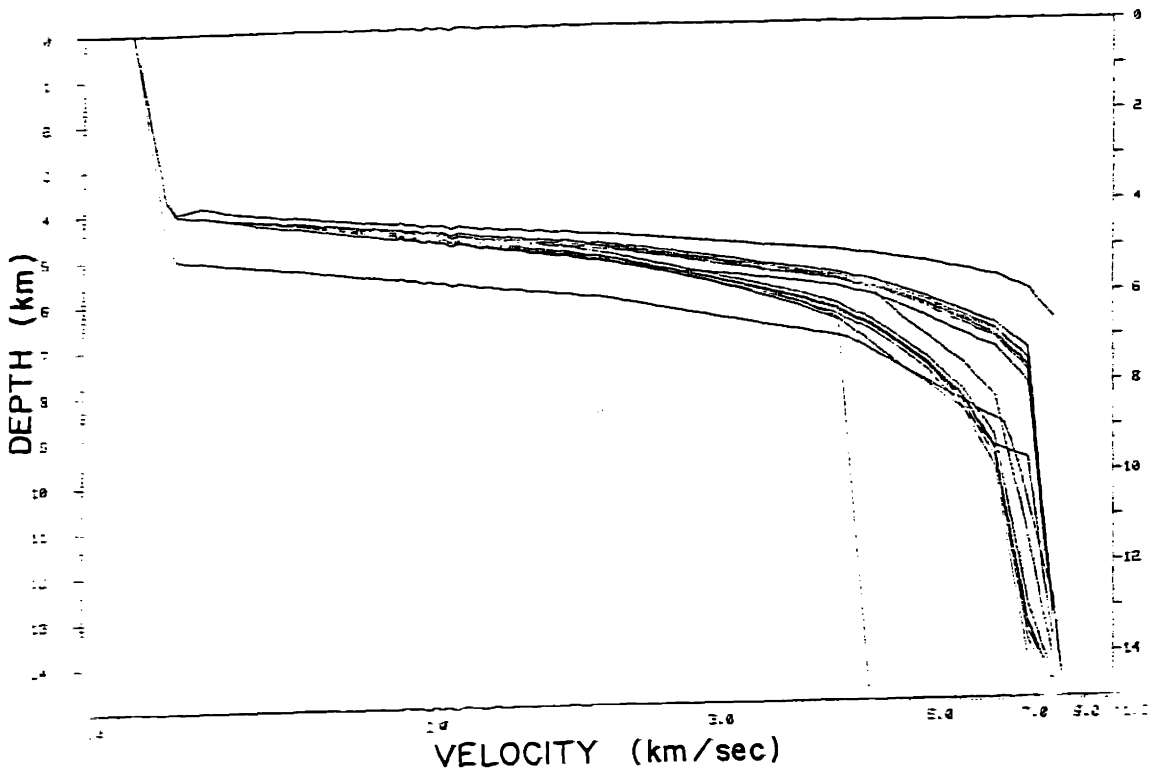

Fig. 4.22a) Migration iteration trajectory for 30 data points and $\Delta z = .05$ km starting from model "B" of fig. 4.16.

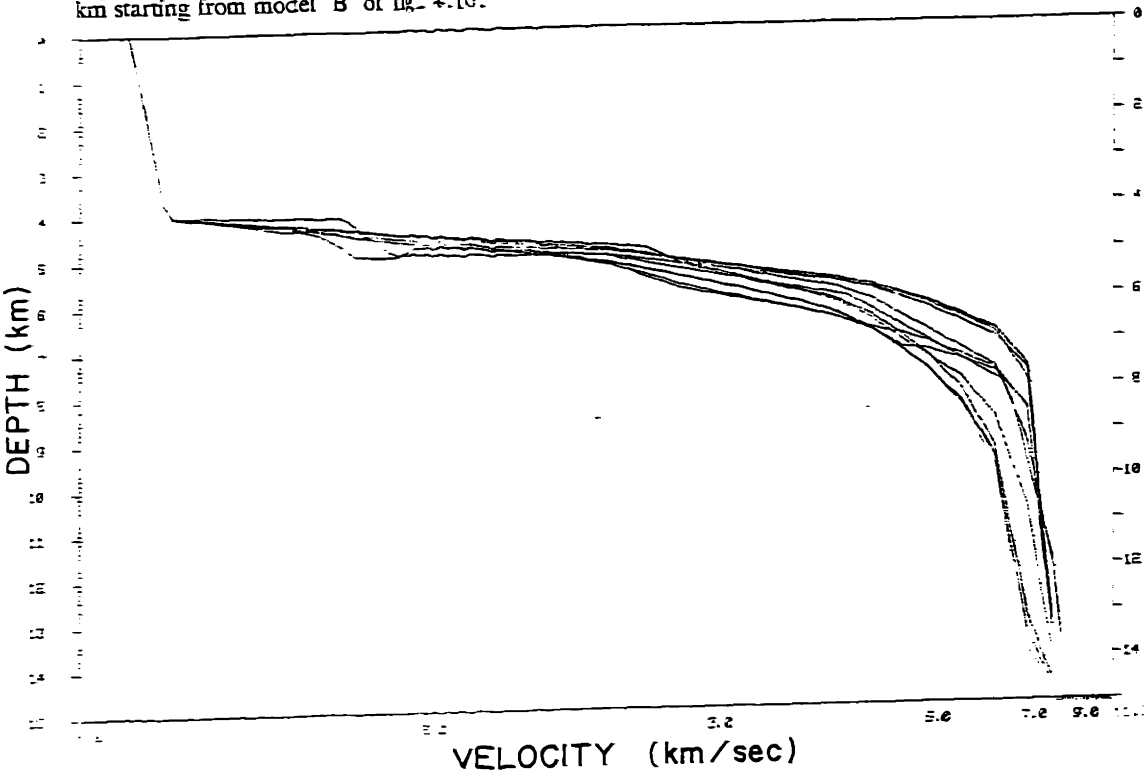

Fig. 4.22b) Migration iteration trajectory for 30 data points and $\Delta z = .05$ km starting from model "C" of fig. 4.16.

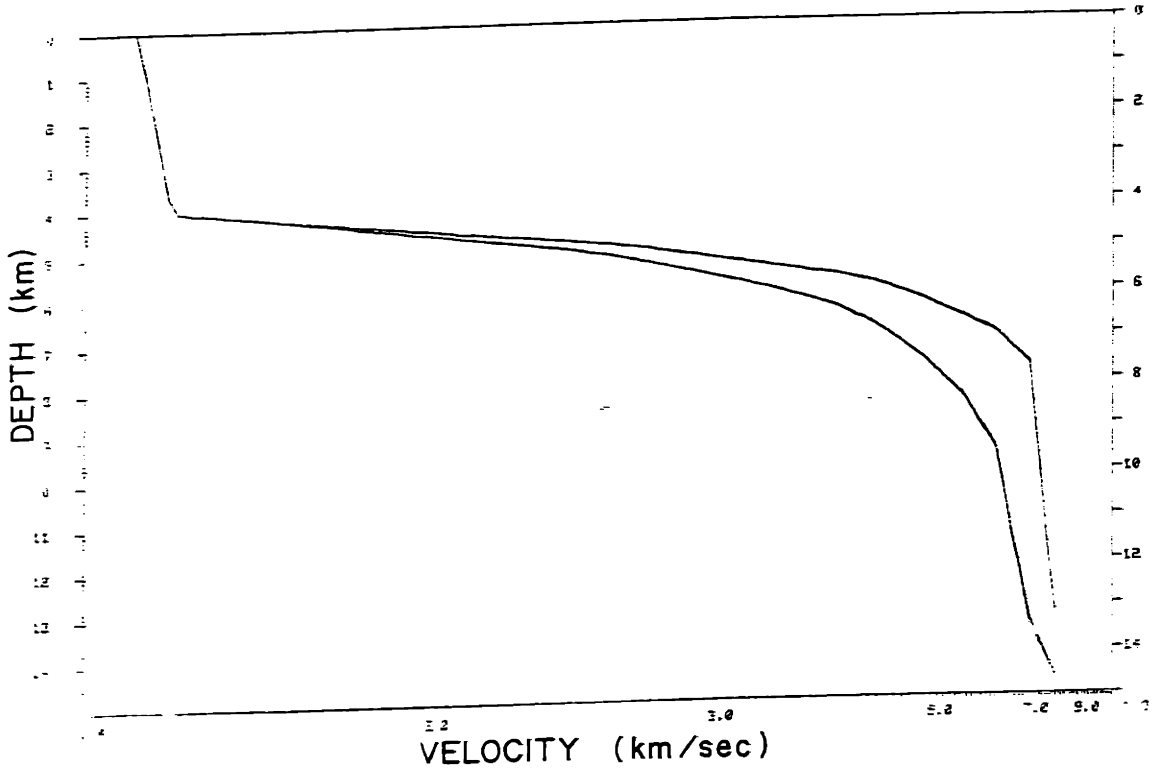

Fig. 4.22c) Migration iteration limit cycles for 30 data points and $\Delta x = .05$ km. The results for starting models "A", "B", and "C" of fig 4.16 are superposed and seen to be identical.

was used as the starting model. Fig 4.22c shows the limit cycles after 10 iterations starting with models "A" (see fig 4.21c for complete trajectory), and "C" and after 15 iterations starting from model "B". The limit cycles are identical within the resolution of the plot.

Now that it has been shown that the original algorithm is prone to non-convergence, we propose a method to stabilize it. The mechanism is very simple, and in fact already resides in the peak migration algorithm described which computes a grid and linear interpolates to find the $z(p)$ image value corresponding to a given peak $\tau(p)$ value. All that need be done is to increase the grid spacing, and to rely more on the linear interpolation. Not only will this tend to stabilize the algorithm, but will also speed the computation because of the fewer number of ray trace evaluations that must be made. How this works to damp the oscillations is illustrated in fig. 4.23. The solid curves in the figure are the $\psi(p_0,z)$ predictions of eqn. 4.47 for the fast (upper limit cycle), $\Psi_f(p_0,z)$, the slow (lower limit cycle), $\Psi_s(p_0,z)$, and true models. These models are shown in figure 4.24. All the curves are computed for imaging of the p_0 = 1/4 s/km slowness value. The way the curves work is that the image depth for the trial models is the depth at which the curves cross the data $\tau(p_0)$ line. Thus the slower limit cycle line, $\Psi_s(p_0,z)$, gives image value $z_s = z_f(p_0)$ and the upper limit cycle line gives $z_f = z_s(p_0)$, and the curves are mutual inverses. Note the inflections in the curves at the points where the model slowness equals the target slowness, p_0. However, if instead of the exact $\Psi_f(p_0,z)$ and $\Psi_s(p_0,z)$ curves being calculated*, the curves are computed on a coarse grid (Δz = 1.0 km shown by dotted lines) and linearly interpolated, then the values $\hat{z}_s$ and $\hat{z}_f$ are obtained as the next model iterations, depending on which curve one is currently on. This has two effects, first, the cycle is broken, and second, the geometry is such that the swing to the other side of the true model is damped- it doesn't overshoot as much as the other limit cycle curve.

*Here exact means that the grid spacing, Δz, is given by 0.05 km.

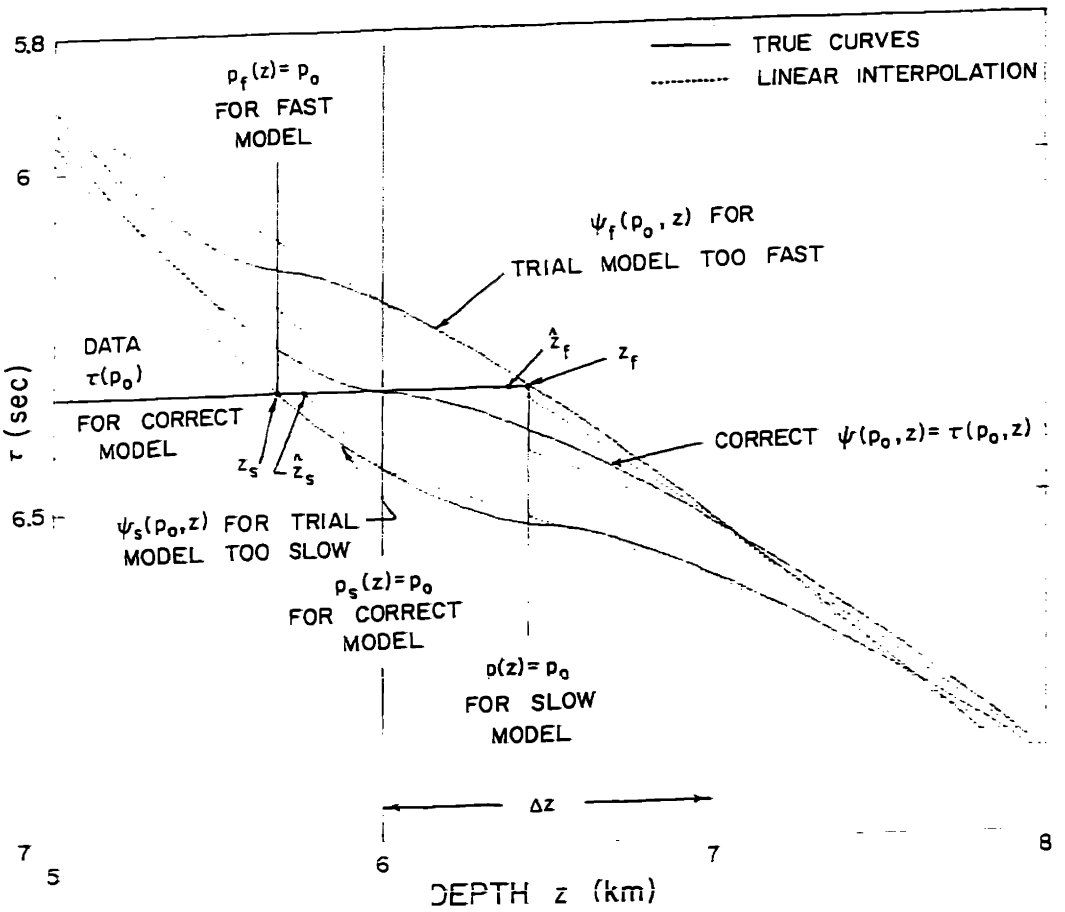

Fig. 4.23) Diagram to accompany discussion of migration convergence and stabilization.

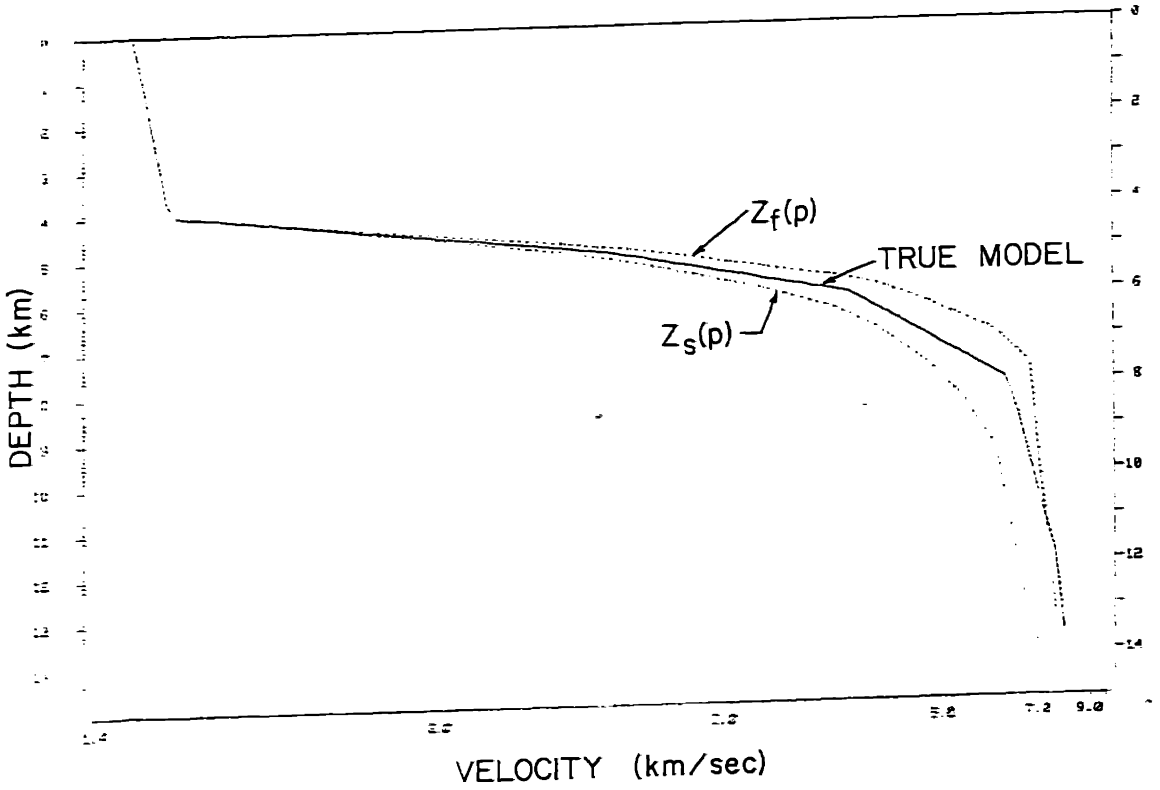

Fig. 4.24: True and limit cycle velocity depth functions for discussion of fig. 4.23.

It appears as though the slowness sampling density and depth grid interval, Δz, are the factors which control convergence. For a larger grid interval, the convergence will be faster, but the converged images will be slightly distorted. For a dense slowness sampling, smaller grid sizes appear to converge. This is why at Δz = .05 km the curve with 100 samples (figs 4.21d & e) was still converging slowly after 39 iterations.

To show the improved convergence of the modified algorithm we consider the same data used for the examples above, but use a grid size of Δz = 1.0 km. Figure 4.25a shows that the algorithm still will not converge with only seven data points, however the bounds given by the limit cycles are tighter than with Δz = .05 km in fig. 4.21a. Figure 4.25b indicates much tighter limit cycles than the corresponding plot in fig. 4.21b when 10 data points are used. For 30 data points, the image trajectories are shown in fig. 4.25c. However, the important result is that in figure 4.25d the converged limit cycles for the 30 slowness sample curve (solid lines for iterations 10 and 11) are very close together and approximate the true model (dotted line) quite well. As was mentioned earlier, this convergence is obtained with an increase in distortion of the final model. However, it should be noted that the distortion encountered for a grid interval of Δz =1.0 km leads to deviations from the correct model that are well within the resolution of most noisy/finite bandwidth data sets, and certainly for those from the Fram 2 experiment.

When 100 data points are used, the image trajectories are given in figure 4.25e for 29 iterations. The converged model (solid line) and the true model (dotted line) are given in fig. 4.25f. Note that with 100 data points, the model is unique.

Finally, the more realistic example with data points computed from peaks in the WKBJ synthetics measured at a set of 7 discrete offsets also yields both a tighter migration trajectory

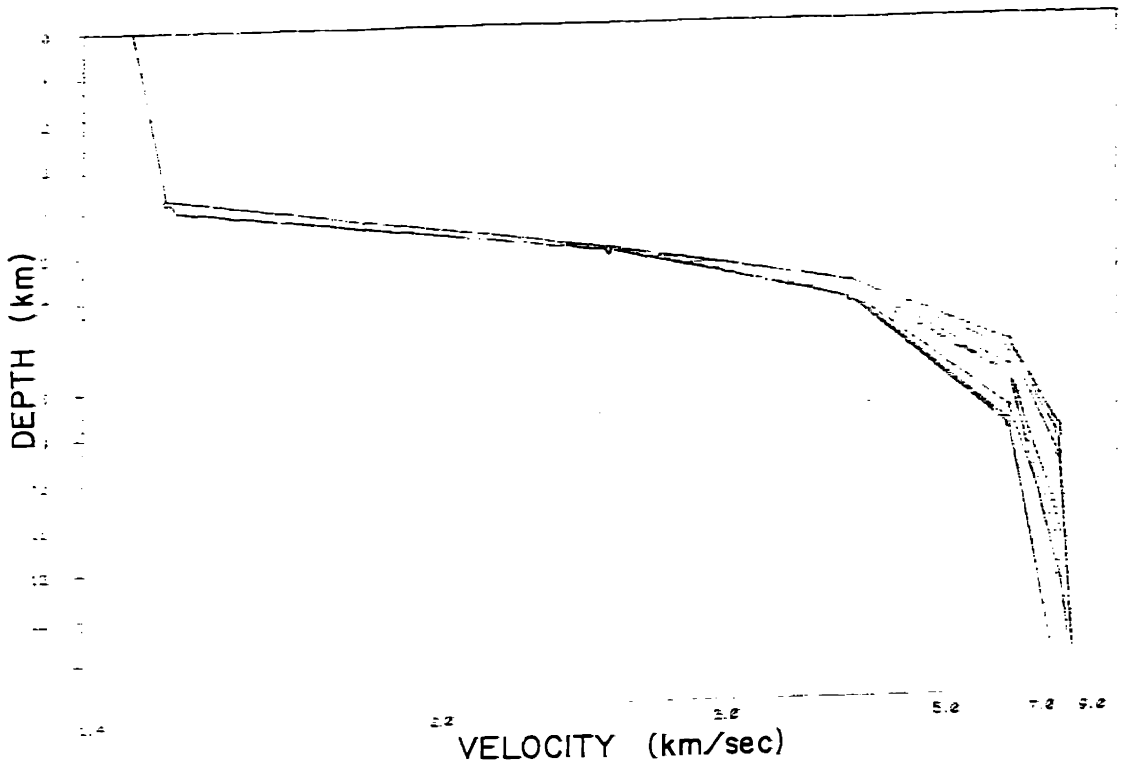

Fig. 4.25a) Migration iteration trajectory for 7 data points at the true vertices of the model. ($\Delta z = 1.0$ km)

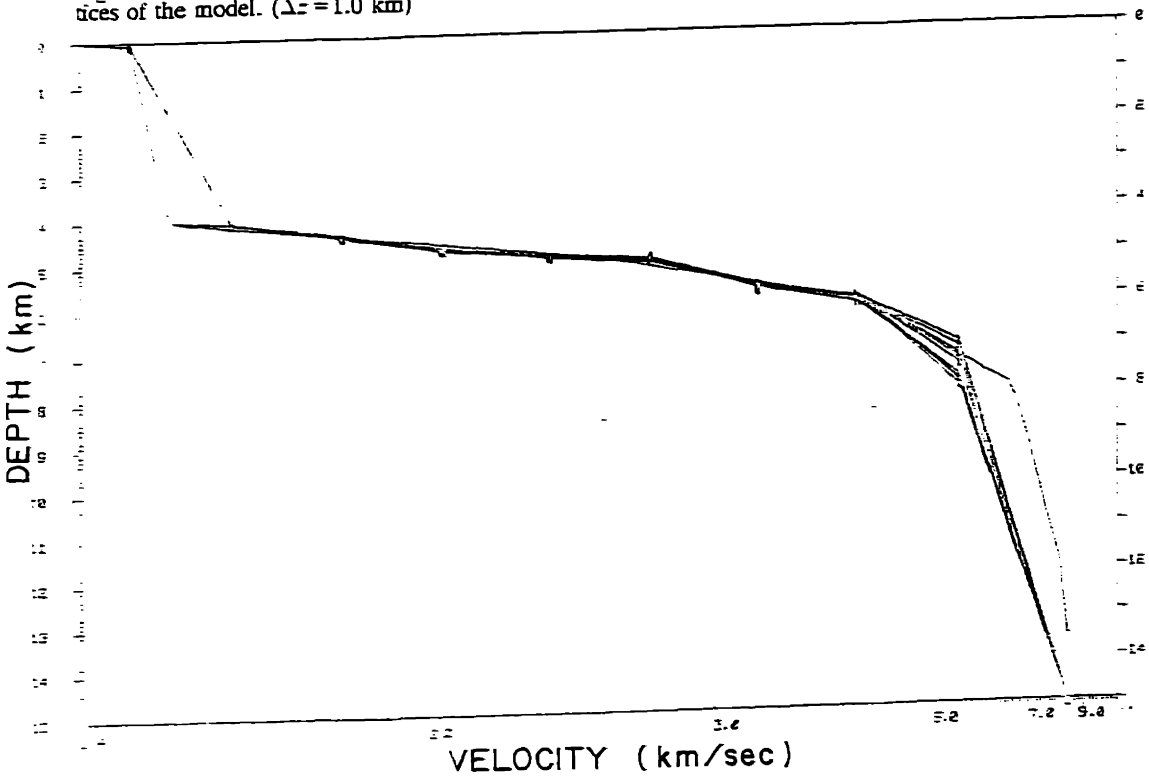

Fig. 4.25b) Migration iteration trajectory for 10 data points. ($\Delta z = 1.0$ km)

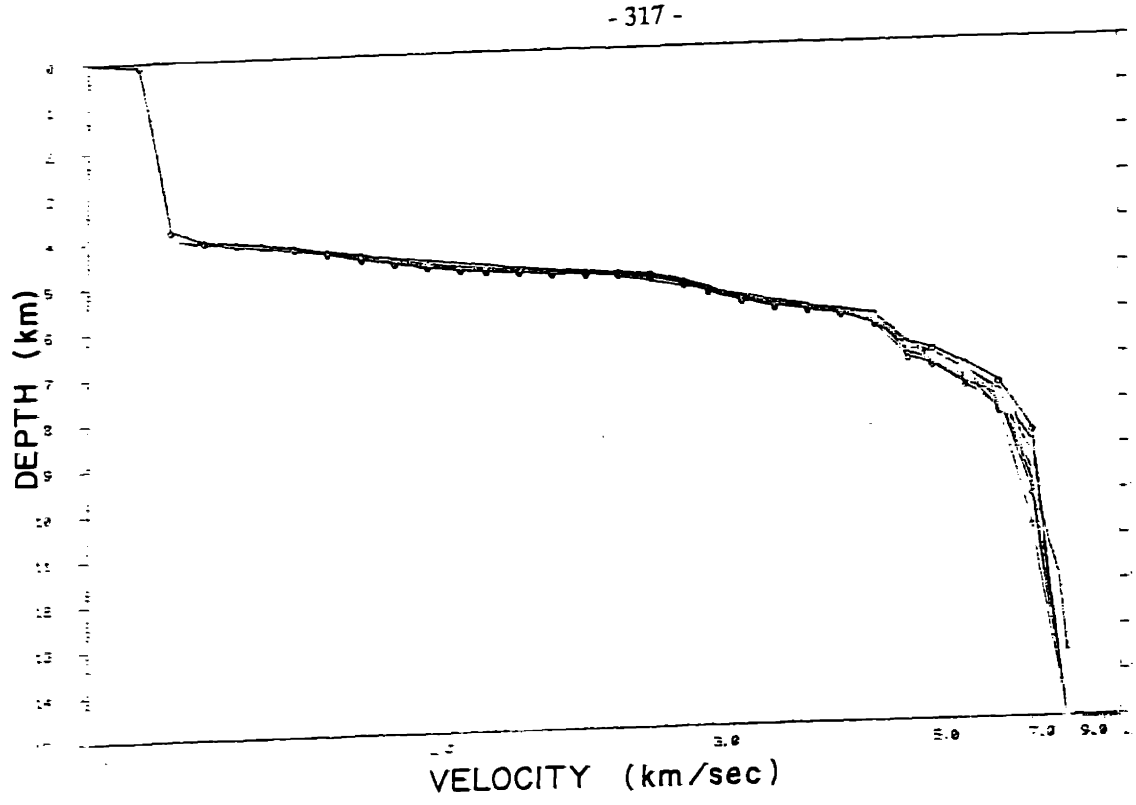

Fig. 4.25c) Migration iteration trajectory for 30 data points. ($\Delta z = 1.0$ km)

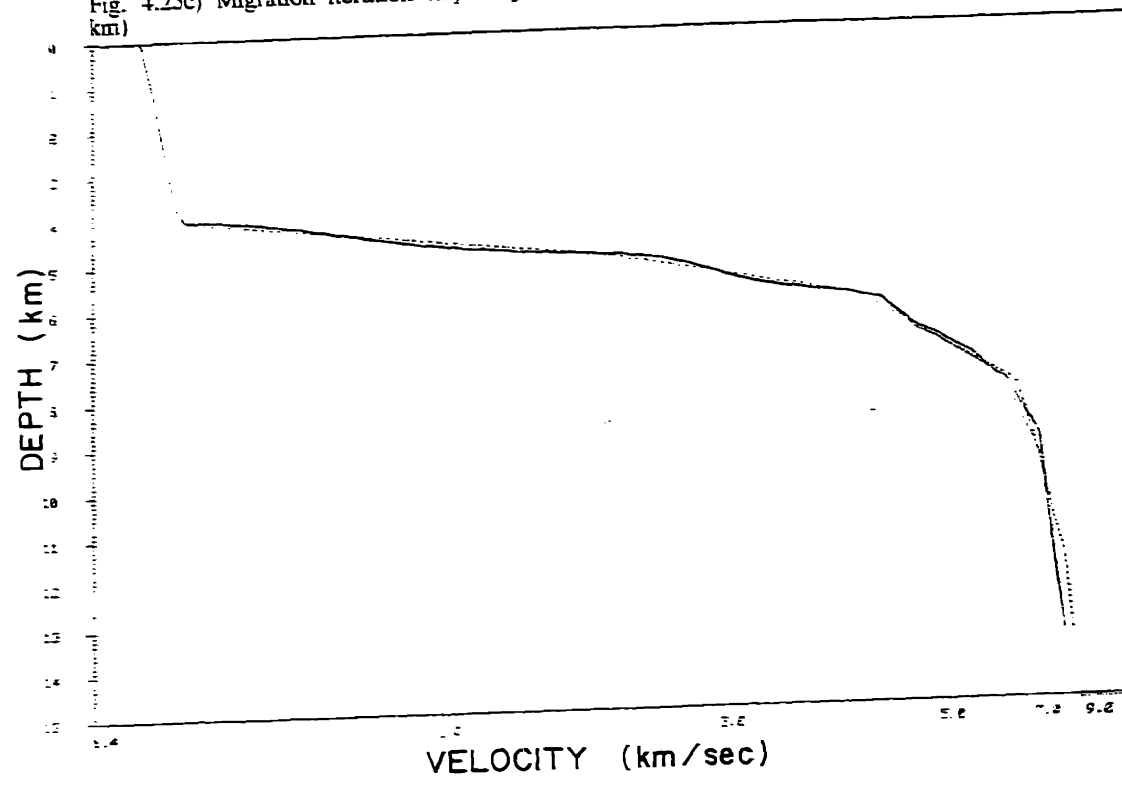

Fig. 4.25d) Migration iteration limit cycles (solid lines) and true model (dotted line) for 30 data points and $\Delta z = 1.0$ km.

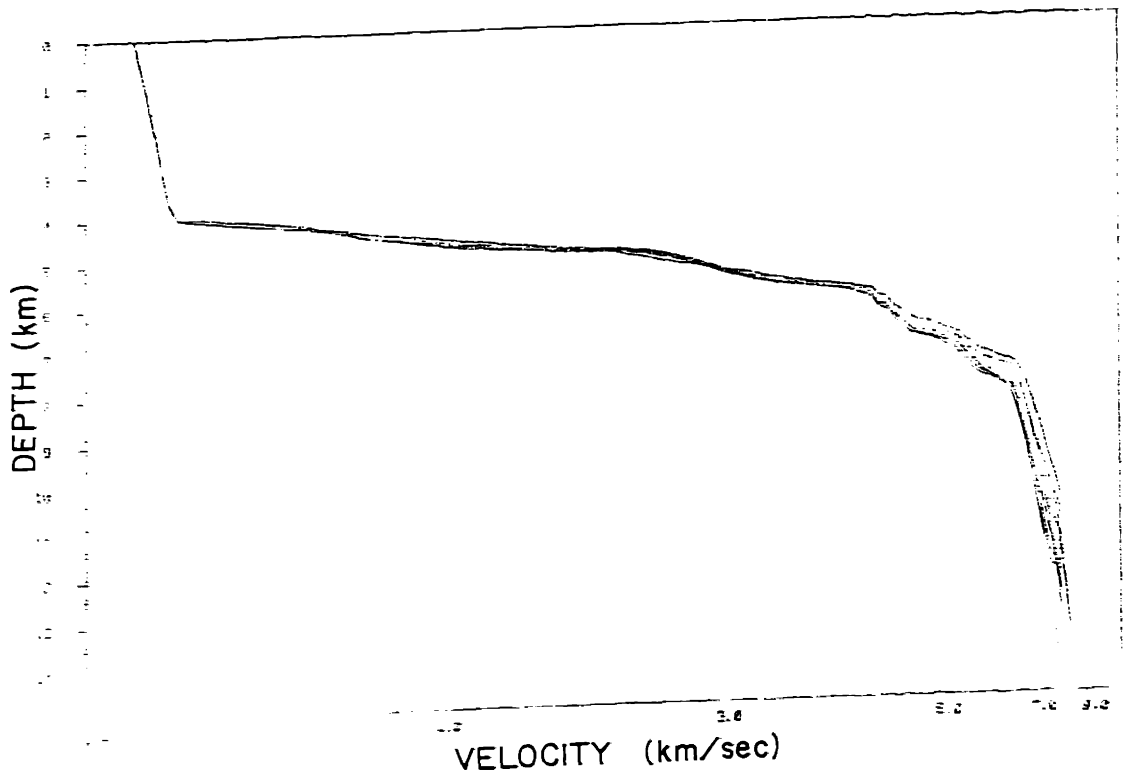

Fig. 4.25e) Migration iteration trajectory for 100 data points. ($\Delta z = 1.0$ km)

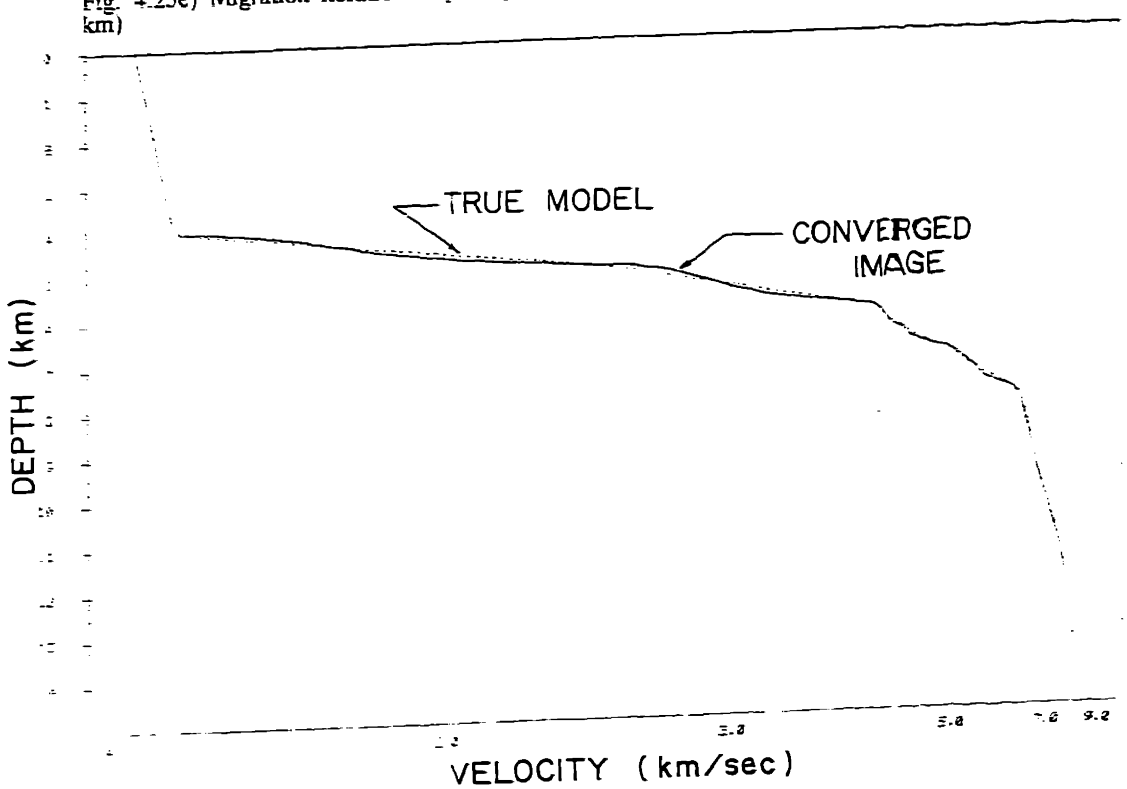

Fig. 4.25f) Migration iteration limit cycle (solid line) and true model (dotted line) for 100 data points and $\Delta z = 1.0$ km.

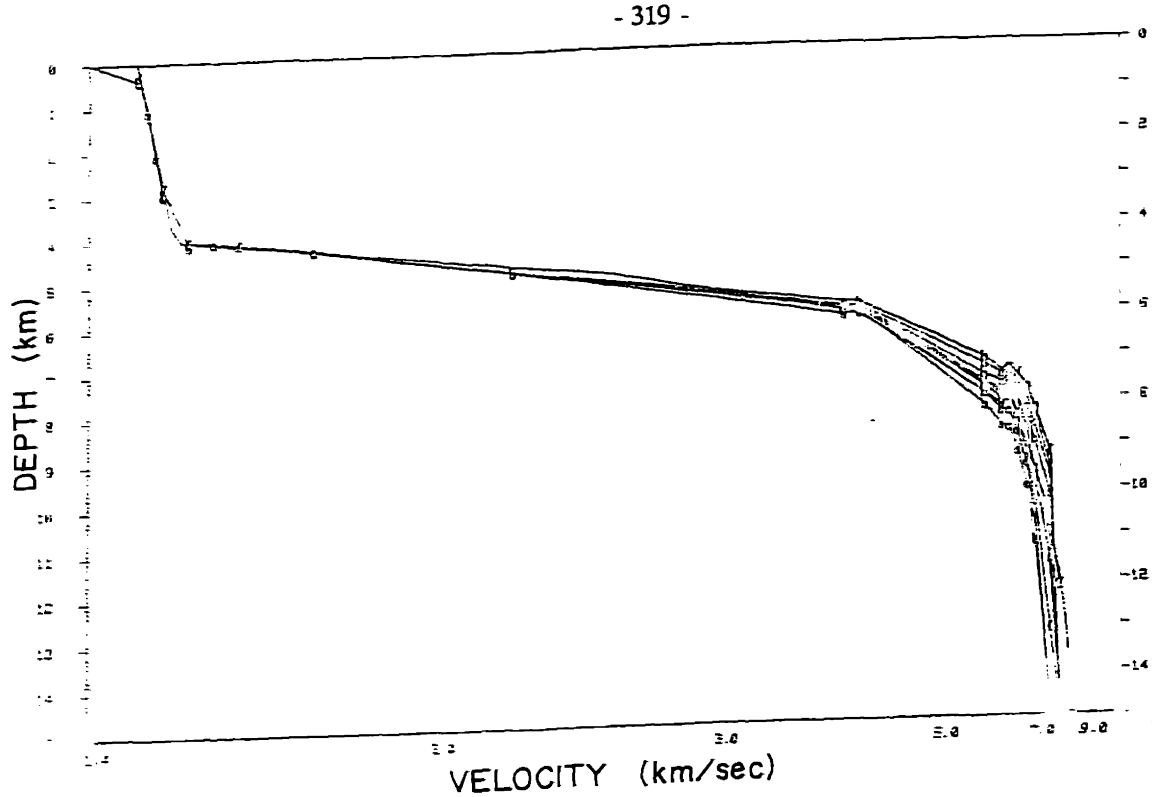

Fig. 4.25g) Migration iteration trajectory for data points from WKBJ synthetics. ($\Delta z = 1.0$ km)

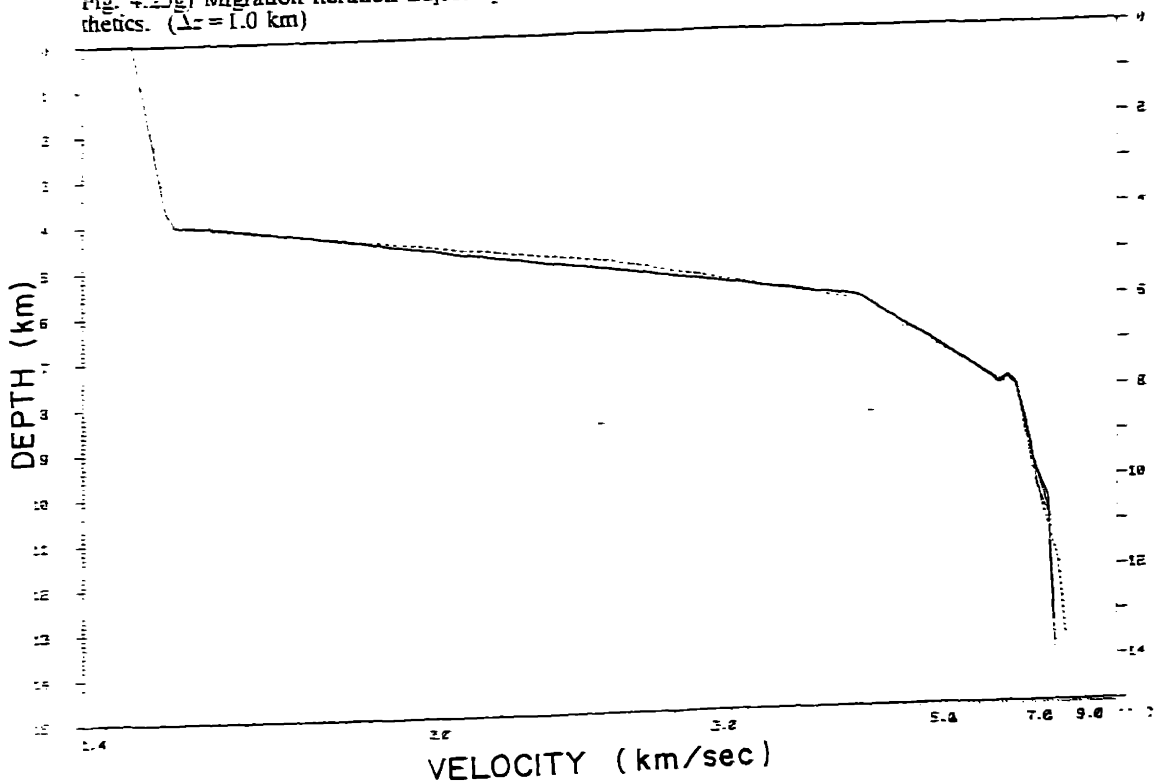

Fig. 4.25h) Migration iteration limit cycles for data points from WKBJ synthetics. ($\Delta z = 1.0$ km)

in fig 4.25g and a very tight set of limit cycles. These are shown in fig. 4.25h (solid lines) and compared to the true model (dotted line). The infeasibility of the model in this plot is due to one erroneous data point.

To complete this discussion of the migration algorithm, we examine the effects of noisy data. For the first example, the 30 sample $\tau(p)$ and $x(p)$ data were perturbed as shown in figure 4.26 (solid lines, the dotted lines are the noiseless curves). To obtain this data, Gaussian random numbers were added to the correct τ and x data. The means were zero, and the standard deviations were 0.1 sec and 2.0 km respectively. Figure 4.27 plots the sixth through tenth iterations for both the $\Delta z = 1$ km case (dotted) and the $\Delta z = .05$ km case (solid bounds). The true model is also plotted (center solid lines). Again, the damping provided by the interpolation seems to improve the convergence of the algorithm.

SUMMARY

In this chapter we have summarized and given details of the various inversion algorithms used to invert the data for crustal models. Much of the material presented was tutorial in nature, but it is hoped that its relative completeness will be of aid to the reader in understanding the work in chapter 5. Some new material was presented, the equations for the tau-sum method with linear slowness gradients, the method for easy modification of the maximum likelihood inversion technique to do stochastic inversion, the inclusion of $x(p)$ data in the migration process, the migration of velocity spectra and the method for compositing short aperture results, and some new insights into the convergence properties of the migration algorithm appear to be original work.

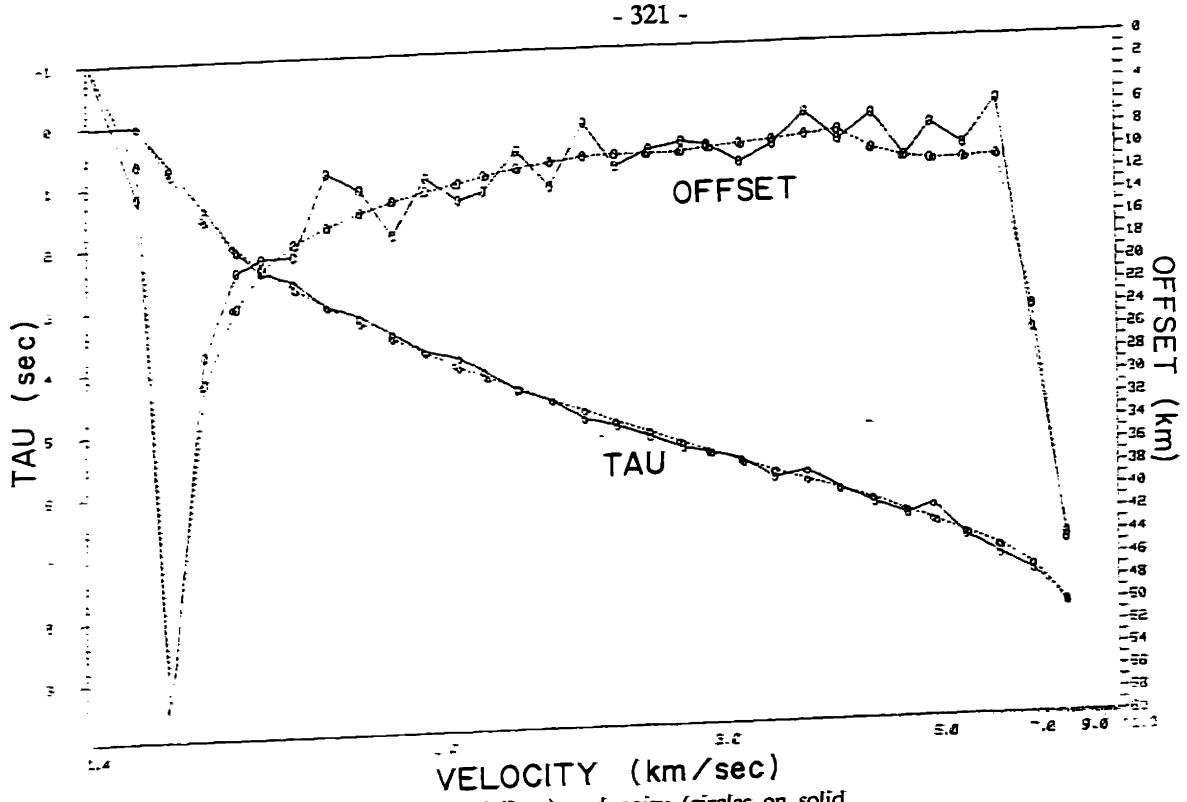

Fig. 4.26) Noiseless (circles on dotted lines) and noisy (circles on solid lines) data. $\sigma_\tau = .1$ sec, $\sigma_x = 2$ km.

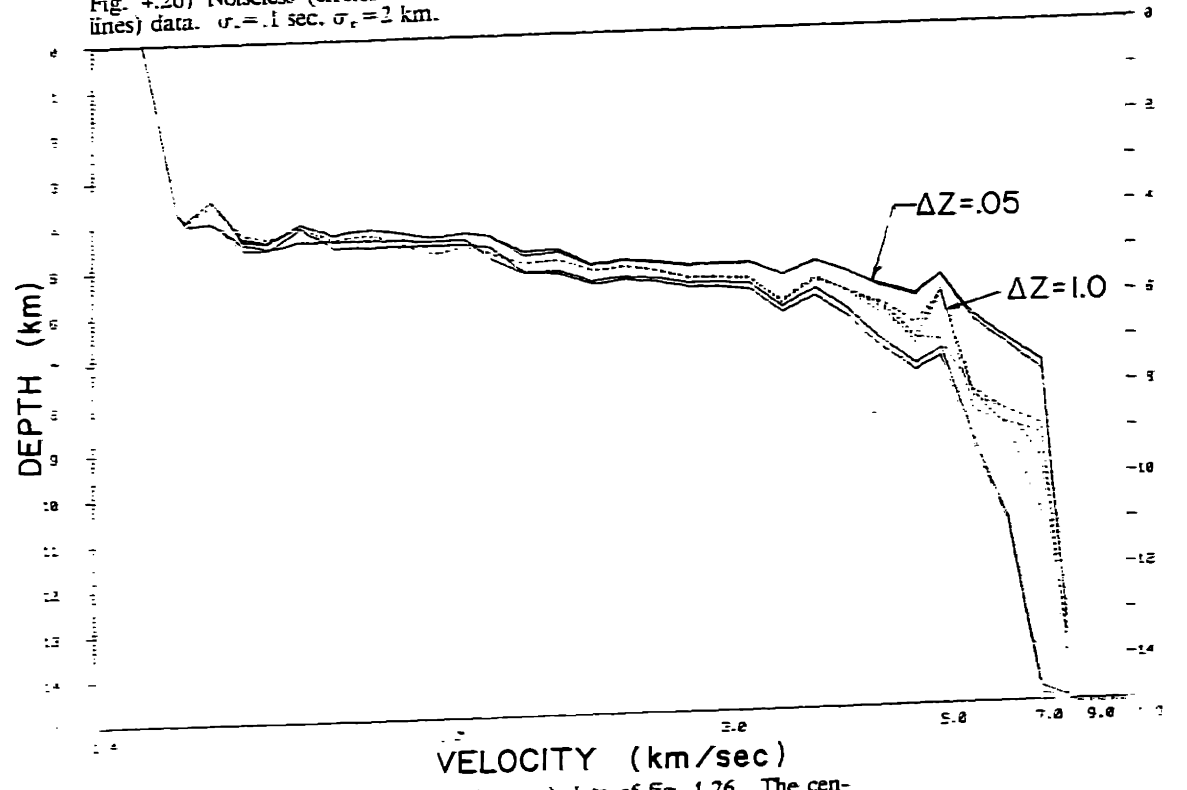

Fig. 4.27) Results of migration of noisy $\tau(p)$ data of fig. 4.26. The central solid curve is the true model. The dotted curves are the migration trajectories for $\Delta z = 1.0$ km, and the solid curves are the limit cycles for $\Delta z = .05$ km.

REFERENCES

Aki, K. and Richards, P.G., in *Quantitative Seismology: Theory and Methods*, San Francisco: W.H. Freeman, 1980.

Claerbout, J.F., *Fundamentals of Geophysical Data Processing*. McGraw Hill, Inc., 1976.

Clayton, R. and McMechan, G., "Inversion of refraction data by wavefield continuation," *Geophysics*, vol. 46, no. 6, p. 860, 1981.

Diebold, J.B. and Stoffa, P.L., "The traveltime equation, tau-p mapping, and inversion of common midpoint data," *Geophysics*, vol. 46, no. 3, pp. 238-254, March, 1981.

Dorman, L. and Jacobson, R.S., "Linear Inversion of Body Wave Data; Part I: Velocity Structure From Travel Times and Ranges," *Geophysics*, vol. 46, no. 2, pp. 138-151, 1981.

Dorman, L.M., "A Linear Relationship between Earth Models and Seismic Body Wave Data," *Geophysical Research Letters*, vol. 6, no. 3, pp. 132-134, 1979.

Franklin, J., "Well posed stochastic extensions of ill-posed linear problems," *Journal of Mathematical Analysis and Applications*, vol. 31, pp. 682-716, 1970.

Garmany, J., "On the Inversion of Travel Times," *Geophysical Research Letters*, vol. 6, no. 4, pp. 277-279, 1979.

Jackson, D.D., "Interpretation of inaccurate, insufficient, and inconsistent data," *Geophysical Journal of the Royal Astronomical Society*, vol. 28, pp. 97-109, 1972.

Jackson, D.D., "The use of a priori data to resolve non-uniqueness in linear inversion," *Geophysical Journal of the Royal Astronomical Society*, vol. 57, pp. 137-157, 1979.

Lanczos, C., in *Linear Differential Operators*, London, England: Van Nostrand, 1961.

Parker, R.L., "Understanding Inverse Theory," *Ann. Rev. Earth Planet. Sci.*, vol. 5, pp. 35-64, 1977.

Purdy, M., *Ocean Industry Program Lecture Series*, Woods Hole Oceanographic Institution, October 1981.

VanTrees, H.L, *Detection, Estimation, and Modulation Theory: Part I*. New York, NY: John Wiley and Sons, 1968.

Wiggins, R.A., "The general linear inverse problem: Implication of surface waves and free oscillations for earth structure," *Reviews of Geophysics and Space Physics*, vol. 10, no. 1, pp. 251-285, 1972.

CHAPTER 5: Processing and Inversion of the Fram 2 Refraction Data

INTRODUCTION

In this chapter I will discuss the inversion of the refraction data from the Fram 2 experiment. This experiment was carried out in the Pole Abyssal Plain or Fram Basin of the eastern Arctic Ocean from March to May of 1980. The shooting geometry for the three non-reversed lines to be discussed is pictured in chapter 1 in figures 1.1 and 1.2a and a general outline of the problems presented by experimentation in the Arctic is given there. The plan for this chapter is to first lay out the experimental particulars for the three refraction lines to be covered. This will include the locations of the lines and the details of the method used for offset determination from the direct water wave path, and the determination of bearing to the shot from the receiving array. Following this, analysis of a small part of the data will be given in detail so that the methods used will become clear. Detailed presentation of all the data analysis is prohibited by the volume of the data. Finally, the thought processes involved in the inversion will be sketched, and models will be given for the three lines analysed. The geological implications of the results will then be discussed.

NAVIGATION, SHOT POINT LOCATION, AND BATHYMETRY

To draw sensible conclusions from a seismic experiment it is necessary to know exactly where the experiment is being conducted. To this end, the camp position was determined by the use of several satellite navigation units using the Navy Transit Satellite network. Although the camp was moving with the ice pack, it was not necessary to use inertial interpolation during the experiment because of the frequent update of the position afforded by the near polar location of the camp. Because the 5 satellites in the system are in polar orbits, a satellite was

nearly always in view, and fixes were obtained approximately every hour. These raw data were then smoothed and interpolated by a Kalman filtering algorithm to yield a densely sampled camp drift track. This data has been published by Allen, et al. [1980]. Because the array was spread in two dimensions over the surface of the ice pack, it was also necessary to get the ranges and relative bearings to each of the sensors (for coherent processing), and the absolute bearing of the entire array with respect to north (for determination of the bearing to the shot). The sensor locations relative to a 200 m optical baseline were determined by standard surveying techniques using a high quality theodolite. This yielded sensor "through-ice" positions* to within a meter at near the vertex of the array, and within 5 meters at the furthest extents of the array (about 600 m from the vertex). The absolute rotation of the array was determined by daily sun shots.

The locations of the shot points were roughly located at deployment time using the *Omega* receiver and magnetic compass navigation system on the Bell 204 Helicopter used for the experiment. This system was adequate to maintain the lines within 5° of linearity, and to locate the shots within a kilometer of the desired range**. The accurate ranges to the shots from the receiving array were determined using an assumed water column structure and an accurately measured time of flight for the direct water column arrival. The satellite receiver was used to synchronize a master clock attached to the computer based acquisition system. The system encoded the time accurate to 1 millisecond from this clock onto the digital data

*We could obviously only survey the surface locations. Because of ocean currents relative to the floe, the actual sensor locations will deviate as a function of watch circle. It was assumed that the currents were of constant direction and magnitude over the entire array and thus the relative locations measured at the surface were correct. The sensors used for this experiment used a heavy 3 conductor shielded cable and a 1/4" polypropalene line supporting a two-mass compliant section for strum decoupling. The depth of the sensors was 300' (93 m) and the total suspended weight was 35 lbs. It is believed that all relative currents were less than .5 kt.

**Local ice conditions also required deviation from the planned shotpoints. To carry out the ambitious experimental goals, time to cut deep holes through the ice could not be afforded. Instead, holes of opportunity in the form of freshly open, or recently frozen leads that could easily be cut with a chain saw next to ice suitable for helicopter landing were sought.

tapes along with the array data. For the refraction runs a portable time base was synchronized to the master clock to within 200 microseconds. This clock was then installed in a portable "shot monitor" system consisting of a two channel analog recorder and a hydrophone or geophone. At the shot point this system was deployed on the ice and the direct wave from the shot was recorded on one channel of the recorder, and an analog time code in the IRIG-B format was recorded from the time base on the other. The shots were deployed at a known depth* of 800' (243 m). After the helicopter returned to the camp, the relative drift of the portable time base was checked. Using this method, the propagation time of the direct water arrival was measured. The shot arrival instant at the shot monitor (delayed by the vertical travel time at the source) could be determined to within than a millisecond using a wide band hydrophone and 15 kHz recording bandwidth on the shock wave. The received time is subject to less accuracy because the digital acquisition system had an anti-aliasing rolloff that began at 80 Hz. Considering the time accuracy to be the inverse of the bandwidth yields 12 msec, or about 20 m at best. This accuracy is further degraded by errors in the modeling of the water column, and a figure of .05 km is estimated for the ranging accuracy for this experiment. The time delays were turned into distances using the following method. First, the delay time from the source to the surface was determined. Although the detonation depths of the SUS charges used to initiate the main TNT charge are close tolerance, the source-surface delay could also be measured by the delay between the bottom bounce directly from the source and that which was delayed by the surface reflection. This source-surface delay was then subtracted from the measured shot instant to get the detonation instant. Next, using a water column profile obtained from an expendable sound velocimeter (XSV) and from the work of chapter 6, a table of propagation times vs. offset distances from a source at 243 m to a receiver at 93 m was

*Using the SUS charge pressure activating mechanism.

computed using ray tracing for both the direct and first free surface multiple. The measured time was then looked up on the appropriate table (depending on whether the offset was beyond the first convergence zone at 55 km) and the offset obtained by linear interpolation of the (already dense) table.

The bearing from the array to the shot was determined by beamforming on the direct water arrival using the maximum likelihood algorithm in bearing at the slowness of the arrival. Because of the high signal to noise ratio for this event, the accuracy was quite high- much better than the 0.5^{o} necessary for fixing the direction to the shot for slowness estimation with the velocity spectral processor. The program used to do this is identical to that used to compute the velocity spectra, except instead of scanning in the vertical plane (over slowness), the horizontal plane was swept out.

In addition to the location, the bathymetric relief is also very important to refraction experimentation. Bathymetric dip can cause the measured slownesses and travel times to be grossly mis-interpreted. Evidence of rough topography should also indicate that inversions for horizontally layered structures is inappropriate. For the Fram 2 experiment the bathymetry at the base camp (denoted Fram 2) was determined by a 12 kHz echo sounder. The raw data from this device were processed and reported by Allen et al. [1980] in the same report as the drift track. They report the travel times and the corrected depth using the standard tables. We found that the travel times used with our water column model and ray tracing at vertical incidence yielded the same depths. For the bathymetry at the source, the difference between direct arrival and the normal incidence reflection of the explosion signature from the bottom was used. It is felt that the accuracy of this method was sufficient to give bathymetry to within 20 m in regions of low relief (all regions encountered).

REFRACTION LINE PARAMETERS

Introduction

Before getting into the specifics of the individual lines, it is useful to glance at the overall setting and ice camp structure. Fig. 5.1 shows the locations of the refraction lines in the Pole Abyssal Plain of the eastern Arctic Ocean. In this work, lines 1, 4 and 6 will be discussed. Line 1 is in a deep region of the Plain with almost no topography and runs at 20° true between magnetic anomalies numbered 21 and 22 corresponding to a crustal age of between 48-53 My [Ness, et al. 1980]. Line 4 runs approximately perpendicular to the lineations at 100° true, and is in a region with no topographic relief, but is generally dipping away from the receiving array. The line spans the region from approximately anomaly 23 to anomaly 20. This is a little hazy because the strength of the anomalies deteriorates in this region as the Morris Jessup Rise is approached. Finally, line 6 was carried out on the flanks of the Morris Jessup Rise as the camp shoaled late in the experiment. This line was shot along a non-negligible dip of 0.5° to 0.7° at approximately 104° true and shows little relief beyond this relatively constant dip. The magnetics in this region are an utter mess. The inset in Fig. 5.1 shows the course of the spreading center at the Atlantic and Arctic Mid-ocean ridges.

The detailed drift track for the camp from April 5 until May 4, 1980 is shown in fig. 5.2, along with the refraction lines and bathymetry. Finally, figure 5.3 shows a plan view of the ice camp *Fram 2* giving the approximate array, living and laboratory structure, and ice activity locations.

Signal levels, noise levels, and dynamic range

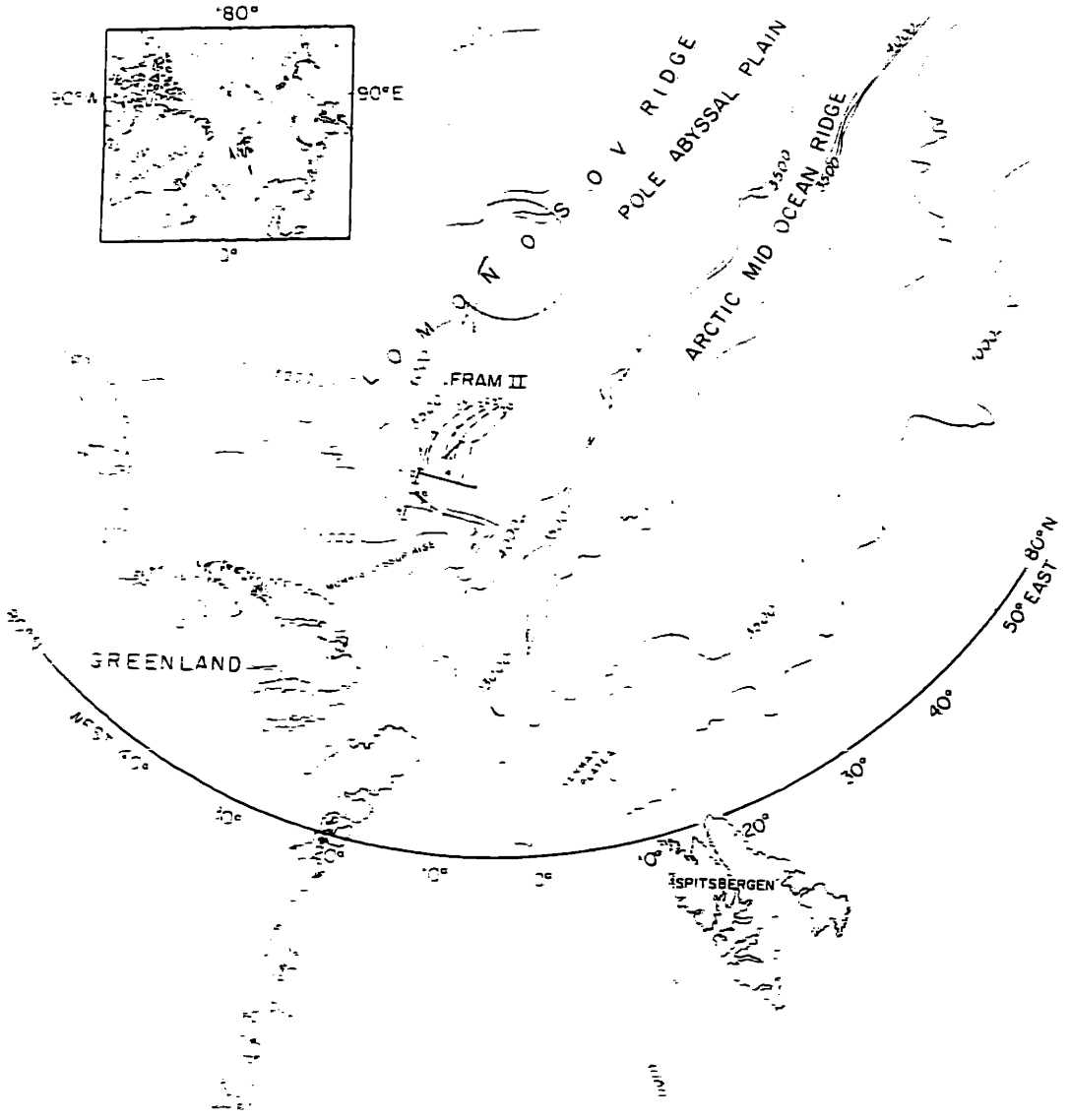

Fig. 5.1) Location and bathymetry of camp Fram 2 in the Pole Abyssal Plain of the Eastern Arctic Ocean. The starting location of the camp was 86° N, 24° W. Also shown are the refraction lines (solid lines labeled 1-6) and the major magnetic anomalies in the area studied (dashed lines labeled 20-23). Inset: location of the Arctic Mid-ocean Ridge spreading center.

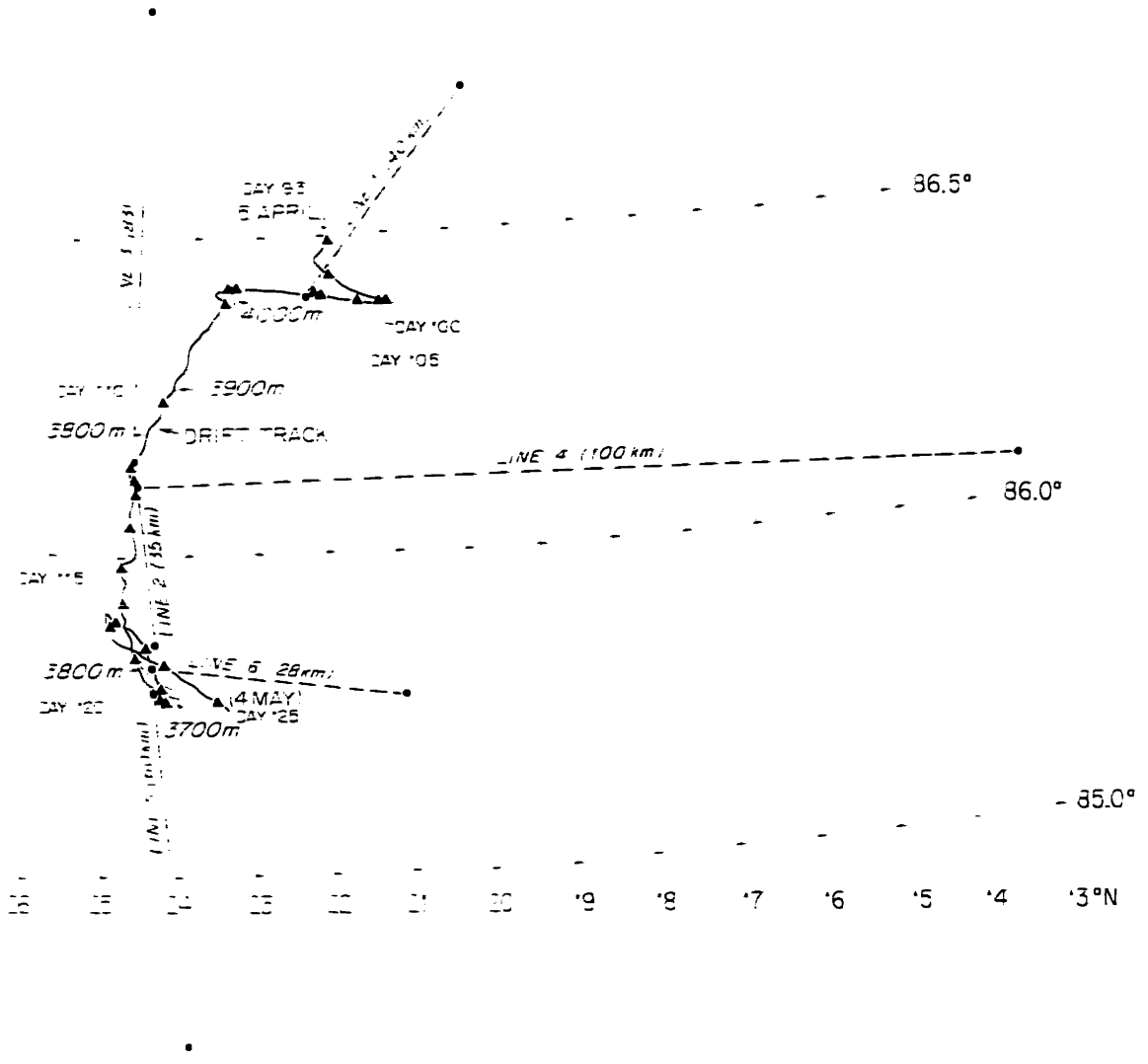

Fig. 5.2) The detailed drift track of camp Fram 2. The noon positions are denoted by triangles. Also indicated are water depths and the refraction lines carried out during the experiment.

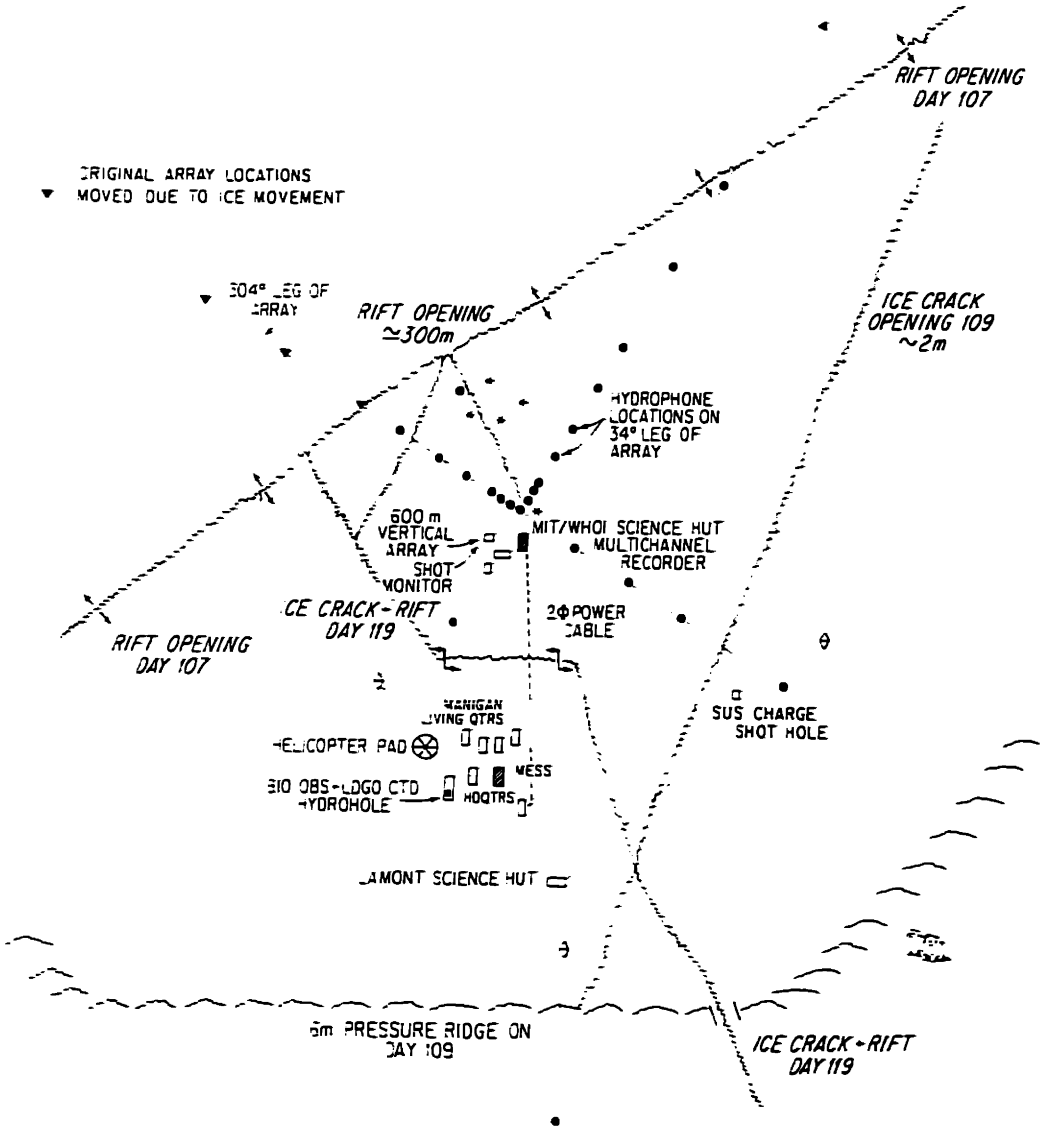

Fig. 5.3) Plan view of the camp layout, local ice rifting, and hydrophone array structure. The hydrophones are deployed to a depth of 93 meters. The triangles indicate sensor locations that were eliminated due to ice movement, circles are the final array locations. (True north is vertical)

For the Fram 2 experiment hydrophones with a sensitivity of -160 dB re 1 volt/μPa were used. The phones and digital acquisition system had a maximum swing of ±5 volts, thus yielding a maximum linearly detectable pressure of 174 dB re 1 μPa. The ambient noise level averaged around 80 dB re 1 $\mu Pa/\sqrt{Hz}$ in the 6 to 20 Hz band of interest, and the wideband rms noise level was about 95 dB re 1 μPa, excluding the noise at 2-4 Hz caused by strumming of the hydrophone suspension system. This strum noise was highly variable temporally, and ranged from undetectable to 160 dB re 1 μPa peak pressures.

The digital acquisition system anti-alias filtered the data at 80 Hz with a 48 dB/octave Butterworth filter, and digitized the 24 channels of data with a 4 msec sampling interval. The system used an instantaneous gain-ranging amplifier system which provided 120 dB of total dynamic range and 72 dB of precision. After digitization, the data were immediately converted to Hewlett-Packard single precision floating point format for storage on the data tapes.

At short ranges (< 40 km) the standard source charge was 25 kg. of TNT detonated at a depth of 243 meters. This yields a spectral peak at 16 Hz, and a spectral level of 225 dB re 1 μPa/Hz at this frequency. In the 40-60 km. and 60-100 km. ranges charges of 50 kg and 100 kg were deployed at the same depth giving spectral peaks of 13 and 10 Hz at 229 and 233 dB re 1 $\mu Pa/\sqrt{Hz}$ respectively.

Line 1

Line 1 was carried out on April 12, 1980. At the start of the run (1400Z), the camp was at 86.401° *N* and 22.196° *W* and had a southerly drift of .7 cm/sec and and easterly drift of 2.3 cm/sec. At the end of the run (1900Z), the camp location was 86.400° *N* and 22.206° *W* and had no north component to the drift and a 1.3 cm/sec westerly drift. The distance between these endpoints is less than 0.1 km, so the camp may be regarded as stationary for the

duration of the line. During the 5 hour interval, the velocities oscillated between north and south and east and west.

For this line, the data acquisition system was not writing the master clock times correctly onto the data tapes, thus disabling the accurate offset determination described above. However, in parallel with our system, the Bedford Institute of Oceanography (BIO) was operating an ocean bottom seismometer (OBS) and an independent shot instant monitor. The experimental geometry for this system is also illustrated in figure 1.2a in chapter 1. Correcting the offset determination of this system for the surface offset between the BIO installation and the estimated wire angle obtained the offsets used to analyse the array data. It is estimated that the offset errors using this method are bounded by .2 to .3 km. The offsets obtained were also corroborated using the travel time and slowness measurements for the direct water arrival and the first bottom bounce (refraction) assuming a sediment model as well as the water column profile. The formula for this offset is:

$$x = \frac{[(t_1 - t_2) - (\tau_1 - \tau_2)]}{[p_1 - p_2]} \qquad 5.1$$

where $\tau_1 = \tau(p_1)$ and $\tau_2 = \tau(p_2)$ from the model prediction, and (t_1, p_1) are the direct water wave coordinates from the velocity spectrum and (t_2, p_2) are the bottom arrival coordinates from the velocity spectrum. The models used to compute the predicted $\tau(p)$ values after linear slowness interpolation are given in table 5.1.

Table 5.1

Direct arrival			Bottom arrival		
z (km)	c (km/s)	nt	z (km)	c (km/s)	nt
0	1.437	0	0	1.437	2
.08	1.44	0	.08	1.44	2
.093	1.441	1	.093	1.441	3
.250	1.455	2	.250	1.455	4
.4	1.460	2	.4	1.460	4
1.6	1.471	2	1.6	1.471	4
4.0	1.510	2	4.0	1.510	4
4.1	1.512	2	4.1	1.512	4
4.3	1.625	2	4.3	1.625	4
5	2.5	2	5	2.5	4

In this table, the parameter "nt" refers to the number of traverses the ray makes through the layer.

The parameters for the shots in line 1 are summarized in table 5.2.

TABLE 5.2 Shot parameters for line 1

reel	charge weight (kg)	depth @ rcvr (km)	depth @ src (km)	dip (deg)	range (BIO) (km)	range (bounce) (km)	bearing (true deg)
3006	25	4.025	3.860	-.71	13.4	13.05	26
3007	25	4.025	4.010	-.05	18.9	18.93	20
3008	25	4.025	4.010	-.05	23	23.34	22
3009	25	4.025	4.320	.62	27.2	27.56	21
3010	25	4.025	4.100	.13	34.1	31.33	20
3011	25	4.025	3.935	-.13	41.1		20

For the velocity spectral processing (see chapter 3) the parameters were set to the values given in table 5.3. The reader is referred to chapter 3 for further information on each of the parameters.

Table 5.3 Velocity spectral processing parameters for line 1		
Parameter	Value	Description
T	.25 sec	window length
w_s	$\sin^2$	window taper
Δt	.004 sec	data sampling interval
α	.002	stabilization fraction
N	18	number of sensors
$\omega_p/2\pi$	6,10,14,18 Hz	processing center freqs.
B / n_{ave}	2π*4 / 1	processor bandwidth / number of coeffs. ave.
normalization	used	covariance matrix normalization
Δp	0.02514 s/km	time steering slowness increment
δp	.00503 s/km	phase steering slowness increment
np	5	number of phase steers per time steer

Finally, this initial line was carried out before the entire 24 channel array was deployed. The sensor locations for the 18 channels in operation are given in table 5.4 in terms of range and bearing from north (true) from the reference sensor at the apex of the array.

Table 5.4	The sensor array locations for line 1	
Channel	range (m)	bearing (^{o} true)
1	0.	0 (apex)
2	16.7	34
3	32.7	34
4	49.7	34
5	101.1	34
6	152.0	34
7	226.1	34
8	302.1	34
9	456.0	34
10	616.3	34
11	NC	
12	NC	
13	17.3	304
14	33.3	304
15	50.0	304
16	100.6	304
17	152.1	304
18	227.6	304
19	302.1	304
20	456.0	304
21	NC	
22	NC	
23	NC	
24	NC	

A schematic view of the array coverage for line 1 is given in figure 1.2b in chapter 1.

Line 4

Refraction line 4 began on April 21, 1980 at about 1900Z. The initial shot used for this work is reel 3042 for which the Fram 2 camp was located at 86.103^{o} *N* and 24.779^{o} *W* and had a south velocity of 4 cm/s and a west velocity of .5 cm/s. At the end of shooting on the 21st (reel 3048) at 2030Z the camp had moved negligibly. The second day of shooting for this line was April 22, and began at 1500Z with reel 3049. The initial location of the camp was 86.065^{o} *N* and 24.871^{o}*W* with a south velocity of 8.4 cm/s and a west velocity of .9 cm/s. This

is 4.3 km south of the previous day's shooting. The final reel (3055) of this line was shot at 2000Z when the receiving array was at 86.053° *N* and 24.876° *W*. The drift was still southerly, and this location is 1.3 km south of the initial shot (reel 3049) on this day, and 5.6 km south of the previous day's shooting.

For this line, the data acquisition software had been fixed to write the master clock time correctly on the tape, thus enabling the accurate determination of the shot offsets. The parameters for the shots in line 4 are summarized in table 5.5.

TABLE 5.5 Shot parameters for line 4

reel	charge weight (kg)	depth @ rcvr (km)	depth @ src (km)	dip (deg)	range (km)	bearing (true deg)
3042	25	3.805	3.85	.195	13.246	91.5
3043	25	3.805	3.855	.17	16.912	89
3044	25	3.805	3.862			
3045	25	3.805	3.88	.17	25.666	93
3046	25	3.805	3.910	.214	28.136	92
3047	25	3.805	3.958	.262	33.449	92
3049	50	3.806	3.99	.244	43.228	93
3050	50	3.807	4.002		45.791	94
3051	50	3.807	4.028	.24	52.696	95
3052	50	3.807	4.048	.24	57.251	95
3053	50	3.807	4.075	.244	63.040	91
3054	100	3.808	4.100	.233	71.822	92
3055	100	3.808	4.150	.223	87.883	93

For the velocity spectral processing the parameters were set as given in table 5.3 for line 1. Refer to chapter 3 for further information on each of the parameters.

For this line the entire 24 channel array had been deployed. However, three hydrophone channels were omitted from the data processing because of excessive noise or because geophones were being recorded. The sensor locations for the 21 channels used are given in table

5.6 in terms of range and bearing from north (true) from the reference sensor at the apex of the array. These locations are different from line 1 because the array had to be reorganized (and was forceably "reorganized") by ice movement on April 16, 1980. This movement is illustrated in fig. 5.3.

Table 5.6 The sensor array locations for line 4

Channel	range (m)	bearing ($^{o}true$)
1	0	0 (apex)
2	16.7	26
3	NC	
4	49.7	26
5	101.1	26
6	152.0	26
7	226.1	26
8	302.1	26
9	456.0	26
10	616.3	26
11	200.0	206
12	NC	
13	17.3	296
14	33.3	296
15	50.0	296
16	100.6	296
17	152.1	296
18	227.6	296
19	102.1	116
20	204.3	116
21	306.6	116
22	515.6	116
23	NC	
24	204.2	333.8

Line 6

This short 5-shot line was carried out on April 18, 1980. The first shot, at 1400Z, was initiated when the camp was located at 85.771° *N* and 24.235° *W* as the camp began to shoal

on the Morris Jessup Rise. The line was completed by 1530Z and camp movement was negligible (1.2 cm/s north velocity, .5 cm/s west velocity) during this period. For this line all systems were operating well, and the parameters for the shots are tabulated in Table 5.7.

TABLE 5.7 Shot parameters for line 6

reel	charge weight (kg)	depth @ rcvr (km)	depth @ src (km)	dip (deg)	range (km)	bearing (true deg)
3071	25	3.655	3.745	.546	9.445	104
3072	25	3.655	3.845	.768	14.183	100
3073a	25	3.655	3.890	.737	18.278	98
3073b	25	3.655	3.900	.649	21.642	97
3074	25	3.655	3.895	.588	23.369	97

The array locations were nearly the same as those for line 4, although one more sensor had been reactivated. The sensor locations for line 6 are given in Table 5.8.

Table 5.8 The sensor array locations for line 6		
Channel	range (m)	bearing (^{o} true)
1	0	0 (apex)
2	16.7	26
3	32.7	26
4	49.7	26
5	101.1	26
6	152.0	26
7	226.1	26
8	302.1	26
9	456.0	26
10	616.3	26
11	200.	206
12	NC	
13	17.3	296
14	33.3.	296
15	50.0	296
16	100.6	296
17	152.1	296
18	227.6	296
19	102.1	116
20	204.3	116
21	306.6	116
22	515.6	116
23	NC	
24	204.2	333.8

The processing parameters for this line were nearly the same as those given in Table 5.3 for line 1. The only change is that the center frequencies for the processing were changed to 8.10.14.and 18 Hz. in accordance with the true "bin" center frequencies from the FFT used in the temporal spectral decomposition. It was found that this change did not alter the features of the spectra noticibly.

AN EXAMPLE INVERSION OF THE FRAM 2 DATA

The velocity spectrum

To acquaint the reader with the use of velocity spectral processing output, and how it compares to the waveforms themselves, we consider a typical set of traces and their corresponding spectrum at a single frequency, 6 Hz. For the plots in figures 5.4a-e the contour intervals for the spectral plots are 3 dB. The spectrum used is from reel 3009 of line 1 has reference offset of 27.2 km. This distance is approximately the midpoint of the projection of the 2-D array along the line of propagation from the shot, and is the range to the apex (channel 1) phone which was designated to be the reference point. The waveforms plotted at the top of the figures are lowpassed at 30 Hz and are taken at sensors 0.6 km apart to indicate coherency. The traces are uncorrected for moveout, and the top trace is the reference for the velocity spectrum. It should be noted that the data are exceptionally coherent and noise free for refraction data. This can be attributed to the quiet platform provided by the ice, the high dynamic range of the acquisition system, and the relatively large charge sizes employed (25 kg of TNT). As can be seen from the ambient noise level preceding the initial arrival the differences between the two traces in figs. 5a-e are variations due to differential propagation paths for the sensors, not independent sensor noise. The arrival path identifications have been made by first determining a model using much more data than this single shot. The predictions of this model were then compared to the arrivals at 27.2 km to make the identifications. One can clearly not ascribe paths based on observation of the velocity spectra alone.

In figure 5.4a the waveforms are plotted with a gain of 20 in amplitude. Event A has been identified as the layer 3 primary* at about 7 km/s. The four peaks in the received complex on the spectrum are due to surface reflections at the source and receiver. How these multipaths may be used to the interpreter's advantage will be discussed in a later section. The

Fig. 5.4a) Waveform and velocity spectrum for Fram II seismic refraction experiment with source/receiver offset = 27.2 km. The waveforms are lowpassed at 30 Hz and are taken at sensors 0.6 km apart to indicate coherency. The traces are uncorrected for moveout, and the top trace is the reference for the velocity spectrum. For the spectrum, the contour intervals are 3 dB. The waveforms are plotted with a gain of 20 in amplitude. Event A is the layer 3 primary. The four peaks are due to surface reflections at the source and receiver. Event B is the Moho compressional arrival.

Fig. 5.4b) Waveform and velocity spectrum of fig. 5.4a continued. The waveforms are plotted with a gain of 20 in amplitude. Event C is a layer 3 shear primary arrival. Event D is a deep sediment compressional primary. Events E and F are layer 3 and Moho water column pegleg multiples. Arrival G is a deep layer 2 second multiple, and event H is the layer 3 free surface multiple. Note that the events that are clearly delineated on the spectrum are not easily picked on the waveforms themselves.

Fig 5.4c) Waveform and velocity spectrum of fig. 5.4a continued. The waveforms are plotted with a gain of 0.5 in amplitude. Event I is the direct water arrival. Note that at 27.2 km the offset is exactly half the distance to the first convergence zone and the arrival is relatively weak. Arrival J is the primary refraction from the upper sediments. Event K is the compressional arrival from the deeper sediments, and L is a shear multiple from layer 3. Complex M is the second free surface multiple from a sediment refraction path. A high sediment velocity gradient causes the rise in phase velocity as the near source/receiver free surface ghosts arrive. Event M' is probably the water column pegleg multiple for a deep sediment compressional path.

Fig. 5.4d) Waveform and velocity spectrum of fig. 5.4a continued. The waveforms are plotted with a gain of 2.0 in amplitude. Event N is an internal multiple of undetermined path. Arrival O is the layer 2 compressional third free surface multiple. The complex P is the third free surface multiple of the sediment refraction. The event labeled Q is probably a deep layer 2 shear path third free surface multiple. Weak arrival R is a shallower layer 2 shear third free surface multiple.

Fig. 5.4e) Waveform and velocity spectrum of fig. 5.4a continued. The waveforms are plotted with a gain of 5.0 in amplitude. Event S is probably a layer 2 shear path. Complex T is the sediment compressional refraction fourth free surface multiple.

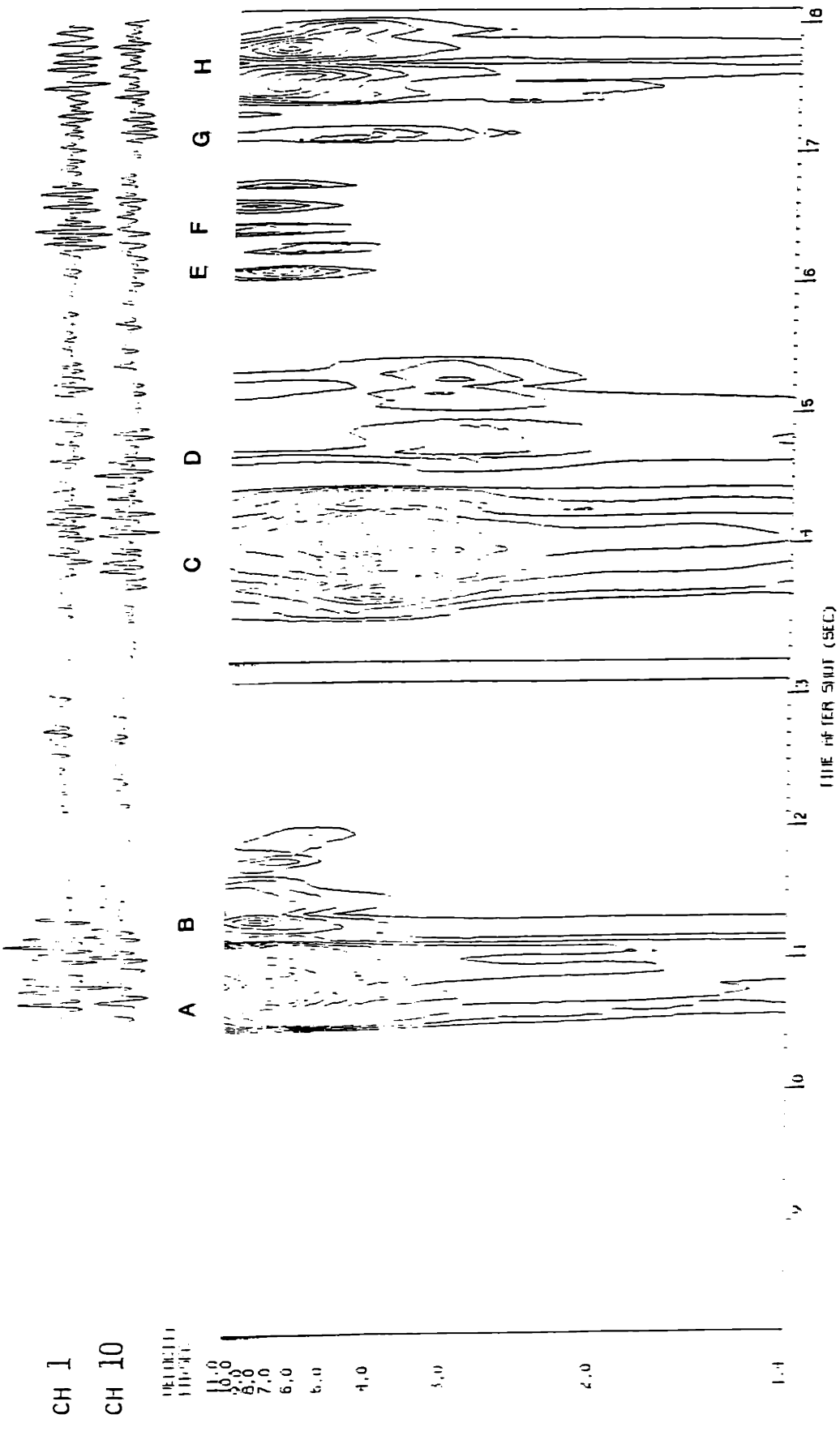

Fig. 5.4a)

Fig. 5.4b)

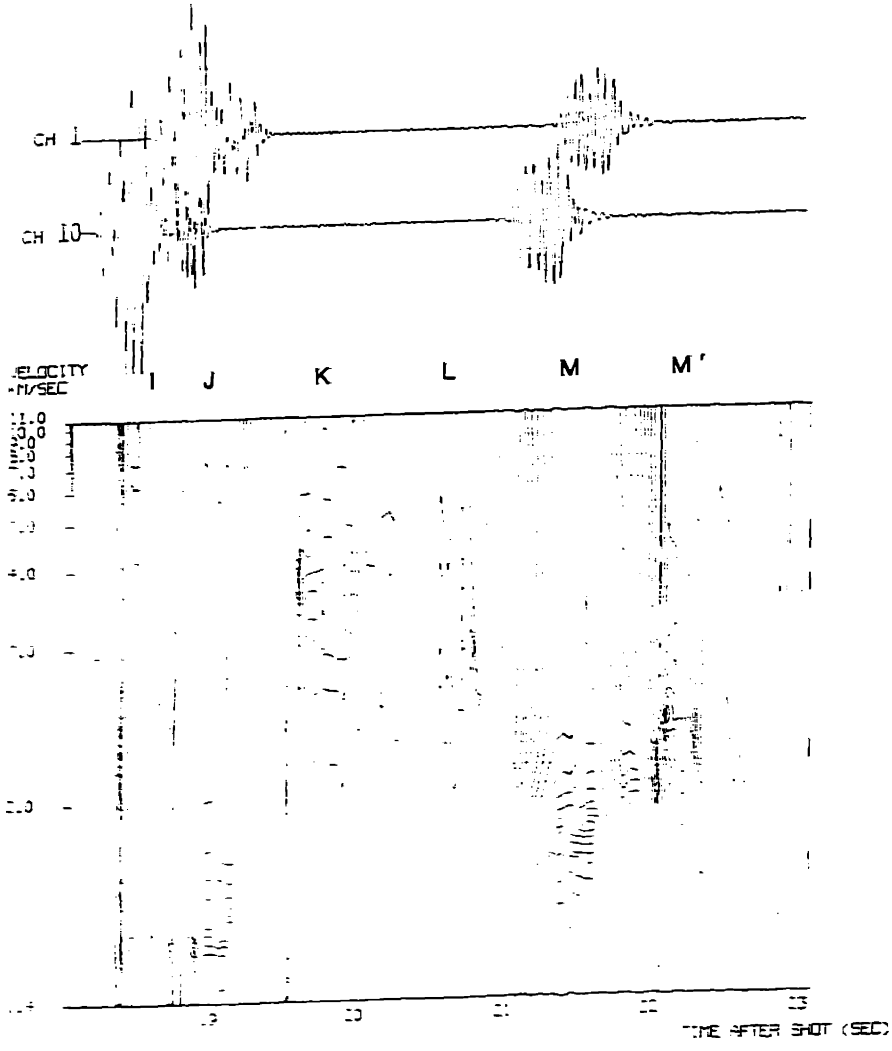

Fig. 5.4c)

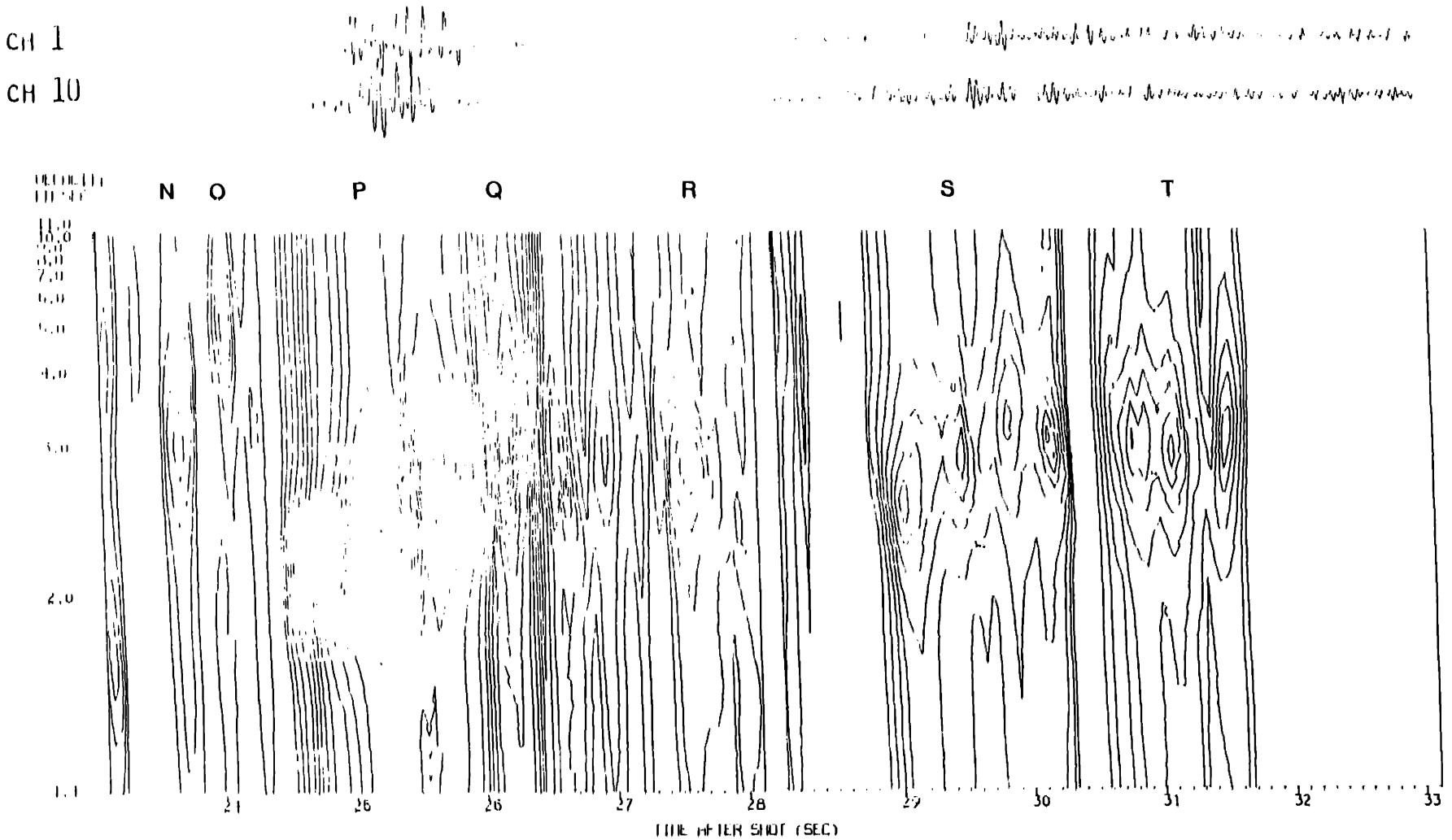

Fig. 5.4d)

Fig. 5.4e)

arrival labeled B is interpreted as the Moho compressional arrival. As expected, it has a phase velocity of around 8 km/s. One can observe that the important events stand out much more clearly on the spectrum than on the waveforms themselves.

Fig. 5.4b continues with another 5 second record of the received and processed data. The waveforms are again plotted with a gain of 20. Event C is a layer 3 shear primary arrival. Event D is probably a deep sediment compressional primary. Events E and F are layer 3 and Moho water-column pegleg multiples. Arrival G is a deep layer 2 second multiple, and event H is the layer 3 free surface multiple. Note that the events which are clearly delineated on the spectrum are not easily picked on the waveforms themselves, and that despite the lack of obvious coherency in the data, the arrivals are clearly revealed by the velocity spectrum.

The next 5 second record is plotted in fig. 5.4c. For these traces the waveforms are plotted with a gain of 0.5 in amplitude due to the large amount of energy in the direct water column arrival (event I) and bottom return (event M). However, at 27.2 km the offset is exactly half the distance to the first convergence zone (range where the water column rays constructively interfere to form a region of increased intensity, about 55 km for the Arctic profile used) for the Arctic profile and the direct arrival is relatively weak. Arrival J has been identified as the primary refraction from the upper sediments and event K is the compressional arrival from the deeper sediments or wide angle reflection from the basement. The weak peak L is a shear multiple from layer 3. Complex M is the second free surface multiple from a sediment compressional refraction path. A high sediment velocity gradient causes the rise in phase velocity as the near source/receiver free surface ghosts arrive. This slowness "dispersion" can be used to extract qualitative information about the gradients in the sediments. An analysis of why the "dispersion" occurs is given in a later section. Event M' is probably the water column

pegleg multiple for a deep sediment compressional path.

The records following the direct water arrival show a multitude of complex reverberations. Fig. 5.4d contains the waveforms plotted with a gain of 2.0 in amplitude. Event N , which would normally be lost in waveform picking is an internal multiple of undetermined path. Arrival O is the layer 2 compressional third free surface multiple. The complex P is the third free surface multiple of the sediment refraction. It again exhibits the slowness "dispersion" which will be seen to be indicative of a fairly strong gradient. The event labeled Q is a deep layer 2 shear path third free surface multiple. The weak and rather poorly defined arrival R is a shallower layer 2 shear third free surface multiple.

Figure 5.4e continues the record with waveforms plotted with a gain of 5.0. Event S has not been unambiguously identified, but is probably a layer 2 shear path. Complex T is the sediment compressional refraction fourth free surface multiple.

The $\tau-p$ spectrum

Obviously, identification of all the paths noted in figs. 5.4a-e is not possible from the one velocity spectrum alone, especially not in the $t-p$ domain in which arrivals have no well defined organization in terms of order of arrival. The procedure by which the identifications were made is roughly the following. First, the data from this offset and frequency, and other offsets and frequencies were converted to the $\tau-p$ domain. The conversion of this velocity spectrum at a single offset is given in fig. 5.5. The events labeled on figs. 5.4 are also noted there. When the $\tau-p$ spectra from other offsets are composited, and only the primary (non-multiple) arrivals are used, the result in figure 5.6 is obtained. For this plot the inner six shots of line 1 at 14 Hz have been combined, and are contoured at 10 dB intervals. Note that

---

*In this discussion I construe primary to denote no free surface reflections, not the compressional wave.

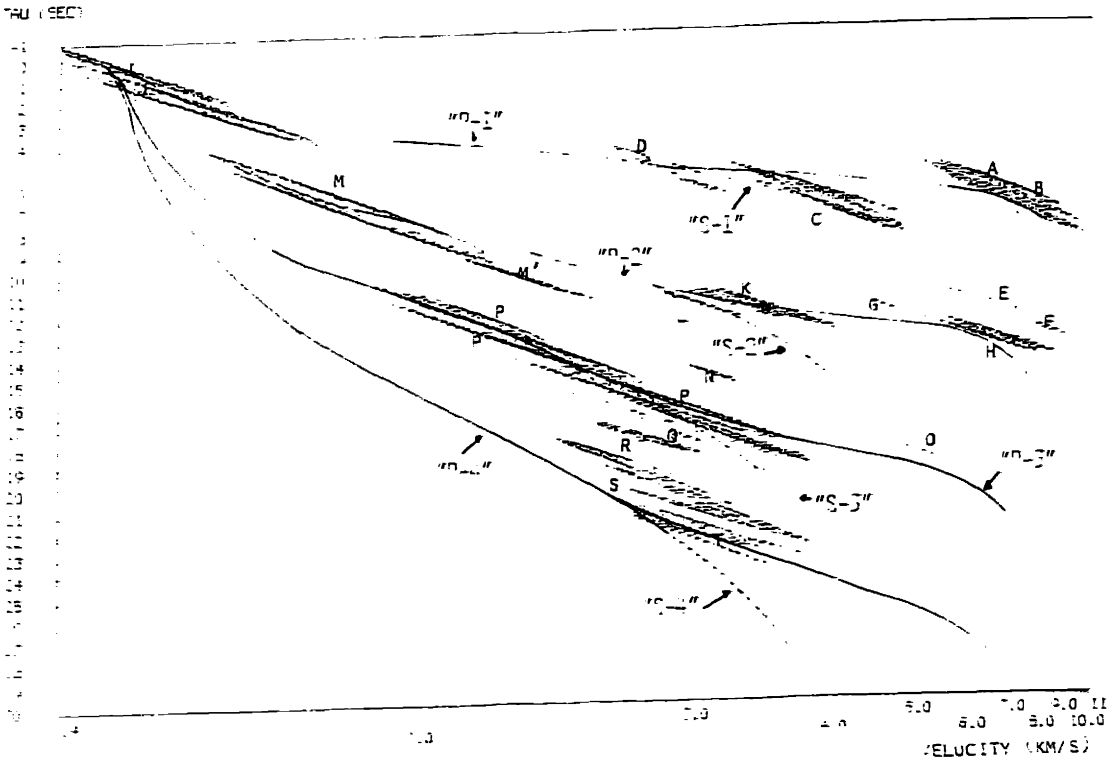

Fig. 5.5) Tau-slowness spectrum at 6 Hz of the shot in figs. 5.4. Tau-slowness curves from a possible model obtained from this and other shots is shown superposed on the spectrum. Solid lines are curves for the compressional model. dotted lines are curves for the shear model. The events indicated in figs. 5.4 are labeled. Contour intervals are 10 dB.

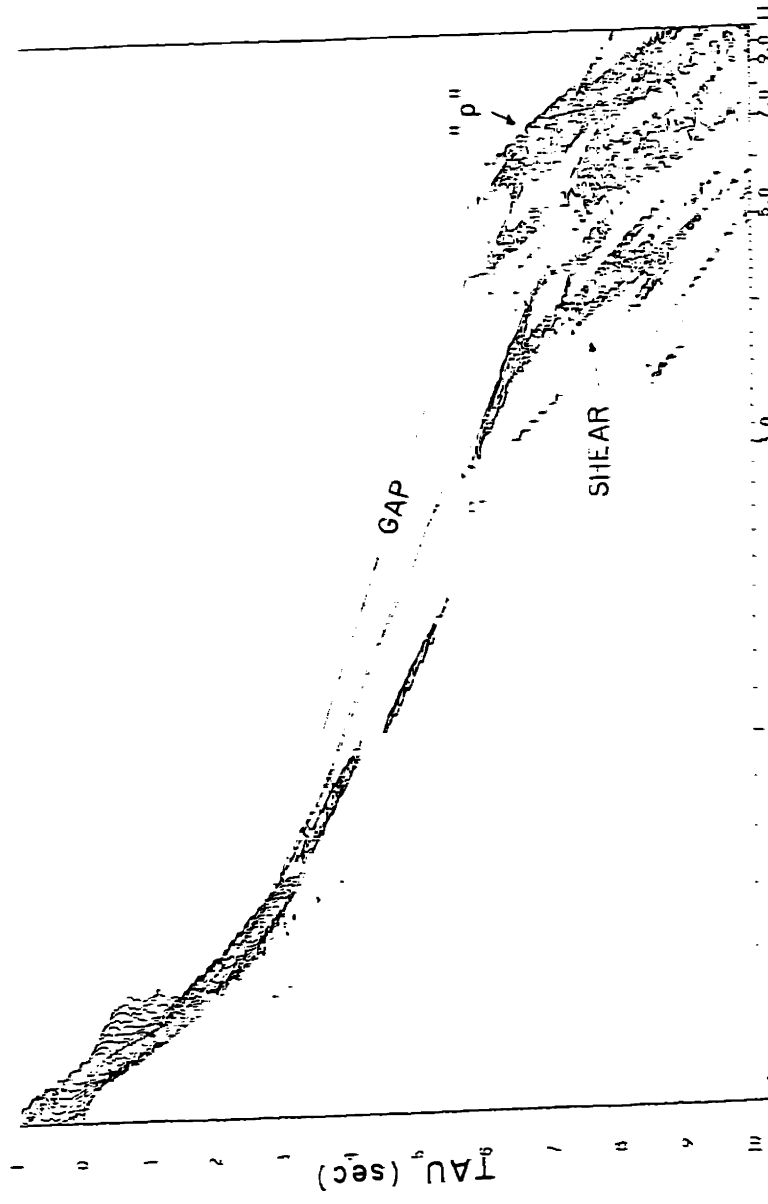

Fig. 5.6) The tau-slowness spectrum at 14 Hz for line 1. This plot contains the direct arrivals from all six shots in the line. The $tau(p)$ curves for a possible model have been added to aid in interpretation of the arrivals. Contour intervals are 10 dB.

because of the sparse offset sampling outside of the actual array locations there is a large gap in the slowness coverage in the deep sedimentary to layer 2 region*. This data alone would obviously lead to a very ambiguous model. The situation can, however, be greatly improved by utilizing the free surface multiples. As was discussed earlier, once these are identified, which is quite easy after the transformation to the $\tau-p$ domain in fig. 5.5, they may be "condensed" to their equivalent single "loop" paths by dividing their $\tau(p)$ and $x(p)$ coordinates by the appropriate multiplicity. The condensed result of fig. 5.5 is shown in fig 5.7 for the offset of 27.2 km. For this figure only the first two free surface multiples have been condensed, and are labeled as p-2 for the first free surface multiple, and p-3 for the second free surface multiple.

When this procedure is carried out for the six inner shots of line 1, the resulting $\tau-p$ spectrum for a center frequency of 14 Hz in fig. 5.8 is obtained. Using all the multiples (which of course makes strong assumptions about lateral homogeneity**) results in a very densely sampled $\tau-p$ curve. An interesting thing to note from fig. 5.8 is that the lack of compressional arrivals in the velocity region from 3.0 to 4.5 km/s corresponds to a region in which strong shear arrivals break away from the compressional curve. This indicates that there is probably a smooth basement with a strong velocity contrast at the base of the sediments, yielding strong shear conversions. The weak contrast between what appears to be a thin, high velocity layer 2 and layer 3 yields strong layer 3 shear arrivals in the 2.9 to 4.4 km/s range.

---

*The curves on the plot are the $\tau-p$ loci for the model that will eventually be extracted from this data.

**Strong support for the validity of compositing the multiples for this line is given by the fact that the second free surface multiple data for this shot at 27.2 km looks almost identical to the primary data from from reel 3006 at an offset of 13.4 km.

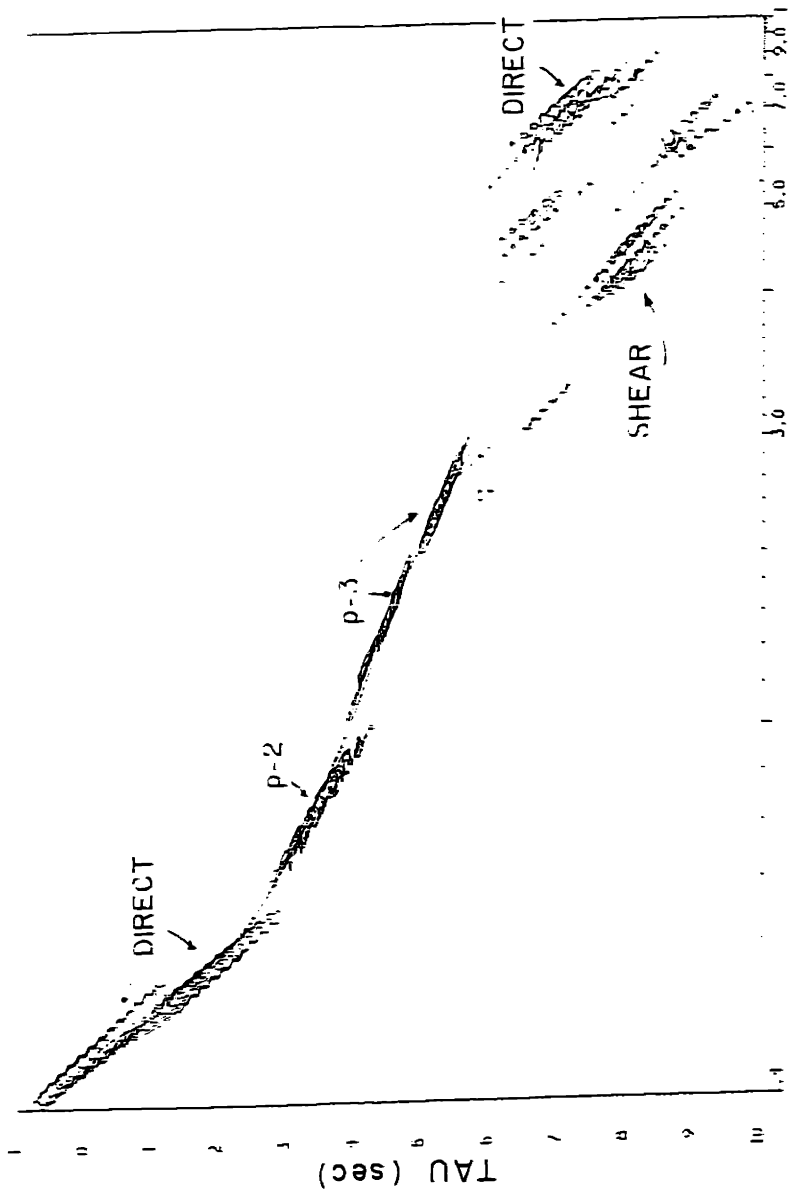

Fig. 5.7) The tau-slowness spectrum at 14 Hz for the shot in figs. 5.4 after "condensing" the free surface multiples to their equivalent primary curves. Note, this plot is for one offset only, 27.2 km. The individual contributions of the different multiples have been labeled. Contour intervals are 10 dB.

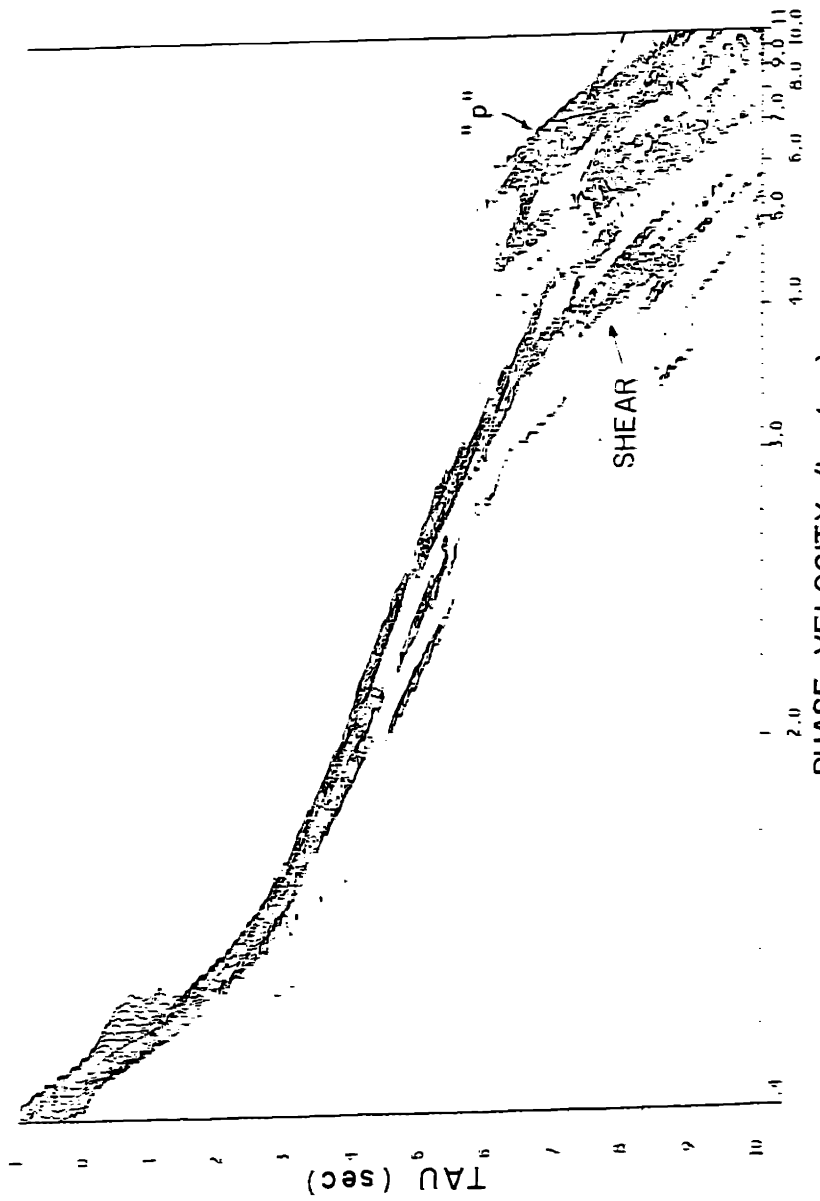

Fig. 5.8) The 14 Hz tau-slowness spectrum of all six shots and all multiples "condensed" to the primary curve. Contour intervals are 10 dB.

Inversion of the $\tau-p$ spectrum

In addition to the use of the migration technique, these data were also picked for $t(p)$ and $x(p)$ values in the velocity spectral domain. In figure 5.9 the data from 27.2 km (fig 5.7) are imaged by the model determined through a $\tau-$sum inversion of the picked data for a homogeneous layered model. The peaks appear to image onto the trial model quite well. The image of the data from all the offsets and multiples migrated by the compressional wave velocity profile is shown in fig. 5.10. In figure 5.11, the image of all the data after migrating with a shear profile below the conversion at the base of the sediments (about 5 km below the ocean surface) is shown.

In figure 5.12 the models are plotted without the confusion of the imaged data. The compressional model plotted is the result of the τ-sum inversion which was verified by the migration. The shear model was obtained independently by use of the migration algorithm only, and is thus parameterized differently. Finally, the extremal bounds on the model computed using the method of Bessonova, et al. [1974] assuming an uncertainty of 0.1 seconds in the data τ values. These curves are given by the dashed lines and are seen to bound the model well.

Interpretation of near source/receiver surface multiples

Because the source and receivers are located at 243 m and 93 m below the surface of the ocean, each major event will typically consist of a four arrival complex. Each of the four multipaths making up the complex will have a slightly different geometrical ray path, and will thus sample the medium slightly differently. Initially, one would consider this added complexity to the data as just one more problem to deal with, and in many cases it is, since the elongated impulse response for one event can obscure another, weaker arrival. However, the fine struc-

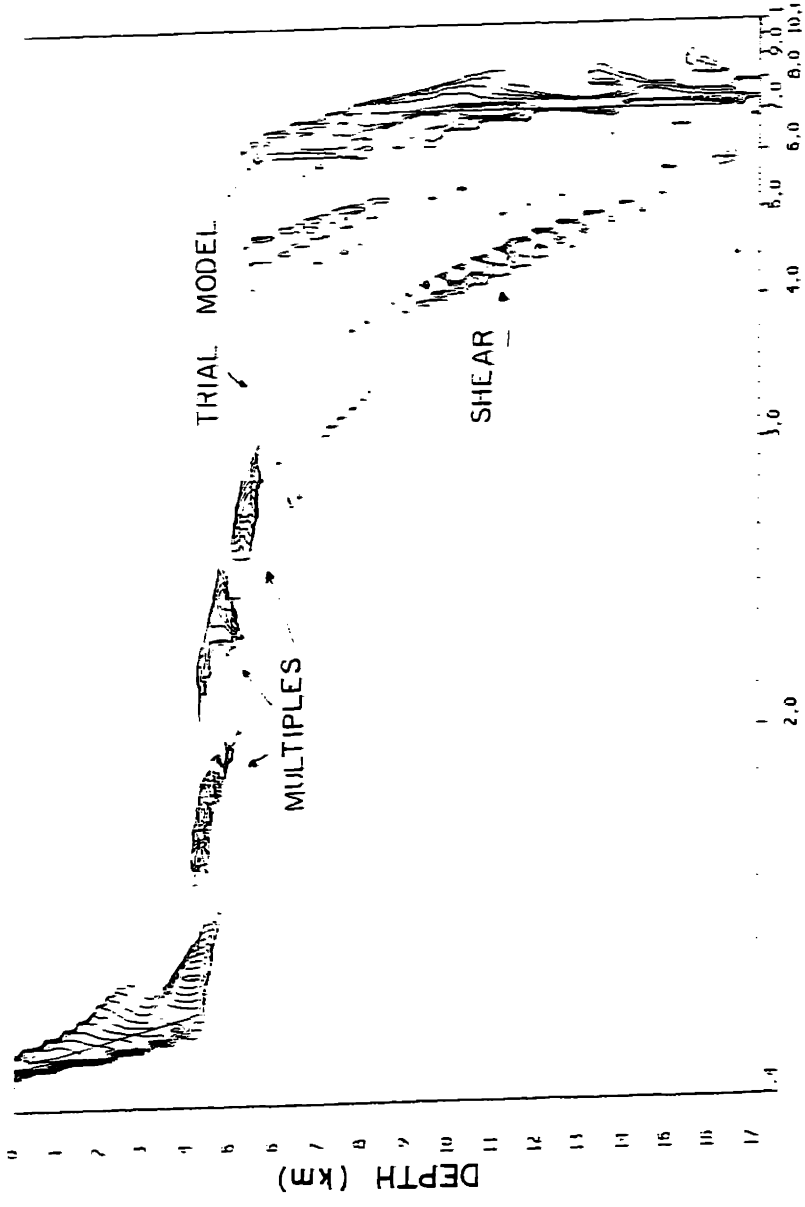

Fig. 5.9) Compressional velocity/depth migration image of data consisting of all multiples from 27.2 km. Contour intervals are 10 dB.

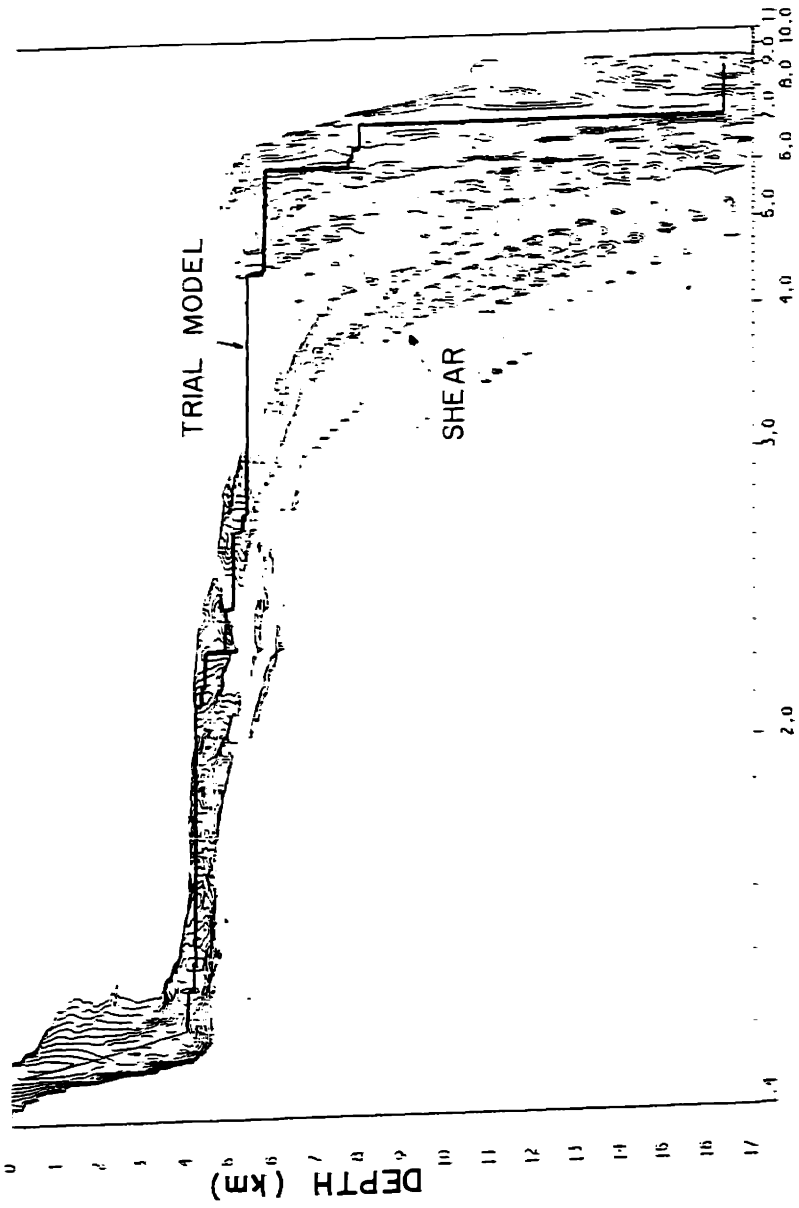

Fig. 5.10) Compressional velocity/depth migration image of data consisting of all multiples from all six offsets in line 1. Contour intervals are 10 dB.

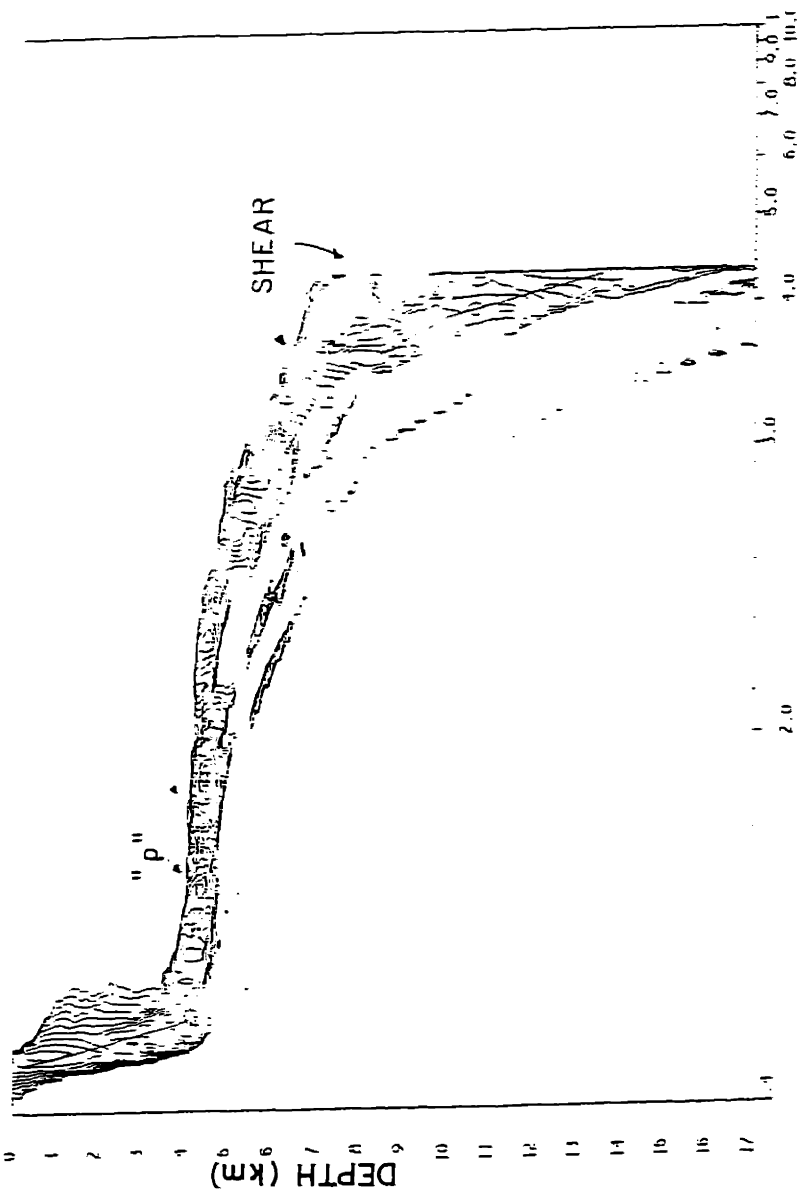

Fig. 5.11 Shear wave velocity/depth migration image of data consisting of all multiples from all six offsets in line 1. Contour intervals are 10 dB.

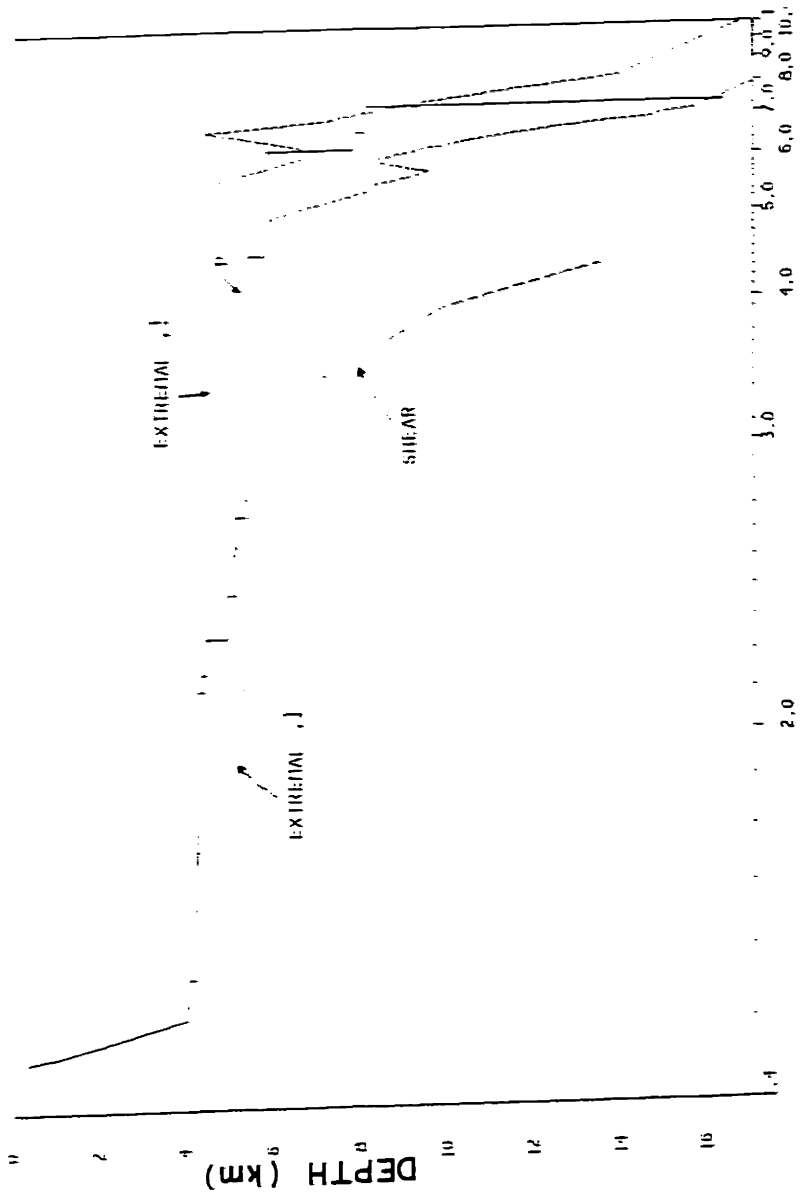

Fig. 5.12) Summary of the profiles obtained in this example. The solid curve labeled "P" is a possible compressional profile, and the dashed curve marked "SHEAR" is a possible shear profile. The curves marked "EXTREMAL, I" are the extremal bounds determined by the method of Bessonova et al, 1974.

ture of these multipaths can be used to an advantage in the interpretation if the data are processed by the short-aperture, short-time velocity spectral analysis algorithm. How this is done is illustrated in figs. 5.13. The plate a in this figure shows a hypothetical velocity/depth function. A simplified ray diagram showing only the multipaths at the source is given in plate b. The arrival "1" is the direct path, and the arrival "2" is the path that initially travels to the surface, then is reflected* specularly. For moderate values of slowness, the effective offset is reduced by over .2 km, thus sampling a different region in slowness of the geometrical curves. A qualitative picture of the geometrical offset function is given in figure 5.13c. Drawing lines at constant offset, we see that whether the travel time curves are on a forward (low gradient) or reversed branch (high gradient) determines whether arrival "1" or "2" has a higher apparent velocity across the array. Finally, this can be translated to the velocity spectra (plate d) at the two offsets, x_1 and x_2. The "2" arrival will always have a larger τ value due to the extra path to the surface, and for the depths of our source and receiver, the surface multiple will never arrive in advance of the direct arrival, even if the surface multiple ray penetrates to a faster layer.

Summary

One of the important points of this example is to show that the multi-channel data and the velocity spectra identify many more events in the data from a single source/receiver offset than just the first arrival detection historically done in refraction analysis. In addition, the

*It was initially thought that the surface reflection at the source would be much less powerful than the direct arrival. The argument for this was that the peak pressure of the shock wave at the surface for a 25 kg charge detonated at 243 m was 231 dB re 1 μPa. Since the ambient air pressure is 220 dB re 1 μPa, it was assumed that the reflected pulse would cavitate, and only a 220 dB reflection would be supported. However, experiments conducted by Weston [1960] indicated that the surface cavitation threshold for explosions was about 246 dB re 1 μPa, mostly said to be due to the tensile strength of water. In addition, in the arctic another 2 dB is gained due to the depression of the water interface by the ice layer. Our data indicate that there is little loss in the surface reflection, and the reflection coefficient is well modeled by -1. The appearance of the thin (1-4 m) ice layer does not seem to complicate the reflection coefficient very much for the wavelengths of interest (50 - 300 m).

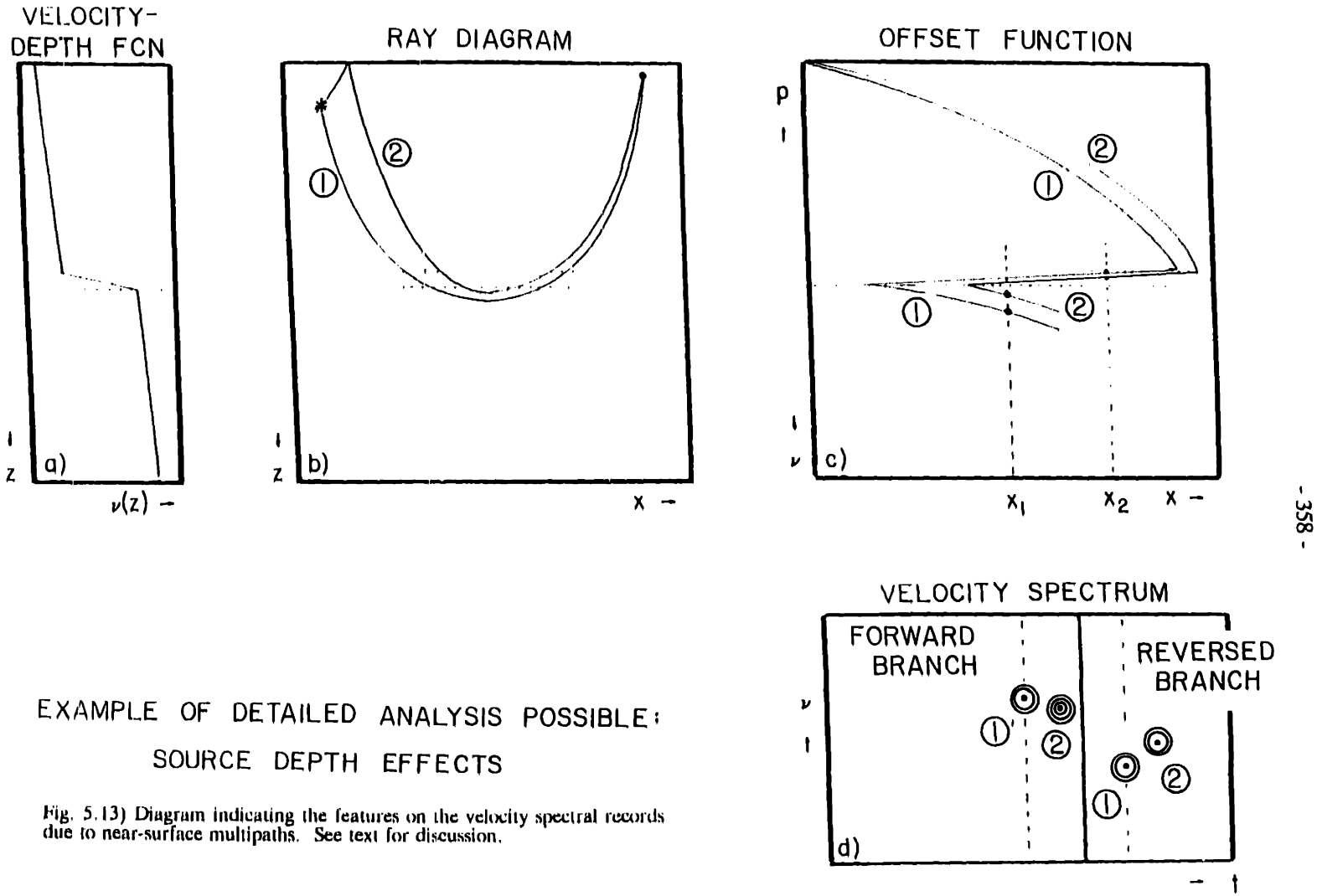

EXAMPLE OF DETAILED ANALYSIS POSSIBLE:

SOURCE DEPTH EFFECTS

Fig. 5.13) Diagram indicating the features on the velocity spectral records due to near-surface multipaths. See text for discussion.

phase velocity, or its inverse, horizontal slowness, are directly estimated from the data when arrays are used. These identifications are especially useful in filling in the gaps in the offset coverage imposed by the ice cover.

INVERSION OF LINE 1 DATA

The picked data curves

An example of the processing of the transformed velocity spectra was given in an earlier section for this line. In this section we will concentrate on the treatment of picked data. These data were obtained from the velocity spectra by a numerical 2-D gradient pick peaking algorithm. The algorithm implemented the first difference approximation to the gradient, and generated contour maps of the data with the local maxima of the plot indicated on them. Although absolute power windowing was done to eliminate the peaks from local maxima in regions of no coherent arrivals, it was necessary to use an interactive program to weed out other spurious peaks. Once a table of peak power, time of arrival, τ, slowness, p, and offset, x, was obtained, it was corrected to the surface datum using the known water column profile above the source and receiver. These data were then used in the inversion programs.

In the following figures the notation given in table 5.9 is used to identify the reel from which the data point came.

Table 5.9 The label assignments for Figs. 5.14a-5.14e		
reel	offset (km)	label
3006	13.4	a#, as#
3007	18.9	b#, bs#
3008	23	c#, cs#
3009	27.2	d#, ds#
3010	34.1	e#, eg#, es#
3011	41.1	f#, fs#

The number following the label indicates which free surface multiple the arrival corresponds to, and all arrivals have been reduced by this multiplicity before plotting for clarity. The number has been omitted when it is 1. The presence of an "s" in the label indicates that the point has been identified as having part of its path as a shear wave.

A plot of the corrected peaks corresponding to compressional arrivals at 6 Hz is given in figure 5.14a. Note that some surface ghosts are present in these data, thus increasing their apparent spread in τ and x. The 6 Hz data contributing to the shear path (some of which is compressional before the conversion at the base of the sediments) are plotted in fig. 5.14b. The plots for other center frequencies are similar, with fewer detectable arrivals present on the highest frequency data, 18 Hz, due to increased attenuation by the intrinsic Q of the medium, and because the higher frequencies are scattered by small scale inhomogeneities more effectively. The τ and x curves after reduction to the primary arrival curves and composited over all frequencies are shown in fig. 5.14c and 5.14d. As with the $\tau-p$ migration example given in the example above, there is a paucity of compressional arrivals in the layer 2 velocity region.

Finally, to show the order of the multiples, and the ranges at which each type of multiple can be detected, a plot of the "uncondensed" $\tau(p)$ data is given in figure 5.14e. This plot contains both the compressional and shear data picked from the velocity spectra of line 1. This plot is the composite of the data at 6, 10, 14, and 18 Hz center frequencies.

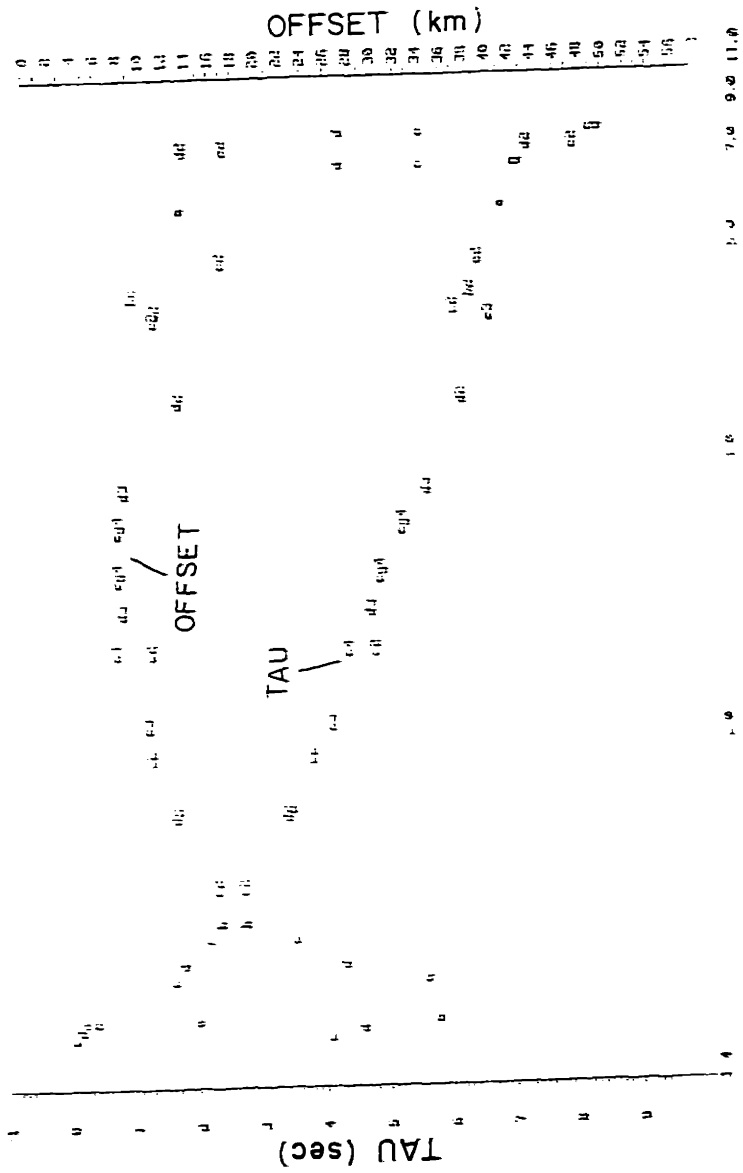

Fig. 5.14a) Plot of the compressional $\tau(p)$ and $v(p)$ data picked from the velocity spectra of line 1 at a 6 Hz center frequency.

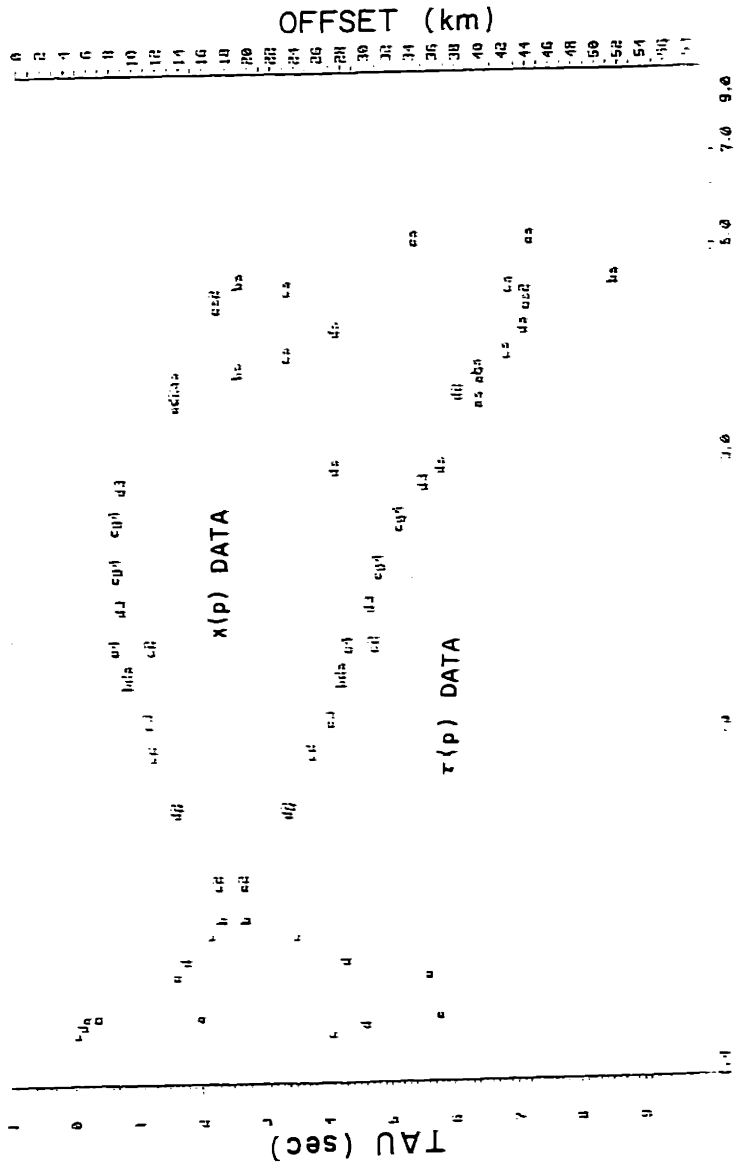

Fig. 5.14b) Plot of the shear path $\tau(p)$ and $x(p)$ data picked from the velocity spectra of line 1 at a 6 Hz center frequency.

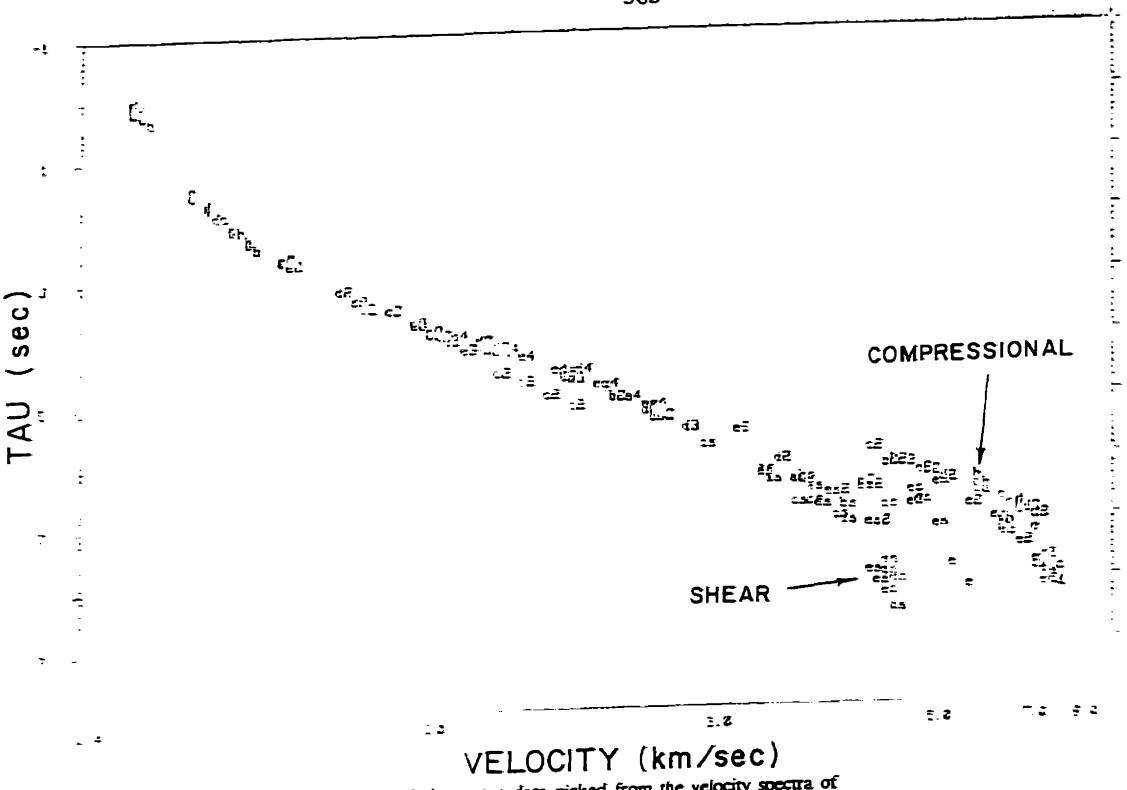

Fig. 5.14c) Plot of the compressional and shear $\tau(p)$ data picked from the velocity spectra of line 1. This plot is the composite of the data at 6, 10, 14, and 18 Hz center frequencies and has been reduced by the order of its free surface multiplicity.

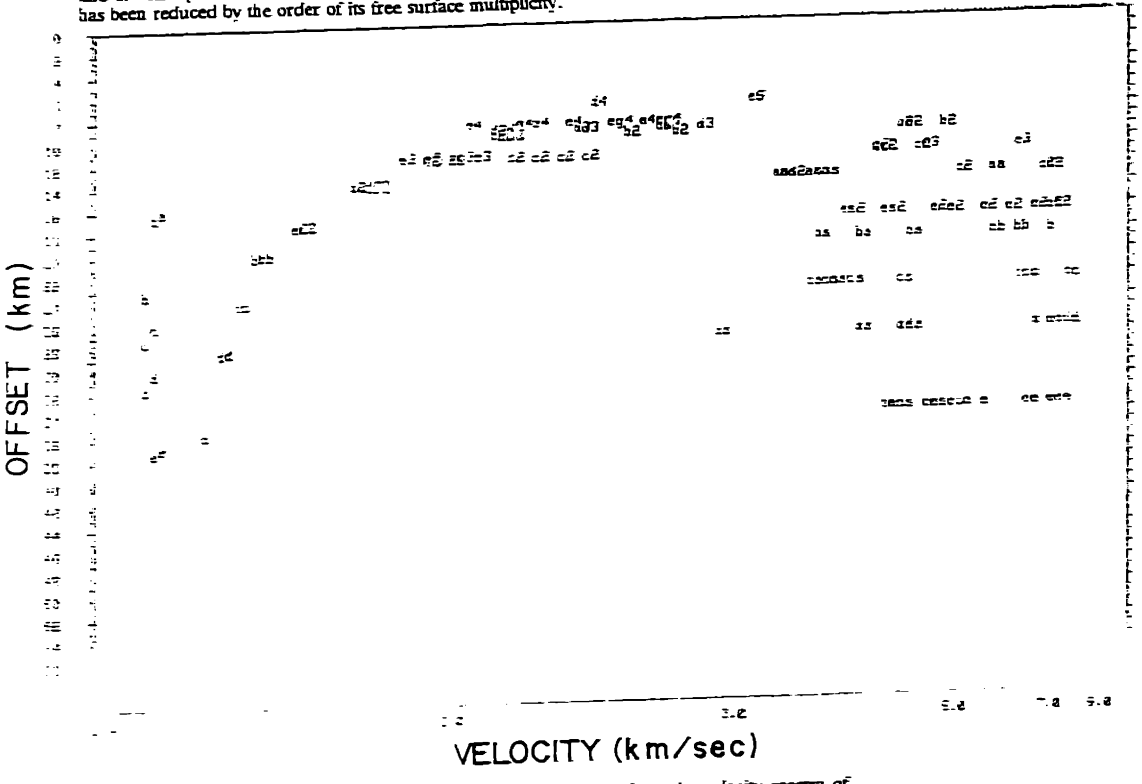

Fig. 5.14d) Plot of the compressional and shear $\tau(p)$ data picked from the velocity spectra of line 1. This plot is the composite of the data at 6, 10, 14, and 18 Hz center frequencies and has been reduced by the order of its free surface multiplicity.

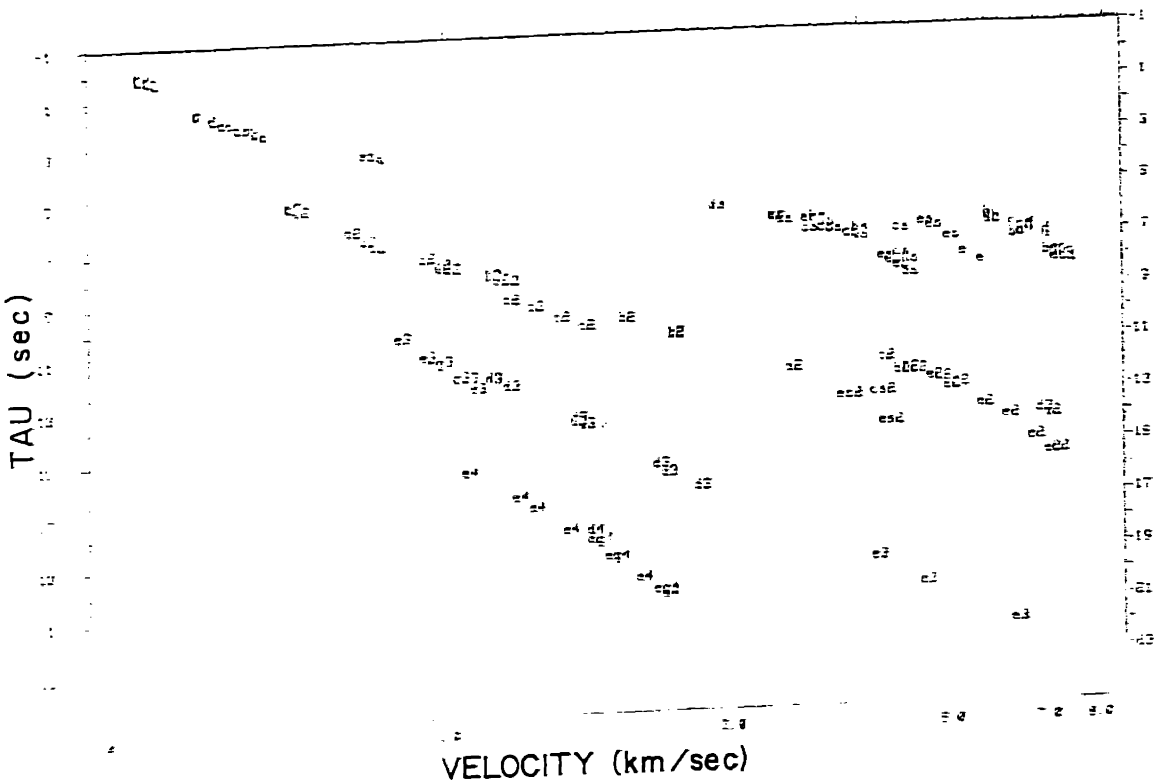

Fig. 5.14e) Plot of the compressional and shear $\tau(p)$ data picked from the velocity spectra of line 1. This plot is the composite of the data at 6. 10. 14. and 18 Hz center frequencies. The data are "uncondensed" to show the order of the multiples that may be detected by the velocity spectral processing.

Inversions by the τ-sum method

The τ-sum method proposed by Diebold and Stoffa [1981] is the perhaps the easiest inversion method to understand, computer code, and use. The initial data analysis for line 1 was carried out using this method, and was reported by Duckworth, Baggeroer, and Jackson [1982]. The models determined using this method are given in figure 5.15. For this analysis, the data at different center frequencies were treated separately, thus yielding the suite of models in the figure. The spread in the models is indicative of the uncertainty in the data. Note that although there is some variability, the sediments start with an initially moderate gradient (.6 s^{-1}) for the upper .3 km, then increase in gradient very sharply, perhaps even having a velocity discontinuity to about 1.9 km/s at .4 km into the sediments, then exhibit a gradient of 1.8 s^{-1} down to a depth of 5 km. As discussed before, there is evidence of a large velocity discontinuity at the basement interface, or at least a very high gradient. The τ-sum inversions bear this out, however, since there is no compressional data observed in this velocity region, it is impossible to tell unequivocally. To determine the structure will require observations at offsets smaller than those observed. Some additional data may be obtained from reel 3006 at 13.4 km, which was not processed much past the direct water arrival, and should be examined for multiples that may fill in the missing slowness region. It is intrinsic to the homogeneous layered tau-sum inversion that large slowness gaps of missing data will be interpolated by a large velocity jump. The models in fig. 5.15 indicate that the layer 2 region is approximately 0.5 km thick and has a velocity of 4.5 km/s. This is underlain by a layer 3 region with a velocity from 6 to 7.2 km/s, an initial gradient of 0.4 s^{-1}, and a total thickness of 2.5 to 6 km. The Moho depth is not well constrained by this line. To indicate how the model predicts the $\tau(p)$ data, fig. 5.16 shows the 14 Hz. data and $\tau(p)$ curve predicted by the 14 Hz. model. The solid lines in the figure show the interpolating quarter ellipses characteristic of the

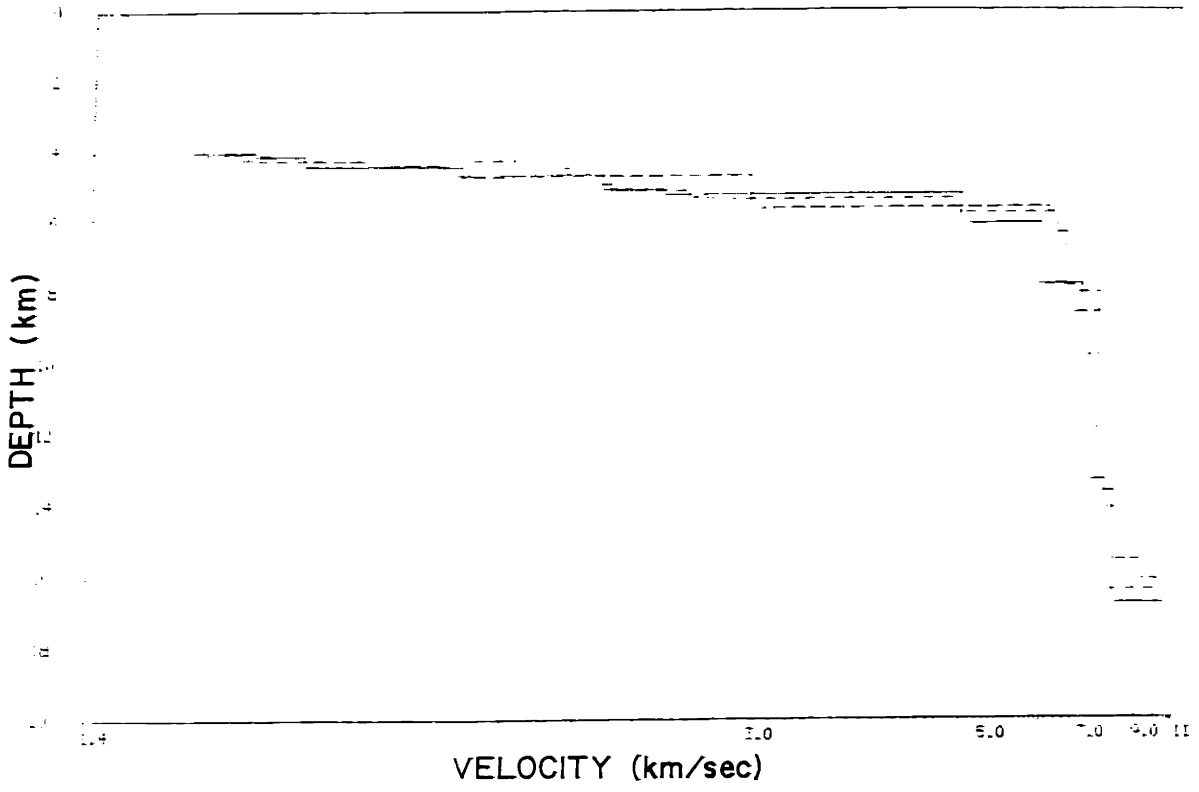

Fig. 5.15) The models resulting from the inversion of the line 1 data using the homogeneous layered formulation of the τ-sum method. The 6 Hz. data are indicated by the solid curve, the 10 Hz. data by the dotted curve, the 14 Hz. data by the dot-dashed curve, and the 18 Hz. data by the dashed curve.

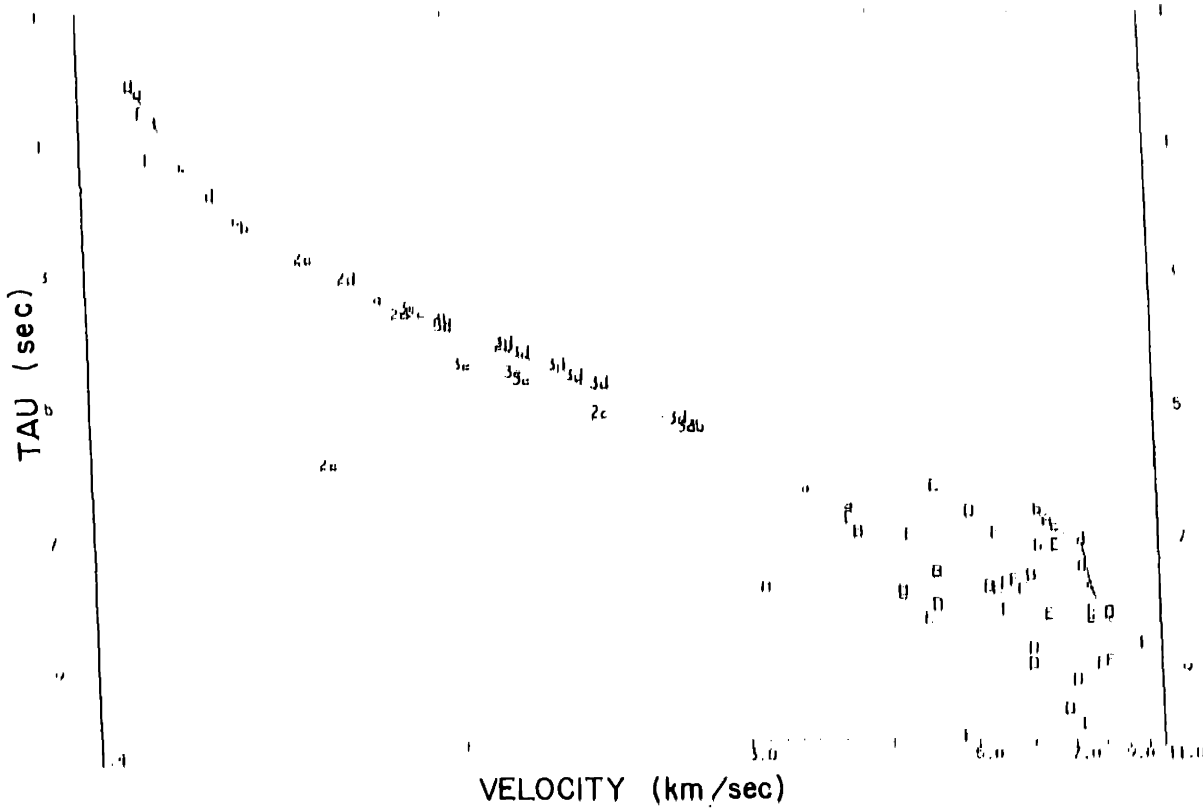

Fig. 5.16) The $\tau(p)$ data for 14 Hz. (labels) and the curve predicted by the resulting model (solid line). The light dotted line interpolates the data points that were used in the inversion.

homogeneous layered model. The letters use the same system as outlined in table 5.9, however, the upper case letters indicate arrivals that have less power, and are thus less reliable.

Inversions by velocity/depth migration

The example earlier in this chapter showed (see figs. 5.7-5.12) that one of the models determined by the τ-sum method for the compressional profile imaged the $\tau-p$ spectrum reasonably well, certainly within the resolution inherent in the bandwidth of the data. In this section we will image the peaks picked from the data and discussed in the section before last. For this work we will use both the $\tau(p)$ and $x(p)$ data to try to constrain the models resulting from the sparsely sampled slowness data curves.

Before giving some of the intermediate steps in the determination of the models, fig. 5.17 summarizes the results of migrating the peak $\tau(p)$ and $x(p)$ data to obtain the compressional profile. Again, the curves for each center frequency were analysed separately. In some cases more than one model was obtained when a single model could not fit all the features of the data. This method thus has the effect of constructing an envelope of possible models, indicating the resolution of the method. The models obtained agree quite well with those obtained by the tau-sum method. The major features are again the very high gradient in the middle of the sediments, followed by a more moderate one down to basement at 5 to 5.2 km total depth (1.2 km of sediments). A high gradient or discontinuity is indicated at this depth up to the basement velocity of 4.3-4.5 km/s. Again, layer 2 appears to be less than 1 km thick, and appears to have a gradient which is moderately high. This is difficult to say with confidence because of the paucity of arrivals, however, it leads to the best overall agreement with both types of data. Since the major region missing from the offset sampling is the region less than 13 km, and no layer 2 arrivals appear at larger offsets, we assume that they must reside there.

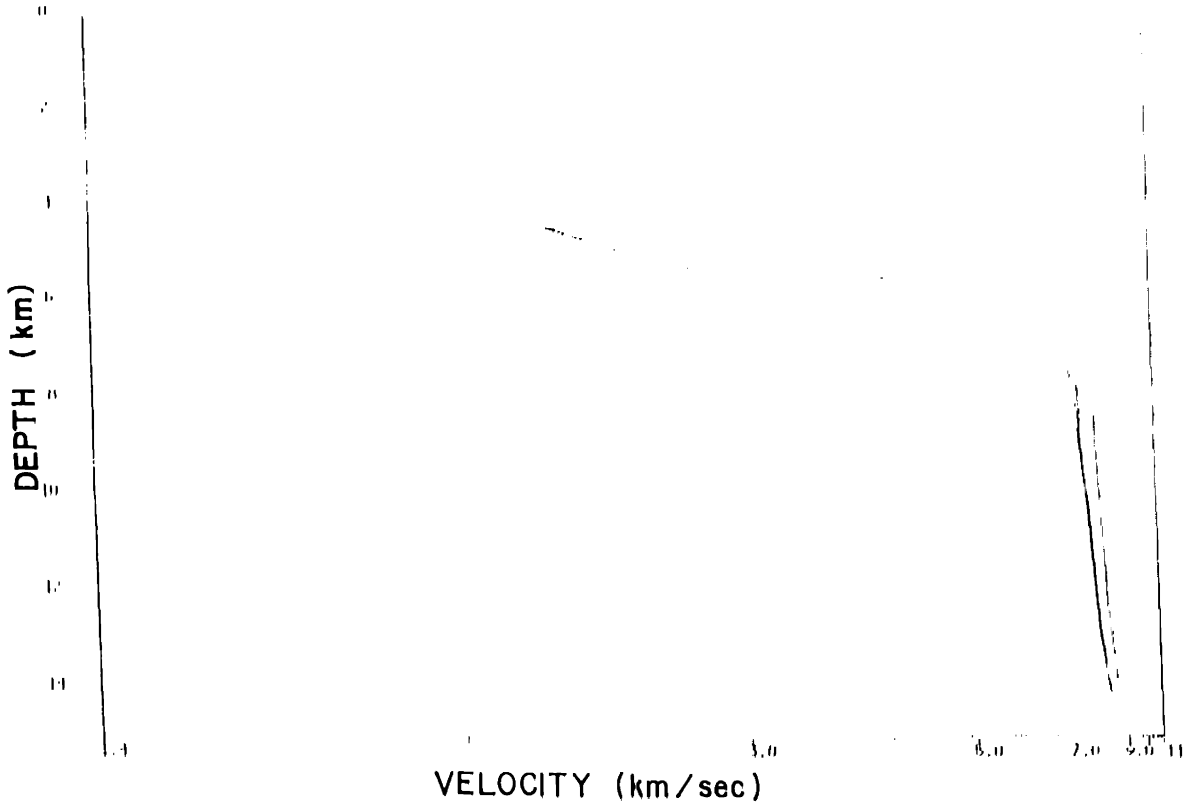

Fig. 5.17) The suite of compressional models resulting from the inversion of the *tau* (p) and x (p) peak data. The inversion was carried out by individual center frequencies using the velocity/depth migration algorithm.

Such small offsets are indicative of high gradient reversed branches of the travel-time curve. The gradient and thickness for layer 3 velocities is similar to that obtained by the previous analysis, and the (still poorly constrained) total thickness of layer 3 averages about 4-5 km. The major difference between this profile and that obtained from the τ-sum technique is the omission of the lower gradient layer at the top of the sedimentary column. We will see on the imaged peak plots that the offset data indicate the need for this lower gradient layer. Note that one of the models in the suite has a stair-step appearance, similar to a homogeneous layered model. Arrivals at velocities typical of layer 3 appeared over large ranges in offset, indicating rapid changes in gradient in this region. The slowness stability of the velocity spectral estimator was not adequate to develop a consistent $x(p)$ curve that could closely determine the velocity discontinuities. However, it is worthwhile noting that such discontinuities are not inconsistent with the data.

The shear wave velocity-depth profiles obtained below the conversion depth at the basement interface are shown in fig. 5.18. Again, each frequency has been imaged separately and a suite of curves is obtained indicating the range of models that fit the data reasonably. These models are compared with the shear wave profiles predicted by using the compressional models of fig. 5.17 and assuming a Poissons ratio of $\sigma = .25$ in fig. 5.19. The estimated shear profiles indicate that the crust is generally "less rigid" than a Poisson solid, with the measured shear profiles being generally of lower velocity than the predictions. Using the average P and S profiles from figs. 5.17 and 5.18 gives the estimate of the Poisson ratio from the relation

$$\sigma = \frac{\frac{1}{2}(V_p/V_s)^2 - 1}{(V_p/V_s)^2 - 1}$$

where V_p is the compressional velocity, and V_s is the shear velocity at a given depth. The values obtained agree well with those tabulated from the literature by Christensen and

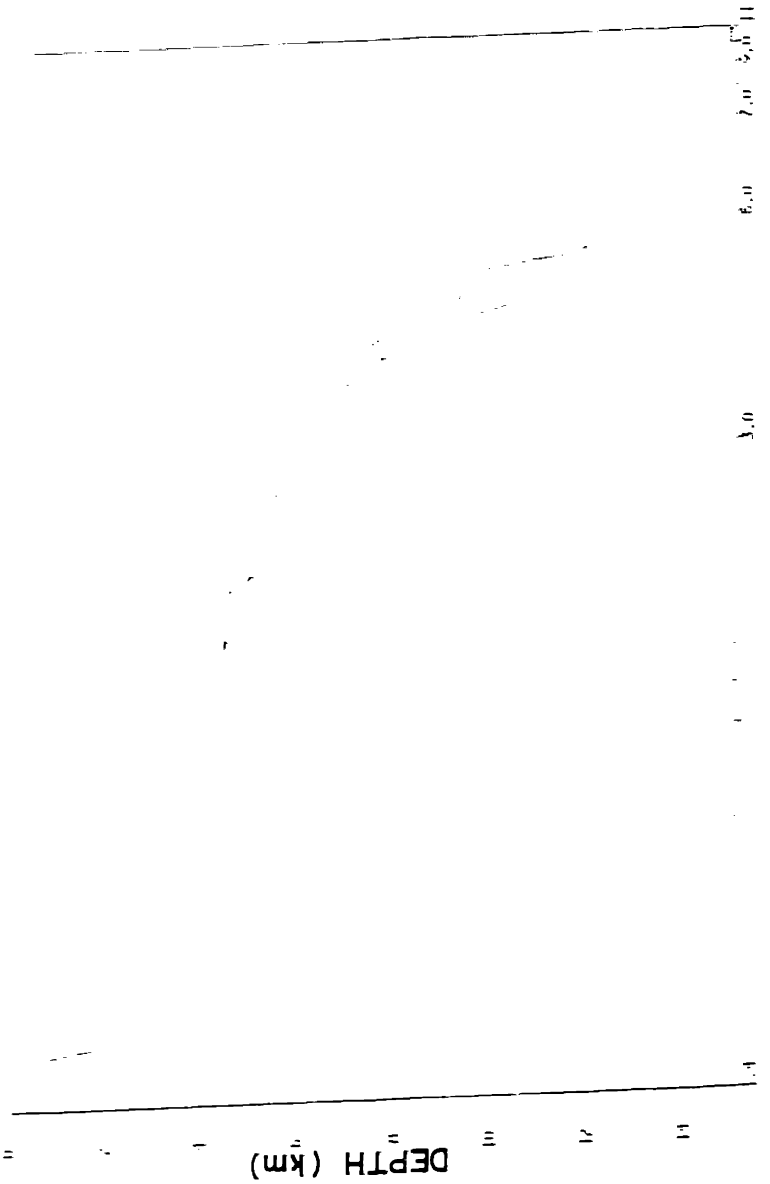

Fig. 5.18) The suite of shear velocity models resulting from the inversion of the $\tau_{AM}(p)$ and $x(p)$ peak data. The inversion was carried out by individual center frequencies using the velocity/depth migration algorithm.

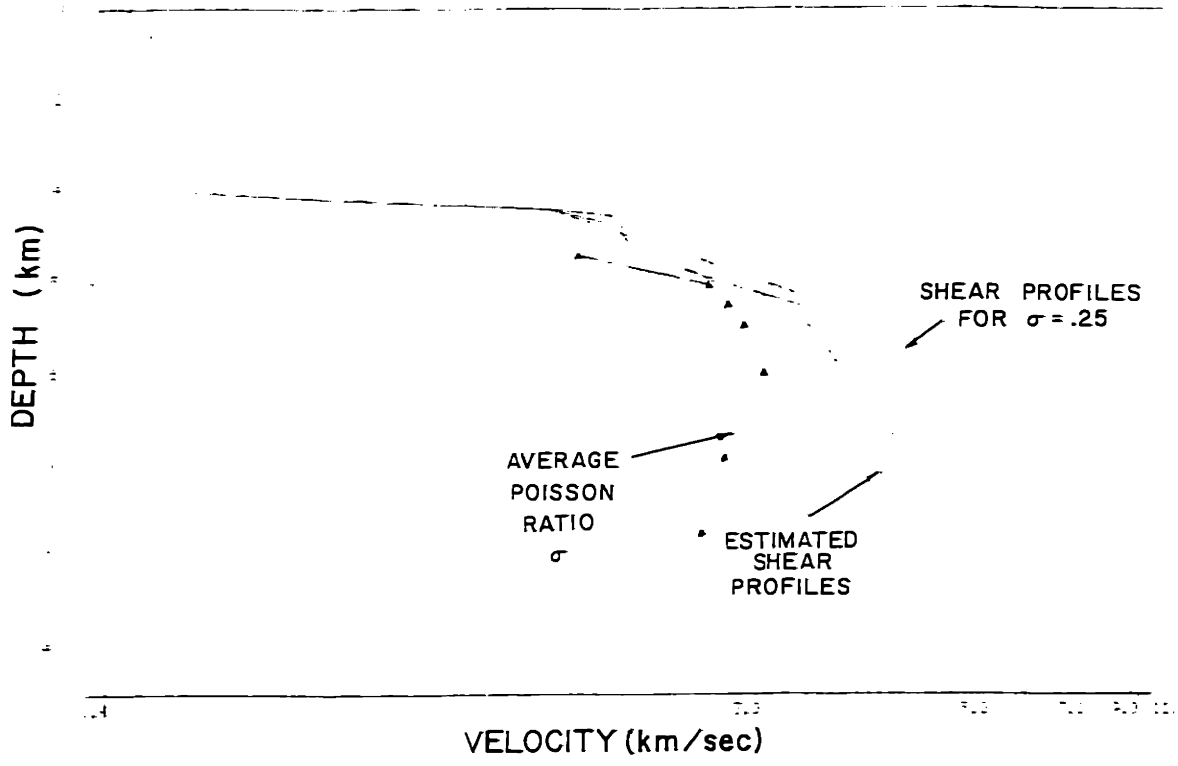

Fig. 5.19) The suite of shear wave models obtained from the compressional models of fig. 5.17 assuming the Poisson ratio. $\sigma = .25$ (dotted curves). Show also are the shear models of fig. 5.18 directly estimated from the data using the migration of the peak data. The Poissons ratio calculated for the crustal model obtained by averaging the curves in figs. 5.17 and 5.18 is indicated by the triangles.

Salisbury [1975] and support a gabbroic petrology for layer 3, the most popular interpretation. These are plotted as the triangles with connecting lines in fig. 5.19. The scale for these is just the velocity scale divided by 10. The values are also tabulated in table 5.10.

Table 5.10 Average values of Poissons ratio for line 1

Depth (km)	V_p (km/s)	V_s (km/s)	Poissons Ratio σ
5.5	4.5	2.65	.23
6	5.5	3.05	.28
6.5	6.1	3.3	.29
7	6.5	3.5	.3
8	7.2	3.75	.31
9	7.6	4.15	.29
11.5	8	4.4	.28

The abnormally low σ for the 5.5 km depth is a result of being near the conversion region from compressional to shear.

To indicate how the velocity/depth migration works, we will examine a few of the plots of migrated peaks, and of the predicted τ and x values vs. those of the data. Fig 5.20 gives one of the trial models (heavy solid line) and the results of imaging the 14 Hz compressional peaks. The set of lower case letters connected by the dotted line is the image of the $\tau(p)$ peaks. The set of upper case letters is the corresponding image of the offset data. Note that at the base of the water column the image of the $x(p)$ data indicates that the gradient is too large. The image of the $\tau(p)$ data also reflects this, but not so dramatically. The scatter in the higher velocity regions is primarily due to incomplete editing of near surface multiple peaks from the data. As was mentioned earlier, one advantage of the migration method is that it allows the operator to eliminate data at any time, and after viewing its image directly in model space where more intelligent decisions can be made. Although it was a little hard to see on the image, the agreement of the predictions of deeper regions of the model with the observed

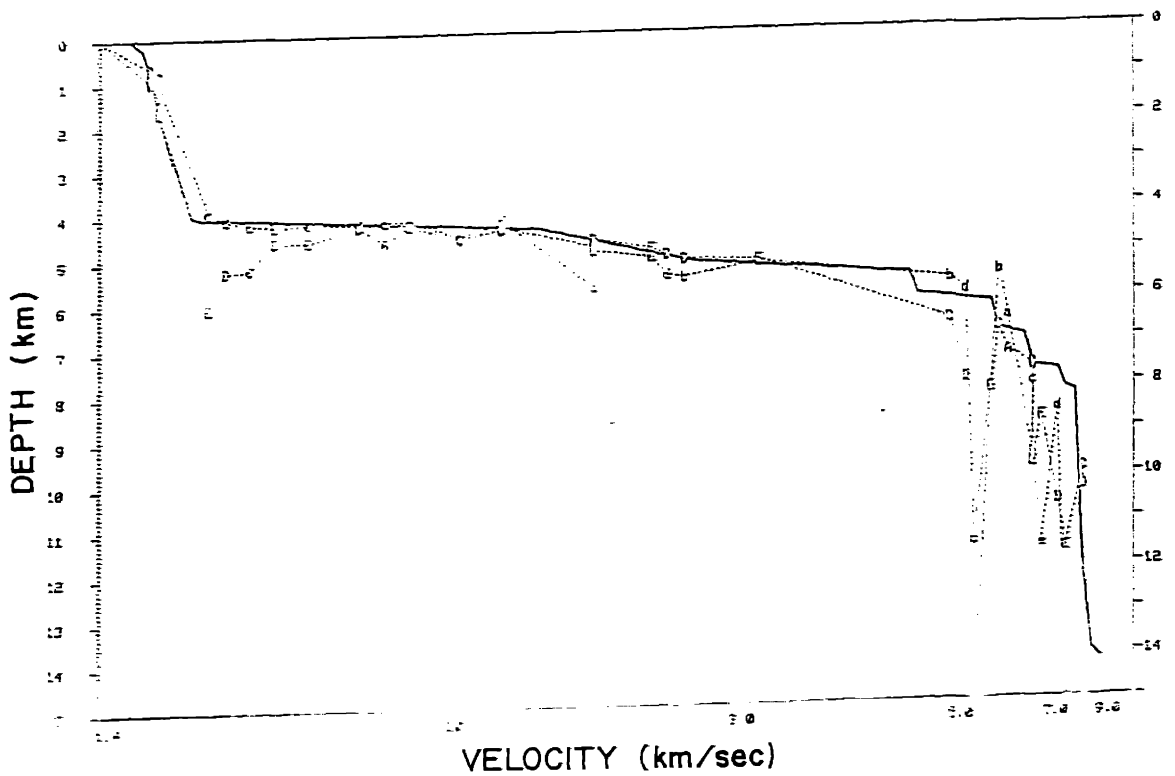

Fig. 5.20) Trial compressional model and data image for 14 Hz. data from all six shots and multiples. The heavy solid curve is the trial model. the dotted curve with lower case labels is the τ data image, and the dotted curve with the upper case labels is the offset image.

offset data is quite good. This is seen more readily in fig. 5.21. In this plot, both the $x(p)$ and $\tau(p)$ data and predictions from the model in fig. 5.20 are shown.

Fig 5.22 shows a trial model (solid line) and the imaged τ (lower case letters and dotted line) and x (upper case letters and dotted line) data for the shear conversions at the basement. The agreement is quite good, except just at the base of the water column, which indicates the need for a decreased gradient. The data and predicted curves are given in fig. 5.23. The offset matching by this model is seen to be very good.

Summary for Line 1

The results of refraction Line 1 indicate a crust that is slightly thinner than average oceanic crust [Christensen and Salisbury, 1975] in this region of slow crustal spreading (0.5 cm/yr). The high gradient sediments overlie a basement which is seemingly smooth and has a high velocity contrast with the base of the sediments, thus supporting strong shear conversions. The results of calculating the unloaded depth to basement for the resulting model yields an estimate of crustal age using the Parsons-Sclater [1977] relationship which is in agreement with the interpretation of the magnetic anomaly pattern [Vogt et al., 1979]. Both of these techniqes estimate the age of the crust for this line at around 50 My (late Eocene) [Duckworth and Baggeroer, 1983]. The estimated offset function from this line also gives evidence of a variable gradient structure in the deep layer 2 and layer 3-Moho region. [Spudich and Orcutt, 1980].

INVERSION OF LINE 4 DATA

Comparison with line 1

From the earlier section on the refraction line parameters, it will be recalled that line 1 was deeper into the abyssal plain, and ran 20° off true north, while the receiving end of line 4

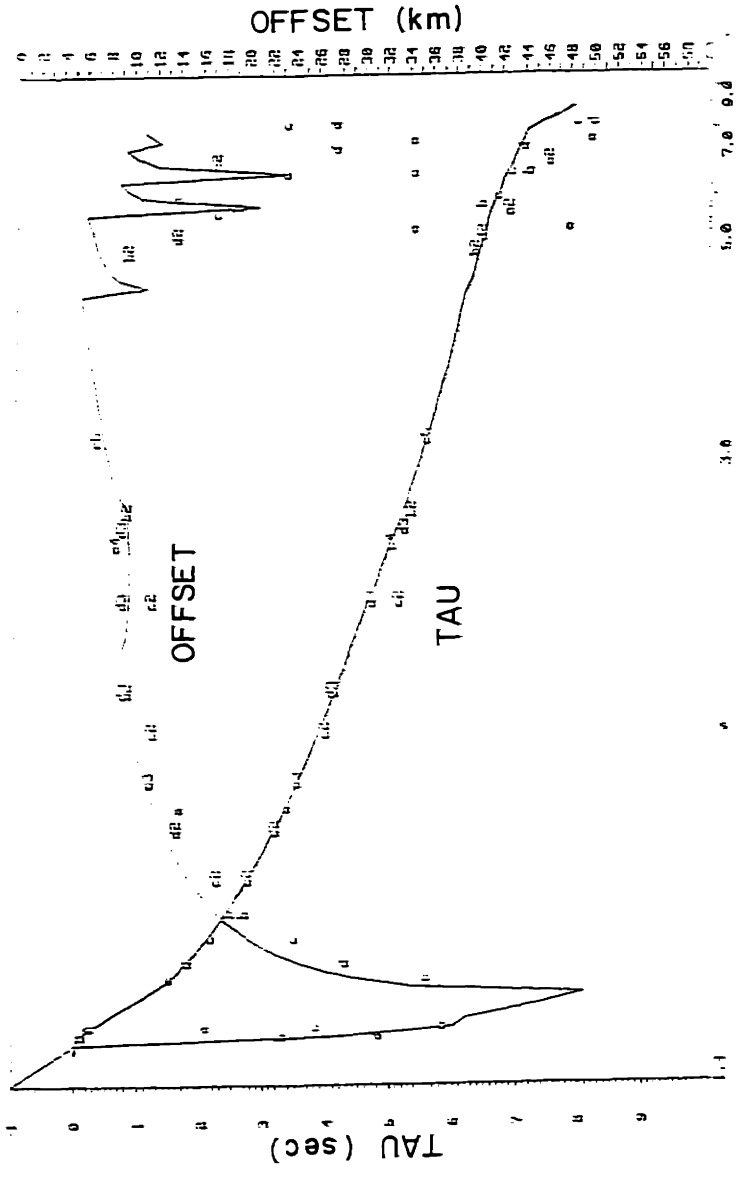

Fig. 5.21 The 14 114 peak $\tau(p)$ and $x(p)$ data (letters) and the curves predicted by the model of fig. 5.20 (solid curves).

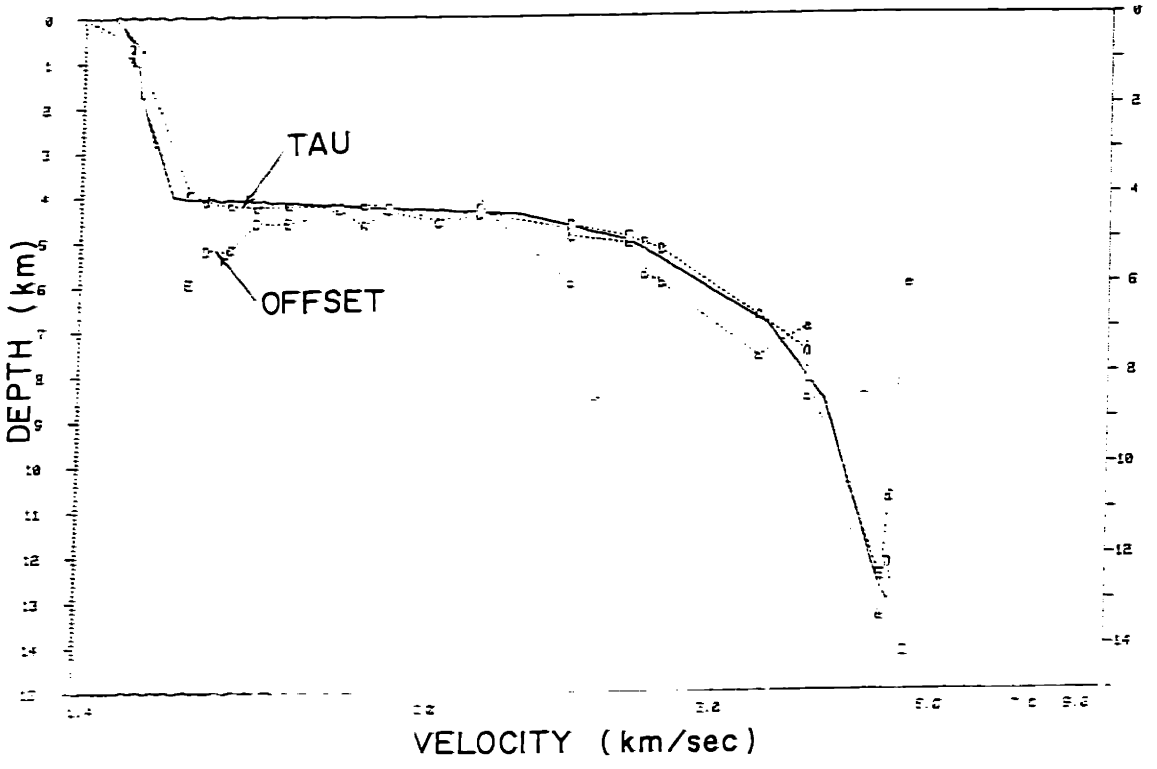

Fig. 5.22) Trial shear wave model and data image for 14 Hz. data from all six shots and multiples. The heavy solid curve is the trial model, the dotted curve with lower case labels is the τ data image, and the dotted curve with the upper case labels is the offset image.

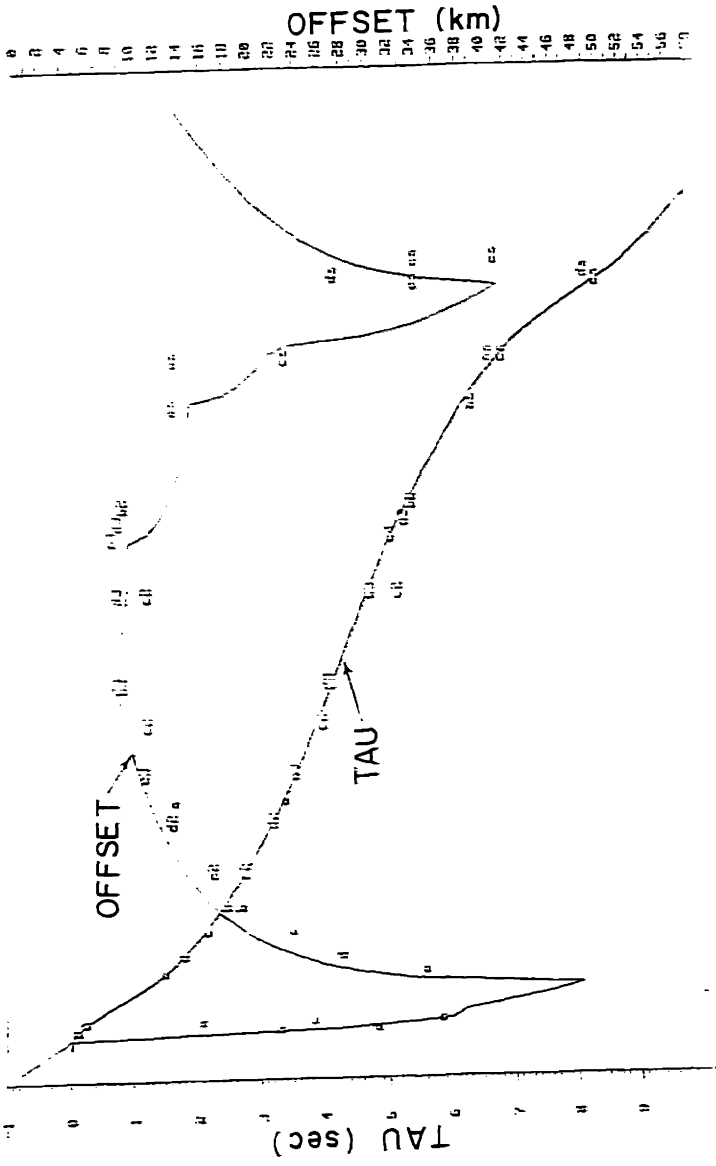

Fig. 5.23) The 14 114 peak $\tau(p)$ and $x(p)$ data (letters) and the curves predicted by the model of fig. 5.22 (solid curves).

is 200 m shallower, and the line runs almost directly east from the camp. The overall location is south of line 1, and closer to the Morris Jessup Rise. Since this line runs perpendicular to the isochrons, it is expected that the structure will adhere less to laterally homogeneous assumptions than line 1. The receiving array was located at magnetic anomaly 23. Anomaly 22 was at a range of 16 km, anomaly 21 at 43 km, and anomaly 20 at 77 km to the east. The bathymetry shoaled toward the receivers with a dip of .25°, thus possibly biasing the measured phase velocities upward. Apart from differences in the crustal structure, we would expect that because of the shallower water, the τ values will be .2 to .3 seconds less than those of line 1 because of the shallower water column.

To first get an idea of what to expect from line 4, we compare some of the features of the velocity spectra from line 4 to those of the already analysed line 1. Only one of the shots of line 4 is at nearly the same offset as one of line 1. This expedites comparison, and we will note some qualitative features. At an offset of 13.25 km on line 4 (fig. 5.24a*) and 13.4 km on line 1 (fig. 5.24b) the main difference noted is that the deep arrival at 5.8-6.0 km/s that has broken out in front of the direct water arrival on line 1 has not yet appeared on line 4 (it is probably lost in the water wave side-lobe). This indicates that despite the shallower water, there is a larger delay time, τ, at a given slowness for line 4, indicating a thickening of the sedimentary layers. Since we are certainly in a region of oceanic crust, this indicates that the oceanic layers are beginning their slide to oblivion. Adhering to isostatic gravity arguments, the bathymetric shoaling would also support this interpretation.

The similarity of the rest of the section is high, and we again expect a high gradient in the sediments. The arrivals from line 4 (fig. 5.24a) and line 1 (fig. 5.24b) at 9.6 and 9.9

*The numbers on the plots 5.24a&b are the local maxima picks of the peak picking algorithm before editing out the unimportant detections. These should be ignored.

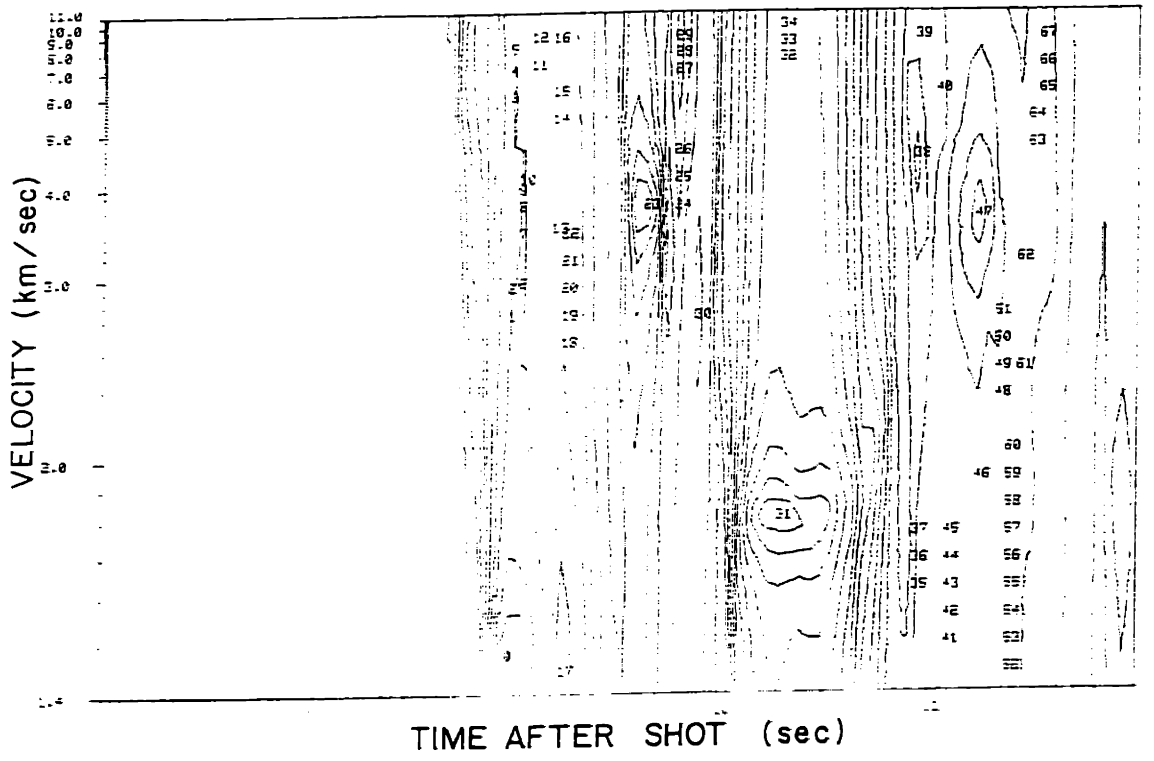

Fig. 5.24a) The 6 Hz velocity spectrum for line 4 at an offset of 13.25 km. The contour intervals are 5.0 dB.

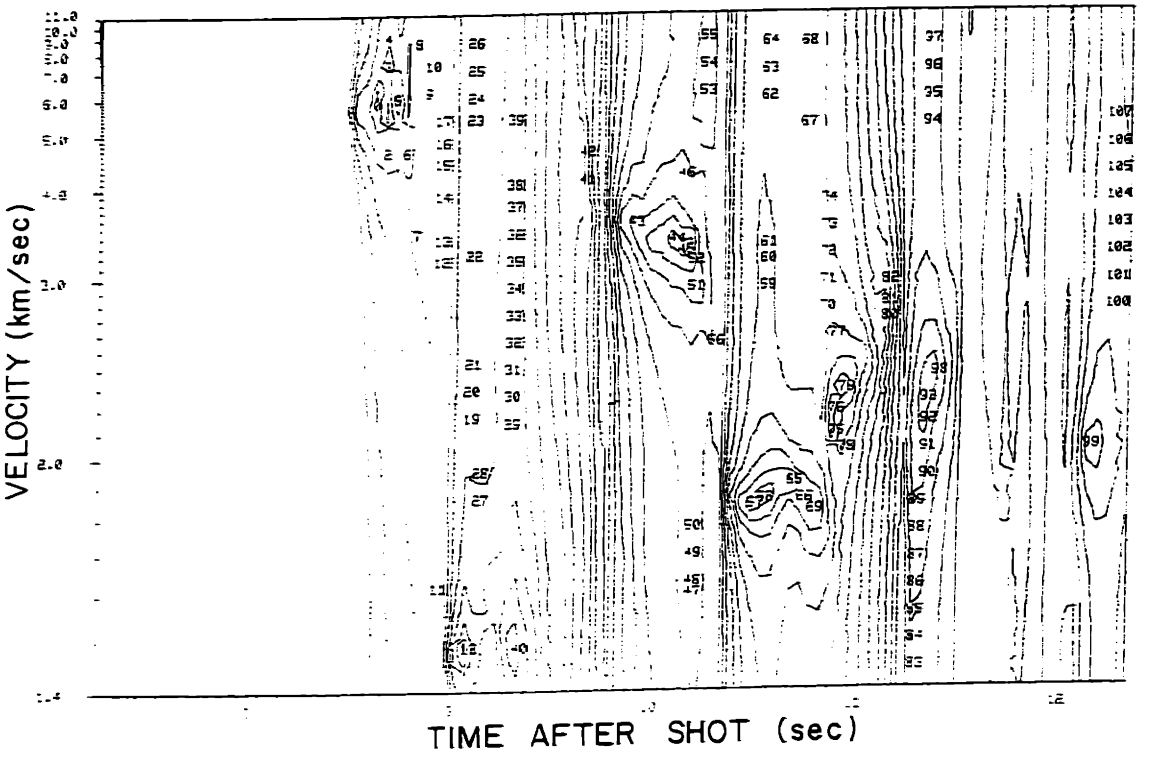

Fig. 5.24b) The 6 Hz velocity spectrum for line 1 at an offset of 13.4 km. The contour intervals are 5.0 dB.

seconds, and 3.8 and 3.5 km/s which have been identified as having been converted to shear at the basement interface also show a .2 second larger τ for the line 4 events. The velocity spectra for other offsets of line 4 are similar to those of nearby offsets on the line 1, although there is significantly more multipathing on line 4, a result, perhaps, of greater lateral heterogeneity.

The τ and offset data

Figures 5.25a&b show the "condensed" $\tau(p)$ and $x(p)$ data for the 6 Hz band of line 4. These curves are quite similar to those of fig. 5.14c and 5.14d of line 1. The major differences lie in the grouping of multiples noted on the plots and in the slightly greater delay times measured on line 4. It is believed that multiples noted are due to water column pegleg paths, and are not true free surface multiples. Because of this, treating them as free surface multiples by dividing their total (datum corrected) τ by their assumed multiplicity will lead to primary arrival τ estimates which are too small. Similarly, the offset data shows arrival distances which are smaller than expected for these arrivals.

Inversions by velocity-depth migration

Line four has not been analysed in detail for this work, however the initial inversions using the velocity-depth migration algorithm on peak picked data support the qualitative features mentioned above. Although the Moho is poorly constrained on this line, the τ values for layers 2 and 3 are larger, leading to a model with a thicker sedimentary region. Fig. 5.26a shows the $\tau(p)$ picks for the line 4 data and the $\tau(p)$ curve for a representative inversion of the data (solid line). Also indicated is a $\tau(p)$ curve representative of the inversion from line 1 (dotted line). The compressional models for line 4 and line 1 for the τ curves of fig. 5.26a are given in fig. 5.26b.

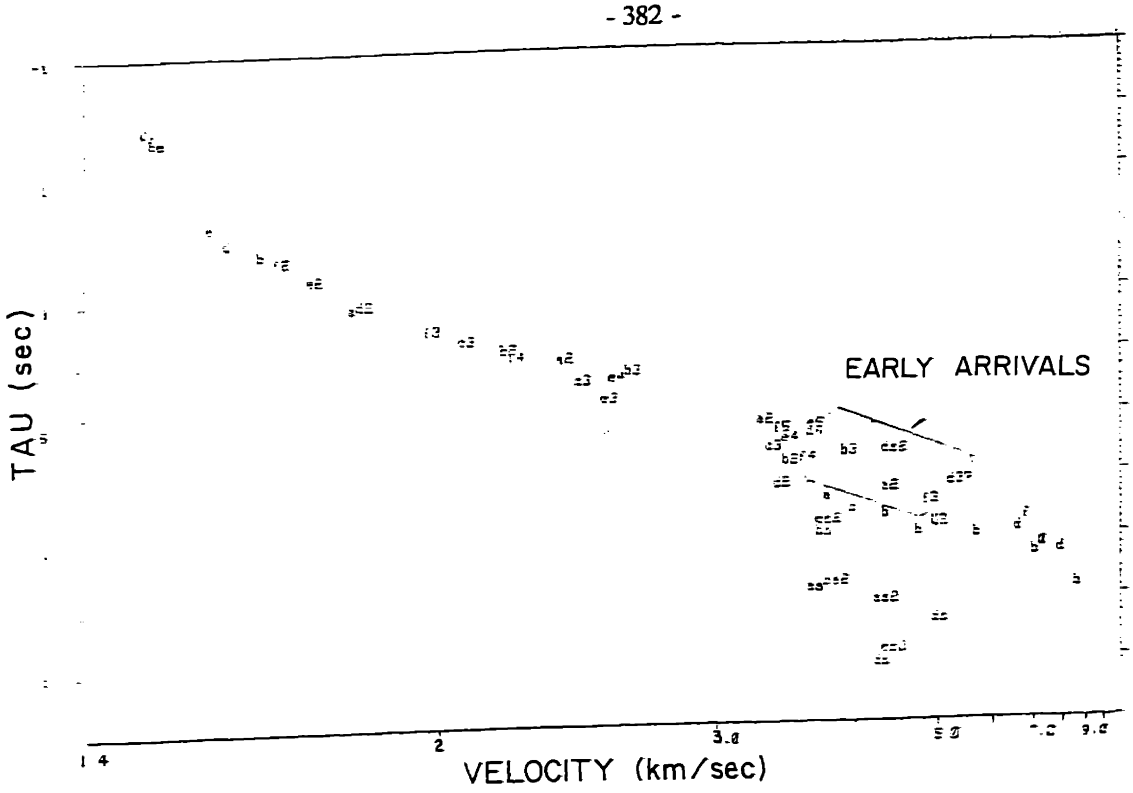

Fig. 5.25a) The $\tau(p)$ data for 6 Hz from line 4. Note the early arrivals of the second through fifth multiples.

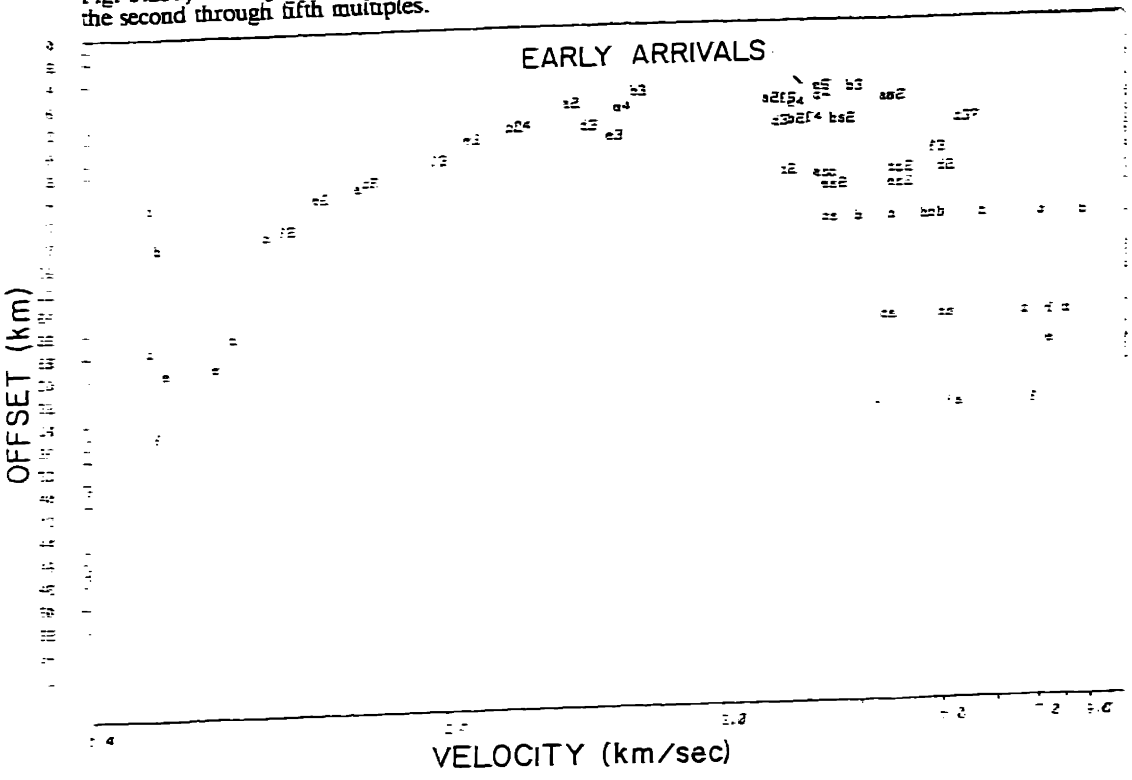

Fig. 5.25b) The $x(p)$ data for 6 Hz from line 4.

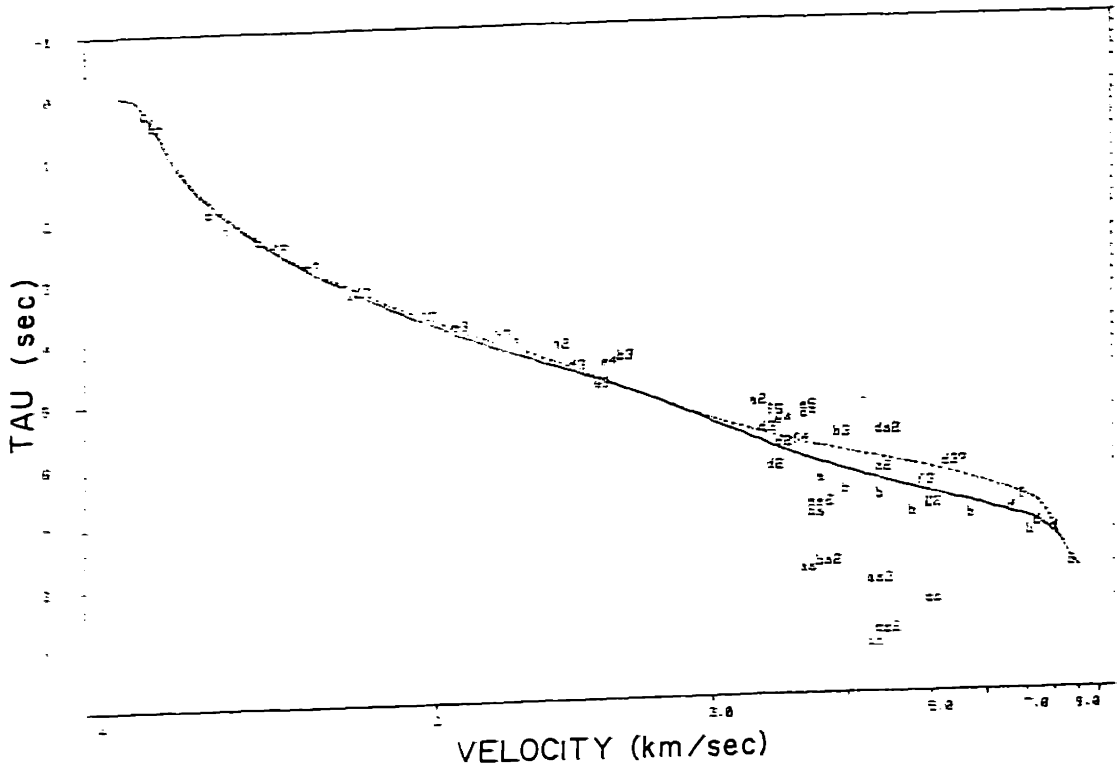

Fig. 5.26a) The $\tau(p)$ data for 6 Hz from line 4. The $\tau(p)$ curves for models from line 1 (dotted) and the inversion of line 4 (solid) are shown.

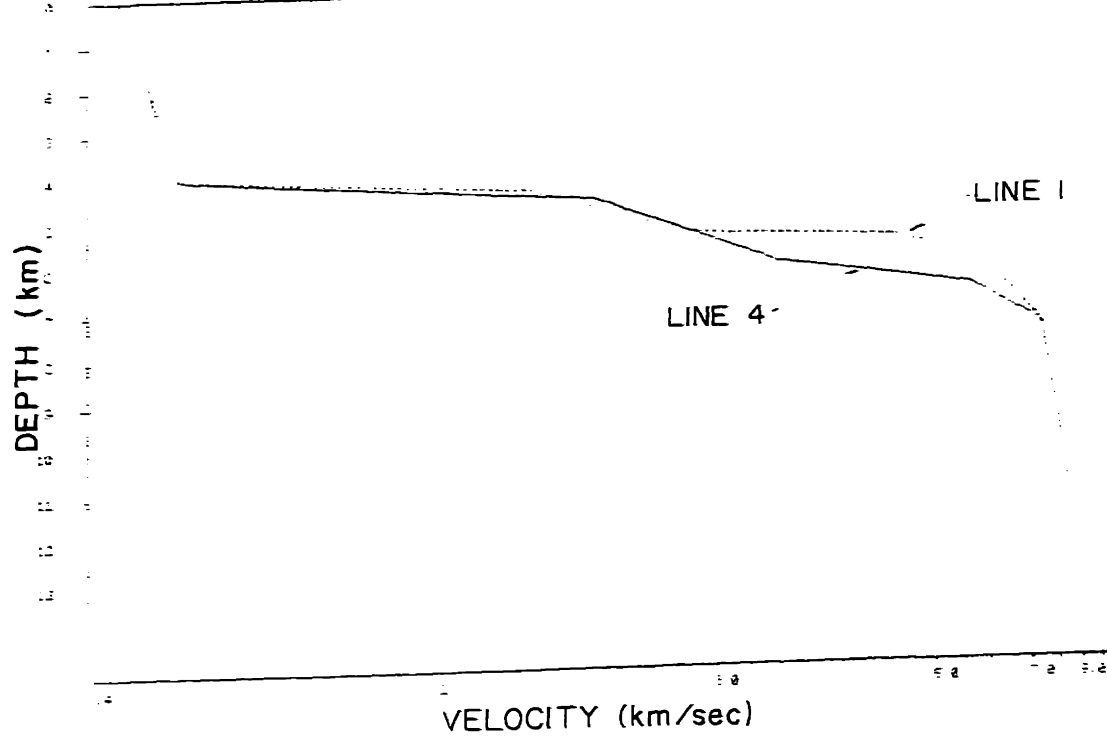

Fig. 5.26b) The compressional models for line 1 (dotted) and line 4 (solid).

As with the compressional data, the shear arrivals show significant scatter. Again, this is probably due to the direction in which the line was shot leading to significant lateral heterogeneity. The $\tau(p)$ data at 6 Hz is shown in fig. 5.27a along with a the $\tau(p)$ curve resulting from the shear wave model in fig. 5.27b. The shear conversions are again at the basement interface as in line 1. It should be noted that the observed shear data indicate a deeper depth to lower layer 3 and mantle velocities than the compressional data. This discrepancy cannot be reconciled due to the large scatter in the data.

Discussion

A more conventional display of the data and model predictions is shown in fig. 5.28. The data are plotted by the letters on the plot after datum corrections and reduction of the free surface multiples to the primary curve. The $x-t$ curve of the line 4 compressional model in fig. 5.27b is shown by the solid line. The plot is reduced on 8 km/s. The first arrivals are well modeled according to this plot. An interesting feature of the data is the long string of arrival peaks at an offset of 16.9 km. The later components of this series are in a position to result from shadow zone arrivals from the triplication with cusp reaching out to 11 km. The earlier arrivals would also be better predicted if the model had included some gradient changes in layer 3. The arrivals in this complex are quite powerful, and the 6 Hz, 16.9 km velocity spectrum from which the arrivals were picked is shown in fig. 5.29. The numbers on the plot are the local maxima picks of the peak picking algorithm before editing out the unimportant detections and should be ignored. The heavy solid line is the θ function defined in chapter 2. This was computed using the compressional model of fig 5.27b and the experimental source and receiver depths. The non-infinite slope of the line shows that the arrivals after the first (at about 7.3 km/s) are not geometrical for the model used. However, a model close to the model

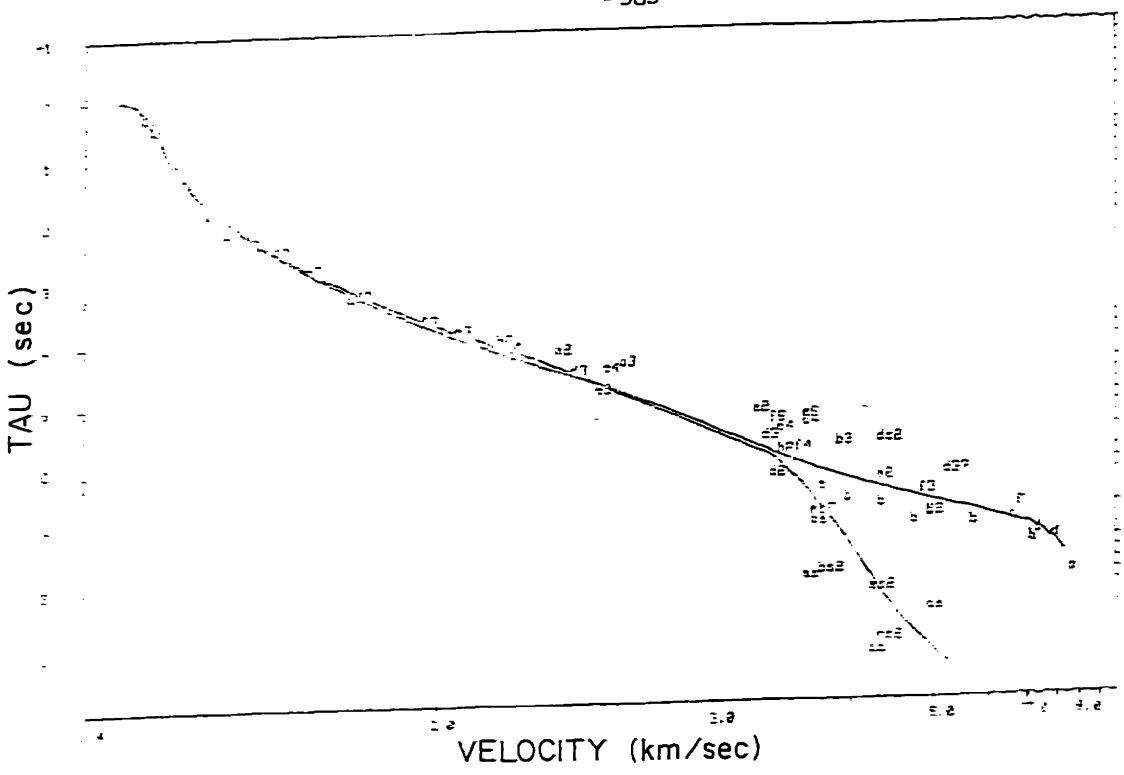

Fig. 5.27a) $\tau(p)$ data (letters) from line 4 at 6 Hz with compressional $\tau(p)$ curve from line4 model in fig. 5.26b (upper solid line) and shear $\tau(p)$ curve from line 4 shear model of fig. 5.27b (lower solid line).

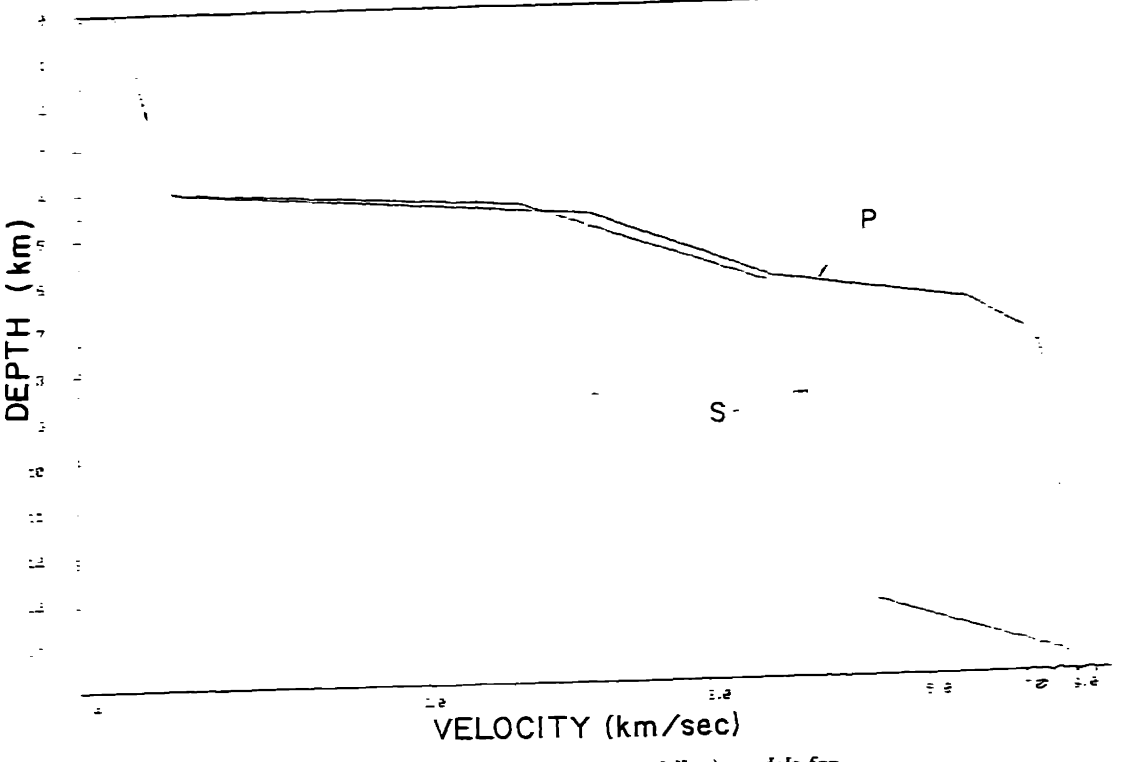

Fig. 5.27b) Compressional (solid line) and shear (dashed line) models for line 4.

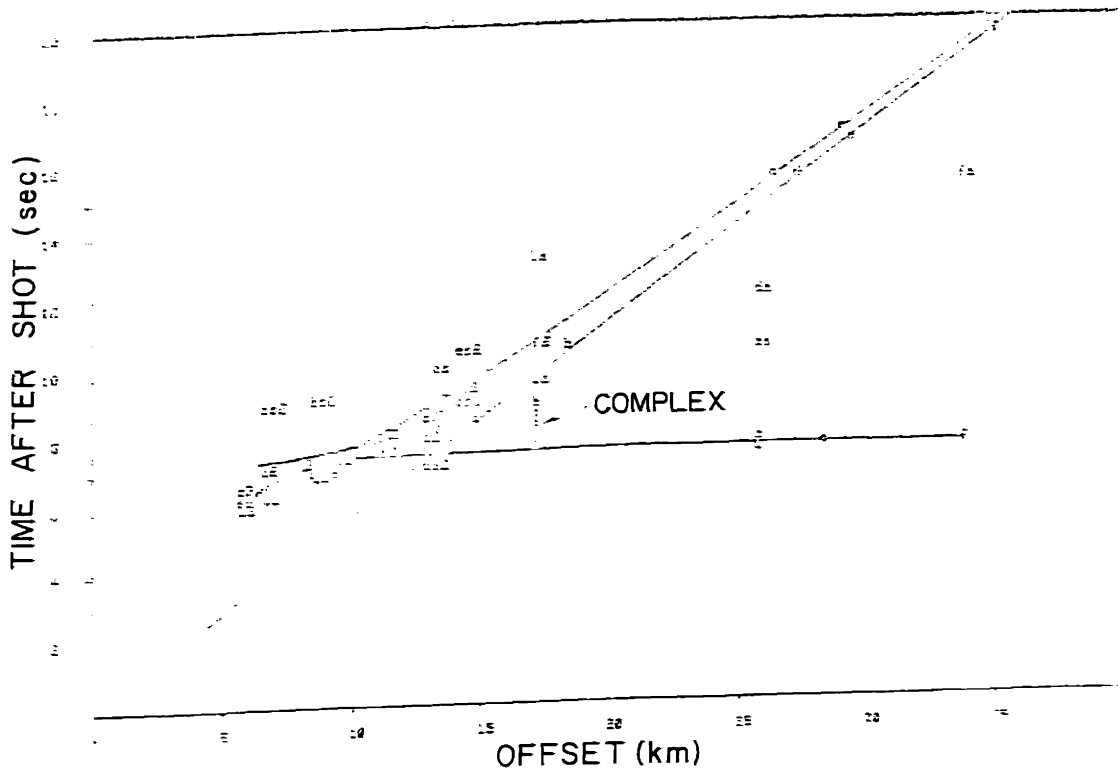

Fig. 5.28) Datum corrected and free surface "condensed" data for 6 Hz band on line 4 (letters). A number appearing in the labels indicates the suspected free surface multiplicity. An "s" in the label indicates a suspected shear path. The plot is reduced on 8 km/s.

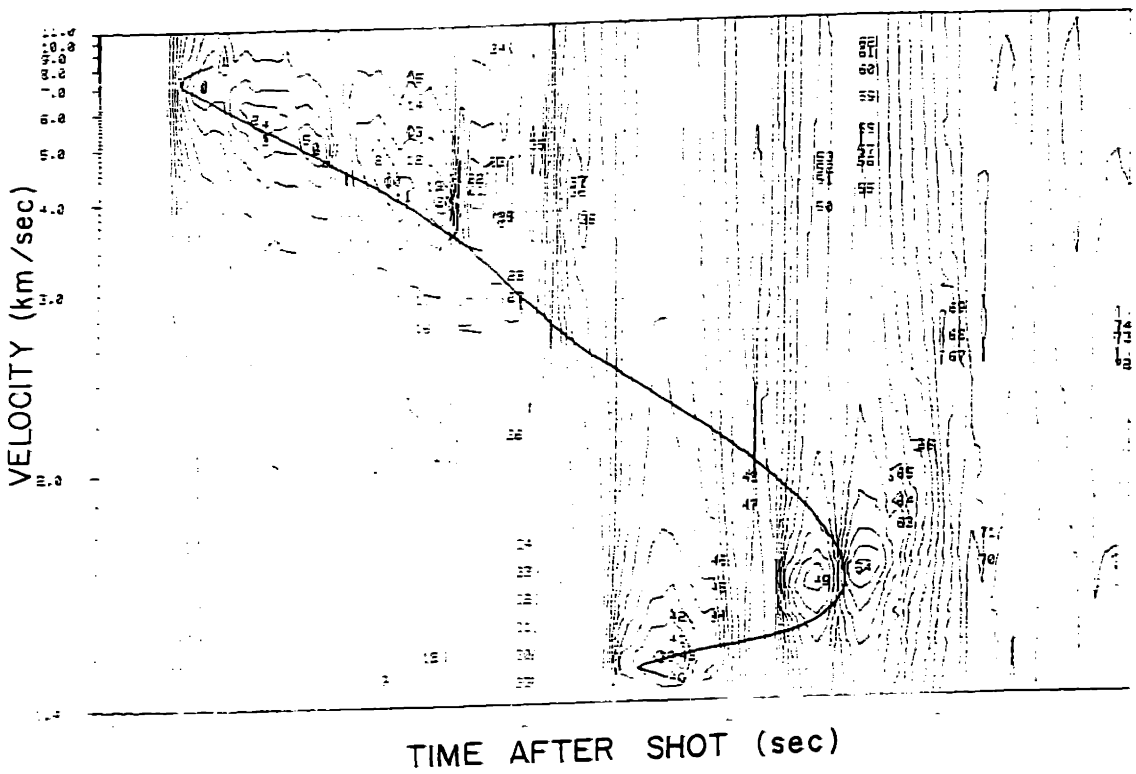

Fig. 5.29) Velocity spectrum at 6 Hz. for line 4. reel 3043. at an offset of 16.9 km (contours). The θ function defined in chapter 2 is plotted for the primary arrival with no free surface interactions by the heavy solid line. This was computed using the compressional model of fig 5.27b and the experimental source and receiver depths.

used, but with more definite layering would have larger cusps, and would have more "ripples" in the theta function in the area between 4 and 6 km/s, thus leading to significant amplitudes in this region. This supports the indications noted in the discussion of line 1 that there could be significant gradient changes in the layer 2 - layer 3 depth regions.

INVERSION OF LINE 6 DATA

Setting

Line 6 is similar to line 4 in that the shots were deployed in ever younger oceanic crust as the offset increased. Although the line ran obliquely to the bathymetric contours, there was still a significant dip of about 0.6°, with depth increasing with offset. Since the bathymetry is decreasing, an isostatic argument would infer that the Moho would be depressed, igneous crustal thickness would be constant, and thicker sediments would be found in this region than deeper in the Pole Abyssal Plain. This would be the case if this were completely normal oceanic crust beginning to meet the continental margin. However, the Morris Jessup Rise on which this line was shoaling is not normal oceanic crust. It is instead hypothesized to be a region of thickened oceanic crust which formed at the Arctic Mid-ocean Ridge at anomaly 18-13 time, along with the Yermak Plateau [Feden, et al., 1979]. One of the major arguments for this is that plate reconstructions for this time require that the Morris Jessup Rise and the Yermak Plateau be oceanic to avoid continental overlap. Another piece of corroborative evidence for crustal thickening is the "magnetic high" [Vogt, et al., 1979; Feden, et al., 1979] observed in the magnetic anomaly over the Rise. This could be due to increased magnetization, or increased thickness of the layer 2 region of the crust in that region.

Ostenso and Wold [1977] ran a single channel seismic reflection profile across the Morris Jessup Rise during the ARLIS 2 experiment (1964). Their stations numbered 63-65 were very close (30 km distant) to the area surveyed by line 6. The penetration of the single channel system was only about .5 sec (2-way travel time) and basement is not defined in our area. They concluded that the sediment was generally thick in this region, but the paucity and quality of the data makes the seismic results somewhat inconclusive. In addition, their coverage is not exactly for the line 6 location. My reasons for this discussion are, of course, a result of the fact that the refraction data indicate a somewhat different structure for the sediments on this line.

Data and interpretation

The $\tau(p)$ and $x(p)$ data for line 6 at all frequencies are composited in figs. 5.30a&b. For fig. 5.30a the data are not "condensed", while for fig. 5.30b they have been in order to describe the single primary offset function. Note that the scatter on this line is very low. In figure 5.31 the τ data are condensed, corrected to the surface datum, and the observed phase velocities corrected for the .6° dip on the line. The $\tau(p)$ curve from line 1 superposed on this plot shows that the water column is thinner (the decreased τ for most regions of the curve for line 6) but that the total depth to Moho must be somewhat larger than that of line 1 due to the matching of the τ values at velocities of 7.4-8 km/s. Since this profile has lost .35 km of very slow water column, the crust and sediments must thicken noticibly, or have a larger region of lower velocity rock, or both, to obtain this feature. The presence of the water column pegleg arrivals (noted on the plot) indicates that the top of the sediments is fairly solid. This concurs with the turbidite sediment constitution hypothesis of Ostenso and Wold [1977].

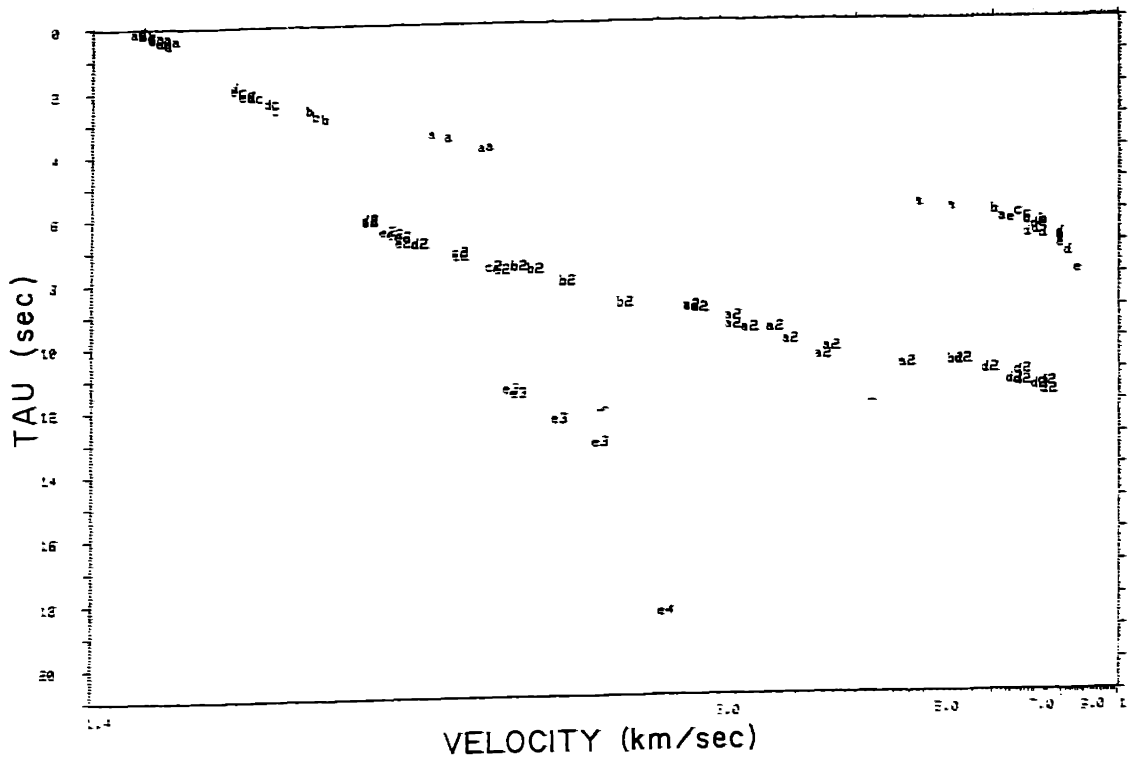

Fig. 5.30a) The $\tau(p)$ data for all frequencies for line 6.

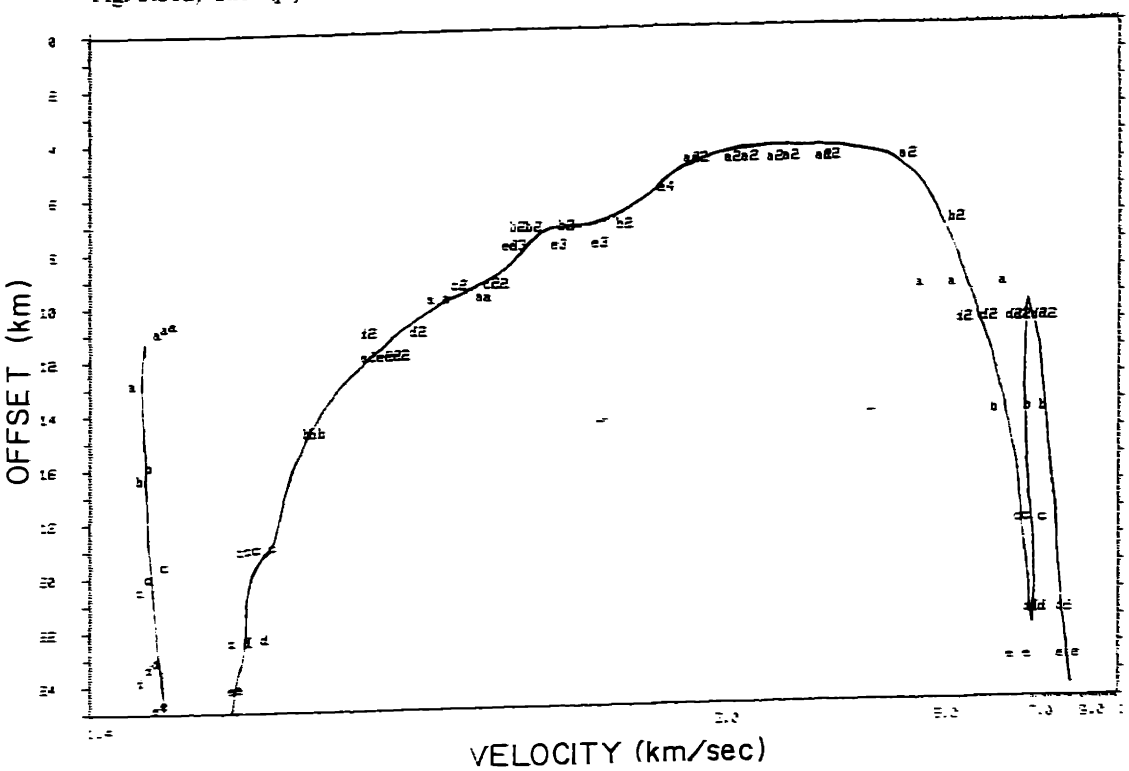

Fig. 5.30b) The $x(p)$ data for all frequencies for line 6.

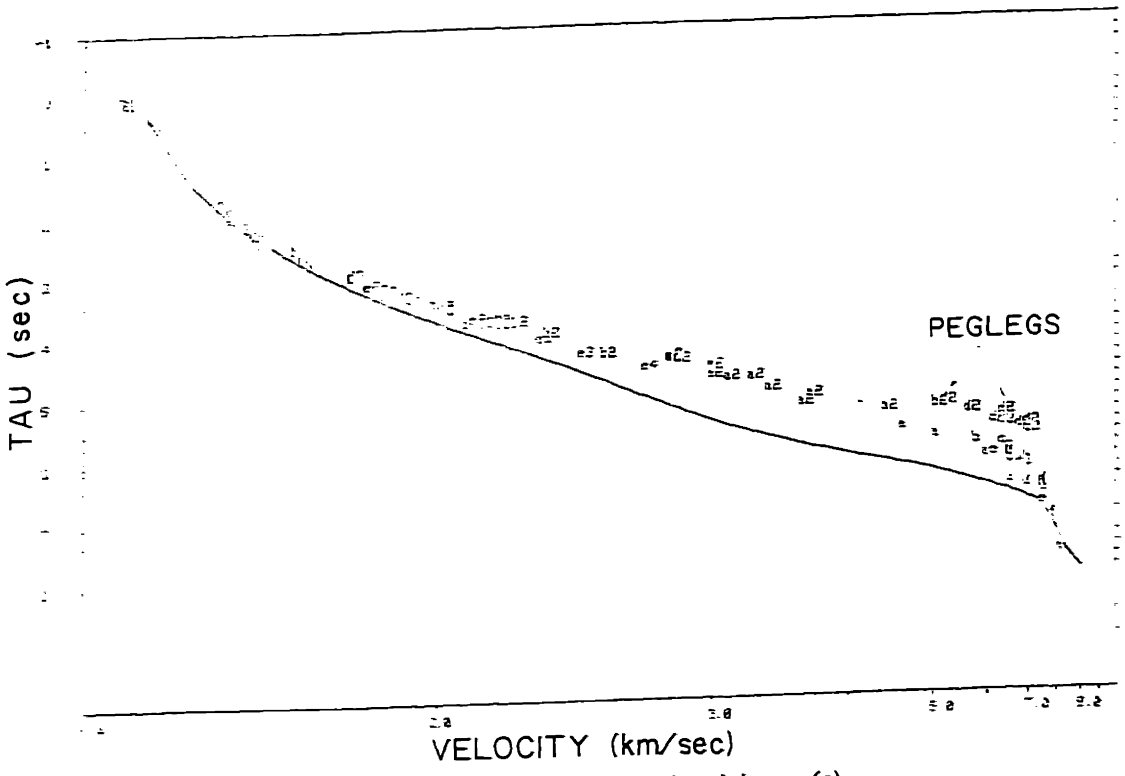

Fig. 5.31) The condensed and corrected $\tau(p)$ data (letters) and the tau (p) curve representative of the data from line 1 (solid line).

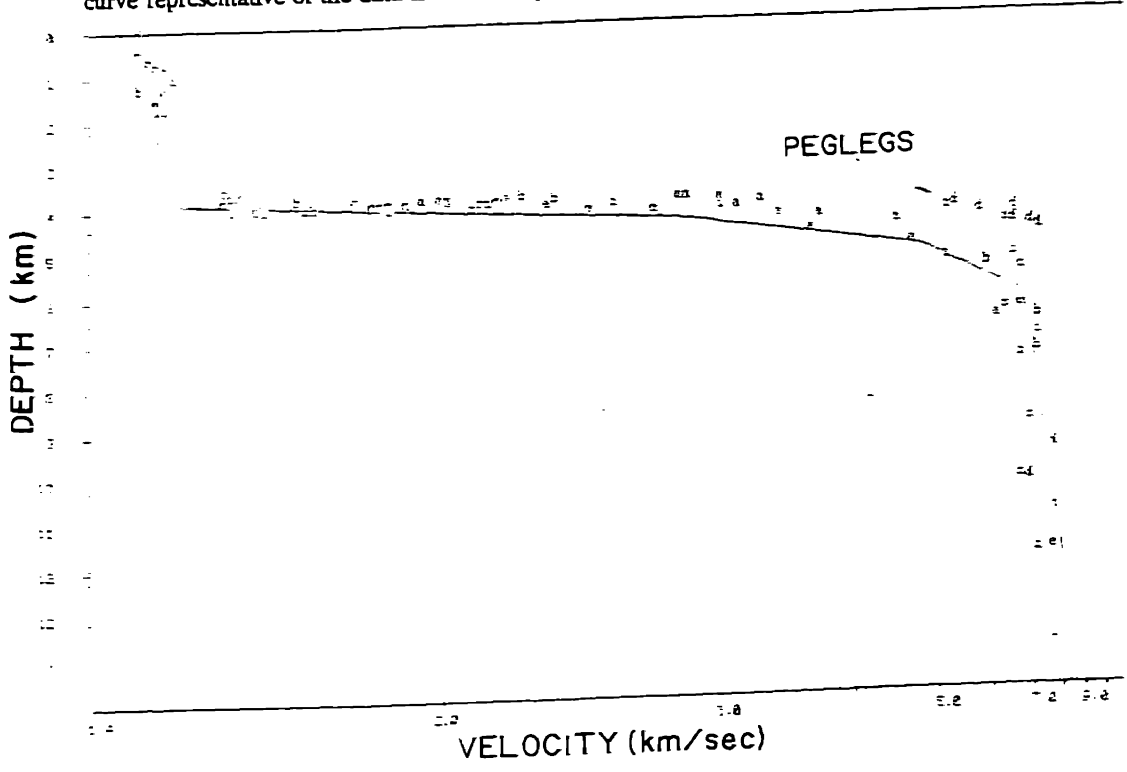

Fig. 5.32a) The velocity-depth migration results for line 6.

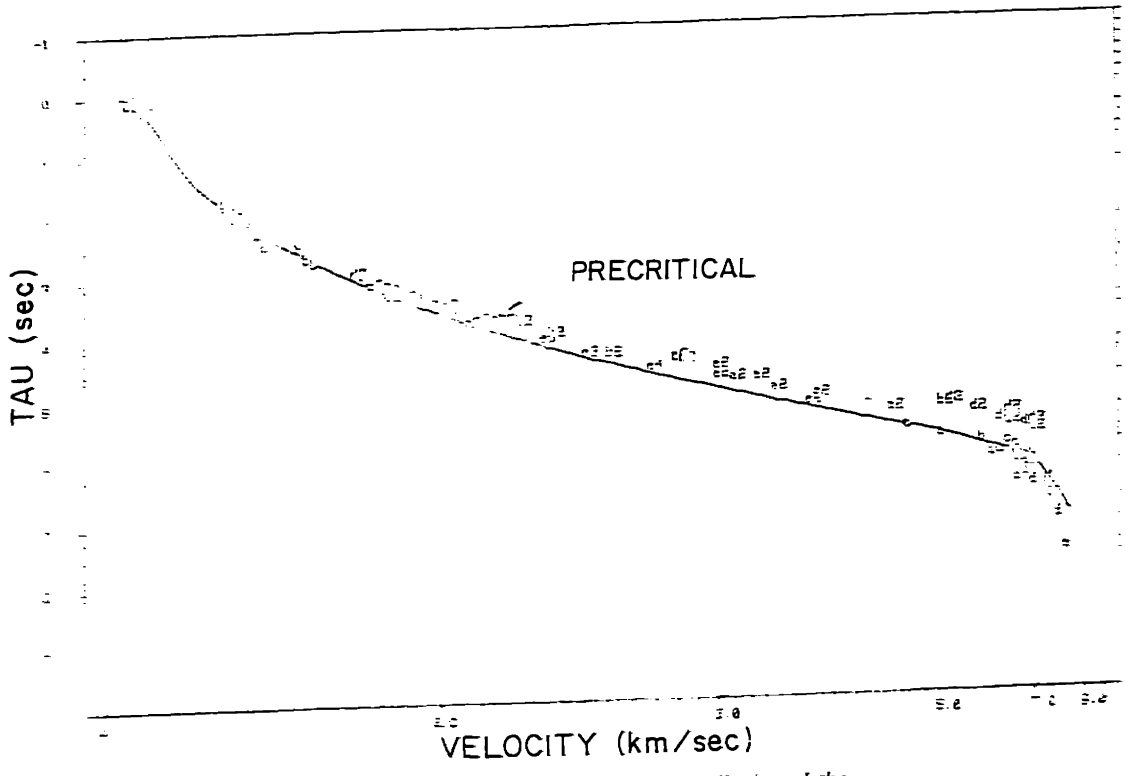

Fig. 5.32b) The $\tau(p)$ curve for the model in fig 5.32a (solid line) and the data (letters).

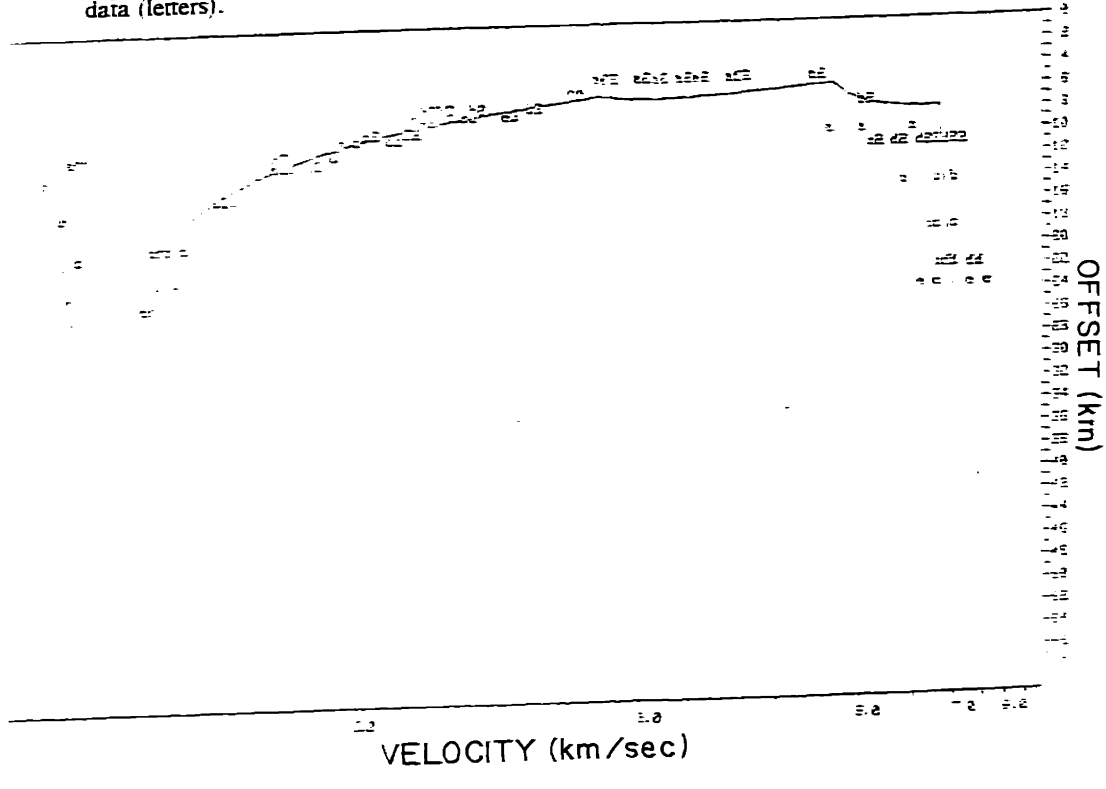

Fig. 5.32c) The $x(p)$ curve for the model in fig 5.32a (solid line) and the offset data (letters).

The results of velocity-depth migration on this data are shown in figs. 5.32. In fig. 5.32a the data and trial model are shown by the letters and solid line, respectively. The pegleg data at layer 2-layer 3 velocities have been ignored, as have some of the early arriving multiples in the sedimentary velocity region. This is because it is felt that a significant portion of the early arriving energy is due to water column pre-critical peglegs, although the differences in τ for the shallower events do not allow good separation of the direct and true free surface multiples from the pegleg paths. The data and predicted $\tau(p)$ curve are compared for this model in fig. 5.32b. Note that the suspected pre-critical arrivals proceed horizontally from the $\tau(p)$ curve as discussed by Clayton and McMechan [1981]. The agreement of the data and the predicted offset function is shown in fig. 5.32c.

The tau-sum method for homogeneous layers was used on the data in fig. 5.33a. The lower dashed curve is the lowest frequency (8 Hz) and is the least influenced by the pre-critical reflections which I hypothesize to cause the bulge between 2 and 3 km/s. The higher velocity peglegs mentioned earlier are not included in these curves. The results of the tau-sum inversions are in fig. 5.33b. These are in good agreement with the migration result. The envelope of the curves is indicative of the uncertainty in the resulting model. In general, the models indicate a slightly shallower depth to basement than is correct because of the use of the precritical reflection peglegs. However, because these arrivals tend to make infeasible models, they are often eliminated by the recursion discussed in chapter 4.

The use of the Dorman-Jacobson type linear least squares formulation in chapter 4 results in the models of fig. 5.34. For this inversion, only offset data were used and a 10 layer parameterization of the model with equal velocity interval partitions was solved for. These results, while scattered, concur with the previous determinations. The model for a 20 Hz

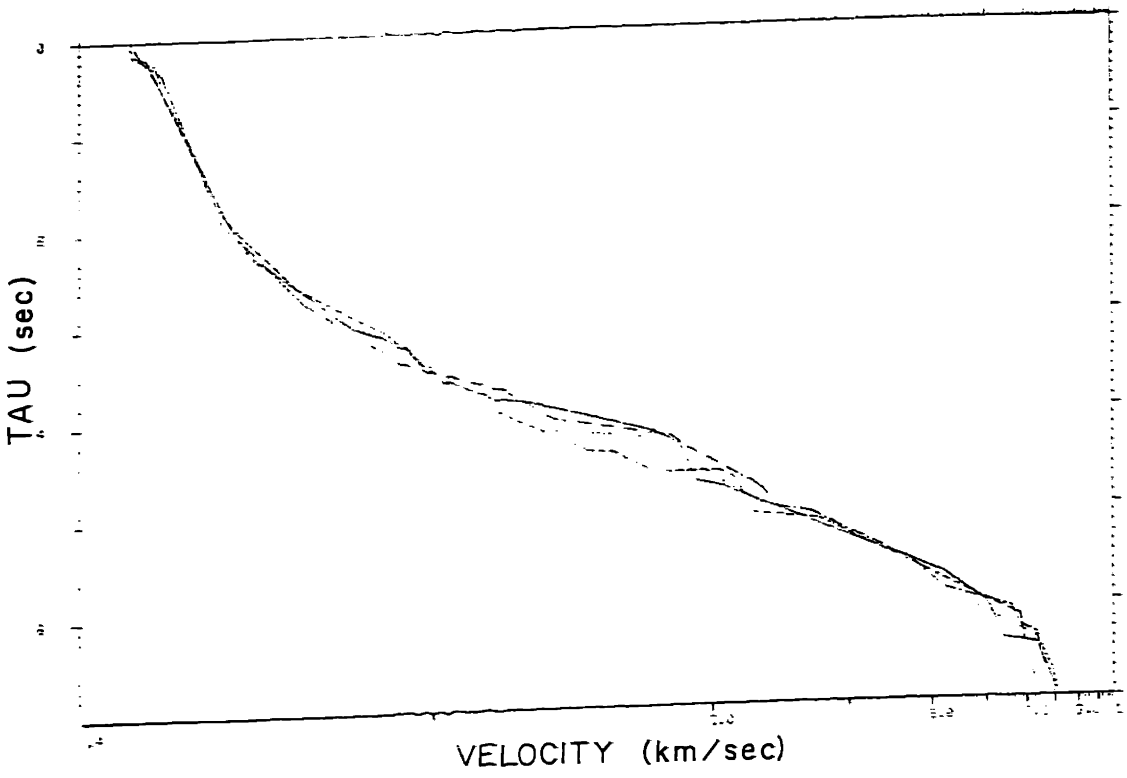

Fig. 5.33a) The $\tau(p)$ curves for the different velocity spectral analysis frequencies.

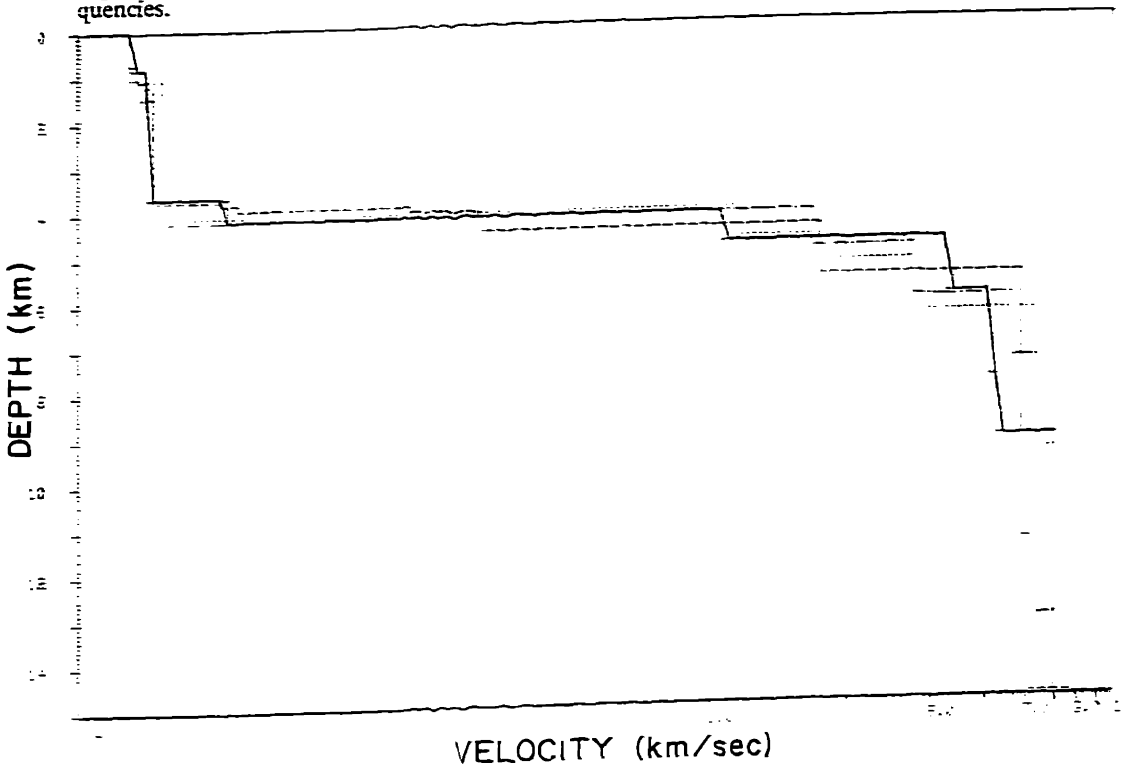

Fig. 5.33b) The models resulting from inversion of the data used to make the $\tau(p)$ curves in fig. 5.33a by the tau-sum method.

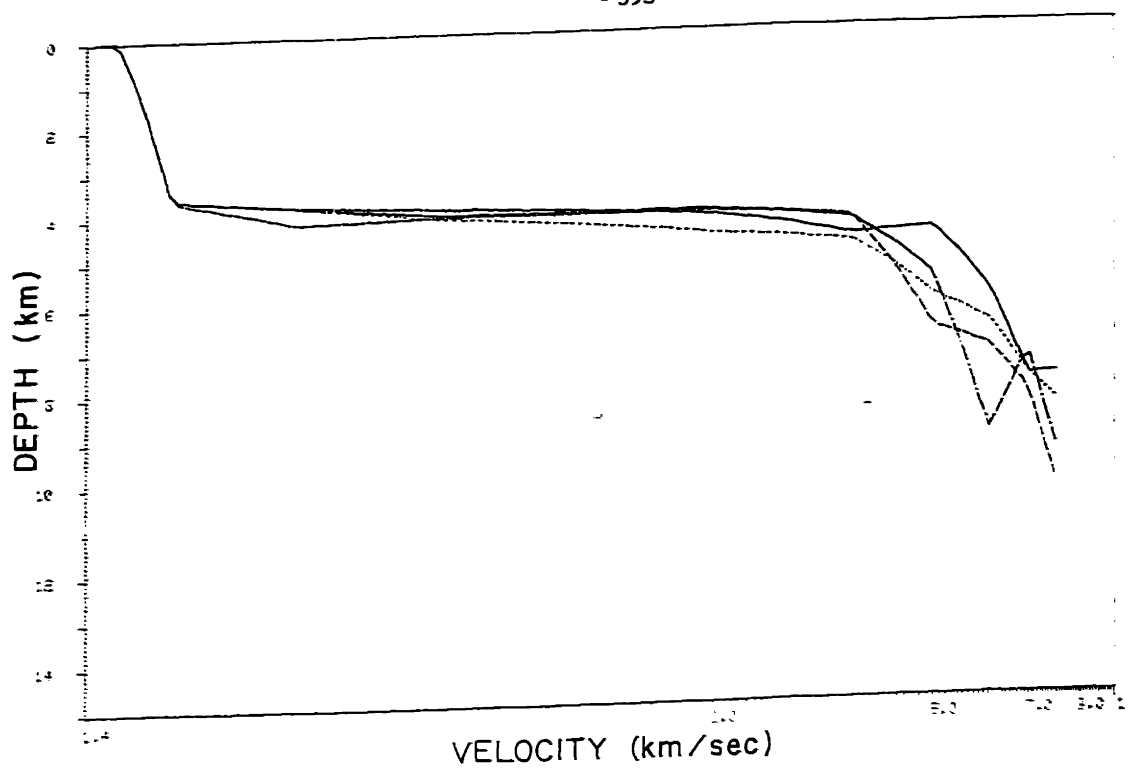

Fig. 5.34 Models resulting from linear least squares inversion of the offset data at each frequency of the velocity spectral analysis.

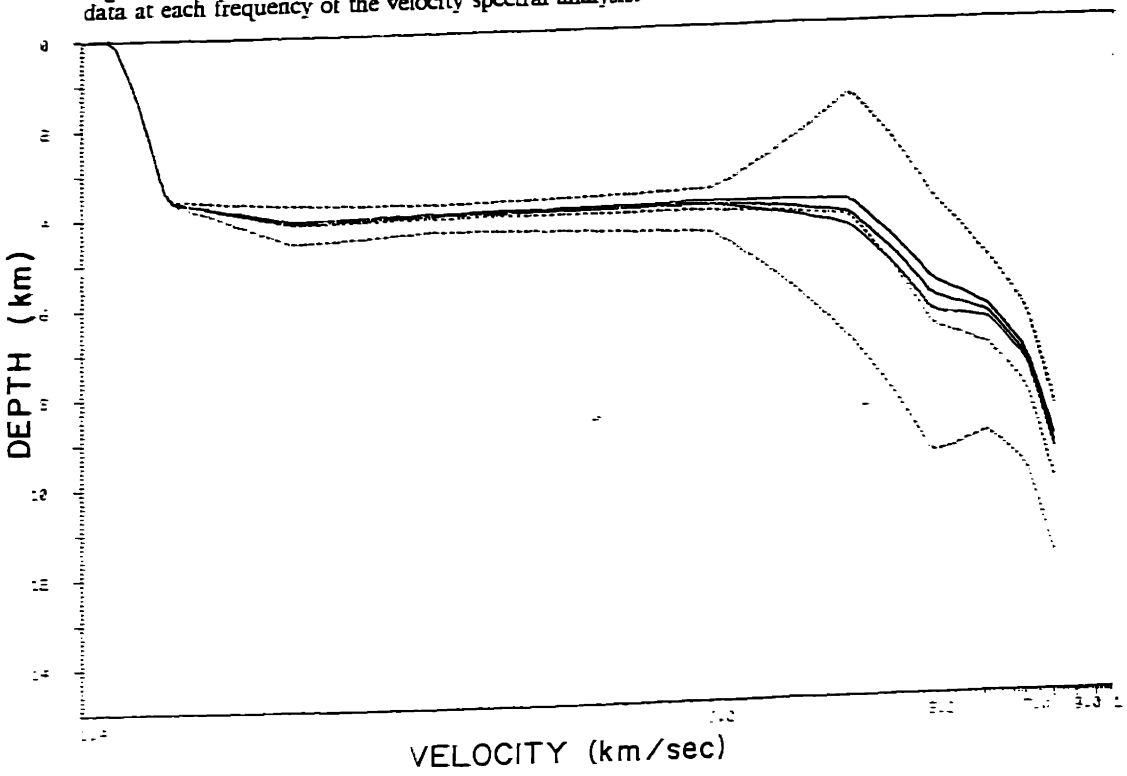

Fig. 5.35 Models resulting from linear least squares inversion of the 20 Hz travel time (t) (solid curves) and the offset (dotted curves) data.

center frequency is repeated by the central dotted line in fig. 5.35. The bounding dotted lines are the 2σ error bounds assuming a 3 km standard deviation for the offset measurements. (Which was excessive.) The results for inversion of the travel time data at 20 Hz are also shown on this plot by the solid lines. The central line is the resulting model and the bounding curves are the 2σ lines for an assumed standard deviation of the travel times of 0.1 sec. The linearized least squares formulation used assumed an a priori model with .1 km depth standard deviations in the water column regions in order to force the known water column and bathymetry, and a 10 km standard deviation in all other regions.

Summary

The results for line 6 indicate a thinner sedimentary region than that observed on lines 1 and 4. They also indicate a thicker igneous crust, concurring with current hypotheses that attribute a thickened oceanic crustal structure to the Morris Jessup Rise. Another line which is as yet un-interpreted (line 5, see fig 5.1) samples the Rise much more extensively and should confirm the data reported here. The only anomalous result is the lack of a thick sedimentary cover on line 6.

CONCLUSIONS

This chapter has shown that the processing and inversion techniques outlined in the previous regions of this work can, in fact, be used to interpret actual crustal structures with data taken under the tough experimental conditions of the Arctic environment.

REFERENCES

Allen, B., Ardai, J., Hunkins, K., Lee, T., Manley, T.O., and Tiemann, W., "Observations of Position, Ocean Depths, and Gravity Taken from the Fram II and Camp I Drifting Ice Stations," Lamont-Doherty Geological Observatory Technical Report CU-13-80, August, 1980.

Bessonova, E.N., Fishman, V.M., Ryaboyi, V.Z., and Setnikova, G.A., "The Tau Method of Inversion of Travel Times- I. Deep Sounding Seismic Data," *The Geophysical Journal of the Royal Astronomical Society*, vol. 36, pp. 377-398, 1974.

Christensen, N.I. and Salisbury, M.H., "Structure and Consititution of the Lower Oceanic Crust," *Reviews of Geophysics and Space Physics*, vol. 13, no. 1, pp. 57 - 86, February 1975.

Clayton, R. and McMechan, G., "Inversion of refraction data by wavefield continuation," *Geophysics*, vol. 46, no. 6, p. 860, 1981.

Diebold, J.B. and Stoffa, P.L., "The traveltime equation, tau-p mapping, and inversion of common midpoint data," *Geophysics*, vol. 46, no. 3, pp. 238-254, March, 1981.

Duckworth, G.L., Baggeroer, A.B., and Jackson, H.R., "Crustal Structure Measurements near FRAM II in the Pole Abyssal Plain," *Tectonophysics*, vol. 89, pp. 172-215, 1982.

Duckworth, G.L. and Baggeroer, A.B., "Crustal Refraction Results from the Fram and Nansen Basins of the Arctic Ocean," *(In press)*, 1983.

Feden, R.H., Vogt, P.R., and Fleming, H.S., "Magnetic and Bathymetric Evidence for the Yermak Hot Spot Northwest of Svalbard in the Arctic Basin," *Earth and Planetary Science Letters*, vol. 44, pp. 18-38, 1979.

Ness, G., Levi, S., and Couch, R., "Marine magnetic anomaly timescales for the Cenozoic and late Cretaceous: a precis, critique, and synthesis," *Reviews of Geophysics and Space Physics*, vol. 18, pp. 753-770, 1980.

Parsons, B. and Sclater, J.G., "An analysis of the variation of ocean floor bathymetry and heat flow with age," *Journal of Geophysical Research*, vol. 82, pp. 803-827, 1977.

Spudich, P. and Orcutt, J. "A new look at the seismic velocity structure of oceanic crust," *Rev. Geophys. and Space Phys.*, vol. 18, pp. 627-645, 1980.

Vogt, P.R., Taylor, P.T., Kovacs, L.C., and Johnson, G.L., "Detailed Aeromagnetic Investigations of the Arctic Basin," *Journal of Geophysical Research*, vol. 84, pp. 1071-1089, 1979.

Weston, D.E., "Underwater Explosions as Acoustic Sources," *Proceedings of the Physical Society*, vol. 76, p. 233, 1960.

CHAPTER 6: Inversion of Long-range Propagation Data

INTRODUCTION

The background material on the study of long-range propagation data was given in chapter 1, and the reader is urged to read that section prior to proceeding through this one. With that behind us, the primary intent of this chapter will be to indicate how the use of an array of hydrophones to receive long range propagation data allows a much more complete analysis to be carried out than is possible with single channel systems. In addition to the *sonogram* or short-time spectral analysis usually carried out to determine the group velocity vs. frequency dispersion curves, multichannel acquisition also allows the phase velocity dispersion curves to be estimated, and allows better determination of the group velocity dispersion curves when the modes are not easily separable on the sonogram. This is done by applying the *velocity spectral analysis* procedures usually used to process refraction data to the long-range data. (See fig. 2.5 for the relationship between these decompositions.) The application of these algorithms allows the data to be decomposed by group velocity, phase velocity, and frequency simultaneously.

The utility of this decomposition is that it breaks the complex received waveforms down into components that may be understood and easily predicted by theoretical models. The ability to write down a relatively simple prediction physics is a large step toward the solution of the *inverse* problem of determination of model parameters from the observations. Observation of the waveform and the ability to predict the wave shape through synthetic seismogram techniques does not constitute a truly reasonable solution of the inverse problem. Even if the propagation physics are described perfectly, when one tries to predict the entire waveform the deviation of one small part of the model from the true model may make the prediction look

very wrong when, in fact, the model is nearly correct. In this case, even with an excellent description of the physics, one is often in the dark as to how to change the model to make it predict the observed data better, and just how close the model is to the correct result is unknown. However, if the basic physics behind the generation of the waveform is understood, and more fundamental components of the phenomenon can be separated and predicted, then very often a methodology for deviating a trial model toward one that predicts the observed data more closely can be constructed. In addition, if the decomposition is chosen wisely, individual properties of the medium, in this case the velocity and velocity gradient at different depths in the water column and crust, may manifest themselves in relatively disparate regions of the decomposition. When this occurs, and when the relationship between the observables (the output of the decomposition) and the model is known through the analysis of the physics of the situation, then the model may be easily deviated to bring its predictions into accordance with the observed data. In general, the waveforms are much too complicated to use as an observable directly, for it is very difficult to describe the influence of a model on each individual point of a multichannel time series. In addition, this observation is extremely noise sensitive. For this reason we have developed methods for estimating the group and phase velocity dispersion characteristics from the acquired multichannel data.

From these measured curves the physics may theoretically be run backwards to obtain the model. Unfortunately, this cannot usually be done directly for three reasons: i) models are generally not uniquely specified by practically obtainable amounts of data: ii) the *complete* physics are generally impossible to describe in perfect detail mathematically because of their complexity; and iii) the analytical inversion of the physics can be very difficult. The limit on the amount of data that can be taken is set by both the acquisition geometry, and the observation noise. What is essentially done by the decomposition algorithms is the distillation of the best

observables possible from these limited and noisy data. For these *smoothed* observables, we may use smoothed physics, that is to say somewhat incomplete and approximate models, to predict them. In many cases such physical descriptions are invertible directly, as in the case of ray theoretical predictions of travel time data using the Herglotz-Wiechert-Bateman formulae [Aki and Richards, 1980], or may be done computationally by iterative methods. For analysis of the long-range propagation data in this work both methods have been applied to invert multichannel data recorded from a distant (341.3 km) explosive shot for water column and crustal velocity structure [see also: Baggeroer and Duckworth, 1982]*. The models determined are, of course, valid only to the point where the physics used to obtain them breaks down. This usually manifests itself in the blurring of fine scale structure, since an important assumption is often spatial invariance of the model in the horizontal dimension. (This is enforced by both mathematical and experimental expediency in Arctic work.) The models thus represent an average of what might really exist in nature. Finally, before proceeding to the sections concerning the estimation of the dispersion curves and inversion of these, and the bottom interaction travel-time data, the particulars of the experimental procedure carried out on the Fram 2 experiment will be summarized.

THE EXPERIMENT

The data which motivate this work are the multichannel waveforms recorded from a 55# TNT charge detonated at a depth of 93 meters 341.3 km from the 24 channel horizontal hydrophone receiving array at the Fram 2 camp. This experiment was carried out on April 26, 1980 at 1421Z. The location of the Fram 2 receiving array was 85.786° *N*, 24.408° *W*. The source charge was deployed at approximately 88.85° *N*, 18.75° *W*, at an initial bearing of

*The range to the shot-point had mistakenly been taken as 389 km for the analysis performed in this work. This was due to an error in the navigation computations that was discovered too late.

2.11° true [Allen, et al., 1980]. The depth at the Fram 2 camp was 3.68 km directly underneath the array, however this shoaling was very fast, and the depth at the slant range for the highest velocity rays was 3.8 km for their first interaction, then 4.0 to 4.15 km for all bottom interactions thereafter. The bathymetric dip in the along the direction of propagation appears to be less than 0.2° from the measured bathymetry near the Fram 2 camp [Allen, et al., 1980] and currently available bathymetric maps of the Pole Abyssal Plain. This dip is small enough that it should not affect apparent phase velocities measured by the array.

One small note must be made before proceeding. To properly carry out the inversions for velocity/depth structure both the distance between the source and receiver, and the absolute difference between the shot instant and received times must be known. For the Fram 2 experiment clocks at the source ("Camp 1") and receiving (Fram 2) camps were to be synchronized to the satellite navigation receivers so that these times could be measured. Unfortunately, an older model receiver (the Magnavox MX-709) was used at Camp 1 and could not acquire the fiducial time mark, nor calculate the position accurately because of interference of the 5 polar orbiting satellites with one another. Because the Camp 1 position was so close to the North Pole, more than one satellite was in view almost all the time. Apparently the locking algorithm in the early receivers was inadequate in this situation, and one satellite could not be tracked long enough to obtain a position fix. As a result, the desired time synchronism between the camps was not obtained, and positions for Camp 1 had to be obtained by sunshots. The inversions thus depend on the assignment of a reference time to the first arrival. This time was obtained by dividing the distance between camps by the assumed group velocity of the first arrivals. The group velocity was determined by starting with a profile which was measured at the Fram 2 camp using an XSV (eXpendable Sound Velocimeter) down to 2 km, then using the canonical curves for the deep arctic ocean [Urick, 1975]. This was then

perturbed until the group velocity curves of the first 3 modes and the first arrivals (due to higher order modes) were matched by the predictions of the normal mode program. In essence, what the loss of the time synchrony required was relative deviation of the dispersion curves, not absolute movement, thus making the inverse problem a little bit more difficult. A more complete discussion of the technique will follow in a later section of this chapter.

THE DATA

Figure 6.1 shows the waveform from a single channel for the duration of the dominant arrivals. This data is on digital tape reel 5293 from the Fram 2 experiment. Each trace in this figure is 10 seconds long, with the vertical axis being correct for the first trace. After the 60 second period shown, most arrivals are from scattering mechanisms that are both very difficult to describe, and not of immediate interest in determination of the mechanisms for the long-distance transport of the bulk of the explosive energy. The long, intense arrival beginning at 233 seconds is the sum of the arrivals that are transported by strictly water column paths and are best described in this example of strong lateral homogeneity by a modal solution of the wave equation (see chapter 2). The later, more discrete, arrivals are caused by the superposition of a number of modes, many of which interact strongly with the seafloor structure. In this region, the arrivals are more efficiently described by ray theory and the WKBJ approximation to the wave equation. This is because the dispersion characteristics of the different modes and frequencies converge, making it impossible to resolve their individual components with our experimental geometry. It turns out very handily that one may first solve the normal mode dispersion curve inversion problem for the water column structure, then deal with the later arrivals with ray and WKBJ theoretic techniques to determine the sedimentary structure. One should note, however, that some of the later sediment multiples after approximately 265

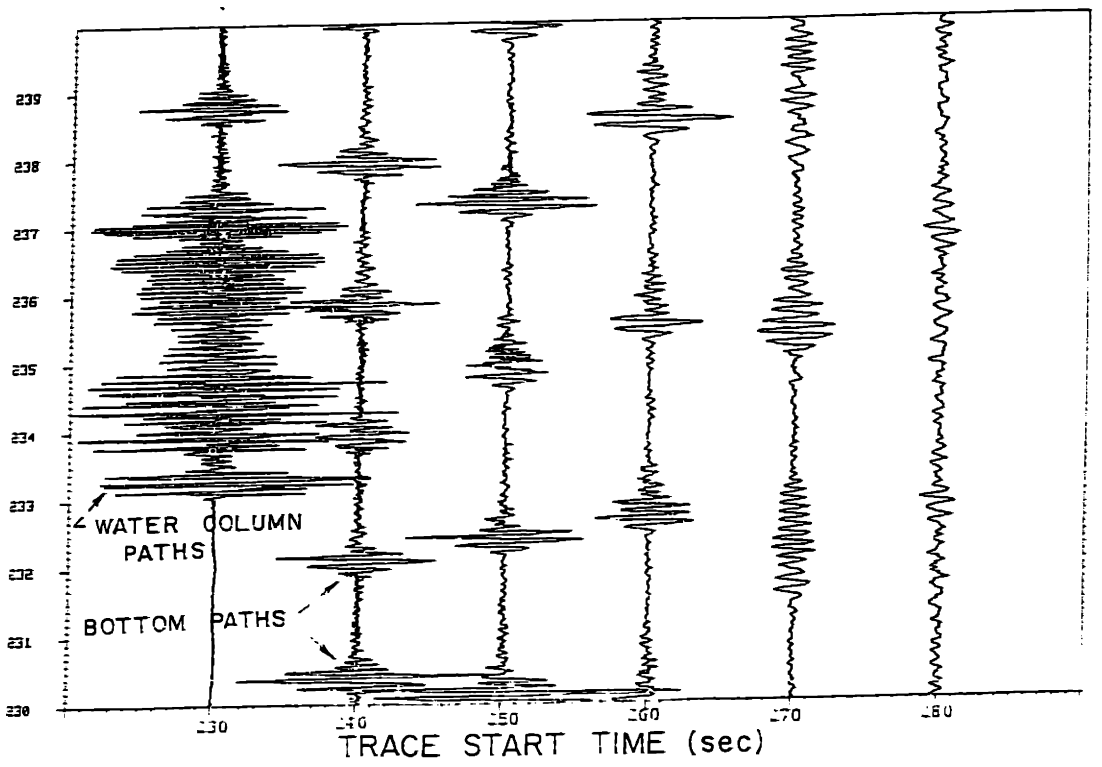

Fig. 6.1) A long-range propagation waveform received at a distance of 341.3 km. The water column and bottom interacting paths are indicated. Some bottom interacting paths are time coincident with the water arrivals and cannot be discerned on this plot.

seconds do appear to be dispersive. This can be seen on the *sonogram* or spectrogram (see chapter 2, fig 2.5) analysis and on the velocity spectra of the multichannel data. To fully utilize these arrivals, the full wave solution must again be used, and has not been done for this work.

MODAL ANALYSIS

Introduction

In normal mode analysis [eg. Tolstoy and Clay, 1966] it is found that the only components of the acoustic energy put into the water column by an explosion that get propagated for long ranges are those that satisfy certain boundary conditions. This allows the wave equation equation to be solved for these discrete "eigenmodes", or normal mode components which are supported by a given water column model and may be described by their phase velocity dispersion curve, $c_p^m(\omega)$, or vertical direction of propagation vs. frequency characteristic for each mode, along with the mode amplitude function. The phase velocity dispersion is more commonly expressed by the wavenumber dispersion curve, $k_m(\omega) = \omega / c_p^m(\omega)$ because this quantity is the most natural to use in analytical work. It can also be shown that the speed of propagation of a wave packet with a certain frequency is given by the group velocity, $c_g^m(\omega) = d\omega / dk_m(\omega)$ [Tolstoy and Clay, 1966]. A more detailed discussion of dispersion relations is given in chapter 2, and the results of that chapter indicated that if the group and phase velocity curves could be estimated, then the inverse problem relating these curves to the velocity-depth model in the water column could be defined. This will be done by the linearized inversion technique outlined in chapter 4. However, before describing the inversion algorithm I will first discuss the methods used to estimate the dispersion curves from the data.

Dispersion curve estimation

Since this experiment was conducted in an ocean basin with a 4 km water depth there are many normal modes supported for each frequency, corresponding to different phase and group velocities. The lower order modes are dispersive enough in group velocity to allow them to be separated by sonogram analysis. Such a sonogram for the water column component is shown in fig. 6.2. Using this single channel analysis, phase velocity, c_p, cannot be obtained, however, the group velocity, c_g, as a function of frequency can be measured indirectly through the time of arrival, t, and the known offset of r=341.3 km through the simple relation:

$$c_g^m(\omega) = \frac{r}{t_m(\omega)} \qquad 6.1$$

In this equation the dependence on the mode, m, chosen and the frequency, ω, is noted. In this figure, the vertical axis is frequency (Hz), and the horizontal axis is time after the shot initiation. The power in a single channel waveform as a function of these two variables is contour plotted after being analysed by Fourier transform over tapered 0.5 second intervals advanced every 0.1 seconds. The contour intervals are 3 dB. A $\sin^2$ spectral analysis window was used for sidelobe control. Superposed on this contour plot are predictions of arrival time vs. frequency for the first 7 modes predicted by the state-space normal mode program outlined in chapter 2. (The solid lines are for one model, the dotted lines for another. The reason for the two sets will be given shortly.) This program assumes a constant density, does not model shear waves, and allows description of the sound speed structure in terms of linear velocity gradient segments between specified grid points [Baggeroer, unpublished].

The sonogram method for group velocity dispersion curve estimation from a single trace is the most popular technique for oceanic modal analysis [Kutschale, 1981]. As was seen in chapter 2 (fig. 2.5) the sonogram is only the projection of the higher dimensional

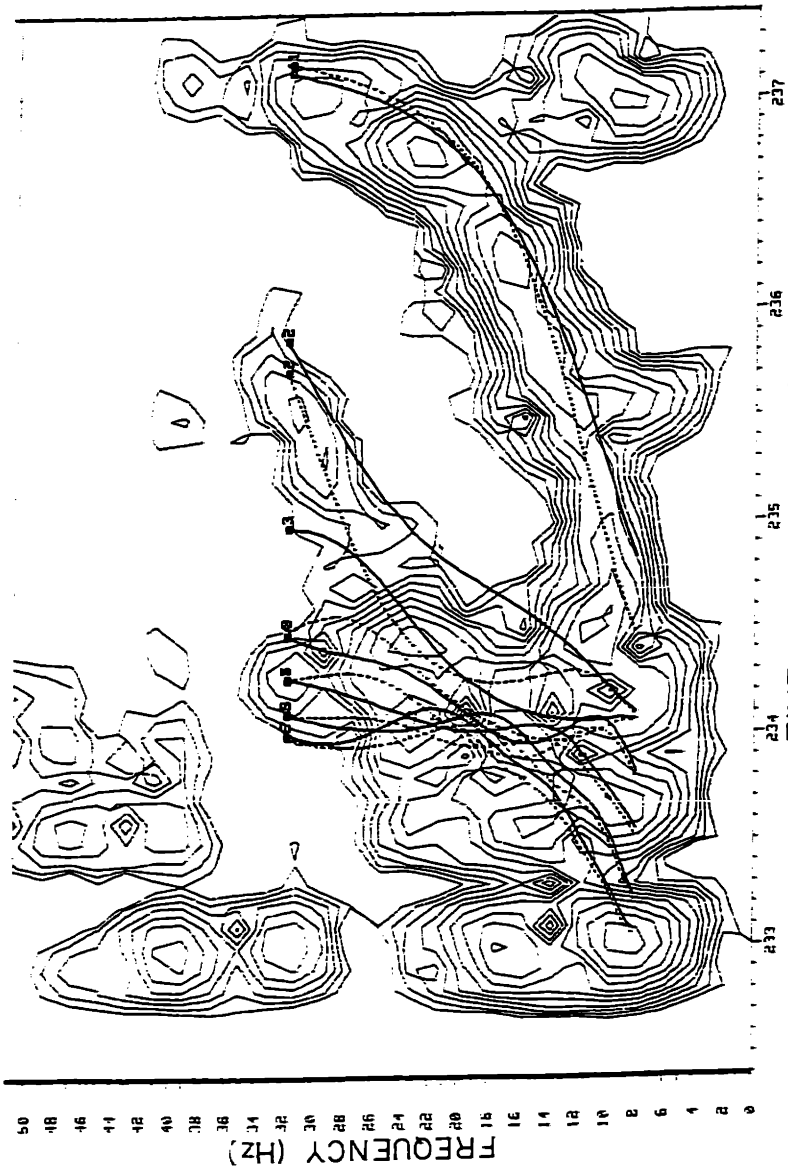

Fig. 6.2) Sonogram for part of the the data trace in fig. 6.1. The heavy solid and dotted lines are mode dispersion curve model predictions. The contour intervals are 3 dB, and the heavy curves are dispersion relation predictions for 2 different models.

decomposition done by velocity spectral analysis obtained by integrating the velocity spectra over slowness or phase velocity. Fig. 6.3 shows the sonogram of the Fram 2 data with the modal dispersion curves predicted by a trial velocity depth model in the water column and sediments. From this plot it is quite easy to see that the long low frequency to high frequency *chirp*, or frequency sweep, observed in the first data trace of figure 6.1 is primarily due to the dispersion of mode 1. This plot also shows that the large bandwidth first arrival at approximately 233 seconds on fig. 6.1 is due to the superposition of many of the higher order modes (in this case, modes 6-30). It must be noted that the existence of a predicted group velocity curve at a given point on the sonogram does not ensure that an arrival will appear there. (Although the converse is true.) For example, the decreasing arrival time with increasing frequency for the first arrivals as the mode number goes up does not make the higher frequencies come in slightly earlier. This fact is the result of consideration of the amplitudes of the modes which can also be computed by the normal mode program. From chapter 2 it will be recalled that the measured mode amplitudes are set by the values of the mode eigenfunctions at the source and receiver depths. To show that this is true, a waveform was synthesized from the superposition of the normal mode components for the dispersion curves in fig. 6.3. This was done using the "non-aliasing" method outlined in chapter 2, and the sonogram computed from this synthetic data is shown in fig. 6.4, along with the group velocity dispersion curves for the first 7 modes. Note that the first arrivals do not "lean" forward, as do the dispersion curves in fig. 6.3.

Before going on to the advantages of the higher dimensional decomposition afforded by the multichannel data, the sonogram analysis can be improved by using spectral analysis techniques other than the simple windowed Fourier transform used for these examples. One possible method is to use an MEM technique such as the Burg algorithm [Lacoss, 1971] to achieve

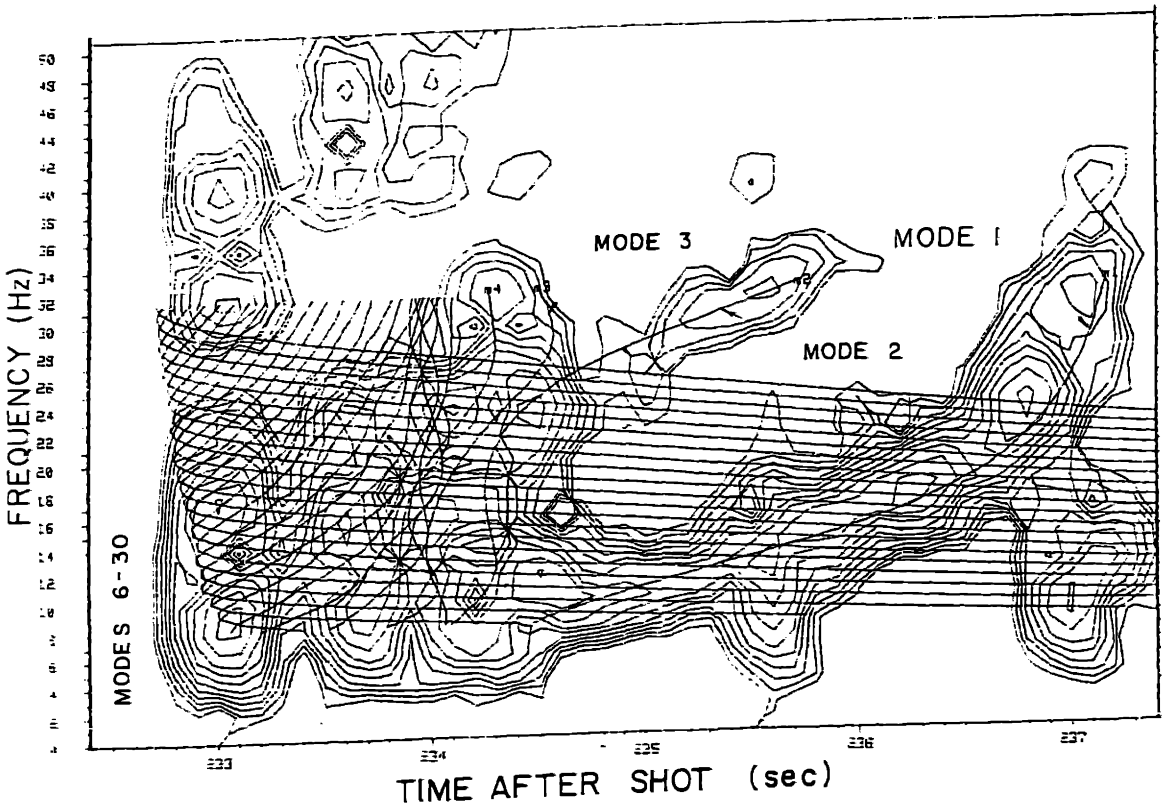

Fig. 6.3) Sonogram of the Fram 2 data showing the group velocity dispersion curves for the first 30 modes.

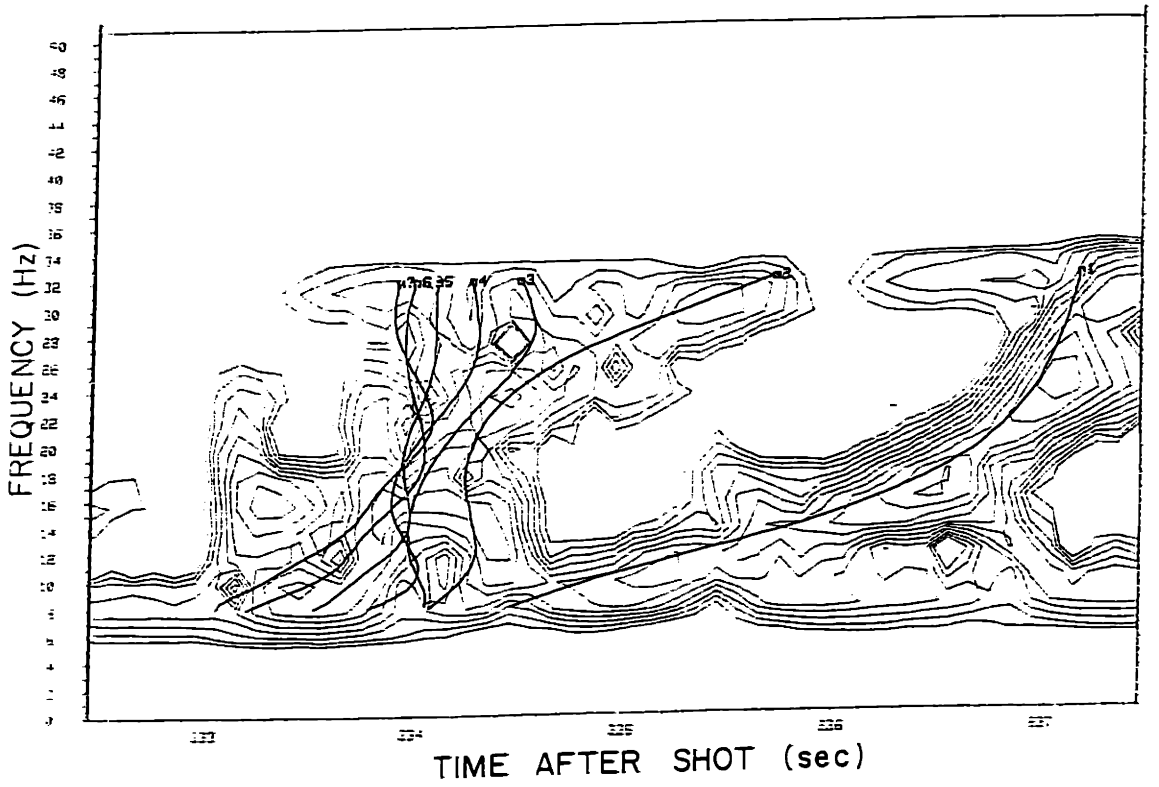

Fig. 6.4) Sonogram for synthetic data and the dispersion curves for the model used to generate the data.

higher frequency resolution with shorter data segments, thus obtaining better localization of the dispersion curves in frequency and time*.

The advantages of decomposing the modal data by phase velocity, as well as the sonogram coordinates, are two-fold. First, the phase velocity datum is useful in itself as an observable in the inversion. Second, different mode number trajectories which are too close to resolve in their projection onto the sonogram plane can be separated in the three dimensions afforded by the velocity spectral decomposition (again, see fig 2.5). To see this, an example velocity spectrum at a 12 Hz center frequency is given in fig. 6.5 for noisy synthetic data. This velocity spectrum was computed using the MLM method and a $T = .25$ second window which was advanced in was 0.9 km in length and uniformly sampled. The points marked "X#" on the plot are peaks which have been picked and identified with a particular mode, #. The peaks marked with "o" have not been identified with any one mode. The points marked "m#" are the (t, f, p) coordinates of the mode dispersion curves used to calculate the data using the "no-alias" technique. When the "X" peaks are picked at all frequencies and projected onto the sonogram plane, the results are in figure 6.6. In this plot the true model dispersion curves are given by the usual solid lines. The sonogram computed with .5 second periodograms advanced every .1 seconds is contoured. The "X#" values from the velocity spectral peak picks are plotted every 4 Hz, as are the unidentified peaks marked by "o". Note that the true dispersion curves are well picked by the "X" data, while interpretation of the sonogram contours is very difficult beyond the first two modes. Thus, using the complete decomposition from array data, more dispersion curves can be estimated, and thus used to invert for the water column velocity

*Note, this does not necessarily imply that the actual peak locations are more accurate, but will often allow picking individual dispersion curves which are too close together for periodogram type spectral analyses to resolve. It should further be noted that the Burg algorithm, or any method which uses forward and backward errors, is probably a bad one to use on this asymmetrical and almost deterministic data, since the dispersive chirps clearly do

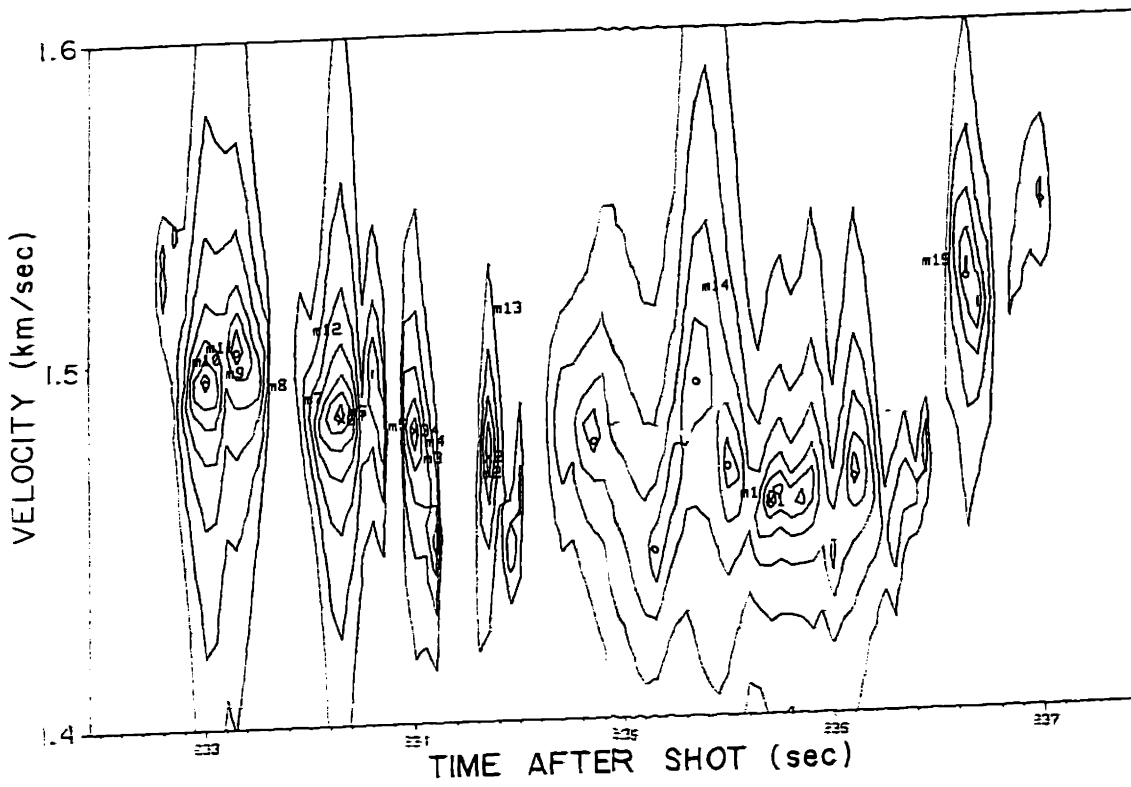

Fig. 6.5) A velocity spectrum of the dispersive water column arrivals. This spectrum is for the analysis in the 4 Hz band centered at 12 Hz and is contoured with 5 dB intervals.

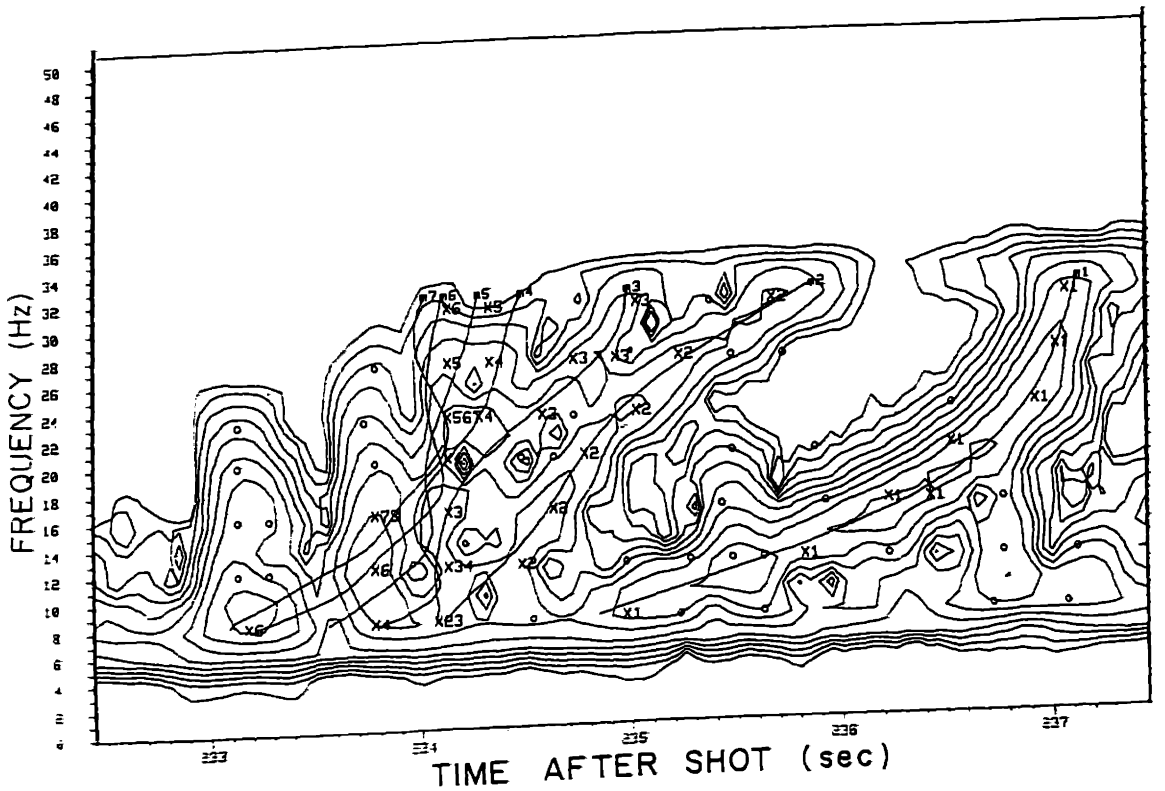

Fig. 6.6) The projection of the peaks of the MLM velocity spectrum onto the sonogram plane. The various features are discussed in the text.

structure.

To carry out the 3-dimensional decomposition for which a single frequency plane is shown in fig. 6.5, and discussed in the previous paragraph, the standard velocity spectral analysis algorithm described in chapter 3 was used. This method first temporally Fourier transforms the multichannel data over short data segments, then at each frequency uses the MLM spectral analysis method in the spatial dimension to estimate the spatial frequency, which is just the slowness or inverse phase velocity. The segmented short-time temporal analysis gives the group velocity (arrival time) resolution. An alternative method to carrying out this decomposition would be to do the spatial transform first, via a slant stack, then to temporally Fourier transform the waveform at each slowness. The disadvantage of this for short arrays has already been seen in chapter 2 (see discussion around figs. 2.3). However, if the STFTSS using the MLM method is employed, then the short aperture slant-stack* can be obtained that has good slowness resolution. This is shown in fig. 6.7. To then obtain the 3-dimensional transform, short-time temporal Fourier transforms are carried out at each slowness. The result of this operation at a slowness of 1/1.448 s/km, the inverse phase velocity of a large part of the first mode, is shown in fig 6.8. To carry out the temporal spectral estimates for this plot periodograms were not used, but rather the Burg algorithm on a .125 second window (32 points) using a 10^{th} order model. Because each short velocity filtered time segment had only one frequency component in it, the low model order, and the short data length may be used to achieve good temporal and frequency resolution simultaneously. Note the sharpness of this dispersion curve vis a vis that of fig 6.6. Part of the gain comes from the additional noise

---

not look the same going forward and backward in time.

*The term slant-stack is not quite appropriate here. We are not using the true offset of 341.3 km in the computation of τ, but rather referencing the sensors in the array to one of their number, which has been defined as zero. The result is the travel time vs. slowness plot for the reference sensor shown.

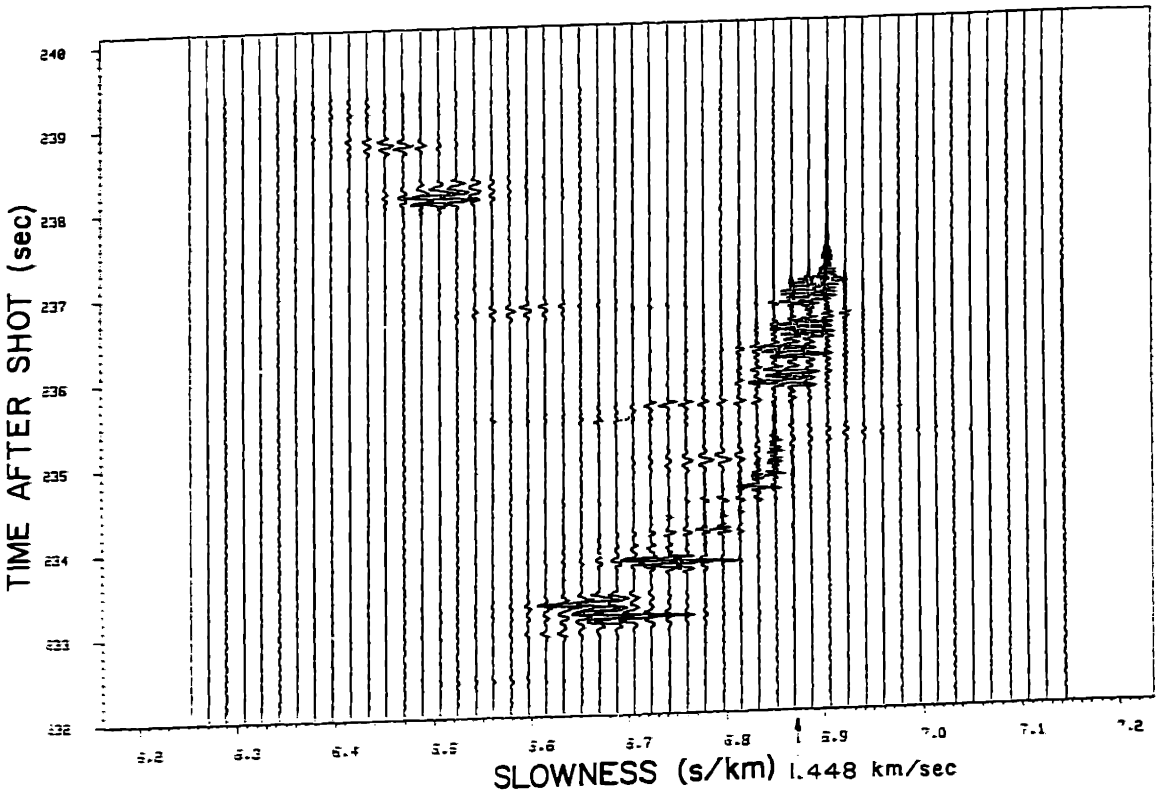

Fig. 6.7) Decomposition of the wavefield data using the MLM STFTSS. The axis is in slowness, p, with increasing phase velocity to the left.

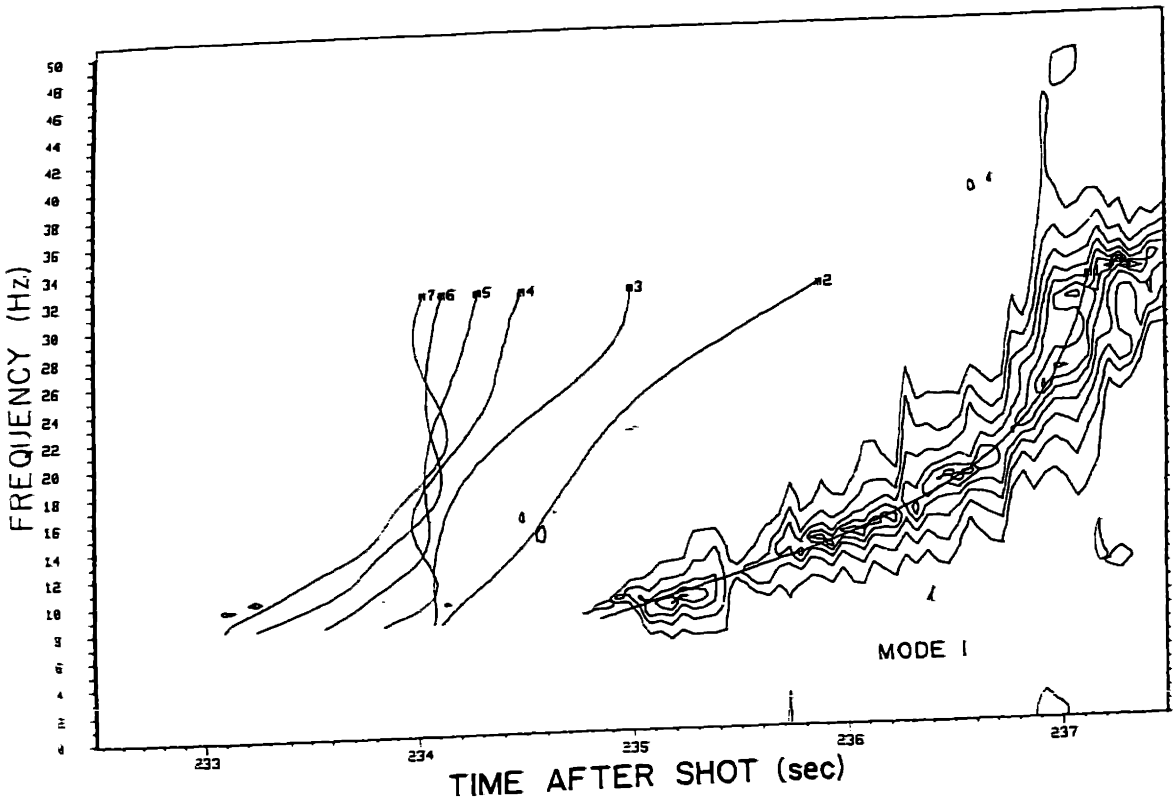

Fig. 6.8) Short time spectral estimate using the Burg algorithm on the mode I data after velocity filtering by the MLM STFTSS at 1.448 km/s.

suppression of th velocity filtering by the STFTSS, and part from the use of the MEM spectral analysis technique.

In conclusion, these results indicate that the use of adaptive and high-resolution processing on multichannel long-range propagation data allow very good phase and group velocity dispersion curve estimation to be carried out.

Inversion of the dispersion data

Using the relation 6.1, the predictions of the arrival time data are easily computed from the group velocity curves calculated by the normal mode program. For this work, the travel time datum has been used in the linearized least-squares inversion instead of the group velocity. There is no particularly good reason for this. The partial derivative matrices are nearly the same for both arrival time and group velocity. These have elements $\partial t_i/\partial m_j$ and $\partial c_{gi}/\partial m_j$ related by:

$$\partial t_i/\partial m_j = -\frac{1}{c_{gi}^2}\,\partial c_{gi}/\partial m_j \qquad 6.2$$

where m_j is the velocity at depth grid point j, and t_i is the travel time for some frequency and mode number. The matrix is made up by scanning over frequency, mode, and depth. An example partial derivative matrix, H, is shown in figure 6.9a where $\Delta\underline{d}$ is the vector of data residuals, and the elements $\Delta\underline{m}$ are the model residuals. This matrix was computed using first differences calculated from 1.0 meter per second model deviations at each of the 7 model layers. The group velocities were computed in the normal mode program by first differences of the wavenumber using 0.5 Hz deviations. Note that mode 1 samples the water column near the surface, mode 2 goes a little deeper and model 3 is deeper still. For each of the 3 modes, the dispersion curves were specified at 14 frequency points between 8 and 32 Hz. The qualita-

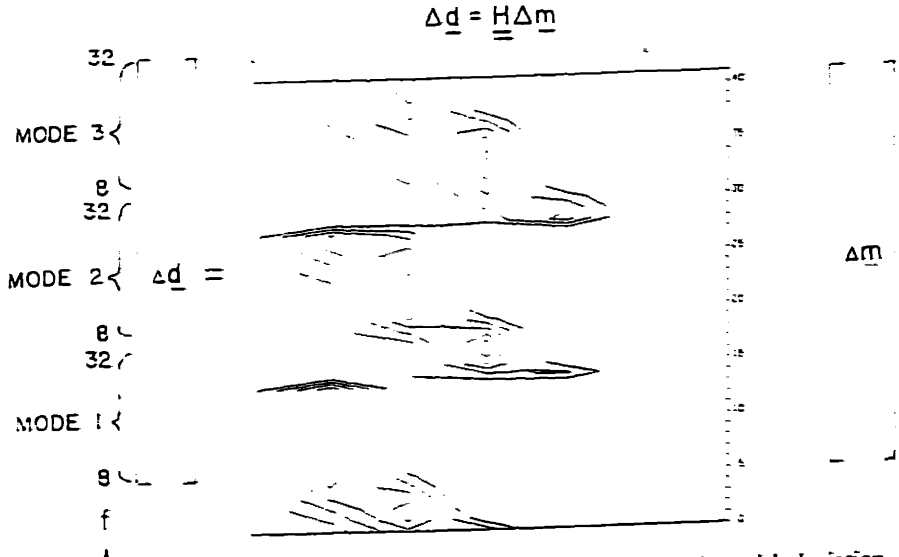

Fig. 6.9a) The partial derivative matrix and data and model deviation vectors for the linearized inversion of the travel time data for the first 3 modes. The dispersion curves were used between 8 and 32 Hz for a total of 42 data points.

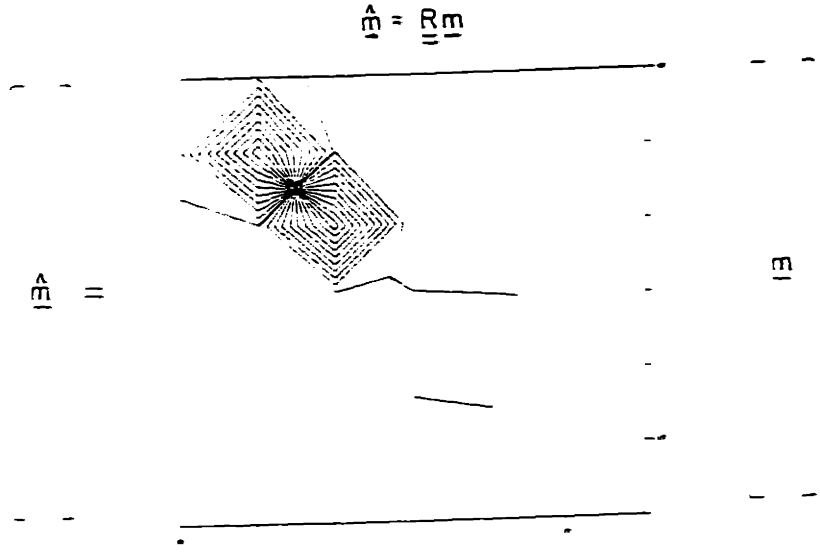

Fig. 6.9b) The resolution matrix for the inversion of the mode 1 travel-time curves only. Only the 2 largest eigenvectors have been retained, and only the depth region of the model for which the mode amplitude was the largest is resolved. (This is somewhat spread out by the frequency band used, since different frequencies sample different depths.)

tive features of the contour plot of the partial derivative matrix are as expected. For example, the higher frequencies sample the water column more shallowly, and as the mode number increases, the deeper into the model the the main energy lies.

If we consider the inversion problem for only the first mode, the resolution matrix for a condition number of 50 is shown in fig. 6.9b. For this matrix, only 2 eigenvalues have been kept, and it is seen that only the velocities at the second and third depth grid points are resolved, precisely the depths where the partial derivative matrix is large, and mode one has its largest amplitude.

To return to fig. 6.2, the solid lines are the dispersion characteristics predicted by the initial trial model for which the partial derivative matrix in fig. 6.9a was calculated, and are seen to deviate from the observed data, especially for mode 2. Using the "inverse" of this partial derivative matrix (see chapter 4 on linearized inversion), the corrections to the model indicated by the multiplying the error between the observations and predictions of the model by the "inverse" matrix were used to calculate the model which gives the dispersion characteristics indicated by the dotted lines in fig. 6.2.

To calculate the inverse matrix, only the two largest eigenvalues for the matrix were kept, and these caused the main change to the trial model to be an increase of 2.5 m/s at a depth of .3 km. The dispersion curves of fig 6.2 predicted by the corrected model are in reasonable agreement with the observed data, and we use this model for the average water column velocity structure. In fact, our determination by this technique agrees quite well with that measured by expendable sound velocimeter (XSV) readings in the upper regions of the water column covered by these measurements, and also agrees well with the standard relations given in the literature for the very stable deep ocean levels. The XSV data were taken at both the

transmitting and receiving ends of the propagation path. The initial trial and final (corrected) models are shown in fig. 6.10.

As an aside, the inversion procedure currently being discussed can be turned around when the water column structure is known. In this case, the observed dispersion and relative amplitude characteristics can be used to estimate the range and depth from the receiver to an unknown source. If multichannel data from a horizontally oriented array are used, then beamforming (analogous to our vertical velocity analysis, except that the azimuth domain instead of elevation is searched) can also be used to obtain the source azimuth.

Figure 6.11 compares the observed data with the waveform predicted by superposing the first 30 modes over the frequency band of 8-32 Hz, and then convolving with the source pulse appropriate for the charge weight and depth. In addition, the measured data are band-passed filtered over the same band as the synthetics. Note that the agreement is quite good after compensation for the (arbitrary) differing gain factors.

WKBJ and RAY ANALYSIS

From figure 6.3 one can see that the discrete bottom interacting paths, such as the one appearing at 8 Hz and approximately 237 seconds after shot initiation, cannot easily be described by a single mode. However, since these arrivals are not strongly dispersive, this indicates that they may be adequately modeled by ray theory. If so, it is much easier to analyse these arrivals using WKBJ or ray techniques. Figure 6.12 gives a velocity spectrum of the long-range propagation data for which a single channel was shown in fig. 6.1. On this plot the vertical axis is phase velocity, plotted linearly in its inverse, slowness. The horizontal axis is again time after shot initiation. The analysis shown was carried out for the 4 Hz band cen-

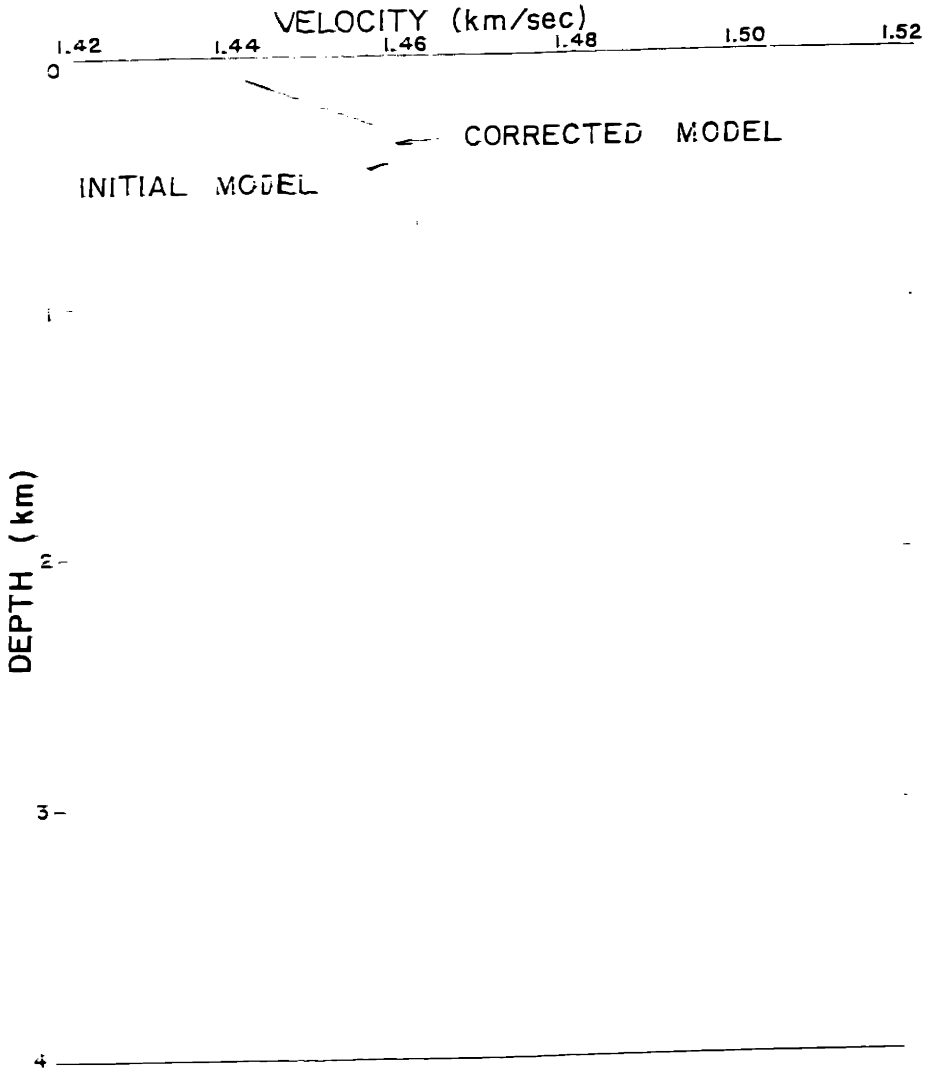

Fig. 6.10) The initial trial model, and the corrected model from the inversion of the dispersion curves.

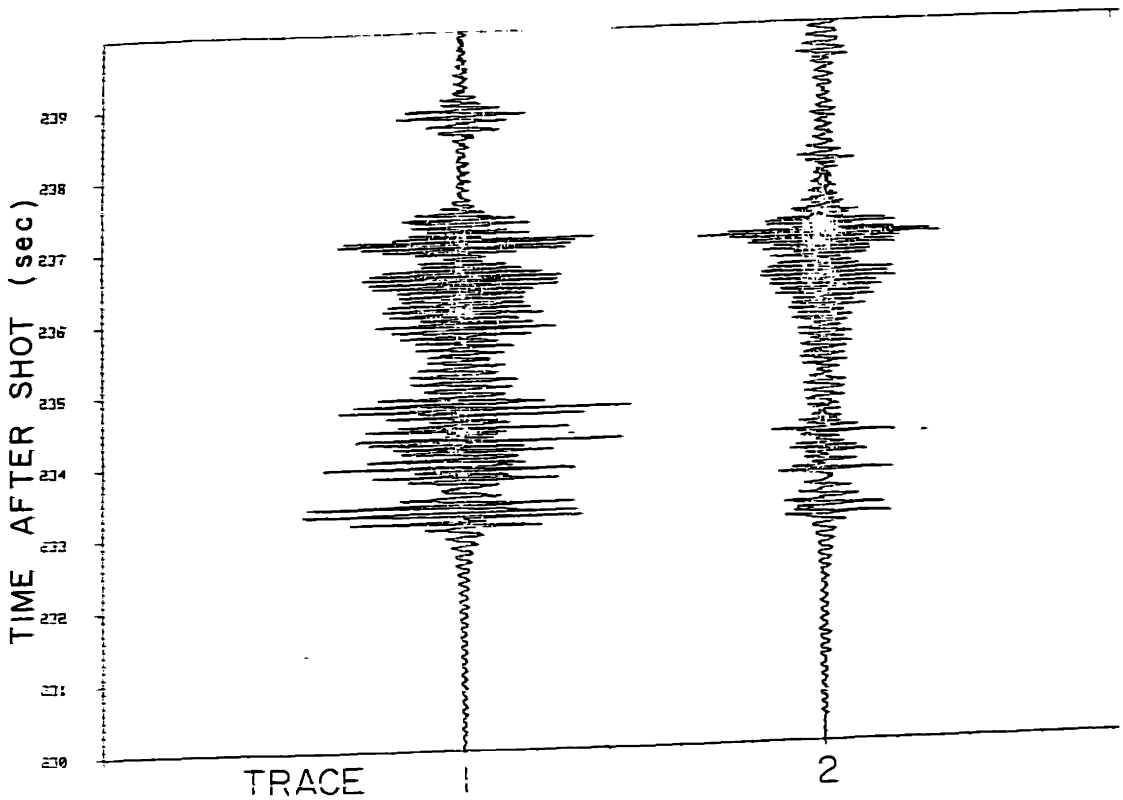

Fig. 6.11) Comparison of the observed dispersive water column arrivals (Trace 1) and the predictions (Trace 2) obtained using a mode synthesis algorithm on the model profile obtained from inversion of the measured dispersion characteristics of the data. The text discusses the parameters of the synthesis.

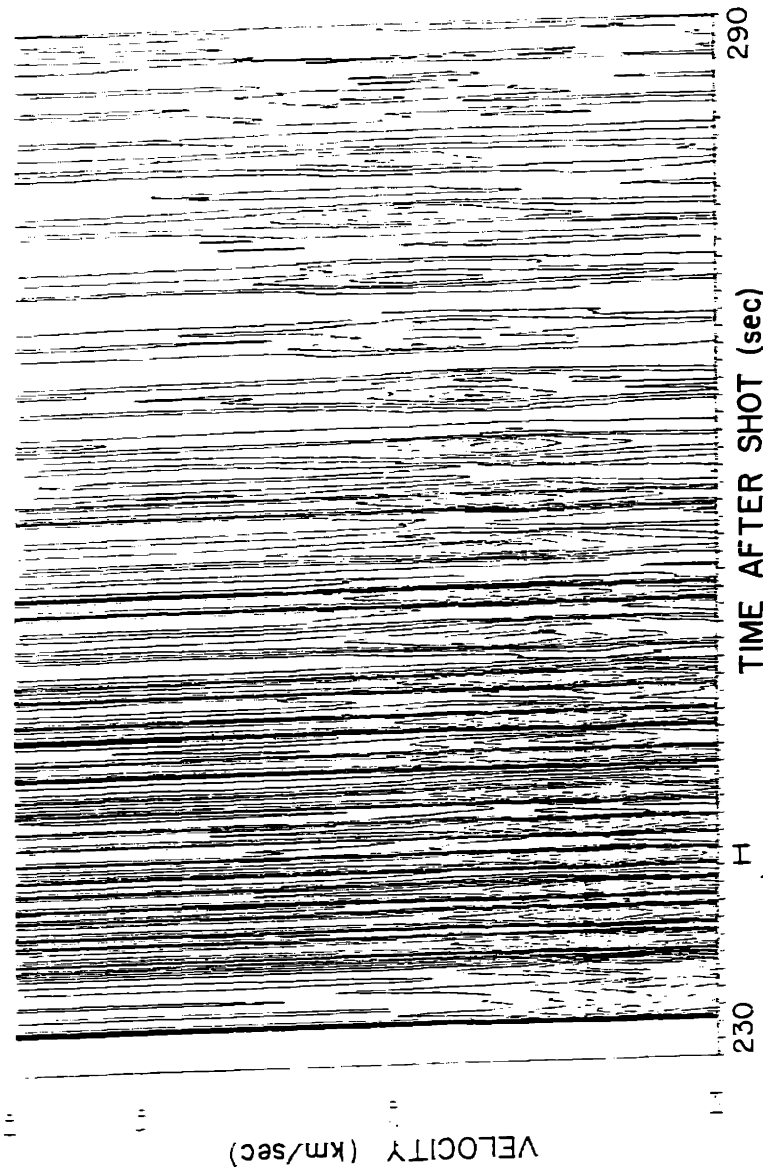

Fig. 6.12) The 12 Hz velocity spectrum for the long-range propagation shot. Contour intervals are 5 dB over a 70 dB range.

tered about 12 Hz. From this plot it is clear that very little scattering of the multiply turning rays is taking place, and good coherency in the arrivals is being maintained for 30 bottom interactions. To begin the inversion, velocity spectra similar to this for bands from 6 to 44 Hz were peak-picked, and the travel time data resulting were converted to $t(x)$, $\tau(p)$ and $x(p)$ curves for the equivalent multi-shot experiment by reducing the observations by the multiplicity of their turning points. this was done in the same manner as for the free surface multiples in the refraction experiments. (See the discussion at the beginning of chapter 4.) The travel time curve for the 6 Hz data after reduction by 1.5 km/s is given in fig 6.13. The lack of scatter in the arrivals is quite apparent. These picked data were then inverted for the velocity structure by the tau-sum implementations of the Herglotz-Wiechert-Bateman formulae to obtain a velocity-depth models shown for the 5 lowest frequencies (the ones with the greatest sediment penetration). The resulting models are shown in fig. 6.14 (the deeper homogeneous layered models), and are averaged to give the linear slowness gradient model given by the heavy line. The sediment model at 6 Hz from line 1 is also shown (upper homogeneous layered model) and is seen to be a little shallower than the average basin depth.

Finally, all the data are summarized in fig. 6.15. This plot is a detail of the 16 Hz velocity spectrum for the first 16 free surface multiples. The velocity spectral peak locations and free surface multiplicity (#) are indicated by "o#". The solid lines are the WKBJ synthetic seismogram "θ" curves for the various multiples [Chapman, 1978] corresponding to the arrival time/slowness locus for this model at an offset of 341.3 km. In the WKBJ approximation, the amplitude of an arrival is proportional to the derivative of the slowness with respect to arrival time along these curves. The inflection points in the curves where this value is infinite correspond to geometric arrival times. Note that these inflections agree well with the contour plot peaks of the velocity spectrum for this shot.

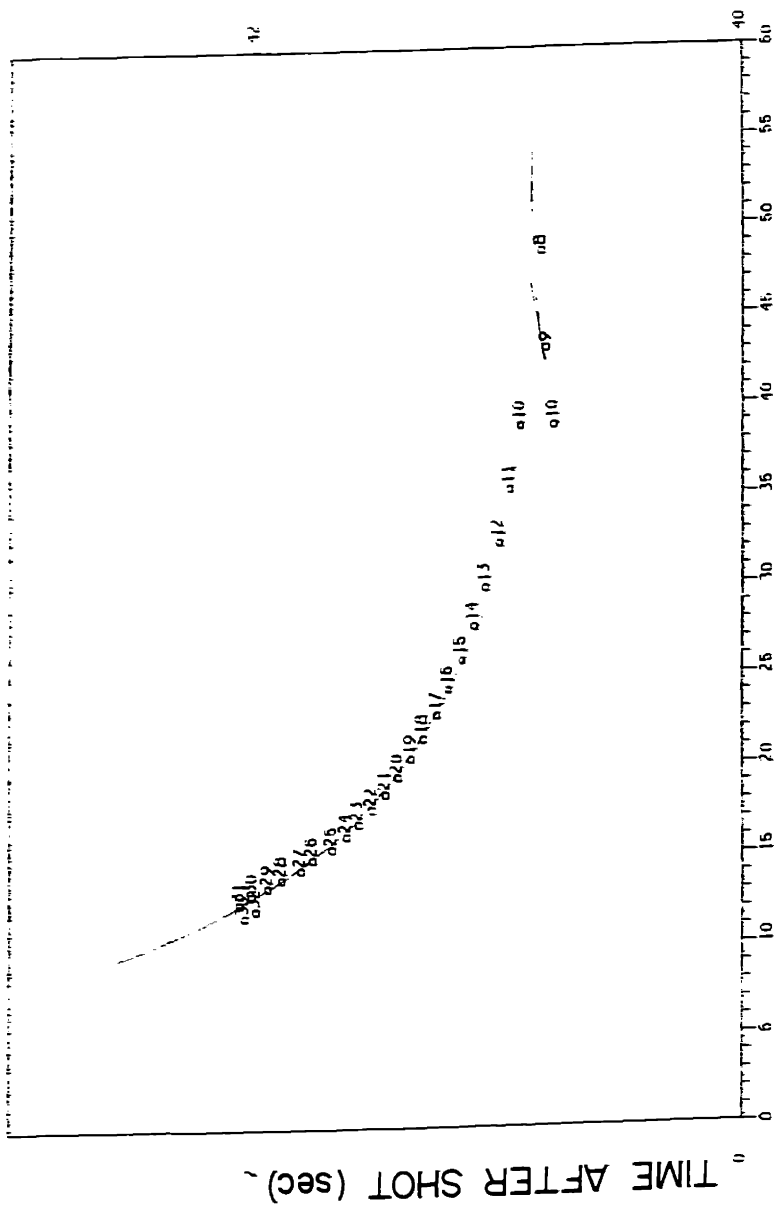

Fig. 6.13)
The picked peaks from the 6 Hz velocity spectrum (denoted by "o#" where # is the order of the multiple) after condensation to the first multiple curve. This display is the travel time vs. offset reduced by 1.5 km/s. The solid line is the prediction of the model obtained by inverting the observed points.

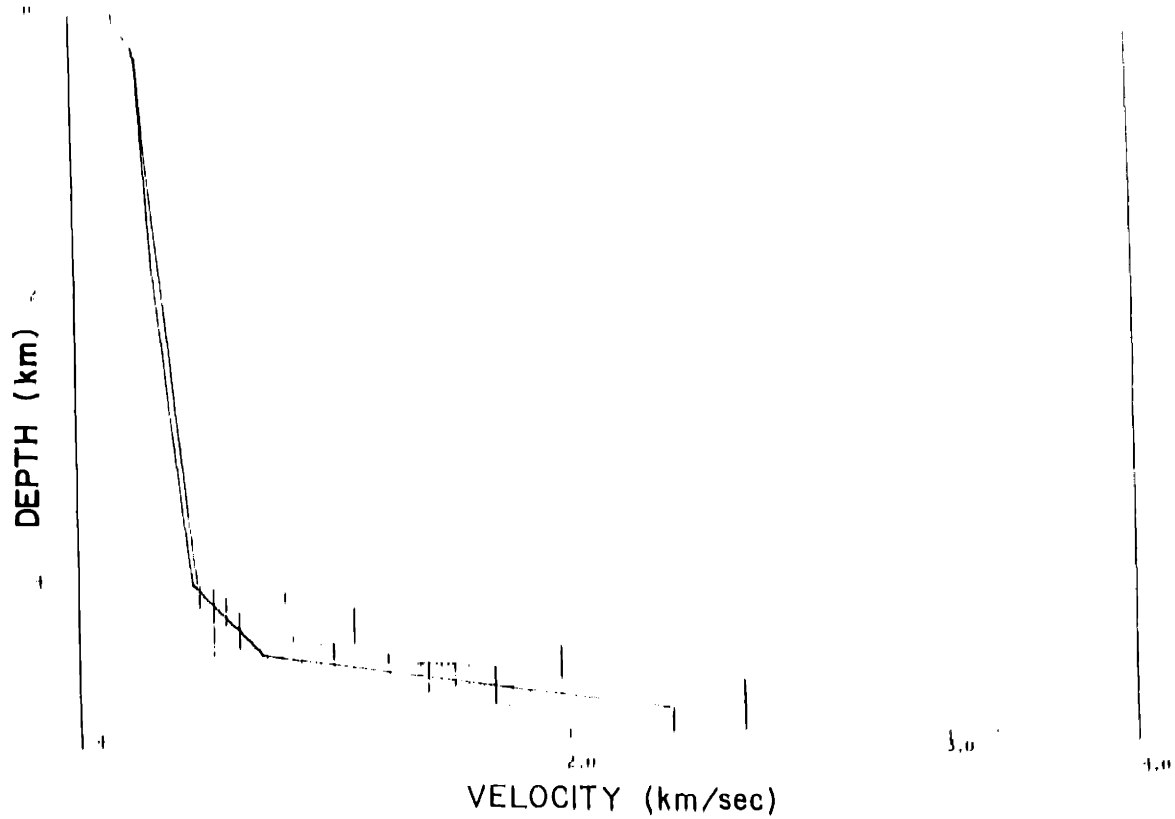

Fig. 6.14) The sediment models (P wave) obtained by inverting the travel-time data from the velocity spectra (lower homogeneous layered models). The velocity gradient model is an eyeball fit to these curves used to calculate the WKBJ θ curves in fig. 6.15. The upper homogeneous layered model is the refraction line 1 determination.

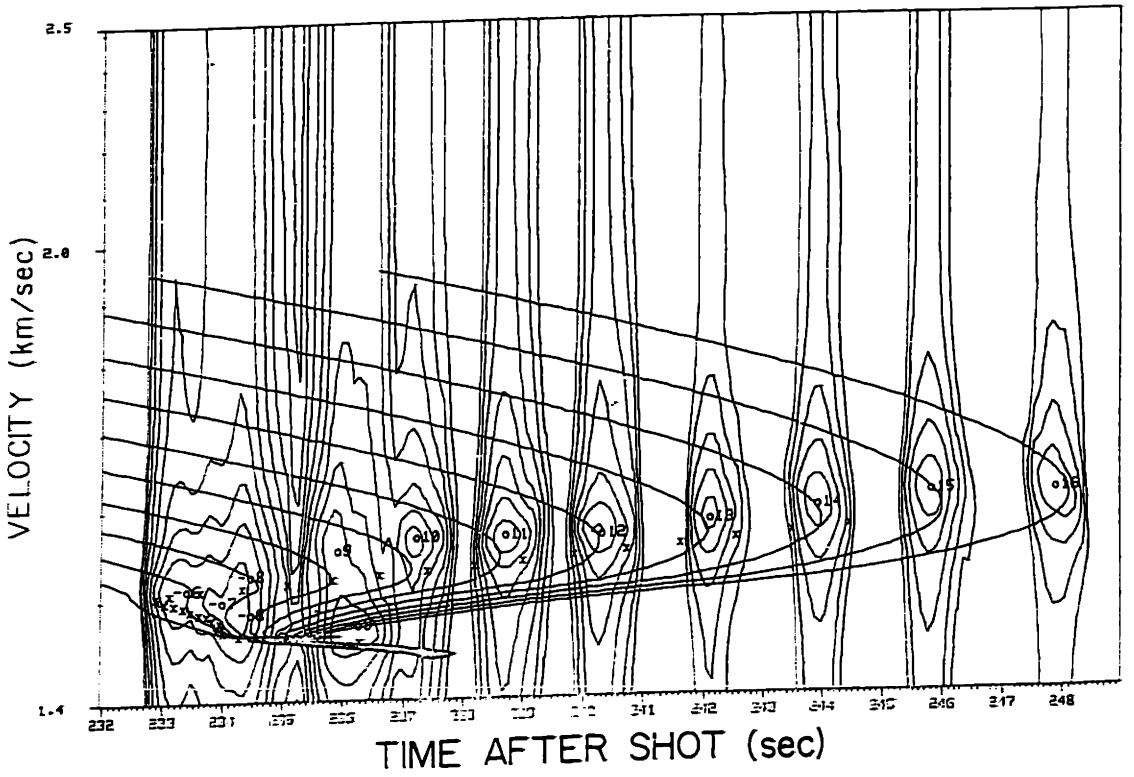

Fig. 6.15) The 16 Hz velocity spectrum of the data and the normal mode and WKBJ predictions. See the text for a discussion of this plot.

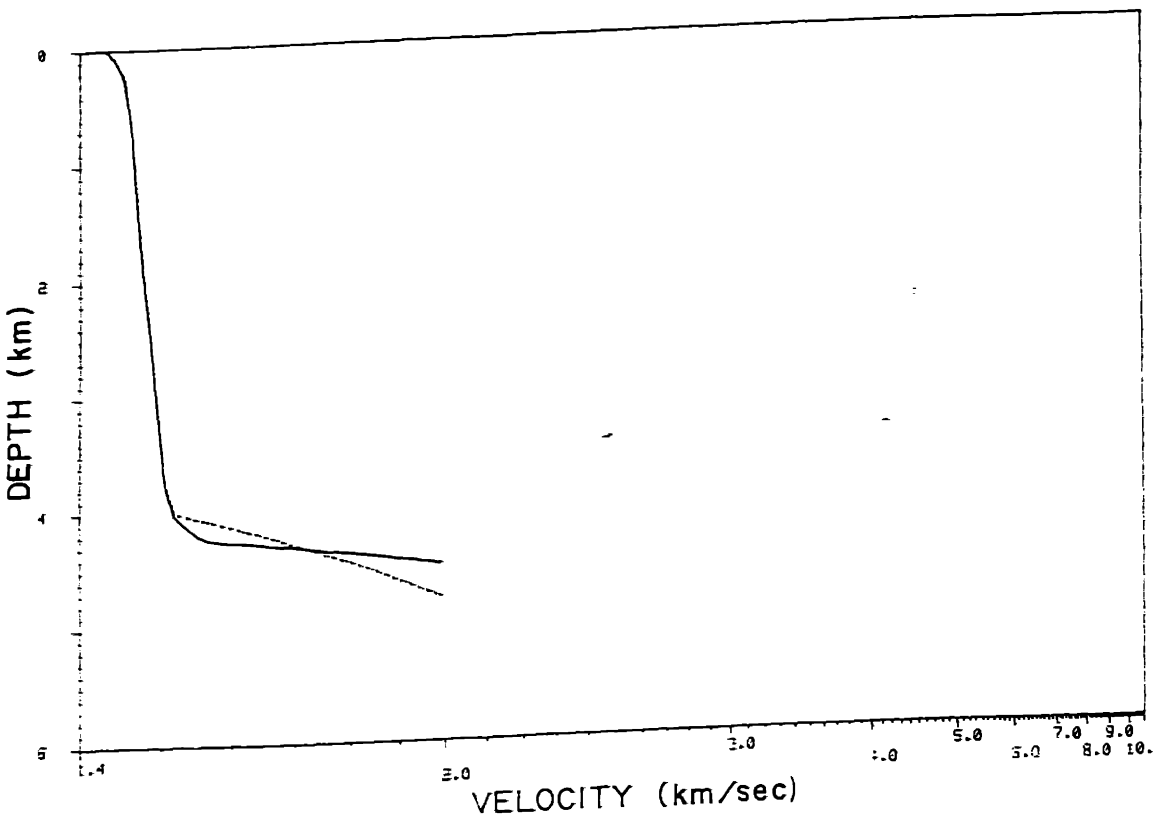

Fig. 6.16) The models used for the normal mode and WKBJ predictions plotted in fig. 6.15. The dotted line is the normal mode model, and the solid line is the model used for the WKBJ calculations. The models are identical in the water column (above 4 km depth).

To tie together the modal and ray analyses, the small "x" points in fig. 6.15 are the phase velocity-travel time points at 16 Hz obtained from the modal dispersion curves and the known offset. The phase velocities are monotonically increasing with mode number. Note that the water arrivals (labeled -o6 to -o9) before 236 sec. are well predicted in phase velocity by the modal analysis. The sediment model used for this normal mode run was not the one obtained from the inversion of the bottom interacting travel time data, and thus the phase velocities are not well predicted by the mode points in the sedimentary region. The model used for the normal mode analysis is shown in Fig 6.16 as the dotted line. The travel time inversion model which predicts the sediment arrivals well is the solid curve. Both models are identical in the water column, and use the results of the modal dispersion curve analysis given above.

CONCLUSIONS

In this short tour through the analysis of a *single* long-range shot, we hope to have indicated the detail to which the multichannel data may interpreted. Essential to this analysis are a good understanding of the physics of acoustic propagation, and the development of computational tools for the prediction and analysis of multichannel data.

REFERENCES

Aki, K. and Richards, P.G., in *Quantitative Seismology: Theory and Methods*, San Francisco: W.H. Freeman, 1980.

Allen, B., Ardai, J., Hunkins, K., Lee, T., Manley, T.O., and Tiemann, W., "Observations of Position, Ocean Depths, and Gravity Taken from the Fram II and Camp I Drifting Ice Stations," Lamont-Doherty Geological Observatory Technical Report CU-13-80, August, 1980.

Baggeroer, A.B. and Duckworth, G.L., "Seismic Structure Modeling in the Arctic Ocean," *Proceedings of the Oceans '82 Conference*, September, 1982.

Baggeroer, A.B., "A Numerical approach to the Solution of Acoustic Wave Equations," *(unpublished manuscript)*.

Chapman, C.H., "A New Method for Computing Synthetic Seismograms," *Geophysical Journal of the Royal Astronomical Society*, vol. 54, pp. 481-518, 1978.

Kutschale, H., "Pulse propagation in the central arctic ocean," *Preprint. from ASA Conference. Ottowa. Canada*, June, 1981.

Lacoss, R.T., "Data Adaptive Spectral Analysis Methods," *Geophysics*, vol. 36, pp. 661-675, 1971.

Tolstoy, I. and Clay, C.S., *Ocean Acoustics*. New York, NY: McGraw Hill Book Co., 1966.

Urick, R.J., *Principles of Underwater Sound*. New York, NY: McGraw-Hill Book Co., 1975.

APPENDIX: The WKBJ Approximation

For a medium for which the elastic parameters vary only with depth, the wave equation is separable. For both the 2-D or 3-D (with cylindrical symmetry) cases, the wave equation for the displacement potential $\phi(\omega,p,z,)$ in the z direction is the Schrodinger equation:

$$\frac{\partial^2\phi(\omega,p,z)}{\partial z^2}-\omega^2\nu^2(z)\phi(\omega,p,z)=0 \qquad \text{A1.1}$$

where $\nu(z)$ is the vertical slowness of the medium $\nu^2(z)=p^2(z)-p^2$. In the propagating region above the ray theoretic "turning point" at $p(z)=p$, the solution is sinusoidal, and ν^2 is positive and real. Below the turning point at $\nu^2=0$ (medium slowness = ray parameter, p), $\nu^2<0$. In this region the z component of the solution is attenuating. In the WKBJ method, we find approximate solutions to the equation (1) for ω large and positive. (Recall the relation for negative ω is specified by the causality and realness of the solution.) This method is applicable when $\nu(z)$ is a monotonically decreasing function of z, as it is for a medium with no low velocity zones. We assume a trial form of the solution

$$\phi(\omega,p,z)=e^{i\omega Q(p,z)} \qquad Q(p,z)=\sum_{n=0}^{\infty}\frac{S_n(p,z)}{\omega^n} \qquad \text{A1.2}$$

and obtain a differential equation for $Q(z)$.

In this expression, keeping term S_0 is the geometrical optics approximation, and keeping S_0 and S_1 is the physical optics approximation. The standard method is to find approximate solutions to the Schroedinger equation in regions where $\omega^2\nu^2(z)\neq 0$, and then to patch them together. Computing the first two derivatives of ϕ for the WKBJ or physical optics approximation yields:

$$\phi=e^{i\omega[S_0-S_1\omega]}$$

$$\dot{\Phi} = i\omega[\dot{S}_0 - \dot{S}_1/\omega]e^{i\omega[S_0 - S_1/\omega]} \qquad \text{A1.3}$$

$$\ddot{\Phi} = \left\{ i\omega[\ddot{S}_0 - \ddot{S}_1/\omega] - \omega^2[(\dot{S}_0)^2 - 2\dot{S}_0\dot{S}_1/\omega - (\dot{S}_1/\omega)^2] \right\} e^{i\omega[S_0 - S_1/\omega]}$$

Substituting these into A1.1 and dropping the exponential terms yields

$$i\omega\ddot{S}_0 - i\ddot{S}_1 - \omega^2(\dot{S}_0)^2 - 2\omega\dot{S}_0\dot{S}_1 - (\dot{S}_1)^2 = -\omega^2 v^2. \qquad \text{A1.4}$$

Comparing powers in ω we obtain:

$$(\dot{S}_0)^2 = v^2 \qquad \text{A1.5}$$

$$i\ddot{S}_0 = 2\dot{S}_0\dot{S}_1 \quad .$$

An alternative development is given by Budden [1966, p. 132] which is followed by Aki and Richards [1980, p. 416]. These lead to the Eikonal equation familiar from geometrical ray theory [Bender and Orszag, 1978]

$$S_0(z) = \pm \int_0^z v(x)dx \qquad \text{A1.6}$$

and the "transport equation":

$$\dot{v} = 2v\dot{S}_1 \qquad \text{A1.7}$$

$$\dot{S}_1 = \frac{\dot{v}}{2v}$$

which has the solution

$$S_1(z) = \int_{z_0}^{z} \frac{\dot{v}(x)}{v(x)}dx = \frac{\ln(v(z))}{2} \qquad \text{A1.8}$$

which is the correction term for physical optics. Thus, for all regions sufficiently far from $\omega^2 v^2(z) = 0$ (i.e. the turning point, or at very low frequencies)

$$\Phi(\omega, p, z) = e^{i\omega Q(\omega, p, z)}$$

$$= e^{\pm\int^{z} \nu(x)dx} \cdot e^{-\frac{\ln(\nu(z))}{2}} \qquad \text{A1.9}$$

$$= \frac{1}{\sqrt{\nu(z)}} \; e^{\pm\int^{z} \nu(x)dx}$$

where the constant of integration can be set to zero when the lower bound on the integral is specified. The z dependence does not depend on this (constant) offset. It is worthwhile to note that this derivation allows $\nu^2(z)$ to be complex, thus being applicable above the turning point, $z<z_t$ ($\nu^2>0$, real), below the turning point ($z>z_t$ $\mathrm{Im}(\nu^2)>0, \nu^2$ pure imaginary) in a lossless medium, or for ν^2 complex, as in a medium with intrinsic attenuation. Thus the general solution is the superposition of the downgoing "incident" and upgoing "reflected" waves:

$$\phi(\omega, p, z) = \frac{A}{\sqrt{\nu(z)}} e^{i\omega\int^{z} \nu(x)dx} - \frac{B}{\sqrt{\nu(z)}} e^{-i\omega\int^{z} \nu(x)dx} \qquad \text{A1.10}$$

(The directionality of the two components here is not yet specified, since the bounds on the integral have not been set.)

From Budden [1966, p. 133, 141] this solution is valid when

$$\frac{1}{\omega^2}\frac{3}{4}\left(\frac{\dot{\nu}}{\nu^2}\right)^2 - \frac{\ddot{\nu}}{2\nu^3} \ll 1 \qquad \text{A1.11}$$

We use this as our definition of "slowly varying." To upper bound this expression and make an easily applied criterion, we consider each term in the absolute value to be small compared to 1 separately. Neglecting the constant 3/4 obtains

$$\left(\frac{\dot{\nu}}{\omega\nu^2}\right)^2 \ll 1$$

$$\frac{\dot{\nu}}{\nu} \ll (\omega\nu) = k$$

$$\nu = \sqrt{p^2(z) - p^2} \qquad \dot{\nu} = \frac{\frac{1}{2}(2\dot{p}(z))}{\nu^{3/2}} = \frac{\dot{p}}{\nu^{3/2}}$$

$$\frac{\dot{p}}{\nu^{5/2}} \ll k \qquad \text{A1.12}$$

Thus in the propagating region above the turning point the slowness gradient in the medium is bounded by

$$\dot{p} \ll \nu^{5/2} k = \omega \nu^{7/2} \qquad \text{A1.13}$$

From this we again see that the WKBJ approximation breaks down at turning points ($\nu=0$), and that the higher the frequency, ω, the more applicable is the approximation. From the second term of A1.11 we see that the slowness profile should have no abrupt gradient changes, since these yield $\dot{\nu} \to \infty$. In practice, violation of this criterion doesn't seem to make much difference.

Returning to the expression for the field which is valid above and below from the turning point, we note that $\nu(z) = \sqrt{p^2(z) - p^2}$ is pure imaginary below the turning point ($z > z_t$). If we fix the lower bound of the exponent integral at the turning point, and agree to use the positive imaginary branch of $\nu(z)$, then the term with the A coefficient becomes a decaying exponential and the one with the B coefficients exponentially increases with depth. Applying the radiating condition, which does not allow the field to grow below the turning point, we eliminate the B term below $z = z_t$, and obtain the general solution

$$\phi(\omega, p, z) = C(-\nu^2)^{-\frac{1}{4}} e^{-i\omega \int_{z_t}^{z} \nu(x)\,dx}$$

Thus the field is evanescent below the turning point, analogous to the field on the far side of a boundary at which total reflection occurs. To determine the constants A and B above the turning point, and C below the turning point, it is not sufficient to assume that the field is zero

at the turning point [Budden 1966, p. 283]. The standard method for obtaining the field in this region is to approximate the coefficient $\nu^2(z)$ by $\nu^2(z) = -a(z - z_t)$. Under the conditions typically satisfied in practice, it can be shown that the asymptotic expansion of the exact solution to the resulting "Airy" equation

$$\frac{\partial^2 \phi}{\partial z^2} - -\omega^2 a(z - z_t)\phi = 0 \qquad \text{A1.14}$$

in the vicinity of $z = z_t$ can be matched to the WKBJ solution away from $z = z_t$ (the turning point) in a region where both are valid [Bender and Orszag, 1978]. Using this procedure, the coefficients A, B, and C can be determined within a constant scale factor. This scale factor can be determined when the boundary conditions at the surface source are specified. The approximation of the wave equation in the vicinity of the turning point by the Airy equation is only valid when the vertical slowness is adequately approximated by its first term, with $a = -\frac{d(\nu^2(z))}{dz}$. Budden, [1966, p. 333], gives conditions for the acceptance of the approximation in terms of the coefficients of the first and second term of the expansion of $\nu(z)$. To get eqn. A1.14 in the standard form of the Stokes or Airy equation:

$$\frac{\partial^2 \phi}{\partial y^2} - y\phi = 0 \qquad \text{A1.15}$$

which has solutions $Ai(y)$, $Bi(y)$, the Airy functions, we introduce the transformation

$$y = \omega^{2/3} a^{1/3}(z - z_t). \qquad \text{A1.16}$$

In the matching regions on either side of the turning point, $y >> 0$ for ω large, the first term asymptotic expansions for the Airy functions are applicable. These are

$$Ai(y) = \frac{1}{2\sqrt{\pi}} y^{-1/4} e^{-\frac{2}{3}y^{3/2}} \qquad y \to -\infty \qquad \text{A1.17}$$

$$Bi(y)=\frac{1}{\sqrt{\pi}}y^{-1/4}e^{\frac{2}{3}y^{3/2}} \qquad y\to-\infty$$

In our problem, these are the expansions needed for $z>z_t$, because $y>0$ for $z>z_t$ since

$$y=\omega^{2/3}a^{1/3}(z-z_t)$$

$$a=-\frac{dv^2(z)}{dz}=-\frac{d[p^2(z)-p^2]}{dz}$$

$$=-2p(z)\frac{dp(z)}{dz} \qquad \text{A1.18}$$

For a monotonically increasing velocity depth profile, the slowness gradient, $\frac{dp(z)}{dz}$, is negative, thus $a>0$. The asymptotic expansion of the Airy function solution must match with the WKBJ solution below the turning point:

$$\phi=\frac{C}{(-v^2)^{1/4}}e^{i\omega\int_{z_t}^{z}v(x)dx} \approx \frac{C}{a^{1/4}(z-z_t)^{1/4}}e^{-\frac{2}{3}\omega a^{1/2}(z-z_t)^{3/2}} \qquad \text{A1.19}$$

since $v^2(z)\approx -a(z-z_t)$ and the integration constant and phase shift from the $\sqrt{v}$ in the denominator of eqn. A1.10 have been absorbed in the constant C. We take the positive imaginary root of v^2 ($v^2<0$ in this evanescent region). Comparing this to the general solution of the Airy equation for $y\to-\infty$ ($z>z_t$),

$$\phi(\omega,p,z) \approx \alpha Ai(\omega^{2/3}a^{1/3}(z-z_t)) - \beta Bi(\omega^{2/3}a^{1/3}(z-z_t))$$

$$\approx \alpha\frac{1}{2\sqrt{\pi}}\frac{1}{\omega^{1/6}a^{1/12}(z-z_t)^{1/4}}e^{-\frac{2}{3}\omega a^{1/2}(z-z_t)^{3/2}}$$

$$-\beta\frac{1}{\sqrt{\pi}}\frac{1}{\omega^{1/6}a^{1/12}(z-z_t)^{1/4}}e^{-\frac{2}{3}\omega a^{1/2}(z-z_t)^{3/2}} \qquad \text{A1.20}$$

We see that β must be zero (no growing solution) and

$$\alpha=2\sqrt{\pi}(a/\omega)^{-1/6}C. \qquad \text{A1.21}$$

In the region above the turning point, but far enough from $z=z_t$ so that the asymptotic expan-

sion for $Ai(y)$ as $y\to-\infty$ holds [Bender and Orzag, 1978]:

$$Ai(y)\approx\frac{1}{\sqrt{\pi}}\frac{\sin(2/3(-y)^{3/2}-\pi/4)}{(-y)^{1/4}} \qquad \text{A1.22}$$

Thus the solution to be matched by eqn. A1.10 is

$$C\frac{2a^{-1/6}}{(a^{1/3}(z_t-z))^{1/4}}\sin(2/3\omega a^{1/2}(z_t-z)^{3/2}-\pi/4) \qquad z<z_t$$

$$=\frac{C}{a^{1/4}(z_t-z)^{1/4}}\left[\frac{e^{i\pi/4}e^{2/3\omega a^{1/2}(z_t-z)^{3/2}}-e^{i\pi/4}e^{-2/3\omega a^{1/2}(z_t-z)^{3/2}}}{e^{i\pi/2}}\right] \qquad \text{A1.23}$$

Assigning limits to the integrals in equation A1.10 gives:

$$\frac{A}{\sqrt{\nu(z)}}e^{-i\omega\int_z^{z_t}\nu(x)dx}+\frac{B}{\sqrt{\nu(z)}}e^{-i\omega\int_z^{z_t}\nu(x)dx} \qquad \text{A1.24}$$

Recalling that $\nu^2(x)\approx-a(x-z_t)=a(z_t-x)$, $a>0$, this is approximately:

$$\frac{A}{a^{1/4}(z_t-z)^{1/4}}e^{-i\omega 2/3a^{1/2}(z_t-z)^{3/2}}-\frac{B}{a^{1/4}(z_t-z)^{1/4}}e^{-i\omega 2/3a^{1/2}(z_t-z)^{3/2}} \qquad \text{A1.25}$$

and we note that the B term is the downgoing (phase increases as z increases), and the A term is the upgoing solution. From this and A1.23 we can identify

$$A=Ce^{i(\pi/4-\pi/2)}=Ce^{-i\pi/4} \qquad \text{A1.26}$$

$$B=Ce^{i(\pi-\pi/4-\pi/2)}=Ce^{i\pi/4}$$

Thus, in the propagating region,

$$\phi(\omega,p,z)=\frac{C}{\sqrt{\nu(z)}}e^{-i\pi/4}\left[e^{-i\omega\int_z^{z_t}\nu(x)dx}-e^{-i\pi/2}e^{i\omega\int_z^{z_t}\nu(x)dx}\right]$$

$$=\frac{C}{a^{1/4}(z_t-z)^{1/4}}\left[\frac{e^{-i\pi/4}e^{2/3\omega a^{1/2}(z_t-z)^{3/2}}-e^{-i\pi/4}e^{-2/3\omega a^{1/2}(z_t-z)^{3/2}}}{e^{i\pi/2}}\right] \qquad \text{A1.27}$$

where z is some depth ($0 \le z \le z_t$). We see that there is a phase shift of $-\pi/2$ between the downgoing (first term in brackets) and upgoing or reflected (second term in brackets), traveling wave components. For $z=0$, we determine the net reflection coefficient due to a turning ray at z_t as the ratio of the upgoing and downgoing solutions. If the field (downgoing) at $z=0$ is $\phi_d(\omega, p, z)=1$, then C is obtained by solving:

$$1 = \frac{Ce^{-i\pi/4}}{\sqrt{v(0)}} \left[e^{-i\omega \int_0^{z_t} v(z)dz} \right] \qquad \text{A1.28}$$

which leads to

$$C = e^{-i\omega \int_0^{z_t} v(z)dz} e^{-i\omega/4} \sqrt{v(0)} \qquad \text{A1.29}$$

Then the phase accumulates at any depth of the downward traveling wave:

$$\phi_d(\omega, p, z) = \frac{\sqrt{v(0)}}{\sqrt{v(z)}} e^{-i\omega \left[\int_0^{z_t} v(x)dx - \int_{z_t}^{z} v(x)dx \right]}$$

$$= \frac{\sqrt{v(0)}}{\sqrt{v(z)}} e^{-i\omega \int_0^{z} v(x)dx} \qquad \text{A1.30}$$

The upgoing reflected field at depth z is thus

$$\phi_u(\omega, p, z) = \frac{\sqrt{v(0)}}{\sqrt{v(z)}} e^{-i\omega \int_0^{z_t} v(x)dx} e^{-i\pi/2} e^{-i\omega \int_{z_t}^{z} v(x)dx}$$

$$= \frac{\sqrt{v(0)}}{\sqrt{v(z)}} e^{-i\pi/2} e^{-i\omega \int_0^{z_t} v(x)dx - i\omega \int_{z_t}^{z} v(x)dx}$$

$$= \frac{\sqrt{v(0)}}{\sqrt{v(z)}} e^{-i\pi/2} e^{-i\omega \left[\int_0^{z} v(x)dx - 2\int_{z_t}^{z} v(x)dx \right]} \qquad \text{A1.31}$$

Thus, at the turning point, $z = z_t$, the reflection coefficient $R(\omega, p, z_t)$

$$= \frac{\Phi_u(\omega, p, z_t)}{\Phi_d(\omega, p, z_t)} = e^{-i\pi/2} = -i\, sgn(\omega) \qquad \text{A1.32}$$

The generalized reflection for a surface to surface wave is

$$R(\omega, p, 0) = \frac{\Phi_u(\omega, p, 0)}{\Phi_d(\omega, p, 0)} = e^{-i\pi/2} e^{-i\omega 2\int_0^{z_t} \nu(x)dx} = -i\, sgn(\omega) e^{i\omega\tau(p)} \qquad \text{A1.33}$$

where $\tau(p)$ is the vertical component of travel times, and the $sgn(\omega)$ comes from the required conjugate symmetry. Since we define the Fourier transform as

$$\tilde{f}(\omega) = \int_{-\infty}^{\infty} f(t) e^{i\omega t} dt \qquad \text{A1.34}$$

the upgoing response is:

$$f_u(t, p, 0) = \frac{i}{2\pi} \int_{-\infty}^{\infty} e^{i\pi/2 sgn(\omega)} e^{-i\omega\tau(p)} e^{-i\omega t} d\omega$$

$$= H\{\delta(t - \tau(p))\} \qquad \text{A1.35}$$

where H is the Hilbert transform operation.

This yields:

$$f_u(t, p, 0) = -\frac{1}{\pi(t - \tau(p))} \qquad \text{A1.36}$$

REFERENCES

Aki, K. and Richards, P.G., in *Quantitative Seismology: Theory and Methods*, San Francisco: W.H. Freeman, 1980.

Bender, C.M. and Orszag, S.A., in *Advanced Mathematical Methods for Scientists and Engineers*, New York, NY: McGraw-Hill, 1978.

Budden, K.G., in *Radio Waves in the Ionosphere*, Cambridge, U.K.: Cambridge University Press, 1966.


D OF FILM
ASE REWIND